THÈSE

Intitulée

Impacts of Volatile Organic Compounds Emissions from Maritime Traffic on Air Quality in Harbour Cities of Northern France

Préparée et soutenue publiquement par

Erwan Volent

le 05 décembre 2025

Pour obtenir le grade de

DOCTEUR

En Terre, Enveloppes Fluides

DOCTORAT DE L'UNIVERSITÉ DE LILLE
DELIVRÉ PAR IMT NORD EUROPE

Membres du jury :

Charbel AFIF	*Professeur*	*Univ. Saint Joseph de Beyrouth, Liban*	**Rapporteur**
Anne MONOD	*Professeure*	*LCE, CNRS/Aix-Marseille Université*	**Rapportrice**
Valérie GROS	*DR CNRS*	*LSCE, IPSL/CNRS, Gif-sur-Yvette*	**Présidente du Jury**
Juliane FRY	*Professeure*	*Wageningen University, Pays-Bas*	**Examinatrice**
Alexandre ARMENGAUD	*Docteur*	*AtmoSud, Marseille*	**Examinateur**
Stéphane SAUVAGE	*Professeur*	*CERI EE, IMT Nord Europe*	**Directeur de thèse**
Liselotte TINEL	*Docteure*	*CERI EE, IMT Nord Europe*	**Encadrante**

Laboratoire d'accueil : CERI EE, IMT Nord Europe
Ecole doctorale SMRE 104 (ULille, UPHF, Centrale Lille, Chimie Lille, IMT Nord Europe)

Je dédie ce manuscrit à celles et ceux que j'aime sans toujours le dire, à l'amour discret qui traverse le temps, les absences et les silences.

À Nini.

« For those who come after. »
***Clair Obscur: Expedition 33*, Sandfall Interactive, 2024.**

« I learned a lot, by the end of everything. The past is the past now, but that's okay ! It's never really gone completely. The future is always built on the past, even if we don't get to see it. »
***Outer Wilds*, Mobius Digital, 2019.**

Remerciements

Nous y voilà : le manuscrit est soumis, inspecté, la défense est passée, le diplôme est (à priori) délivré. Quand je repense à ce que je m'étais dit avant mon stage de Master 2 : "jamais de thèse", c'est un résultat surprenant. C'est précisément depuis ce stage que des rencontres et des échanges enrichissants, avec des personnes aux métiers passionnants, ont jalonné mon parcours. Ils m'ont permis de prendre conscience, d'une part, de ma capacité à mener un projet concret, et d'autre part, que nos réussites ne sont jamais uniquement le fruit de performances individuelles. Sans l'accompagnement de chercheurs brillants et le soutien indéfectible de mes proches, ce manuscrit n'aurait jamais vu le jour.

Je tiens tout d'abord à saluer l'investissement du jury qui a évalué mon travail, les professeurs Anne Monod et Charbel Afif, qui ont accepté de rapporter ce manuscrit, ainsi que les examinateurs, la professeure Juliane Fry et les docteurs Alexandre Armengaud et Valérie Gros, que je remercie particulièrement pour avoir présidé ce jury. Vos retours ont grandement amélioré la qualité du manuscrit et de ma soutenance, dont les discussions qu'elle a suscitées ouvrent des perspectives prometteuses pour la caractérisation des émissions des navires.

Avant même de commencer mes recherches d'une thèse, l'on m'avait indiqué que 80% de la réussite d'un doctorat est provoquée par la qualité de l'encadrement : c'est vrai. De mon expérience, il est difficile d'estimer les atomes crochus lors d'un entretien. En revanche, après trois ans, je mesure la chance que j'ai eue d'être encadré par deux chercheurs incroyables et inspirants, à qui je dois beaucoup de ce que je suis aujourd'hui. Merci infiniment Stéphane, pour m'avoir accordé ta confiance tôt et d'avoir vu en moi le meilleur que je ne pensais jamais voir. Tu es de ceux qui donnent envie d'apprendre ! Merci, Liselotte, pour ton soutien inconditionnel, à tout moment et en toute situation. Nos rendez-vous hebdomadaires vont me manquer, car ta bienveillance et ton humanité ont toujours fait de mon travail un vrai plaisir, menant à des discussions qui, parfois, en voiture, nous ont emmenés plus loin que notre destination. Je vous remercie tous les deux pour les opportunités que vous m'avez offertes pendant ces trois ans, et pour m'avoir permis de prendre conscience de ce qu'il y a de mieux en moi.

Je tiens à remercier les collaborateurs du projet pour leur investissement sans faille, notamment Quentin et Barbara du LCE, qui ont participé à la rédaction de l'article. Plus largement, j'exprime ma gratitude envers toutes les personnes avec qui j'ai eu l'occasion de collaborer et d'échanger dans le cadre des projets PIRATE (ADEME), SHIPAIR (ANR) et Labex CaPPA.

Il est difficile d'arriver à Douai uniquement à dos de Citroën Saxo (bic !). À chaque déplacement, ma famille a toujours répondu présente. Je leur dois ma mobilité, mon désir d'apprendre et de comprendre ce qui m'entoure, ainsi que l'élan qui m'a permis de m'engager et de persévérer. Chaque appel hebdomadaire a constitué, durant ces trois années, une véritable bouffée d'air, me rappelant pour qui et pour quoi je me suis engagé, depuis plus ou moins longtemps, sur les questions de l'environnement, de l'air et de la santé. Je dédie à ma mère, à mon père et à mon frère la motivation qui m'a permis de travailler et de mener ce manuscrit à son aboutissement.

Parfois, le soutien de nos proches est précieux, même s'il est à distance. C'est le cas de Benoit, Mattis et Florian, mes amis de toujours de Couëron, qui prouvent une fois de plus que l'amitié profonde résiste à la distance et au temps. Vous avez toujours été présents dès que j'en avais besoin, lors de mes retours ponctuels dans la région nantaise. Merci pour votre soutien, qui était inconscient mais nécessaire, et je vous souhaite à tous le meilleur. Dans un autre registre, mais avec une importance tout aussi réelle, je tiens également à remercier Pierrot et Lewis. Votre présence régulière, notamment sur Discord, a constitué un espace précieux pour me vider la tête, prendre du recul et souffler lorsque le travail se faisait plus dense. Je remercie plus largement l'équipe de l'étang de Romo pour ce rendez-vous annuel devenu incontournable. Merci pour ces parenthèses hors du temps, propices au ressourcement. Elles rappellent, année après année, l'importance de ces espaces communs qui nourrissent l'esprit et les liens humains.

Merci Colwyn et Perrine, mes Dunkerquois préférés, pour m'avoir fait découvrir votre incroyable carnaval, mais surtout pour votre gentillesse et votre accueil inconditionnel. Je me rends compte de la chance que j'ai de vous compter parmi mes proches et je vous adresse tous mes vœux de bonheur pour vos fiançailles. Merci à Lola, Yoan et Elisa, dont la bonne humeur me manque souvent, et que j'ai toujours hâte de retrouver dès que je sais que nos chemins vont à nouveau se croiser.

Après ces trois années, je tiens à remercier chaleureusement toutes les personnes du CERI EE qui ont contribué à rendre mon passage inoubliable. Je tiens tout particulièrement à remercier Marvin, qui a partagé mon bureau pendant tout ce temps. Sans toi, ce manuscrit n'aurait pas du tout la même tête. C'est grâce à ta capacité précieuse à transmettre tes connaissances que j'ai pu en arriver là. Je te remercie également pour ta présence et pour cet espace propice au travail et à la rigolade que tu as contribué à créer. Je te souhaite une belle réussite, largement méritée, dans tes futurs projets. J'adresse une pensée émue à Bérénice, que j'ai eu le plaisir de retrouver à Douai après nous être croisés à Lyon. Merci pour le rayon de soleil que ta présence a apporté à toute l'équipe et pour ton énergie contagieuse. Je te souhaite de finir ta thèse aussi brillamment que tu l'as menée jusqu'à présent.

Let me thank Olatunde, my "thesis cousin". I am deeply grateful for your presence, your constant encouragement, and your strong friendship. Thank you for standing by my side during conferences, and for the memorable moments we shared discovering Vienna and Budapest together. I wish you a good luck for your own defense !

Je salue également les amitiés qui se sont créées au sein de l'IMT Nord-Europe, notamment avec Marcela, la personne que j'ai rencontrée de manière la plus inattendue. Merci d'avoir rendu certains moments de ma vie à Douai un peu moins moroses. J'espère te revoir très vite au Hellfest ! D'une manière générale, je suis reconnaissant envers tout le personnel de l'IMT Nord-Europe. Certains sont devenus des amis et, même si j'en oublierai sûrement, je remercie Antoine, Vincent, Adrien, Trinh, Thomas F. et Thomas A., Florent, Clara, Marius, Zahra, Félix, Ezgi, Lakhdar, Théo, Alexis, Mathilde et Audrey. Clin d'œil spécial au groupe de jeu de rôle mené par le meilleur maître du jeu : Loïc. Bonne continuation à tous !

Pour finir, je tiens à remercier toutes les personnes qui m'ont permis de vivre des expériences inoubliables dans le cadre de ma thèse, notamment en formation. Je remercie Didier Voisin de l'IGE de m'avoir permis de participer à l'édition 2023 d'ERCA à Grenoble, où des amitiés se sont forgées autour d'expériences uniques, comme l'observation des astres à partir des télescopes de l'Observatoire de Haute-Provence. Merci à tous les doctorants qui ont participé à ERCA cette année-là. Je tiens également à remercier sincèrement Géraldine Besson et Frédéric Luginsland, pour leur accompagnement tout au long de la formation "Ma thèse en 180 secondes", grâce à qui j'ai eu la chance d'atteindre la finale régionale et de créer des souvenirs qui me resteront à vie. Je vous remercie de m'avoir transmis le goût de la vulgarisation et de la médiation, ainsi que votre volonté de rendre la science accessible à tous.

J'achève mes remerciements en les dédiant à Anaïs, qui illumine ma vie depuis bientôt un an et y occupe une place essentielle. Tu es la preuve que le bonheur peut surgir là où l'on ne l'attend pas, parfois simplement dans le bâtiment d'à côté. Merci pour ton soutien précieux durant les derniers mois de cette thèse, pour ta patience et la douceur que tu as su insuffler à mon quotidien. J'espère continuer à avancer avec toi, porté par ce petit nuage que nous partageons.

Contents

General Introduction **1**

1 State of the art: shipping as a source of interest for Volatile Organic Compounds **5**
1.1 Volatile Organic Compounds: sources, chemistry and fate 5
1.1.a Definition of Volatile Organic Compounds 5
1.1.b Primary sources of VOCs 7
1.1.c Generalities on chemistry of VOCs in the atmosphere 9
1.1.d Formation of secondary pollutants 14
1.1.e Elements of transport of VOC 17
1.1.f Impacts of VOCs 18
1.2 Shipping as a source of VOCs 21
1.2.a Ship traffic trends, impacts and regulations 21
1.2.b Volatile Organic Compounds emissions by ships 24
1.3 State-of-the-art of VOCs in Dunkirk 28
1.3.a Overview 28
1.3.b Sources of VOCs identified in Dunkirk 28
1.3.c Regional emission inventories : focus on VOC speciation of shipping 29
1.4 Scientific questions 32

2 Sites, instrumentation and methods of analysis in the study area **33**
2.1 Site location and instrumentation 33
2.1.a Overview 33
2.1.b Instrumentation 34
2.2 VOC measurements 39

2.2.a TD-GC-FID . . . 39
2.2.b PTR-ToF-MS . . . 42
2.3 Description of the dataset . . . 50
2.3.a Data validation . . . 50
2.3.b Statistics and trends . . . 60
2.3.c Comparison to other study . . . 67
2.4 Combined approaches of data analysis . . . 68
2.4.a Wind Analysis . . . 68
2.4.b Source apportionment . . . 71
2.4.c Application in the study and strategy . . . 78
2.5 Conclusion . . . 80

3 Ship Emission Factors for Volatile Organic Compounds and PM_1 from land-based observations in an Emission Control Area of France 81
3.1 Introduction . . . 84
3.2 Methodology . . . 87
3.2.a Site description and meteorology . . . 87
3.2.b VOC measurements . . . 89
3.2.c Measurements of sub-micronic aerosol composition . . . 89
3.2.d Regulated pollutants . . . 90
3.2.e Ship plume identification . . . 90
3.2.f Emission Factors . . . 91
3.3 Results and discussions . . . 92
3.3.a Identification of a ship tracer . . . 92
3.3.b Background influence on Emission Factors . . . 93
3.3.c Emission Factors of the ferries . . . 95
3.3.d Variability of EFs . . . 102
3.4 Conclusion . . . 107

4 Characterisation of the shipping source from near field-measurements using Positive Matrix Factorisation in an industrial area 109
4.1 Prior knowledge on the VOC sources in Dunkirk . . . 110
4.2 Native PMF of TD-GC-FID . . . 112
4.2.a Solutions . . . 112
4.2.b Interpretation . . . 113
4.2.c Limitations . . . 118
4.3 Native PMF of PTR-ToF-MS . . . 119
4.3.a Solutions . . . 119
4.3.b Interpretation . . . 120
4.3.c Partial conclusion . . . 127
4.4 Application of MTR-PMF with PTR-ToF-MS and TD-GC-FID . . . 128
4.4.a Solutions . . . 129
4.4.b Interpretation . . . 131

4.4.c Isolating a shipping profile . . . 135
4.4.d Constrained MTR-PMF . . . 137
4.5 Implications for the identification of ship emissions from TD-GC-FID observations. . 143
4.6 Indications on air quality impacts . . . 149
4.6.a Ozone formation . . . 149
4.6.b SOA formation . . . 152
4.7 Conclusion . . . 155

5 Cross-validation of the Volatile Organic Compounds emitted by ships in the harbour of Le Havre 157
5.1 Context of Le Havre . . . 157
5.2 Site description and instrumentation . . . 158
5.2.a Overview . . . 158
5.2.b VOC measurements in Le Havre . . . 165
5.3 Indications on a shipping profile in Le Havre . . . 177
5.3.a Stabilizing a PMF solution . . . 177
5.3.b Overview of the factors . . . 177
5.4 Conclusion . . . 182

General Conclusion 183

Bibliography 189

Appendices 217

A Additional Tables of Chapter 2 217

B Supplementary Information of Chapter 3 225
B.1 Transmission coefficient of the flow tube for correcting the HR-ToF-AMS measurements 226
B.2 m/z 69 parent ion identification . . . 226
B.3 Additional tables . . . 227
B.4 Additional figures . . . 231

C PMF solution fraction time series of Chapter 4 239

D Appendices of Chapter 5 243
D.1 Deliverable report of the PIRATE Project by Atmo Normandie . . . 243

Scientific Valorisation 253

List of Figures

1-1 Evolution of NMVOC in France depending on the sector, adapted from CITEPA (2022a) . . . 9
1-2 General mechanism of oxidation of VOCs (Atkinson, 2000). . . . 11
1-3 Vertical distribution of O_3. Adapted from King et al. (2010). . . . 12
1-4 From Cooper et al. (2014): Surface ozone time series at several rural sites around the world. Trend lines are fit through the yearly average ozone values using the linear least-square regression method. Trend lines in Europe only extend through 2000 when the positive trend appears to have ended. This figure is modified from the original that appeared in IPCC (2013). . . . 13
1-5 Initialisation reaction of ozonolysis and Criegee intermediates formation (Johnson and Marston, 2008) . . . 13
1-6 Photostationary state of O_3, NO_2 and NO (left) and VOC-disturbed equilibrium (right) (Atkinson, 2000). . . . 15
1-7 Isopleth and O_3 formation regimes (Dodge, 1976). . . . 16
1-8 Saturation pressure of VOCs depending on their number of carbons, adjusted from Goldstein and Galbally (2007). . . . 16
1-9 Mixing height variation during the night (a) and during the day (b) (Seinfeld and Pandis, 2016). . . . 17
1-10 Sea breeze and land breeze. . . . 18
1-11 Evolution of the quantity of unloaded goods since 1970. Data were extracted from the United Nations Conference on Trade and Development data hub (UNCTAD, 2021). 21
1-12 Speciated VOC profiles reported by studies. *OGV; Ocean-Going Vessels, ($^{\square}$) Off-line GC/MS analysis from canisters, ($^{\triangle}$) On-line GC measurements, ($^{\oplus}$) On-line GC-MS measurements. . . . 25

1-13 VOC profile from observations of ships at berth in the Jingtang Port (Xiao et al., 2018). 26
1-14 From Timonen et al. (2022): VOC EFs reported in the SCIPPER C2 campaign according to the load, the fuel used and the additional of urea (+, on, -, off). 27
1-15 Stages of ship journey in harbours taken into consideration for the regional emission inventories, adapted from the LCSQA (2018) guide. 30
1-16 Evolution of total NMVOC EF for the datebase of EMEP and CITEPA via OMINEA. 31
1-17 Pie chart of the sectors contributing to NMVOC emissions in the Urban Community of Dunkirk in 2021, adapted from the TrACE website https://www.trace-hdf.fr/air. The remaining 0.2% are the contribution of tertiary activities on NMVOC emissions. 31
1-18 Evolution of the VOC emissions by sector of activity in the Urban Community of Dunkirk from 2008 to 2021. Green: Agriculture; orange: non-road transport; light blue: Energy; Dark blue: Industrial; Yellow: Residential; red: Road transport.From https://www.trace-hdf.fr/air 32

2-1 (a) Location of Dunkirk in France and site location in the Dunkirk agglomeration; (b) Zoom-in of the western terminal and the ferries' docking trajectories; (c) View of the measurement site; (d) Aerial view of the site showing the docking location of the Dunkirk-Dover ferries. 36
2-2 Location of the measurement site in the western terminal in Dunkirk, in perspective of the environmentally classified industries of the agglomeration. Spatialised data were taken from the Dunkirk agglomeration data hub (https://data.dunkerque-agglo.fr/explore). Total Flandres is not a classified infrastructure but was added for comprehensiveness. 37
2-3 The three ferries (passenger/RoRo ships) operated by DFDS in the Dunkirk to Dover ferry line. Pictures were taken from Vessel Finder (https://www.vesselfinder.com). . 38
2-4 Details on the instruments deployed on site and partners operating them. 38
2-5 Evolution of the temperature in the oven of the AirmoVOC. 40
2-6 Calibrations of the two GC during the Dunkirk 2022 campaign. 41
2-7 PTR-ToF-MS. Water is drawn into the cathode to produce H_3O^+, then meets an ambient air flow in the drift tube where trace gases are ionised. 43
2-8 From Gueneron et al. (2015): proton affinity of VOCs found in urban air: alkenes (red circles), aromatics (blue diamonds), alkanes (black squares), OVOCs (black stars), cycloalkanes reported in vehicular exhaust (white squares) and biogenic VOCs (green triangles). The proton affinity of water and the water dimer (first water cluster) are represented in the dashed lines, 691 kJ·mol^{-1} and 808 kJ·mol^{-1} respectively. 44
2-9 Illustration of the measurement cycles during PTR-ToF-MS operation in the Dunkirk campaign. 47
2-10 Transmission for calibrated m/z for each calibration (symbols) and interpolated transmission for other masses (lines). 48
2-11 Mass calibration on PTRMS Viewer 3. 50
2-12 Average contribution of each uncertainty component relative to the summed contributions for the whole campaign. 54

2-13 Zoom in on the time series of ambient signal of m/z 79.054 ($C_6H_6{\cdot}H^+$) during the VOC measurement cycles (red) and blank cycles (green). 55
2-14 Comparison of GC measurements of aromatics with those of PTR, expressed in $\mu g{\cdot}m^{-3}$. 59
2-15 Time series of the sum of VOC concentrations measured with the TD-GC-FID during the whole campaign, colour-coded with the wind direction. 63
2-16 Complete time series of the concentrations of $CH_3OH{\cdot}H^+$ (methanol) measured by the PTR-ToF-MS. 66
2-17 Zoom-in of the sum of concentrations time series of VOCs measured by PTR-ToF-MS within the favourable wind period. The blue shaded areas correspond to a ferry presence in the Dunkirk – Dover dock. 66
2-18 Complete time series of the concentrations of VOCs measured by PTR-ToF-MS, colour-coded with the wind direction. 67
2-19 Wind rose observed during the campaign. 69
2-20 NWR plot of toluene during the whole campaign. 70
2-21 Various approaches to determine sources contribution depending on the prior knowledge required on the sources. p denotes the number of species in the model, k denotes the number of factors, x_t denotes the observational matrix, Λ denotes the profile matrix, f_t denotes the factor contribution matrix and e_t denotes the residual matrix (Schauer et al., 2006). 73
2-22 Illustration of the matrices mentioned in the PMF Equation 2.66. 74
2-23 Principle of the MTR-PMF if a 1 min dataset is used as reference, associated with a lower time-resolution dataset with a 1 h timestamp. 78

3-1 (a) Dunkirk location in the north of France. (b) Site location in the western harbour of Dunkirk. (c) Site location (red dot) with respect to ferries, arrival trajectory (red arrows), ferry (green full line) and RoRo (pink full line) docking locations. (d) Distance between the site (red dot) and the ferry dock (picture taken from DUNKERQUE PORT http://www.dunkerque-port.fr/en/). 88
3-2 Wind rose of the whole campaign. The contributions of western and south-eastern wind direction highlight the sea and land breezes impacting the site. 88
3-3 Concentrations of SO_2 (pink), CO_2 (blue), NO_2 (red) and $PM_{2.5}$ (green) observed on the 16 of September 2022, under favourable wind for sampling ferry emissions. The blue shaded areas indicate the presence of a ship at berth, according to the ferries time schedule. 93
3-4 EFs of the gas phase components: (top-left) NO_x, (top-right) CH_4, CO and SO_2 (all in $g{\cdot}kg^{-1}_{fuel}$) and (bottom) the 20 highest EFs for VOCs (in mg/kg_{fuel}). 97
3-5 EFs of the components of the particulate phase: (a) mass concentrations determined by FIDAS (pink, left Y axis) and by SMPS (green, right Y axis), (b) number concentrations measured by FIDAS (pink, left Y axis) and SMPS (green, right Y axis), (c) organic (red, left Y axis) and inorganic (brown, right Y axis) mass concentrations determined by AMS and (d) black carbon measured by the aethalometer. 98
3-6 Comparison of VOC EFs from Dunkirk (blue) with those obtained from stack measurements in the Baltic Sea by Timonen et al. (2022) (orange). 102

3-7 Comparisons of EFs for the gas phase components, including inorganic pollutants (SO_2, CO, NO_2, NO) and the 6 largest VOC EFs for the different ferries: ferry A (red), B (green) and C (blue). . . . 103
3-8 Comparisons of EFs for PM variables for the different ferries: ferry A (red), B (green) and C (blue). . . . 103
3-9 Comparisons of EFs for the gas phase components, including inorganic pollutants (SO_2, CO, NO_2, NO) and a selection of 6 VOCs, according to the directions of travel of the ships, arrivals (red), departures (blue). The VOCs selected show the highest difference between arrival and departure according to the two samples t-test. . . . 105
3-10 Comparison of EFs for PM variables between the directions of travel of the ships: arrivals (red), departures (blue) . . . 105
3-11 Comparisons of EFs for a selection of 6 VOC, BC and PM_{SMPS}, and the three ferries (A, B and C), according to the direction of travel, arrivals (red), departure (blue), and identification of the ferry (A, B and C). . . . 106

4-1 NWR plots of a selection of VOC over the whole campaign. . . . 111
4-2 Evolution of the correlation coefficient between observed and modelled concentration depending on the number of factors for the GC-only PMF solutions. . . . 112
4-3 Pie chart of average contribution of the PMF factors in the GC-PMF 5-factor solution. 112
4-4 Contribution time series and chemical profiles of the 5-factor solution of the GC-PMF. 113
4-5 Identification of 'background' Factor 2 in the 5-factor solution of the GC-PMF. . . . 114
4-6 NWR of 'hydrocarbon industry' Factor 1 of the 5-factor solution from the TD-GC-FID PMF. . . . 115
4-7 Identification of 'toluene' Factor 3 in the 5-factor solution of the GC-PMF. . . . 116
4-8 Identification of 'combustion' Factor 4 in the 5-factor solution of the GC-PMF. . . . 116
4-9 Identification of 'evaporation' Factor 5 in the 5-factor solution of the GC-PMF. . . . 117
4-10 Evolution of the correlation coefficient between observed and modelled concentration depending on the number of factors for the PTR-only PMF solutions. . . . 119
4-11 Pie chart of average contribution of the PMF factors in the 7-factor solution. . . . 119
4-12 Correlation between the observed and modelled concentration for the 6- and 7-factor solutions. . . . 120
4-13 (a) Time series and (b) chemical Profiles of the 7-factor solution of the PMF on the PTR-ToF-MS data. The bar plot in (b) corresponds to the contribution of the variable to the profile (left axis), the dotted plot corresponds to the contribution of the factor to the observed mass of each variable (right axis). . . . 121
4-14 NWR of 'background' Factor 2 the 7-factors solution from the PTR-ToF-MS PMF . 122
4-15 NWR of the 'methanol' Factor 6 of the 7-factors solution from the PTR-ToF-MS PMF. . . . 122
4-16 (a) NWR of 'traffic' Factor 4 in the 7-factors solutions of PMF of PTR-ToF-MS; (b) Correlation between NO_x and Factor 4 in the 100 – 135° wind directions; (c) Correlation between BC and Factor 4 in the 100 – 135° wind directions. . . . 123
4-17 NWR of 'aromatics' Factor 3 in the 7-factors solutions of PMF of PTR-ToF-MS. . . . 124

4-18 (a) Time series of 'shipping' Factor 7 and SO_2 on the 16th of September, the blue shaded areas indicate the presence of a ship in the dock; (b) scatter plot of Factor 7 and SO_2 from 16th at midnight to 20th at 8 am; (c) NWR of Factor 7; (d) scatter plot of Factor 7 and CO from 16th at midnight to 20th at 8 am 125

4-19 Comparison of the top 30 contributors to Factor 7 'shipping' from the PMF with those determined in Chapter 3 for the ship Emission Factors. Major contributors to Factor 7 are shown as blue bar plot, left Y-axis,; the box plots, right Y-axis, shows the EFs calculated in Chapter 3. 126

4-20 Time series: (blue) Factor 7 'shipping': (red) Factor 5 'shipping OVOC'. 127

4-21 NWR of Factor 5 'shipping OVOCs'. 127

4-22 Evolution of the correlation coefficient between observed and modelled concentration depending on the number of factors for the MTR-PMF. 129

4-23 Pie chart of average relative contributions of the MTR-PMF factors in the 5-factor solution. 129

4-24 (a) Time series and chemical profiles for the PTR (b) and GC (c) of the 5-factor solution MTR-PMF. The bar plots in (b and c) correspond to the contribution of the variable to the profile (left axis), the dotted plot corresponds to the contribution of the factor to the observed mass of each variable (right axis) 130

4-25 NWR of 'methanol' Factor 5. 131

4-26 NWR of 'background' Factor 1. 131

4-27 NWR of Factor 4 'traffic exhaust'. 132

4-28 XY plot of Factor 3 'aromatic' with Factor 4 'traffic exhaust'. 133

4-29 NWR of Factor 3 'aromatics'. 133

4-30 Identification of 'shipping' Factor 2 in the MTR-PMF; (a) Time series of Factor 2 and SO_2 on the $17^{th}$of September, the blue shaded areas indicate the presence of a ship in the dock; (b) scatter plot of Factor 2 and SO_2 from 16th at midnight to 20th at 8 am; (c) Contribution of Factor 2 to the modelled concentrations color-coded for the wind direction; (d) NWR of Factor 2. 134

4-31 Comparison of the top 30 contributors to 'shipping' Factor 3 from the MTR-PMF with the Emission Factors determined in Chapter 3. Major contributors to Factor 2 'shipping' of the MTR-PMF profile are shown as a blue bar plot (left Y-axis); the box plots, right Y-axis, represent the associated EF calculated in Chapter 3. 135

4-32 Zoom-in on the time series of the 5-factors solution of the MTR-PMF. 136

4-33 Time series and profiles of the 2-factors solution of the wind-constrained MTR-PMF. The bar plot of the profiles corresponds to the contribution of the variable to the profile (left axis), the dotted plot corresponds to the contribution of the factor to the observed mass of each variable (right axis). 139

4-34 Time series and profiles of the 5-factors solution of the fully constrained MTR-PMF (a-value = 0). The bar plot of the profiles corresponds to the contribution of the variable to the profile (left axis), the dotted plot corresponds to the contribution of the factor to the observed mass of each variable (right axis). 140

4-35 Evolution of the correlation coefficient between observed and modelled concentrations for two a-values of the constrained 'shipping' Factor 1; (a) a-value = 0.9; (b) a-value = 0. 141
4-36 Evolution of the relative contributions of each modelled ship peak of Factor 1 to the total modelled concentrations during ship emissions. The full line in each box in the median, the bottom and top edges of each box are 1st and 3rd quartiles respectively, the bottom and top whiskers are the 10th and 90th percentiles respectively. Triangle/lines indicate the average contribution for each a-value. 141
4-37 Pie chart of average contribution of the constrained MTR-PMF factors in the 5-factor solution. 142
4-38 Comparison of the top 30 contributors to the ship emissions profile on the fully constrained MTR-PMF with the Emission Factors determined in Chapter 3. (left axis, blue bar plot) Major contributor to the Factor 1 ship emissions MTR-PMF profile; (box plots, right axis) associated EF calculated in Chapter 3. 142
4-39 Comparison between the PTR time series of Factor 1 and the GC time series of 'shipping' Factor 1 in the constrained MTR-PMF. 143
4-40 Comparison between the GC time series of 'shipping' Factor 1 in the MTR-PMF and the total concentration of VOCs observed by the TD-GC-FID. 143
4-41 Time series and profiles of the 2-factors solution of the wind-constrained GC-PMF. The bar plot of the profiles corresponds to the contribution of the variable to the profile (left axis), the dotted plot corresponds to the contribution of the factor to the observed mass of each variable (right axis). 145
4-42 Comparison of the GC 'shipping' profile obtained in the wind-constrained MTR-PMF (blue) versus the GC 'shipping' profile obtained in the wind-constrained GC-PMF (orange). 146
4-43 Correlation between the relative contributions (%) of each species to the GC profile of the constrained MTR-PMF (x-axis) and the GC profile of wind-constrained GC-PMF (y-axis), for the calculation of the Pearson Distance (PD). The colorbar refers to the compound number and give an indication on the mass. 146
4-44 Time series and profiles of the 4-factor solution of the GC-PMF. The bar plot of the profiles corresponds to the contribution of the variable to the profile (left axis), the dotted plot corresponds to the contribution of the factor to the observed mass of each variable (right axis). 147
4-45 Comparison of the GC profile obtained in the 'shipping' factor of constrained MTR-PMF (blue) versus the GC profile obtained in the standard GC-PMF (orange) . . . 148
4-46 Temporal evolution of the relative contribution of each factor to the total OFP. . . . 151
4-47 Blue, left axis: VOC contribution to Factor 1; Red crosses, right axis: VOC contribution to the OFP of 'shipping' Factor 1. 152
4-48 Temporal evolution of the relative contribution of each factor to the total SOAP. . . 154
4-49 Blue, left axis: VOC contribution to the 'shipping' Factor 1; Red crosses, right axis: VOC contribution to the SOAP of Factor 1. For SOAPs = 0, no symbol is used fo clarity. Only the top 40 contributors to the ship emission profile are represented. . . 154

5-1 Location of the measurement site at the "Écluse François 1er" in Le Havre. (a) Location of Le Havre in France; (b) Location of the lock in Le Havre; (c) Location of the measurement site next to the terminal and the industrial zone; (d) View on the lock and the bridge used to cross it. 160

5-2 Location of the site in the harbour of Le Havre, in perspective of environmentally classified industries of the industrial park. Spatialized data were taken from the GéoRisques French state data hub. An important number of storage facility of unspecified various materials are present therefore not documented in this map. . . . 161

5-3 Wind rose of the 2023 campaign of Le Havre. 162

5-4 Time series of criteria pollutants; violet: SO_2 (ppb); blue: CO (ppm); red: NO (ppb); green : NO_2 (ppb); olive: PN (particles·cm^{-3}, CPC). 164

5-5 Diurnal cycles related to NO_x, local time. Full lines: hourly medians; shaded area: hourly Inter-Quartile Range (IQR), 25th -the 75th percentiles. 165

5-6 Various views of the measurement site of the 2023 campaign in Le Havre. 165

5-7 Calibration factors of the two TD-GC-FID during the 2023 campaign of Le Havre. . 167

5-8 Top 20 most abundant VOCs based on their average in each campaign, respectively (a) Le Havre (without benzene) and (b) Dunkirk, selected for the common species with Le Havre. Error bars: the standard deviation throughout the campaigns. 170

5-9 Sum of the VOC concentrations from the TD-GC-FID observed in the 2023 campaign of Le Havre, color coded for wind direction. Black lines represent an absence of wind data. 171

5-10 Diurnal cycles of (a) summed concentration of the VOCs deducted from benzene, (b) Boundary Layer Height during the 2023 campaign of Le Havre, local time. Full lines: hourly medians; shaded area: hourly Inter-Quartile Range (IQR), 25th -the 75th percentiles. 172

5-11 Diurnal cycles of 2-methylpentane (a) and n-hexane (b) during the 2023 campaign of Le Havre, local time. Full lines: hourly medians; shaded area: hourly Inter-Quartile Range (IQR) (25th – 75th percentile) 172

5-12 Near Wind Regression (NWR) plots of 2-methylpentane (a) and n-hexane (b). . . . 173

5-13 Co-variability of 2-methylpentane (blue, left axis) with n-hexane (orange, right axis). 173

5-14 Diurnal cycles of butane (a) and propane (b) during the 2023 campaign of Le Havre, local time. Full lines: hourly medians; shaded area: hourly Inter-Quartile Range (IQR) (25th -75th percentile) 174

5-15 Near Wind Regression (NWR) plots of n-butane (a) and n-propane (b). 174

5-16 Time series of n-propane, butane, pentane and hexane. 175

5-17 Near Wind Regression (NWR) plots of the sum of VOCs. 175

5-18 Time series of benzene (blue, left axis); and n-heptane (orange, right axis). 176

5-19 Time series and profiles of the 7-factor solution. (a) Time series (µg·m^{-3}) of each factor and chemical profiles of (b) Factors 1, 2, 3, 4 and (c) Factors 5, 6, 7 . Left axis (blue): contributions to the profile (µg·m^{-3}); right axis (red): contributions to the variable (%). Absence of black cross means that the factor contribution is 0. . . 179

5-20 Time series (µg·m^{-3}). (blue): Factor 5 in the 7-factor solutions of Le Havre; (red): SO_2. 180

5-21 Comparison of the GC profiles. (blue, left axis): GC profile of Factor 5 in the 7-factor solutions of Le Havre; (red, right axis): GC profile in the 'shipping' factor of the fully constrained MTR-PMF in Dunkirk (2022). 181

BF1 Meteorological conditions recorded at the sampling site in Dunkirk. temperature (purple, in °C), pressure (green, in mbar), wind direction (blue, in °), wind speed (red, m·s^{-1}) 231

BF2 Transmission curves for the PTR-ToF-MS determined for each calibration of the campaign. 231

BF3 Setup of the Aerosol Flow Tube (AFT). 232

BF4 Flow tube transmission determined in laboratory experiment. A nebulised ammonium sulphate solution was used and the ratio between inlet (green dots) and outlet (blue dots) masses results in a diameter-dependant transmission efficiency (black dots). Mass distributions were determined using a SMPS, and the final transmission was calculated using the ratio of medians of the inlet and outlet of the distributions at each diameter. 232

BF5 Top (1-4): mass distributions of particles at the inlet of the flow tube, corrected (blue dots) and non-corrected (black dots), for each time that is indicated in the time series below. Bottom: concentration time series of corrected OA (dark green), non-corrected OA (light green). Black dots correspond to the mass-weighted mean diameter-dependant transmission efficiency, determined at each time step. 233

BF6 Linear fit Based EF (LEF, blue), Median-based EF (MEF, orange) and rolling-median based EF (REF, yellow) distributions for NO, SO2, CO, BC and CH4. The line within the box is the median, the upper and lower edges of the box are respectively 25th and 75th percentile respectively, the bottom and top edges of the whiskers correspond to the median ± 1.5 × Interquartile Range (IQR) of the distributions, outliers are shown as individual points. 233

BF7 Median-based EF distributions (blue) and rolling-median based EF distributions for the 6 major VOCs. The line within the box is the median, the upper and lower edges of the box are respectively 25th and 75th percentile respectively, the bottom and top edges of the whiskers correspond to the median ± 1.5 × Interquartile Range (IQR) of the distributions, outliers are shown as individual points. 234

BF8 Linear fit Based EF (LEF, blue), Median-based EF (MEF, orange) and rolling-median based EF (REF, yellow) distributions for PM_1 composition and PN and mass from the SMPS. The line within the box is the median, the upper and lower edges of the box are respectively 25th and 75th percentile respectively, the bottom and top edges of the whiskers correspond to the median ± 1.5 × Interquartile Range (IQR) of the distributions, outliers are shown as individual points. For readability, some outliers are indicated as values or a range of values that are off-scale. 234

BF9 Distribution of the FSC derived from each EF of SO_2. The line within the box is the median, the upper and lower edges of the box are respectively 25th and 75th percentile respectively, the bottom and top edges of the whiskers correspond to the median ± 1.5 × Interquartile Range (IQR) of the distributions, outliers are shown as individual points. For readability, some outliers are indicated as values or a range of values that are off-scale. 235
BF10 Scatter plot of CO vs CH_4. (Red line) linear regression of CO vs CH_4, associated coefficients are in the upper left of the figure. (Color bar) Number of days spent throughout the campaign, 0 is September 9th 2022. 236
BF11 Size distributions within the ship plumes determined by the SMPS: (left) normalised mass size distribution , (right) normalised number size distribution 236
BF12 Left : time series of raw signals (in Counts Per Second, CPS) of m/z 69 (blue), m/z 111 (red) and m/z 125 (green). Right : bar plots of the mean sum of twice m/z 125 (green) in CPS, half m/z 111 (red) in CPS, and mean m/z 69 in CPS. 237
BF13 Additional comparisons of VOC EF distributions depending on the direction of travel with arrivals EF in red and departures EF in blue. 237

CF1 Times series of the mass fraction of the 5-factor solution of the PMF ran with TD-GC-FID data. 239
CF2 Times series of the mass fraction of the 7-factor solution of the PMF ran with PTR-ToF-MS data. 240
CF3 Times series of the mass fraction of the 5-factor solution of the MTR-PMF ran with PTR-ToF-MS and TD-GC-FID data. 240
CF4 Times series of the mass fraction of the 5-factor solution of the constrained MTR-PMF ran with PTR-ToF-MS and TD-GC-FID data. 241

List of Tables

1-1 Structures of VOCs by chemical family. 6
1-2 Emission Control Areas (ECAs) set by the Annex VI of MARPOL, adapted from the IMO IMO (b). 23

2-1 Departure timetable of the Dunkirk – Dover and Dunkirk – Rosslare ferry lines (local time). Adjusted from DFDS (https://www.dfds.com/en). 34
2-2 Key pollutants under focus in this study. 35
2-3 Coefficients used for calculating Effective Carbon Number for uncalibrated compounds. 42
2-4 Correction coefficient and offset for VOC concentrations as a function of humidity. [H_2O] is the absolute humidity in ppmv, the concentrations of VOC in ppb have to be multiplied by the obtained coefficient. 49
2-5 Parameters of the drift tube. 50
2-6 Limits of Detection (LOD) taken for the VOCs measured by the GC-FID. 52
2-7 Linear correlation ($y = ax+b$) between the two TD-GC-FID for common compounds during the whole campaign. 58
2-8 TD-GC-FID of reference for each VOC. 60
2-9 Statistics of the measurements of VOC from the two TD-GC-FID during the Dunkirk 2022 campaign. Concentrations are expressed in µg·m^{-3}. 61
2-10 Statistics of the uncertainties on the TD-GC-FID measurements of VOCs and associated SNR based on Norris et al. (2014). SNR inferior to 10^{-3} were written as 0. 62
2-11 Statistics of the measurements of VOCs from the PTR-ToF-MS during the Dunkirk 2022 campaign. Concentrations are expressed in µg·m^{-3}. The availability of the data is calculated upon the VOC measurement cycles of the PTR-ToF-MS at the native time resolution (1 s). 64

2-12 Statistics of the uncertainties on the PTR-ToF-MS measurements of VOCs and associated SNR based on Norris et al. (2014). The calculations were performed on the 1 min-averaged concentrations of PTR-ToF-MS. 65
2-13 Mean levels of VOCs observed in Dunkirk in 2022 and in previous studies. Concentrations are expressed in µg·m^{-3}. (*): graphical reading. ($^{\triangle}$) converted from ppb to µg·m^{-3}. 68

3-1 Comparison of the EF determined in this study with the OMINEA database for shipping in 2021. 98
3-2 Measured FSCs and methodology of previous studies investigating ship emissions. . 101
3-3 Comparisons of EFs from this study with literature for inorganic and regulated compounds. (*) indicates that EFs taken from the study were converted from g/kWh to g·kg$_{\text{fuel}}^{-1}$ using the Low Heating Value of the corresponding fuel from The Engineering Toolbox (2003). 101

4-1 MIR coefficients of the VOCs retained for the OFPs determination. 150
4-2 SOAP coefficients used in this study, taken from Derwent et al. (2010). 153

5-1 Key pollutants under focus in the campaign of Le Havre. 161
5-2 Statistics of the concentrations of the criteria pollutants. 163
5-3 Statistical overview of the VOC concentrations observed in the 2023 campaign of Le Havre. Concentrations are expressed in µg·m^{-3}. 168
5-4 Statistical overview of the uncertainties of the VOC measurements in the 2023 campaign of Le Havre. Uncertainties are expressed in µg·m^{-3}. 171

AT1 Composition of the NPL gas standard used to calibrate the TD-GC-FID (Chromatotec) and TD-GC-2FID (Perkin-Elmer). Reference of the standard is D723268. . 217
AT2 Composition of the NPL gas standard used to calibrate the PTR-ToF-MS. 217
AT3 Calibration factors for calibrated VOCs and uncalibrated VOCs and their compound of reference (if any) for the Chromatotec TD-GC-FID. 218
AT4 Calibration factors for calibrated VOCs and uncalibrated VOCs and their compound of reference (if so) for the Perkin-Elmer TD-GC-2FID. 219
AT5 Peak list (1st part) used in the PTRMS Viewer 3. Columns 'low' and 'high' indicate the limits for the peak, 'center' indicates the mass at the maximum of the peak. kRate refers to the ionisation rate k of each ion (Equation 2.5). 220
AT6 Peak list (2nd part) used in the PTRMS Viewer 3. Low and high columns indicate the limit of the position of the peak, center indicates the maximum position of the peak in mass. kRate refers to the production rate k of each ion (Equation 2.5). . . . 221
AT7 Peak list (3rd part) used in the PTRMS Viewer 3. Low and high columns indicate the limit of the position of the peak, center indicates the maximum position of the peak in mass. kRate refers to the production rate k of each ion (Equation 2.5). . . . 222
AT8 Peak list (4th part) used in the PTRMS Viewer 3. Low and high columns indicate the limit of the position of the peak, center indicates the maximum position of the peak in mass. kRate refers to the production rate k of each ion (Equation 2.5). . . . 223

BT1 Composition of the NPL cylinder used for calibration of the PTR-ToF-MS 227
BT2 Coefficients of correction for humidity for 16 VOCs. [H_2O] is the concentration of water (absolute humidity) expressed in ppm. The obtained coefficient has to be multiplied by the raw concentrations of VOCs to obtain the final humidity-corrected concentrations. 228
BT3 Statistics of the EFs and FSCs calculated in this study. 229
BT4 Comparison of VOC and PM_1 EF with previous studies. 230

DT1 Composition of the NPL gas standard used to calibrate the TD-GC-FID. 252

General Introduction

On 1st April 2021, French television broadcast a 3-minute report entitled: *In Marseille, when cruise ships stay at port, pollution soars*[1]. The concerns of inhabitants of the areas surrounding the port of Marseille about ships as an emission source were shared with a large audience during primetime. Indeed, during the 2020 pandemic, more ferries remained docked in the port than normal. According to Atmo Sud (2021), this strongly suggested increased emissions of nitrogen oxides (NO_x, NO + NO_2) and Particulate Matter (PM) by ships, occasionally exceeding the World Health Organisation's (WHO) recommendations. This Tv reports illustrates the growing concern about emissions from maritime activities, that are receiving increasing attention over time from the global to regional scale.

Although 70% of ship emissions were found to occur within 400 km of the coastline worldwide (Capaldo et al., 1999), harbours are hotspots of ship emissions, where inhabitants living at their vicinity are particularly exposed to their exhaust plumes. Indeed, ship emissions account for 24% of the annual mean concentrations of NO_x and SO_2 in coastal areas of Europe (Viana et al., 2014), causing concentrations to exceed recommended limits. Due to these emissions, shipping is estimated to be responsible between 60,000 and 400,000 premature deaths worldwide (Corbett et al., 2007; Sofiev et al., 2018).

[1] https://www.franceinfo.fr/replay-jt/france-2/20-heures/video-a-marseille-quand-les-paquebots-restent-a-quai-la-pollution-decolle_4356041.html

In response, the International Maritime Organisation (IMO) implemented new shipping practices through the Annex VI of the MARPOL convention, which focuses particularly on emissions. This involved the creation of Emission Control Areas (ECAs), enforced in 2005, where sulphur SO_2 and NO_x emissions are reduced through the use of compliant low-sulphur fuels or after-treatment technologies, such as scrubbers or catalytic systems. Harbours within these ECAs are submitted to the same restrictions, or sometimes voluntarily apply even stricter norms, as requested by the harbour of Marseille since 2021. Consequently, greenhouse gases (GHGs), SO_2 and NO_x emissions have been quite extensively recorded in ports around the world. However, in the context of these evolving practices, the composition of ship emissions is also expected to change, and new, emerging pollutants may be substituting the regulated pollutants. It seems thus important to assess the new emissions and address their impacts on air quality and climate change.

Among these emerging pollutants are the Volatile Organic Compounds (VOCs), trace gases that are mostly unregulated. Currently in Europe, only one VOC has regulated ambient concentration levels: benzene, a carcinogen. Other VOCs are not regulated, but their monitoring is recommended due to their role in the formation of secondary pollutants. In particular, VOCs contribute to ozone (O_3) formation, an oxidant harmful for the human respiratory system and affecting plants and crops, as well as to the formation of Secondary Organic Aerosols (SOAs), which contribute to the burden of cardiovascular, respiratory and cerebrovascular diseases associated with PM. Given their impact on the formation of secondary pollutants, the study and monitoring of VOCs are of growing interest for the implementation of reduction policies and extensive surveillance.

The existing literature on VOC emissions from ships shows that there is significant variability in ship emissions of VOCs, depending on the fuel used, the type of ship, its loading and the navigational phase (Huang et al., 2018; Timonen et al., 2022; Zhang et al., 2024). Overall, the existing literature on VOC emissions in harbours is limited (Le Berre et al., 2025). Not only are the VOCs emitted by ships not well identified in these areas, but their contribution to O_3 and SOA formation is still not fully understood. In France, for example, only the ports of Marseille and Toulon have been investigated in terms of ship emissions, limiting the scope for assessing changing VOC emissions from ships under new practices, as the Mediterrenean Sea only became ECA in 2025. This makes it particularly important to investigate VOC emissions from ships in other harbours, situated in a stricter regulated area. For instance, Dunkirk, the main harbour of northern France, lays in the the North Sea ECA, where stricter regulations were in place since 2006. Furthermore, shipping traffic is globally expected to increase double (Faber et al., 2020). This can have direct repercussions on the air quality of the harbour cities.

For example, the relative contribution of the 'other transportation' sector to the VOC emission inventory in the Urban Community of Dunkirk keeps increasing, making the accurate assessments of the VOC emitted by ships more pressing, in order to more precisely evaluate their impact on the city's air quality. Currently, one of the main limitation for the accurate assessment of the impact of VOCs from ships on air quality is their current state in the regional emission inventories. In these inventories, VOCs emitted by ships are aggregated as an annual sum rather than individually quantified species. This poorly reflects the reactivity and concentrations of the individual species, obstructing the accurate assessment of their impact on air quality. This thesis aims to address knowledge gaps related to the identification of VOCs emitted by ships in harbours, using data collected during an intensive field campaign in Dunkirk in 2022 and a simplified field campaign in Le Havre in 2023. As busy ports with significant industrial activity, both harbours are representative of highly industrialised urban area, which can be encountered in other European location, such as Rotterdam, Antwerp, Barcelona or Hamburg. This work will contribute to regional emission inventories and support the assessment of VOC emissions by ships in these contexts. This work relies on the use of advanced data analysis and explores source-receptor modelling to assess the ship emissions. The outputs of the source-receptor approach developed in this study will inform the deterministic modelling approach adopted for the local impacts within the framework of SHIPAIR project.

This thesis was achieved in the framework of the Laboratory of Excellence-Chemical and Physical Properties of the Atmosphere (Labex CaPPA), funded by the National Research Agency (ANR-11-LABX-0005-01), and benefited from the financial support of the Hauts-de-France region and the CPER ECRIN. This work was part of the SHIPAIR project, through the ANR contract ANR-21-CE22-0015, and the PIRATE project (AQACIA), funded by the French Agency for Ecological Transition (ADEME).

Structure of the thesis This manuscript is divided into five distinct chapters. The first chapter covers the generalities of VOCs, from their origin to their impacts, and discusses their known emission by ships in the context of increasing traffic and stricter regulations. It also presents the methods used to investigate ship emissions in the literature.

Chapter 2 provides a detailed description of the main field campaign in Dunkirk in 2022. It describes the experimental and analytical tools that were deployed in the Dunkirk and Le Havre campaigns to identify ship emissions of criteria pollutants and VOCs. The chapter also explains how these tools will help us to achieve our objectives and provide a meaningful approach.

Chapter 3 is an article submitted to the journal Atmospheric Environment: X, currently under review. It focuses on the determination of Emission Factors to characterize ship emissions of VOCs in Dunkirk for the first time, which required a methodology to isolate shipping peaks using high-time resolution mass spectrometry data. Background considerations are also discussed, which are an important feature in EF calculations. The variability of EFs depending on the ship and its navigational phase is also discussed, and compared to EFs from the literature.

Chapter 4 confronts the chemical fingerprint determined in chapter 3 with a source-apportionment method, the Positive Matrix Factorisation (PMF). The methodology developed to produce the most accurate modelling is discussed, combining datasets with high and low time resolutions. A shipping factor is isolated, by combining time-resolved and chemically-resolved VOC measurements, and its characteristics discussed.

Chapter 5 aims to test the robustness of the VOC chemical fingerprint determined in previous chapters by exploring the less time-resolved data obtained in the harbour of Le Havre in 2023. Prior to data analysis, the campaign and experimental site are presented, and the assessment of the VOCs observed in Le Havre are explored. The results presented in this chapter are preliminary and prompt further investigation into performing the best PMF modelling, which was also used with Le Havre data, for resolving a ship emission factor.

CHAPTER 1

State of the art: shipping as a source of interest for Volatile Organic Compounds

The aim of this first chapter is to address the generalities of Volatile Organic Compounds (VOCs) and their importance for air quality. The emissions of VOCs are considered in relation to their sources, with a particular focus on shipping, which is discussed in the second half of the chapter in a context of evolving practices and regulations.

1.1 Volatile Organic Compounds: sources, chemistry and fate

1.1.a Definition of Volatile Organic Compounds

The definition given by the European Directive 1999/13/CE relates organic compounds as "*any compound that contains at least one carbon element, with one or more of the following elements: hydrogen, oxygen, sulphur, phosphorus, silica, or nitrogen, excluding carbon oxides, carbonates, and inorganic carbonates*" (EU, 1999). Volatile Organic Compounds (VOCs) are defined by the same directive as organic compounds with a vapour pressure of more than 0.01 kPa at 293.15 K. VOCs refer to a large variation of trace gases, that can be classified in function of their elemental composition and chemical bonds. VOCs that contain only carbon and hydrogen are referred to as hydrocarbons, mostly alkanes, alkenes and aromatics, while the most prominent constituents of Oxygenated Volatile Organic Compounds (OVOCs) are alcohols, carboxylic acids, aldehydes and ketones. Table 1-1 illustrates the chemical structure of these groups. Note that methane (CH_4) is considered a VOC but has a much smaller reactivity than other VOCs (Seinfeld and Pandis, 2016), therefore, CH_4 is usually excluded from VOCs, thus referred as Non-Methane Volatile Organic Compounds (NMVOCs). Although the term NMVOCs appears in some references, its use remains relatively limited. In this work, the term VOCs will be used throughout the manuscript to denote NMVOCs unless otherwise specified.

Table 1-1: *Structures of VOCs by chemical family.*

Alkanes	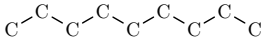 *Octane*	**Alcohols**	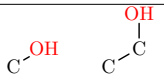 *Methanol* *Ethanol*
Alkenes	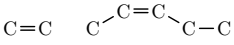 *Ethylène* *(Z) pent-2-ene*	**Carboxylic acids**	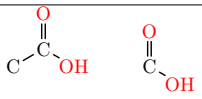 *Acetic acid* *Formic acid*
Alkynes	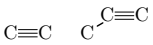 *Ethyne* *Propyne*	**Aldehydes**	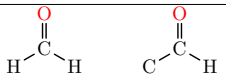 *Formaldehyde* *Acetaldehyde*
Aromatics	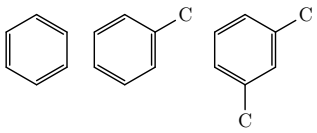 *Benzene* *Toluene* *Xylenes*	**Ketones**	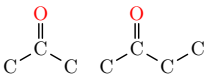 *Acetone* *Butanone*

VOCs can also be classified according to their volatility, i.e. their capacity to vaporise into the atmosphere in standard conditions. Shiraiwa and Seinfeld (2012) suggested the use of the effective saturation mass concentration C^* (µg·m^{-3}) to describe the volatility (Equation 1.1):

$$C_i^* = \frac{M_i p_i^0}{760RT} 10^6, \tag{1.1}$$

for a compound i, with M_i its molar mass (g·mol^{-1}), p_i^0 (Torr) its saturation vapour pressure, R the gas constant (m^3·atm·mol^{-1}·K^{-1}) and T the temperature (K). This metric can be used to classify VOCs according to their volatility. Note that the following criteria are examples that can be found in the literature and do not constitute an absolute indication of the nomenclature:

- VOC: $C_i^* > 10^6$ µg·m^{-3} and less than 11 carbon atoms,
- Intermediate-volatility VOC (IVOC): $10^3 < C_i^* < 10^6$ µg·m^{-3} and between 12 and 18 carbon atoms (Tkacik et al., 2012),
- Semi-Volatile VOC (SVOC): $0.1 < C_i^* < 10^3$ µg·m^{-3} and between 29 and 32 carbon atoms (Robinson et al., 2007),
- Non-Volatile Organic Compounds (NVOC): $C_i^* < 0.1$ µg·m^{-3} and more than 32 carbon atoms (Robinson et al., 2007).

1.1.b Primary sources of VOCs

VOCs are primarily emitted by both anthropogenic (human-made) and biogenic (natural) sources. Model estimations show that global emission rates are larger for biogenic than for anthropogenic VOCs (Guenther et al., 1995). For example, Guenther et al. (2006) reported emission rates of approximately 600 Tg/year for biogenic and Piccot et al. (1992) roughly 120 Tg/year for anthropogenic VOCs. Although biogenic emissions of VOC dominate globally, anthropogenic sources contribute significantly in urban environment. This section discusses the different sources responsible for both anthropogenic and biogenic VOC emissions.

1.1.b.i Biogenic sources

The total flux of biogenic VOCs (BVOCs) over one year is estimated at 600 – 1,150 Tg (Guenther et al., 1995, 2000, 2006, 2012). More specifically, VOC emissions from vegetation account for 98% of the total BVOCs flux, primarily from foliage (Guenther et al., 2000). On average, isoprene (C_5H_8) accounts for 70% of BVOC emissions (Sindelarova et al., 2014), followed by terpenoids, which include all terpenes and their derivatives. Of these, monoterpenes ($C_{10}H_{16}$) are the second most important contributor to atmospheric emissions of VOCs from vegetation, accounting for 10% on average (Kesselmeier and Staudt, 1999; Sindelarova et al., 2014). Monoterpenes can be acyclic (myrcene), cyclic (limonene) or bicyclic (α-/β-pinenes) (Graedel, 1979). Alcohols, in particular methanol, aldehydes (formaldehyde, acetaldehyde) account for only an insignificant proportion of BVOC emissions (Graedel, 1979; Kesselmeier and Staudt, 1999). The latest estimates of BVOC emissions used the MEGAN model to provide a total emission rate of 835.4 Tg·year^{-1}, with a majority of isoprene (347.7 Tg·year^{-1}) (Wang et al., 2024).

The ocean plays a key role in the production and consumption of Oxygenated Volatile Organic Compounds (OVOCs) in the atmosphere, as it controls largely the atmospheric concentrations of certain compounds, such as methanol, acetaldehyde and acetone. For instance, the marine environment releases 85 Tg of methanol yearly, which is comparable to the rate at which methanol is oxidised in the atmosphere (Millet et al., 2008). OVOC production by the ocean is linked to marine vegetation, therefore, concentrations at the surface of the ocean depend on photochemical processes and microbial oxidation (Dixon et al., 2013), and ocean conditions (ocean vs. upwelling) which influence the lifetime of OVOCs. The ocean can also be a source of organosulphur compounds such as dimethylsulphide (DMS) (Hopkins et al., 2016).

1.1.b.ii Anthropogenic sources

Piccot et al. (1992) reported early anthropogenic VOC inventories from modelling, showing that burning fuelwood and savannas were the main contributors to global VOC emissions (20% and 16%, respectively), next to gasoline consumption, storage and transport (16%). Finally, the rubber, plastic and organic chemicals industries, along with solvent use and surface coatings, were also notable contributors.

Among the various anthropogenic sources identified, road transport stands as the most ubiquitous in urban environments. Vehicle emissions represent a more localised yet significant source of VOCs, particularly in densely populated areas. VOCs from road transport are mainly present in the exhaust plumes and are produced by the incomplete combustion of fuel in vehicles or by fuel evaporation. Numerous studies have determined the main combustion-related VOCs, either by identifying them under laboratory conditions (Schauer et al., 2002; Montero et al., 2010; Yamamoto et al., 2012; Marques et al., 2022) or by identifying the sources of road transport in tunnels or urban environments (Olson et al., 2009; Salameh et al., 2014; Baudic et al., 2016; Dufresne et al., 2025). The main VOCs from road transport identified are alkanes (iso-/n-pentane, isooctane, heptane), aromatic compounds (toluene, benzene) and certain OVOCs (acetaldehyde, methanol). Due to their low saturation vapour pressure, hydrocarbons present in fuels are likely to evaporate at ambient temperatures, resulting in VOC emissions that depend on external conditions and the climate in which the vehicle is used (Borbon et al., 2002). Non-exhaust vehicle emissions of VOCs are associated with the abrasion of brakes and tyres, as well as fuel evaporation which releases aromatic VOCs and alkenes, and also include alcohols originating from de-icing products used in cars (Harrison et al., 2021). Asphalt-covered surfaces were also identified as a significant source of VOCs in Paris, contributing an amount equivalent to 21.3% of annual VOC emissions from road transport, with emissions from aged asphalt being particularly significant during summer (Lasne et al., 2023; Lostier et al., 2025).

Industrial activities, which were also identified in early inventories, remain a substantial and diverse contributor to ambient VOCs, particularly through the use of solvents and chemical processing operations. These sources often emit a wide variety of VOC species with different emission profiles to those of combustion-related sources. Industrial sources of VOCs include metallurgy, the petrochemical industry, printing, the food industry and agriculture. The variety of sources and species involved makes speciation difficult and has prompted numerous studies in urban areas (Badol et al., 2008a,b; Borbon et al., 2002; Salameh et al., 2014; Wang et al., 2012; Xiang et al., 2012). These studies observed that industrial activities and solvent manufacturing mainly emitted BTEX (benzene, toluene, ethylbenzene and xylenes), as well as isopentane, trimethylbenzenes and 1-hexene to a lesser extent.

In France, the French National Institute for Emission Inventories (CITEPA) develops emission inventories for greenhouse gases (GHGs) and other pollutants at national scale. One of CITEPA's latest reports examined the evolution of VOC emissions by originating sector and revealed a decline in VOC emissions in France since 1990 as shown Figure 1-1. This decrease was attributed to the implementation of regulations on fuel storage and distribution, a reduction in the quantity of solvents in paints used in the housing and industrial sectors, the adoption of more efficient after-treatment systems for transport, cleaner fuels and electric vehicles (CITEPA, 2022a). Most importantly, the benzene fuel content of vehicles was reduced to a 1% maximum in volume since 2000 (Légifrance, 1999). However, the report also states that the solvent use still makes up around 31.3% of VOC emissions in France.

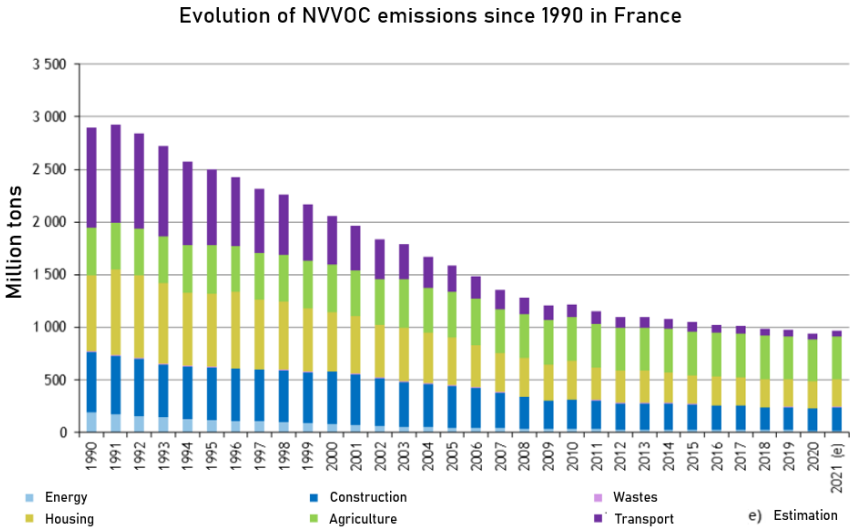

Figure 1-1: *Evolution of NMVOC in France depending on the sector, adapted from CITEPA (2022a)*

1.1.c Generalities on chemistry of VOCs in the atmosphere

Historically, the study of *smog* (contraction of *smoke* and *fog*) observed in the cities of London (Bell and Davis, 2001) or Los Angeles (Haagen-Smit, 1952), causing concerning health hazards to the populations, uncovered the role of hydrocarbons, nitric oxides (NO_x = NO_2 + NO) and photolysis in the formation of ozone (O_3) and Secondary Organic Aerosols (SOAs). Automobile exhaust was then specifically found to be the main responsible for ozone formation in Los Angeles (Haagen-Smit and Fox, 1954). These constituted the onset of the atmospheric chemistry of VOCs and their impacts on air quality, which will be presented in the following sections with a focus on the main oxidants of VOCs and their origins. There are many other reactions involving VOCs in the troposphere, such as those involving halogen atoms and heterogeneous reactions, but these play a minor role in the global troposphere and will not be discussed in the present work.

1.1.c.i Reaction with OH·

The hydroxyl radical (OH·) is the most important oxidant of VOCs with reported yearly mean concentration of $1.16{\cdot}10^6$ molecules·cm^{-3} (Spivakovsky et al., 2000). OH· radicals form from photodissociation of tropospheric O_3 ($290 \leq \lambda \leq 335$ nm), which produces O_2 and one excited oxygen (O^1D) (Equation 1.2). This oxygen relaxes in collision with an inert molecule M, such as N_2 in ambient air, to its ground state (O^3P) (Equation 1.3). Then, it creates O_3 with O_2 (O^3P) (Equation 1.3). However, in the presence of water, $O(^1D)$ preferably reacts with H_2O to create two OH radicals (Equation 1.5) (Atkinson, 2000):

$$O_3 + h\nu \longrightarrow O_2 + O(^1D), \tag{1.2}$$

$$O(^1D) + M \longrightarrow O(^3P) + M, \tag{1.3}$$

$$O(^3P) + O_2 + M \longrightarrow O_3 + M, \tag{1.4}$$

$$O(^1D) + H_2O \longrightarrow 2OH. \tag{1.5}$$

This is the main formation mechanism of OH· radicals encountered in the troposphere (Clemitshaw, 2015), favoured by sunlight and humidity, leading to maximum concentrations mid-day. However, multiple other sources contribute to the formation of OH· radicals, such as H_2O_2 photodissociation (Li et al., 2015), hydroperoxyl radical reaction with NO and photolysis of HONO.

The initial oxidation of VOCs by OH· produces an alkyl radical R which transforms into a peroxy radical RO_2 when combined with O_2. This radical may react with multiple species, causing propagation reactions (Kroll and Seinfeld, 2008). As example, its reaction with a hydroperoxy radical HO_2 form a hydroperoxide ROOH (Equation 1.6), a major component of SOA. In presence of NO_x, RO_2 reacts with NO and forms either a alkoxy radical ·RO (Equation 1.7) or an organic nitrate $RONO_2$ (Equation 1.8). It can also produce a peroxynitrate ($ROONO_2$) when reacting with NO_2 (Equation 1.9).

$$RO_2 + HO_2 \longrightarrow ROOH + O_2, \tag{1.6}$$

$$RO_2 + NO \longrightarrow \cdot RO + NO_2, , \tag{1.7}$$

$$RO_2 + NO + M \longrightarrow RONO_2 + M, \tag{1.8}$$

$$RO_2 + NO_2 + M \longrightarrow ROONO_2 + M. \tag{1.9}$$

Therefore, O_3 formed during the day through the photolysis of NO_2 is not consumed as long as NO can react with peroxy radicals (HO_2, RO_3) produced by the oxidation of VOCs. Termination reactions can slow down or stop O_3 accumulation by forming stable species, by removing radicals that can react with each other to form peroxides H_2O_2 (Equation 1.10). NO_2 can also be oxidised by OH· to form nitric acid without producing O_3 (Equation 1.11) (Seigneur, 2018). The general mechanism is presented in Figure 1-2.

$$HO_2 + HO_2 \longrightarrow H_2O_2, \tag{1.10}$$

$$NO_2 + \cdot OH + M \longrightarrow HNO_3 + M. \tag{1.11}$$

1.1.c.ii Reaction with ozone

Tropospheric O_3 has to be distinguished from stratospheric O_3 in respect to its formation mechanisms and compounds that disturb their equilibrium.

Stratospheric O_3 represents 90% of the total O_3 in the atmosphere, concentrated in the ozone layer between 10 and 40 km altitude (WMO, 2015), as represented in Figure 1-3, and acts as a primary UV radiation shield. Upon photodissociation of O_2 when absorbing UV solar radiation ($\lambda \leq 242$ nm), a formed molecular oxygen (O^1D) (Equation 1.12) combines with O_2 to reform O_3 (Equation 1.13) :

$$O_2 + h\nu \longrightarrow 2O(^1D), \tag{1.12}$$

$$O(^1D) + O_2 \longrightarrow O_3. \tag{1.13}$$

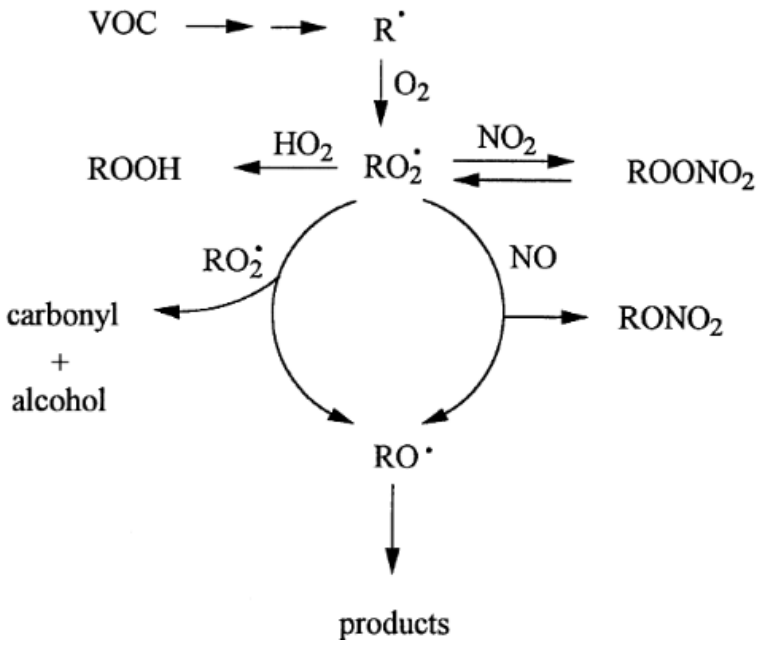

Figure 1-2: *General mechanism of oxidation of VOCs (Atkinson, 2000).*

Additionally, O_3 absorbs solar UV radiation ($240 \leq \lambda \leq 320$ nm) and photodissociates to form O_2 and $O^1(D)$ (Equation 1.14), then $O^1(D)$ recombines with O_3 to reform O_2 as presented in Equations 1.15.

$$O_3 + h\nu \longrightarrow O(^1D) + O_2, \tag{1.14}$$

$$O(^1D) + O_3 \longrightarrow 2O_2. \tag{1.15}$$

This mechanism is known as the Chapman cycle, leading to an equilibrium between O_2 and O_3 in the stratosphere (Chapman, 1930):

$$3O_2 \rightleftharpoons 2O_3. \tag{1.16}$$

Tropospheric O_3 is formed by the photodissociation of NO_2 ($\lambda \leq 400$ nm) leading to the formation of NO and one oxygen $O^3(P)$ (Equation 1.17). This oxygen combines with O_2 to form O_3 (Equation 1.18) after which NO reacts with O_3 to reform NO_2 and O_2 (Equation 1.19). This explain the equilibrium of O_3 in the troposphere ($\leq$ 10 km altitude) referred to as the Leighton photostationary state (Seigneur, 2018):

$$NO_2 + h\nu \longrightarrow NO + O(^3P), \tag{1.17}$$

$$O(^3P) + O_2 + M \longrightarrow O_3 + M, \tag{1.18}$$

$$NO + O_3 \longrightarrow NO_2 + O_2. \tag{1.19}$$

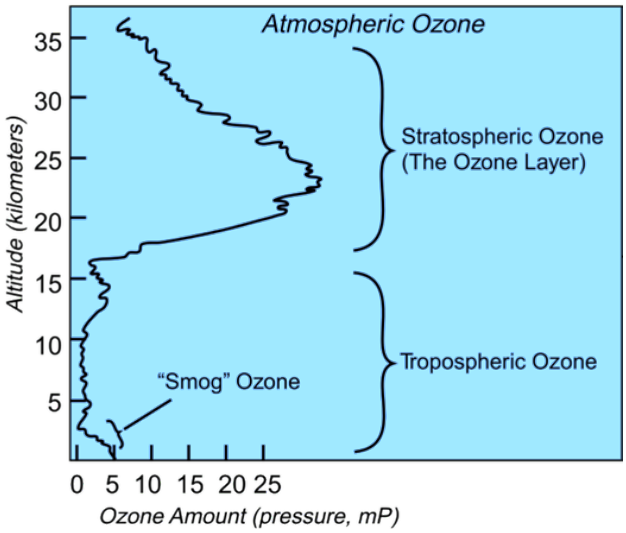

Figure 1-3: *Vertical distribution of O_3. Adapted from King et al. (2010).*

As shown in Figure 1-4 of Cooper et al. (2014), global trends were reported from observational data in various rural sites around the world. Ozone levels have increased steadily since the mid-20th century, due to the accumulation of its anthropogenic precursors. However, since 2000, O_3 levels have remained high at 30 — 50 ppb in Europe (Cooper et al., 2014), showing little decrease since then.

VOCs notably undergo oxidation from ozonolysis as O_3 during both night and day times, especially for alkenes. The addition of O_3 on the double bond C=C initiates the ozonolysis reaction, forming a primary ozonide (POZ). The POZ is consequently decomposed by the exothermic reaction and then forms two primary carbonyls called Criegee intermediates (Figure 1-5) that act as precursors of OH radicals (Johnson and Marston, 2008).

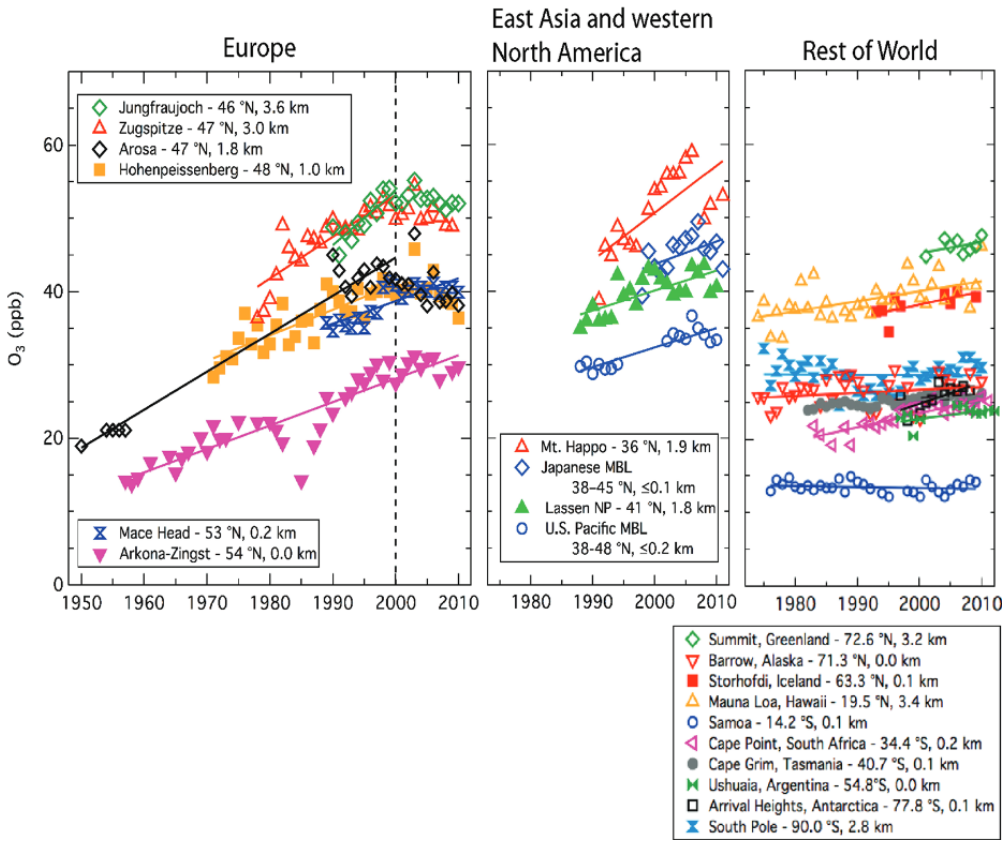

Figure 1-4: *From Cooper et al. (2014): Surface ozone time series at several rural sites around the world. Trend lines are fit through the yearly average ozone values using the linear least-square regression method. Trend lines in Europe only extend through 2000 when the positive trend appears to have ended. This figure is modified from the original that appeared in IPCC (2013).*

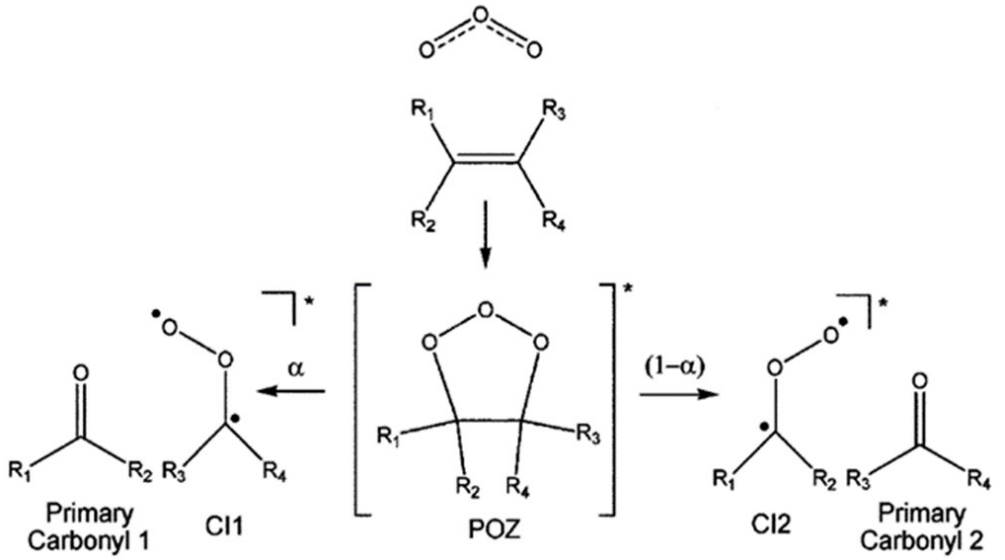

Figure 1-5: *Initialisation reaction of ozonolysis and Criegee intermediates formation (Johnson and Marston, 2008)*

1.1.c.iii Reaction with nitrate

Nitrate (NO_3) is formed by the the combination of NO and O_3 (Equation 1.20), creating NO_2 and O_2 that combine into NO_3 (Equation 1.21). It can photodissociate ($380 \leq \lambda \leq 690$ nm) into NO_2 and $O(^3P)$ (90%) or into NO and O_2 (10%) (Equation 1.22), consequently day time concentrations of NO_3 are lower than at night, as its lifetime in sunlight is about 5 seconds. Nighttime concentrations were reported up to $1{\cdot}10^{10}$ molecules·cm^{-3} (Atkinson, 2000) making NO_3 the main oxidant of VOCs during the night.

$$NO + O_3 \longrightarrow NO_2 + O_2, \tag{1.20}$$

$$NO_2 + O_3 \longrightarrow NO_3 + O_2, \tag{1.21}$$

$$\begin{cases} NO_3 + h\nu \longrightarrow NO + O_2, \\ NO_3 + h\nu \longrightarrow NO_2 + O(^3P). \end{cases} \tag{1.22}$$

1.1.c.iv Photolysis

Aldehydes (RCHO) may decay by photodissociation, forming a radical R and HCO, or an hydrocarbon RH and carbon monoxide (CO) (Calvert and Pitts, 1966). This mechanism is a minor phenomenon for most VOC and quite specific to certain compounds like formaldehyde (HCHO).

1.1.d Formation of secondary pollutants

It is important to distinguish between primary pollutants, which are emitted directly into the atmosphere and whose impact is directly linked to their concentration, and secondary pollutants, which are formed from the transformation of other chemical compounds, known as precursors, in the atmosphere. While the precursors themselves are not necessarily harmful, most secondary pollutants are considered harmful to human health and the environment because they contribute to atmospheric pollution (Seigneur, 2018).

1.1.d.i Ozone

As seen in Section 1.1.c.ii, NO reacts preferably with most VOC oxidation products from OH oxidation, to create carbonyl compounds, alkoxy radicals (RO) or OH radicals (Jenkin and Clemitshaw, 2000). The equilibrium of O_3, NO_2 and NO disturbed by VOCs is schematized in Figure 1-6. The O_3 formed by the photolysis of NO_2 isn't consumed while NO can react with VOC oxidation products (HO_2, RO_2). Only termination reactions can limit or stop the accumulation of O_3 by forming stable compounds, as represented in Equation 1.23 where two HO_2 radicals combine to form peroxides (H_2O_2). Also, NO_2 can be oxidised by OH to form nitric acid (HNO_3, Equation 1.24):

$$HO_2 + HO_2 \longrightarrow H_2O_2 + O_2, \tag{1.23}$$

$$NO_2 + OH + M \longrightarrow HNO_3 + M. \tag{1.24}$$

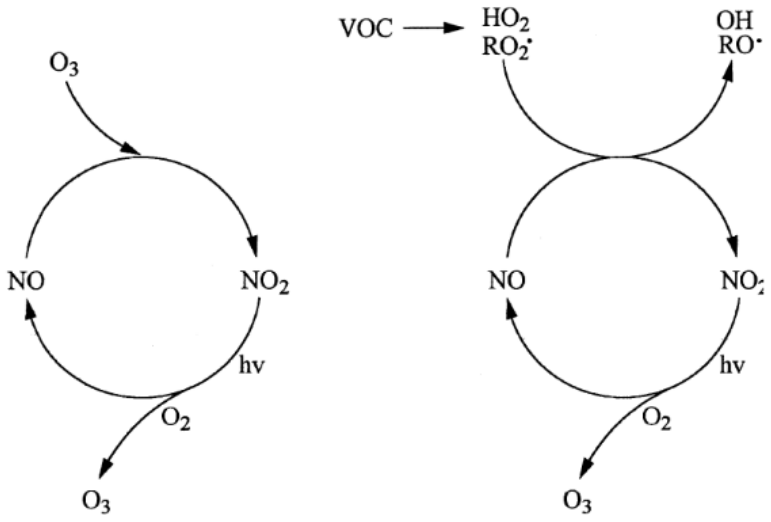

Figure 1-6: *Photostationary state of O_3, NO_2 and NO (left) and VOC-disturbed equilibrium (right) (Atkinson, 2000).*

The VOC/NO_x ratio is commonly used to describe O_3 destruction or formation regimes. The non-linearity of reactions between VOC and NO_x leads to complex assessments of theses regimes, thus O_3 isopleths are calculated by models as represented in Figure 1-7. They describe the sensitivity of various locations to VOCs and NO_x in O_3 formation (Ashok and Barrett, 2016; Shen et al., 2021; Santos et al., 2021). For example, in urban areas where NO_x emissions are important, concentrations like [VOC] = 0.4 ppmC and [NO_x] = 0.18 ppm, results in 0.12 ppm of O_3 based on the upper left side of Figure 1-7. The O_3 formation is VOC-limited thus O_3 reduction strategies should focus on the reduction of VOCs. On the other hand, VOCs are prominent in rural or sub-urban areas, resulting in concentrations like [VOC] = 1.6 ppmC and [NO_x] = 0.04 ppm, resulting in 0.20 ppm of O_3 and a NO_x-limited regime, corresponding to the lower right side of Figure 1-7. Reducing NO_x would lead to a reduction in O_3 formation. Note that Ivatt et al. (2022) reported the complementary role of aerosols in the VOC/NO_x model of O_3 formation in highly polluted urban areas, to account for heterogeneous reactions and modification of photolysis rates in the atmosphere.

1.1.d.ii Secondary Organic Aerosols

VOCs that undergo oxidation, can become Semi-Volatile Organic Compounds (SVOCs). These are characterised by a saturation vapour pressure lower than VOCs (10^{-14} – 10^{-4} atm) (Goldstein and Galbally, 2007; Weschler and Nazaroff, 2008), meaning they have lower volatility (as shown by Equation 1.1). SVOCs can be found in both the gaseous and condensed phases. The oxidation of VOCs generally leads to functionalisation, which reduces volatility and favours partitioning into the particulate phase. However, high oxidation can lead to fragmentation, increasing the volatility of specific oxidation products (Seigneur, 2018).

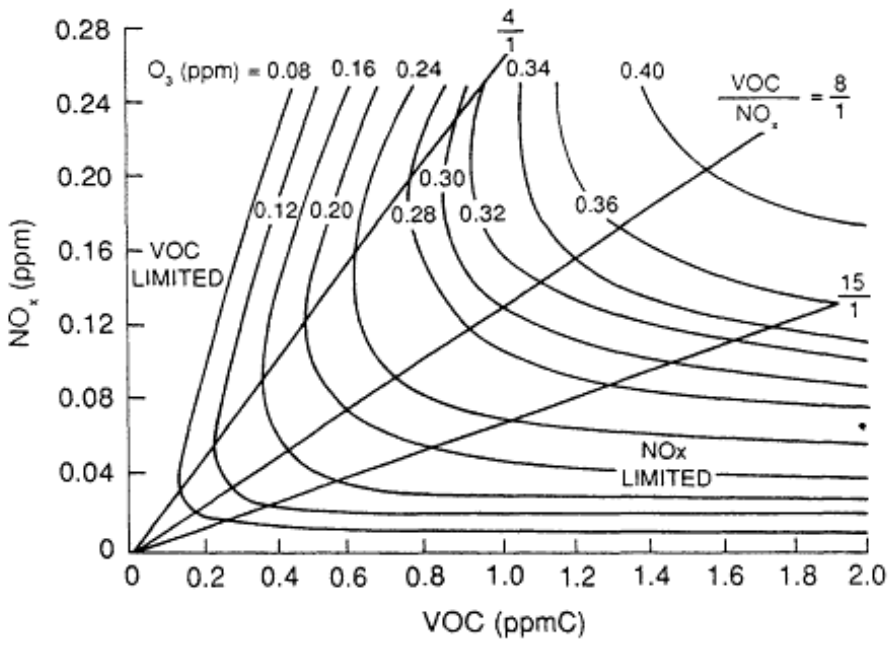

Figure 1-7: *Isopleth and O_3 formation regimes (Dodge, 1976).*

Figure 1-8 shows that compounds with more functional groups than alkanes (alcohols, carboxylic acids) have lower saturation vapour pressure, illustrating that oxidation products have lower volatility and are expected to be more present in the particulate phase without fragmentation. The assessment of SOA formation depending on the type of oxidant and the VOC group leads to complex studies, that confronts field studies with lab observations in order to identify the precursors of the SOAs and the oxidation or fragmentation processes that they underwent (Freney et al., 2018).

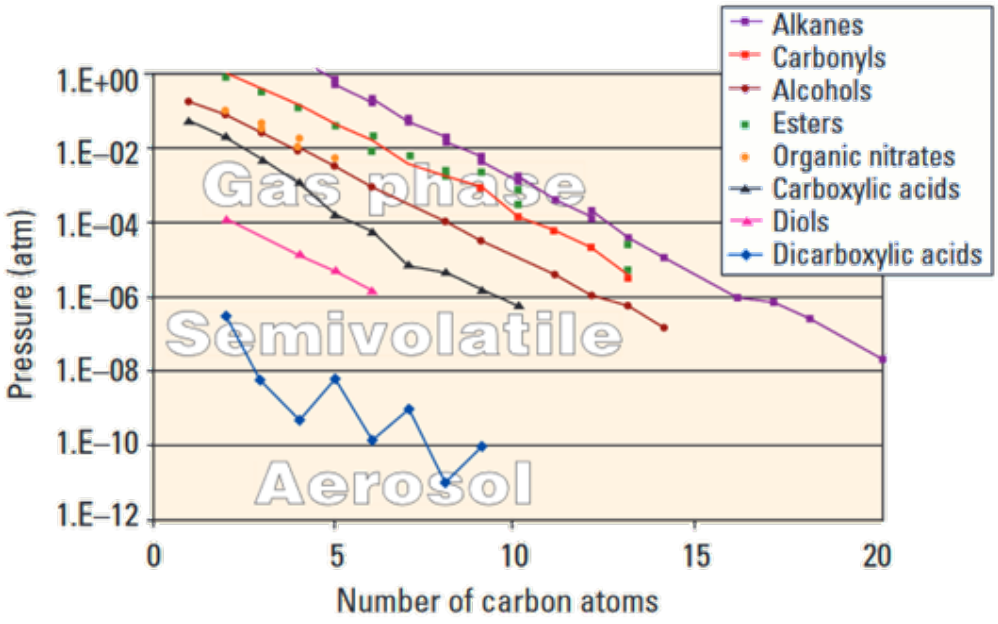

Figure 1-8: *Saturation pressure of VOCs depending on their number of carbons, adjusted from Goldstein and Galbally (2007).*

1.1.e Elements of transport of VOC

1.1.e.i Vertical transport in the Planetary Boundary Layer

The Planetary Boundary Layer (PBL) constitutes the lowest section of the troposphere (100 m – 1 km above the surface) that is most sensitive to Earth's surface radiative forcing. As solar radiation heats the PBL, air masses rise and cool as they gain altitude. During the day, an increase in temperature elevates the mixing height, creating a large volume for the dispersion of pollutants and resulting in a turbulent atmosphere with favoured vertical transport of pollutants. However, progressive cooling of the surface, for instance at night, creates an inversion layer, with hotter air masses remaining above. This creates a reduced mixing height between the surface and the inversion layer (Figure 1-9), trapping pollutants between the surface and the mixing inversion layer (Seinfeld and Pandis, 2016). Therefore, at night, the mixing height is lower, favouring pollutant accumulation at ground levels with less dispersion, as the atmosphere is more stable. Lower winter temperatures reduce the mixing height, resulting in higher VOC concentrations near the surface than in summer (Filella and Penuelas, 2006).

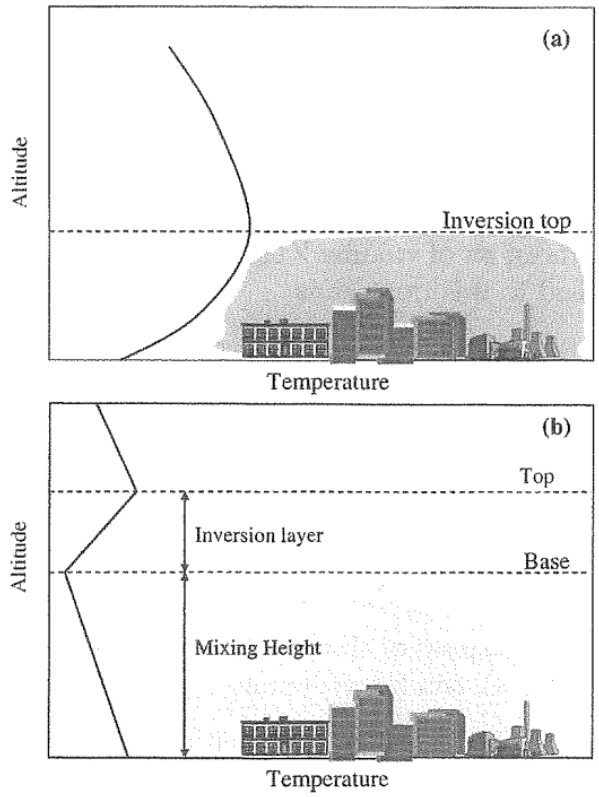

Figure 1-9: *Mixing height variation during the night (a) and during the day (b) (Seinfeld and Pandis, 2016).*

1.1.e.ii Wind regimes

Winds are one of the main driving forces behind the dispersion of pollutants. Breeze regimes particularly influence local air circulation, as shown in Figure 1-10. During the day, solar radiation heats both the land and the sea. However, as the land has a lower thermal capacity than the sea, it warms quicker. The air above land areas becomes hotter and less dense, and rises. This creates a decrease in pressure at the surface, which is compensated by the displacement of cooler air from the sea surface to the land, creating the so-called *sea breeze*. Without radiation, at night, the cooling of the ground is slower than the sea surface, resulting an opposite displacement of cooler air from above land towards the sea, identified as *land breeze*. Further details about land- and sea breezes and their dynamics are presented in Miller et al. (2003).

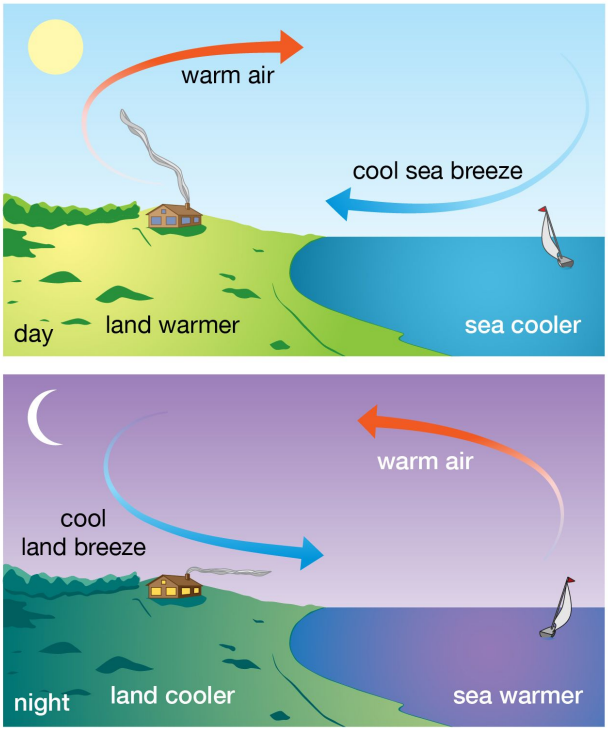

Figure 1-10: *Sea breeze and land breeze.*

The breeze dynamics have an impact on the pollutant dispersion in coastal areas, particularly the sea breeze which tends to dilute pollutant concentrations over land, including VOCs (Sauvage et al., 2009; Dufresne et al., 2025).

1.1.f Impacts of VOCs

In addition to impacting air quality, as demonstrated so far, VOCs significantly influence the climate through complex interactions between the environment, atmospheric chemistry, and GHGs. VOCs also have important direct and indirect impacts on human health through their contribution to the formation of secondary pollutants, such as ozone and SOAs.

1.1.f.i Climate

As mentioned in Section 1.1.b.i, biogenic emissions of VOCs (BVOCs) dominate the global VOC emission budget. BVOCs emitted from terrestrial ecosystems were found to directly impact the radiative forcing of the Earth, as their oxidation products induce a net chemical cooling effect on the global climate of -0.17 W·m^{-2} (Unger, 2014). However, when anthropogenic VOC emissions are taken into account, this forcing increases up to $+0.10$ W·m^{-2}, resulting in a warming effect on the climate. This is consistent with the results of Fry et al. (2014), who determined that a 50% global reduction in VOCs could lead to an average net radiative forcing of -9.73 W·m^{-2}. However, uncertainties remain as regional global warming potential estimates range from -1.13 to $+18.9$ W·m^{-2} over a 20-year period (Fry et al., 2014).

VOCs react with NO_x, enhancing tropospheric O_3 levels, which has doubled over the last two centuries, making O_3 the third most important anthropogenic GHGs after CO_2 and CH_4 (Helmig et al., 2009). Elevated O_3 produced through VOC reactions damages vegetation and reduces its ability to absorb O_3 which limits natural carbon sinks (Helmig et al., 2009). Furthermore, the O_3 damage on vegetation increases the impacts of VOCs by reducing the quantity of CO_2 absorbed by the biosphere (Collins et al., 2010). Moreover, chronic exposure of plant growth to O_3 leads to a reduction of yields (Krupa and Manning, 1988).

1.1.f.ii Health

Exposure to air pollution contributes significantly to the global burden of human disease, causing acute and chronic diseases that cause millions of deaths worldwide. The World Health Organisation (WHO) estimates that the combined effects of ambient air pollution and household air pollution is associated with 7 million premature deaths annually (WHO, 2021). Unlike PM, NO_x, SO_2 and O_3, for which the WHO has historically provided health-based guidelines because they are relatively well documented, assessing the health impacts of VOCs is particularly complex. This is due not only to the unequal availability of exposure data for individual compounds, but also to the fact that their effects depend on whether they act as primary pollutants or contribute to the formation of secondary pollutants, such as O_3 and SOAs. This contribution to secondary pollution involves non-linear atmospheric processes and varies depending on environmental conditions, making it challenging to quantify their impact. Furthermore, the relative importance of direct versus indirect health effects varies depending on the context. For example, in indoor environments or occupational settings, where concentrations are higher, exposure data may be lacking.

Direct health impacts Amongst the VOCs with demonstrated direct health, benzene (C_6H_6) can be cited as the only VOC with regulatory limits. The yearly exposure limit for benzene is set by the French Décret n°2010-1250 at 5 µg·m^{-3}, with the aim of achieving 2 µg·m^{-3} (Légifrance, 2010), in line with the European Union's directives 2000/68/CE and 2008/50/CE (EU, 2000, 2008). Half of the inhaled benzene is absorbed by the lungs (ORS, 2007), and acute exposure can lead to irritation of the eyes, nose and throat or vertigo.

The International Agency for Research on Cancer (IARC) has compiled cohort studies on the health impacts of chronic benzene exposure, reporting links between chronic benzene exposure and leukaemia, lung cancer, and possibly childhood cancer (IARC, 2018).

The IARC also reported on the health hazards linked to exposure to formaldehyde (HCHO), which originates from various industrial activities, such as resin, paper and plastic production, and coating processes. In their review, they highlight an increased mortality rate from nasopharyngeal, leukaemia and sinonasal cancers following chronic exposure to formaldehyde. In the short term, formaldehyde is the most irritating VOC (IARC, 2008b).

Further, the VOC 1,3-butadiene (C_4H_6), linked to industrial emission sources, has been identified as a carcinogenic compound. Exposure to this substance has been associated with an increased risk of lymphatic and haematopoietic cancers, as well as renal cell carcinoma for workers in the styrene-rubber industry (IARC, 2008a).

Indirect health impacts As explained Section 1.1.c.ii, ozone is a secondary pollutant resulting from the reaction of VOCs and sunlight, particularly in urban areas where NO_x emissions are significant. Exposure to ozone can cause respiratory irritation and inflammation of the airways. It favours lung diseases such as asthma, chronic bronchitis and emphysema. Long-term exposure to ozone makes the lungs more vulnerable to infection, leading to higher rates of hospitalisation and even death from respiratory causes (US EPA, 2015). Therefore, ozone is one of the regulated pollutants in France and Europe, with an air quality guideline of 100 $\mu g \cdot m^{-3}$ on an 8-hour average (WHO, 2021).

The impact of SOAs is linked to their size and composition, and they contribute to fine particulate matter (PM) (Wang et al., 2022; Chebaicheb et al., 2023), which poses health risks. Orellano et al. (2020) published a review of evidence showing that short-term exposure to PM with aerodynamic diameters of less than 10 µm (PM_{10}) and 2.5 µm ($PM_{2.5}$) leads to cardiovascular, respiratory and cerebrovascular mortality. These are also regulated pollutants, and the WHO air quality guidelines for short-term exposure (24 hours) are 45 $\mu g \cdot m^{-3}$ for PM_{10} and 15 $\mu g \cdot m^{-3}$ for $PM_{2.5}$ (WHO, 2021). PM with a diameter of less than 100 nm are referred as Ultra Fine Particles (UFPs). These are emitted by sources such as wildfires or exhaust systems and are a leading cause of neurodegenerative diseases such as Alzheimer's and Parkinson's (Calderón-Garcidueñas and Ayala, 2022). Long-term exposure to PM increases mortality from PM_{10} and $PM_{2.5}$, as well as from cardiovascular and respiratory disease and lung cancer, even at levels below the WHO guideline exposure levels. This has prompted new guidelines for both PM_{10} and $PM_{2.5}$ (Chen and Hoek, 2020).

1.2 Shipping as a source of VOCs

1.2.a Ship traffic trends, impacts and regulations

According to the International Maritime Organisation (IMO), shipping accounted for the transport of 80% of global trade in 2020. The intensity of ship traffic can be measured by the tonnage of goods unloaded, as shown in Figure 1-11 and presented by the United Nations Conference on Trade and Development (UNCTAD). Over the past 30 years, this quantity has increased by 30% and is expected to grow further. According to the IMO's projection scenario, maritime traffic is estimated to double by 2030 compared to 2016, as reported in the fourth IMO study of 2020 (Faber et al., 2020).

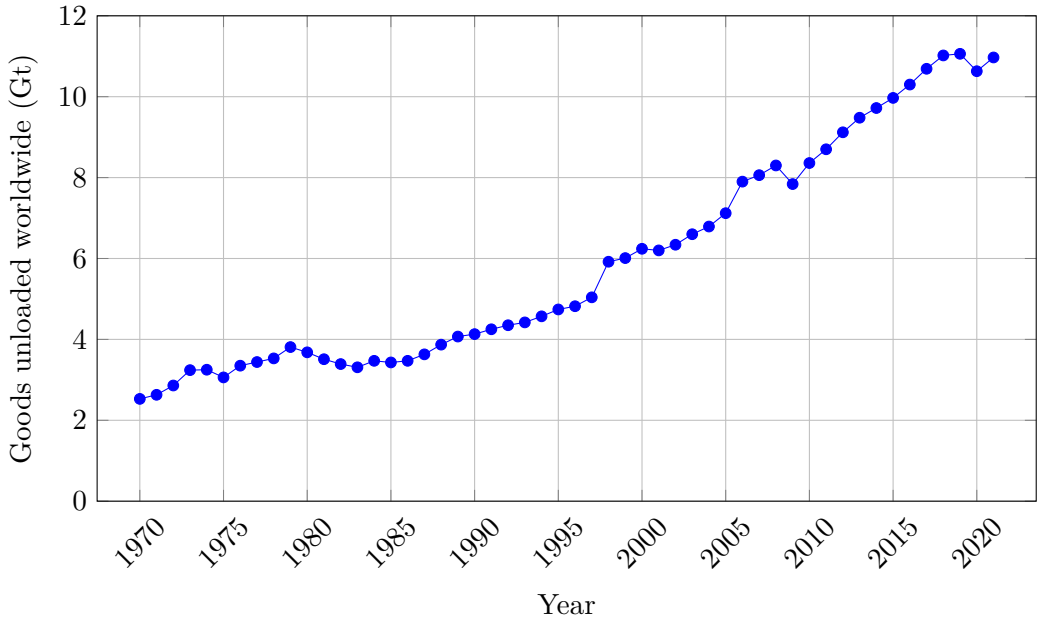

Figure 1-11: *Evolution of the quantity of unloaded goods since 1970. Data were extracted from the United Nations Conference on Trade and Development data hub (UNCTAD, 2021).*

Ship emissions accounted for 2,89% of total GHG emissions in 2018 (Faber et al., 2020). For comparison, the same year saw greenhouse gases (GHG) emissions from aviation contribute 2.6% to global GHG emissions (Graver et al., 2019), highlighting the importance of shipping as a major and concerning source of GHGs worldwide. Since shipping traffic is increasing, emissions follow this increasing trend. Indeed, the IMO reported a 9.3% increase in GHG emissions from ships in 2018, with a particular acceleration observed for CO_2 emissions, which increased by 2.76% (Faber et al., 2020). The IMO estimates that CO_2 emissions will increase by 30% in 2050 compared to 2008, accounting for 17% of global CO_2 emissions (Cames et al., 2015).

In addition to GHG, co-emitted species affect climate and air quality, particularly in coastal and port areas. Corbett et al. (2007) show that ship emissions are a major source of NO_x, and report yearly estimates of 5 – 9.0 Tg, representing 15% of global NO_x emissions. They also represent 4.7 – 6.5 Tg of sulphur oxides (SO_x, mainly sulphur dioxide, SO_2), accounting for 5 – 8% of global SO_x.

For particles, total PM_{10} emissions from ships were estimated at 1.2 – $1.6{\cdot}10^6$ Tg (Corbett et al., 2007). These last two pollutants have direct impacts on air quality, but are also important for the radiative forcing of the global climate. In particular, SO_2 converts quickly to sulfate, which is a major contributor to particle nucleation. Sulfate particles have a brightening effect, and, hence, are climate coolers. However, black carbon, another type of particles emitted by ships, has a warming effect (Bond et al., 2013).

70% of ship emissions occur within 400 km of the coast (Capaldo et al., 1999), where they impact the air quality of densely populated coastal areas. Viana et al. (2014) demonstrated that ships can contribute up to 24% of the annual mean concentrations of NO_x and SO_2 on European coasts. The impact of ship emissions in coastal areas was also demonstrated in Copenhagen, Denmark, where legal limits for NO_x were frequently exceeded due to ships (Saxe and Larsen, 2004).

Ship emissions regulations were set to address these issues. Historically, the IMO adopted the International Convention for the Prevention of Pollution from Ships (MARPOL) in 1973, which was enforced by the 1978 Protocol (IMO, a). This was in response to oil pollution in the sea caused by a series of oil tanker accidents between 1976 and 1977. The first air pollution regulations for ships were added in 1997 in Annex VI of MARPOL, which came into force in 2005. This enforced Emission Control Areas (ECAs) that comprise the Baltic and North Seas, the North American ECA and the United States Caribbean Sea ECA, as presented in Table 1-2. Here, the emissions of NO_x and SO_2 from ships are reduced. PM are indirectly concerned by the SO_2 regulations in ECAs as PM emissions are linked to the SO_2 emissions. In 2005, the Fuel Sulphur Content used by ships in SECAs was limited at 1.5%. In 2008, Annex VI was modified to introduce a more stringent 0.1% FSC limit in SECAs, that was to be achieved by 2020. The same year, the global FSC limit for ships was also reduced to 0.5%, compared to 3.5% prior to this amendment, according to the Resolution MEPC.308(73) (IMO, 2018). The NO_x emissions from ships are controlled by Annex VI of MARPOL, as set out in Resolution MEPC.251(66) (IMO, 2014), which indicates that ships constructed after January 1st 2016 must comply with the most stringent Tier III limits within the ECAs. These limits correspond to a total weighted emission of NO_x, depending on the rated engine speed (n, revolutions per minute, rpm):

- 3.4 g·kWh^{-1} if $n < 130$ rpm,
- $9 \times n^{-0.2}$ g·kWh^{-1} if $130 \leq n < 2000$ rpm,
- 2.0 g·kWh^{-1} if $n \geq 2000$ rpm.

These controls allow an Engine International Air Pollution Prevention (EIAPP) Certificate to be issued, demonstrating that a ship's engine complies with the requirements of the regulation. Finally, the shipping sector CO_2 emissions sector needs to decrease by half by 2050 compared to 2008 levels, in order to meet IMO goals (IMO, 2018). Since their enforcement, a wide majority of ships seem to comply with these regulations, as reported in the Southern North Sea (Van Roy et al., 2022b, 2023), and positive impacts on public health were observed. Decreases in premature mortality and morbidity from $PM_{2.5}$ of ships have already been observed, highlighting the benefits of regulating emissions from shipping (Sofiev et al., 2018).

Table 1-2: *Emission Control Areas (ECAs) set by the Annex VI of MARPOL, adapted from the IMO IMO (b).*

Area	Pollutants	Adoption date	Enforcement date	Effective date
Baltic Sea	SO_2	September, 26th 1997	May, 19th 2005	May, 19th 2006
	NO_x	July, 7th 2017	January, 1st 2019	January, 1st 2021
North Sea	SO_2	July, 22nd 2005	November, 22nd 2006	November, 22nd 2007
	NO_x	July, 7th 2017	January, 1st 2019	January, 1st 2021
Northern America	SO_2 + PM	March, 26th 2010	August, 1st 2011	August, 1st 2012
	NO_x			January, 1st 2016
US Caribbean	SO_2 + PM	July, 26th 2011	January, 1st 2013	January, 1st 2014
	NO_x			January, 1st 2016

There are two ways in which ships can comply with the SO_2 and NO_x regulations within ECAs. Regulation 14 of the IMO recognises two methods: the primary method avoids the formation of pollutants, while the secondary method removes them prior to exhaust. The primary method is applied by ships using low-sulphur fuel, for example. Prior to the recent regulations, most ships in international waters used Heavy Fuel Oil (HFO), also referred to as Residual Fuel Oil (RFO), which has an FSC of 0.83 – 3.15% (Lack and Corbett, 2012), which is higher than the 2020 global limit of 0.5%. Therefore, fuels with a lower FSC are used to comply with the regulations, such as diesel fuels like Marine Gas Oil (MGO) or Marine Diesel Oil (MDO), or Light Fuel Oil (LFO). These have an FSC of less than 0.01 – 0.1%, leading to a 10 – 15% reduction and a 13 – 30% decrease in PM and BC, respectively, when switching from HFO to MGO (Petzold et al., 2011). Biomass fuels, such as biodiesel derived from palm oil, animal fat, soya bean oil or sunflower oil, can also be used to comply with FSC regulations (Petzold et al., 2011). The secondary method involves using after-treatment devices such as Selective Catalytic Reduction (SCR), which effectively reduce NO_x emissions from catalytic processes. In addition, SCR was found to reduce the SOA formation potential of ship emissions (Karjalainen et al., 2022). SO_2 emissions are notably reduced when ships use scrubbers, such as wet scrubbers, which dilute SO_2 to transform it into sulphurous acid:

$$SO_2 + H_2O \longrightarrow H_2SO_3, \tag{1.25}$$

therefore removing SO_2 from the exhaust. There are two types of wet scrubber: the open-loop scrubber, which discharges the scrubber water into the sea, and the closed-loop scrubber, which recycles the scrubber water (García-Gómez et al., 2023; Le Berre et al., 2025).

Any solution used to remove pollutants prior to exhaust must comply with Resolution MEPC.259(68) (IMO, 2015). It has been proven that using the combination of SCR and scrubbers effectively reduces SO_2, NO_x and PM emissions in line with ECA regulations (Lack and Corbett, 2012; Fridell and Salo, 2016; Jeon et al., 2023).

As emissions from ships continue to evolve in response to regulatory changes and new practises, it is crucial to thoroughly characterise them in order to accurately assess their impact in coastal areas, where human exposure is the most significant. VOC emissions in particular deserve close attention, as they become relatively more prominent compared to regulated pollutants such as SO_2 and NO_x, especially when low-sulphur fuels or after-treatment technologies are employed.

1.2.b Volatile Organic Compounds emissions by ships

While most studies focused on emissions of SO_2, NO_x or CO_2, less studies report VOC emissions of ships in various locations in the world, yet, the VOC impact from ships on the exposure of populated coastal areas was demonstrated in locations such as Shanghai, China (Feng et al., 2019), the Ionian Sea, southern Italy (Lonati et al., 2010) and the Candarli Gulf, Turkey (Deniz et al., 2010). Some studies report total VOC emissions (NMVOCs) or hydrocarbons (HC) without speciation of VOCs (Dalsøren et al., 2008; Eyring et al., 2010; Fan et al., 2016; Alver et al., 2018; Grigoriadis et al., 2021; Warneke et al., 2014). However, speciation of VOCs is important for the estimation of their impact, not only directly on human health, especially for the formation of secondary pollutants.

Different approaches are used to derive information on VOC speciation from ships. Agrawal et al. (2010) measured speciated VOC emissions using Gas Chromatography (GC) from samples taken at the stack of container ship running on HFO, whereas Zhang et al. (2024) collected VOC from the exhaust stacks of various ships in canisters then analysed the samples off-line using the GC/MS methodology TO-15 (EPA, 1999). The GC-MS was also used by Huang et al. (2018) who performed on-line measurements of VOC on a bulk carrier on various loads. Particularly at berth and upon arrival or departure, this ship used low-sulphur fuel (FSC 0.38%) to comply with the Chinese legislation (maximum 0.5% in ports). The mentioned studies reported Emission Factors (EFs) which represent the quantity of pollutant emitted by the consumption of one unit of fuel, and were able to create VOC profiles for shipping. Figure 1-12 shows a comparison of these EFs for these studies. They indicate that OVOCs are the most emitted species according to the EFs of acrolein and acetone. The comparison also highlights the differences in emissions between ships of different types or in different navigational phases. For example, the EFs of the outgoing bulk carrier in Huang et al. (2018) are higher for all compounds than its emissions at berth. They indicate that this may be linked to the ship's engine optimisation for HFO use, resulting in less efficient LSF combustion in the sulphur-regulated port and higher EFs during manoeuvring. The cruising container ship studied in Agrawal et al. (2010) displays lower levels of benzene, toluene, m&p-xylenes, and ethylbenzene than the Ocean-Going Vessel (OGV) studied by Zhang et al. (2024), but lower o-xylenes values. Xiao et al. (2018) reported a ship VOC emission profile from a ship using diesel in the Jingtang Port, China, which is presented in Figure 1-13.

The study did not measure OVOCs, allowing the main contributors to the non-oxygenated VOC fraction of total VOC emissions from various ships to be identified: benzene, toluene, and alkanes (n-heptane, n-octane, and n-nonane).

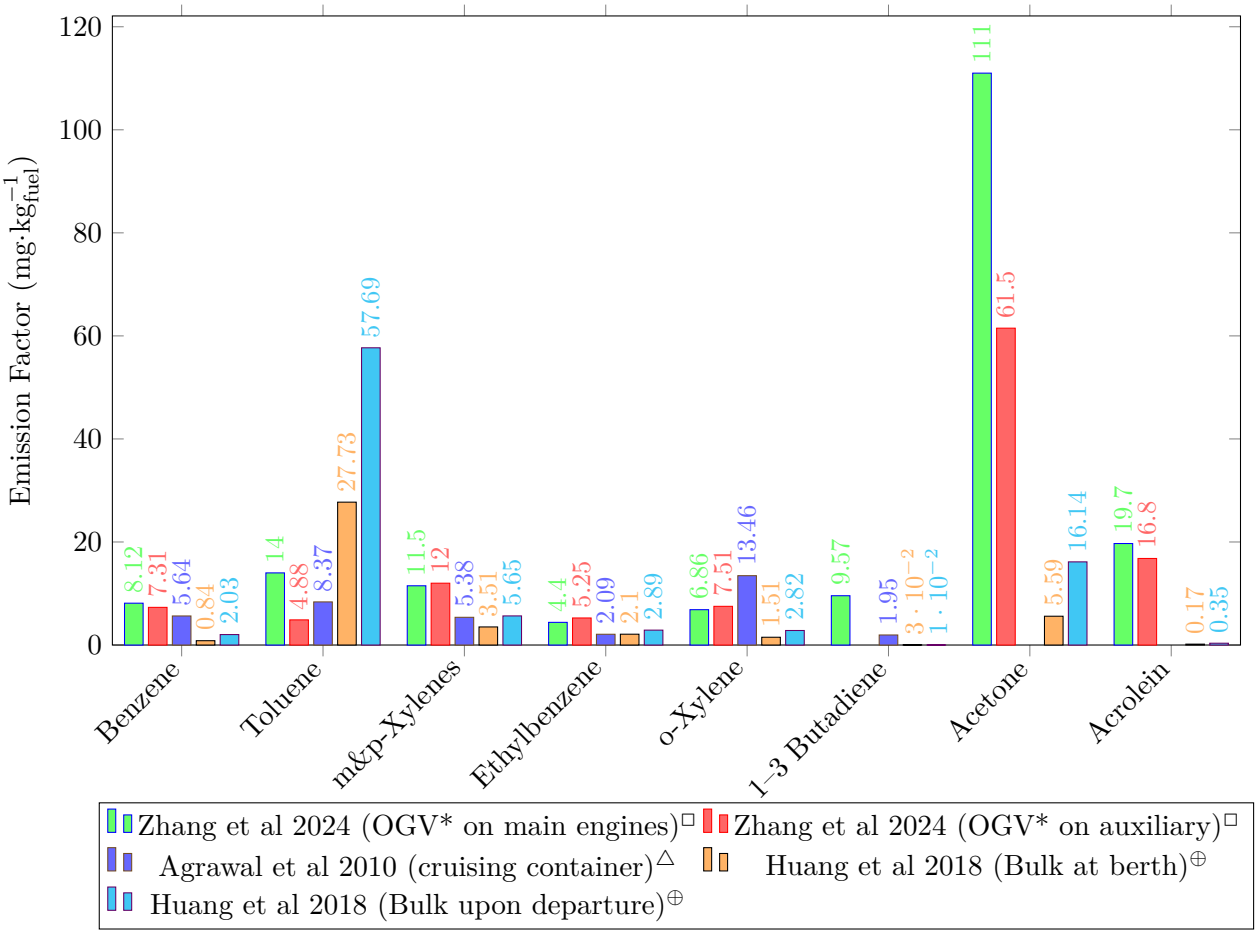

Figure 1-12: *Speciated VOC profiles reported by studies. *OGV; Ocean-Going Vessels, (□) Off-line GC/MS analysis from canisters, (△) On-line GC measurements, (⊕) On-line GC-MS measurements.*

More recently, the SCIPPER project (Shipping Contributions to Inland Pollution Push for the Enforcement of Regulations[1]) examined shipping emissions using stack measurements during a campaign on a ferry travelling between Kiel (Germany) and Gothenburg (Sweden), which is located within the Baltic Sea ECA, during the C2 campaign (Timonen et al., 2022). They measured VOCs on-line by Proton-Transfer-Reaction Mass Spectrometry (PTR-MS, see Section 2.2.b) and GC and report speciated VOC EFs as shown in Figure 1-14 for C_6 – C_{10} compounds (Figure 1-14a), C_2 – C_6 (Figure 1-14b) and OVOC (Figure 1-14c). Compared to other studies, the benzene EF equals that reported for a cruising tanker using HFO fuel by Agrawal et al. (2010). However, the toluene EF reported by Timonen et al. (2022) is much lower than in all other studied in Figure 1-12.

[1]https://www.scipper-project.eu

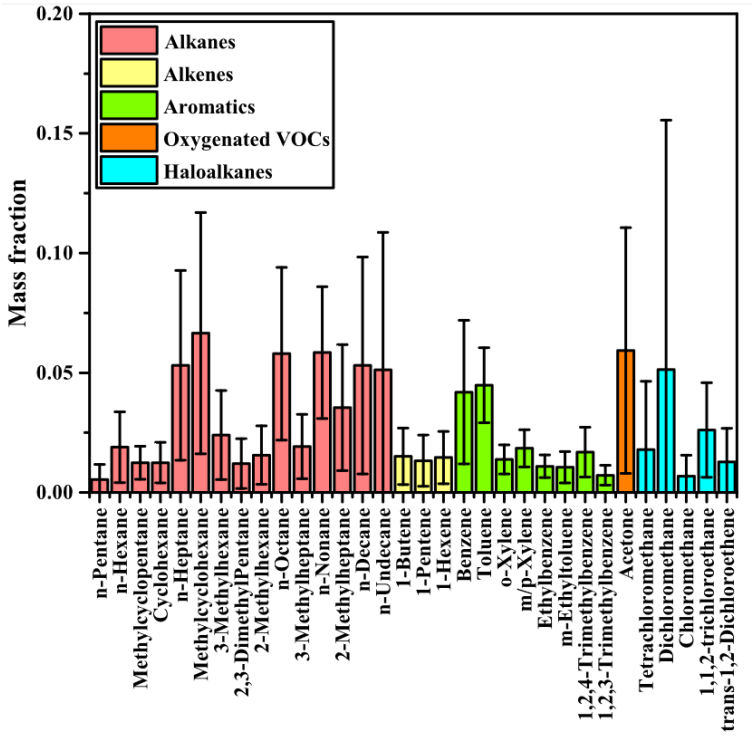

Figure 1-13: *VOC profile from observations of ships at berth in the Jingtang Port (Xiao et al., 2018).*

The SCIPPER campaign confirms that OVOCs are a major contributor to VOC emissions from ships, even when measured at the stack, with formaldehyde and acetic acid accounting for a significant proportion of the reported compounds. This study also presents EFs under different sailing conditions, namely with and without the use of SCR (urea) to remove NO_x, with different fuel types and for different engine loads. Higher emissions of non-oxygenated VOC were obtained at low load (10%) and higher emissions when Marine Gas Oil (MGO) is used compared to methanol. Methanol is an alternative fuel with lower carbon content than other conventional fuels such as MGO, explaining the discrepancies observed for VOC EFs (Grigoriadis et al., 2021; Fridell et al., 2021). According to Figure 1-14c, EFs of OVOCs show less variation across the different loads and after-treatment for each fuel used. Particularly, the use of an urea-SCR as used by (Timonen et al., 2022) is expected to reduce the amount of VOC emitted, with a particular decrease for benzene, styrene, ethylbenzene and some OVOCs like acetaldehyde, acrolein and acetone (Jiang et al., 2010; Shah et al., 2011), the main contributors observed by Huang et al. (2018) and Zhang et al. (2024). These findings emphasise the significant variability in VOC emissions depending on fuel type, engine load and after-treatment technologies. Such variability underlines the importance of conducting field measurements in order to capture real-world conditions and emissions, particularly in port environments, in order to highlight the operational context, as performed by (Diesch et al., 2013) in the banks of the Lower Elbe, Germany, in the Rotterdam Port, Germany (Alföldy et al., 2013) or in the harbour of Helsinki, Finland (Pirjola et al., 2014), as examples.

(a) C_6 – C_{10} *VOC EFs at the stack of the ferry.*

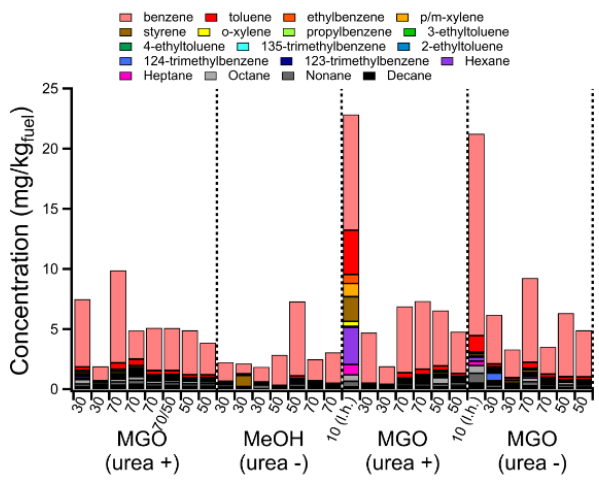

(b) C_2 – C_6 *VOC EFs at the stack of the ferry.*

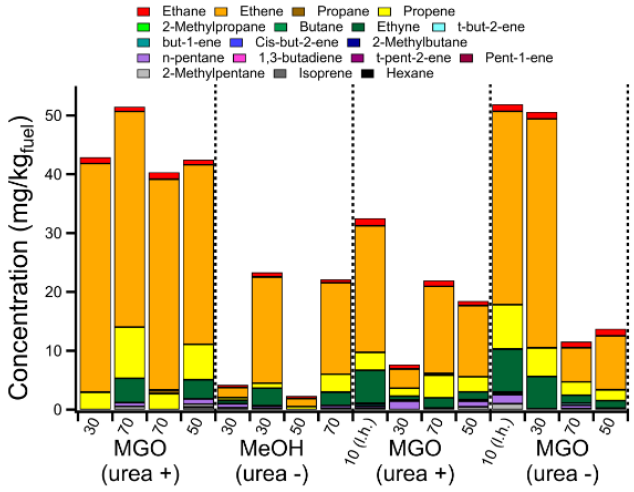

(c) *OVOC EFs at the stack of the ferry.*

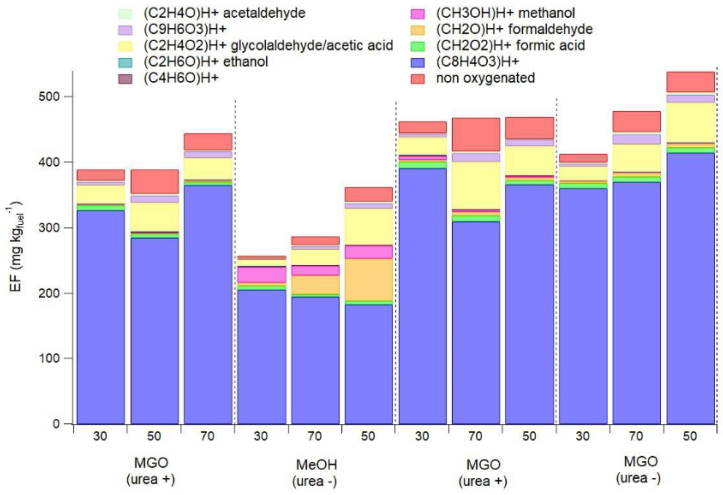

Figure 1-14: *From Timonen et al. (2022): VOC EFs reported in the SCIPPER C2 campaign according to the load, the fuel used and the additional of urea (+, on, -, off).*

Studies that examined VOCs emitted by ships from land-based measurements are rarer in France. One recent study reported speciated VOCs from ships in the harbour of Marseille. (Le Berre et al., 2025). At the time of the measurements, Marseille was not situated in an ECA zone, and only ships at berth for more than two hours had to comply with the ECA sulphur limit (0.1% by mass). Since, the Mediterranean Sea has been classified as a SECA in May 2025. Le Berre et al. (2025) measured the EFs of multiple compounds, including metals and organic aerosols. However, the levels of most VOCs were too low to calculate EFs and only the EFs for summed xylenes (C_8H_{10}) are reported.

These results highlight a gap in the literature: few studies have combined GC and PTR-MS to investigate ship emissions, and even fewer have performed land-based measurements. However, such an approach is essential for evaluating the evolving emission profiles of ships in the context of new practices. In particular, land-based studies offer a representative and operational perspective on the real-world impact on port cities, where population exposure is most acute.

1.3 State-of-the-art of VOCs in Dunkirk

1.3.a Overview

The Directorate for the Environment, Planning and Housing of Hauts-de-France (Grandjean and Tapadinhas, 2019; Labit and Grandjean, 2021) publishes reports on industrial emissions of VOCs in the region. The 2021 report indicates that the industries emitting the most VOCs were textiles, surface treatment and metallurgy. Particularly, 3 out of the 47 establishments responsible for 80% of VOC emission in the Hauts-de-France region are present in Dunkirk (Labit and Grandjean, 2021).

The Urban Community of Dunkirk (UCD) is located in the Hauts-de-France region and comprises 17 cities, with a total population of 192,000 inhabitants in 2021 across an area of 300 km^2. The autonomous harbour of Dunkirk is the third largest port in France in terms of goods (Bauer, 2025) and the seventh largest in Europe. The harbour covers an area of 7,000 hectares and has 120,000 m^2 of storage space.

At the regional scale, the Regional Network for Air Quality Monitoring (AASQA) of Hauts-de-France (Atmo Hauts-de-France[2]) measures concentrations of regulated pollutants (SO_2, NO_2, NO, PM_{10}, BTEX) to assess population exposure and potential guideline concentration exceedances. Throughout 2019, they conducted a study in the cities of Mardyck and Grande-Synthe, to the west of Dunkirk and at the heart of the Dunkirk industrial area, near the Versalis chemical production site and the Total Flandres petrochemical storage facility (Saison, 2020). Overall, guideline levels were respected, except for three hourly levels of SO_2 that occasionally exceeded the limit value of 300 $\mu g \cdot m^{-3}$ and seven that exceeded 100 $\mu g \cdot m^{-3}$, showing that the industries are a prompt hotspot of SO_2 in Dunkirk. However, the trend in hourly levels for all pollutants demonstrates the influence of these industries, which produce occasional peaks in concentration. This influence is particularly evident for benzene and toluene, whose concentration peaks reflect a strong industrial contribution. These observations call for a closer examination of VOC levels and their specific characteristics in the Dunkirk area.

1.3.b Sources of VOCs identified in Dunkirk

Various studies have confirmed the influence of industries on VOC concentrations in Dunkirk. For example, the study of regulated pollutants (SO_2, PM_{10}, NO_x) has highlighted the importance of the wind regimes in dispersing the pollution caused by industrial activities towards the North Sea (Rimetz-Planchon et al., 2008). In addition, Badol et al. (2008a) used a Chemical Mass Balance (CMB) model and reported that the industrial sources can contribute up to 70% to VOC concentrations, particularly when their receptor site was downwind of oil refineries, which represent 40% this industrial contribution. In other wind sectors, its contribution was reduced to 2%, highlighting the influence of wind on the exposure of episodic pollution.

[2] https://www.atmo-hdf.fr

The VOCs contributing most to the refinery source were ethane, ethylene, propene, and alkanes (2-methylpentane, iso-/n-pentane and n-hexane). Roukos et al. (2009) approached VOC studies by spatialising the VOC measurements in Dunkirk, and confirmed that the industrial sector contributed to 75% of the VOC emissions, the main contributor was the hydrocarbon cracking industry, which had high BTEX (Benzene, Toluene, Ethylbenzene, Xylenes) concentrations. Recently, Farhat et al. (2024) showed that the mixing ratio of terpenoids increased significantly downwind of industrial plumes during a campaign that occurred in 2014. In other wind sectors, the contribution of industry may decrease, leading to an increase in the importance of other sources, such as traffic exhaust, that contributes up to 40% in all other wind directions and represents the highest observed contribution of VOCs in Badol et al. (2008a). The VOCs observed in traffic exhaust in Dunkirk were ethylene, toluene, m-/p-xylenes, isopentane, benzene, propene and acetylene. Concentrations of long-lived VOCs such as ethane may be explained by natural sources or remote sources, while fuel evaporation sources are mainly composed of butane and iso-/n-pentane.

Meteorological factors are a key determinant of the VOC concentrations in Dunkirk. In addition, atmospheric turbulence influences the dispersion and concentration of VOCs (Xiang et al., 2012). Seasonal variability further shapes the observed profile, with higher influences from anthropogenic sources in winter and from biogenic and long-distance sources in summer (Badol et al., 2008a; Roukos et al., 2009).

Although industrial sources were shown to be strong contributors to the total VOC burden in Dunkirk, shipping might be an overlooked source. Indeed, Xiang et al. (2012) noted that some outliers strongly contributed to a emission profile, in particular from 2,2-dimethylbutane, 2-methylpentane and 2,3-dimethylbutane, and hypothesized that this could be linked to the passage of ships through channels. Other studies however did not detect the influence of shipping in the VOCs measured, which can for some be explained by sampling sites away from shipping sources (Roukos et al., 2009; Badol et al., 2008b). The lack of detailed information on VOC emission profiles from ships in Dunkirk, given the significance of shipping activities here, highlights a critical gap in current regional emission inventories.

1.3.c Regional emission inventories : focus on VOC speciation of shipping

As mentioned above, EFs are a metric that characterise emissions based on energy consumption in the industrial and transport sectors. Generally, the emission factors, expressed per unit of fuel consumption or per unit of power, are multiplied by the activity of the source (e.g. number of cars, fuel volume purchased by industries, ship traffic) to obtain its emission inventory. Various emission inventories exist, differing in the number of sources described and the EFs used, particularly for shipping. Some of the most widely used inventories are organised by the US Environmental Protection Agency (EPA, 2022), TNO in the Netherlands (Denier van der Gon and Hulskotte, 2010) or CITEPA in France (CITEPA, 2022a).

French regional emission inventories for transport, and specifically shipping, are reported by the AASQAs, which uses the EFs from the OMINEA database of CITEPA (CITEPA, 2022b), combined with a methodology to estimate ship activities that is defined by the European Monitoring and Evaluation Programme (EMEP) (De Lauretis, 2023). Briefly, the specific stages of a ship's route within a harbour are considered, as illustrated in Figure 1-15. These phases are assigned based on the times of arrival and departure, the destination and origin ports, and the location of the docks. Furthermore, weighting factors are applied depending on the type of ship, its motorisation or its equipment. More details are given in the Central Laboratory for Air Quality Monitoring guide for emission inventories (LCSQA, 2018).

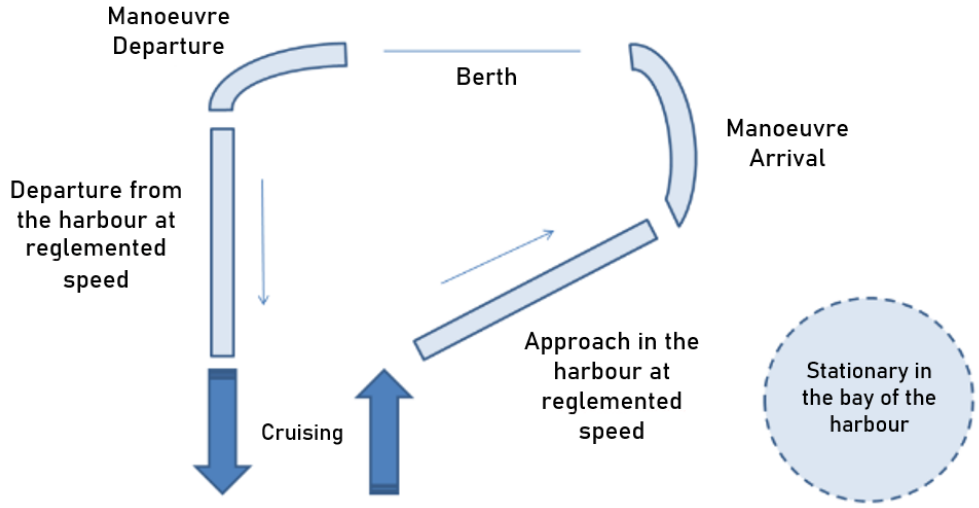

Figure 1-15: *Stages of ship journey in harbours taken into consideration for the regional emission inventories, adapted from the LCSQA (2018) guide.*

Finally, the total calculated activity is multiplied by the EFs that are provided by either the EMEP or by CITEPA via its OMINEA database (CITEPA, 2022b) for ships. Regarding VOCs, both inventories only report total NMVOCs and no speciation is found in the EFs. Furthermore, NMVOC values haven't changed since 2010 in the case of OMINEA as can be seen in Figure 1-16. Therefore, the regional emission inventories face a challenge in correctly assessing VOC emissions from ships, because they do not take speciation into account, which hinders the correct assessment of their chemistry. Furthermore, the EFs haven't evolved in response to changes in ship emission regulations, highlighting the importance of characterising ship emissions of speciated VOCs in regulated harbours.

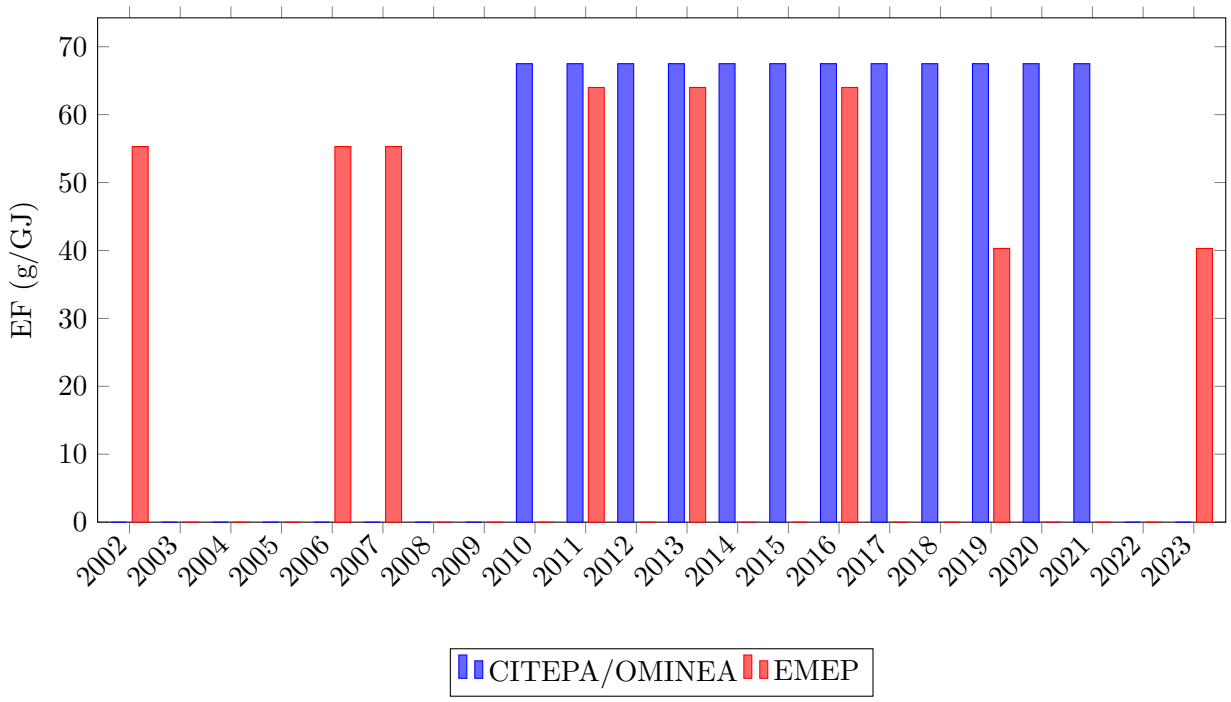

Figure 1-16: *Evolution of total NMVOC EF for the datebase of EMEP and CITEPA via OMINEA.*

The TrACE website (Air-Climat-Energy Trajectories[3]) was developed by Atmo Hauts-de-France and the Resource Center for Sustainable Development (Cerdd) to report the regional emissions inventories of the Hauts-de-France region. More particularly for the Urban Community of Dunkirk, the transportation sector apart from automobile accounted for 6.2% of the NMVOC emissions of 2021, as seen in Figure 1-17, representing 2,956,561 kg. The same year saw the contribution of road transport contribute 1.7%. The contribution of ship emissions to the 2021 inventory results from an increase of the importance of this sector that accompanied a decrease of total VOC emissions in Dunkirk, as presented in Figure 1-18.

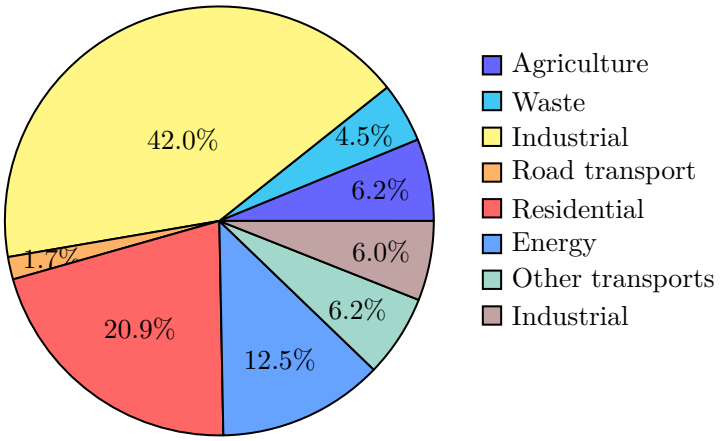

Figure 1-17: *Pie chart of the sectors contributing to NMVOC emissions in the Urban Community of Dunkirk in 2021, adapted from the TrACE website https://www.trace-hdf.fr/air. The remaining 0.2% are the contribution of tertiary activities on NMVOC emissions.*

[3]https://www.trace-hdf.fr/air

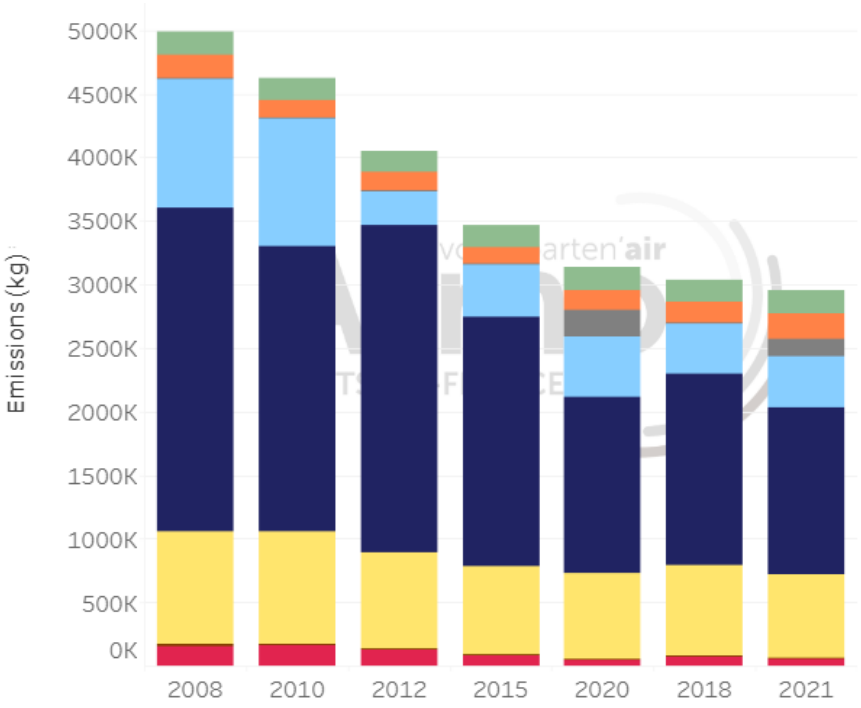

Figure 1-18: *Evolution of the VOC emissions by sector of activity in the Urban Community of Dunkirk from 2008 to 2021. Green: Agriculture; orange: non-road transport; light blue: Energy; Dark blue: Industrial; Yellow: Residential; red: Road transport.From https://www.trace-hdf.fr/air*

1.4 Scientific questions

The Dunkirk harbour is the third largest port in France. It belongs to the Northern and Baltic Seas Emission Control Area (ECA), where emissions of NO_x and SO_2 are regulated within a framework of constantly evolving regulations. VOC studies show the strong influence of industrial activities, notably from metallurgical and petrochemical industries, as well as road traffic. However, some studies have highlighted the importance of VOCs emitted by ships in Dunkirk without providing clear identification or chemical profiles. This forms a gap in the literature that will be addressed in this thesis. This work aims to identify the VOCs emitted by ships in the Dunkirk harbour, in light of new emission regulations and emerging technologies that aim to reduce port emissions. Moreover, VOC speciation will be addressed to accurately assess the impact of shipping emissions. The questions addressed in this thesis are:

- How to identify VOC ship emissions amongst other VOC sources an industrial harbour ?
- What are the VOC emissions of ships under the new sulphur regulations ?
- What is the contribution of ships to the total VOC concentrations in an industrial harbour ?
- How does the VOC emissions of ships in Dunkirk compare to the other harbours ?

CHAPTER 2

Sites, instrumentation and methods of analysis in the study area

To address the knowledge gaps identified in the previous chapter regarding VOC emissions by ships in harbours, a field campaign was conducted in Dunkirk harbour in September 2022. This campaign combined high-resolution time measurements with chemically resolved VOC measurements. A second campaign occurred in 2023 in Le Havre, with only the chemically resolved measurements of VOCs. This second chapter describes the instruments and analytical tools used for this work, with a focus on the campaign of Dunkirk, and details the application strategy employed to achieve the objectives defined in the previous chapter.

2.1 Site location and instrumentation

2.1.a Overview

The intensive field campaign took place in Dunkirk, northern France, from 2nd to 29th September, 2022. As shown in Figure 2-1, the campaign site was located in the western harbour, approximately 13 km west of the center of Dunkirk. Refinery, petrochemical, metallurgy and chemical storage infrastructures are located in the surroundings, as shown in Figure 2-2, representing the classified installations for the protection of the environment (ICPE) sites of Dunkirk. A petrochemical site specialised in the production of ethylene and polyethylene (Versalis) is located 5 km E-NE from the site. To the east of the site is the Total Flandres oil depot, and further towards the city is a refinery (Société de la Raffinerie de Dunkerque) at the entrance to the eastern port terminal. Further south (SE), an alcohol production facility is located (Ryssen Alcools). To the West and to the East of the site, metallurgical activities were established, with the presence of two companies to the West (Befesa Valera and Aluminium Dunkerque) and ArcelorMittal to the East. All these industrial activities influence pollutant levels in arriving at the site.

The measurement site was installed on a roll-on-roll-off (RoRo) berth on the water, between the docks of two ferry lines as shown in Figure 2-1. The main line was the Dunkirk to Dover (England) route operated by DFDS. The dock for this line was located 230 m north of the site, as indicated by the green star on Figure 2-1d. This line comprises three sister-ferries that depart every two hours during the week, with fewer departures at weekends, according to the timetable in Table 2-1. The three passenger/RoRo ships (Dover Seaways, Delft Seaways, Dunkerque Seaways, Figure 2-3) were built around the same time (Dunkerque in 2005 and Dover and Delft in 2006) by the same manufacturer. They are each equipped with four medium-speed, four-stroke diesel engines (MAN L48/60B, 9,200 kW) and have no exhaust after-treatment system. In order to comply with the SECA regulations in the North and Baltic Seas, they use low-sulphur fuel such as Marine Diesel Oil (MDO), also known as Marine Gas Oil (MGO), which has a fuel content of less than 0.1% (Petzold et al., 2011; Zhou et al., 2019). Approximately 300 m to the west of the site was a dock for the ferry line between Dunkirk and Rosslare (Ireland), which was also operated by DFDS. According to the timetable in Table 2-1, there were five departures per week, on Monday, Wednesday, Thursday, Friday and Sunday, at night (9 pm and 1 am) or early in the morning (5 am). Further south of the site, there were several docks for various container ships.

Table 2-1: *Departure timetable of the Dunkirk – Dover and Dunkirk – Rosslare ferry lines (local time). Adjusted from DFDS (https://www.dfds.com/en).*

Dunkirk – Dover												
Monday – Friday	02:00	04:00	06:00	08:00	10:00	12:00	14:00	16:00	18:00	20:00	22:00	23:59
Saturday	02:00	04:00	06:00	08:00	10:00	12:00	14:00	16:00		20:00		
Sunday			06:00		10:00	12:00	14:00	16:00	18:00	20:00	22:00	23:59
Dunkirk – Rosslare												
Monday											21:00	
Wednesday	00:55											
Thurday			05:00									
Friday											21:00	
Sunday			05:00									

2.1.b Instrumentation

The measuring equipment comprised three mobile laboratories, each operated by a campaign partner: IMT Nord-Europe, Atmo Hauts-de-France (the Regional Network for Air Quality Monitoring of Hauts-de-France) and the Laboratoire Chimie Environnement (LCE, Aix-Marseille Université). Figure 2-4 lists the instruments set up in each laboratory. Each laboratory had its own separate inlet, all of which were mounted on masts at a height of 3 m to effectively capture the ship plumes. The wide range of measured pollutants (VOCs, PM_1/sub-micron aerosol composition and regulated pollutants) allowed for a large and robust basis for the characterisation of ship emissions. The partners of the LCE were responsible for advanced, particle-focused measurements with HR-ToF-AMS and SMPS to assess the sub-micron aerosol composition and the size and mass distributions of aerosols, but these are not of focus in this work and will not be discussed.

The targeted pollutants are summarised in Table 2-2. Ubiquitous and frequently detected gases, namely CO_2, CO and CH_4, were measured using a built-in Cavity Ring-Down Spectroscopy (CRDS, Picarro) deployed by IMT Nord-Europe. Additionally, NO_x were measured using a Teledyne chemiluminescence detector (API 200E) and SO_2 was measured using a UV-fluorescence detector from Envea (AF22E), both deployed, operated and processed by Atmo Hauts-de-France. Similarly, they provided PM data (PM_{10}, $PM_{2.5}$, PM_1) from a FIDAS 200E. IMT Nord-Europe performed the VOC measurements with GC-FID and PTR-ToF-MS directly at the outlet of the sampling line. These measurements are presented in detail in the following section.

Table 2-2: *Key pollutants under focus in this study.*

Compounds	Instrument	Principle	Time resolution
VOCs	Ionicon Analytic PTR-QI-ToF-MS	Proton-Transfer Reaction + Time Of Flight (PTR-ToF)	1 s
	Chromatotec C_6-C_{12}	Gas Chromatography (GC)	60 min
	Perkin-Elmer C_2-C_6	Gas Chromatography (GC)	60 min
CO_2, CO, CH_4, H_2O	Picarro G2401	Cavity Ring-Down Spectroscopy (CRDS)	1 s
SO_2	Envea AF22E	UV-fluorescence detector	10 s
NO_x	Teledyne API 200E	Chemiluminescence detector	10 s
PM_{10}, $PM_{2.5}$, PM_1, PN	Palas FIDAS 200E + SMPS	Optical light scattering	10 s
Wind direction, speed, RH, P, T°	Vaisala WXT520	Ultrasonic signals, capacitive silicon sensor	10 s
Black Carbon	Magee Scientific AE33	Particle optical attenuation	10 s
PM_1 composition	Aerodyne Research Inc. HR-ToF-AMS	High-resolution Time-Of-Flight Aerosol Mass Spectrometer	10 s

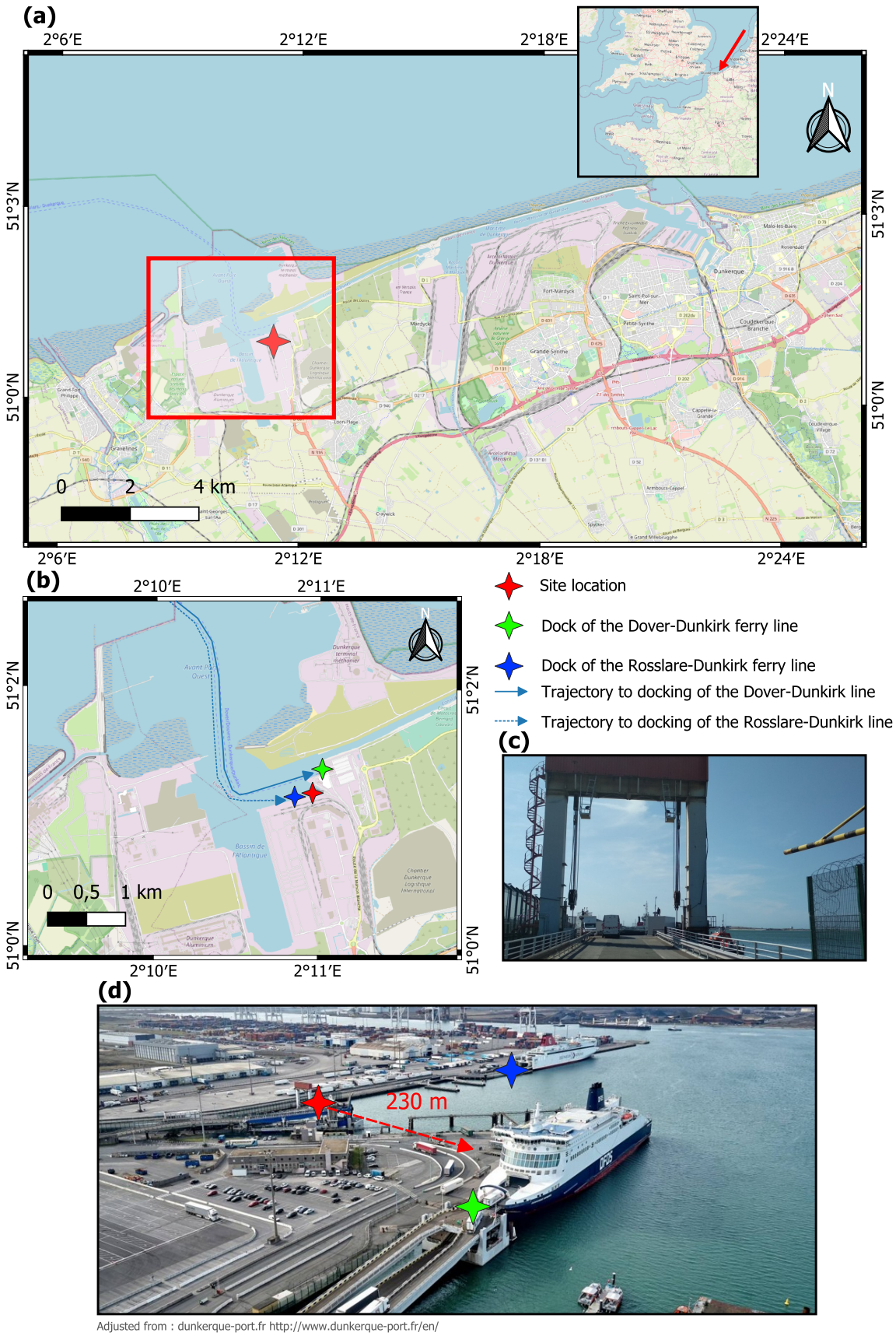

Adjusted from : dunkerque-port.fr http://www.dunkerque-port.fr/en/

Figure 2-1: *(a) Location of Dunkirk in France and site location in the Dunkirk agglomeration; (b) Zoom-in of the western terminal and the ferries' docking trajectories; (c) View of the measurement site; (d) Aerial view of the site showing the docking location of the Dunkirk-Dover ferries.*

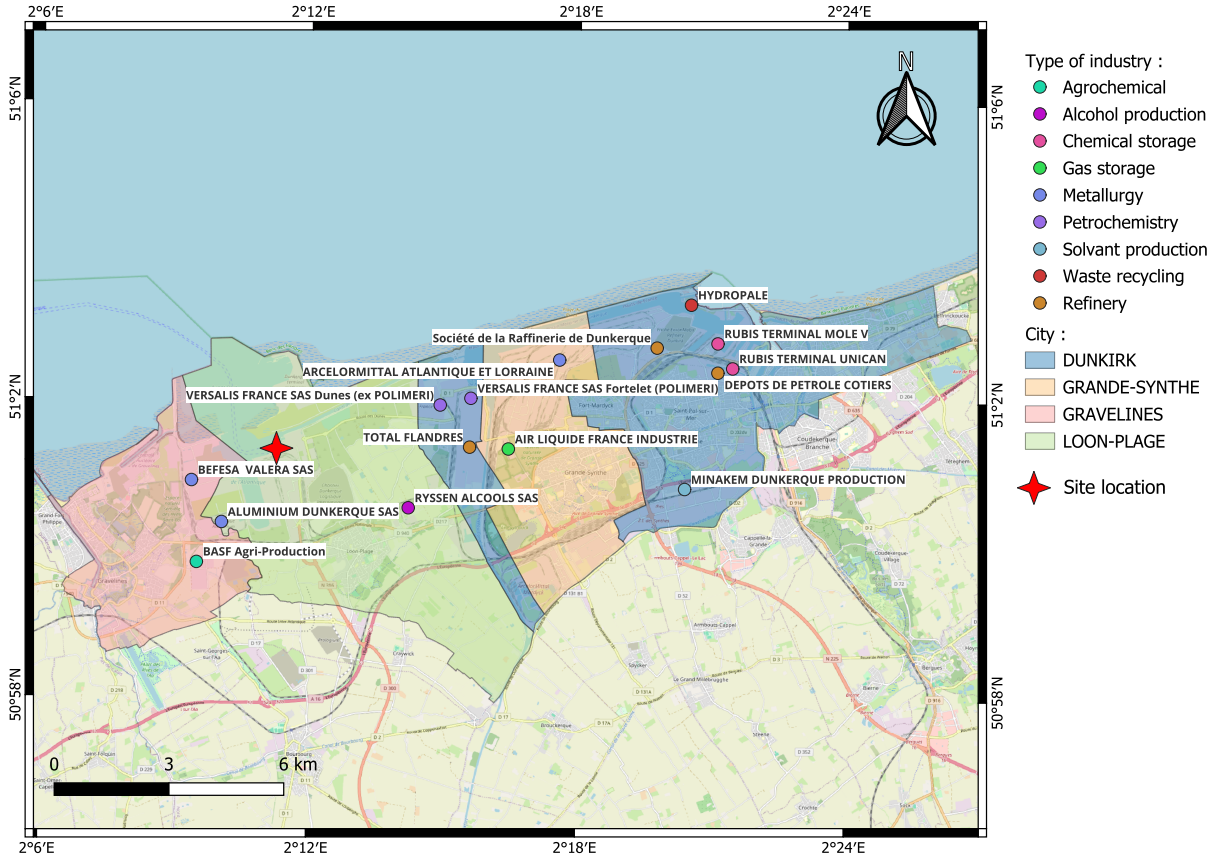

Figure 2-2: *Location of the measurement site in the western terminal in Dunkirk, in perspective of the environmentally classified industries of the agglomeration. Spatialised data were taken from the Dunkirk agglomeration data hub (https://data.dunkerque-agglo.fr/explore). Total Flandres is not a classified infrastructure but was added for comprehensiveness.*

(a) Dover Seaways.



(b) Delft Seaways.



(c) Dunkerque Seaways.



Figure 2-3: *The three ferries (passenger/RoRo ships) operated by DFDS in the Dunkirk to Dover ferry line. Pictures were taken from Vessel Finder (https://www.vesselfinder.com).*



Figure 2-4: *Details on the instruments deployed on site and partners operating them.*

2.2 VOC measurements

This section describes the origin of the VOC data processed in this study. As the campaign occurred prior to this work, this study wasn't involved in the setup of the instruments but the general principles of measurements are reported here with their operation during the campaign.

2.2.a TD-GC-FID

2.2.a.i Principle

Two gas chromatographs (GC) were deployed in the 2022 Dunkirk campaign, namely the Thermo Desorber-Gas Chromatography-Two Flame Ionization Detectors (TD-GC-2FID) from Perkin-Elmer, which measured C_2 – C_9 VOCs, and the TD-GC-FID AirmoVOC from Chromatotec, which measured C_6 – C_{16} VOCs. As both instruments operate in a similar way, their principles of function will be described through the same sequence of steps.

Sampling and capture: Ambient air is sampled and the VOCs contained within it are adsorbed on a sorbent trap, contained at low temperature in the thermo-desorber. The two adsorbents used are Carbopack B, which is used for heavier VOCs (C_5 – C_9), and Carbosieve III, which is used for lighter VOCs (C_2 – C_5). The adsorbents are maintained at a negative temperature to increase the retention of the compounds on the sorbent. Air was sampled at 60 ml/min for 1825 s ($\approx$ 30 min), resulting in a total sampled volume of 1783.2 ml. This step captures the VOCs and pre-concentrates them on the sorbents over 30 minutes.

Desorption and analysis: At the end of the sampling, the trap is heated at 300°C for 240 s to provoke the desorption of the compounds from the trap, that is continuously swept by hydrogen (vector gas). Next, the gases are injected, through a heated injector, in the chromatographic column, where compounds are separated from each other according to their affinity for the stationary phase and their volatility. On the C_2 – C_9 instrument (Perkin Elmer), two column were used in parallel. One chromatographic column (CP Sil 5CB, 50 m × 0,25 mm × 1 µm) is used to separate compounds with more than 6 carbons. A second column (Al_2O_3/Na_2SO_4, 50 m × 0,32 mm × 5 µm) separates compounds with less than 6 carbons. Both end in a distinctive Flame Ionisation Detector (FID).

Quantification: When a compound arrives at the FID, it produces a signal peak occurring at a specific retention time and VOCs can be identified based on their retention time. All peaks of all different compounds form a chromatogram. The specific retention times for each compound are determined using a relative method or a reference compound. Retention times are calibrated based on the chromatograms obtained when passing a gas standard, and a calibration factor (area/ppt) is calculated for each calibrated compound:

$$f_{cal} = \frac{A_i - A_{i,BG}}{C_i}, \tag{2.1}$$

with A_i denoting the area of the peak of the compound i, $A_{i,BG}$ denoting the area of the peak during blank determination and C_i denoting the calibrated concentration.

2.2.a.ii Operation

Each GC was operated with a sampling time of 30 min, after which the sample was analysed over 30 min. The separation was optimized using a temperature program for the GC oven according to Figure 2-5 for the AirmoVOC.

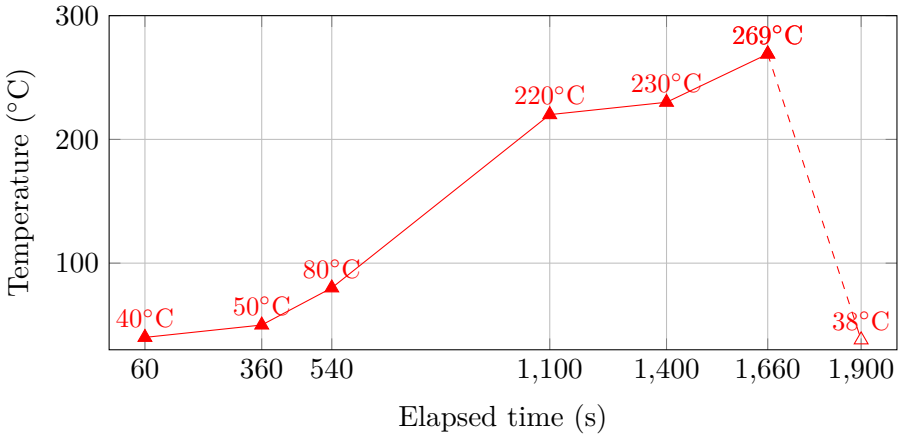

Figure 2-5: *Evolution of the temperature in the oven of the AirmoVOC.*

For the AirmoVOC, the Chromatotec software Vistachrom was used to process the chromatograms and extract the concentrations. Two calibrations were performed on 1st and 28th September using a gas standard from the National Physical Laboratory (NPL), the composition of which is presented in Appendix AT1. For each calibration, three chromatograms were obtained to calculate a mean area and a standard deviation, shown shown in Figures 2-6a and 2-6b. Overall, the two calibrations show good agreement, with low deviation for each calibration for the C_6 – C_{16} AirmoVOC. The C_2 – C_9 Perkin-Elmer shows slightly different areas for the two calibrations, with increased standard deviation for the heavier species, from isooctane to 1,2,3-trimethylbenzene. This is much higher than for the same species in the AirmoVOC. To account for the variation in area for the two gas chromatographs (GCs), the mean area was considered for each species and the mean squared error was calculated.

(a) *Calibrations of 1st and 28th September for the AirmoVOC, Chromatotec, TD-GC-FID, C_6 – C_{16}.*

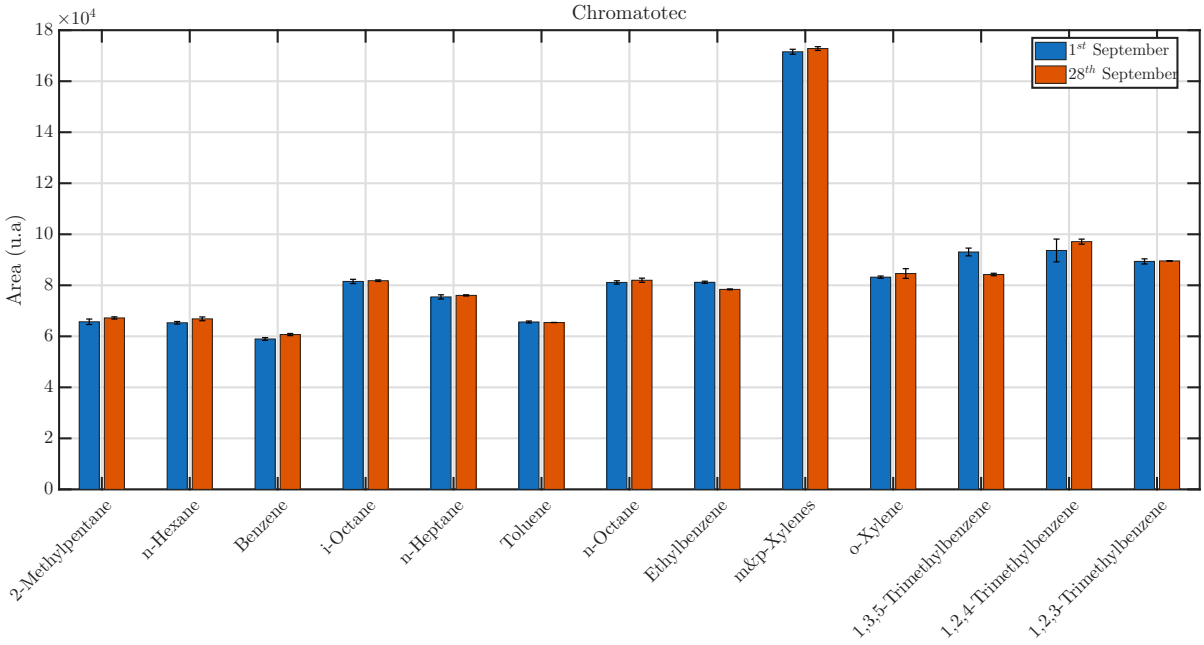

(b) *Calibrations of 1st and 28th September for the Perkin-Elmer TD-GC-2FID, C_2 – C_9.*

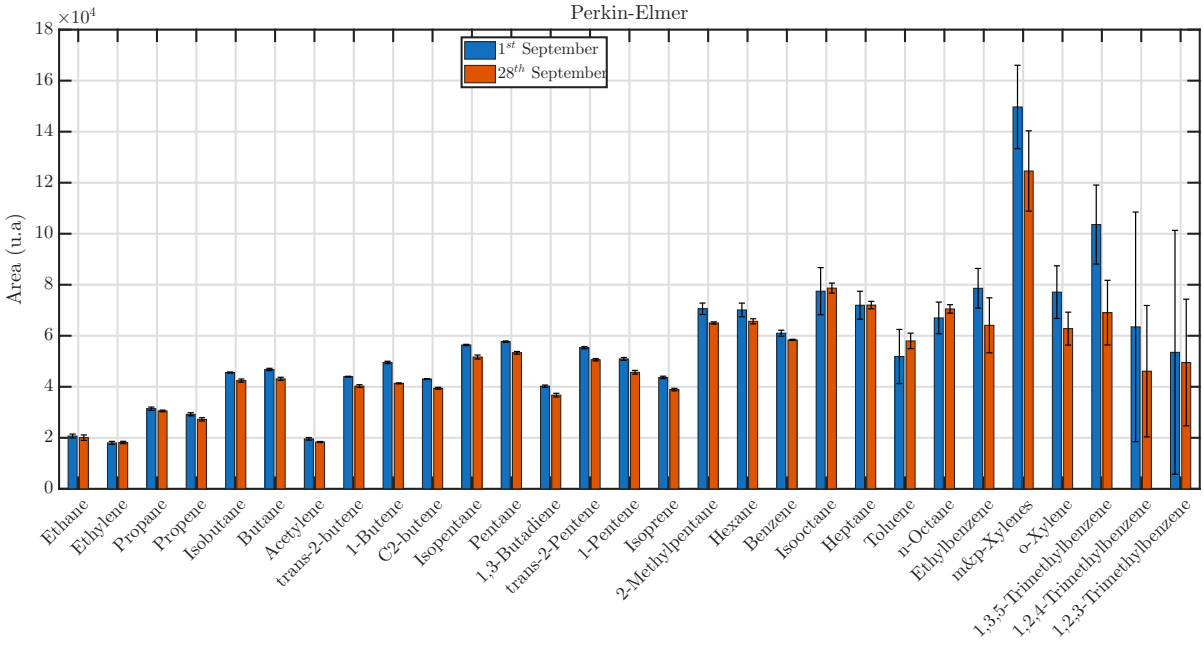

Figure 2-6: *Calibrations of the two GC during the Dunkirk 2022 campaign.*

Calibration factors (area/ppt) were determined using the calibrated areas and concentrations. For non-calibrated compounds, a reference compound must be identified based on similarities in functional groups or behaviour. For that, the Effective Carbon Number is used, that depends on the carbon bonds, chemical functionalities and composition of the compound. Table 2-3 shows the coefficient used for calculating the Effective Carbon Number. Then, the conversion factor of the uncalibrated compound is expressed as:

$$f_{uncal} = f_{cal_{ref}} \times \frac{C_{eff}}{C_{ref}}, \tag{2.2}$$

where $f_{cal_{ref}}$ refers to the calibration factor of the compound of reference, C_{eff} refers to the Effective Carbon Number and C_{ref} refers to the Effective Carbon Number of the compound of reference. Once identified, the median relative standard deviation (RSD) of the reference compound is used as the RSD for all observations of the uncalibrated compound. Appendices AT3 and AT4 summarise the calibration factors of all compounds and their respective reference compounds for the AirmoVOC and the Perkin-Elmer respectively.

Table 2-3: *Coefficients used for calculating Effective Carbon Number for uncalibrated compounds.*

Chemical bond	Type	Effective Carbon Number
C–C	aliphatic	1
C∘C	aromatic	1
C=C	olefin	0.95
C≡C	acetylenic	1.3
C=O	carbonyl	0
C–N	nitrile	0.3
O	ether	-1
O	primary alcohol	-0.6
O	secondary alcohol	-0.75
O	tertiary alcohol / ester	-0.25
Cl	2 or more on aliphatic C	-0.12
Cl	on olefin C	0.05
N	primary amine	-0.6
N	secondary amine	-0.75
N	tertiary amine	-0.25

2.2.b PTR-ToF-MS

High time-resolution measurements of VOCs were performed using a Proton-Transfer-Reaction Quadripole-Interface Time-Of-Flight Mass Spectrometer (PTR-Qi-ToF-MS) from Ionicon Analytik (Figure 2-7). This instrument allowed for high time-resolution (1 s), high sensitivity measurements of trace gases (Hansel et al., 1995; Lindinger et al., 1998).

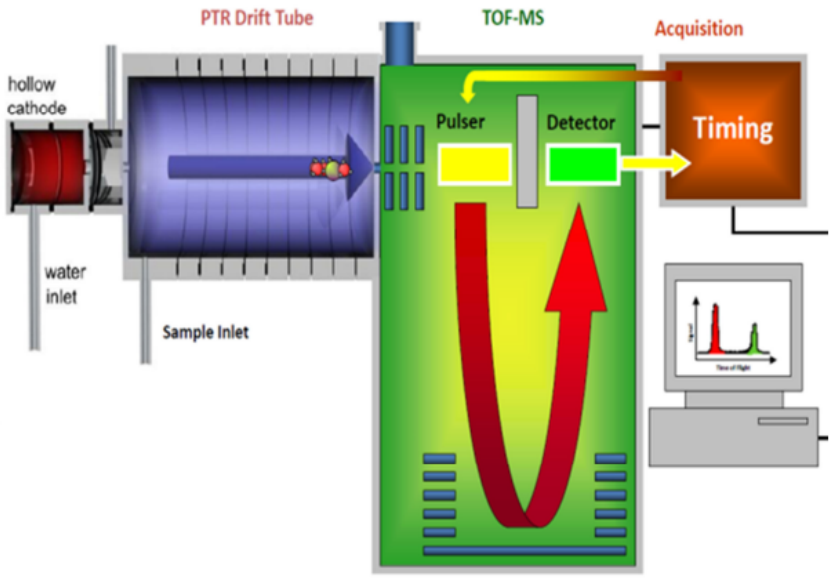

Figure 2-7: *PTR-ToF-MS. Water is drawn into the cathode to produce H_3O^+, then meets an ambient air flow in the drift tube where trace gases are ionised.*

2.2.b.i Principle

The ion source comprises a hollow cathode, in which pure water (H_2O) is softly protonated to form hydronium ion (H_3O^+), which is the proton donor used in our study. At this stage, clusters may form from the water, oxygen and nitrogen contained in the air that comes into contact with the cathode ($H_2O{\cdot}H_3O^+$, O_2^+, NO_2^+, CO_2^+...). The air samples are drawn into the drift tube, where compounds with higher proton affinities than water are ionised by the proton transfer reaction (PTR) process (Equation 2.3):

$$R + H_3O^+ \xrightarrow{k} RH^+ + H_2O, \tag{2.3}$$

with R denoting the reactant gas. Figure 2-8 was produced by Gueneron et al. (2015) and shows the proton affinity of a selection of VOCs. The proton affinity of alkanes is lower than water, therefore, they are hardly detected by this instrument as they are not ionised during the PTR. Details of the PTR-ToF-MS equations are given by de Gouw and Warneke (2007) and reported here. The rate at which the product ions of a given concentration of reactant molecules R, $[RH^+]$, are produced is expressed as follows:

$$[RH^+] = [H_3O^+]_0(1 - e^{-k[R]t}), \tag{2.4}$$

$$\approx [H_3O^+]_0[R]kt, \tag{2.5}$$

with $[H_3O^+]_0$ denoting the initial concentration of H_3O^+ ions, k denoting the reaction rate constant of proton transfer reaction as given by Equation 2.3 and t denoting the time spent in the reactor (Hansel et al., 1995). An electric field E is applied inside the reactor to drive the ions to the outlet.

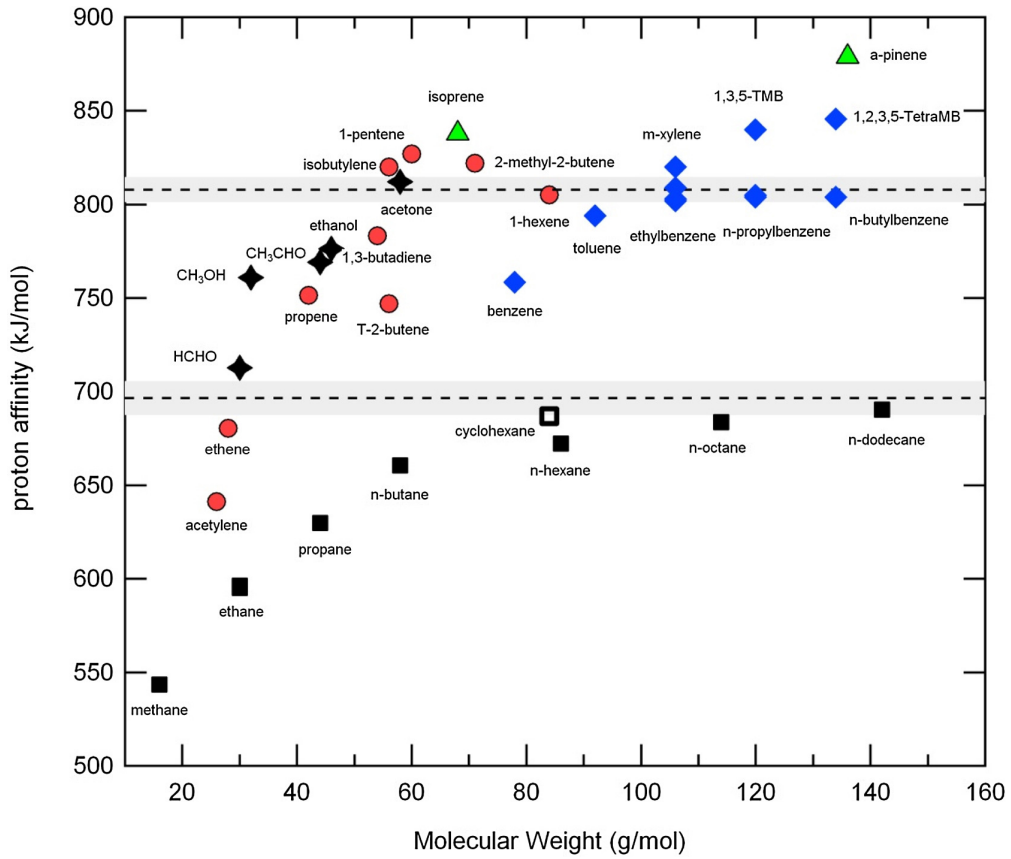

Figure 2-8: *From Gueneron et al. (2015): proton affinity of VOCs found in urban air: alkenes (red circles), aromatics (blue diamonds), alkanes (black squares), OVOCs (black stars), cycloalkanes reported in vehicular exhaust (white squares) and biogenic VOCs (green triangles). The proton affinity of water and the water dimer (first water cluster) are represented in the dashed lines, 691 kJ·mol^{-1} and 808 kJ·mol^{-1} respectively.*

The speed to which the ions are accelerated is expressed as ν_d (Equation 2.6):

$$\nu_d = \mu E, \tag{2.6}$$

where μ refers to the ion mobility and the electric field E is the voltage applied in the reactor per unit of length:

$$E = \frac{U_{drift}}{L}, \tag{2.7}$$

U_{drift} is the voltage inside the reactor and L its length. One can express the reduced mobility μ_0:

$$\mu_0 = \left(\frac{p}{p_0}\right)\left(\frac{T_0}{T}\right)\mu, \tag{2.8}$$

$$\text{with} \begin{cases} pV = nRT, \\ n = \dfrac{N}{N_A}, \end{cases} \tag{2.9}$$

$$\mu_0 = \left(\frac{N}{N_0}\right)\mu, \tag{2.10}$$

with p and p_0 denoting the pressure and standard pressure (1 atm) respectively, T and T_0 denoting the temperature and standard temperature (273.15 K) respectively, N denoting the number of molecules of the gas and N_0 denoting the number of molecules in standard conditions. Equations 2.7 and 2.10 result in:

$$\nu_d = \mu_0 N_0 \left(\frac{E}{N}\right). \tag{2.11}$$

E/N is expressed in Townsend units (1 Td = 10^{-17} V$\cdot$ cm^2) and characterizes the kinetic energy of the ions inside the drift tube. The time spent in the reactor, as defined in Equations 2.4 and 2.5 is then expressed as follows:

$$\Delta t = \frac{L}{\nu_d}, \tag{2.12}$$

$$= \frac{L}{\mu_0 N_0} \left(\frac{E}{N}\right)^{-1}. \tag{2.13}$$

Increasing the voltage in the drift increases E/N, leading to more energetic collisions between the reactants and H_3O^+. This reduces the number of clusters, but increases the probability of ion fragmentation.

The PTR-Qi-ToF-MS comprises a Quadrupole interface (Qi) between the drift tube and the mass spectrometer (ToF-MS). This consists of a quadrupole ion guide that focuses ions more effectively than common lens systems. This way, losses during ion transport after the drift tube decrease, thereby increasing the sensitivity (Sulzer et al., 2014).

In the Time-of-Flight Mass Spectrometer, ion pulses are injected into a flight chamber where they are separated based on the time it takes each ion to reach the detector. The ions are then deflected by a reflector and directed towards a microchannel plate detector (MCP). Through calibration, the time of flight of each ion can be attributed to a mass to charge ratio (m/z), meaning that each ion pulse generates a mass spectrum. According to Equations 2.5 and 2.13, the quantity of analyte R can be expressed as:

$$[R] = \frac{1}{k\Delta t} \frac{[RH^+]}{[H_3O^+]_0}, \tag{2.14}$$

$$= \frac{\mu_0 N_0}{kL} \left(\frac{E}{N}\right) \frac{[RH^+]}{[H_3O^+]_0}. \tag{2.15}$$

Technically, the $[RH^+]/[H_3O^+]_0$ ratio is obtained by the ratio of counts per second (cps) detected by the MCP. This signal depends on the transmission efficiency of the drift tube to the ToF-MS, and the ToF-MS to the MCP, as well as the MCP's detection efficiency.

The total transmission (%) for each RH^+ ion is determined experimentally:

$$T(RH^+) = \frac{i(RH^+)}{[RH^+]}, \tag{2.16}$$

with i denoting raw signal in cps and T denoting the transmission. It leads to:

$$\frac{[RH^+]}{[H_3O^+]_0} = \frac{i(RH^+)}{i(H_3O^+)} \frac{T(H_3O^+)}{T(RH^+)}, \tag{2.17}$$

$$[R] = \frac{\mu_0 N_0}{kL} \left(\frac{E}{N}\right) \frac{T(H_3O^+)}{T(RH^+)} \frac{i(RH^+)}{i(H_3O^+)}, \tag{2.18}$$

according to Equation 2.15. The mixing ratio σ_R can be expressed by taking into account the total gas concentration N defined above with Equation 2.18:

$$\sigma_R = \frac{[R]}{N} \cdot 10^9, \tag{2.19}$$

$$= \frac{\mu_0 N_0}{kL} \left(\frac{E}{N}\right) \frac{T(H_3O^+)}{T(RH^+)} \frac{1}{N} \frac{i(RH^+)}{i(H_3O^+)} \cdot 10^9, \tag{2.20}$$

with σ_R expressed in ppbv (10^9). Equation 2.20 reveals the expression of the sensitivity of the PTR-Qi-ToF-MS for each ion, $S(RH^+)$ (cps·ppbv^{-1}), that gives the value of the mixing ratio σ_R (ppbv) depending on the raw signal $i(RH^+)$ (cps):

$$\chi_R = \frac{i(RH^+)}{S(RH^+)}, \tag{2.21}$$

with

$$S(RH^+) = \left[\frac{\mu_0 N_0}{kL} \left(\frac{E}{N}\right) \frac{T(H_3O^+)}{T(RH^+)} \frac{1}{N} \frac{1}{i(H_3O^+)} \cdot 10^9\right]^{-1}. \tag{2.22}$$

Usually, the sensitivity and raw signals are normalised to 10^6 cps of $i(H_3O^+)$, expressed in units of normalised cps (npcs/ppbv):

$$S(RH^+)_{norm} = \left[\frac{\mu_0 N_0}{kL} \left(\frac{E}{N}\right) \frac{T(H_3O^+)}{T(RH^+)} \frac{1}{N} 10^3\right]^{-1}, \tag{2.23}$$

$$\chi_R = \frac{i(RH^+)}{i(H_3O^+)} \frac{10^6}{S(RH^+)_{norm}}. \tag{2.24}$$

2.2.b.ii Operation

The PTR-Qi-ToF-MS sampling line was positioned at the inlet of the mast of IMT Nord-Europe laboratory. During the campaign, the PTR-ToF-MS did not only measure VOCs; SVOCs and organic aerosols were analysed using the CHARON inlet (CHemical analysis of AeRosols ON-line, Ionicon Analytik), that will not be discussed in this study. However, they did impact the measurement operation of the PTR-ToF-MS according to Figure 2-9. First, VOCs were measured for 2 hours and 40 minutes, then the blank gas phase measurements were performed for 20 minutes.

Next, the particle blanks were measured using a High Efficiency Particulate Air (HEPA) filter for 40 minutes, followed by a measurement of the particles with the CHARON inlet for 1 hour and 20 min (Figure 2-9a). These timings were kept from 1st until 8th September, when the cycles changed according to Figure 2-9b to allow for slightly shorter blank measurements of VOCs and particles.

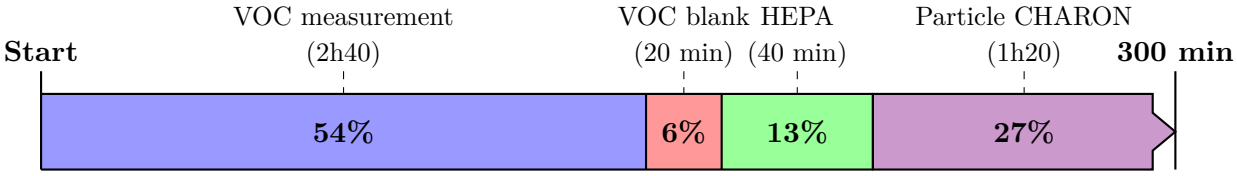

(a) Cycles from 2nd to 7th September 2022.

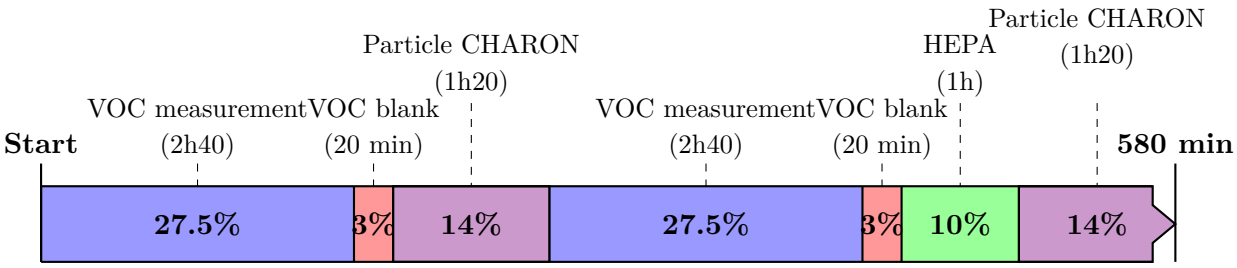

(b) Cycles from 8th to 29th September 2022.

Figure 2-9: *Illustration of the measurement cycles during PTR-ToF-MS operation in the Dunkirk campaign.*

In total, 315 m/z were recorded, including clusters. Five calibrations were performed during the campaign using a gas standard from the National Physical Laboratory (NPL, Teddington, U.K.), the composition of which is detailed in Appendix AT2. These were notably used to fit a transmission curve based on the transmissions of 11 m/z, the transmissions of the other m/z were interpolated according to Figure 2-10:

- 21.022 (H_3O^+)
- 33.035 ($CH_3OH{\cdot}H^+$, Methanol)
- 45.036 ($CH_3CHO{\cdot}H^+$, Acetaldehyde)
- 59.049 ($C_3H_6O{\cdot}H^+$, Acetone)
- 79.054 ($C_6H_6{\cdot}H^+$, Benzene)
- 93.069 ($C_7H_8{\cdot}H^+$, Toluene)
- 107.078 ($C_8H_{10}{\cdot}H^+$, Xylenes/ethylbenzene)

- 121.101 (1,2,4-Trimethylbenzene)
- 223 (Hexamethycyclotrisiloxane)
- 297 (Octamethylcyclotetrasiloxane)
- 371 (Decamethylcyclopentasiloxane)

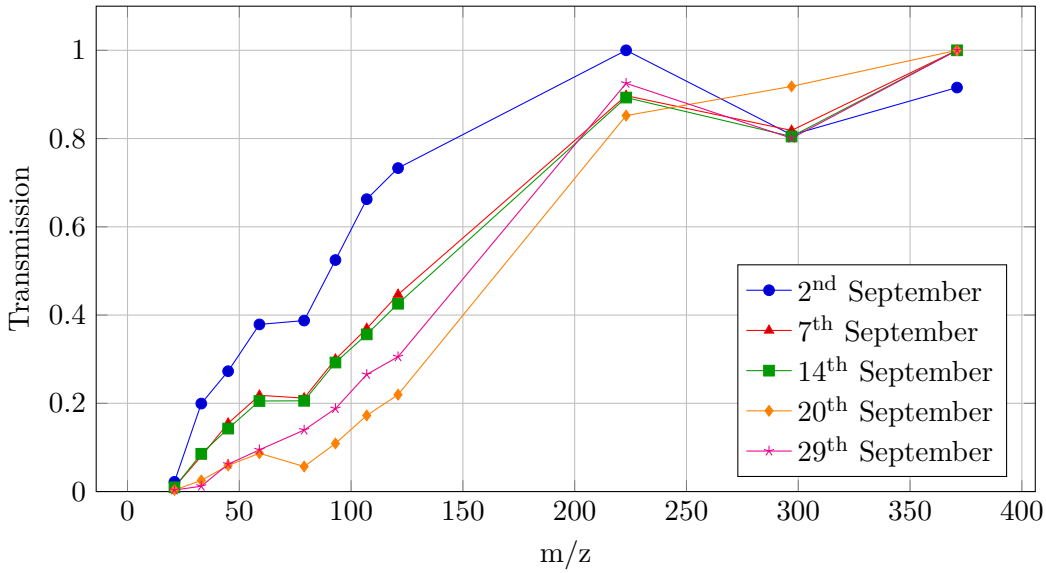

Figure 2-10: *Transmission for calibrated m/z for each calibration (symbols) and interpolated transmission for other masses (lines).*

In addition, 16 VOCs were corrected for humidity impacts on transmission and fragmentation, according to Table 2-4.

Table 2-4: *Correction coefficient and offset for VOC concentrations as a function of humidity. $[H_2O]$ is the absolute humidity in ppmv, the concentrations of VOC in ppb have to be multiplied by the obtained coefficient.*

Compound	Coefficient
Methanol	$-0.43\times$ [H_2O] $+7.67$
Acetonitrile	$-0.08\times$ [H_2O] $+2.15$
Acetaldehyde	$-0.02\times$ [H_2O] $+1.36$
Acetone	$-0.03\times$ [H_2O] $+1.38$
Isoprene	$-0.02\times$ [H_2O] $+1.26$
2-Butanone	$-0.03\times$ [H_2O] $+1.46$
Benzene	$0.03\times$ [H_2O] $+0.55$
Toluene	$0.01\times$ [H_2O] $+0.86$
o-Xylene	$-0.01\times$ [H_2O] $+1.11$
1,2,4-Trifluorobenzene	$0.04\times$ [H_2O] $+0.33$
3-Carene	$-0.01\times$ [H_2O] $+1.20$
1,2,4-Trimethylbenzene	$-0.01\times$ [H_2O] $+1.19$
DMS	$-0.001\times$ [H_2O] $+1.01$
Hexamethylcyclotrisiloxane	$-0.04\times$ [H_2O] $+1.55$
Octamethylcyclotetrasiloxane	$-0.05\times$ [H_2O] $+1.68$
Decamethylcyclopentasiloxane	$-0.23\times$ [H_2O] $+4.42$

The PTRMS Viewer 3 software was used to process and export raw data and convert it into concentrations. First, mass calibration was performed (Figure 2-11) based on on four primary ions, present on all mass spectra of both ambient and blank measurements of the PTR-ToF-MS (Dusanter et al., 2025): m/z 21.022 (H_3O^+), 37.0275 (water cluster $H_2O\cdot H_3O^+$), 203.943 (di-iodobenzene fragment) and 330.848 (di-iodobenzene), the two last necessitating the addition of high weight compounds in the drift tube during the mass calibration, using the PerMaScale function of the PTR-ToF-MS from IONICON (Dusanter et al., 2025). Using interpolation, the timebins of these compounds serve as references for other ions, enabling the attribution each m/z to be attributed to a time of flight. Next, the peak table (Appendix AT5, AT6 AT7 and AT8) was used to assign a mass peak to a molecular formula. Finally, the drift tube parameters U_{drift}, p_{drift} and T_{drift} were set according to the parameters used during the measurement campaign and resumed Table 2-5. These were chosen to limit fragmentation in the PTR-ToF-MS during the campaign. During analysis of the extracted data, the GLOVOCS[1] database was used to help attribute each m/z to a compound or fragment (Yáñez-Serrano et al., 2021).

[1]https://glovocs.creaf.cat

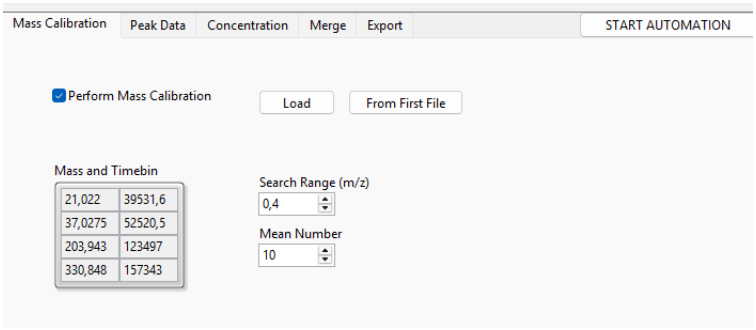

Figure 2-11: *Mass calibration on PTRMS Viewer 3.*

Table 2-5: *Parameters of the drift tube.*

Parameter	Value	Unit
U_{drift}	478	V
U_{dx}	35.5	V
T_{drift}	80	°C
P_{drift}	2.6	mbar
E/N	80	Td

2.3 Description of the dataset

The concentrations of VOCs measured by the two TD-GC-FID were provided prior to this work. Concentrations extracted from PTRMS Viewer 3 were also provided for the PTR-ToF-MS, and the raw data was already available. However, data validation and uncertainty calculations for these instruments had yet to be performed. Therefore, this thesis involved validating VOC concentrations alongside uncertainty calculations, which provided a statistical description of VOC observations and allowed the Dunkirk 2022 campaign to be positioned alongside previous ones. Note that for the determination of the uncertainties of the GC, the aforementioned coefficients not concerning calibration were provided from campaigns occurring prior to 2022 and were kept for consistency and less processing time.

2.3.a Data validation

2.3.a.i Uncertainties

TD-GC-FID The determination of the uncertainties on the TD-GC-FID were performed in agreement with guidelines provided by the Global Atmosphere Watch (GAW, 2023). They are determined by two components defining the systematic and random errors:

$$u_{GC} = \sqrt{\sigma_{acc}^2 + \sigma_{sys}^2}. \tag{2.25}$$

Often the expanded uncertainty is reported, integrating a coverage factor k, set at 2 for a 95% confidence interval.

$$U_{GC} = k \times \ u_{GC} \tag{2.26}$$

$$= k\sqrt{\sigma_{acc}^2 + \sigma_{sys}^2}. \tag{2.27}$$

The **accuracy** reflects the variability of the instrument due to random errors, also called precision. Precision covers the random error contributions due to the sampling volume, the integration (only random errors of volume determination and peak integration are captured, the systematic errors are considered hereafter), the sampling system and the blank variation. The latter was added from the guidelines of the GAW for consistency with previous campaigns performed by the data curators. The precision error will increase for low concentrations, therefore its determination depends on the Limit Of Detection (LOD), the lowest measurable concentration:

$$\sigma_{acc}^2 = \frac{LOD_i^2}{9} + (C_i \times \sigma_i^{rel})^2, \tag{2.28}$$

with LOD_i denoting the detection limit of the compound i, C_i denoting its concentration and σ_i^{rel} denoting the Relative Standard Deviation (RSD) of each compound i during calibration (area or concentration), also called the Coefficient of Variation (CV), representing the variability of the instrument. Distinctive methods exist for calculating the LOD on both Perkin-Elmer and AirmoVOC GCs, so the LOD were taken from studies using graphical method for consistency. It involves comparing the height of the background with the height of the peak of the compound on the chromatogram :

$$LOD_i = \frac{3H_{BG}C_i}{H_i}, \tag{2.29}$$

where H_{BG} denotes the height of the background, C_i denotes the concentration of the compound and H_i denotes the height of the peak. The LOD of the VOCs that were measured are presented in Table 2-6.

Table 2-6: *Limits of Detection (LOD) taken for the VOCs measured by the GC-FID.*

VOC	LOD Perkin-Elmer (ppt)	LOD Chromatotec (ppt)	VOC	LOD Perkin-Elmer (ppt)	LOD Chromatotec (ppt)
Ethane	128		2,4-Dimethylpentane	43	3
Ethylene	54		2,2,3-Trimethylbutane	8	3
Propane	162		Benzene	51	12
Propene	62		3,3-Dimethylpentane	32	3
Isobutane	45		Cyclohexane	47	3
Butane	45		2-Methylhexane	18	3
Acetylene	118		2,3-Dimethylpentane	30	
trans-2-butene	31		Trichloroethylene	22	
1-Butene	29		Isooctane	39	11
Isobutene	26		Heptane	23	12
Neopentane	24		Toluene	27	10
cis-2-butene	43		n-Octane	15	2
Isopentane	30		Ethylbenzene	18	7
Pentane	33		m&p-Xylenes	30	8
1,3-Butadiène	24		Styrene	14	2
Propyne	4		o-Xylene	18	7
3-Methyl-1-butene	14		n-Nonane	9	2
trans-2-Pentene	44		Isoprobylbenzene	41	
2-Methyl-2-butene	34		Propylbenzene	3	3
2-Methyl-1-butene	21		3-Ethyltoluene	12	
1-Pentene	13		4-Ethyltoluene	15	
cis-2-Pentene	10		1,3,5-Trimethylbenzene	8	11
2,2-Dimethylbutane	41		2-Ethyltoluene	7	
Butyne	14		1,2,4-Trimethylbenzene	10	9
Isoprene	36		n-Decane	8	2
Cyclopentene	53		1,2,3-Trimethylbenzene	10	12
Cyclopentane	36		n-Undecane	10	
2-Methylpentane	66	7	1,2-Dichloropropane	6	
3-Methylpentane	39	3	1,2-Dibromomethane	8	
Hexene	4	3	Chlorobenzene	3	
Hexane	51	9	α-pinene	3	
2,2-Dimethylpentane	20	3			

The **systematic error** σ_{sys} is composed of three combined errors :

$$\sigma_{sys}^2 = \sigma_{cal}^2 + \sigma_{int}^2 + \sigma_{bg}^2, \tag{2.30}$$

The calibration error σ_{cal} is determined from the calibration of the GC, in our case with a National Physical Laboratory (NPL) gas standard (Reference 2019040353). It is expressed as follows :

$$\sigma_{cal}^2 = \left(\frac{A_i \times V_{cal}}{A_{i,cal} \times V_i} \times \delta_{cal} \right)^2, \tag{2.31}$$

with $V_{cal} = V_i$ denoting the volume sampled from the calibration and the compound i, A_i the area of the sample, $A_{i,cal}$ denoting the area of calibration of i and δ_{cal} denoting the uncertainty associated to each compound inside of the NPL gas standard.

The **integration error** σ_{int} represents the variation in the integration window used for each chromatogram. For well-defined and symmetrical peaks, this error is negligible. Otherwise:

$$\sigma_{int}^2 = \left(\frac{f_{cal}}{V_i} \times \delta A_i \right)^2 + \left(\frac{A_i \times V_{cal} \times C_{cal}}{V_i \times A_{cal}^2} \times \delta A_{cal} \right)^2, \tag{2.32}$$

with

$$f_{cal} = \frac{V_{cal} \times C_{cal}}{A_{cal} - A_{bg}}, \tag{2.33}$$

$$\delta A_i = \frac{A_{i,max} - A_{i,min}}{6}, \tag{2.34}$$

$$\delta A_{cal} = \frac{A_{cal,max} - A_{cal,min}}{6}. \tag{2.35}$$

f_{cal} denotes the calibration factor for each compound (ppt/area), V_{cal} and V_i denote the volume sampled ($V_{cal} = V_i$ if the volumes for samples and calibrations are the same), A_{cal} denotes the calibration area, A_{bg} denotes the area of the background, A_i denotes the area of the compound, δ_i and δ_{cal} denote the errors on the peak integration for each compound and calibration, respectively, determined on 6 repeated measurements.

The **background error** σ_{bg} takes into account the instrumental background that impacts mostly the low concentrations that reach the noise levels.

$$\sigma_{bg}^2 = \left(\sigma_{bg} \times \frac{1}{\sqrt{n-1}}\right)^2, \tag{2.36}$$

with σ_{bg} denoting the standard deviation of concentrations during background measurement and n denoting the number of observations.

The average contribution of each component of the total uncertainties of the two TD-GC-FID is represented in Figures 2-12a and 2-12b. The uncertainties for light VOC on the Perkin-Elmer (ethane, ethylene, propane and propene) are mainly driven by the integration error (60 – 80%), while other VOCs measured by this GC are mainly to totally driven by the accuracy component. This is particularly understandable for species with an important standard deviation on their area of calibration, as used in Equation 2.28 and that can be observed in calibration in Figure 2-6b, starting with isooctane. Uncertainties determined for the AirmoVOC are more balanced between their component, but a high contribution of the accuracy component can here also be seen for isooctane, n-heptane and the trimethylbenzenes.

(a) *Contribution of each component of the uncertainties to the total uncertainty of the calibrated VOC on the TD-GC-2FID from Perkin-Elmer.*

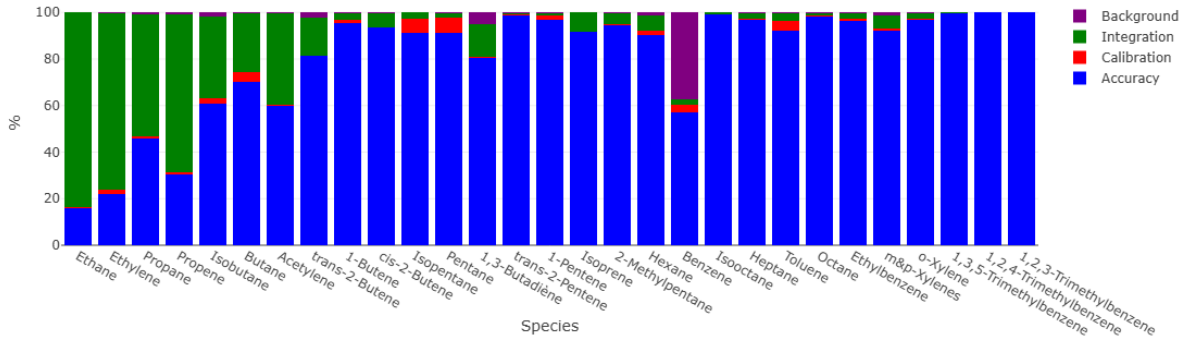

(b) *Contribution of each uncertainty component to the total uncertainty of the calibrated VOC on the TD-GC-FID AirmoVOC from Chromatotec.*

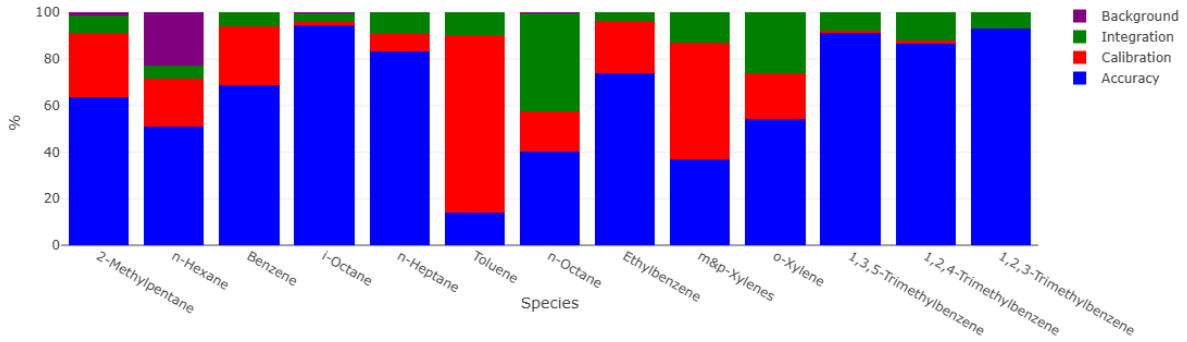

Figure 2-12: *Average contribution of each uncertainty component relative to the summed contributions for the whole campaign.*

PTR-ToF-MS Let $i(RH^+)$ the intensity of an analyte signal R result from the subtraction of the blank signal $i(RH^+)_{blank}$ to the ambient signal determined during sampling $i(RH^+)_{ambient}$:

$$i(RH^+) = i(RH^+)_{ambient} - i(RH^+)_{blank}. \tag{2.37}$$

The uncertainties on this signal are calculated according to the measurement guidelines of ACTRIS (Dusanter et al., 2025), to which this work actively contributed by assisting with the calculations presented here. The expression of the total uncertainty for an observation is given by the quadratic sum of the random error (precision) and the systematic error (accuracy). The coverage factor k is taken as 2 for a 95% confidence interval:

$$U_{PTR} = k \cdot \sigma, \tag{2.38}$$

$$= k\sqrt{\sigma^2_{precision} + \sigma^2_{accuracy}}. \tag{2.39}$$

The **precision** on $i(RH^+)$ results from the propagation of errors of $i(RH^+)_{ambient}$ and $i(RH^+)_{blank}$ using the standard deviation determined by Poisson noise.

$$\sigma_{precision} = \sqrt{i(RH^+)_{ambient} + i(RH^+)_{blank}}. \tag{2.40}$$

Then, $\sigma_{precision}$ is normalized by the net signal $i(RH^+)$ to provide a dimensionless Relative Standard Deviation (RSD) that can apply to the mixing ration χ_R:

$$RSD_{precision} = \frac{\sigma_{precision}}{i(RH^+)}, \tag{2.41}$$

$$= \frac{\sqrt{i(RH^+)_{ambient} + i(RH^+)_{blank}}}{i(RH^+)_{ambient} - i(RH^+)_{blank}}, \tag{2.42}$$

according to Equations 2.37 and 2.40. Likewise:

$$\sigma_{precision} = RSD_{precision} \times \chi_R, \tag{2.43}$$

$$= \frac{\sqrt{i(RH^+)^2_{ambient} + i(RH^+)^2_{blank}}}{i(RH^+)_{ambient} - i(RH^+)_{blank}} \times \chi_R. \tag{2.44}$$

As shown in Figure 2-13, each blank cycle was associated with the preceding measurement cycle. The mean blank value was calculated for each blank cycle and subtracted from every point in the preceding VOC cycle.

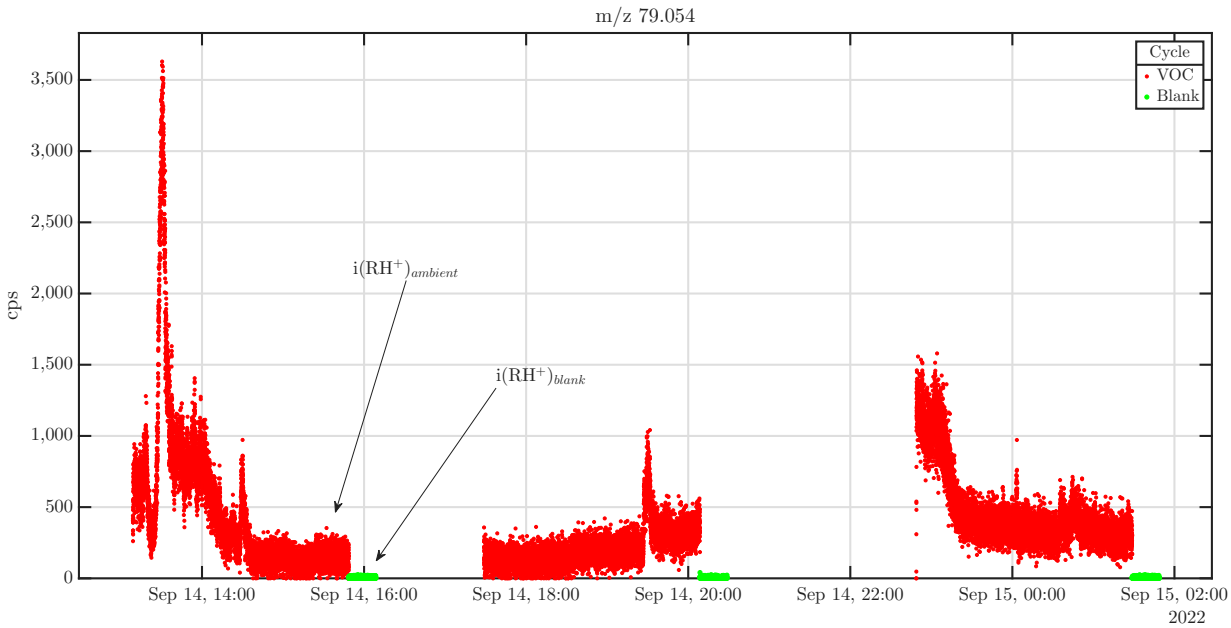

Figure 2-13: *Zoom in on the time series of ambient signal of m/z 79.054 ($C_6H_6{\cdot}H^+$) during the VOC measurement cycles (red) and blank cycles (green).*

The **accuracy** is considered systematic, estimated by the calibrations and given by:

$$RSD_{accuracy} = \sqrt{\left(\frac{\sigma_{cal}}{\chi_{R_{cal}}}\right)^2 + \frac{1}{(F_{cal}+F_{air})^2}\left(\frac{F_{air}^2}{F_{cal}^2} \times \sigma_{F_{cal}}^2 + \sigma_{F_{air}}^2\right)}, \tag{2.45}$$

with $\chi_{R_{cal}}$ denoting the volume mixing ratio indicated by the gas standard, σ_{cal} denoting the associated uncertainty, F_{air} and F_{cal} denoting the flow rate of dilution air and gas standard respectively, and $\sigma_{F_{air}}$ and $\sigma_{F_{cal}}$ denoting the associated uncertainties. As F_{air} and F_{cal} were not recorded and a limited amount of VOCs was calibrated, $\text{RSD}_{accuracy}$ was taken as 5% of the concentration for each component, calibrated and uncalibrated, based on the relative uncertainty of the concentration of the calibrated compounds in Table AT2.

$$\sigma_{accuracy} = 0.05 \times \chi_R. \tag{2.46}$$

The **Limit Of Detection** (LOD) is also calculated using the standard deviation determined by Poisson noise for $i(RH^+)_{blank}$ and the sensitivity $S(RH^+)$calculated using Equation 2.20:

$$LOD = \frac{3\sqrt{i(RH^+)_{blank}}}{S(RH^+)}. \tag{2.47}$$

Alternatively, the sensitivity can be calculated by dividing the mean value of the subsequent blank cycle used in the Equation 2.37 by the extracted concentration. The latter was used and resulted in a single LOD associated to a single observation point.

The LOD were taken into account for data validation by comparing the observed concentration with the LOD. For all observations, if the concentration is below the LOD, its value is replaced by half the LOD in anticipation of its use in Positive Matrix Factorisation (Norris et al., 2014). This produced robust VOC datasets, and similarly, the associated uncertainty was replaced by 5/6 of the LOD. This operation was performed for both GC and PTR.

$$\text{if } [VOC]_i > \text{ LOD} \Rightarrow \begin{cases} [VOC]_i = [VOC]_i, \\ \sigma[VOC]_i = \sigma[VOC]_i, \end{cases} \tag{2.48}$$

$$\text{if } [VOC]_i \leq \text{ LOD} \Rightarrow \begin{cases} [VOC]_i = \frac{1}{2}\text{LOD}, \\ \sigma[VOC]_i = \frac{5}{6}\text{LOD} \end{cases} \tag{2.49}$$

In addition, the signal-to-noise ratio (**SNR**) of each VOC was calculated to indicate how significant a measurement is, relatively to its uncertainty. The method used to calculate the SNR in this study is the one presented by Norris et al. (2014) in anticipation of its use in the PMF.

SNRs are calculated using the criterion d_{ij}, which is employed when the concentration value exceeds its uncertainty:

$$d_{ij} = \left(\frac{x_{ij} - s_{ij}}{s_{ij}} \right) \text{ if } x_{ij} > s_{ij}, \tag{2.50}$$

$$d_{ij} = 0 \text{ if } x_{ij} \leq s_{ij}. \tag{2.51}$$

Then, the criteria are totalled:

$$\text{SNR}_j = \frac{1}{N_d} \sum_{i=1}^{n} d_{ij}, \tag{2.52}$$

with N_d denoting the total length of d_j. This method calculates one SNR for each compound.

2.3.a.ii Intercomparison

The two GCs measured 25 compounds in common, which can be used to compare the performance of the two instruments and determine which will report which VOC throughout the rest of the work. Table 2-7 summarises the comparison between the two instruments from the perspective of their availability, i.e. the proportion of observations above the LOD, using a linear relationship. Overall, the two GCs showed poor agreement, primarily due to being unsynchronised during the campaign and the analysis time of the Perkin-Elmer instrument varying between samples due to temperature regulation malfunction. The two instruments were resynchronised using the interpolation method, which produced the best agreement. Additionally, the two instruments display significant differences in the LODs of 2- and 3-methylpentane, 2,2- and 3,3-dimethylpentane and benzene, with the AirmoVOC more frequently displaying the highest LODs. For this reason, most VOCs measured in common will be reported by the AirmoVOC GC. However, octane and nonane will be reported from the Perkin-Elmer, even though they are more available in the AirmoVOC, as the Perkin-Elmer can resolve these compounds more effectively, and that they may co-elute in the AirmoVOC chromatogram. Also, only the Perkin-Elmer reported undecane, so for consistency alkanes were kept with the Perkin-Elmer. 2-Methylhexane will also be reported by the Perkin-Elmer due to its higher efficiency for measuring this compound. Finally, propylbenzene will be reported by the Perkin-Elmer because it is the only GC to report isopropylbenzene, therefore, it was kept for consistency. 1,3,5- and 1,2,4-trimethylbenzenes show a greater availability in the AirmoVOC, so, for consistency, 1,2,3-trimethylbenzene will also be reported by this GC even if it shows a much more important availability from the Perkin-Elmer. Otherwise, every compound solely reported by a GC will be reported by the same instrument. Table 2-8 summarises the GC attribution for all compounds used in this study.

Table 2-7: *Linear correlation ($y = ax + b$) between the two TD-GC-FID for common compounds during the whole campaign.*

VOC	R^2	a	b	% >LOD Perkin	% >LOD chromatotec
2-Methylpentane	0.34	0.41	0.11	13.91	73.06
3-Methylpentane	0.29	0.22	0.11	18.09	95.88
Hexene	0.003	0.03	0.05	67.83	69.26
Hexane	0.62	0.90	0.11	52.70	57.37
2,2-Dimethylpentane	0.01	0.08	0.06	7.13	36.13
2,4-Dimethylpentane	0.10	0.37	0.15	22.26	39.62
2,2,3-Trimethylbutane	0.52	0.09	0.03	4.52	13.00
Benzene	0.52	0.82	-0.02	27.30	78.92
3,3-Dimethylpentane	0.0002	-0.001	0.07	0.87	32.01
Cyclohexane	0.40	0.55	0.07	7.65	58.32
2-Methylhexane	0.50	0.80	0.02	17.22	47.54
Isooctane	0.57	0.80	0.06	9.22	31.06
Heptane	0.71	1.02	0.02	18.43	30.11
Toluene	0.45	0.60	0.12	76.52	86.37
n-Octane	0.61	0.72	0.03	19.65	58.95
Ethylbenzene	0.36	0.47	0.03	43.83	68.78
m&p-Xylenes	0.34	0.46	0.17	59.30	74.17
Styrene	0.0003	0.02	0.04	15.48	13.00
o-Xylene	0.24	0.38	0.09	48.52	60.54
n-Nonane	0.54	0.77	0.05	46.61	65.45
Propylbenzene	0.02	-0.10	0.02	11.30	34.55
1,3,5-Trimethylbenzene	0.08	0.13	0.03	18.78	20.44
1,2,4-Trimethylbenzene	0.18	0.47	0.02	8.70	30.90
1,2,3-Trimethylbenzene	0.17	1.17	0.02	30.78	7.92
n-Decane	0.25	0.48	0.04	30.09	60.06

In addition to GC measurements, the PTR-ToF-MS also measured common species, even though it reported m/z. Some of the compounds measured by the PTR in Dunkirk can be confidently associated with particular compounds, such as aromatic VOCs like benzene ($C_6H_6 \cdot H^+$), toluene ($C_7H_8 \cdot H^+$) and C_8 aromatics (xylenes and ethylbenzene) ($C_8H_{10} \cdot H^+$). Cyclopentane and styrene could be compared to $C_5H_{10} \cdot H^+$ and $C_8H_8 \cdot H^+$, respectively, but they showed poor availability from the GC. The PTR observations were averaged over the GC sampling time and Figure 2-14 shows the correlation coefficients for the aromatic VOCs. These indicate a high level of agreement between the instruments throughout the entire campaign, with a minimum R^2 of 0.86 and slopes close to unity. It can therefore be concluded that PTR measurements strongly match the GC measurements. This agreement between low- and high-time resolution measurements sets the scene to investigate speciated VOCs with greater temporal resolution.

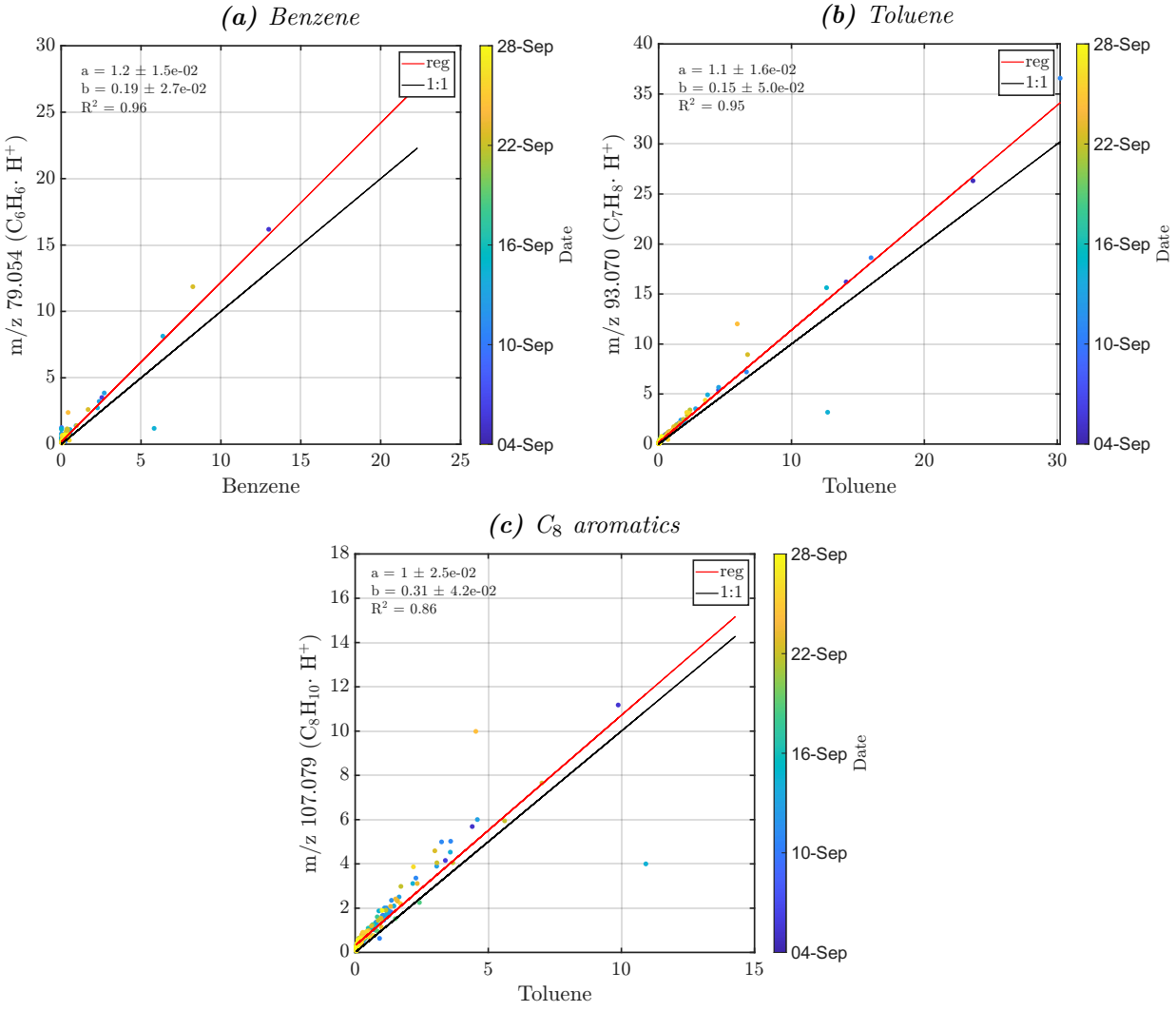

Figure 2-14: *Comparison of GC measurements of aromatics with those of PTR, expressed in* $\mu g \cdot m^{-3}$.

Table 2-8: *TD-GC-FID of reference for each VOC.*

VOC	Instrument	VOC	Instrument
Ethane	Perkin-Elmer	2,4-Dimethylpentane	AirmoVOC
Ethylene	Perkin-Elmer	2,2,3-Trimethylbutane	AirmoVOC
Propane	Perkin-Elmer	Benzene	AirmoVOC
Propene	Perkin-Elmer	3,3-Dimethylpentane	AirmoVOC
Isobutane	Perkin-Elmer	Cyclohexane	AirmoVOC
Butane	Perkin-Elmer	2-Methylhexane	Perkin-Elmer
Acetylene	Perkin-Elmer	2,3-Dimethylpentane	Perkin-Elmer
trans-2-butene	Perkin-Elmer	Trichloroethylene	Perkin-Elmer
1-Butene	Perkin-Elmer	Isooctane	AirmoVOC
Isobutene	Perkin-Elmer	Heptane	AirmoVOC
Neopentane	Perkin-Elmer	Toluene	AirmoVOC
C2-butene	Perkin-Elmer	n-Octane	Perkin-Elmer
Isopentane	Perkin-Elmer	Ethylbenzene	AirmoVOC
Pentane	Perkin-Elmer	m&p-Xylenes	AirmoVOC
1,3-Butadiène	Perkin-Elmer	Styrene	AirmoVOC
Propyne	Perkin-Elmer	o-Xylene	AirmoVOC
3-Methyl-1-butene	Perkin-Elmer	n-Nonane	Perkin-Elmer
trans-2-Pentene	Perkin-Elmer	Isoprobylbenzene	Perkin-Elmer
2-Methyl-2-butene	Perkin-Elmer	Propylbenzene	Perkin-Elmer
2-Methyl-1-butene	Perkin-Elmer	3-Ethyltoluene	Perkin-Elmer
1-Pentene	Perkin-Elmer	4-Ethyltoluene	Perkin-Elmer
cis-2-Pentene	Perkin-Elmer	1,3,5-Trimethylbenzene	AirmoVOC
2,2-Dimethylbutane	Perkin-Elmer	2-Ethyltoluene	Perkin-Elmer
Butyne	Perkin-Elmer	1,2,4-Trimethylbenzene	AirmoVOC
Isoprene	Perkin-Elmer	n-Decane	Perkin-Elmer
Cyclopentene	Perkin-Elmer	1,2,3-Trimethylbenzene	AirmoVOC
Cyclopentane	Perkin-Elmer	n-Undecane	Perkin-Elmer
2-Methylpentane	AirmoVOC	1,2-Dichloropropane	AirmoVOC
3-Methylpentane	AirmoVOC	1,2-Dibromomethane	AirmoVOC
Hexene	AirmoVOC	Chlorobenzene	AirmoVOC
Hexane	AirmoVOC	Alphapinene	AirmoVOC
2,2-Dimethylpentane	AirmoVOC	1,2-Dichlorobenzene	AirmoVOC

2.3.b Statistics and trends

After validating the concentrations and selecting one instrument to report each VOC, a descriptive analysis of the dataset is performed. This includes statistics of measurements and time series, which are often necessary when analysing variables before using more complex tools. Uncertainties are also discussed in perspective of the SNRs. While these are basic descriptions, they are key to gaining insight into the data. These analyses and the development of various analytical tools to ease data management were performed using MatLab software (The MathWorks, Inc.).

GC The data availability of each VOC measured by the GC, i.e. the quantity of observations superior to the LOD, is presented in Table 2-9 alongside their statistical indicators. Most light VOCs (C_2 – C_4) show high availability, with proportion above 88%, except for acetylene (53.9%) and trans-2-butene (49.1%). In contrast, C_5 compounds demonstrate poor availability, with almost no data above the LOD for neopentane, propyne, 3-methyl-1-butene or trans-2-pentene. There are no concentration above the LOD for 2-methyl-2-butene. 1-pentene stands out of the C_5 compounds with 32.5% of availability, whereas isoprene, a key indicator of biogenic emissions, is limited to a poor availability of 8.7%.

This small number of significant measurements already suggests that the contribution of biogenic emissions to the VOC concentrations is minimal. However, α-pinene, another strong marker of biogenic emissions, has 54.2% of data above the LOD, but was found in the industrial plumes of Dunkirk by Farhat et al. (2024). The industrial contribution to VOC concentrations is particularly evident when investigating the proportion of values above the LOD for 2-methylpentane (73,1%) or hexene (69.3%) and hexane (57.4%), corroborating the VOCs found to be markers for refinery activities in Dunkirk reported by Roukos et al. (2009). Other indicators for industrial activities or traffic exhaust are BTEX, among which toluene has the highest availability (86,4%), followed by benzene (78.5%), m&p-xylenes (74.2%), ethylbenzene (68.8%) and o-xylene (60.5%). Toluene was found to be the most abundant VOC, with an average concentration of 1.17 ± 3.18 µg·m^{-3}, and the overall BTEX average concentrations are 0.44 ± 1.74 µg·m^{-3} for benzene, 0.47 ± 1.15 µg·m^{-3} for m&p-xylenes, 0.25 ± 0.81 µg·m^{-3} for ethylbenzene and 0.24 ± 0.59 µg·m^{-3} for o-xylene. Ethane was also a major VOC observed during the campaign, with an average of 1.03 ± 0.44 µg·m^{-3}. Light VOCs such as propane (0.64 ± 0.63 µg·m^{-3}), butane (0.88 ± 0.81 µg·m^{-3}), 1-butene (0.77 ± 0.33 µg·m^{-3}) and iso/n-pentane (0.69 ± 1.50 / 0.52 ± 1.17 µg·m^{-3}) exhibited significant levels.

Table 2-9: *Statistics of the measurements of VOC from the two TD-GC-FID during the Dunkirk 2022 campaign. Concentrations are expressed in µg·m^{-3}.*

VOC	mean	median	min	max	std	% >LOD	VOC	mean	median	min	max	std	% >LOD
Ethane	1.03	0.94	0.08	4.33	0.44	99.7	2,4-Dimethylpentane	0.07	0.01	0.01	5.49	0.32	39.6
Ethylene	0.40	0.28	0.03	5.41	0.50	99.8	2,2,3-Trimethylbutane	0.05	0.01	0.01	21.53	0.86	13.0
Propane	0.64	0.47	0.15	5.96	0.63	88.7	Benzene	0.44	0.08	0.02	23.48	1.74	78.9
Propene	0.18	0.11	0.05	4.52	0.32	69.7	3,3-Dimethylpentane	0.10	0.01	0.01	6.87	0.61	32.0
Isobutane	0.62	0.49	0.22	3.03	0.43	99.8	Cyclohexane	0.09	0.01	0.01	3.97	0.33	58.3
Butane	0.88	0.62	0.20	5.68	0.81	99.8	2-Methylhexane	0.08	0.04	0.04	3.05	0.19	29.2
Acetylene	0.11	0.07	0.06	0.66	0.07	53.9	2,3-Dimethylpentane	0.07	0.06	0.06	0.87	0.05	4.8
trans-2-butene	0.06	0.04	0.04	0.34	0.05	49.1	Trichloroethylene	0.17	0.06	0.06	4.44	0.46	28.2
1-Butene	0.77	0.67	0.38	3.48	0.33	99.8	Isooctane	0.08	0.03	0.03	1.87	0.19	31.1
Isobutene	0.22	0.20	0.03	0.87	0.13	97.8	Heptane	0.12	0.02	0.02	5.92	0.45	30.1
Neopentane	0.04	0.04	0.04	0.27	0.01	1.0	Toluene	1.17	0.18	0.02	31.52	3.38	86.4
cis-2-butene	0.05	0.05	0.05	0.24	0.02	6.8	n-Octane	0.09	0.04	0.04	2.56	0.19	27.9
Isopentane	0.69	0.26	0.04	13.67	1.50	90.8	Ethylbenzene	0.28	0.07	0.02	10.91	0.81	68.8
Pentane	0.52	0.17	0.05	11.86	1.17	85.6	m&p-Xylenes	0.47	0.11	0.02	11.29	1.15	74.2
1,3-Butadiène	0.14	0.14	0.03	0.53	0.04	99.0	Styrene	0.02	0.01	0.01	0.94	0.05	13.0
Propyne	0.00	0.00	0.00	0.08	0.00	1.3	o-Xylene	0.24	0.05	0.02	6.03	0.59	60.5
3-Methyl-1-butene	0.02	0.02	0.02	0.13	0.01	4.0	n-Nonane	0.14	0.05	0.02	4.17	0.37	65.8
trans-2-Pentene	0.07	0.06	0.06	0.42	0.03	7.3	Isoprobylbenzene	0.10	0.10	0.10	0.50	0.02	1.7
2-Methyl-2-butene	0.05	0.05	0.05	0.05	0.00	0.0	Propylbenzene	0.02	0.01	0.01	0.22	0.03	18.5
2-Methyl-1-butene	0.04	0.03	0.03	0.41	0.04	13.9	3-Ethyltoluene	0.04	0.03	0.03	0.65	0.04	10.8
1-Pentene	0.04	0.02	0.02	6.83	0.29	32.5	4-Ethyltoluene	0.06	0.04	0.04	1.72	0.11	14.1
cis-2-Pentene	0.02	0.01	0.01	0.24	0.02	10.0	1,3,5-Trimethylbenzene	0.07	0.03	0.03	2.65	0.16	20.4
2,2-Dimethylbutane	0.09	0.07	0.07	1.21	0.09	12.5	2-Ethyltoluene	0.24	0.19	0.02	0.99	0.19	94.6
Butyne	0.07	0.06	0.02	0.56	0.05	94.1	1,2,4-Trimethylbenzene	0.07	0.02	0.02	1.20	0.13	30.9
Isoprene	0.06	0.05	0.05	1.26	0.07	8.7	n-Decane	0.09	0.03	0.02	2.21	0.23	50.7
Cyclopentene	0.08	0.07	0.07	0.26	0.01	0.6	1,2,3-Trimethylbenzene	0.04	0.03	0.03	0.39	0.04	7.9
Cyclopentane	0.08	0.05	0.05	2.00	0.16	13.2	n-Undecane	0.06	0.03	0.03	1.66	0.12	20.4
2-Methylpentane	0.25	0.04	0.01	8.31	0.73	73.1	1,2-Dichloropropane	0.18	0.05	0.03	7.60	0.48	61.2
3-Methylpentane	0.14	0.03	0.01	12.83	0.73	95.9	1,2-Dibromomethane	0.24	0.07	0.07	8.91	0.66	32.2
Hexene	0.05	0.02	0.01	1.55	0.11	69.3	Chlorobenzene	0.05	0.02	0.02	1.97	0.13	57.8
Hexane	0.21	0.05	0.02	10.63	0.74	57.4	α-pinene	0.06	0.02	0.01	2.08	0.14	54.2
2,2-Dimethylpentane	0.05	0.01	0.01	1.64	0.13	36.1	1,2-Dichlorobenzene	0.05	0.02	0.02	1.43	0.10	40.6

The uncertainties of the concentrations of VOCs measured by TD-GC-FID are presented in Table 2-10. Their SNR is also shown in this table. The results show that toluene has the highest SNR at 8.23, followed by m&p-xylenes at 7.06, ethylbenzene at 4.31, o-xylene at 3.69 and benzene at 3.61. This emphasises the high quality and importance of the BTEX measurements taken during this campaign compared to those of other compounds. 2-Methylpentane is close with an SNR of 3.81, followed by hexane with an SNR of 2.80, isopentane with an SNR of 3.19, and pentane with an SNR of 2.64. Remarkable SNRs are also exhibited by isobutane, butane, 1-butene and isobutene, with SNRs of 3.90, 4.38, 3.60 and 3.43 respectively. In contrast, 3-methyl-1-butene, 2-methyl-1/2-butene, cyclopentene, 3,3-dimethylpentane, 1,2-dichloropropane and α-pinene have and SNR of 0. However, these compounds will remain in the study for the TD-GC-FID but analysed in perspective of their quality.

Table 2-10: *Statistics of the uncertainties on the TD-GC-FID measurements of VOCs and associated SNR based on Norris et al. (2014). SNR inferior to 10^{-3} were written as 0.*

VOC	mean	median	min	max	std	SNR	VOC	mean	median	min	max	std	SNR
Ethane	0.35	0.34	0.13	0.49	0.02	1.95	2,4-Dimethylpentane	0.05	0.01	0.01	3.77	0.22	0.18
Ethylene	0.12	0.12	0.05	0.42	0.02	2.08	2,2,3-Trimethylbutane	0.04	0.01	0.01	14.77	0.59	0.06
Propane	0.28	0.29	0.24	0.48	0.02	1.21	Benzene	0.04	0.03	0.03	0.99	0.07	3.61
Propene	0.12	0.12	0.09	0.50	0.03	0.47	3,3-Dimethylpentane	0.14	0.01	0.01	9.76	0.87	0
Isobutane	0.12	0.11	0.10	0.28	0.03	3.90	Cyclohexane	0.06	0.01	0.01	2.73	0.22	0.46
Butane	0.15	0.13	0.11	0.67	0.07	4.38	2-Methylhexane	0.09	0.06	0.06	2.21	0.16	0.03
Acetylene	0.11	0.11	0.10	0.12	0.003	0.25	2,3-Dimethylpentane	0.11	0.10	0.10	0.83	0.04	0.01
trans-2-butene	0.06	0.06	0.05	0.06	0.002	0.35	Trichloroethylene	0.19	0.10	0.10	3.76	0.39	0.04
1-Butene	0.17	0.15	0.09	0.68	0.06	3.60	Isooctane	0.04	0.04	0.04	0.06	0.004	1.36
Isobutene	0.05	0.04	0.01	0.19	0.03	3.43	Heptane	0.04	0.04	0.03	0.17	0.01	1.65
Neopentane	0.06	0.06	0.04	0.08	0.001	0.02	Toluene	0.06	0.04	0.03	0.88	0.09	8.23
cis-2-butene	0.08	0.08	0.07	0.08	0.002	0.04	n-Octane	0.06	0.06	0.05	0.40	0.02	0.46
Isopentane	0.11	0.07	0.07	1.54	0.15	3.19	Ethylbenzene	0.03	0.02	0.02	0.50	0.03	4.31
Pentane	0.10	0.08	0.07	1.17	0.10	2.64	m&p-Xylenes	0.04	0.03	0.03	0.32	0.03	7.06
1,3-Butadiène	0.04	0.04	0.04	0.07	0.002	2.07	Styrene	0.005	0.003	0.003	0.24	0.01	2.98
Propyne	0.01	0.01	0.01	0.03	0.002	0.01	o-Xylene	0.03	0.03	0.03	0.27	0.02	3.69
3-Methyl-1-butene	0.04	0.03	0.03	0.28	0.01	0	n-Nonane	0.10	0.04	0.03	3.40	0.23	0.36
trans-2-Pentene	0.10	0.10	0.09	0.11	0.003	0.04	Isoprobylbenzene	0.17	0.17	0.14	0.33	0.01	0.005
2-Methyl-2-butene	0.08	0.08	0.08	0.08	0	0	Propylbenzene	0.02	0.01	0.01	0.13	0.02	0.12
2-Methyl-1-butene	0.07	0.05	0.05	0.83	0.07	0	3-Ethyltoluene	0.05	0.05	0.04	0.37	0.02	0.04
1-Pentene	0.03	0.03	0.03	0.62	0.03	0.25	4-Ethyltoluene	0.07	0.06	0.04	0.99	0.06	0.07
cis-2-Pentene	0.03	0.02	0.02	0.14	0.01	0.06	1,3,5-Trimethylbenzene	0.05	0.05	0.04	0.30	0.01	0.51
2,2-Dimethylbutane	0.12	0.12	0.06	0.55	0.02	0.11	2-Ethyltoluene	0.13	0.10	0.03	0.53	0.10	0.77
Butyne	0.04	0.03	0.02	0.25	0.03	0.74	1,2,4-Trimethylbenzene	0.04	0.04	0.03	0.10	0.01	0.95
Isoprene	0.09	0.08	0.06	0.68	0.03	0.04	n-Decane	0.13	0.04	0.04	3.17	0.32	0.01
Cyclopentene	0.13	0.12	0.12	0.56	0.02	0	1,2,3-Trimethylbenzene	0.05	0.05	0.04	0.05	0.002	0.18
Cyclopentane	0.14	0.09	0.09	3.64	0.30	0.001	n-Undecane	0.09	0.05	0.05	2.93	0.18	0.01
2-Methylpentane	0.03	0.02	0.02	0.37	0.03	3.81	1,2-Dichloropropane	0.25	0.07	0.04	10.79	0.68	0
3-Methylpentane	0.10	0.02	0.01	8.80	0.50	0.46	1,2-Dibromomethane	0.16	0.05	0.05	6.11	0.45	0.46
Hexene	0.03	0.01	0.01	1.06	0.08	0.46	Chlorobenzene	0.03	0.01	0.01	1.35	0.09	0.46
Hexane	0.03	0.03	0.03	0.43	0.03	2.80	α-pinene	0.14	0.04	0.01	4.77	0.33	0
2,2-Dimethylpentane	0.04	0.01	0.01	1.13	0.09	0.17	1,2-Dichlorobenzene	0.03	0.01	0.01	0.98	0.07	0.46

Figure 2-15 shows the sum of VOC concentrations determined by the TD-GC-FID, in perspective of the various wind regimes that were observed during the campaign. It began with a period from 3rd to 7th September, during which wind directions oscillated between north and east. This suggests an impact from the Dunkirk industrial park, which could explain the peaks (105 – 192 µg·m^{-3}) encountered during this period. Next, lower levels of VOCs were found in winds from the south to south-east (180 – 270 °), spanning areas with metallurgical activities, until 13th. This wind sector could be identified as having a mixed origin of VOCs (western industrial area and urban).

Then, a major north wind sector is encountered, starting from the 14th, and gaining in importance to create a period ranging from the 15th to the 21st September under the exclusive influence of northern winds. This period is favourable for sampling ship plumes, as the ferry dock was directly north of the measuring site. However, the levels of VOCs observed during this period by the TD-GC-FID show low variability, with occasional peaks of 40 to 60 µg·m^{-3}on 19thand 21st September. Next and until the end of the VOC measurements, mixed wind regimes are found, showing peaks in the range of 20 – 55 µg·m^{-3} with one peak at 50 µg·m^{-3} on 25th September found in the northern wind sector.

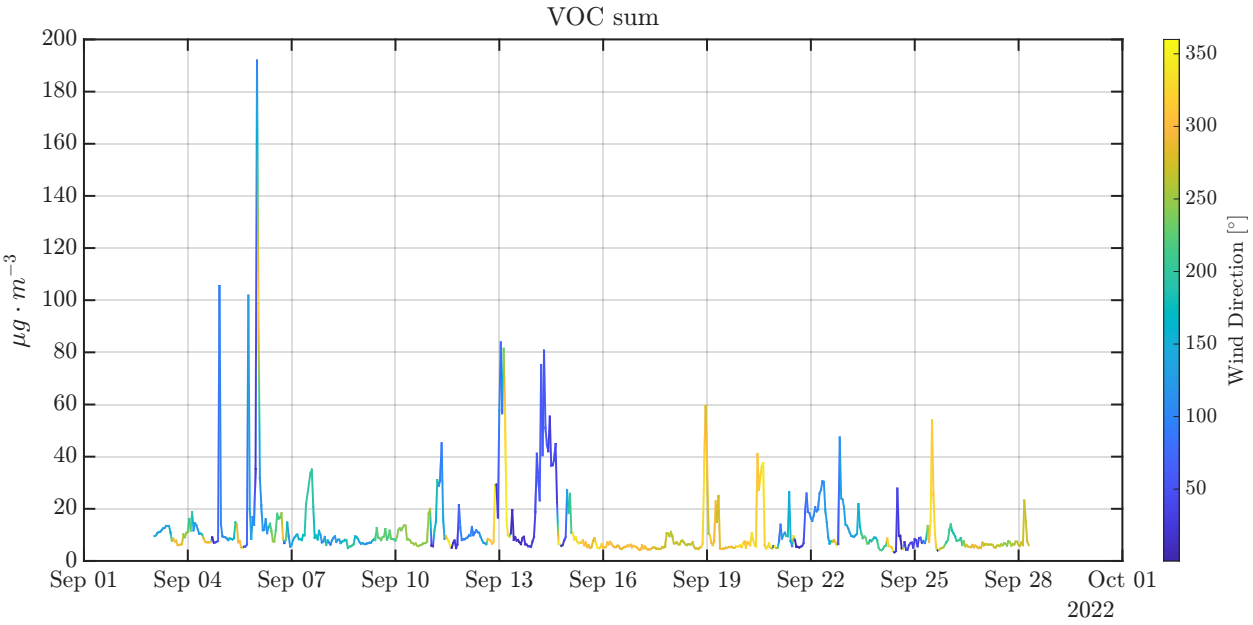

Figure 2-15: *Time series of the sum of VOC concentrations measured with the TD-GC-FID during the whole campaign, colour-coded with the wind direction.*

PTR The statistics of the measurements from this instrument are summarised in Table 2-11 for the 72 VOCs that were clearly identified and selected in the study. By far, methanol (CH_3OH) is the most abundant compound in both the PTR-ToF-MS and TD-GC-FID measurements, with an average of 24.22 ± 29.48 µg·m^{-3}. The next most abundant VOCs are acetic acid ($C_2H_4O_2$, 3.35 ± 12.16 µg·m^{-3}), acetone (C_3H_6O, 3.26 ± 1.40 µg·m^{-3}), acetaldehyde (CH_3CHO, 1.10 ± 1.06 µg·m^{-3}) and ethanol (C_2H_6O, 0.73 ± 2.63 µg·m^{-3}). This is consistent with the fact that these oxygenated compounds are abundant in the atmosphere. The average concentration of C_4H_8 is 0.88 ± 1.28 µg·m^{-3} but can be identified butenes (1-butene, Z-2-butene and E-2-butene) or as a fragmentation product of valeric acid, hexanol or butanal (Yáñez-Serrano et al., 2021). Data availability is complete for the long-lived OVOCs in the atmosphere, such as formaldehyde (HCHO), methanol, acetaldehyde, ethanol, acetone or acetic acid.

The availability of BTEX: benzene (C_6H_6), toluene (C_7H_8) and xylenes + ethylbenzene (C_8H_{10}) is higher than for TD-GC-FID, with 91.6%, 88% and 95% respectively, versus 78.9%, 86.4% and 67.8% (average xylenes and ethylbenzene) for GC. The proportion of concentrations above the LOD of C_5H_8, that could be associated with isoprene, is almost complete (92.3%) whereas isoprene was not significantly detected by the GC (8.7%). This confirms the attribution of C_5H_8 (m/z 69.070) as a fragmentation product of cycloalkanes or cycloalkenes (Yuan et al., 2017; Coggon et al., 2024).

Table 2-11: *Statistics of the measurements of VOCs from the PTR-ToF-MS during the Dunkirk 2022 campaign. Concentrations are expressed in $\mu g{\cdot}m^{-3}$. The availability of the data is calculated upon the VOC measurement cycles of the PTR-ToF-MS at the native time resolution (1 s).*

VOC ($\cdot H^+$)	m/z	mean	median	min	max	std	% >LOD	VOC ($\cdot H^+$)	m/z	mean	median	min	max	std	% >LOD
HCHO	31.016	0.76	0.57	0.04	21.66	0.48	100.0	$C_3H_4O_3$	89.024	0.06	0.05	0.02	10.66	0.04	20.4
CH_3OH	33.035	24.22	14.86	0.30	608.63	29.48	100.0	$C_3H_8N_2O$	89.072	0.10	0.04	0.01	44.95	0.16	54.3
C_2H_3N	42.037	0.25	0.24	0.01	2.76	0.10	99.4	C_7H_8	93.070	0.98	0.27	0.01	120.59	3.69	88.0
C_2H_3O	43.018	0.64	0.47	0.03	156.80	0.81	98.3	$C_2H_6S_2$	94.999	0.03	0.02	0.004	4.77	0.03	43.7
C_3H_7	43.054	0.35	0.21	0.01	24.93	0.43	91.5	C_6H_6O	95.047	0.08	0.06	0.02	63.14	0.22	17.4
CH_3CHO	45.036	1.10	0.78	0.02	103.97	1.06	98.6	C_7H_{10}	95.086	0.08	0.06	0.01	12.82	0.10	66.5
CH_2O_2	47.025	0.13	0.14	0.02	54.51	0.12	8.5	$C_5H_4O_2$	97.027	0.06	0.03	0.01	11.60	0.08	42.0
C_2H_6O	47.049	0.73	0.27	0.01	123.50	2.63	92.7	C_6H_8OH	97.064	0.05	0.03	0.01	2.53	0.05	50.8
C_3H_4O	57.033	0.16	0.11	0.01	83.22	0.24	76.2	C_7H_{13}	97.101	0.16	0.11	0.01	15.45	0.21	89.0
C_4H_8	57.070	0.88	0.46	0.02	134.26	1.28	97.5	H_2SO_4	98.950	0.02	0.02	0.005	4.62	0.02	40.2
C_3H_6O	59.049	3.26	2.95	0.04	92.75	1.40	100.0	$C_4H_2O_3$	99.004	0.09	0.05	0.01	9.94	0.19	56.4
$C_2H_4O_2$	61.028	3.35	1.60	0.06	1150.16	12.16	99.4	$C_5H_2O_2$	99.044	0.10	0.08	0.01	5.03	0.09	57.5
DMS	63.026	0.08	0.06	0.01	2.10	0.08	62.3	$C_6H_{10}O$	99.080	0.08	0.06	0.01	12.84	0.09	70.9
$C_2H_2F_2$	65.020	0.04	0.02	0.005	18.51	0.05	44.9	C_7H_{14}	99.114	0.04	0.02	0.005	24.55	0.04	50.7
$C_2H_8O_2$	65.059	0.10	0.07	0.01	73.41	0.28	25.6	$C_4H_4O_3$	101.023	0.07	0.05	0.02	17.42	0.05	34.5
C_5H_6	67.054	0.06	0.04	0.01	7.67	0.07	29.7	$C_5H_8O_2$	101.060	0.21	0.15	0.01	66.76	0.23	87.2
C_4H_4O	69.033	0.07	0.04	0.01	16.24	0.06	38.6	$C_6H_{12}O$	101.096	0.10	0.07	0.01	35.88	0.13	72.6
C_5H_8	69.070	0.52	0.33	0.02	31.19	0.75	92.3	$C_4H_6O_3$	103.039	0.05	0.03	0.01	4.04	0.04	33.7
C_4H_6O	71.050	0.20	0.13	0.01	14.23	0.21	86.3	$C_5H_{10}O_2$	103.075	0.06	0.04	0.01	11.54	0.08	60.9
C_5H_{10}	71.089	0.43	0.23	0.01	65.83	0.61	87.4	$C_6H_{14}O$	103.112	0.02	0.01	0.004	3.52	0.02	20.4
$C_3H_4O_2$	73.032	0.14	0.11	0.02	34.94	0.14	59.6	C_8H_8	105.070	0.08	0.03	0.003	9.91	0.24	59.1
C_4H_8O	73.066	0.63	0.45	0.01	71.57	0.58	99.5	C_7H_6O	107.053	0.02	0.01	0.004	10.73	0.03	23.9
$C_2H_4O_3$	77.023	0.32	0.29	0.05	21.83	0.23	65.5	C_8H_{10}	107.079	0.91	0.40	0.01	69.66	1.91	95.0
$C_3H_8O_2$	77.060	0.08	0.06	0.02	20.95	0.06	20.4	C_7H_8O	109.065	0.03	0.02	0.005	3.07	0.03	44.9
C_6H_5	78.046	0.05	0.05	0.01	8.23	0.04	11.0	C_8H_{12}	109.102	0.06	0.05	0.004	10.51	0.07	74.0
C_2H_6SO	78.997	0.02	0.02	0.01	0.41	0.01	12.5	$C_7H_{10}O$	111.079	0.04	0.02	0.01	4.51	0.04	48.6
$C_2H_6O_3$	79.040	0.08	0.04	0.01	69.21	0.25	17.1	C_8H_{14}	111.117	0.12	0.08	0.01	13.99	0.15	84.2
C_6H_6	79.054	0.52	0.25	0.01	110.27	2.13	91.6	$C_5H_4O_3$	113.026	0.05	0.02	0.01	8.52	0.05	42.6
C_6H_8	81.072	0.23	0.14	0.01	6.98	0.27	75.7	$C_6H_8O_2$	113.060	0.06	0.03	0.01	11.54	0.06	48.0
H_3PO_3	82.990	0.02	0.02	0.004	5.34	0.02	35.8	$C_7H_{12}O$	113.095	0.04	0.03	0.005	3.63	0.04	57.0
C_2HF_3	83.011	0.03	0.02	0.01	0.98	0.02	25.5	$C_4H_4O_4$	117.021	0.02	0.01	0.01	6.02	0.01	14.7
C_5H_6O	83.050	0.08	0.05	0.01	12.11	0.09	58.0	$C_5H_8O_3$	117.055	0.04	0.02	0.005	7.67	0.05	38.2
C_6H_{10}	83.086	0.25	0.17	0.02	26.40	0.33	87.4	$C_6H_{12}O_2$	117.092	0.05	0.03	0.004	13.08	0.07	59.9
C_5H_8O	85.065	0.10	0.08	0.01	13.70	0.11	63.7	$C_7H_4O_3$	137.017	0.01	0.01	0.002	0.84	0.01	20.5
$C_4H_6O_2$	87.045	0.17	0.15	0.02	23.16	0.16	75.2	$C_8H_8O_2$	137.059	0.02	0.01	0.003	0.97	0.02	41.7
$C_5H_{10}O$	87.080	0.16	0.12	0.01	21.91	0.17	82.2	$C_{15}H_{24}$	205.195	0.02	0.01	0.003	14.15	0.03	40.9

Table 2-12 shows the results of the uncertainty calculations on the PTR-ToF-MS. Overall, the SNRs obtained for this instrument are lower than those for the TD-GC-FID. For example, the SNR of toluene is 2.02 and is among the highest. This may be due to a significantly larger matrix or a decrease in the signal after averaging. Still, the SNRs of BTEX remain relatively high compared to those of the other compounds, at 2.64 for xylenes+ethylenzene and 1.60 for benzene. However, the highest SNRs are found for methanol (4.34), acetaldehyde (2.98), acetic acid (2.61) and acetone (6.41), which is consistent with the trends observed in Table 2-11.

Table 2-12: *Statistics of the uncertainties on the PTR-ToF-MS measurements of VOCs and associated SNR based on Norris et al. (2014). The calculations were performed on the 1 min-averaged concentrations of PTR-ToF-MS.*

VOC ($\cdot H^+$)	m/z	mean	median	min	max	std	SNR	VOC ($\cdot H^+$)	m/z	mean	median	min	max	std	SNR
HCHO	31.016	14.21	1.42	0.06	31273.66	410.77	0.28	$C_3H_4O_3$	89.024	0.08	0.07	0.04	5.28	0.05	0.02
CH_3OH	33.035	4.69	3.34	1.28	752.65	10.70	4.34	$C_3H_8N_2O$	89.072	0.06	0.05	0.02	9.70	0.08	0.56
C_2H_3N	42.037	0.11	0.11	0.02	0.83	0.03	1.44	C_7H_8	93.070	0.19	0.12	0.04	11.15	0.38	2.02
C_2H_3O	43.018	0.27	0.17	0.05	389.21	3.10	2.04	$C_2H_6S_2$	94.999	0.03	0.03	0.01	4.55	0.04	0.07
C_3H_7	43.054	0.12	0.11	0.03	7.56	0.08	1.45	C_6H_6O	95.047	0.10	0.10	0.06	24.40	0.27	0.05
CH_3CHO	45.036	0.80	0.23	0.07	2403.97	24.17	2.98	C_7H_{10}	95.086	0.06	0.05	0.01	24.33	0.20	0.46
CH_2O_2	47.025	0.29	0.24	0.04	239.61	2.21	0.003	$C_5H_4O_2$	97.027	0.06	0.05	0.02	15.55	0.12	0.20
C_2H_6O	47.049	0.14	0.09	0.02	60.58	0.52	2.61	C_6H_8OH	97.064	0.05	0.04	0.02	47.99	0.37	0.18
C_3H_4O	57.033	0.14	0.08	0.01	79.17	1.05	0.71	C_7H_{13}	97.101	0.09	0.06	0.01	38.03	0.56	1.09
C_4H_8	57.070	0.50	0.18	0.06	1129.60	10.77	2.21	H_2SO_4	98.950	0.03	0.03	0.01	1.01	0.01	0.02
C_3H_6O	59.049	0.43	0.40	0.15	9.89	0.16	6.41	$C_4H_2O_3$	99.004	0.06	0.05	0.02	1.65	0.03	0.37
$C_2H_4O_2$	61.028	0.60	0.39	0.11	103.51	1.79	3.57	$C_5H_2O_2$	99.044	0.08	0.07	0.03	38.89	0.38	0.40
DMS	63.026	0.07	0.06	0.01	14.89	0.12	0.28	$C_6H_{10}O$	99.080	0.05	0.05	0.01	3.13	0.03	0.52
$C_2H_2F_2$	65.020	0.05	0.04	0.01	4.05	0.03	0.06	C_7H_{14}	99.114	0.04	0.03	0.01	5.30	0.05	0.15
$C_2H_8O_2$	65.059	0.23	0.11	0.02	584.75	6.25	0.10	$C_4H_4O_3$	101.023	0.08	0.07	0.05	4.95	0.07	0.06
C_5H_6	67.054	0.07	0.06	0.01	2.70	0.03	0.09	$C_5H_8O_2$	101.060	0.09	0.08	0.02	149.54	1.11	1.22
C_4H_4O	69.033	0.08	0.07	0.02	48.25	0.36	0.06	$C_6H_{12}O$	101.096	0.06	0.06	0.01	4.84	0.05	0.55
C_5H_8	69.070	0.19	0.17	0.04	9.03	0.12	1.33	$C_4H_6O_3$	103.039	0.05	0.05	0.03	1.60	0.02	0.06
C_4H_6O	71.050	0.08	0.07	0.01	3.92	0.05	1.34	$C_5H_{10}O_2$	103.075	0.04	0.04	0.01	3.01	0.04	0.31
C_5H_{10}	71.089	0.15	0.12	0.02	71.22	0.53	1.43	$C_6H_{14}O$	103.112	0.02	0.02	0.01	2.23	0.02	0.004
$C_3H_4O_2$	73.032	0.10	0.10	0.03	7.66	0.09	0.38	C_8H_8	105.070	0.04	0.03	0.01	2.00	0.04	0.49
C_4H_8O	73.066	0.15	0.13	0.04	6.96	0.09	2.69	C_7H_6O	107.053	0.03	0.03	0.01	3.28	0.04	0.05
$C_2H_4O_3H$	77.023	0.22	0.19	0.07	136.22	1.15	0.76	C_8H_{10}	107.079	0.36	0.13	0.04	476.30	5.53	2.64
$C_3H_8O_2H$	77.060	0.11	0.09	0.05	63.73	0.55	0.01	C_7H_8O	109.065	0.03	0.03	0.01	11.36	0.09	0.11
C_6H_5	78.046	0.08	0.08	0.04	2.74	0.05	0.01	C_8H_{12}	109.102	0.07	0.04	0.01	364.44	2.69	0.44
C_2H_6SO	78.997	0.04	0.03	0.02	0.52	0.01	0.003	$C_7H_{10}O$	111.079	0.04	0.03	0.01	2.51	0.02	0.12
$C_2H_6O_3$	79.040	0.09	0.08	0.03	8.16	0.08	0.05	C_8H_{14}	111.117	0.40	0.05	0.01	5446.86	40.13	0.85
C_6H_6	79.054	0.14	0.11	0.03	10.25	0.22	1.60	$C_5H_4O_3$	113.026	0.05	0.04	0.02	8.26	0.07	0.13
C_6H_8	81.072	0.12	0.09	0.03	233.67	1.73	0.89	$C_6H_8O_2$	113.060	0.06	0.05	0.02	90.76	0.69	0.19
H_3PO_3	82.990	0.03	0.03	0.01	1.62	0.01	0.01	$C_7H_{12}O$	113.095	0.04	0.03	0.01	1.14	0.01	0.19
C_2HF_3	83.011	0.04	0.04	0.02	1.58	0.02	0.01	$C_4H_4O_4$	117.021	0.03	0.03	0.02	1.30	0.01	0.001
C_5H_6O	83.050	0.06	0.06	0.02	9.20	0.08	0.33	$C_5H_8O_3$	117.055	0.04	0.04	0.01	35.05	0.27	0.09
C_6H_{10}	83.086	0.10	0.09	0.02	7.27	0.08	1.23	$C_6H_{12}O_2$	117.092	0.06	0.04	0.01	30.29	0.50	0.29
C_5H_8O	85.065	0.07	0.07	0.02	4.92	0.04	0.44	$C_7H_4O_3$	137.017	0.02	0.02	0.01	0.38	0.004	0.004
$C_4H_6O_2$	87.045	0.10	0.09	0.02	9.99	0.08	0.76	$C_8H_8O_2$	137.059	0.03	0.03	0.01	37.65	0.38	0.04
$C_5H_{10}O$	87.080	0.08	0.08	0.01	5.85	0.06	0.84	$C_{15}H_{24}$	205.195	0.04	0.03	0.01	73.45	0.66	0.07

As can be seen in Figure 2-16, methanol is the main contributor to the observed VOC mass. For example, it accounted for 58% of the mass observed during the peak on 11th September and 64% during the peak on 25th September. While the lowest variability of the TD-GC-FID measurements is encountered in the northern wind direction, the PTR-ToF-MS measurements show a greater variability during this period. Winds between 270 and 60° are favourable for sampling ship plumes, resulting in transient peaks corresponding to the ship's arrival and departure, as shown in Figure 2-17. The total time series of VOC measured by PTR-ToF-MS is shown in Figure 2-18, showing a great variability at the 1 min timestep.

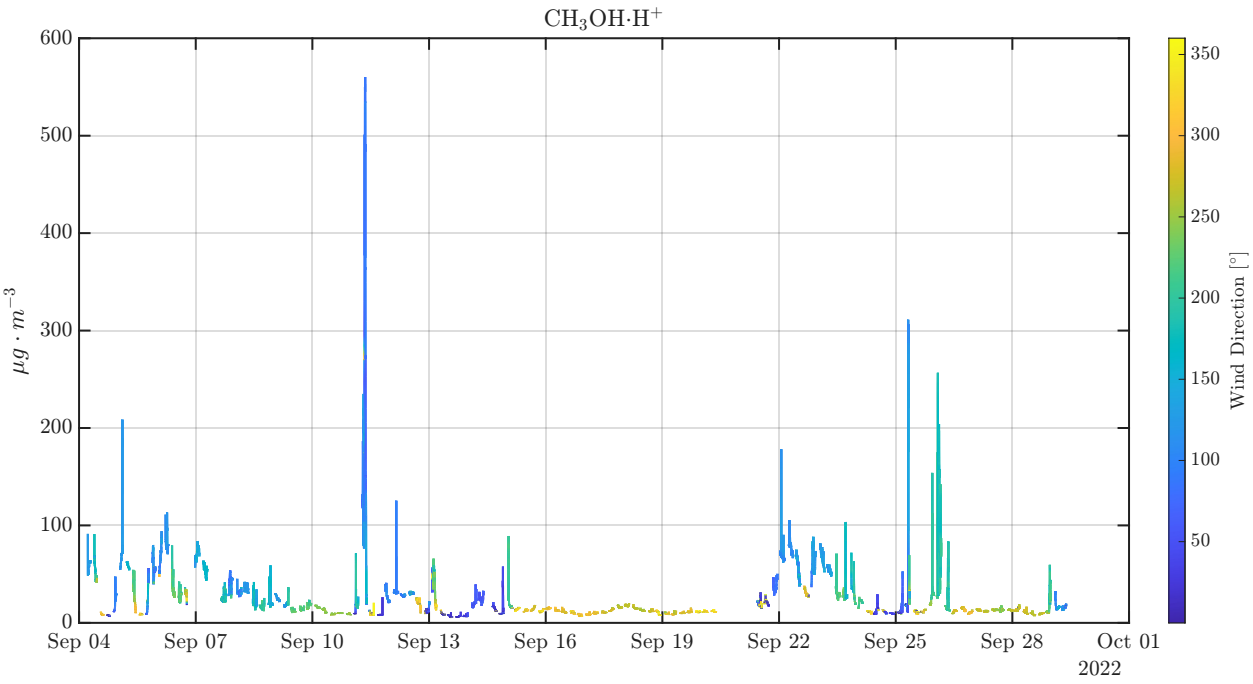

Figure 2-16: *Complete time series of the concentrations of $CH_3OH{\cdot}H^+$ (methanol) measured by the PTR-ToF-MS.*

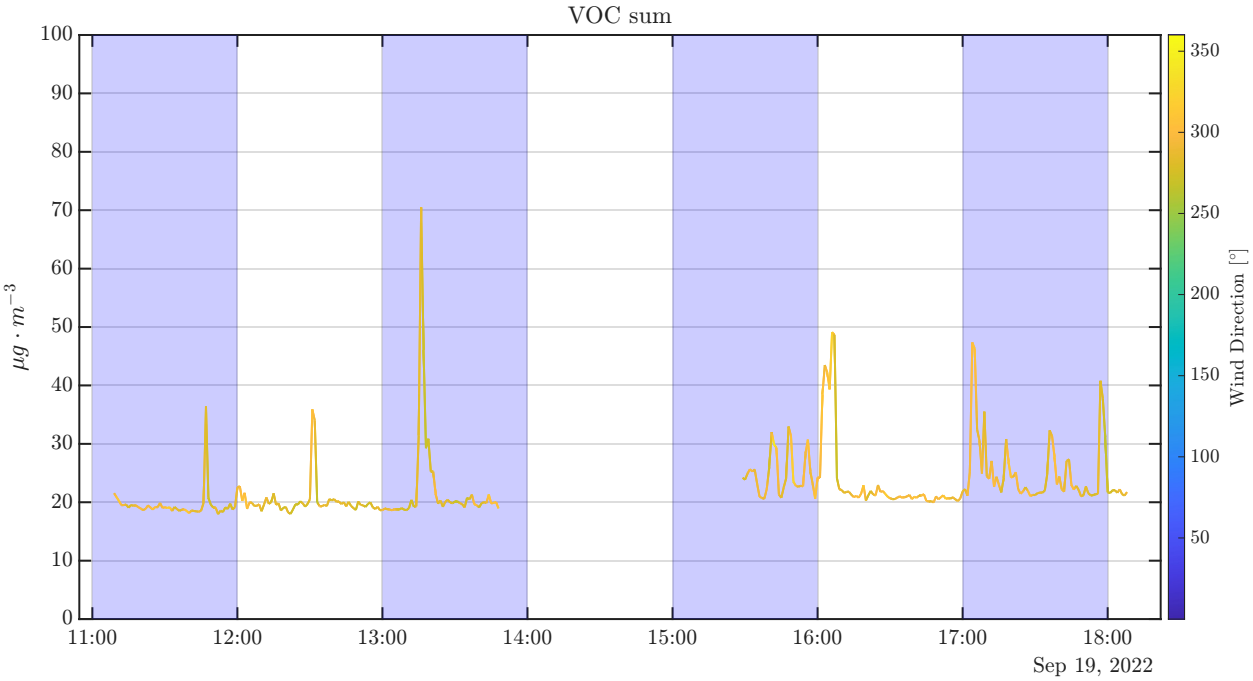

Figure 2-17: *Zoom-in of the sum of concentrations time series of VOCs measured by PTR-ToF-MS within the favourable wind period. The blue shaded areas correspond to a ferry presence in the Dunkirk – Dover dock.*

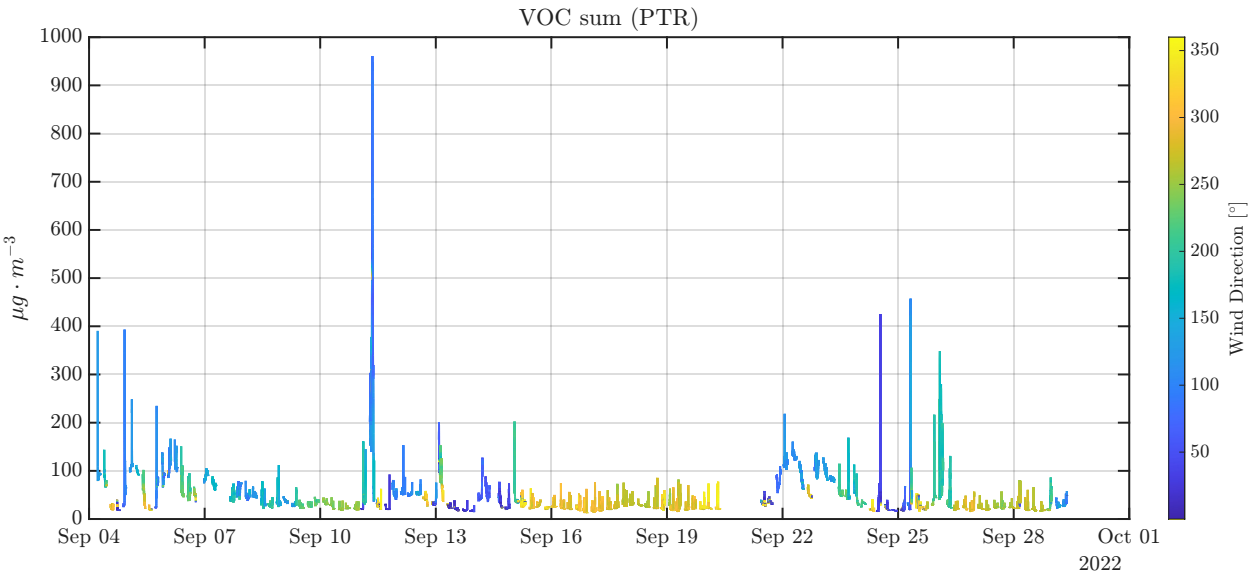

Figure 2-18: *Complete time series of the concentrations of VOCs measured by PTR-ToF-MS, colour-coded with the wind direction.*

2.3.c Comparison to other study

The levels observed in September 2022 are lower than those reported in the literature, as shown in Table 2-13. In particular, toluene was found to be the most abundant aromatic compound in all reported studies (Badol et al., 2008a; Roukos et al., 2009; Xiang et al., 2012; Farhat et al., 2024), but its mean concentration in 2022 is the lowest compared to all studies. To the best of our knowledge, the VOCs compared are the lowest ever recorded in Dunkirk in 2022, except for benzene, which is slightly higher that the levels observed in 2009 (Xiang et al., 2012). While these differences can be partially explained by changes in regulations regarding fuel storage or solvents used, the closure of the Total Flandres refinery in 2010 may have affected VOC levels, which could account for the decrease in BTEX levels.

Table 2-13: *Mean levels of VOCs observed in Dunkirk in 2022 and in previous studies. Concentrations are expressed in $\mu g{\cdot}m^{-3}$. (*): graphical reading. ($^{\triangle}$) converted from ppb to $\mu g{\cdot}m^{-3}$.*

Study	This study	Farhat et al. (2024)$^{*,\triangle}$	Xiang et al. (2012)	Roukos et al. (2009)	Badol et al. (2008a)$^{\triangle}$
Location	Industrial	Industrial	Industrial	Industrial	Urban
Date	September, 2022	July, 2014	July, 2009	June, 2007	September, 2002 – August, 2003
Ethane	1.03 ± 0.44	2.54			5.49
Propane	0.64 ± 0.63	8.69			4.17
Butane	0.88 ± 0.81	2.72			2.49
Isobutane	0.62 ± 0.43	1.24			1.64
pentane	0.52 ± 1.17	2.68			1.59
isopentane	0.69 ± 1.5	3.96			2.82
Ethylene	0.40 ± 0.50	4.71			2.56
Propene	0.18 ± 0.32	3.14			1.87
Acetylene	0.11 ± 0.07	0.20			0.84
Styrene	0.02 ± 0.05	1.14			0.17
Isoprene	0.06 ± 0.07	0.33			0.11
alphapinene	0.06 ± 0.14	0.83			
2-Methyl-pentane	0.25 ± 0.73		0.81 ± 2.91 (+2.2-dimethylbutane)		0.82
Heptane	0.12 ± 0.45		0.63 ± 0.67		0.46
Octane	0.09 ± 0.19				0.24
Isooctane	0.08 ± 0.19				0.24
Benzene	0.44 ± 1.74	1.03	0.40 ± 0.71	1.55 ± 0.62	1.72
Toluene	1.17 ± 3.3	3.39	1.22 ± 1.97	2.10 ± 2.66	4.06
Ethylbenzene	0.28 ± 0.81	1.11	0.37 ± 0.50	0.56 ± 0.77	0.75
m&p-Xylenes	0.47 ± 1.15	2.53	0.86 ± 1.20	0.82 ± 0.95	0.53
o-Xylene	0.24 ± 0.59	1.78	0.3 ± 0.38	0.32 ± 0.39	0.88
1,3,5-Trimethylbenzene	0.07 ± 0.16		0.25 ± 0.30		
1,2,4-Trimethylbenzene	0.07 ± 0.13		0.43 ± 0.54		
1,2,3-Trimethylbenzene	0.04 ± 0.04		0.19 ± 0.13		

2.4 Combined approaches of data analysis

The large number of variables studied in this thesis results in a complex dataset that necessitates advanced analytical tools for effective processing. This section presents the analytical tools used in this work to identify sources, whether in terms of origin, chemical fingerprint, or contribution, ranging from simple data visualisation to factor analysis.

2.4.a Wind Analysis

This section presents the various analytical tools used in this thesis to identify the location of sources of pollutants, with a particular focus on methods requiring wind information, mainly direction and velocity. When working with concentrations of pollutants from various instruments, averaging will inevitably be required at some point, so the geometric mean must be used to calculate the average of wind direction and velocity. Let θ be the wind direction expressed in $^{\circ}$ and υ the velocity expressed in $\mathrm{m{\cdot}s^{-1}}$: υ should be projected in cartesian coordinates using θ to account for the difference in both wind direction and speed during averaging:

$$\begin{cases} Y = \upsilon \cdot \sin\left(\theta \times \dfrac{\pi}{180}\right), \\ X = \upsilon \cdot \cos\left(\theta \times \dfrac{\pi}{180}\right), \end{cases} \tag{2.53}$$

Next, the arithmetic means of projected X and Y can be computed, resulting in X_{av} and Y_{av}. Finally, the averaged wind speed and direction are recovered:

$$v_{av} = \sqrt{X_{av}^2 + Y_{av}^2}, \tag{2.54}$$

$$\theta_{av} = \tan^{-1}\left(\frac{Y_{av}}{X_{av}}\right) \times \frac{180}{\pi}. \tag{2.55}$$

in case the resulting θ_{av} is below 0°:

$$\text{if } (\theta_{av} < 0), \theta_{av} = \theta_{av} + 360°. \tag{2.56}$$

This averaging step is necessary to accurately assign a wind direction and speed to a concentration observation. This enables the observations to be used in wind models, such as the ones presented below. Such modelling can be performed using the built-in analytical tool ZeFir, implemented in Igor Pro and developed by Petit et al. (2017), or the Positive Matrix Factorisation tool SoFi Pro, which is described further down.

2.4.a.i Wind and pollution roses

The simplest visualisation of the impact of wind on the site is the wind rose. It is a polar representation in which the polar axis corresponds to the wind direction (usually, north = 0° and east = 90°) and the radial axis corresponds to the frequency, i.e. the number of occurrences, of the directional wind bin which width is user-defined. Each of these bins can be divided into a user-defined number of wind speed, as shown in Figure 2-19. This figure shows that the most frequent winds come from the west, and that the highest wind velocities are met in the west also. When pollutant concentration ranges are used instead of velocity ranges, this representation becomes a pollution rose.

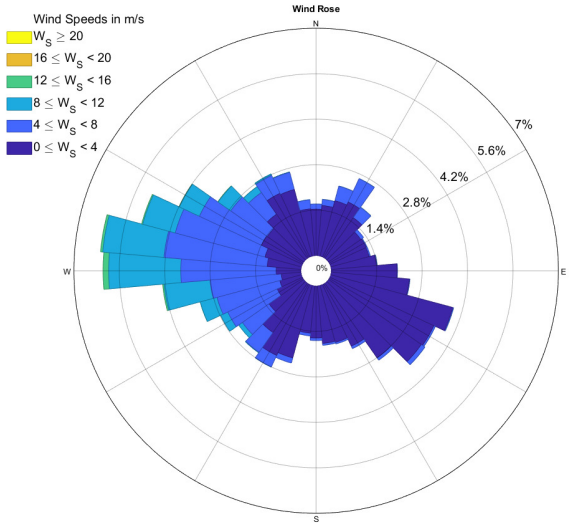

Figure 2-19: *Wind rose observed during the campaign.*

2.4.a.ii Non-parametric Wind Regression

Henry et al. (2009) describe the use of the Non-parametric Wind Regression (NWR) in receptor-oriented models to help locate and quantify local emission sources using wind speed and direction. In the NWR model, each concentration is associated with a wind direction θ and velocity υ and plotted at the (θ,υ) coordinates. The concentration C of a certain pollutant observed at a given (θ,υ) is computed as the weighted average of the concentration data in the vicinity of that direction and velocity. This concentration is then smoothed on the map using the user-defined parameters σ and h, which lead to a kernel (weighting) function K, $K(\theta, \upsilon, \sigma, h) = K_1(\theta, \sigma)K_2(u, h)$:

$$E(C|\theta, \upsilon) = \frac{\sum_{i=1}^{N} K_1\left(\frac{\theta - W_i}{\sigma}\right) K_2\left(\frac{u - U_i}{h}\right) C_i}{\sum_{i=1}^{N} K_1\left(\frac{\theta - W_i}{\sigma}\right) K_2\left(\frac{u - U_i}{h}\right)}, \tag{2.57}$$

with C_i, U_i and W_i denoting the concentration and the resulting wind speed and direction respectively. N is the total number of samples. This results in a representation as presented in Figure 2-20.

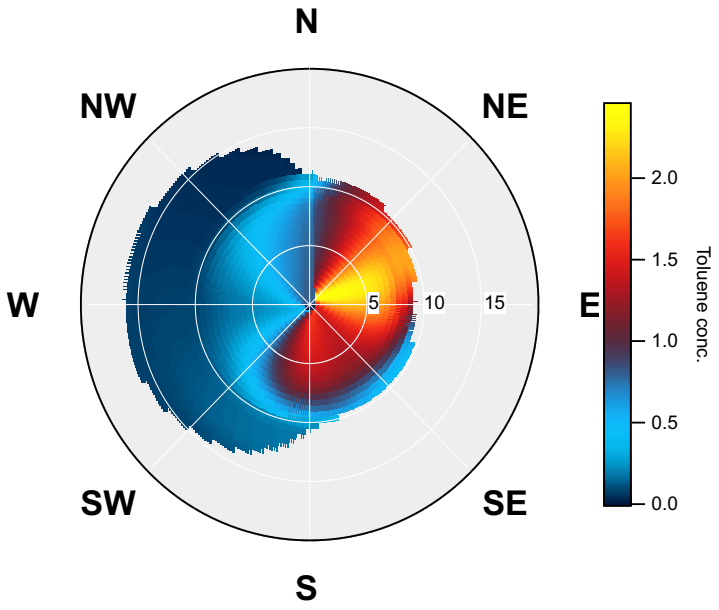

Figure 2-20: *NWR plot of toluene during the whole campaign.*

2.4.b Source apportionment

2.4.b.i Emission Factors

The chemical fingerprint of a source can be determined using Emission Factors (EFs), also known as the carbon ratio method. Used in emission inventories, as presented in Section 1.3.c, EFs are a quantity expressed in mass emitted per energy unit. The energy to fuel conversion is performed using the lower heating value (LHV), which reports the heat energy released by the combustion of 1 kg of fuel when considering that water vapour is part of the combustion products and its heat is not recovered. Each fuel has a different LHV [1] and results in EFs to be expressed in mass of pollutants emitted per mass of fuel consumed ($g \cdot kg_{fuel}^{-1}$). Equation 2.58 is applied to observations under the net exclusive influence of the source in question. Therefore, the background concentrations of pollutants are subtracted in the selected period, as expressed in Equation 2.59 (Diesch et al., 2013; Alföldy et al., 2013; Pirjola et al., 2014; Van Roy et al., 2022a; Le Berre et al., 2025; Celik et al., 2020):

$$EF = \frac{\int \Delta X(\mu g \cdot m^{-3})}{\frac{M_c}{M_{CO_2}} \cdot \int \Delta CO_2(mg \cdot m^{-3})} \cdot \omega_c, \tag{2.58}$$

$$= \frac{\int X - X_{bg}(\mu g \cdot m^{-3})}{\frac{M_c}{M_{CO_2}} \int CO_2 - CO_{2_{bg}}(mg \cdot m^{-3})} \cdot \omega_c, \tag{2.59}$$

where ΔX refers to the net concentration of the pollutant of interest, ΔCO_2 refers to the net concentration of CO_2 and ω_c refers to the carbon mass fraction ($kg\ C \cdot kg_{fuel}^{-1}$) in the fuel used by the ships. The EFs of ships can be determined from airborne observations, as reported in the Belgian waters (Van Roy et al., 2022a,b). They can also be directly determined from stack measurements, which allow sampling of the fresh plume and ensure that the observed signal is exclusively attributable to ship emissions (Cooper, 2003; Timonen et al., 2022; Zhang et al., 2024; Celik et al., 2020; Agrawal et al., 2008). Access to direct measurements at ship stacks is more limited than to field campaigns within port areas, as accessing ship exhaust stacks is logistically challenging and often restricted due to safety and operational regulations and requires the involvement of the ship operating company. In this context, ambient on-site measurements provide a valuable added value, as they allow the emissions from multiple vessels and other port-related activities to be characterised simultaneously, offering a more comprehensive view of their real-world contributions (Diesch et al., 2013; Alföldy et al., 2013; Pirjola et al., 2014; Le Berre et al., 2025). In such cases, specific tracers and favourable wind conditions are needed in order to identify periods during the campaign that are affected by emissions from ships. In this thesis, the conditions of identification of ship emissions are presented in Section 3.2.e.

[1] https://www.engineeringtoolbox.com/fuels-higher-calorific-values-d_169.html

In addition, the Fuel Sulphur Content (FSC) can be calculated to assess ships' compliance with regulations. It can be calculated in units of % based on EF(SO_2), assuming that all sulphur in the fuel is oxidised to SO_2 (Petzold et al., 2008; Pirjola et al., 2014). If SO_2 is expressed in ppb and CO_2 in ppm, the FSC results from the integration of the peaks over the background (Pirjola et al., 2014):

$$FSC(\%) = \frac{M_s}{M_{CO_2}} \times EF_{CO_2} \times \frac{10^{-3} \int \Delta SO_2(ppb)}{\int \Delta CO_2(ppm)} \times 100, \tag{2.60}$$

$$FSC(\%) \approx 0.232 \times \frac{\int \Delta SO_2(ppb)}{\int \Delta CO_2(ppm)}, \tag{2.61}$$

as EF_{CO_2} is taken in the literature around 3107 $g \cdot kg_{fuel}^{-1}$ (Petzold et al., 2008), when converted in $g \cdot g_{fuel}^{-1}$ results in the FSC to be calculated with a 0.232 coefficient in the literature (Balzani Lööv et al., 2014; Pirjola et al., 2014; Beecken et al., 2015; Van Roy et al., 2022a,b), and was kept here for consistency with other studies. Then, ppb and ppm are converted in mass concentration:

$$FSC(\%) \approx 0.232 \times \frac{\int SO_2 - SO_{2_{bg}}(\mu g \cdot m^{-3})}{\int CO_2 - CO_{2_{bg}}(mg \cdot m^{-3})} \times \frac{M_{CO_2}}{M_{SO_2}}, \tag{2.62}$$

which can be expressed as EF_{SO_2} according to Equation 2.59, that results in the final expression of the FSC in our study:

$$FSC(\%) \approx 0.232 \times EF_{SO_2}(g \cdot kg_{fuel}^{-1}) \times \frac{M_C}{M_{CO_2}} \times \frac{1}{\omega_c} \times \frac{M_{CO_2}}{M_{SO_2}}, \tag{2.63}$$

$$FSC(\%) \approx 0.232 \times EF_{SO_2}(g \cdot kg_{fuel}^{-1}) \times \frac{M_c}{\omega_c M_{SO_2}}. \tag{2.64}$$

2.4.b.ii Generalities on source-receptor models

Source-receptor models are one of the approaches used to analyse air pollution sources and apportion emissions. In contrast to source-oriented dispersion models, which take into account the transport of pollutants from the source to the site, receptor-oriented models focus on observations of the mass of pollutants at the impact point. Receptor-oriented models are based on the principle of mass conservation from the emission source to the receptor site (Hopke, 2006) which is expressed as follows (Hopke, 2000):

$$x_{ij} = \sum_{k=1}^{p} f_{ik} \cdot g_{kj} + e_{ij}, \tag{2.65}$$

with x_{ij} denoting the concentration observed of ith compound of the jth sample, f_{ik} denoting the fraction of the ith compound of the kth source, g_{kj} denoting the contribution of the kth source to the jth sample and e_{ij} denoting the unmodelled part of the observations. This type of model uses a given number of factors to explain the observed concentrations, each factor representing a source impacting the site. The question these models answer is expressed as follows: *Which pollution sources, when reconstructed in different proportions, best explain a series of observations?* The identification of the sources is derived from the chemical profiles and contributions obtained using the model. There are multiple receptor models in the literature which vary in the prior knowledge required about the sources, as presented in Figure 2-21. For example, the Chemical Mass Balance (CMB) model requires full a-priori knowledge of the pollution sources (Hopke, 2006), whereas multivariate models such as the Positive Matrix Factorisation (PMF) and the Principal Component Analysis (PCA) require little knowledge about the pollution sources (Paatero and Tapper, 1994; Viana et al., 2008).

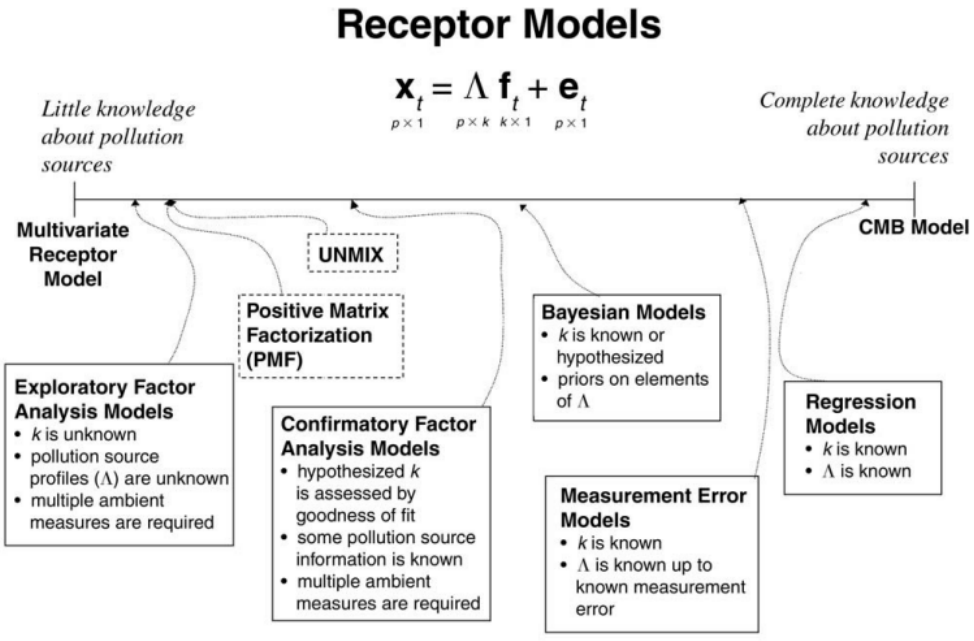

Figure 2-21: *Various approaches to determine sources contribution depending on the prior knowledge required on the sources. p denotes the number of species in the model, k denotes the number of factors, x_t denotes the observational matrix, Λ denotes the profile matrix, f_t denotes the factor contribution matrix and e_t denotes the residual matrix (Schauer et al., 2006).*

2.4.b.iii Positive Matrix Factorisation

Theory of PMF The PMF was first introduced by Paatero and Tapper (1994) and uses the covariation of input variables to perform the source apportionment. It is broadly used in the literature, for PM (Brown et al., 2015; Mooibroek et al., 2022; Stanimirova et al., 2023) and for VOCs (Sauvage et al., 2009; Slowik et al., 2010; Salameh et al., 2016; Gu et al., 2023; Simon et al., 2025; Dufresne et al., 2025). Although some prior assumptions about the sources were present in Dunkirk, we opted for the PMF approach over the PCA approach. The advantage of the PMF approach over other approaches with low prior knowledge is that it relies on the non-negativity of the sources. This allows for environmentally realistic emission profiles. This constraint was first introduced by Paatero (1997), illustrated in Figure 2-22 and written as follows:

$$X = GF + E, \tag{2.66}$$

with X referring to the observational matrix $(n \times m)$, composed of n samples and m compounds. F refers to the profile matrix $(p \times m)$, representing the contribution of each compound to each factor p. G refers to the contribution matrix $(n \times p)$, representing the contribution of each factor to the modelled concentration of a sample. E refers to the matrix of unmodelled concentrations $(n \times m)$, namely the residuals.

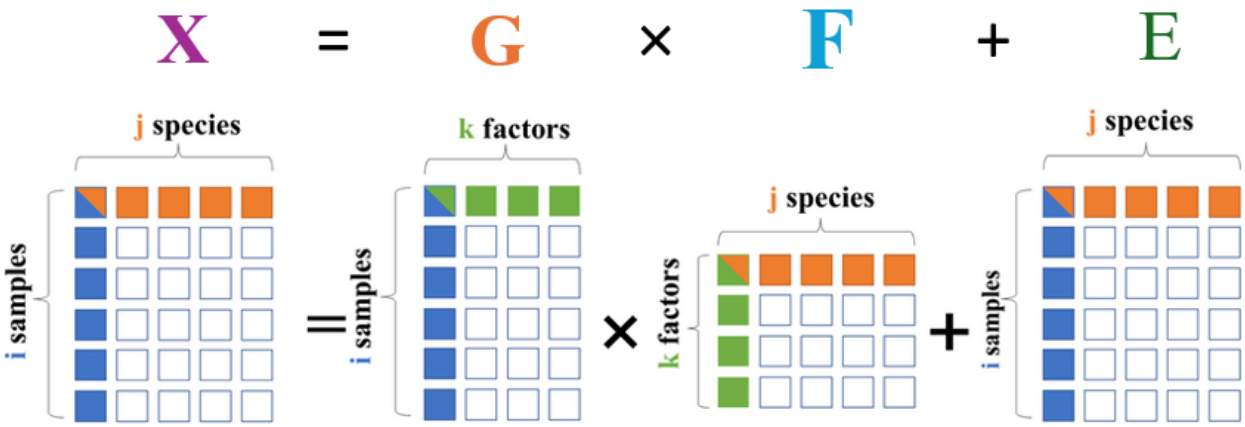

Figure 2-22: *Illustration of the matrices mentioned in the PMF Equation 2.66.*

This quantity is used to minimise the sum of squared residuals, $Q(E)$, to achieve a stable solution of the PMF:

$$Q(E) = \sum_{i=1}^{n} \sum_{j=1}^{m} \left(\frac{e_{ij}}{s_{ij}} \right)^2, \tag{2.67}$$

with e_{ij} denoting the elements of the unmodelled matrix E and s_{ij} denoting the components of the uncertainty matrix. Therefore, the uncertainties of concentrations are mandatory inputs for performing PMF analysis.

Convergence of the criteria is achieved through an iterative process using a solver called the Multilinear Engine (ME), which was first introduced by Paatero (1999). The second version of this solver, ME-2, is now in use (Norris et al., 2014). Briefly, the convergence process comprises three stages, each with increasingly stringent criteria for the change in $Q(E)$ (called dQ) over a set number of steps. The first step identifies the region of the general solution, the second narrows this down to the neighbourhood of the final solution and the third aims to achieve optimal $Q(E)$ values. ME-2 usually requires between a few hundred and 2,000 iterations, depending on the size of the data set. If none of these levels are met, the solution is considered non-convergent. The ME-2 engine is integrated in recent models such as the EPA PMF 5.0[1] or SourceFinder Pro (SoFi Pro, Datalystica Ltd.[2]).

Data quality PMF can be ran in robust mode to limit the impact of outliers with high Signal-to-Noise Ratios (SNRs), rare events that can drive the solution. Their impact is reduced by defining a threshold α, the ratio of residuals to uncertainties, taken as 4 (Paatero, 1997):

$$\text{outlier} = \left|\frac{e_{ij}}{s_{ij}}\right| \geq \alpha. \tag{2.68}$$

The residuals are reweighted to prevent them from determining the solution in the current version of PMF (PMF 5.0), to ensure that each compound impacts the PMF in proportion to its uncertainty, weighting factors are applied to the uncertainties depending on the SNR (Equation 2.52). This means that poor-quality measurements contribute less importantly to the model's convergence than high-quality ones. The criteria used in this study are:

- Strong : SNR ≥ 1, no weighting,
- Weak : $1 >$ SNR ≥ 0.2, $\mathrm{U_{weighted}} = 2\times\mathrm{U_{unweighted}}$,
- Bad : SNR < 0.2, $\mathrm{U_{weighted}} = 10\times\mathrm{U_{unweighted}}$.

PMF solutions To determine the best PMF solution, the sum of squared residuals $Q(E)$ is normalized by the the degree of freedom of the model:

$$Q_{exp} \cong n \cdot m - p(m+n). \tag{2.69}$$

[1] https://www.epa.gov/air-research/positive-matrix-factorization-model-environmental-data-analyses
[2] https://datalystica.com

This accounts for the size of the data matrix (n × m) and the number of factors (p) impacting $Q(E)$ during modelling. Ideally, the value of $Q(E)/Q_{exp}$ is 1, indicating that the solution was modelled with the correct number of factors that captured the full variability of the measured concentrations. However, the $Q(E)/Q_{exp}$ ratio is subject to limitations when the wrong number of factors are chosen, when transient sources are found in the data, or when errors are present in uncertainty estimations and should therefore not be the unique criterion to judge the quality of the modelled solution (Canonaco et al., 2013). In PMF modelling, the difference in $Q(E)/Q_{exp}$ between PMF runs is monitored as indicator of the improvement in the solutions using different parameters. Other methods to ensure the reliability of the solution is to calculate the correlation coefficient (R^2) between the modelled and observed concentrations, or the correlation coefficient between the resulting factor and specific tracers, in order to identify environmentally reasonable factors. The analytical tools presented in Section 2.4.a are used to help explain the PMF factors.

Constrained PMF The factor profiles (F) and contributions (G) in Equation 2.66 can be constrained by the user. To do so, the user must first provide either factor profiles or time series of their contributions as inputs (seeds), meaning that the model will initiate the solutions using these predefined characteristics. The constraint is defined using a scalar known as the a-value, which determines the extent to which the solution matrices are allowed to deviate from the seed (Canonaco et al., 2013):

$$f_{j,final} = f_j \pm a \cdot f_j, \tag{2.70}$$

$$g_{i,final} = g_i \pm a \cdot g_i, \tag{2.71}$$

where f_j denotes a column of the factor profile matrix F, representing the jth compound, and g_i denotes a row of the contribution time series matrix G, corresponding to the ith sample. The parameter a, the a-value, defines the allowable deviation from the seed and can be specified in various ways: either as a fixed scalar value or as a vector with elements ranging from user-defined values between 0 and 1. An a-value = 0.1 means that the factor profile can variate by ±10%. Therefore, an a-value = 0 indicates that the factor is fully constrained and must exactly follow the seeded profile/time series. In opposition, an a-value = 1 allows a variation of 100% and the profile is almost unconstrained. Reference mass spectra are commonly used to perform PMF analysis with organic aerosol (OA) data. They are used to analyse ACSM data and identify a-priori sources, therefore reducing the uncertainty of source apportionment based on profiles representing Biomass OA (BBA), Highly Oxidised Aerosols (HOA) or Oxygenated OA (OOA) for examples (Lin et al., 2017, 2021; Fossum et al., 2024; Simon et al., 2025). However, constraints on VOC data are rarely used (Gkatzelis et al., 2021), because the VOC profiles have a higher variability compared to aerosols. Therefore, the constraint of VOC data in PMF will be explored in this thesis, in order to provide insights into their application with GC and PTR data to resolve shipping emissions.

Multi-time resolution PMF The Multi-Time Resolution PMF (MTR-PMF) is broadly used to combine datasets of various instruments with different time resolutions. This approach allows, for example, a combinatory PMF on 30 min non-refractory PM_1 (NR-PM_1) composition and 24 hours filter black carbon analyses (Via et al., 2023). It has also been used to combine aerosol data with selected VOCs to improve the interpretation of the sources (Slowik et al., 2010; Liao et al., 2013; Kuo et al., 2014; Simon et al., 2025). More generally, this method avoids the disadvantages of averaging and interpolating, which can deteriorate datasets. This results in increased sensitivity, as the method uses the best available time resolution and the greater number of observations (Zhou et al., 2004; Ogulei et al., 2005). The receptor model described by Equation 2.65 is modified to take into account the different time resolutions of each instruments:

$$x_{sj} = \frac{1}{(t_{s2} - t_{s1} + 1)} \sum_{p=1}^{P} \left(f_{jp} \sum_{i=ts_1}^{t_{s2}} g_{ip}\eta_{jm} \right) + e_{sj}, \tag{2.72}$$

with s denoting the sample number, j denoting the compound, t_{s2} and t_{s1} denoting the time units (scalars) of reference, which are those of the dataset with the shortest time interval. x_{sj} denotes the concentration of jth compound in s^{th} sample, f_{jp} denotes the mass fraction of compound j in factor p, g_{ip} denotes the p_{th} factor's mass contribution during the interval of the s_{th} sample and e_{sj} denotes the residual. Adjustments factors η_{jm} are used in case of replicated species between the datasets of different time resolution. The way MTR-PMF operates is represented in Figure 2-23: first, datasets with different time resolutions are combined, the low-resolution data are aligned with the high-resolution time grid, filling missing timestamps with null values and appropriately large uncertainties. The PMF model then estimates the time-resolved factor contribution matrix G only over the finest time scale, and the factor profiles matrix F across all compounds, from both high- and low-resolution instruments. At this point, G is only computed for the highest time resolution (i.e. same number of rows as the high-resolution matrix, and p columns), while F is computed for every variable from the combined matrices. For compounds measured at a lower time-resolution, their modelled concentrations are computed by averaging the corresponding high-resolution factor contributions g_{ip} over the relevant time window, between t_{s2} and t_{s1} expressed in time units from the finest grid. For example, if the highest time-resolution is in minutes, and the lowest in hours, the first sample of the low time-resolution modelled concentrations will be the average of every minutely contributions of the factor g_{ip} between $t_{s2} = 60$ and $t_{s1} = 0$ (if the first sampling of low time-resolution is synchronous with the first timestamp of the high time-resolution) multiplied by its profile f_{jp}. This ensures that each modelled data point is expressed on the same time base as it associated observation. Note that if all compounds are measured at the same time resolution, then t_{s2} will equal t_{s1} for all observations and Equation 2.72 reverts to the common source-receptor Equation 2.65. G and F are then adjusted using the sum of squared residuals to better fit the observations of each instrument.

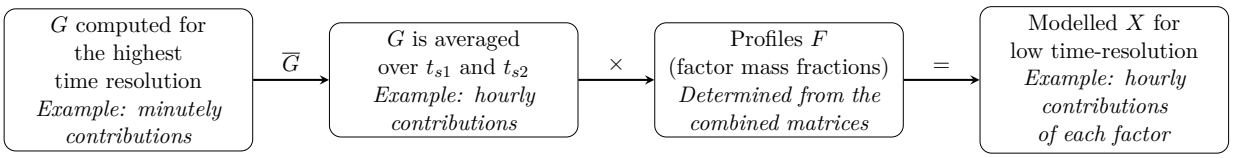

Figure 2-23: *Principle of the MTR-PMF if a 1 min dataset is used as reference, associated with a lower time-resolution dataset with a 1 h timestamp.*

2.4.c Application in the study and strategy

2.4.c.i Period of focus for EF calculation

As mentioned in Section 2.3.b, a favourable wind period for sampling ship plumes was encountered between 14th to 21st September 2022 in Dunkirk, as their main direction was from the north. This resulted in transient peaks of various regulated pollutants, which were also visible on the PTR-ToF-MS signal upon the arrival and departure of the ferries travelling between Dunkirk and Dover. This behaviour was used for the initial VOC source apportionment of the ferry source, as Emission Factors (EFs) were calculated from the peaks, which had to be isolated using a specific tracer. This was achieved using auxiliary data provided by Atmo Hauts-de-France, which had to be filtered from the validated data. Once the ship peaks had been identified, they could be used to perform various classifications depending on the manoeuvre direction and individual ship.

2.4.c.ii PMF: Inputs and strategy

The concentration and uncertainty matrices described previously allowed the measurements of VOCs to be validated and prepared for use in PMF. Inspection of the uncertainty and concentration matrix meant that each compound could be attributed a quality criterion, as mentioned in Section 2.4.b.iii. This results in a 631×64 matrix comprising 20 compounds with a strong quality, 16 with a weak quality and 28 with a bad quality for the TD-GC-FID. The initial matrix of PTR-ToF-MS measurements resulted in a 1,100,854×72 matrix at its native resolution (1 s), which was averaged over 1 min for optimisation. This produced a 18,463×72 matrix. According to SNR-based quality criteria, 19 compounds are of strong quality, 21 are of weak quality, and 32 are of poor quality. SourceFinder Pro (SoFi Pro), developed by Datalystica Ltd. (2021), was used to perform PMF in this study.

SoFi Pro is an IgorPro-based interface for initialising PMF runs, feeding the ME-2 solver with user-defined parameters, and analysing the PMF results. It was originally developed for Aerosol Chemical Speciation Monitor (ACSM) data (Canonaco et al., 2013, 2015), and the most recent developments allow PMF analysis to be performed with time-dependent factors, including rolling PMF (Canonaco et al., 2021; Chen et al., 2021; Via et al., 2022). This possibility was not explored in this thesis as the dataset spanned less than a month, and rolling PMF is recommended for datasets spanning different seasons which impact the composition of the factors. However, SoFi Pro was used for constraints and MTR-PMF, the details of which are presented by Datalystica Ltd. (2021) and Chebaicheb et al. (2025).

The strategy for performing PMF and find the best solution is presented step by step as follows:

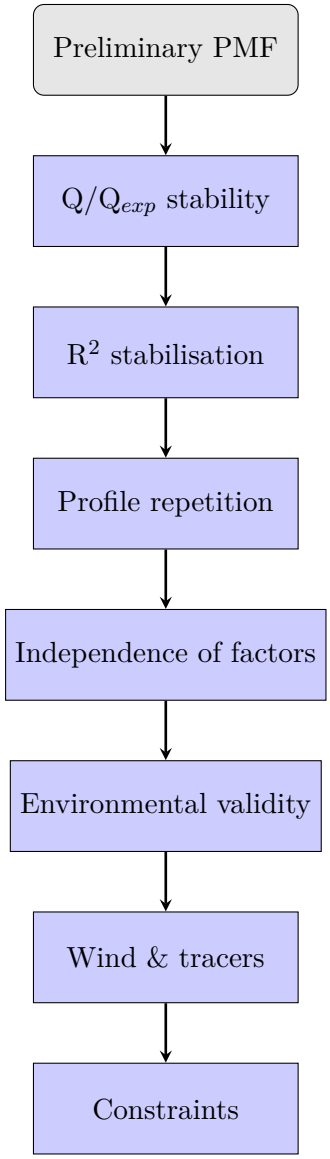

1. A preliminary PMF is systematically performed spanning up to 10 factors with more than 20 runs each to explore the variability of the solutions.
2. Stable solutions are compared if their Q/Q$_{exp}$ is stable, and ideally close to 1.
3. The number of factors for which the R^2 starts to stabilised is suspected as the best solution.
4. The repetition of the profile is recognised as a confirmation of the stable solution.
5. The absence of correlation (R^2) between factors shows that no factor has split in multiple profile and that sources were correctly apportioned.
6. The profiles are investigated and the environmental validity of factors show a good modelling.
7. Wind analysis and tracer comparison is performed to identify the factors.
8. In need of constraint, various a-values are explored and all compounds of the seeded profile vary with the same range.

2.4.c.iii Representativity of the results

The resulting PMF factor in Dunkirk will be compared with the previously calculated EFs to assess the robustness of the chemical fingerprints determined by each method. Further, the field campaign in Le Havre will be analysed in terms of VOC levels and variability to contrast concentration trends observed in Dunkirk and evaluate the potential for sampling shipping emissions in a representative harbour. Additionally, PMF analysis will be conducted in Le Havre to evaluate the applicability of the factors identified in Dunkirk to other harbours.

2.5 Conclusion

The location of the site and the instrumentation in Dunkirk set the stage for studying various pollutants and meteorological conditions in an area affected by ship emissions from the Dover to Dunkirk ferry route. Moreover, as is often the case for harbour sites, the site is in proximity to various industrial sources. This thesis focuses on VOCs, which were measured using two TD-GC-FIDs to provide chemical-resolved VOC data and a PTR to provide a high-time-resolution dataset of unspeciated VOCs. This thesis involved calculating uncertainties for both GCs and the PTR, as well as validating the PTR data. This process ensures the reliability of the data and prepares the dataset for use with the advanced analytical methods and tools described in this chapter. Among these methods, EFs enable emissions from ferries to be calculated based on field measurements, complementing the PMF analysis which provides chemical profiles for ships and their contribution to concentrations at the site compared to other sources. These tools and methods have been used to inform the subsequent two chapters: EFs will be the focus of Chapter 3, while PMF will be discussed in particular in Chapter 4 and the robustness of its profiles will be compared with the results of another campaign in Le Havre in 2023 in Chapter 5.

CHAPTER 3

Ship Emission Factors for Volatile Organic Compounds and PM_1 from land-based observations in an Emission Control Area of France

This first chapter introduced the impact of ship emissions, highlighting their effect on air quality and the growing interest in their VOC emissions. This is a poorly understood source in terms of its chemical fingerprint and contribution to ambient VOCs, which has a direct impact on populations living near harbours. Chapter two presented two complementary approaches to characterise this source: the calculation of emission factors to provide a chemical fingerprint of ship-related VOCs and PMF to quantify the real-world contribution of ships to ambient VOCs. The instrumental setup was also discussed, emphasising the complementary of TD-GC-FID, which offers high chemical resolution, and PTR-ToF-MS, which provides high temporal resolution. This dual perspective motivated their combined use in determining Emission Factors and applying PMF, enabling a more complete description of shipping emissions.

The first chapter of results in this thesis is dedicated to calculating VOC EFs based on PTR-ToF-MS observations from the Dunkirk campaign in 2022. It is written as an article in its second revised state following review, with supplementary information provided in Appendix B. This article was submitted in Atmospheric Environment: X and is currently under review. First, the site and experimental setup are described, paying particular attention to VOC and PM_1 composition measurements (HR-ToF-AMS), which add value to the knowledge of ship emissions provided by this article. The EFs of these compounds are compared with the EFs of regulated pollutants such as SO_2, NO_x, BC, and regulated PM_{10}, $PM_{2.5}$ and PM_1.

The discussion begins with the identification of a specific ship emission tracer to bound the EF calculation. A thorough assessment of the impact of the background calculation method on the resulting EF is provided, the first of its kind for EFs determined in a field campaign, to the best of our knowledge. The values of the EFs are then discussed for both the gaseous and particulate phases, and are put into perspective with regard to the literature and regulated areas.

Finally, the variability of our EFs is presented depending firstly on the ship and secondly on the direction of manoeuvre. Statistical methods are used to highlight significant differences in the EFs of some VOCs when ships are entering or leaving the harbour. This is an interesting outcome, as these differences do not seem to be linked to the regulations in place in Dunkirk.

Ship Emission Factors for Volatile Organic Compounds and PM_1 from land-based observations in an Emission Control Area of France

Submitted on June 13th 2025 in Atmospheric Environment: X

Erwan Volent[a], Quentin Gunti[b,c], Barbara D'Anna[b], Joel F. De Brito[a], Marina Jamar[a], Brice Temime-Roussel[b], Jana Moldanova[d], Hilkka Timonen[e], Heidi Hellen[e], Grazia Lanzafame[b], Miikka Dal Maso[f], Sylvain Roze[g], Véronique Riffault[a], Liselotte Tinel[a], Stéphane Sauvage[a,h]

[a] *IMT Nord-Europe, Institut Mines-Télécom, Univ. Lille, Centre for Energy and Environment, Lille, F-59500, France*

[b] *Aix-Marseille Université, CNRS, LCE, Marseille, France*

[c] *AtmoSud, Regional Network for Air Quality Monitoring of Provence-Alpes-Côte-d'Azur, Marseille, France*

[d] *IVL, Swedish Environmental Research Institute, Gothenburg, Sweden*

[e] *Atmospheric Composition Research, Finnish Meteorological Institute, Helsinki, Finland*

[f] *Aerosols Physics, Faculty of Engineering and Natural Sciences, Tampere, Finland*

[g] *Atmo Hauts-de-France, Regional Network for Air Quality Monitoring of Hauts-de-France, France*

[h] *Université Grenoble-Alpes, CNRS, IRD, INP, INRAE, Grenoble, France*

Abstract This study presents new Emission Factors (EFs) for regulated and non-regulated pollutants from ferries obtained from a land-based measurement campaign in the harbour of Dunkirk, northern France. Despite Dunkirk being in a sulphur and NO_x Emission Control Area (ECA), we show that SO_2 remains a reliable tracer of ship emissions in this harbour. A comprehensive suite of gas and particulate phase pollutants was investigated, focusing on 68 Volatile Organic Compounds (VOCs) and 5 components of PM_1. In total, 149 plumes were detected from three similar ferries. Individual EFs were calculated for 84 pollutants, including different navigational phases. Clear identification of the ship plumes led to the robustness of EF estimates, as shown by the low sensitivity to the background correction method. Particle Number (PN) showed a ship specific unimodal distribution around 91 nm. The EF(PN) ranged from $1.04{\cdot}10^{16}$ to $2.57{\cdot}10^{16}$ particles$\cdot kg_{fuel}^{-1}$, which is about three times higher than those recently reported in Marseille, southern France. The EFs of the particulate phase components are dominated by organics with an interquartile range between 3.79 and 6.82 g$\cdot kg_{fuel}^{-1}$, two to three orders of magnitude higher than nitrates (NO_3^-) and sulphates (SO_4^{2-}). The EFs of VOCs are dominated by oxygenated species, such as acetaldehyde (165.6 - 278.9 mg$\cdot kg_{fuel}^{-1}$) and methanol (94.56 - 309 mg$\cdot kg_{fuel}^{-1}$). The second most emitted group of VOCs are the C_5 compounds, with notably cyclopentane ($C_5H_{10}{\cdot}H^+$) (73.2 – 145.2 mg$\cdot kg_{fuel}^{-1}$) and the fragment $C_5H_8{\cdot}H^+$ (144.2 – 247 mg$\cdot kg_{fuel}^{-1}$). Aromatic VOCs, such as benzene ($C_6H_6{\cdot}H^+$), toluene ($C_7H_8{\cdot}H^+$) and xylenes/ethylbenzene ($C_8H_{10}{\cdot}H^+$), are also detected with individual EFs below 70 mg$\cdot kg_{fuel}^{-1}$. This study also investigated the emissions as a function of the operational phases, suggesting that some VOCs, BC and PM_1 are more emitted during the arrival than the departure of the ferries. The EFs of the speciated VOCs and PM_1 reported here provide a comprehensive database for improving current emission inventories and a better understanding of the role of shipping emissions on air quality degradation, notably along coastal areas.

3.1 Introduction

Shipping ensures 80% of the world's trade volume and its traffic is expected to double by 2030 compared to 2016. CO_2 emissions from marine transport, which have already increased by 9.3% between 2012 and 2018, are expected to continue to rise, according to the International Maritime Organisation's scenario (IMO, 2023), leading to a 30% increase of CO_2 emissions by 2050 compared to 2008 levels (Faber et al., 2020). CO_2 emissions from shipping contribute to long term global warming (Eyring et al., 2010), and other co-emitted species affect air quality locally, as in coastal and port areas. Around 70% of Particulate Matter (PM) emissions occur in coastal areas (Eyring et al., 2010; Alanen et al., 2020; Jeong et al., 2023; Kuittinen et al., 2021), and shipping is estimated to cause between 60,000 and 400,000 premature deaths worldwide (Corbett et al., 2007; Sofiev et al., 2018). Particulate emissions from shipping contribute 5% of European PM_{10} and significantly degrade air quality in port cities, with impacts comparable to those of road traffic (Contini et al., 2015; Russo et al., 2018; Tang et al., 2020; PACA, 2017). The number concentration of PM emitted by ships is dominated by Ultrafine Particles (UFP) with health and climate related impacts (González et al., 2011; Healy et al., 2009). The chemical composition of ship-emitted particles consist primarily of Organic Aerosols (OA), including polycyclic aromatic hydrocarbons (PAH), Black Carbon (BC), sulphates (SO_4^{2-}), and trace metals such as Vanadium (V) and Nickel (Ni).

The characteristic V/Ni ratio is widely used as a specific tracer of ship-related emissions (Karl et al., 2023; Celik et al., 2020; Viana et al., 2009).

Gaseous emissions from ships can contribute up to 24% of the annual mean concentrations of NO_2 and SO_2 in several European coastal areas (Viana et al., 2014). In Copenhagen, Saxe and Larsen (2004) showed that NO_x emissions from ships caused several exceedances of legal air quality limits around the harbour. Emissions of ships include further Volatile Organic Compounds (VOCs), that represent a wide range of compounds. VOCs play a key role in atmospheric chemical processes by taking part in photochemical reactions with NO_x leading to the formation of Secondary Organic Aerosols (SOAs), ozone (O_3) and peroxyacetyl nitrates (PANs) which are harmful to human health (Fry et al., 2014). VOC emissions from shipping are relatively understudied, and their impact on harmful SOA and ozone formation in coastal areas is not well documented.

Focusing on the impact of maritime emissions on port cities historically prompted authorities to act to limit this pollution. In 1997, the Annex VI of the MARPOL convention (MARine POLlution) was adopted, setting out measures to reduce pollutant emissions from ships. In particular, it stated on the creation of Sulphur Emission Control Areas (SECA), where the Fuel Sulphur Content (FSC) of ships is limited to 0.1% by mass. In Europe, this is notably the case for the Baltic Sea and both the North Sea and the English Channel since 2005 and 2006 respectively. In 2020, new regulations in the Annex VI of MARPOL reinforced the global regulation of ship emissions by restraining the FSC to 0.5% by mass (Contini et al., 2015). In 2021, the North and Baltic Seas also became Nitrogen oxides Emission Control Areas (NECAs). Therefore, the use of low sulphur fuels is expected to change the profile of the emissions, including of VOCs (Timonen et al., 2022). To the best of our knowledge, only one study reported speciated VOCs from ships in France (Le Berre et al., 2025), measured in 2021 in the harbour of Marseille. In Marseille only ships at berth for more than two hours had to comply with the EU sulphur limit of 0.1% by mass (Directive EU 2016/802).

The relative lack of information on VOCs emitted by ships in ports is also reflected in the shipping Emission Factors (EFs), a key metric for building emission inventories used in air quality models. An EF describes the quantity of a pollutant emitted by a unit activity of a given source, usually expressed in grams per unit of energy output, or for transport sources, per unit of mass of fuel consumed by the engine. In France, the national emission inventory follows the methodology of the EMEP guidelines as a reference for calculating total ship emissions (De Lauretis, 2023). EFs are multiplied by the energy or fuel consumption of ships, depending on the operational phase: at berth, manoeuvring or cruising, but also the type of ship (ferry, carrier, etc). EFs depend on the fuel type, speed, engine type and operation. Reduction coefficients are applied for abatement measures such as Selective Catalytic Reduction (SCR) or Diesel Particulate Filter (DPF). In France, the EFs used for national emission inventories are reported by the CITEPA and originate from the OMINEA dataset, where only the sum of Non-Methane VOCs (NMVOCs) are reported. Yet, speciated data on VOCs are important to accurately assess the impact of shipping on emissions on air quality degradation, either directly or as precursors to O_3 and SOAs.

Additionally, very few studies reported EF of VOC from ships, and even fewer have reported VOC speciation (Agrawal et al., 2010; Huang et al., 2018; Timonen et al., 2022).

In this context of changing emissions and practices, Dunkirk, Hauts-de-France, is a strategic study site to determine speciated VOCs and PM. The Larger Dunkirk agglomeration accounted for 192,000 inhabitants in 2021 within an area of 300 km^2. The harbour of Dunkirk is the third largest port in France (GPMD, 2022), and the seventh in Europe and the 93th in the world in terms of tons of goods. It is located within the Northern and Baltic Sea Sulphur Emission Control Areas (SECAs), where stringent regulations on fuel sulphur content and ship emissions have been in place since 2006. This provides a representative example of an emission regulated European port, comparable to major European harbours such as Rotterdam, Antwerp and Hamburg (Tokaya et al., 2024). This work aims to address knowledge gaps regarding the emissions of passenger vessels, which are an important part of maritime traffic, embarking 395.3 million passengers from the EU in 2023. Therefore, investigating Dunkirk provides valuable insights into the chemical composition of air pollutants from this common type of maritime traffic across Europe.

Observations of particles in the Dunkirk agglomeration showed that the main constituents of the PM_1 composition are OA and nitrate (NO_3^-) (Crenn et al., 2017), with a considerable contribution of SO_4^{2-} originating from industrial activities (Zhang et al., 2021). In winter, higher concentrations of PM are observed in the rural and industrial areas compared to summer (Cazier et al., 2016; Crenn et al., 2017). Dunkirk is also under the influence of long-range transport of continental air masses originating from east to north-eastern Europe and inland France (Waked et al., 2018; Potier et al., 2019).

In terms of NMVOC reported in regional inventories, 6 out of the 44 industrial sites, adding up to 80% of the total regional emissions, are based in the Dunkirk agglomeration. Dunkirk is thus recognised as an urban environment influenced by industrial emissions (DREAL, 2021). Previous studies have investigated the VOC levels in Dunkirk and highlighted the main influence of metallurgical industries and oil refineries on VOC concentrations (Badol et al., 2008a; Roukos et al., 2009). So far, the influence of shipping was pointed out by Farhat et al. (2024), who studied VOC levels in Dunkirk in 2014, but the specific impacts of shipping were not the focus of the paper.

Therefore, this study sets out to provide speciated gaseous and particulate EFs from shipping, determined in the harbour of Dunkirk. The results will allow the development of more accurate emission inventories, and thus a better assessment of the role of shipping activities in the air quality of regulated ports across Europe. We further discuss the variability of the EFs depending on the method of background determination but also on type of ship and manoeuvre, and compare our results with those obtained in other French and international ports.

3.2 Methodology

3.2.a Site description and meteorology

The field campaign was conducted in the harbour of Dunkirk from September 2nd to September 29th 2022. The sampling site was located at the western ferry terminal of the Dunkirk harbour (Figure 3-1). Three mobile laboratories (trailers) were installed 230 m north of the dock towards Dover (England) and 300 m west of the Roll-on/Roll-off (RoRo) terminal towards Rosslare (Ireland) as shown in Figure 3-1. Separate inlets were used for each mobile laboratory, all mounted on masts at a height of 3 m, preventing self-sampling effects. At the Dover terminal, three ferries operated daily, departing every two hours between Monday and Friday. At weekends, there were no ferries at 8 pm, 10 pm and midnight on Saturdays, at 2 am, 4 am and 8 am on Sundays. The second ferry line linking Dunkirk to Rosslare had a frequency of 5 departures per week. The three sister ferries transiting from Dunkirk to Dover, referred to as A, B and C in the study, were built around the same time (C in 2005, A and B in 2006) by the same company, and all three are equipped with four medium-speed 4-stroke diesel engines (MAN L48/60B, 9 200 kW) and have no exhaust after-treatment system. They therefore rely on the use of low-sulphur fuel to comply with SECA standards, like Marine Diesel Oil (MDO), also known as Marine Gas Oil (MGO), whose fuel content is less than 0.1% (Petzold et al., 2011; Zhou et al., 2019). Further south, there were berths for container ships.

Meteorological parameters (wind direction, wind speed, temperature and pressure) were recorded by a meteorological station (Vaisala, WXT520) during the campaign (Supplementary Informations, SI, Figure BF1). The temperature varied from 8.6°C to 25.5°C, with an overall decrease of about 5°C throughout the measurement campaign, marking the end of summer. The dominant wind direction was west during the daytime sea-breeze and south-west during the night, as shown in Figure 3-2. The wind direction was west-north-west and north-north-west during periods like September 15th to 20th as shown in Figure BF1 (290 ± 54°), and occasionally during the rest of the campaign. During these events, the site was downwind of the entry to the channel and the manoeuvring area of the ferries.

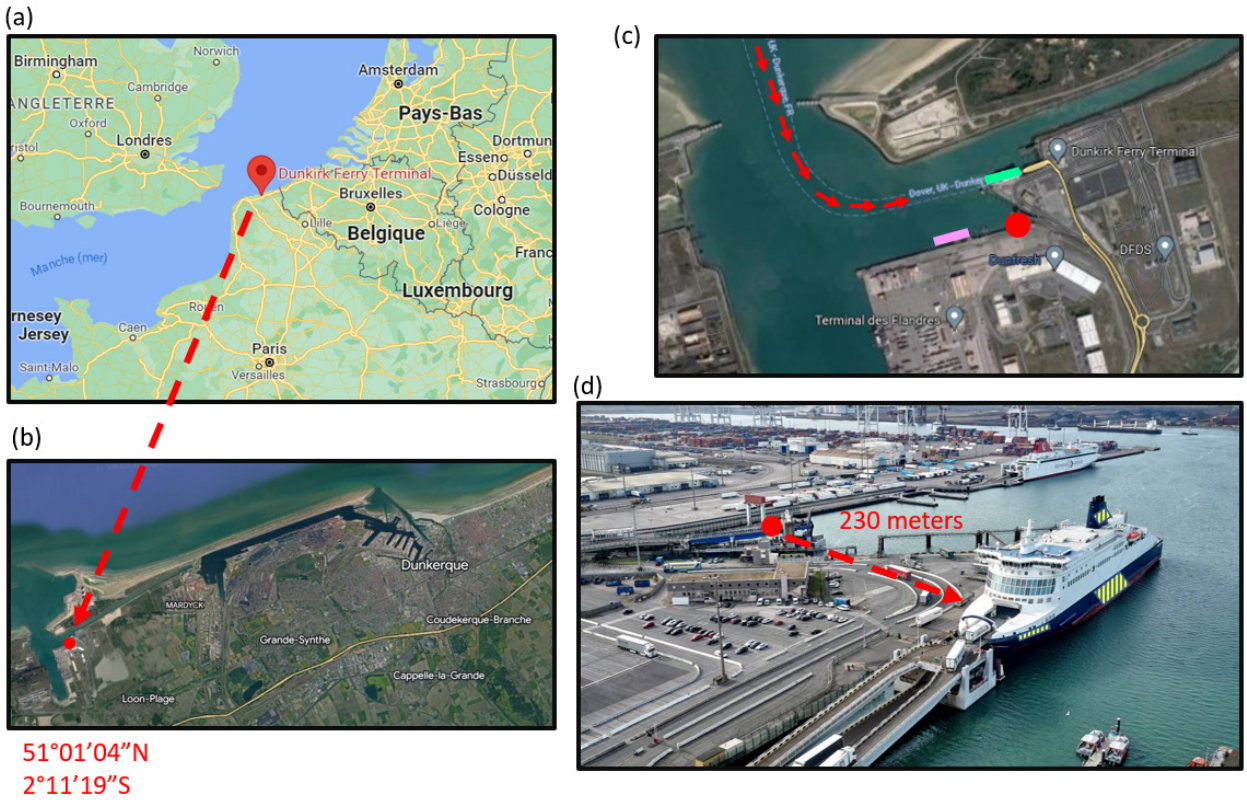

Figure 3-1: *(a) Dunkirk location in the north of France. (b) Site location in the western harbour of Dunkirk. (c) Site location (red dot) with respect to ferries, arrival trajectory (red arrows), ferry (green full line) and RoRo (pink full line) docking locations. (d) Distance between the site (red dot) and the ferry dock (picture taken from DUNKERQUE PORT http://www.dunkerque-port.fr/en/).*

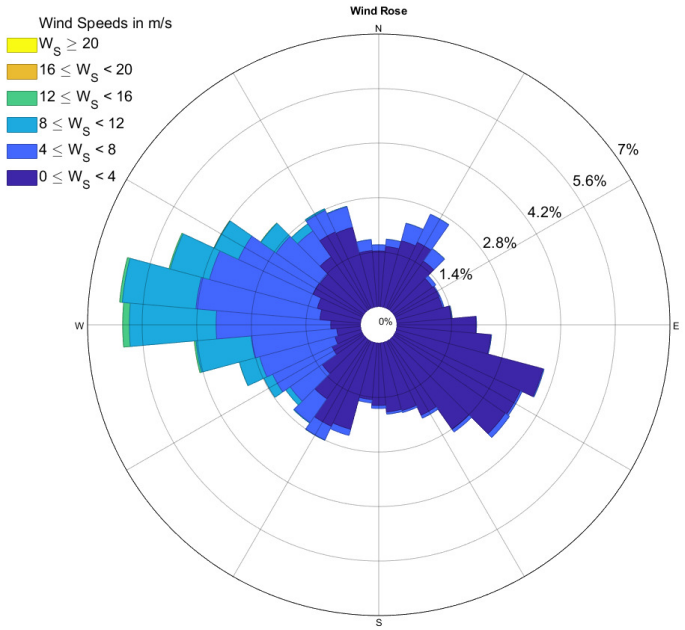

Figure 3-2: *Wind rose of the whole campaign. The contributions of western and south-eastern wind direction highlight the sea and land breezes impacting the site.*

3.2.b VOC measurements

Ambient air for the VOC measurements was sampled using a SilcoNert inlet mounted on a 3 m height mast and VOC concentrations were measured using an online Proton Transfer Reactor coupled to a Time of Flight-Mass Spectrometer (PTR-QI-ToF-MS, Ionicon Analytik), with the drift tube held at 100 Td. This instrument allows high-frequency measurements of trace gases with low detection limits (Lindinger et al., 1998). This method relies on the analysis of soft-ionized gases from a protonation with H_3O^+ :

$$R + H_3O^+ \rightarrow RH^+ + H_2O \tag{3.1}$$

Concentrations were extracted from raw counts-per-second signals using PTR Viewer 3 (v3.2.7, Ionicon). First, the time of flight of each mass to charge (m/z) was calibrated using four ions (m/z 21.022, 37.028, 203.943 and 330.848). Masses from m/z 21 to m/z 372 were identified using a peak table of 315 specific masses. Five calibrations were performed before, during and after the campaign, using a certified National Physical Laboratory (NPL, Teddington, UK) gas mixture (SI, Table BT1), which was used to fit a transmission curve (SI, Figure BF2) to derive the volume mixing ratios of the VOCs. The validation of the concentrations was performed according to the ACTRIS measurement guidelines for VOC analysis on PTR-ToF-MS, which require the calculation of individual Limits of Detection (LoD) for each mass, depending on the raw signals of the blank measurements and the sensitivity. Additional corrections for humidity and fragmentation were applied for 16 VOCs (SI, Table BT2).

3.2.c Measurements of sub-micronic aerosol composition

The mass fraction of sub-micron non-refractory species was measured using a High-Resolution Time-of-Flight Aerosol Mass Spectrometer (HR-ToF-AMS, Aerodyne Research Inc). It detects particles with aerodynamic diameters between 70 nm and 700 nm (standard aerodynamic lens, Aerodyne), including OAs, SO_4^{2-}, NO_3^-, and ammonium (NH_4^+) with a time resolution of 30 s. The vaporizer temperature was set at 600-650°C and the tungsten filament for electron ionization was run at an accelerating voltage of 70 eV. The sampling time resolution was 30 s in V-mode. Details about the AMS methodology are given by DeCarlo et al. (2006) and Canagaratna et al. (2007). Data were processed using Squirrel (v1.65B) and Pika (v1.25B). Calibrations of the HR-ToF-AMS were performed at the beginning of the campaign using ammonium nitrate and ammonium sulphate solutions, resulting in an Ionisation Efficiency (IE) value of $4.0 \cdot 10^{-8}$, and a Relative Ionisation Efficiency (RIE) of 4 and 1.8 for ammonium and sulphate respectively. The RIE for NO_3^- and OAs were 1.1 and 1.4 respectively (Canagaratna et al., 2007; Xu et al., 2018). Previous studies have investigated the Collection Efficiency (CE) to be applied depending on the composition of ambient particle composition (Voliotis et al., 2021; Quinn et al., 2006). Specifically for ship emissions, Lack et al. (2009) determined a unit CE in ship plumes derived from their acidic nature and the ability of the AMS to quantitatively measure condensed organic matter. Therefore, the CE was kept at 1.0 for the present study. This is particularly relevant as the EFs are calculated using the concentration peaks observed by AMS from the ship plumes.

In this study, the HR-ToF-AMS was installed at the outlet of an Aerosol Flow Tube (AFT), aiming at characterizing both fresh and aged particles in ship plumes, represented in SI (Figure BF3). Only fresh plume data, when the AFT did not oxidize the particles, were used in this study. Ambient air was sampled from an inlet installed on top of a 3 m height mast at a flow rate of 12 L/min. The AFT residence time was approximately 1 min, and the particle number concentration and size distribution were recorded using a Scanning Mobility Particle Sizer (SMPS, TSI 3936) ranging from 15 to 661.2 nm on 106 size channels at the inlet of the AFT. Concentrations measured by the HR-ToF-AMS were corrected for wall losses in the AFT, using the SMPS data to determine a mean diameter-dependant transmission coefficient at each time step which calculation is detailed and discussed in the SI (Section B.1).

3.2.d Regulated pollutants

Auxiliary measurements of criteria pollutants were performed by the Regional Network for Air Quality Monitoring of Hauts-de-France (Atmo Hauts-de-France). SO_2 was monitored using a gas UV-fluorescence detector (ENVEA AF22E) and NO_x was measured using a chemiluminescence detector (Teledyne API 200E), both with a 10 s time resolution. Ambient CO_2, CO and CH_4 were measured using Cavity Ring-Down Spectroscopy (Picarro, G2401) allowing measurement at a 1 s time resolution. PM_{10}, $PM_{2.5}$ and PM_1 concentrations were measured with a 10 s time resolution using an aerosol spectrometer (FIDAS 200E), which sampled particles with aerodynamic diameters between 180 nm and 18 µm. At the same time, the SMPS described above, which operated at a time resolution of 2 min, informed on the size distribution and PN with mobility diameters between 15 to 661.2 nm. Black Carbon (BC) was measured using an aethalometer (Magee Scientific, AE33).

3.2.e Ship plume identification

The methodology for identifying ship plumes in this study is based on observations of tracer concentrations (SO_2, discussed in section 3.3.a). The three similar ferries presented in section 3.2.a rotating on the dock located on the north of the site, serving the ferry line from Dunkirk to Dover, were characterised. Concentrations in favourable wind directions (W-N-NE, 270° – 60°, north being 0°) were isolated, covering the entrance of the channel and the berth location. Any relative increase of more than 10% of concentration during these periods was marked as a potential peak start, showing the best identification of peaks after various values of relative increases were tested. The end of the peak was determined as the first datapoint of the longest constant concentrations up to 10 minutes after the maximum of the peak. The attribution of a concentration peak to a specific ship's plume was performed using the time schedule of the operating company. In case of ambiguity, camera footage from the northwest of the terminal was used for ship identification. A total of 149 ferry plumes were identified, with 69 plumes measured from arriving ferries and 80 from departing ones. In total, we sampled 47 plumes from ferry A, 51 from ferry B and 51 from ferry C.

The start and end times of the SO_2 ferry peaks were applied to the other pollutants to delimit their peaks. The differences in residence time in the sampling lines, different instrument clocks, or, but less likely, the transport time of the plume within the site could have induced a temporal shift between instruments in neighbouring mobile laboratories. Consequently, an offset was applied as described by Diesch et al. (2013). For instruments measuring multiple compounds, the timing of each SO_2 peak was aligned to that of their most representative species, and the corresponding time offset was then applied to all species measured by that instrument. Reference species were selected if they exhibited the highest response to ship plumes, making them the most reliable tracers for timing corrections. As a result, VOCs from the PTR-ToF-MS were corrected using $C_5H_8{\cdot}H^+$ (m/z 69.069), which showed the highest sensitivity to the ship plumes. HR-ToF-AMS data were aligned using OA, CO and CH_4 from the Picarro were corrected using CO_2, NOx and NO_2 using NO, and PM_{10} and PM_1 from the FIDAS using $PM_{2.5}$.

3.2.f Emission Factors

The EF of the different species were calculated , in units of $g{\cdot}kg^{-1}_{fuel}$, for ship emissions originating from combustion, using the widely-used carbon ratio method following Eq. 3.1 within the integration windows where ship plumes were identified (Diesch et al., 2013; Alföldy et al., 2013; Pirjola et al., 2014; Van Roy et al., 2022a) :

$$EF = \frac{\int \Delta X}{\frac{M_c}{M_{CO_2}} \cdot \int \Delta CO_2} \cdot \omega_c, \tag{3.2}$$

$$= \frac{\int X - X_{bg}}{\frac{M_c}{M_{CO_2}} \int CO_2 - CO_{2_{bg}}} \cdot \omega_c, \tag{3.3}$$

with X the pollutant of interest. The net concentrations ΔX and ΔCO_2 are given by subtracting the background X_{BG} and CO_{2BG} to the peak concentration values. Background considerations are further detailed and discussed in section 3.3.b. w_c corresponds to the carbon mass fraction (kg/kg) in the fuel, taken at 0.865 kg/kg for MGO (Diesch et al., 2013; Zhou et al., 2019). Various values of w_c are reported in the literature, but this value was mostly encountered and was kept as it for consistency. The range of values of w_c encountered vary ±1.5%, which minimally impacts the values of the EFs reported here.

The relative instrumental uncertainty of the EFs is expressed knowing the uncertainties of each component X and CO_2 (Diesch et al., 2013), as well as the uncertainty on ω_c:

$$\sigma(EF) = \sqrt{\sigma(X)^2 + \sigma(CO_2)^2 + \sigma(\omega_c)^2}. \tag{3.4}$$

The error on the CO_2 measurements from the Picarro is 5%, and the uncertainty on the measurements of the criteria pollutants (SO_2, NO_x, PM) are within the regulated quality range of 15%. This value was kept to represent the maximum expected error. Therefore, the instrumental uncertainty of the EFs calculated from Eq. 3.4 for criteria pollutants is 16%.

However, for the PTR, the uncertainties of the most abundant VOCs were estimated at 30%, resulting in a larger uncertainty in their EFs of 31%, showing a minimal impact of the uncertainties induced by CO_2 and ω_c.

Given the HR-ToF-AMS and the SMPS were sampling downstream of the AFT, the EFs of species detected by those instruments were determined using the colocated CO_2 measurement to accurately account for dilution. The FSC in units of % can be calculated based on EF(SO_2) (Pirjola et al., 2014; Van Roy et al., 2022b) :

$$FSC = 0.232 \times \frac{\int SO_2 - SO_{2_{bg}}}{\int CO_2 - CO_{2_{bg}}} \tag{3.5}$$

Once each peak was identified, the EFs of 84 species were calculated using Eq. 3.3. They include 68 VOC masses that were clearly identified from the peak table that was used to process the PTR-ToF-MS data, and 4 components from the PM_1 composition derived from HR-ToF-AMS measurements (OA, SO_4^{2-}, NO_3^-, NH_4^+).

3.3 Results and discussions

3.3.a Identification of a ship tracer

In order to identify ship peaks, a tracer had to be determined. Four pollutants (SO_2, CO_2, NO_2, $PM_{2.5}$) were tested using two criteria, (i) the co-occurrence of a peak with the presence of a ship, (ii) the technical feasibility of automated detection of the peak. The results of the comparison are shown in Figure 3-3. All three gases, SO_2, CO_2 and NO_2 display transient peaks at the beginning and the end of the ship's presence, indicating the influence of a ferry plume upon arrival and departure of the ship, whereas $PM_{2.5}$ peaks were not as clear due to an averaging in the instrument's signal. SO_2 concentrations showed clear and unique spikes which are easier to detect using a single minimum gradient value. Despite the demonstrated influence of ferries on both SO_2 and NO_2 concentrations during the campaign (Mahajan et al., 2024), SO_2 was chosen as the ship tracer in our study because the SO_2 instrument had a better temporal coverage.

Although the background SO_2 levels observed under the influence of most wind directions were relatively high (3.83 ± 8.56 µg·m^{-3}), lower and more stable background levels of SO_2 were observed in the wind directions favourable for ship emissions [270-60]° (2.36 ± 2.96 µg·m^{-3}), supporting the choice of this tracer. Despite the sulphur regulations being in place in Dunkirk, SO_2 still appears as an efficient effective tracer of shipping emissions in the vicinity of the berth for the Dunkirk harbour.

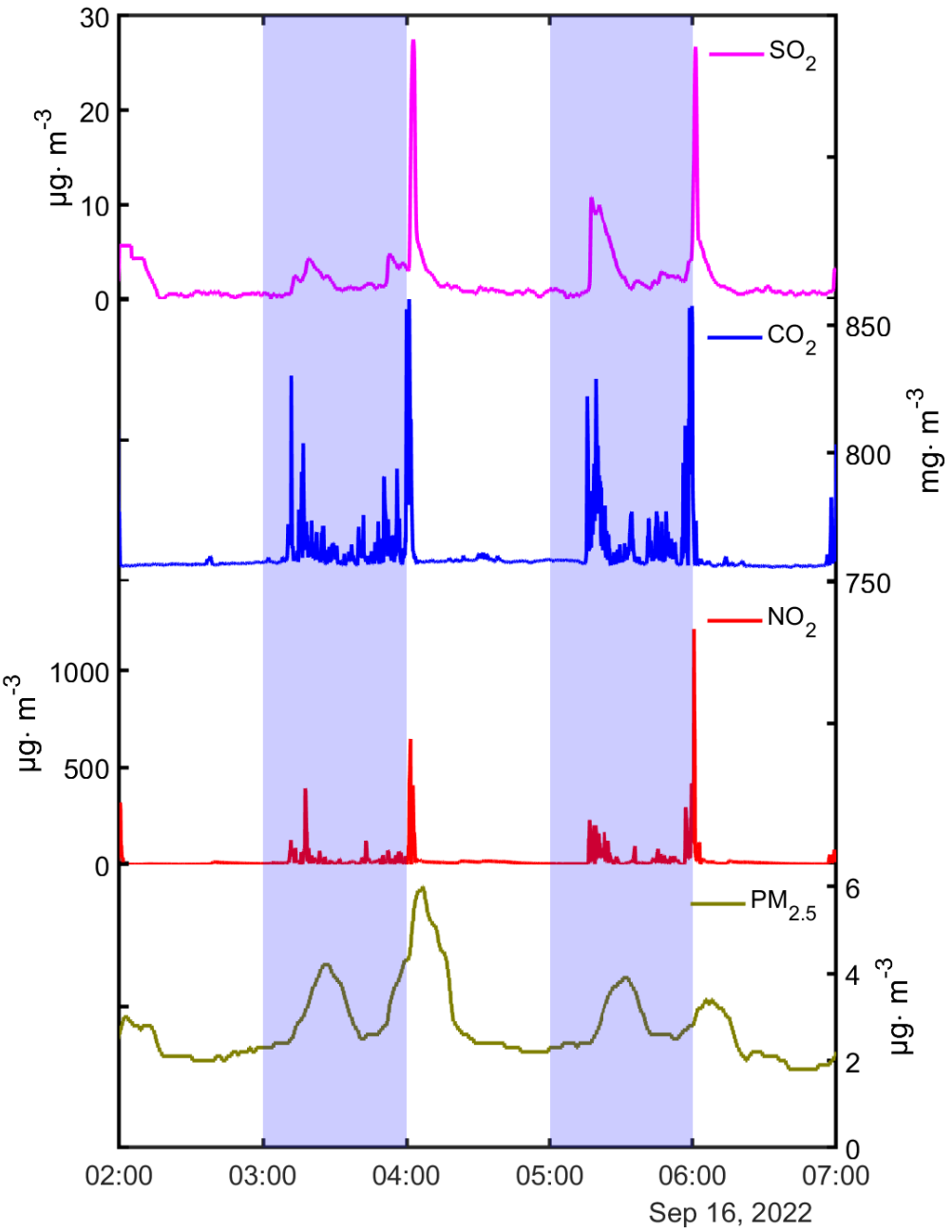

Figure 3-3: *Concentrations of SO_2 (pink), CO_2 (blue), NO_2 (red) and $PM_{2.5}$ (green) observed on the 16 of September 2022, under favourable wind for sampling ferry emissions. The blue shaded areas indicate the presence of a ship at berth, according to the ferries time schedule.*

3.3.b Background influence on Emission Factors

As can be seen in Eq. 3.3, the calculation of EFs requires the use of net concentrations, which means that the background, defined as the concentration levels that are measured without the influence of a ship plume, has to be subtracted from the observed concentrations. A method to calculate the background is to interpolate the baseline before and after the peak, as described by Diesch et al. (2013). They subtracted a linear fit between two manually defined background intervals before and after a concentration increase.

On the other hand, Alföldy et al. (2013) calculated the mean concentrations a few minutes before and after the peak, and subtracted these mean values from the total peak area. Similarly, Celik et al. (2020) calculated the 15 min mean as close as possible to the peak, and subtracted it from the mean concentration of the event. Le Berre et al. (2025) calculated the background of key species using a low-pass filter, considered as a rolling median on a 60 min window. These examples show that no unique method is used for the determination of the background.

In the lack of a standard method, we performed a sensitivity test of background calculations for our conditions to verify their robustness and their impact on EF determination. The choice of a method for our study relies on the analysis that two consecutive ship peaks are separated by approximately one hour (50 ± 24 min). Therefore, considering the background to be the median concentration within the 30 min pre-peak and post-peak gives a good representativeness of the background concentrations, without being influenced by ship emissions. We then integrated the area under the constant line of the median and subtracted it from the total peak to give the net concentration. Sensitivity tests were performed to identify a time window for the background that would influence on the EF significantly, testing time frames from one minute to one hour. No significant variation in EF was observed when varying the time window, therefore we concluded that a 30 min window gave good representativeness of the background. It is worth noting that this time window remains study dependent, so it should be adapted to the dataset studied depending on the variability of the background and the time between successive ship peaks.

For comparison with other methods, the one used here is referred to as Median-based EF (MEF). Other methods from the literature are referred to as the Rolling median-based EF (REF) as in Le Berre et al. (2025), who used a rolling median on a 60 min time window, and the Linear fit-based EF (LEF), where the background is a linear interpolation between the pre- and post- peak observations (Diesch et al., 2013).

Figure BF6 (SI) shows the distributions of LEFs, MEFs and REFs of NO, SO_2, CO and BC. Overall, the EFs of these species are similar between the three methods. Insignificant differences are observed between MEF and REF, which was expected from the fact that both methods calculate a median over the same duration at the vicinity of each peak. The Interquartile Range (IQR) is slightly higher for the LEFs of NO, SO_2, CO and BC, but their medians are similar to those of MEFs. In fact, the median LEF for NO is 23.4 $g{\cdot}kg_{fuel}^{-1}$, while the median MEF is 24 $g{\cdot}kg_{fuel}^{-1}$, therefore the relative difference is not significant (2%). The same observation is made for SO_2 and for CO, which show the smallest differences between the median LEF and MEF, 1% and 4% respectively. BC shows the largest but still small difference of 7%, with a median LEF of 0.44 $g{\cdot}kg_{fuel}^{-1}$ and a median MEF of 0.42 $g{\cdot}kg_{fuel}^{-1}$.

CH_4 shows an important number of outliers for all methods. Although the IQR is higher for CH_4 MEFs, similar values are found for the median LEFs, MEFs and REFs. The IQR and the number of outliers vary for most species, but the median values are similar for each method, suggesting that the background calculation has minimal influence on the EFs of our study.

Background sensitivity tests were performed on the 6 major VOCs with respect to the mean MEF (SI, Figure BF7). No significant influence of the method was found, except for methanol, which shows the largest gap between methods, with a 18% difference between LEF (237.4 mg/kg_{fuel}) and MEF (193.4 mg/kg_{fuel}). In addition, the IQR of LEF is higher and this method shows outliers in the same way as CH_4, suggesting a particular sensitivity to background for compounds with high background levels.

These sensitivity tests were also performed for the particle phase measurements, including PM_1 composition and SMPS measurements of PN and mass (SI, Figure BF8). The tendency towards a higher IQR for LEFs is not observed in these comparisons, except for LEF(PN), which show a significant number of outliers as observed for some previous compounds. Since MEFs and REFs do not have as many extreme values, the differences are mainly a consequence of the linear interpolation method.

The overall good agreement between the three methods underlines a limited influence of the background on the EFs in this study. The absence of difference might be linked to the exclusive influence of ship emissions in the favourable wind periods. We recommend a careful assessment of the impact of the background in studies where the ship peaks occur while influenced by other sources. Considering the agreement between MEFs and REFs and the low number of MEF outliers, MEFs were chosen to describe EFs in the pursuit of the paper.

3.3.c Emission Factors of the ferries

The EF statistics are summarized in SI (Table BT3). The mean FSC observed in Dunkirk is 0.07 ± 0.06% and the median FSC is 0.05%, both below the regulatory limit set at 0.1% in the North Sea ECA that includes Dunkirk. The FSC distribution is presented in SI, Figure BF9. The observed values of FSC are lower than the FSC values of most reported studies for various types of ships and locations, as can be seen in Table 3-2, in line with Dunkirk being located in a SECA, with stricter emission standards than in most other studies. Table 3-2 also summarizes the methodology of the studies that are cited. The EFs obtained in previous studies for regulated pollutants are compared with ours in Table 3-3, VOC and PM_1 EFs are compared in SI (Table BT4)

3.3.c.i Inorganic gasses

Table 3-3 summarizes the EFs from this work and various other studies covering a range of measurement methods and locations over the last two decades. For SO_2, the median EF obtained in Dunkirk is 1.10 $g{\cdot}kg_{fuel}^{-1}$, generally lower than observed in the literature, except for the study of Le Berre et al. (2025) who observed a median EF of 0.4 $g{\cdot}kg_{fuel}^{-1}$in Marseille (France) in 2021. Despite less stringent sulphur regulations in Marseille, that was not part of a SECA at that time, the EF(SO_2) were only about a third of those observed in this study. The exact reason why SO_2 EFs are lower in Marseille than for the ferries that navigate in the SECA of Dunkirk remains elusive, however, the bigger variety of ships sampled in Marseille could lead to discrepancies between the studies.

The SO_2 EFs obtained in Dunkirk are similar to the EFs calculated during a study conducted on a cruising ferry using Marine Gas Oil (MGO), between Kiel, Germany and Gotheburg, Sweden, in September 2021 during the SCIPPER C2 campaign (Timonen et al., 2022), especially during operations at 70% load, where the mean SO_2 EF was 1.5 $g{\cdot}kg_{fuel}^{-1}$.

Figure 3-4 represents the distributions of the EFs for gaseous species calculated here, sorted according to their mean. NO and NO_2 are the most emitted species, with means of 22.18 ± 14.77 $g{\cdot}kg_{fuel}^{-1}$ and 12.28 ± 9.95 $g{\cdot}kg_{fuel}^{-1}$ respectively. EF(NO) are consistent with the values found by Diesch et al. (2013) determined for heavy ongoing vessels of more than 30 Gt, from land-based observations in Germany (25 ± 11 $g{\cdot}kg_{fuel}^{-1}$), however significantly lower than their NO_2 EFs (40 ± 17 $g{\cdot}kg_{fuel}^{-1}$). EF(NO) is also in agreement with measurements performed in China by Zhang et al. (2024) on an ocean-going vessel using Heavy Fuel Oil (HFO) working on its auxiliary engines (20.8 $g{\cdot}kg_{fuel}^{-1}$), yet the NO_2 EF of our study is significantly higher than theirs in the auxiliary engine situation (1.45 $g{\cdot}kg_{fuel}^{-1}$). The differences between EF(NO_2) in these studies can probably be explained, for the study in Germany, by a larger distance between ship and measurement site or to emission after-treatment systems leading to higher NO oxidation, and, for the Chinese study, by measurements at the stack leading to very low EF(NO_2).

The NO_2/NO_x ratio within the plumes, that provides information on ship engine and technology, could not be calculated in our study, because the time resolution of the O_3 measurements on site (15 min) was equal to the plume duration (12 ± 3 min). Therefore, we could not distinguish between NO_2 primarily emitted and produced by the O_3 titration of NO (Kurtenbach et al., 2016), resulting in a lack of data to compare O_3 concentrations with those of NO_x within the plumes. However, the relatively fresh nature of the plumes (3.5 ± 2 min) and the absence of obvious, repeated and simultaneous NO_2 increase and NO depletion indicate a limited influence of O_3 on NO within the plumes. The mean EF(CO) is 6.9 ± 4.2 $g{\cdot}kg_{fuel}^{-1}$. This value is consistent with the range of EF(CO) calculated by Cooper (2003), from 4.20 to 21.80 $g{\cdot}kg_{fuel}^{-1}$, for a passenger ferry in its hotelling phase working on MGO. Our mean EF(CO) is half of the CO EF determined in 2017 in China for a bulk carrier (reported a minimum of 14.40 $g{\cdot}kg_{fuel}^{-1}$ at berth with 50% load), both for a combination of auxiliary and main engines at berth and while manoeuvering (Huang et al., 2018).

As seen in Figure 3-4, CH_4 is one of the most emitted species with a median EF value of 0.87 $g{\cdot}kg_{fuel}^{-1}$ but a much higher mean of 9.6 ± 29.7 $g{\cdot}kg_{fuel}^{-1}$. This is due to the high standard deviation, caused by many outliers. Interestingly, the median CH_4 EF is already an order of magnitude higher than reported in recent literature, (0.02 $g{\cdot}kg_{fuel}^{-1}$ - 0.05 $g{\cdot}kg_{fuel}^{-1}$ - 0.4 $g{\cdot}kg_{fuel}^{-1}$ from Cooper and Gustafsson (2004), Timonen et al. (2022) and Le Berre et al. (2025) respectively). Considering the number of outliers and the standard deviation of the CH_4 EFs, other sources seem to influence the CH_4 concentrations. This is not explained by a particular background, since each peak has its background subtracted after integration. An additional source is evidenced through the poor correlation of CH_4 with CO, tracer of combustion, within the plumes (SI, Figure BF10). High levels of CH_4 are observed without being associated with an increase in CO, which remains at atmospheric levels (about 100 - 150 $\mu g{\cdot}m^{-3}$), showing that CH_4 is not directly related to combustion sources.

Another source of CH_4 indirectly related to the ferry emissions could be originating from the water. Indeed, it was shown that the southern North Sea, near the coasts of England and Belgium, has high CH_4 emitting sediments, leading to higher CH_4 concentrations in the well-mixed water column and thus higher air-sea fluxes compared to fluxes off-shore ($\geq$ 15 km) (Borges et al., 2016). The high concentration of CH_4 in the water could affect the EFs of the ferries when they cause water turbulence during manoeuvres in the harbour. It is important to note that only a few studies report CH_4 EF from ships, and a deeper understanding of CH_4 emissions from shipping in ports, including from water movements, is needed.

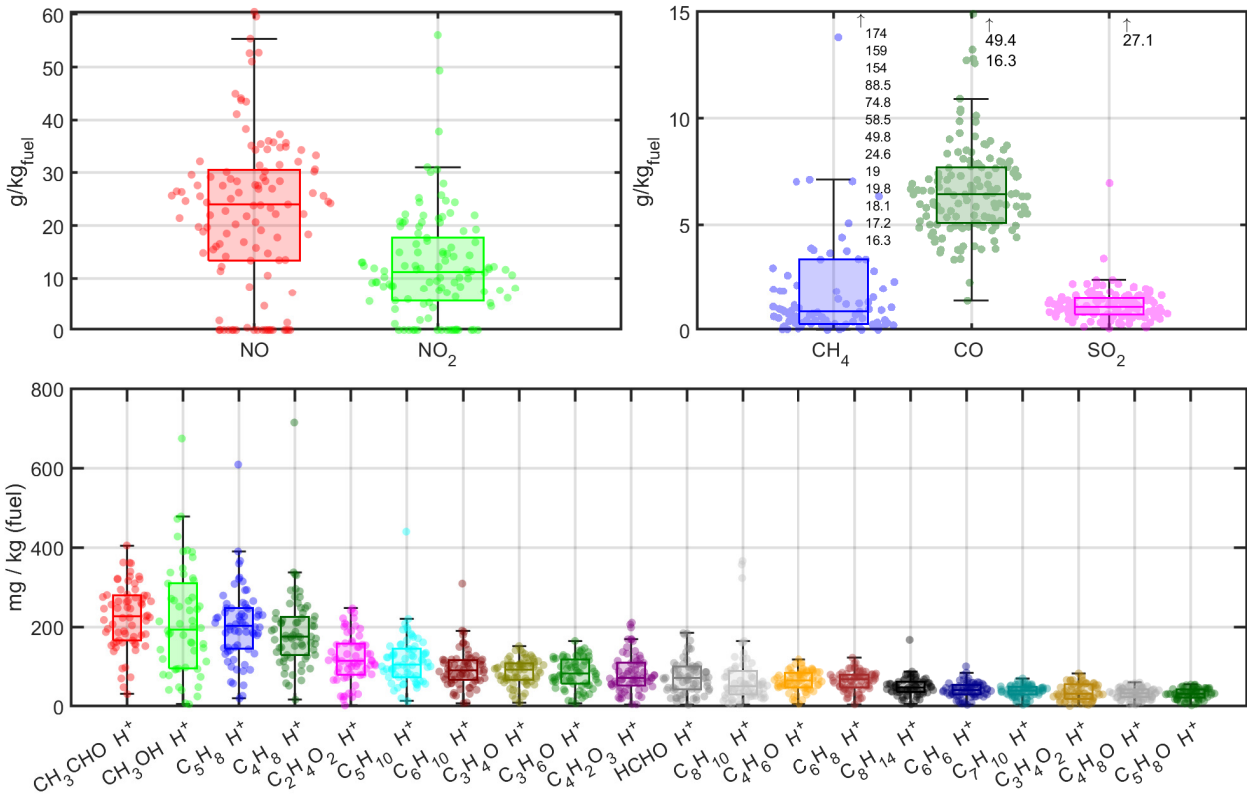

Figure 3-4: *EFs of the gas phase components: (top-left) NO_x, (top-right) CH_4, CO and SO_2 (all in g·kg$^{-1}_{fuel}$) and (bottom) the 20 highest EFs for VOCs (in mg/kg$_{fuel}$).*

The EFs of these criteria pollutants are compared with the OMINEA database for shipping EFs in Table 3-1. This confirms that the mean EF of CH_4 is lower than that reported in this study, which strengthens the hypothesis of an indirect link with the ferries. Moreover, its median EF of CH_4 is close to the EF database. The NO_x EF is consistent with the OMINEA database, but the main difference lies in the EF value of SO_2, which is higher in the EF dataset than in our calculations.

3.3.c.ii Particles

Particulate EFs are shown in Figure 3-5. The median EF(PN) ($1.59{\cdot}10^{16}$ particles/kg$_{\text{fuel}}$) is approximately 3 times the median EF observed in Marseille ($0.67{\cdot}10^{16}$ particles/kg$_{\text{fuel}}$, Le Berre et al. (2025)). As expected, the EFs for PM_{10} (mean 1.1 $\pm$ 1.9 g·kg$^{-1}_{\text{fuel}}$) are higher than the EFs for BC (mean 0.53 $\pm$ 0.45 g·kg$^{-1}_{\text{fuel}}$) and $PM_{2.5}$ (mean 0.35 $\pm$ 1.92 g·kg$^{-1}_{\text{fuel}}$).

Table 3-1: *Comparison of the EF determined in this study with the OMINEA database for shipping in 2021.*

Compound	OMINEA ($g \cdot kg_{fuel}^{-1}$)	Mean EF ($g \cdot kg_{fuel}^{-1}$)
CH_4	0.32	9.60 ± 29.74 (median 0.87)
CO	4.21	6.94 ± 4.24
NO_x	78.22	33.84 ± 22.41
SO_2	11.48	1.36 ± 2.34
PM_1	3.73	0.24 ± 0.18
PM_{10}	4.06	1.11 ± 1.92
$PM_{2.5}$	4.06	0.35 ± 0.38
BC	1.21	0.53 ± 0.45

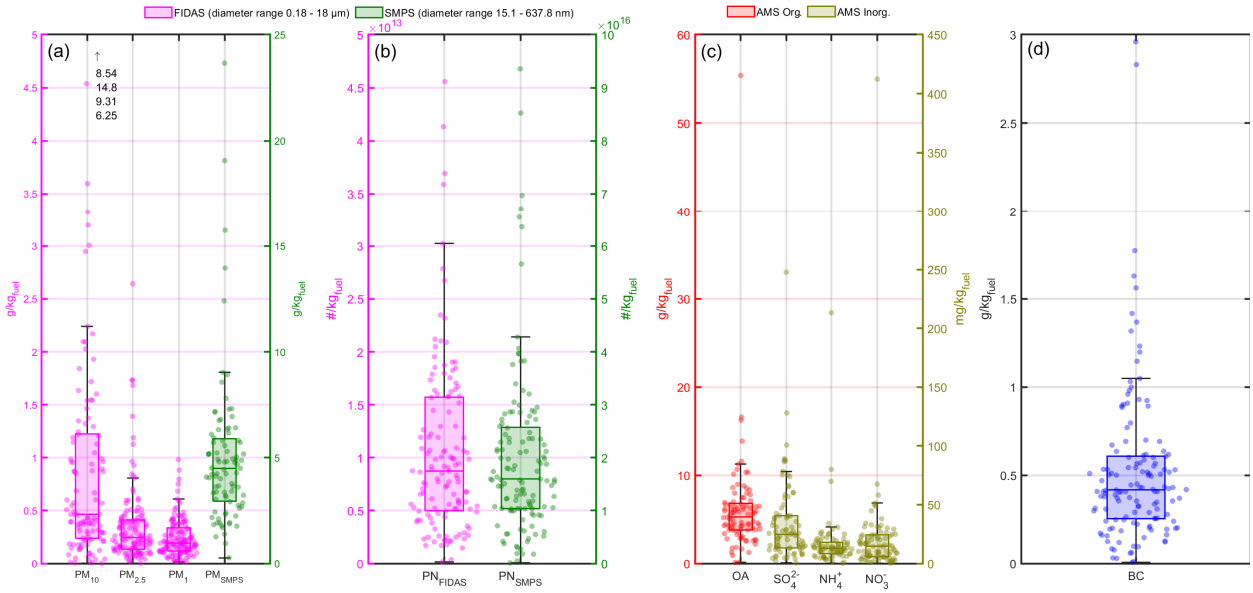

Figure 3-5: *EFs of the components of the particulate phase: (a) mass concentrations determined by FIDAS (pink, left Y axis) and by SMPS (green, right Y axis), (b) number concentrations measured by FIDAS (pink, left Y axis) and SMPS (green, right Y axis), (c) organic (red, left Y axis) and inorganic (brown, right Y axis) mass concentrations determined by AMS and (d) black carbon measured by the aethalometer.*

The EFs for BC are rather poorly described in the litterature, but our mean value is in line with the mean EF observed in the ports of Marseille (0.48 $g \cdot kg_{fuel}^{-1}$) and Toulon (0.38 $g \cdot kg_{fuel}^{-1}$, Gunti et al, 2025, in preparation). As seen in Table 3-1, the EFs of PM determined here are lower than those in the OMINEA database. In contrast, the mean EF of BC is in line with the database.

Ultrafine particles contribute minimally to overall particulate mass in ambient air. However, ships predominantly emit ultrafine particles with sizes between 20 and 100 nm (Gunti, 2025, in preparation; Jeong et al. (2023); Kuittinen et al. (2021)). The mean particle number and mass size distributions of the plumes (SI, Figure BF11) show that $PM_{0.1}$ represent 97% and 61% of the total number and mass distributions, respectively. The mass distribution exhibits a specific unimodal mode at 91 nm, which is below the cut-off diameter range of the FIDAS.

This can also explain the discrepancies in EF(PN) measured by SMPS ([2.01 ± 1.59]·10^{16} particles/kg_{fuel}) and FIDAS (mean [1.06 ± 0.82]·10^{13} particles/kg_{fuel}), because of the different cut-off diameters of FIDAS (180 nm) and SMPS (15 nm). Moreover, the mean EF(PM_1) derived by FIDAS is 0.24 ± 0.18 g·kg_{fuel}^{-1} compared to 5.03 ± 3.57 g·kg_{fuel}^{-1} from the SMPS (PM_{SMPS}).

The EFs for the chemical composition of submicronic particles are dominated by OA with a median of 5.26 g·kg_{fuel}^{-1} (Figure 3-5), which is higher than the median EF determined in the Marseille harbour for manoeuvring ships (1.6 g·kg_{fuel}^{-1}, Le Berre et al. (2025)) and Toulon (1.73 g·kg_{fuel}^{-1}, Gunti et al., in preparation). Opposingly, SO_4^{2-} EF in Dunkirk (24.7 mg/kg_{fuel}) is lower than in Marseille (171 mg/kg_{fuel}) or Toulon (80 mg/kg_{fuel}), despite Dunkirk's higher SO_2. This difference is probably due to the large number of different types of ships in Marseille, some of which use scrubbers that increase the conversion of sulphur into sulphate (Timonen et al., 2022). In addition, many of the ships in Marseille were emitting further away from the monitoring site than in Dunkirk, which could lead to more time for the oxidation of SO_2 to SO_4^{2-}. NO_3^- and NH_4^+ median EFs are 14.4 mg/kg_{fuel} and 12.9 mg/kg_{fuel} respectively in our study, in between EFs obtained in Marseille (5.4 and 5.0 mg/kg_{fuel} respectively) and in Toulon (29.9 and 14.9 mg/kg_{fuel} respectively).

3.3.c.iii VOCs

The VOC EFs display a much smaller number of detected peaks compared to other species, due to the blank cycles of the PTR-ToF-MS. Despite this limitation, 67 peaks were captured during the VOC measurement cycles of PTR-ToF-MS. The sum of the mean EFs of all 68 VOCs studied here is 2.34 g·kg_{fuel}^{-1}, accounting for 4% of the emitted mass per kilogram of fuel for all measured compounds. As only the sum of NMVOCs are reported in the OMINEA database for emission inventories, the sum of VOC EFs reported in this study are put in perspective with the existing database. OMINEA reports a value of 1.8 g·kg_{fuel}^{-1} (converted from 41.8 g/GJ of CITEPA (2022b)) for VOC shipping emissions, thus only about 76% of the results obtained here. Moreover, alkanes are likely underestimated in our study, a known limitation of the PTR-MS method (Warneke et al., 2014). For example, the alkane fraction of VOC EFs determined by Zhang et al. (2024) for ocean-going vessel working on HFO ranged from 15% to 19% for main engines and from 17% to 30% for auxiliary engines, depending on the load. This implies that the discrepancy with existing EF inventory would likely be higher.

The major contributors (27%) to the total emitted VOC mass by ships are light aldehydes, alcohols and acids (formaldehyde, acetaldehyde, methanol and acetic acid), C_5 compounds (14%) ($C_5H_8{\cdot}H^+$ and $C_5H_{10}{\cdot}H^+$, cyclopentane). $C_4H_8{\cdot}H^+$ represents 8% of emitted VOC mass and could be identified as a butene (1-butene, Z-2-butene and E-2-butene) or as a fragmentation product of valeric acid, hexanol or butanal (Yáñez-Serrano et al., 2021). Aromatics (benzene, toluene, xylenes and ethylbenzenes) represent 6% of the emitted VOC mass.

When considering individual contributions of VOCs, it can be seen from Figure 3-4 that the most emitted VOCs are acetaldehyde (CH_3CHO , mean 225.7 ± 80.5 mg/kg$_{fuel}$) and methanol ($CH_3OH{\cdot}H^+$, mean 212 ± 138.7 mg/kg$_{fuel}$). The third most emitted VOC is detected at m/z 69.069 attributed to $C_5H_8{\cdot}H^+$, typically assigned to isoprene. However, Coggon et al. (2024) and Yuan et al. (2017) showed that VOCs from anthropogenic sources, like long-chain aldehydes or cycloalkanes, are strong contributors to this mass. In our study, the m/z 69.069 mostly originates from cycloalkanes or cycloalkenes, as discussed in SI (Section B.2) based on the results of Gueneron et al. (2015).

Most studies so far, have reported speciated VOC EFs using off-line samples (Agrawal et al., 2010; Zhang et al., 2024). From these studies, only a few species were measured in common but using different analytical techniques, mainly GC-MS, that have a much lower time resolution than PTR-ToF-MS and are less sentitive to oxygenated VOCs. These studies point out that toluene and xylenes were the most emitted aromatics and that acetone was the most emitted VOC. In this study, toluene, measured as $C_7H_8{\cdot}H^+$, is not a majorly emitted VOC, with a mean EF of 31 ± 20.7 mg/kg$_{fuel}$, which is comparable to the toluene EF (27.73 mg/kg$_{fuel}$) from a chinese bulk carrier at berth using auxiliary engines as calculated by Huang et al. (2018). Benzene, measured at m/z 79.054 ($C_6H_6{\cdot}H^+$) is among the 20 most emitted VOCs measured in Dunkirk (Figure 3-4) with a mean EF of 41 ± 19.1 mg/kg$_{fuel}$. This is much higher than the speciated EFs reported in literature (maximum of 5.26 ± 0.16 mg/kg$_{fuel}$ by Agrawal et al. (2010), SI, Table BT4). Ethylbenzene, together with m-, p- and o-xylenes are detected at m/z 107.079 ($C_8H_{10}{\cdot}H^+$) by PTR-MS and yielded a mean EF of 70.6 ± 73.4 mg/kg$_{fuel}$, in line with the sum of mean EFs for ocean-going vessels using HFO (22.76 mg/kg$_{fuel}$) calculated by (Zhang et al., 2024). Please note that the studies we compare to here, reported EFs for ships using HFO.

For oxygenated VOC EFs, acrolein (C_3H_4O) and acetone (C_3H_6O) are observed to be respectively the 8th and the 9th most emitted VOCs with mean EFs of 86.8 ± 32 mg/kg$_{fuel}$ and 83.8 ± 38 mg/kg$_{fuel}$ respectively. The acetone EFs is comparable to the EFs calculated by Zhang et al. (2024) (mean 61.5 ± 49.4 mg/kg$_{fuel}$) for stack measurements of an ocean-going vessel using auxiliary engines with HFO, but their value for acrolein (mean 16.8 ± 16.7 mg/kg$_{fuel}$) is much lower than our study.

Comparing the speciated EFs of VOCs leads to discrepancies linked to the analytical technique, such as the contributions of multiple species to a single mass signal for PTR-MS. In conclusion, the complementarity between high time resolved concentrations of VOCs with PTR-MS, mandatory for probing VOC concentrations in ship plumes, and high chemically resolved concentrations using GC-MS have to be explored to ensure reliable determination of VOC EFs from ships.

Timonen et al. (2022) and Le Berre et al. (2025) both used a PTR-MS to determine EFs respectively from the stack of a ferry and from land-based observations in Marseille. In the latter study, most VOCs peaks were below the detection limit and only toluene and heavy aromatics ($\geq C_8$) were occasionally observed in intensive peaks, limiting the comparison between both studies.

The study by Timonen et al. (2022), however, allows for comparisons with precise measurements obtained during the SCIPPER project of stack emissions of a ferry in the Baltic Sea, working on MGO, under various loads and intermittent use of urea. A comparison of the EFs obtained in Dunkirk and the EFs obtained during the SCIPPER campaign are represented in the boxplots of Figure 3-6, where the most emitted VOCs in their study are compared with the same ones in Dunkirk. Important discrepancies between both campaigns are evidenced, where the VOC EFs in Dunkirk are higher by one order of magnitude or more. For benzene, for example, the median EF is 40.8 mg/kg_{fuel} for ferries of Dunkirk versus 4.8 mg/kg_{fuel} for SCIPPER. The smallest differences are encountered for acetic acid ($C_2H_4O_2$), which is higher for Dunkirk (114 mg/kg_{fuel}) than SCIPPER (74.75 mg/kg_{fuel}), and formic acid (CH_2O_2), the only EF higher for SCIPPER (9.83 mg/kg_{fuel}) than Dunkirk (2.8 mg/kg_{fuel}). The ferry used in the SCIPPER campaign was more recent than the ferries studied in Dunkirk, with more efficient combustion that could lead to smaller quantities of emitted VOCs. The SCIPPER ferry was also equipped with after-treatment systems leading to higher oxidation states of VOCs, which could explain the smaller differences of EF for acetic and formic acid. For non-oxygenated VOCs, like benzene on the other hand, this would lead to smaller EFs, as observed. From these comparisons, it can be concluded that after-treatments have an important influence on the intensity and profile of the VOCs emitted, notably shifting towards the emission of smaller, oxygenated molecules. The comparison with EFs obtained from HFO-using ships shows that the use of low sulphur fuel does not automatically lead to lower EFs for VOCs.

Table 3-2: *Measured FSCs and methodology of previous studies investigating ship emissions.*

Study	FSC (%)	Operation	Ship type(s) and number	Fuel, engine, load	Sampling location	Time and place
This study	0,07 ± 0,06	Manoeuvering	3 ferries		Land based	Dunkirk, France 2022
Diesch et al 2013	0,38 ± 0,34	Cruising	13 vessels (5 Gt to 30 Gt)		Land based	Elbe river, Germany, 2011
Diesch et al 2013	0,55 ± 0,20	Cruising	41 vessels, >30 Gt		Land based	Elbe river, Germany, 2011
Agrawal et al 2010	3,01	Crusing	1 Container ship	HFO	Stack	2007
Alföldy et al 2013	0,29 ± 0,07	Hotelling	341 ships		Land based	Rotterdam, Netherlands, 2009
Cooper et al, 2003	0.08	Hotelling	1 passenger ferry	MGO (45 % load)	Engine casing	2002
Cooper et al, 2003	0.53	Hotelling	1 passenger ferry	RO (47 % load)	Engine casing	2002
Zhang et al, 2024	0.43 - 0.50	Crusing	1 ocean going vessel	HFO, auxiliary, 50 %	Stack	China
Zhang et al, 2024	0.43 - 0.50	Crusing	1 ocean going vessel	Diesel, auxiliary. 50 %	Engine casing	China
Zhang et al, 2024	0.43 - 0.50	Crusing	1 ocean going vessel	HFOn main engines, 75 %	Engine casing	China
Zhang et al, 2024	0.43 - 0.50	Crusing	1 ocean going vessel	HFO, main engines, 25 %	Engine casing	China
Pirjola et al, 2014	0.68 ± 0.26		1 ROPAX (RoRo / passenger ship)	HFO	Land based	Helsinki and Turku, Finland, 2010/2011
Timonen et al, 2022		Cruising	1 ferry	MGO (50% load, no urea)	Stack	Gothenburg/Kiel
Le Berre et al, 2024			800 ships, 353 plumes		Land based	Marseille, June 2021
Huang et al, 2018	0.38	At berth	1 bulk carrier (auxiliary)	HFO	Stack	China, 2017
Huang et al, 2018	0.38	Arrival	1 bulk carrier (main engines)	HFO	Stack	China, 2017
Huang et al, 2018	1.12	Departure	1 bulk carrier (main engines)	HFO	Stack	China, 2017

Table 3-3: *Comparisons of EFs from this study with literature for inorganic and regulated compounds. (*) indicates that EFs taken from the study were converted from g/kWh to $g{\cdot}kg_{fuel}^{-1}$ using the Low Heating Value of the corresponding fuel from The Engineering Toolbox (2003).*

Study	NO_x (g/kg_{fuel})	NO (g/kg_{fuel})	NO_2 (g/kg_{fuel})	CO (g/kg_{fuel})	SO_2 (g/kg_{fuel})	PM_{10} (g/kg_{fuel})	PM_1 (g/kg_{fuel})	BC (g/kg_{fuel})	PN (particles./kg_{fuel})
This study	33.84 ± 22.41	22.18 ± 14.77	12.28 ± 9.95	6.95 ± 4.23	1.36 ± 2.33	1.11 ± 1.92	5.03 ± 3.57(SMPS)	0.53 ± 0.45	$1.59 \pm 1.58 \cdot 10^{16}$
Diesch et al 2013	53 ± 27	16 ± 12	37 ± 20		7.7 ± 6.7		2.4 ± 1.8	0.12 ± 0.08	$2.55 \pm 1.91 \cdot 10^{16}$
Diesch et al 2013	65 ± 23	25 ± 11	40 ± 17		11 ± 4.0		3.7 ± 1.7	0.15 ± 0.17	$1.96 \pm 0.7 \cdot 10^{16}$
*Agrawal et al 2010 **	214.11 ± 3.0			3.14 ± 0.22	124.87 ± 2.2	25.98 ± 0.56			
Alföldy et al 2013					5.9 ± 1.5				$1.01 \pm 0.1 \cdot 10^{16}$
*Cooper et al, 2003 **	177.16			6.78	3.92	2.50			
*Cooper et al, 2003 **	145.90			11.63	27.43	5.27			
Zhang et al, 2024	22.3	20.8	1.45	3.33					
Zhang et al, 2024	28.4	27.1	1.38	13.8					
Zhang et al, 2024	59.9	51.7	8.18	2.46					
Zhang et al, 2024	89.1	66.9	22.2	2.59					
Pirjola et al, 2014	65 ± 10	42 ± 6			9.8 ± 1.0				$1.25 \pm 0.17 \cdot 10^{15}$
Timonen et al, 2022		54.8		6.7	1.5			0.14	
Le Berre et al, 2024	37	14		5.4	0.4		1	0.479	$6.70{\cdot}10^{15}$
*Huang et al, 2018 **	49.60			14.40		8.01			
*Huang et al, 2018 **	162.99			73.43		13.32			
*Huang et al, 2018 **	94.65			31.30		11.70			

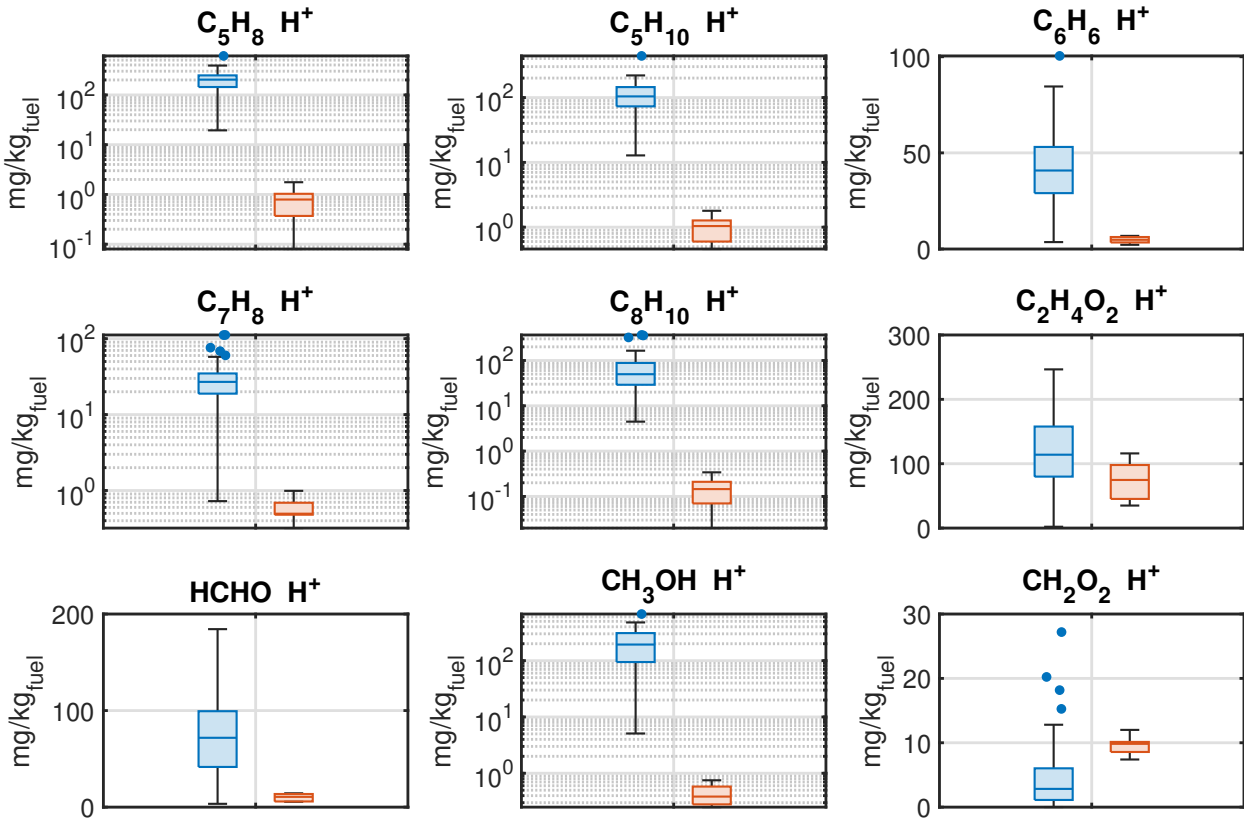

Figure 3-6: *Comparison of VOC EFs from Dunkirk (blue) with those obtained from stack measurements in the Baltic Sea by Timonen et al. (2022) (orange).*

3.3.d Variability of EFs

3.3.d.i Variability of EF depending on the ship

Since our measurement site was next to the docking berth of three rotating ferries, we could evaluate the EFs for each vessel separately. In the gas phase (Figure 3-7), the EFs for all regulated pollutants are not significantly different. The CO EFs from ferry A seem to show a wider range of values but no statistically significant difference was found. The VOC EFs don't display significant discrepancies neither which could be partially due to the lower populations compared to the other components of the gas phase. The median EF(OA) for ferry B (4.05 $g \cdot kg_{fuel}^{-1}$) is lower than for ferry A (6.44 $g \cdot kg_{fuel}^{-1}$) as represented in Figure 3-8, but this difference is not correlated with any other component of the particle phase and also doesn't display a statistical difference. The comparison of EFs between the three vessels demonstrates that they emit very similarly, which is probably related to the ships being built at the same time (C in 2005, A and B in 2006) by the same shipbuilding company and equipped with similar motorization and auxiliary systems.

3.3.d.ii Difference between arrivals and departures

The EFs of the gaseous species classified according to the direction of manoeuvre of the ship, i.e. entry or departure, are represented in Figure 3-9. Firstly, no significant differences are found between entries or departures for most pollutants, such as NO, NO_2, CO and SO_2.

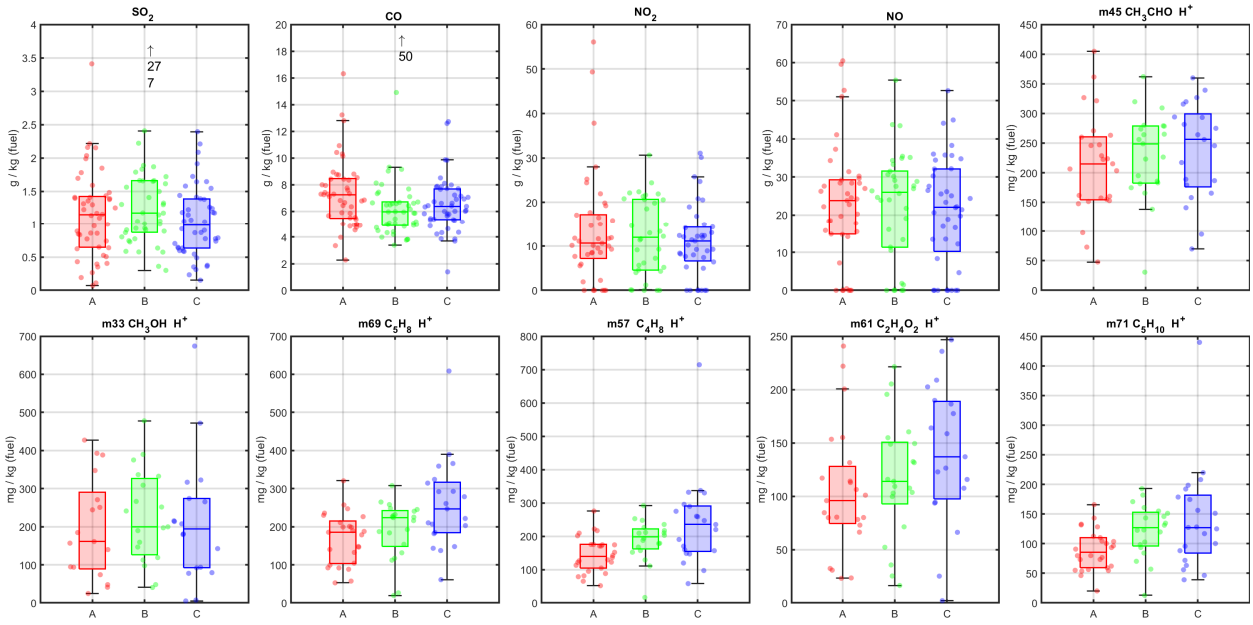

Figure 3-7: *Comparisons of EFs for the gas phase components, including inorganic pollutants (SO_2, CO, NO_2, NO) and the 6 largest VOC EFs for the different ferries: ferry A (red), B (green) and C (blue).*

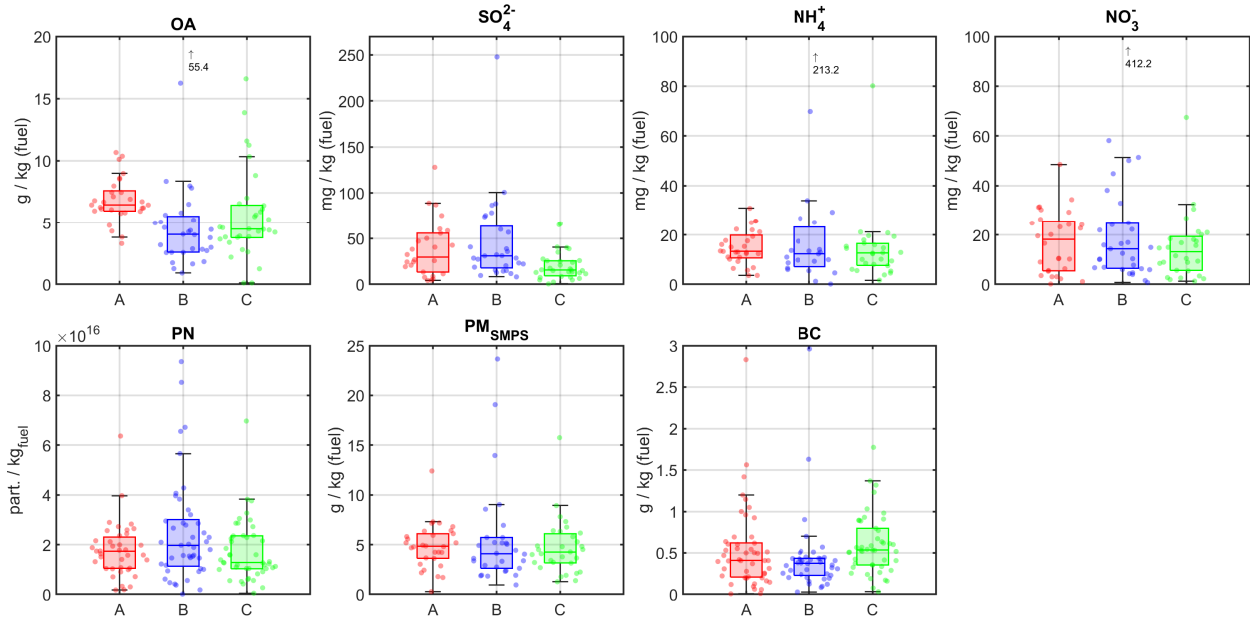

Figure 3-8: *Comparisons of EFs for PM variables for the different ferries: ferry A (red), B (green) and C (blue).*

However, differentiating the EFs based on the direction of manoeuvre is possible for some VOCs (Figure 3-9), PM_{SMPS} and BC (Figure 3-10). These pollutants show significantly higher emissions upon arrival than on departure (two samples t-test, confidence interval 95%). Out of the 68 studied VOCs, 28 show a statistically significant difference between their arrival and departure EF.

The VOCs showing the clearest distinction between arrival and departure EFs are not necessarily the major VOCs shown in Figure 3-4. In SI, Figure BF13 shows a selection of VOC EF distributions corresponding to the VOCs for which the difference is the most obvious, according to p-values of the two samples t-test. Low p-values indicate that the difference between the arrival and departure emissions is significant and that emissions are higher upon arrival. $C_5H_4O_2{\cdot}H^+$ has the lowest p-value of all VOCs and indicates the emissions of furanic compounds, also evidenced by $C_5H_4O_3{\cdot}H^+$ (an oxidation product of $C_5H_4O_2{\cdot}H^+$ from OH) and $C_4H_4O{\cdot}H^+$ (furane) amongst the 10 lowest p-values. It is remarkable that besides benzene ($C_6H_6{\cdot}H^+$), the VOC with the 5th lowest p-value, its oxidation products maleic acid ($C_4H_4O_4{\cdot}H^+$) and maleic anhydride ($C_4H_2O_3{\cdot}H^+$) (Borrás and Tortajada-Genaro, 2012; Priestley et al., 2021) also show low p-value. This is also observed for toluene and one of its oxidation products, formaldehyde (Lannuque et al., 2023). These observations confirm the similar origin of the parent VOCs and their oxidation products.

BC and PM_{SMPS} are the two components of the particulate phase for which there is a statistical difference between arrival and departure EFs. BC median EF is 0.51 $g{\cdot}kg_{fuel}^{-1}$ for arrivals, and only 0.38 $g{\cdot}kg_{fuel}^{-1}$ for departures, which corresponds to a 39% difference. PM_{SMPS} also displays a larger median EF for arrivals (5.17 $g{\cdot}kg_{fuel}^{-1}$) than for departures (4.17 $g{\cdot}kg_{fuel}^{-1}$), a difference of 19%. The ferries are thus more emissive upon arrival than on departure for 28 gaseous species and 2 particulate.

Figure 3-11 represents the classification of EFs according to the identification of the ferry and the direction of manoeuvre for the 6 VOCs that show the largest statistical difference between arrivals and departures, and the 2 particle pollutants, BC and PM_{SMPS}, showing a difference according to the directions of manoeuvre. All of these compounds have a higher mean EF for all ferries (A, B and C) upon arrivals and departures, indicating that the differences observed between arrivals and departures throughout the campaign and for all ferries are not induced by a statistical bias driven by some outliers, since the individual ferries follow the same pattern.

Distinction between arrival and departures EFs has previously been reported for SO_2 EFs in Marseille, where this was ascribed to a fuel switch from a 0.5% to a 0.1% FSC upon arrival in the harbour, due to restrictive norms in the port (Le Berre et al., 2025). However, in our study, SO_2 EFs are independent of the individual ferry and the direction of manoeuvre. Furthermore, in Dunkerque a fuel switch is unlikely, as the ferries' entire navigational route lies within the North Sea SECA (FSC limit of 0.1%). Other hypotheses to explain the observed differences between arrivals and departures include a shift in engine type, engine load or speed upon arrival and departure. We currently lack the detailed information about the manoeuvres and the motorisation of the ships required to identify a specific cause of the observed differences.

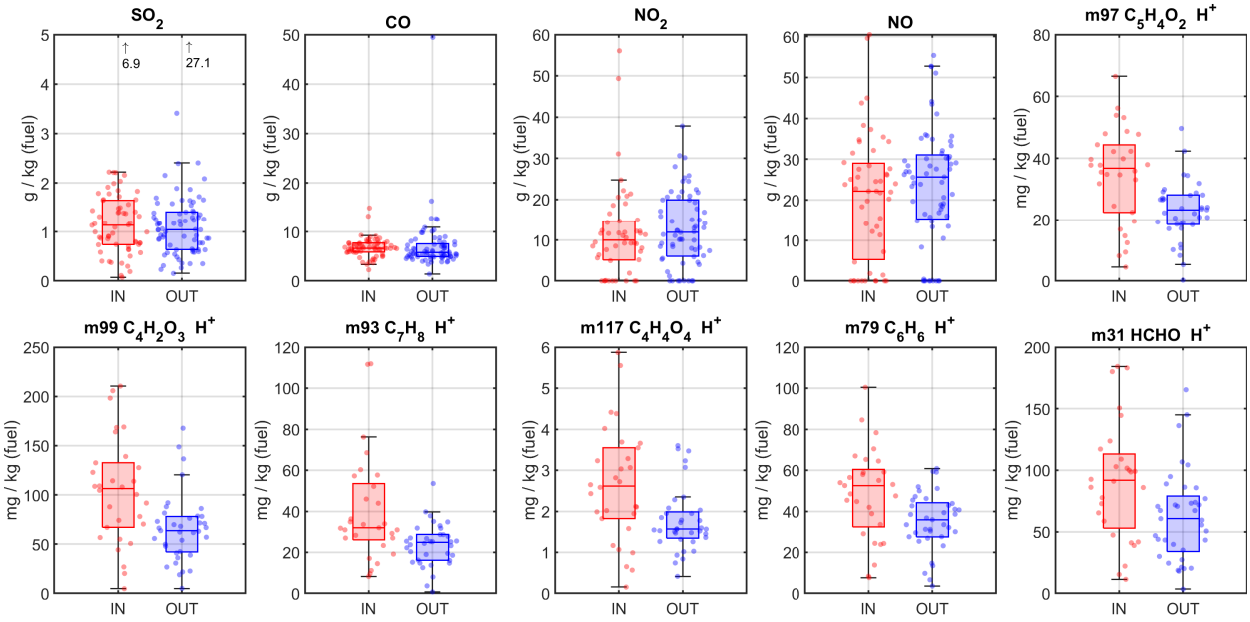

Figure 3-9: *Comparisons of EFs for the gas phase components, including inorganic pollutants (SO_2, CO, NO_2, NO) and a selection of 6 VOCs, according to the directions of travel of the ships, arrivals (red), departures (blue). The VOCs selected show the highest difference between arrival and departure according to the two samples t-test.*

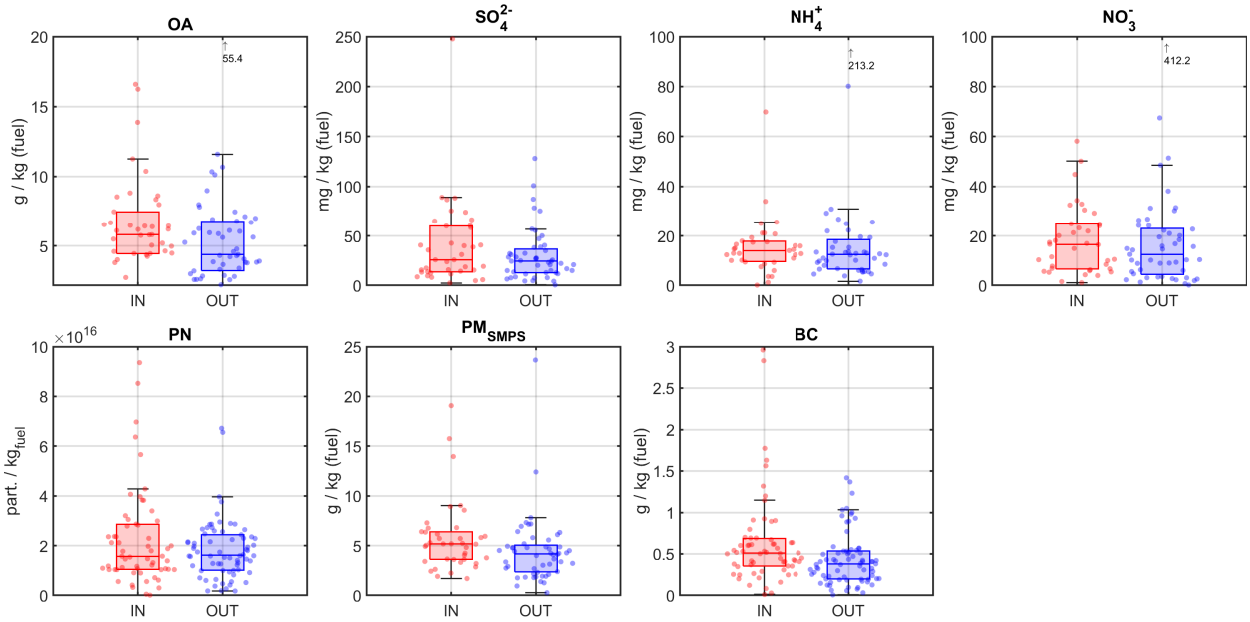

Figure 3-10: *Comparison of EFs for PM variables between the directions of travel of the ships: arrivals (red), departures (blue)*

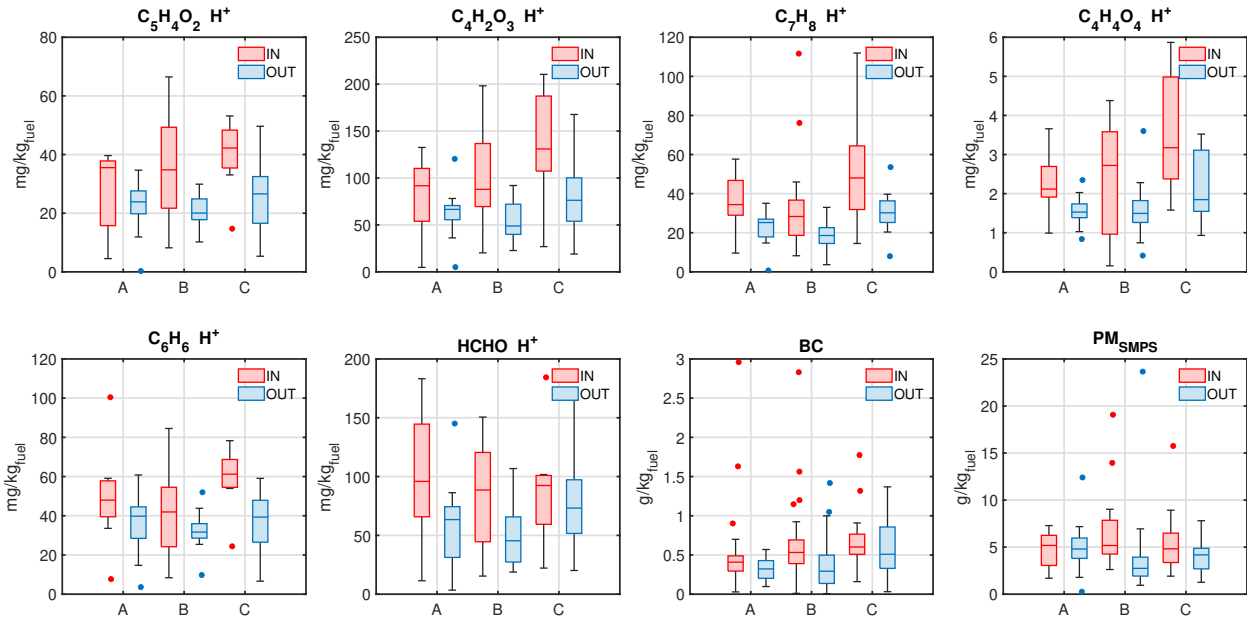

Figure 3-11: *Comparisons of EFs for a selection of 6 VOC, BC and PM_{SMPS}, and the three ferries (A, B and C), according to the direction of travel, arrivals (red), departure (blue), and identification of the ferry (A, B and C).*

3.4 Conclusion

Measurements of 68 VOCs from PTR-ToF-MS, PM_1 chemical composition from HR-ToF-AMS, BC, and other regulated compounds were performed at the ferry terminal of Dunkirk in September 2022. We investigated three similar ferries rotating and departing 30 times a week, allowing intensive measurement of ship plumes under favourable wind directions, from west to north-east.

This study focuses on ferries, a particular type of ship that could be encountered in other harbours within ECAs. This approach is comparable to other field studies conducted in France, such as those carried out in Marseille, shedding light on the emissions of VOCs and PM_1 of these ships in French ports such as Toulon, Calais and Le Havre. The cities of Rotterdam and Gothenburg are regulated European ports with significant ferry traffic, providing insights into their emissions on a larger scale.

Correlation of the SO_2 peaks with ferry arrivals and departures and peak intensity confirm that SO_2 is still a good tracer of ship emissions close to the source, even in a sulphur regulated area. It made it possible to detect 149 peaks, including 68 VOC peaks and 138 PM_1 peaks.

A sensitivity test of the EFs to the background determination was performed for each variable. No major influence was found in our case study, as the measurement site was mainly influenced by the ferries when under favourable wind directions. However, the impact of the background on the EF calculations should always be assessed.

In Dunkirk, NO_x was the most emitted compound (33.8 ± 22.4 $g{\cdot}kg_{fuel}^{-1}$), followed by CO (6.9 ± 4.2 $g{\cdot}kg_{fuel}^{-1}$) and SO_2 (1.4 ± 2.3 $g{\cdot}kg_{fuel}^{-1}$). These results are consistent with the literature. PM_1 composition was dominated by OA (6.12 ± 6.00 $g{\cdot}kg_{fuel}^{-1}$), in line with recent results for manoeuvring ships in the harbour of Marseille, but the median EF(PN) was higher in Dunkirk ($[2.01 \pm 1.59]{\cdot}10^{16}$ particles/kg_{fuel}). As we were very close to the ferries, PN observations may have been higher in Dunkirk compared to Marseille, where the distance to the source was longer and more varied. As a result, particles may have coagulated, leading to a decrease in PN. The high contribution of PN below 100 nm induced large discrepancies between FIDAS and SMPS measurements.

This study provides speciated VOC EFs, including understudied oxygenated species, showing that the EF of total VOCs used for emission inventories, as from the OMINEA database, is lower than the sum of the VOC emissions from ferries observed in our study, despite the relative absence of alkane measurements by the PTR-MS (2.3 $g{\cdot}kg_{fuel}^{-1}$ in our study vs 1.8 $g{\cdot}kg_{fuel}^{-1}$ in OMINEA). VOCs represent 4% of the total mass emitted by the ferries in Dunkirk. The most emitted VOCs are acetaldehyde (CH_3CHO) and methanol (CH_3OH), with mean EFs of 225.7 ± 80.5 mg/kg_{fuel} and 212 ± 138.7 mg/kg_{fuel} respectively. C_5H_8 is the third most emitted VOC but is not related to isoprene in this environment.

Using reported fragmentation patterns and measured concentrations of the parent ions, we show that cycloalkanes and cycloalkenes are the main contributors to the m/z 69 signal.

Finally, we compared EFs from three sister ferries during arrival and departure operations. No difference in EFs were observed among ferries while a statistically significant difference was observed between arrivals and departures of the ferries for 28 VOCs, BC and PM_{SMPS}, indicating that they are more emitted upon arrival. Although a low to high-sulphur fuel switch can cause higher emissions of VOCs upon arrival, as observed in Marseille, the ferries arriving in the Dunkirk terminal transit through a SECA for their entire trajectory, so no fuel switch was occurring. Further investigations, in particular with regard on the engine use and load during the different phases, are required to understand these differences.

The results of this study improve our understanding of the speciation of VOCs and PM_1 of shipping emissions. These are still emerging pollutant categories that require further investigations in light of new emission regulations and evolving practices in the shipping industry (e.g., fuel types, aftertreatment technologies). Comparisons with EFs for speciated VOCs obtained in HFO fuel vessels do not indicate a decrease of VOC emissions when low sulphur fuel is used. Our observations show that benzene, a carcinogenic compound, in particular seems to have higher EFs with low sulphur fuel use. Although VOCs represent a small fraction of the total mass emitted by the ships, some of the VOCs emitted are reactive species that should be taken into account when evaluating the air quality in an industrial harbour like Dunkirk.

The methodology demonstrated a robust approach to determining a relevant chemical fingerprint of ferry emissions. However, such a study needs to be extended to take into account other categories of vessel in order to provide an exhaustive characterisation of shipping pollutant emissions in future work.

CHAPTER 4

Characterisation of the shipping source from near field-measurements using Positive Matrix Factorisation in an industrial area

Validation of the VOC data described previously produced a comprehensive dataset from four instruments, namely two TD-GC-FID from Perkin-Elmer, one AirmoVOC from Chromatotec and one PTR-ToF-MS from Ionicon, some of which measured the same species. As discussed in the previous chapter, the high time resolution of the PTR-ToF-MS was employed to derive Emission Factors (EFs) for VOCs and provide a chemical fingerprint of shipping. However, the low time resolution of the GC measurements remains unused, despite them providing essential VOC speciation information that is important for assessing the impact of VOC sources in Dunkirk. Therefore, the combination of low- and high-time resolution VOC datasets will be explored in this chapter. The objective of this practice is to identify a clear ship emission factor from the solutions provided by the PMF. The optimisation and sensitivity of the PMF solutions in Dunkirk will be explored to provide the most exhaustive shipping factor possible.

4.1 Prior knowledge on the VOC sources in Dunkirk

Although PMF does not require prior knowledge of the source profiles, making an initial inventory of sources impacting the site will facilitate its interpretation. As shown in Figure 2-2, an alcohol source can be expected due to the proximity of an alcohol production facility in the south-east. The NWR plots of methanol and ethanol in Figures 4-1a and 4-1b respectively show that methanol originates from widespread wind directions ranging from the south to the east, which could correspond to the alcohol production facility. In these directions, methanol concentration can reach 200 $\mu g \cdot m^{-3}$ and the higher concentrations are observed with low wind speeds, below 7 $m \cdot s^{-1}$. Otherwise, methanol concentrations under winds outside this sector are around 10 $\mu g \cdot m^{-3}$, indicating a significant background contribution to its concentrations. Ethanol shows higher concentrations when wind speeds are lower and more tightly confined to winds mostly from the east, which deviates from the direction of the alcohol production facility. The NWR plot in Figure 4-1c shows that ethylene predominantly originates from the north-east with wind speed ranging from 0 to 7 $m \cdot s^{-1}$, and that a smaller proportion originates from a broader range of wind directions, from north to east. This suggests an impact from a refinery in the east, which produces ethylene and propene. The same observation is made for propene (Figure 4-1d), which mainly originates from the same direction at the same wind speeds. Finally, the north-east is also the most important wind direction for the observed concentrations of benzene (Figure 4-1e) and toluene (Figure 4-1f) observed at comparable wind speeds. While this may confirm the impact of the refinery on VOC observations, the majority of the observed mass during the Dunkirk 2022 campaign originated from the north-east. The fact that most pollutants share a common direction of origin underscores the need for a more nuanced analysis employing PMF, which facilitates source deconvolution and enhances interpretability.

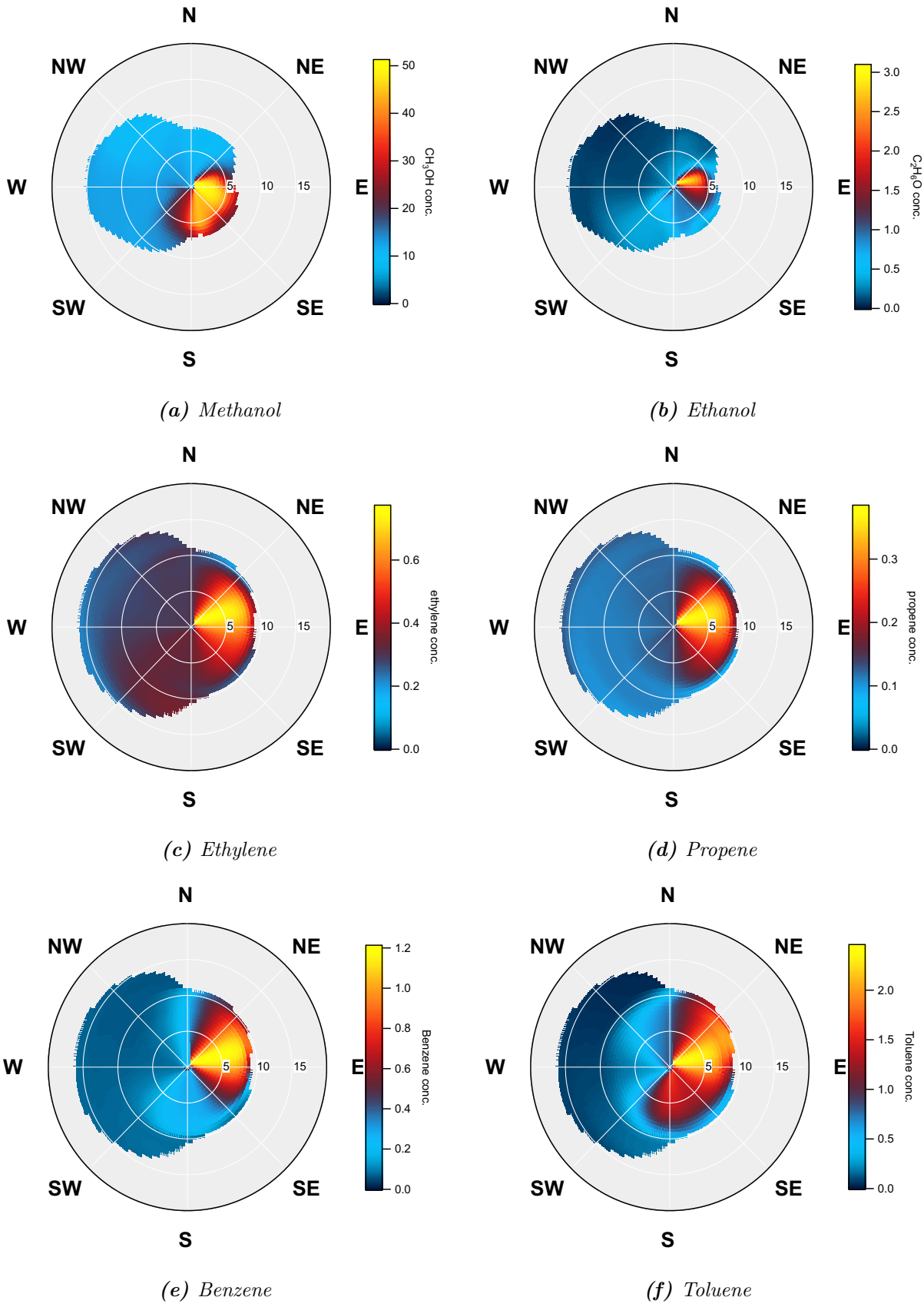

(a) Methanol *(b) Ethanol*

(c) Ethylene *(d) Propene*

(e) Benzene *(f) Toluene*

Figure 4-1: *NWR plots of a selection of VOC over the whole campaign.*

4.2 Native PMF of TD-GC-FID

A standard PMF analysis was first performed using only GC data, to provide a reference framework for the more refined analyses. The input matrix of trhe GC is a 631×64 matrix comprising 20 compounds with a strong quality, 16 with a weak quality and 28 with a bad quality, with a time resolution of 1 hour, which start time is the beginning of the 30 min sampling followed by the 30 min analysis. The main time series and profiles of each solution will be represented within the manuscript and additional information on the time series of the relative contributions of each factor are represented in Appendix C.

4.2.a Solutions

The number of factors tested for the GC-only PMF ranged from 2 to 9 factors. First, the correlation coefficient between the observed and modelled concentrations was investigated, as shown in Figure 4-2. This ranged from 0.74 to 0.97, with the steepest increase observed between 2 and 5 factors, after which it stabilized. This indicates that increasing the number of factors beyond 5 does not improve the quality of the modeling. Therefore, the PMF solution with five factors was used for the study. The time series and profiles of the 5-factor solution are presented in Figure 4-4. The average contribution of each factor is shown in Figure 4-3 revealing that Factor 2 is the main contributor to the modelled mass with 49.4%, followed by Factor 5 (22.2%), Factor 3 (11.7%), Factor 1 (9.7%) and Factor 4 (7.1%). The identification of these factors is discussed in the next section.

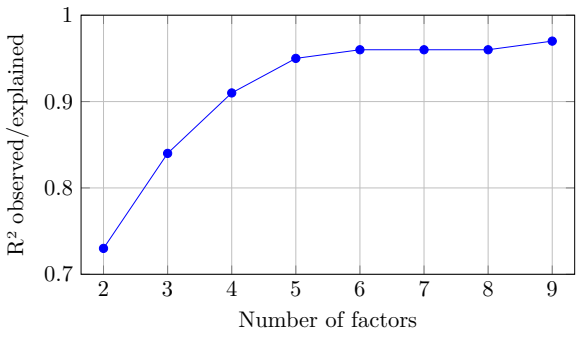

Figure 4-2: *Evolution of the correlation coefficient between observed and modelled concentration depending on the number of factors for the GC-only PMF solutions.*

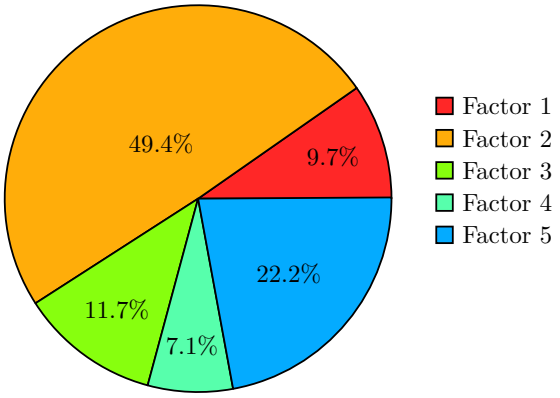

Figure 4-3: *Pie chart of average contribution of the PMF factors in the GC-PMF 5-factor solution.*

(a) *Time series of each factor.*

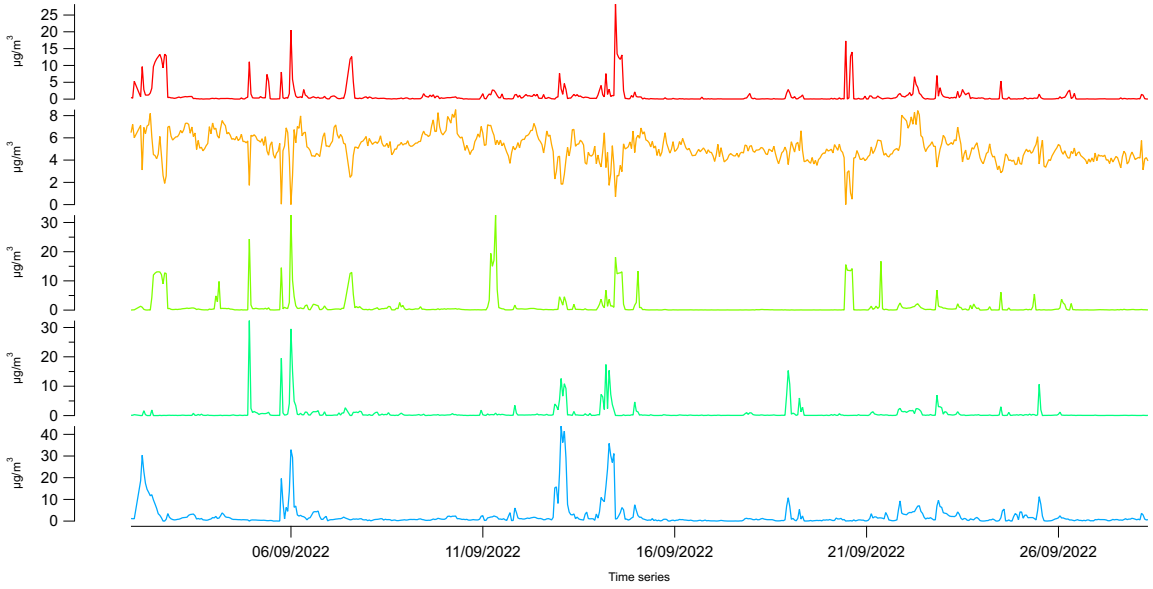

(b) *Profile of each factor. The bar plot corresponds to the contribution of the variable to the profile (left axis), the dotted plot corresponds to the contribution of the factor to the observed mass of each variable (right axis).*

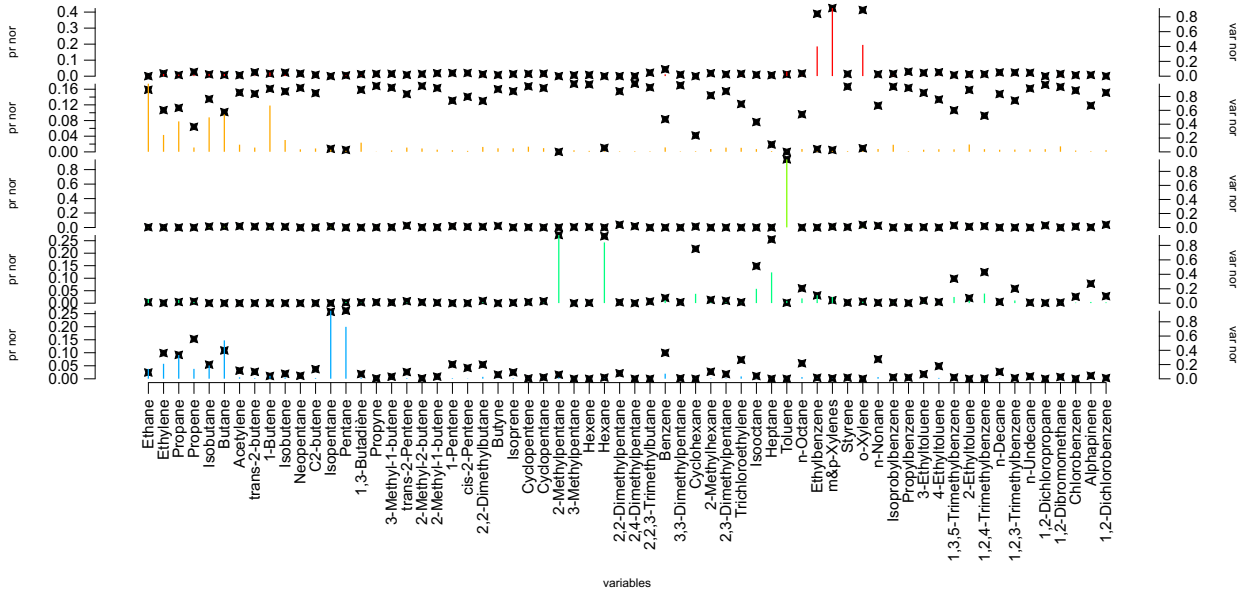

Figure 4-4: *Contribution time series and chemical profiles of the 5-factor solution of the GC-PMF.*

4.2.b Interpretation

Background The factor in position 2 (in orange in Figure 4-4) initially appears to be characteristic of a background source, given its temporal pattern and the nature of its contributing compounds. This interpretation is supported by its low concentration levels, with an average of 5.12 ± 1.22 µg·m^{-3}, and the notable absence of significant peaks compared to the other factors.

Furthermore, the time series showing the relative contribution of the factor ('fraction' time series in Appendix CF1) presented in Figure CF1 indicates that this factor contributes on average 50% up to 80% during the low-level period between 15th and 21st September with N winds. It is mainly composed of light VOCs ranging from C_2 to C_5, and accounts for many observations of these VOCs. In particular, it accounts for 89.6% of the ethane concentrations, representative of the long-lived compounds in this solution (Sauvage et al., 2009; Salameh et al., 2016; Dufresne et al., 2025). Finally, the NWR of factor 2 in Figure 4-5a shows no particular origin according to wind speed or direction, nor any particular concentration distribution, which reinforces the idea of a background factor. However, this background factor explains the majority of the mass of VOCs with 'bad' quality signal-to-noise ratios (SNR < 0.2), including neopentane (92.2%, SNR 0.04), propyne (95%, SNR 0.01), 2,4-dimethylpentane (98.3% SNR < 0.001) or 2-methyl-2-butene (95% SNR < 0.001). The low SNR levels for these compounds suggest that they have a minimal impact on the determination of the factorisation. Moreover, their correlation between modelled and observed correlations are near 0 as most of their observations were below the LOD. However, these correlation for the background-inferring compounds, such as propane and butane, shows satisfactory modelling in this solution, with R^2 of 0.71 and 0.88, respectively. The R^2 for ethane is 0.3, as the PMF mainly captures its low-frequency variability linked to its background presence and struggles to resolve transient increases induced by local sources in addition to this background variability. In conclusion, this factor is partially noise-driven and dominated by compounds with a low SNR, gathering unresolved or weakly explained variability in the dataset. This likely contributes to its low correlation with CH_4 ($R^2 = 0.17$), used as a tracer for background airmasses here, throughout the whole campaign, as shown in Figure 4-5b, despite its apparent background-like behaviour.

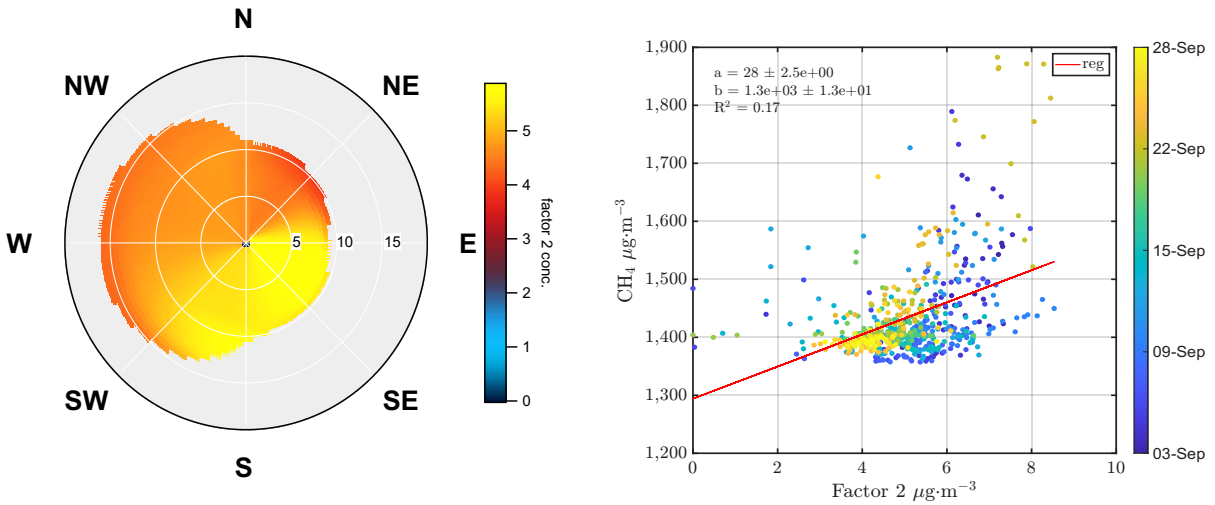

(a) NWR of Factor 2 of the 5-factors solution from the TD-GC-FID PMF.

(b) XY plot Factor 2 with CH_4 in the 5-factors PMF from the TD-GC-FID PMF.

Figure 4-5: *Identification of 'background' Factor 2 in the 5-factor solution of the GC-PMF.*

Hydrocarbon industry The average concentration of Factor 1 is 1.00 ± 2.68 µg·m^{-3} and exhibits some intense peaks (Figure 4-4). As can be seen from its NWR in Figure 4-6, the highest concentrations of this factor originate from high-speed winds (10 m·s^{-1}) from the north-east, suggesting that the refinery at the eastern terminal of Dunkirk could be the source of this factor. Three C_8 compounds: ethylbenzene, m&p-xylenes and o-xylene, contribute to this factor respectively for 18.5%, 42.5% and 19.5% of its total mass. This factor explains 83.9%, 91.7% and 89.1% of the mass of these aromatics, respectively. They are consistent with the VOCs observed for the hydrocarbon cracking industry, as reported by Roukos et al. (2009). They were also found in the chemical profiles linked to industrial sources in Marseille (Dufresne et al., 2025), but never as isolated markers, but present in association with other compounds. Profiles containing C_8 aromatics were also found in solvent use profiles in Beirut (Salameh et al., 2014), and with the widespread origin of Factor 1, from north to east, could suggest a partial impact of solvent production or hydrocarbon evaporation on this factor.

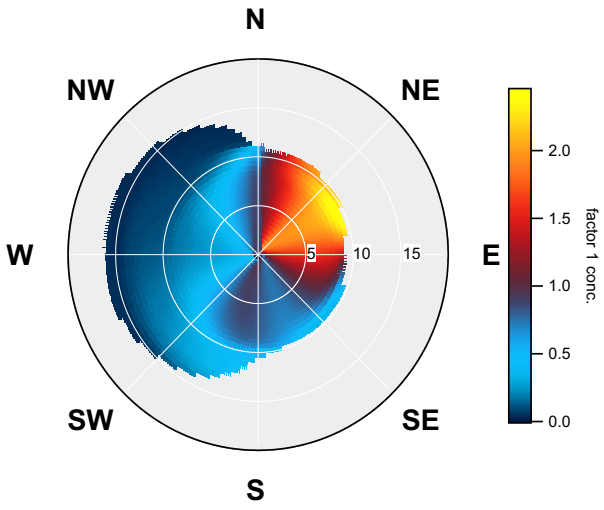

Figure 4-6: *NWR of 'hydrocarbon industry' Factor 1 of the 5-factor solution from the TD-GC-FID PMF.*

Toluene Factor 3 is composed of 94% of toluene and explains 97% of toluene total modelled mass. Moreover, it correlates with a R^2 of 0.55 with Factor 1, meaning that Factor 1 contributes to the refinery source attributed to Factor 3, which is consistent with their co-variability in the NE wind sector. However, Factor 3 has independent peaks compared to Factor 1, such as in 11th September, and similarly Factor 1 displays peaks that are not encountered in Factor 3, such a 07th or 20th September. Average of this 'toluene' factor concentration is 1.2 ± 3.53 µg·m^{-3} and the factor shows a clear variability. As expected, its NWR in Figure 4-7a follows that of toluene in Figure 4-1f, which could potentially highlight the refinery activities as sources. As discussed before, Factor 1 correlates with Factor 3, but also shows a weak correlation with Factor 4, with a R^2 of 0.17, suggesting an independent source from the combustion profile described below. Factor 4 also shares a variability from the eastern wind sector, but show a distinct peak on 18th September that is not present on Factor 3, reversely peaks of 11th or 20th of Factor 3 are absent of Factor 4.

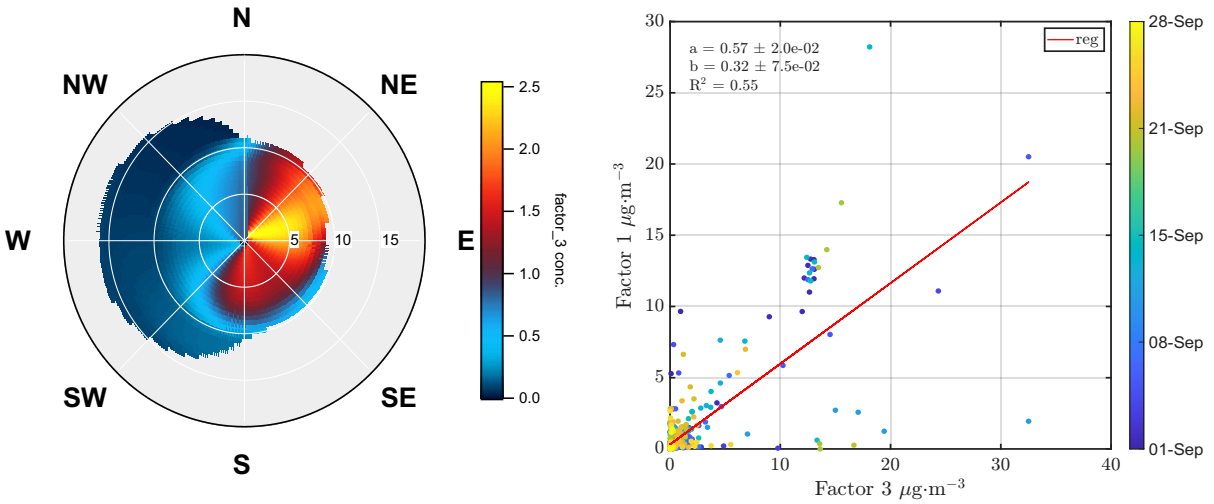

(a) NWR of Factor 3 of the 5-factors solution from the TD-GC-FID PMF.

(b) XY plot Factor 3 with Factor 2 in the 5-factors PMF from the TD-GC-FID PMF.

Figure 4-7: *Identification of 'toluene' Factor 3 in the 5-factor solution of the GC-PMF.*

Combustion The main components of Factor 4 are 2-methylpentane (27.2%), hexane (24.3%), heptane (12.3%) and isooctane (5.7%), which are mostly explained by this factor: 94.3%, 92.6%, 88.1% and 51.3% respectively. 75% of the mass of cyclohexane is explained by this factor, although it contributes little to the total mass of the factor. In addition, Factor 4 explains 33.9% of the variability of 1,3,5-trimethylbenzene, 43% of that of 1,2,4-trimethylbenzene and 20% of that of 1,2,3-trimethylbenzene, all related to combustion sources (Borbon et al., 2002), which seems confirmed by a weak correlation of Factor 4 with CO, a tracer of combustion ($R^2 = 0.27$) as represented in Figure 4-8. The origin of this factor lays north-east to south-east, with more important concentrations when wind are below 5 $m \cdot s^{-1}$, as seen in Figure 4-8b.

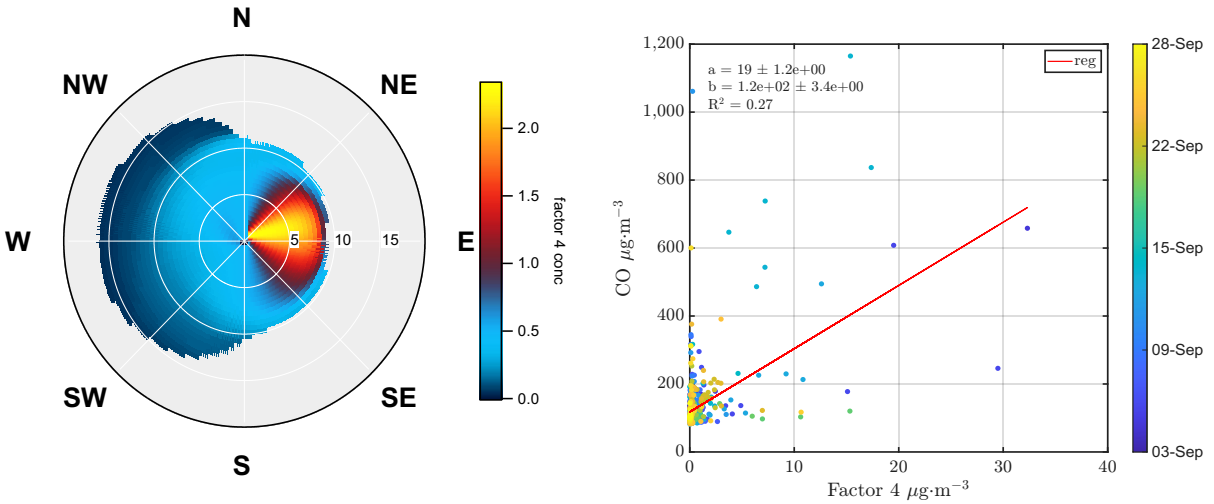

(a) NWR of Factor 4 of the 5-factors solution from the TD-GC-FID PMF.

(b) XY plot Factor 4 with CO in the 5-factors PMF from the TD-GC-FID PMF.

Figure 4-8: *Identification of 'combustion' Factor 4 in the 5-factor solution of the GC-PMF.*

Fuel evaporation The two main components of Factor 5 are isopentane and pentane, accounting for 26.1% and 19.9% respectively. The factor also contains 14.7% butane, 9.1% propane and 5.7% of ethylene. As expected, it largely explains the variability of isopentane and pentane (95.5% and 94%), as well as the different mentioned C_2 – C_4 VOC in a proportion of 20 – 55%. It also contributes 36.4% to the concentration of benzene, 21.7% to octane and 27.5% to nonane. These light hydrocarbons are typical of evaporative gasoline sources (Borbon et al., 2002; Sauvage et al., 2009; Dufresne et al., 2025). This factor originates from a similar direction as Factor 4 (Figure 4-9), and the weak correlation with CO ($R^2 = 0.22$, Figure 4-9b) is consistent with evaporative emissions, that often co-occur with traffic-related combustion sources and can explain the moderate correlation with CO, tracer of combustion.

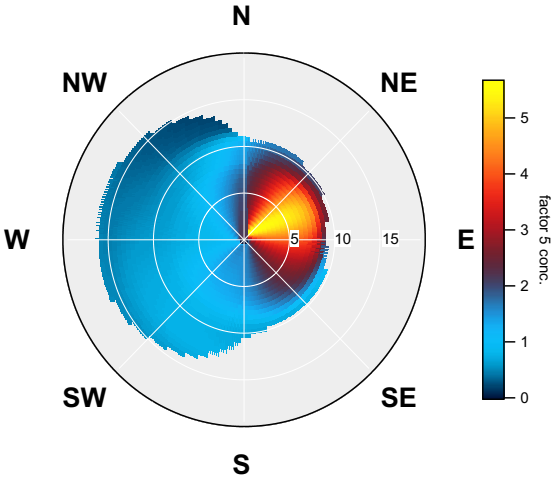

(a) NWR of Factor 5 of the 5-factors solution from the TD-GC-FID PMF.

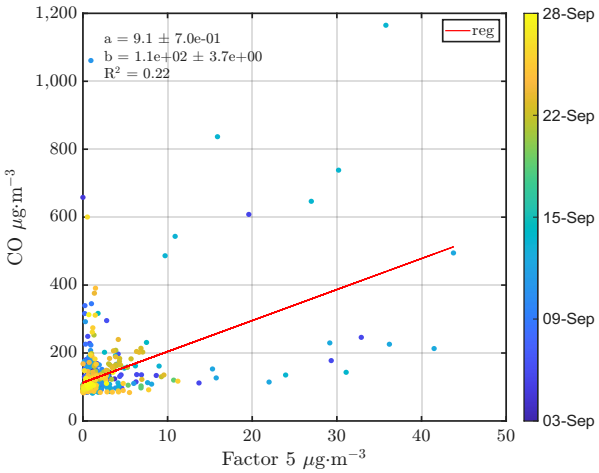

(b) XY plot Factor 5 with CO in the 5-factors PMF from the TD-GC-FID PMF.

Figure 4-9: *Identification of 'evaporation' Factor 5 in the 5-factor solution of the GC-PMF.*

4.2.c Limitations

The main limitation of using the PMF with the GC dataset of Dunkirk is the low time resolution, that, for short-term measurements, leads to an absence of clear correlations with a specific tracer for every factors, with CO, NO_x for traffic exhaust, or, when considering shipping, SO_2, as identified in Chapter 3. In particular for shipping, the GC sampling times of 30 min in a total analytical cycle of approximately 60 mins leads to a loss of information on specific emissions from shipping peaks that show an average duration of 12 ± 3 min, as presented in Chapter 3. A total of 68 SO_2 peaks used for calculating the EFs were completely sampled by the GC, but the VOC concentrations measured by the GCs did not increase because of the 30-minute sampling time. As the GC time series exhibits low variability of concentrations and low levels in the wind periods favourable to sampling ship plumes, the native PMF of GC did not result in a distinctive shipping factor due to the absence of correlation with high time-resolved tracers or recognisable peaks. However, an independent GC-PMF was mandatory to understand the co-variability of the speciated compounds measured in Dunkirk. In the other hand, there is a need to perform a PMF analysis using high time-resolved PTR data, since PTR VOC concentrations are influenced by the arrival and departure of ships. The EF calculations revealed the main contributors, including for VOCs, to ship emissions in Dunkirk. This provides a valuable reference for resolving a shipping profile in subsequent PMF analyses.

4.3 Native PMF of PTR-ToF-MS

Here, we present the PTR-only PMF solutions that differ from GC-based solutions due to the size of the matrix (18,463×72), the different species included, with 19 compounds of strong quality, 21 of weak quality, and 32 of bad quality, and the higher time resolution (1 min).

4.3.a Solutions

The solutions were tested between 2 and 9 factors, resulting in an evolution of the correlation coefficient between the observed and modelled concentrations represented in Figure 4-10. A steep increase in R^2 was observed between solutions with 6 and 7 factors, with R^2 increasing from 0.46 to 0.97. The correlations between the observed and modelled concentrations for these two solutions (Figure 4-12) reveals a poorly modelled period on 11th September between 7 and 9 am. This corresponds to an intense peak of 960.9 µg·m^{-3}, in which methanol accounts for 560.2 µg·m^{-3} (58.3%) and acetic acid for 291.1 µg·m^{-3} (30.3%). Similar but smaller peaks are occasionally observed, for example on the 25th and 26th September. The wind directions during these peaks spanned from east to south, indicating a wide origin and no specific source. However, the very low wind speeds (< 1 m·s^{-1}) during these events point to a local perturbation whose origin is unclear. The PMF may have difficulty resolving rare events, therefore, increasing the number of factors to seven helped to resolve a methanol-containing factor, reproducing the previously mentioned peaks, as shown in the solution plots in Figure 4-13. Figure 4-11 shows the average relative contribution of each factor and highlights the significant contribution of Factor 2 (26.3%), followed by Factor 4 (21.1%).

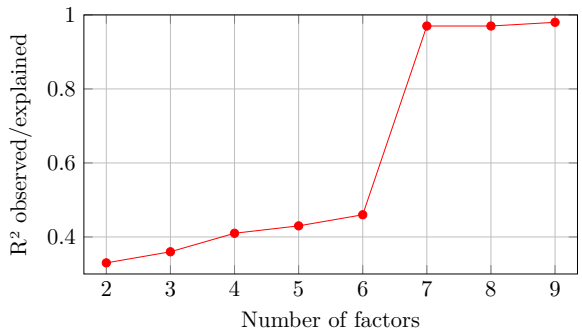

Figure 4-10: *Evolution of the correlation coefficient between observed and modelled concentration depending on the number of factors for the PTR-only PMF solutions.*

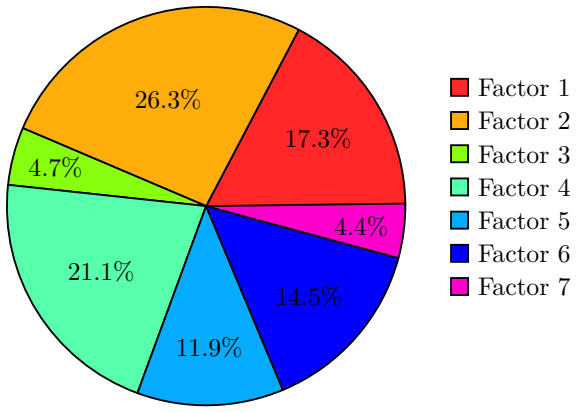

Figure 4-11: *Pie chart of average contribution of the PMF factors in the 7-factor solution.*

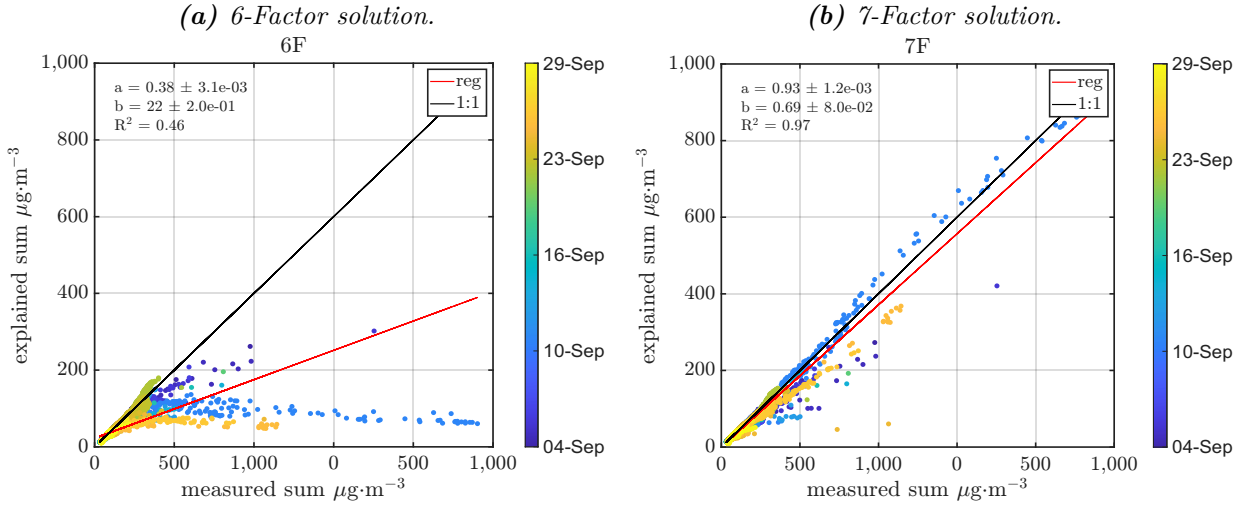

Figure 4-12: *Correlation between the observed and modelled concentration for the 6- and 7-factor solutions.*

4.3.b Interpretation

Methanol As previously explained, the 7-factor solution produced a methanol-containing factor, which is found in position 6 (violet) in Figure 4-13. This factor is composed of 61.5% methanol, and 27.6% acetic acid, which is in direct agreement with the composition of the peaks that this factor mostly explains (11st, 25th and 26th). Additionally, this factor explains 16% of the total mass of methanol and 52% of acetic acid, as well as 29.8% of benzene and 50% of toluene, despite these being minor contributors to the profiles. According to Figure 4-15, this factor mostly originates from the east of the site, where the highest concentrations are encountered in low-speed winds. A smaller contribution from winds coming from the south is encountered. These origins are consistent with the toluene factor presented in Section 4.2.b for the GC-PMF, and the fact that the PMF Factor 6 explains most of the toluene concentration indicates that these profiles refer to the same source and legitimises the seven-factor solution. However, no correlation was observed with a tracer, which leaves uncertainty regarding the identification of the source responsible for this factor. The southern tanker dock or the use of tug boats are possibilities, but no correspondence with the presence of tankers nor tug boats in the harbour was observed based on camera recordings. It should be noted that methanol is the most important contributor to Factors 1, 2, 4 and 6, but given that methanol is the most abundant VOC in the atmosphere after methane (Millet et al., 2008; Bates et al., 2021), it is present in significant amounts in most factors.

Background As in the PMF with GC-FiD data, a background factor is found in this PMF solution, this time in position 2 (orange) in Figure 4-13. While its average level of 7.3 µg·m^{-3} is comparable to the average level of the background factor in the GC PMF, its variability is greater, with a standard deviation of 10.6 µg·m^{-3}. This is consistent with the greater variability observed by the PTR due to its higher time resolution, and the greater number of species, particularly oxygenated VOCs, leads to higher concentrations. This factor is almost exclusively composed of methanol (80.5%), with a smaller portion of acetone (10.3%), two of which are low-reactivity species comprised in regional sources.

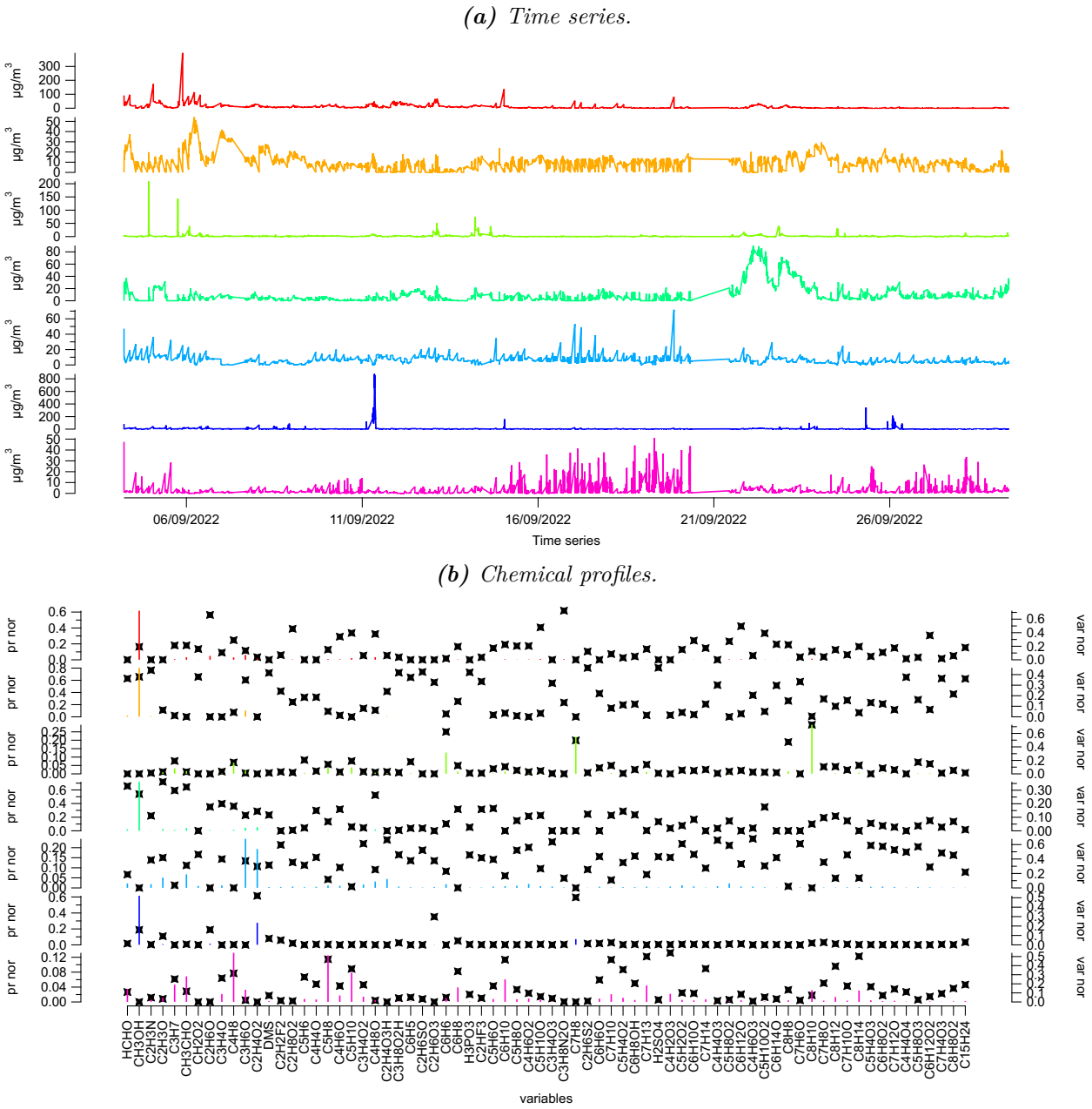

Figure 4-13: *(a) Time series and (b) chemical Profiles of the 7-factor solution of the PMF on the PTR-ToF-MS data. The bar plot in (b) corresponds to the contribution of the variable to the profile (left axis), the dotted plot corresponds to the contribution of the factor to the observed mass of each variable (right axis).*

It explains 37.8% and 34.8% of their observed concentration, respectively. This indicates that factor 2 is a background factor, as confirmed by its spread origin on the NWR plot in Figure 4-14, which is consistent with the origin of the background factor in the 5-factor GC solution. However, as with the GC solutions, this factor is SNR-driven, explaining an important proportion of the mass low-SNR VOCs such as formaldehyde (36.2%) and formic acid (37.8%). Unlike the 'background' factor in the GC-PMF, the PTR-PMF provides a more accurate representation of the compounds comprising its background factor, with R^2 between modelled and observed concentrations of 0.49 and 0.22 for formaldehyde and formic acid, respectively.

In addition, R^2 for acetone and methanol are 0.96 and 0.95 respectively, strengthening the modelling of regional sources and the identification of these compounds in the background factor.

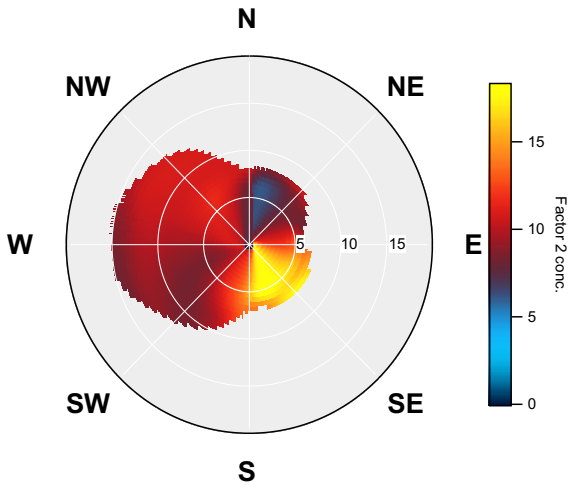

Figure 4-14: *NWR of 'background' Factor 2 the 7-factors solution from the PTR-ToF-MS PMF*

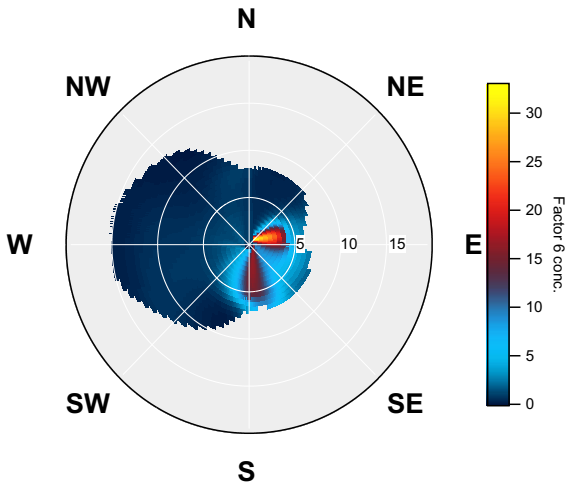

Figure 4-15: *NWR of the 'methanol' Factor 6 of the 7-factors solution from the PTR-ToF-MS PMF.*

Traffic exhaust The factor in position 4 (dark green) in Figure 4-13 also comprise methanol, previously inferred as a background-inferring compound, but it is not driven by low-SNR compounds. It explains compounds such as acetaldehyde (32.3%) or acetone (20%), as well as the fragment C_4H_8 (18.2%), that may originate from 1-butanal, and furan (C_4H_4O, 15%), both of which are related to combustion sources. Additionally, it originates from a narrower wind sector (e.g. the south-east), as shown in Figure 4-16a, potentially passing over the departmental road D601 and the highway A16, where a interchange is present. This is a direction that is not observed as the origin of any other factor, and this factor exhibits a 0.38 correlation coefficient with NO_x (Figure 4-16b) and 0.36 with BC (Figure 4-16c) in this direction, suggesting that traffic exhaust is a source represented by Factor 4 in the south-east. However, the lack of a typical diurnal cycle of traffic prevents the conclusion that traffic has an exclusive influence on this factor, which might explain the low correlation coefficient with NO_x and BC. However, a strong contribution of this factor is encountered between 22th and 25th September, corresponding to wind direction ranging from 90 to 200°, pointing towards the rural urban areas and the main roads surrounding the site.

Aromatics The factor in position 3 (light green) of Figure 4-13 , is composed for 12.6% of benzene, 22% of toluene and 29.2% of xylenes and ethylbenzene. This factor also explains the majority of the concentrations of these compounds, similar to Factor 1 in the GC PMF. The PTR-ToF-MS PMF adds the contributions of the fragments C_4H_8 (6.6%) or the fragments C_5H_8 (3.5%) from cycloalkenes to this factor. Cyclopentane (C_5H_{10}) contributes 3.8% in this factor while its contribution to the aromatic profile in the GC PMF is not significant. The origin of this factor is mainly north-east according to Figure 4-17, in line with the location of the refinery activities next to the eastern terminal.

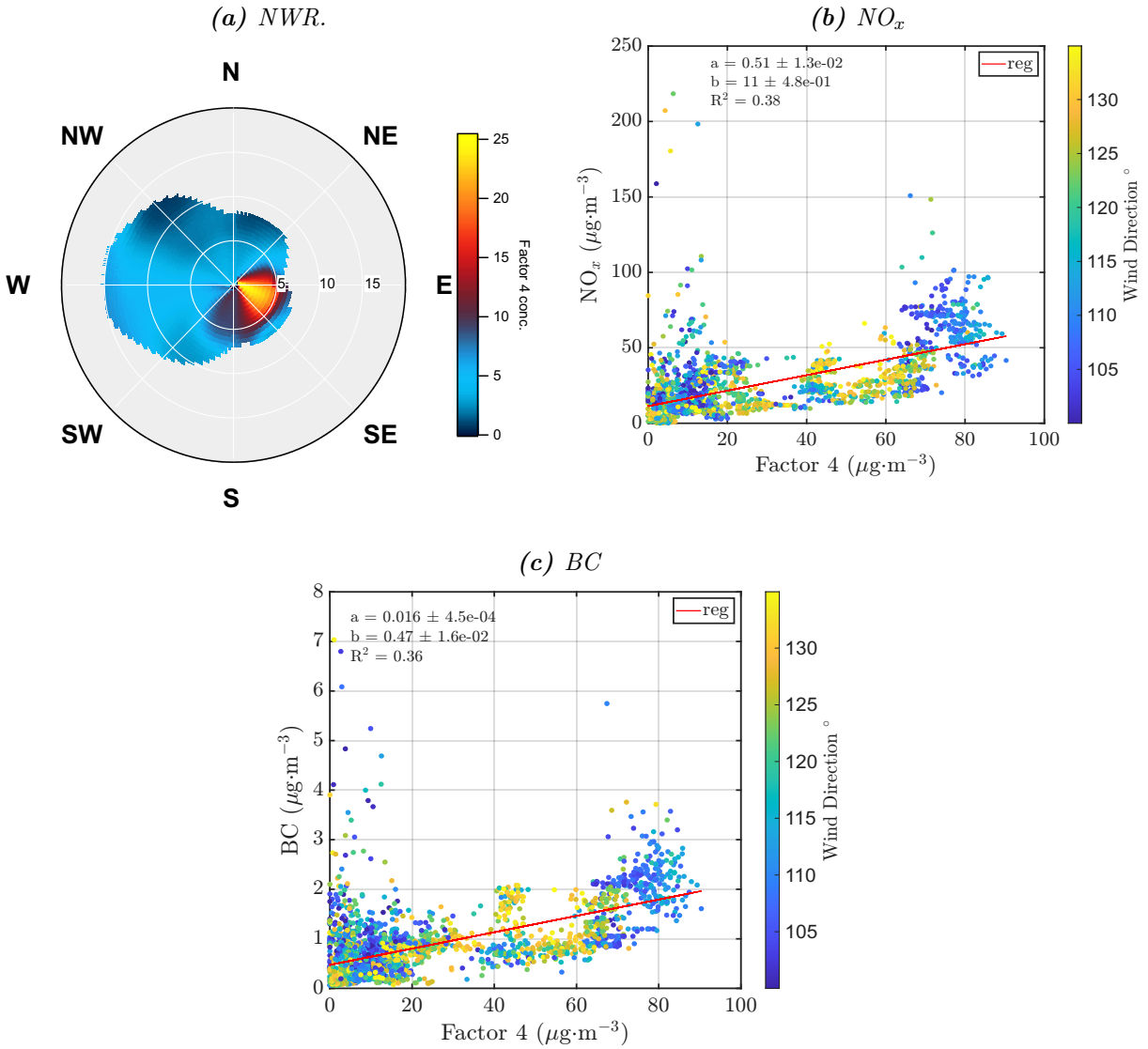

Figure 4-16: *(a) NWR of 'traffic' Factor 4 in the 7-factors solutions of PMF of PTR-ToF-MS; (b) Correlation between NO_x and Factor 4 in the 100 – 135° wind directions; (c) Correlation between BC and Factor 4 in the 100 – 135° wind directions.*

Shipping During the favourable wind period from 16th to 20th September, Factor 7 (pink, Figure 4-13) exhibits the same evolution as the ship emissions tracer SO_2 (discussed in Chapter 3) as illustrated in the zoomed-in plot of Figure 4-18a. During this period, Factor 7 and SO_2 peaks occur during ship arrivals and departures, and exhibit a correlation of $R^2 = 0.21$, as illustrated in Figure 4-18b. This correlation is lower than expected but can be explained by the PTR peaks being shortly ahead of the SO_2 peaks as seen in Figure 4-18a. Although Factor 7 contributes only 4.4% to the total average modelled concentrations, it is the main contributor during this period, with explaining up to 65.1% of the modelled concentration of ship plumes. Factors 4 and 5 show synchronous but smaller peaks during the ship peaks of Factor 7, explaining most of the other mass during these episodes. These three factors share species such as acetone and acetaldehyde, which are abundant in the observations. Finally, the NWR of Factor 7, presented in Figure 4-18c, indicates a predominantly northern origin, along with a smaller contribution from western winds.

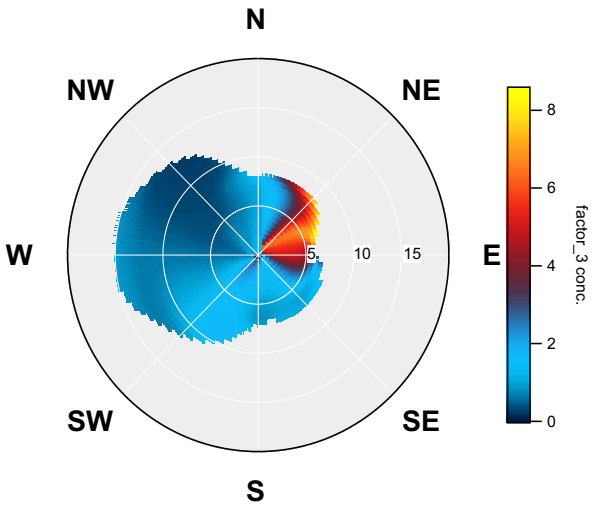

Figure 4-17: *NWR of 'aromatics' Factor 3 in the 7-factors solutions of PMF of PTR-ToF-MS.*

In this predominant northern wind sector, the correlation of this factor with CO, the combustion tracer, reaches $R^2 = 0.6$ (Figure 4-18d) , marking the combustion processes linked to this factor. The combination of northern and western wind observed in the NWR has not been observed for any other factor, and these origins correspond to the location where the ships arrived at the terminal entrance and their manoeuvring position in the dock, respectively. The fact that north winds bring higher concentrations could indicate the spike in emissions upon entrance or departure of the ship from the terminal, as discussed in Chapter 3. The major components of Factor 7 are C_4H_8 (13.2%), C_5H_8 (12.5%), C_5H_{10} (7.8%) and acetaldehyde (6.9%). These components are consistent with the major EFs of VOCs determined in Chapter 3 as shown in Figure 4-19, comforting the attribution of this factor to ship emissions in Dunkirk. The main difference between the EF profile and the PMF profile is that methanol does not contribute to the shipping profile of the PMF, despite being the third biggest VOC EF of ship emissions, according to Figure 3-4. However, methanol is expected to be present in large quantities in ship emissions as the EF calculation takes the precaution of deducting the background level, thereby minimizing the risk of methanols EF being impacted by background levels. The PMF revealed factors (Factors 4 'traffic exhaust' and 6 'methanol') containing almost exclusively methanol, which likely captured most of the variability of methanol. The fact that Factor 4 displays smaller peaks in the ship plumes supports the argument that methanol could be present in ship emissions, thus inferring the need of further inspecting the shipping factors. Indeed, this 'shipping' factor misses the contribution of most OVOCs detected in the EFs.

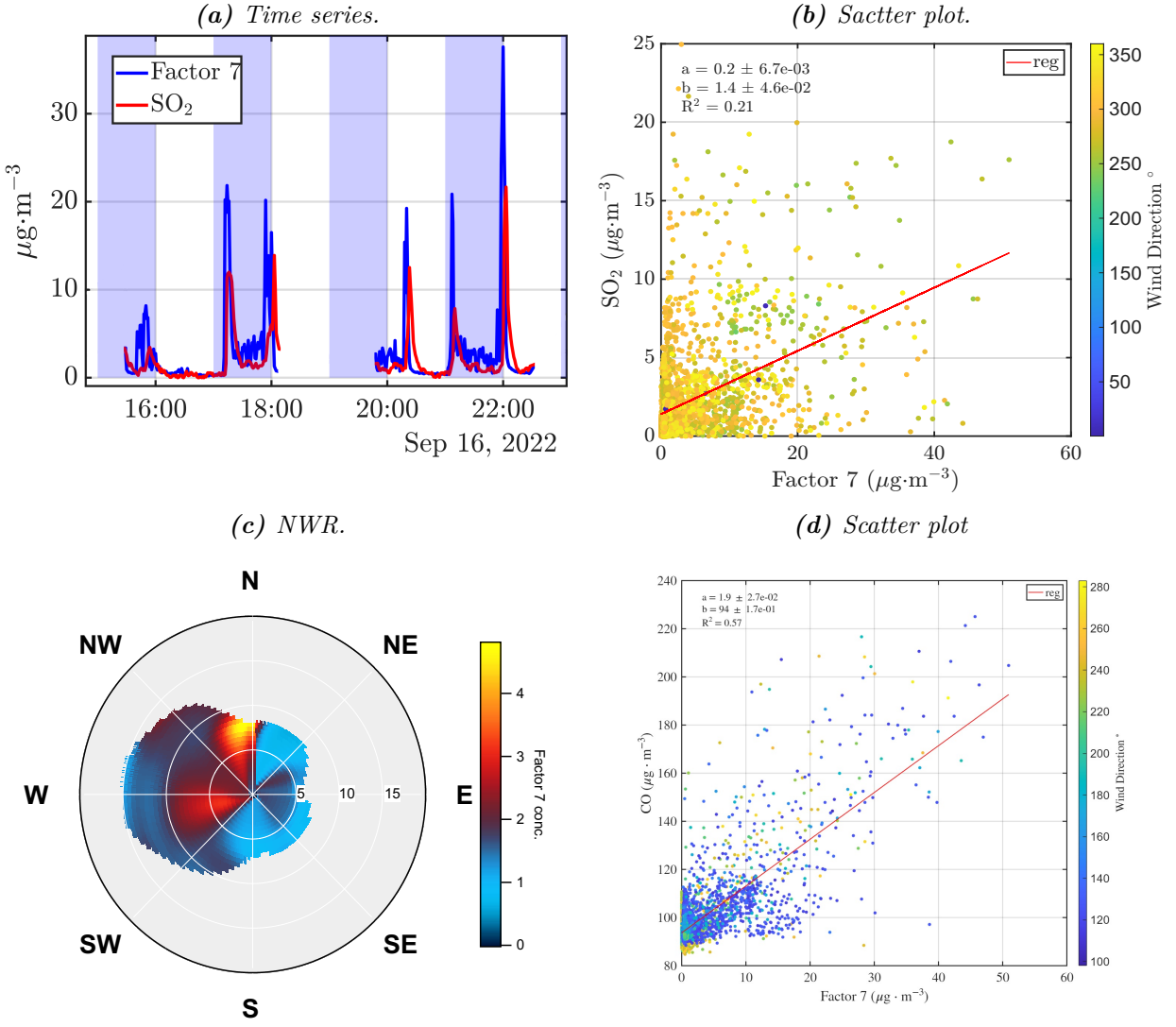

Figure 4-18: *(a) Time series of 'shipping' Factor 7 and SO_2 on the 16th of September, the blue shaded areas indicate the presence of a ship in the dock; (b) scatter plot of Factor 7 and SO_2 from 16th at midnight to 20th at 8 am; (c) NWR of Factor 7; (d) scatter plot of Factor 7 and CO from 16th at midnight to 20th at 8 am*

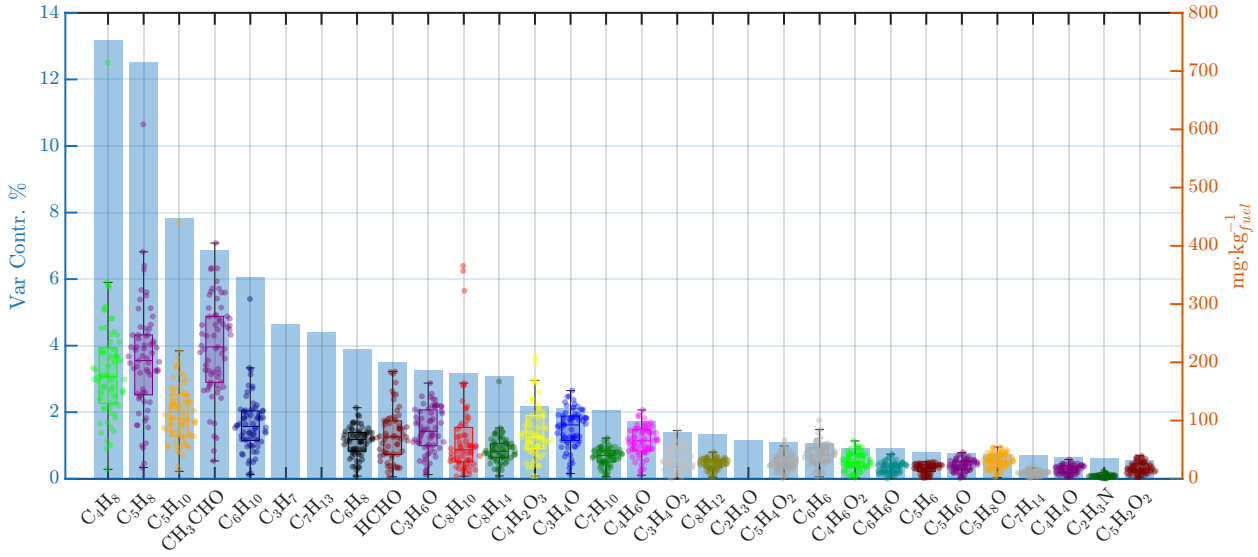

Figure 4-19: *Comparison of the top 30 contributors to Factor 7 'shipping' from the PMF with those determined in Chapter 3 for the ship Emission Factors. Major contributors to Factor 7 are shown as blue bar plot, left Y-axis,; the box plots, right Y-axis, shows the EFs calculated in Chapter 3.*

Shipping OVOCs Inspection of Factor 5 (shown in light blue) reveals that it behaves similarly to ship emissions during the shipping period, exhibiting transient peaks similar to those of Factor 7 ('shipping'), as illustrated in Figure 4-20. Its background level is more significant in this sector and does not approach 0 µg·m^{-3}, unlike the shipping factor. The main contributors to this profile are acetone and acetic acid (24.4% and 19.3% respectively). These compounds were among the major EFs of OVOCs identified in ship emissions, particularly acetic acid, which was the third most prevalent OVOC EF after methanol and acetaldehyde. 'Shipping' Factor 7 misses the contribution of these compounds, and their presence in factor 5 and the peak behaviour encountered during the shipping period could suggest that the factor illustrating ship emissions has split in two. However, outside of this period, the variability of Factor 5 does not correspond to the shipping factor, suggesting that it represents a mixture of sources. Investigating the NWR of Factor 5 in Figure 4-21, which shows high levels across all wind directions and speeds, suggests that this PMF resolved an oxygen-containing background that accounted for the variability of OVOCs linked to ship emissions. Therefore, Factor 5 shares an R^2= 0.19 correlation with Factor 2. This is the greatest correlation observed between any two factors throughout the entire campaign, and it increases outside of periods where the 'shipping' factor is most intense, highlighting the background behaviour of this factor.

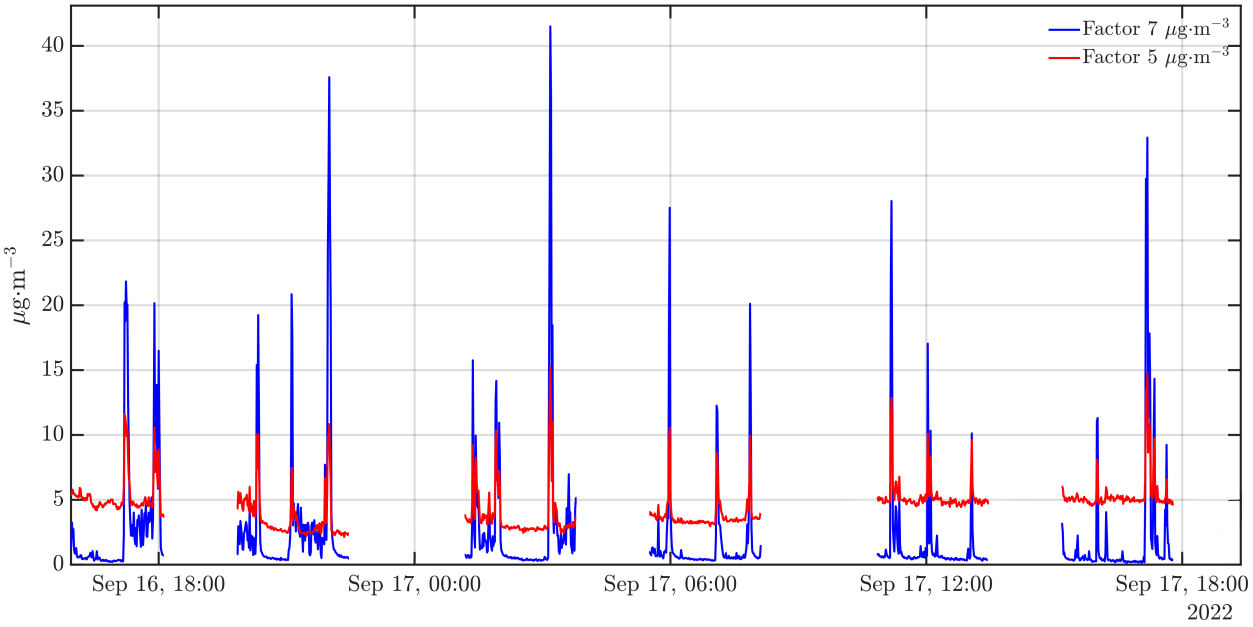

Figure 4-20: *Time series: (blue) Factor 7 'shipping': (red) Factor 5 'shipping OVOC'.*

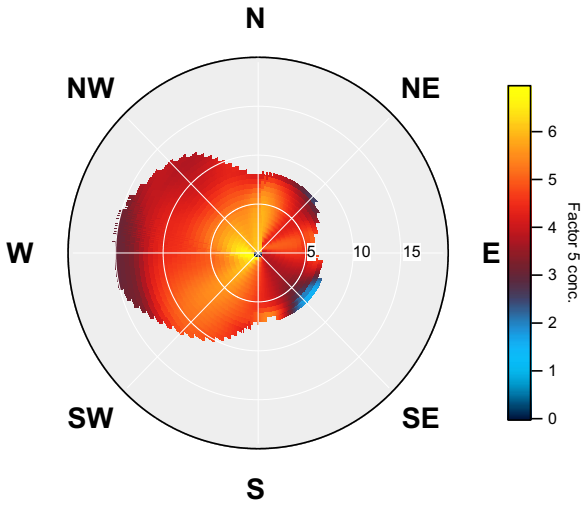

Figure 4-21: *NWR of Factor 5 'shipping OVOCs'.*

4.3.c Partial conclusion

Increasing the temporal resolution and adding oxygenated compounds to the Dunkirk 2022 PMF induces higher sensitivity and variability, revealing 2 additional profiles that were not present in the TD-GC-FID PMF. Primarily, this allowed the identification of a ship emission factor that had previously not been resolved, notably due to the low variability of the GC concentrations during favourable wind periods. The addition of OVOCs contributed to the resolution of a shipping factor in the PMF, as previous EF calculations have shown that these compounds are major contributors to its chemical profile. The agreement between the PMF-derived profiles and the EFs calculated independently underlines the complementarity of the two approaches. By converging on the same chemical signature of the source, the two approaches provide mutual validation and consolidate the identification of Factor 7 as representative of ship emissions in Dunkirk.

However, the PTR-PMF approach detailed here doesn't resolve the contribution of OVOCs found in the EFs, prompting a more detailed PMF analysis. The PTR-PMF revealed factors in common with the GC-PMF, which provides strong motivation for a comparative analysis for a more refined analysis.

In addition, performing a PMF analysis using PTR data lacks chemical identification, as demonstrated for the major components of the shipping profile, C_4H_8 and C_5H_8. To fulfil the need for speciation in our PMF shipping profile, the GC data can be combined with the PTR to perform a Multi-Time Resolutions PMF (MTR-PMF), combining the potential for richer temporal variability captured by the PTR with the greater chemical resolution of the GC measurements. The following section explores the MTR-PMF approach based on this complementarity.

4.4 Application of MTR-PMF with PTR-ToF-MS and TD-GC-FID

The PTR-ToF-MS and the TD-GC-FID were combined with their native PMF time resolution, of 1 min and 1 h, respectively. In accordance with the protocol outlined for Multi Time Resolution-PMF (MTR-PMF) in Section 2.4.b.iii, the instrument of reference is the PTR-ToF-MS because it has the highest time resolution. Consequently, the GC concentrations will be modelled using the average contribution of the PTR time series and its profiles obtained at its native resolution. In the combined GC/PTR MTR-PMF, some VOC species were duplicated across instruments (benzene/$C_6H_6{\cdot}H^+$, toluene/$C_7H_8{\cdot}H^+$, xylenes+ethylbenzene/$C_8H_{10}{\cdot}H^+$, styrene/$C_8H_8{\cdot}H^+$). In such cases, the TD-GC-FID measurements were retained as the unique variables, given their higher chemical resolution compared to PTR-ToF-MS. This choice is consistent with the fact that most factors had already been identified beforehand and were therefore expected to appear similarly in the combined PMF solution. The reader is informed that, when representing MTR solutions from SoFi Pro, the time series will move back and forth in the plots as the second dataset is plotted after the reference dataset, as explained by Datalystica Ltd. (2021).

4.4.a Solutions

A smaller range of solutions was tested, as GC and PTR-PMF revealed optimal solutions for 5 and 7 factors, respectively. As the differences in SNR may lead to unrealistic PMF modelling due to unbalanced representation of the two instruments in the MTR-PMF profiles, e.g. over-presence of one instrument over another, the "C-value" approach have been investigated. Briefly, the uncertainty elements σ_{GC} are weighted by a user defined C-value in order to adjust the SNR between the GC and the PTR ($\sigma'_{GC} = \sigma_{GC}/C_{value}$) (Via et al., 2023). A wide range of C-values were tested, but this did not result in a significant improvement to the solutions. As explained in Chapter 2 regarding the way MTR-PMF works, the fact that the unaligned data points of the GC to the PTR timestep are filled with appropriately small concentrations and very high uncertainty inevitably reduces the contribution of the GC to the MTR profiles. This approach could be performed when combining datasets from different instruments with common timestamps (Simon et al., 2025), e.g. averaging the PTR datasets onto the GC timestep. Although this thesis tested the combination approach of PTR and GC within a one-hour time step, the MTR approach was favoured because it exploited the temporal evolution of the 'shipping' factor evidenced by the high time resolution of the PTR. This overcame the limitations of the GC in resolving a PMF shipping factor. Therefore, solutions with 4 to 8 factors were tested with the native SNRs and timesteps of the GC and the PTR, resulting in a significant improvement in modelling quality when increasing from 4 factors ($R^2 = 0.38$) to 5 factors ($R^2 = 0.94$). This steep increases in R^2 is again explained by poorly modelled peaks, such as the one on 11th September, and the 5-factor solution reveals a factor that explains those peaks similarly to what was seen in the PTR-PMF. Therefore, the 5-factor solution was retained for the analysis, which is two factors less than the PTR-PMF solution, but the same number as the GC-PMF solution. Therefore, the combined PMF solution could still be driven by GC measurements, as it provides a higher SNR for VOCs. The average contributions of each factor is presented in Figure 4-23 and their times series and profiles for this solution are shown in Figure 4-24.

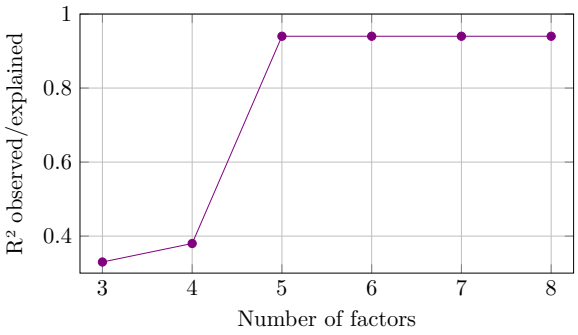

Figure 4-22: *Evolution of the correlation coefficient between observed and modelled concentration depending on the number of factors for the MTR-PMF.*

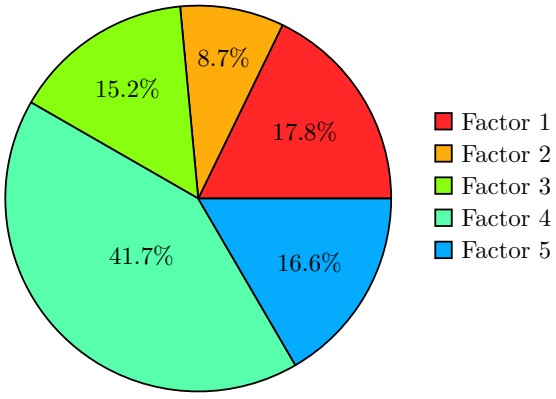

Figure 4-23: *Pie chart of average relative contributions of the MTR-PMF factors in the 5-factor solution.*

(a) *Time series.*

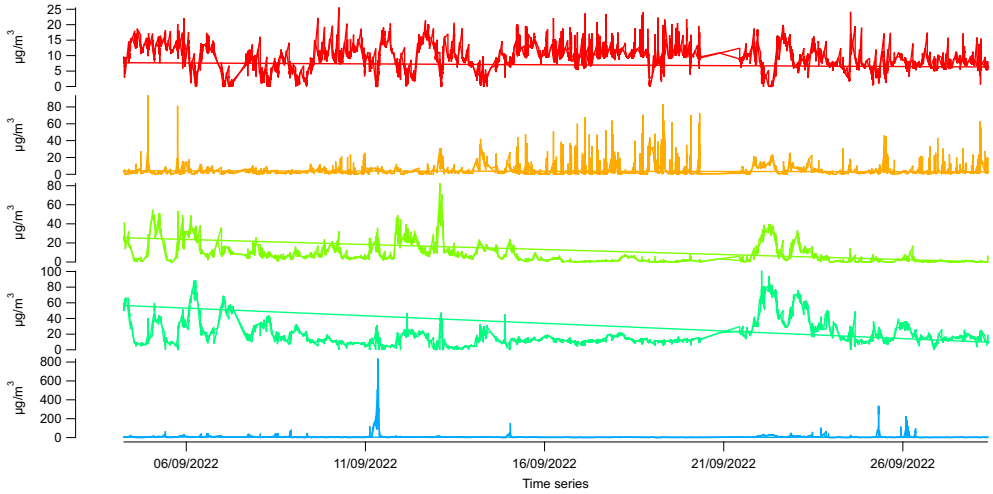

(b) *PTR profiles.*

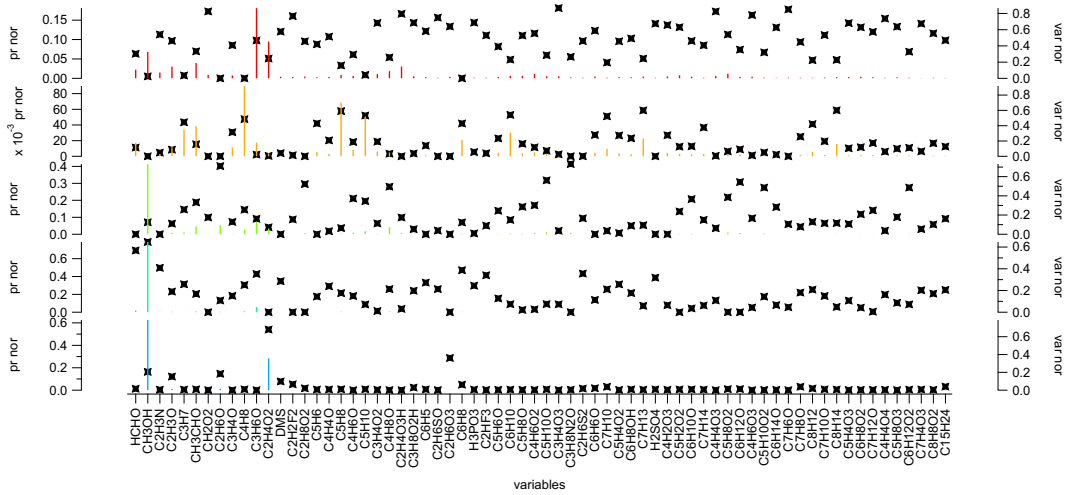

(c) *GC profiles.*

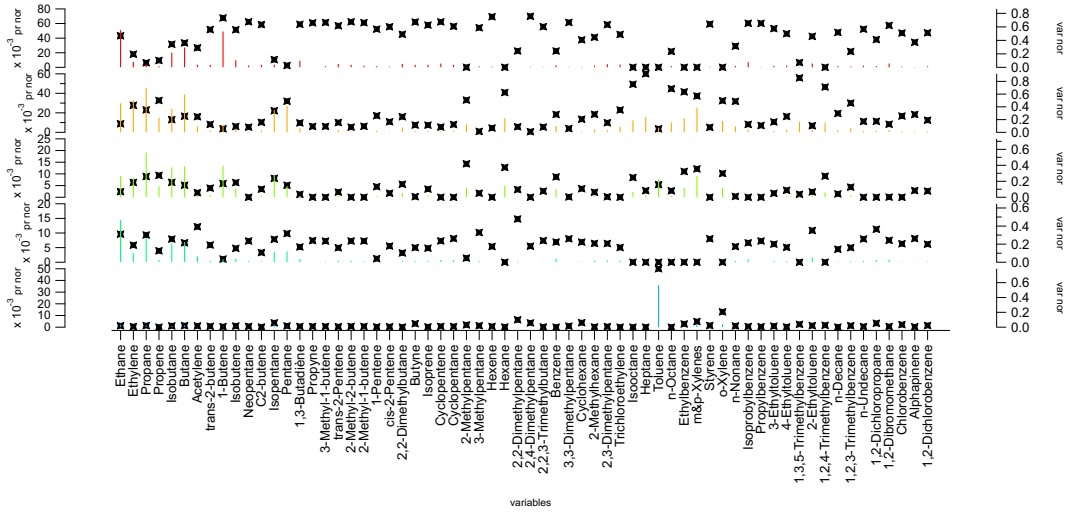

Figure 4-24: *(a) Time series and chemical profiles for the PTR (b) and GC (c) of the 5-factor solution MTR-PMF. The bar plots in (b and c) correspond to the contribution of the variable to the profile (left axis), the dotted plot corresponds to the contribution of the factor to the observed mass of each variable (right axis)*

4.4.b Interpretation

Methanol As previously mentioned, the 5-factor solution reveals a profile (Factor 5, blue, on Figure 4-24) marked by intense peaks on the 11th, 25th and 26th. This factor is very similar to Factor 6 of the PTR-PMF, with major contributions from methanol and acetic acid. Furthermore, Factor 5 explains most of the toluene variability observed in the GC with no significant contribution from other GC VOCs and can thus be linked to the toluene-related Factor 3 of the GC-PMF. In the PTR-PMF, the methanol factor indeed explained 50% of the total toluene mass, although this was a minor contribution to the total mass of the factor. The integration of chemically resolved GC measurements evidences a common source of methanol, acetic acid and toluene, located to the east and south according to Figure 4-25, in accordance with the NWR obtained for the corresponding factors in the PTR-PMF and GC-PMF. Since high concentrations occur mainly under low winds peeds (< 5 m·s^{-1}), this appears to be a local source and could be associated with refinery activities.

Unresolved background Factor 1 explains an important part of ethane (46.7%) and other light VOCs (ethylene, 19.5%, isobutane, 34.2%, butane, 36.1%, acetylene, 29%) of which this factor is mainly composed. Its low average concentration (8.6 $\pm$ 3.7 µg·m^{-3}) reminds the background profile of PTR-PMF and of the GC-PMF. This factor shows little variability and a spread origin (Figure 4-26), confirming the background behaviour of this profile. Here too, the background factor is composed of low-SNR VOC as observed for the background factors in the GC-PMF and PTR-PMF, confirming a mixed background factor gathering species with weak data quality in this MTR-PMF.

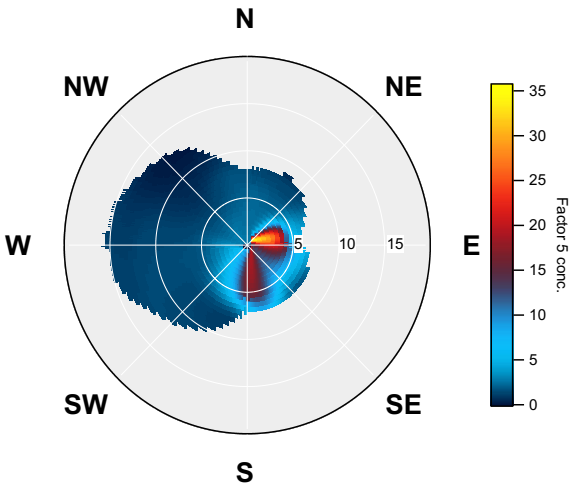

Figure 4-25: *NWR of 'methanol' Factor 5.*

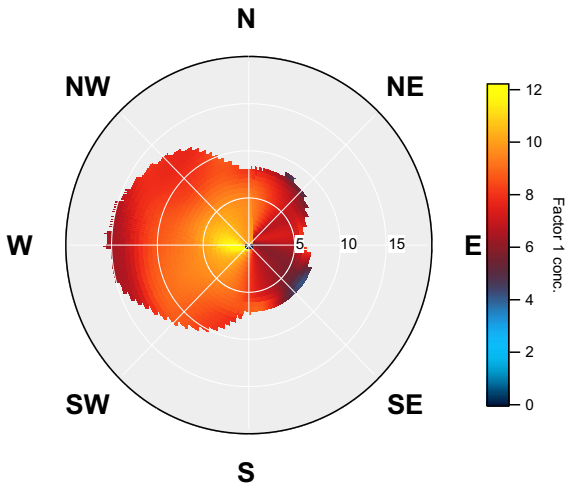

Figure 4-26: *NWR of 'background' Factor 1.*

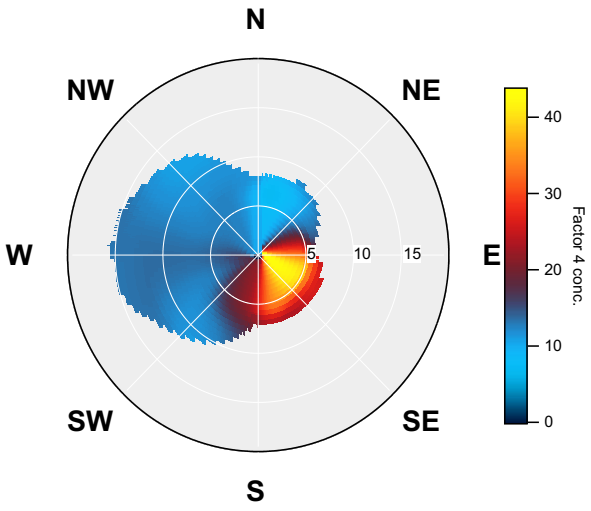

Figure 4-27: *NWR of Factor 4 'traffic exhaust'.*

Traffic exhaust A similar 'traffic exhaust' factor is encountered in Factor 4 (dark green) compared to Factor 4 of the PTR-PMF. It displays the same range of contribution to the mass of acetaldehyde (16.8%), acetone (35.1%), C_4H_8 (25.0%), and furan (C_4H_4O, 23.9%) illustrating a combustion source as discussed in the PTR-PMF. In addition, it originates from the same direction as the Factor 4 of the PTR-PMF, east to south as seen in Figure 4-27, illustrating an influence of the roadway area to this factor. However, in these directions (100 – 135°), the correlations with NO_x and BC are lower, with R^2 of 0.2 and 0.27, respectively. This smaller agreement is attributed to the addition of speciated VOCs, to which isopentane, pentane and lighter VOC contribute the most. In the time series of the factor, these VOCs are expressed in the timestep of the GC (30 min) according to the principle of the MTR-PMF, that lead to a poor agreement of the GC-PMF factors with any tracer, therefore reducing the agreement of the 'traffic exhaust' in the MTR-PMF compared to the PTR-PMF.

Aromatics Factor 3 (light green) of the MTR-PMF solutions appears to correspond to the 'aromatic' factors of both the GC- and PTR-PMF analyses, as BTEX contributes to its profile. However, it only explains around 30% of their mass, whereas the previous factors explained more than 60%. This is the only factor in the MTR-PMF that contains BTEX, apart from Factor 2, which follows the evolution of a shipping factor as seen in the PTR-PMF and discussed further.

Factor 3 also contains light VOCs ranging from ethane to isobutene that were not observed in the other corresponding factors. It also contains isopentane, pentane, 2-methylpentane and hexane. This results in a profile that does not resolve the markers for aromatics as explicitly as the GC- or PTR-PMF. Therefore, there is a link with the traffic exhaust factor ($R^2 = 0.29$), as can be seen in Figure 4-28, which illustrates that these factors can co-evolve as can be seen in their time series. This could suggest a co-variability of traffic exhaust and solvent use in the direction of the urban area, as seen in Figure 4-29.

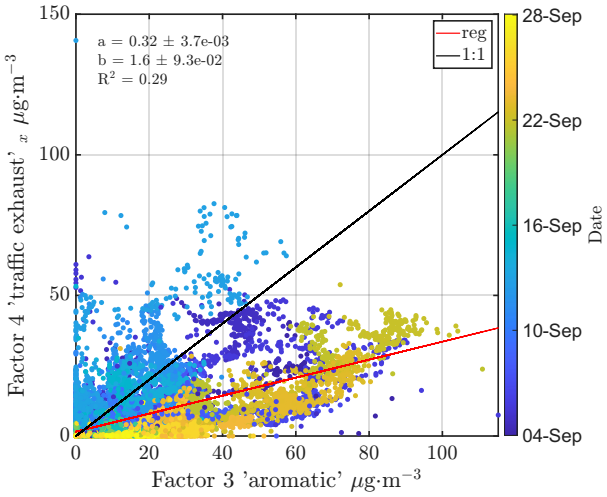

Figure 4-28: *XY plot of Factor 3 'aromatic' with Factor 4 'traffic exhaust'.*

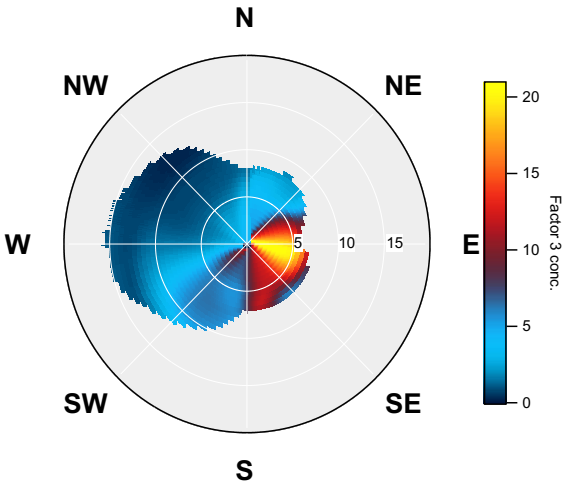

Figure 4-29: *NWR of Factor 3 'aromatics'.*

Shipping Factor 2 of this solution corresponds to a ship emissions profile closely matching with the Factor 7 of the PTR-PMF solution. Their similarity is evident when comparing their chemical profiles, as both are dominated by C_4H_8 (9%), C_5H_8 (6.9%), cyclopentane (5.1%) and acetaldehyde (3.8%). This Factor 2 explains much of the concentrations of these compounds (48.5%, 59.1%, 53.2%, and 15.7%, respectively). Like PTR-PMF Factor 7, it follows the evolution of SO_2 during ship plume events (Figure 4-30a) and shows a similar correlation with SO_2 ($R^2 = 0.18$, Figure 4-30b) during periods favourable to ship emissions. This correlation is also low, given that peaks of the shipping profile occur slightly before the SO_2 peaks, as seen in Figure 4-30a. During the wind period, Factor 2 becomes the dominant contributor (Figure 4-30c), as the 'shipping' Factor 7 in PTR-PMF, and exhibits similar wind origins in its NWR (Figure 4-30d), consistent with the location of the berth of the ships and their manoeuvring location in the dock. The MTR-PMF further enhances the PTR-PMF ship emissions profile by implementing GC-speciated VOCs. From the GC contribution of this factor, propane emerges as the top contributor of the speciated VOCs in ship emissions (4.6%), exceeding the contribution of acetaldehyde. It is followed by butane (3.9%), ethylene (3.3%), and ethane (3%). Notably, pentane (2.7%) and isopentane (2.3%), previously identified as markers of a gasoline evaporation profile in the GC-PMF (Factor 5), are also present. Additional contributors include hexane (1.5%) and 2-methylpentane (0.8%), both previously associated with the hydrocarbon industry profile in the GC-PMF. This indicates that the addition of the GC compounds indeed provide additional chemical identification of the shipping profile. It is worth noting that the two factors 'hydrocarbon industry' and 'fuel evaporation' in the GC-PMF were not found to contribute significantly within the northern wind sector, favourable for sampling the ship plumes. However, the time series of the GC provided by the MTR-PMF is the result of averaging the PTR-MTR factor contribution into the GC timestep. This illustrates that the 'shipping' GC-MTR evolution is not representative of the GC-PMF solution, deriving from the factors presented in the GC-PMF. Furthermore, Factor 2 accounts for nearly all observations of some VOCs: 91.8% of heptane, 85.4% of 1,3,5-trimethylbenzene, 71% of 1,2,4-trimethylbenzene, 75.4% of isooctane, and 56.9% of m&p-xylenes. Figure 4-31 summarises the main contributors of the ship emissions MTR-PMF profile together with the EFs determined in Chapter 3.

This shows that the major components of the shipping profile from the MTR-PMF and the EFs disagree more than the PTR-PMF, mostly because the EFs were based solely on the PTR data. Therefore, the GC speciated measurements gain in importance in the resolution of the shipping factor compared to the PTR alone and modify its main contributors. Although this factor displays a temporal evolution similar to the peaks associated with ships, the lack of correspondence with the EFs reduces confidence in the profile's composition. In addition, a limitation remains in the current MTR-PMF, as shown in Figure 4-32, where shipping peaks are partly redistributed to other factors, as Factor 1 increases up to 20 µg·m^{-3} or Factor 5 up to 6 µg·m^{-3}, thereby reducing the contribution of the shipping factor. This redistribution arises from the overall increase in mass during these peaks and from shared species that generate smaller, synchronous peaks during ship plume events. To address this issue, constraints can be applied in the PMF analysis to better isolate the shipping factor. This can be achieved by seeding the model to obtain a more exclusive ship emission factor. The next focus is to limit the redistribution of shipping peaks into other factors and improve the robustness of the source attribution, therefore refining the methodology for identifying shipping profiles from field observations.

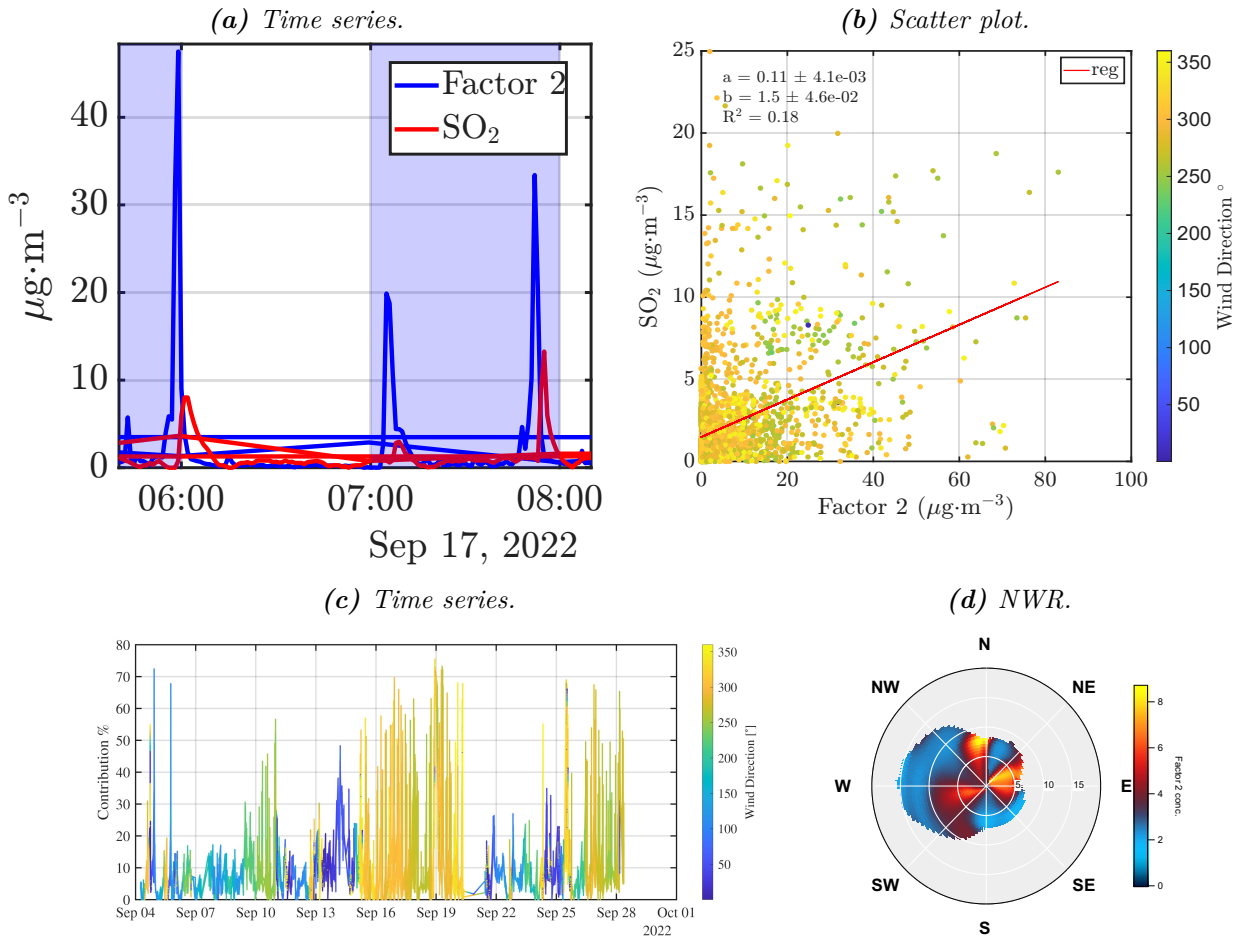

Figure 4-30: *Identification of 'shipping' Factor 2 in the MTR-PMF; (a) Time series of Factor 2 and SO_2 on the 17thof September, the blue shaded areas indicate the presence of a ship in the dock; (b) scatter plot of Factor 2 and SO_2 from 16th at midnight to 20th at 8 am; (c) Contribution of Factor 2 to the modelled concentrations color-coded for the wind direction; (d) NWR of Factor 2.*

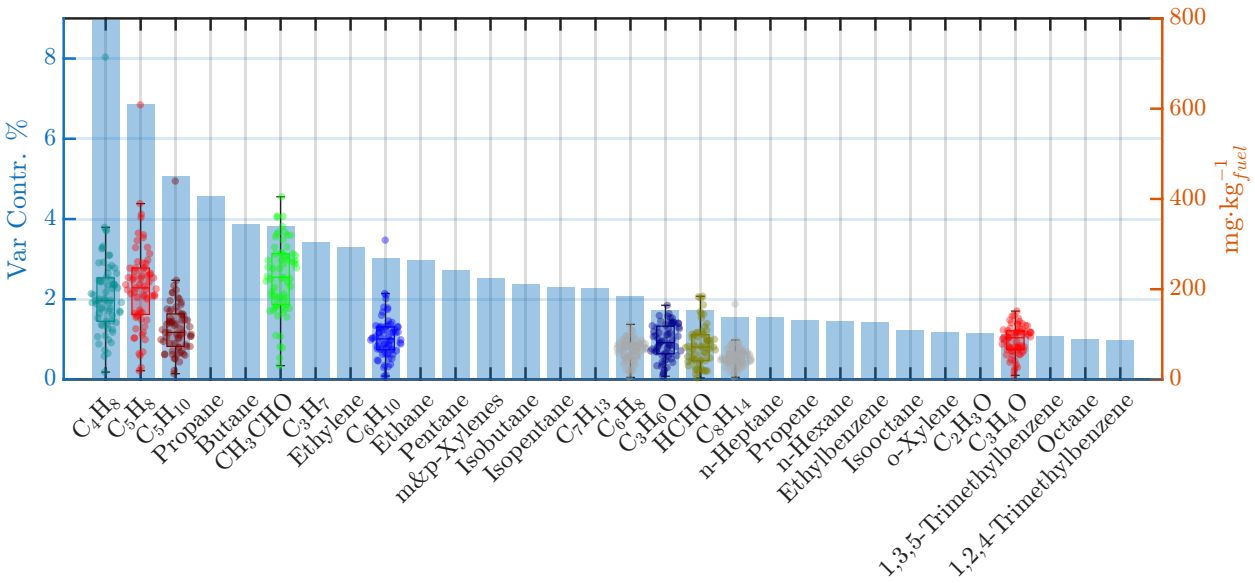

Figure 4-31: *Comparison of the top 30 contributors to 'shipping' Factor 3 from the MTR-PMF with the Emission Factors determined in Chapter 3. Major contributors to Factor 2 'shipping' of the MTR-PMF profile are shown as a blue bar plot (left Y-axis); the box plots, right Y-axis, represent the associated EF calculated in Chapter 3.*

4.4.c Isolating a shipping profile

To isolate the ship's emission profile, we performed a wind-constrained PMF, as more than 60% of the mass of the shipping factor was associated with the northern wind sector. Therefore, when selecting exclusively this wind direction over a favourable period, the influence of other factors should be minimal, with only a small number of factors expected. The combined GC/PTR input matrix was filtered from a narrower range of wind directions than for the EFs, according to the origin of the MTR-PMF profile of shipping (Figure 4-30d). Only the concentrations observed under wind directions between 270 and 20° were kept as inputs, resulting in a 6239×132 matrix. The stable, optimised solution contains two factors, and demonstrates satisfactory modelling quality (R^2 = 0.71). This solution is presented in Figure 4-33. While the second factor is clearly linked to background levels, explaining most of methanol, acetone and acetic acid, the first factor is recognised as the ship emissions factors, as it follows the same temporal evolution as Factor 2 in the MTR-PMF. Interestingly, it is mainly composed of methanol (13.4%), proving right the hypothesis that methanol is indeed part of the ferry emissions.

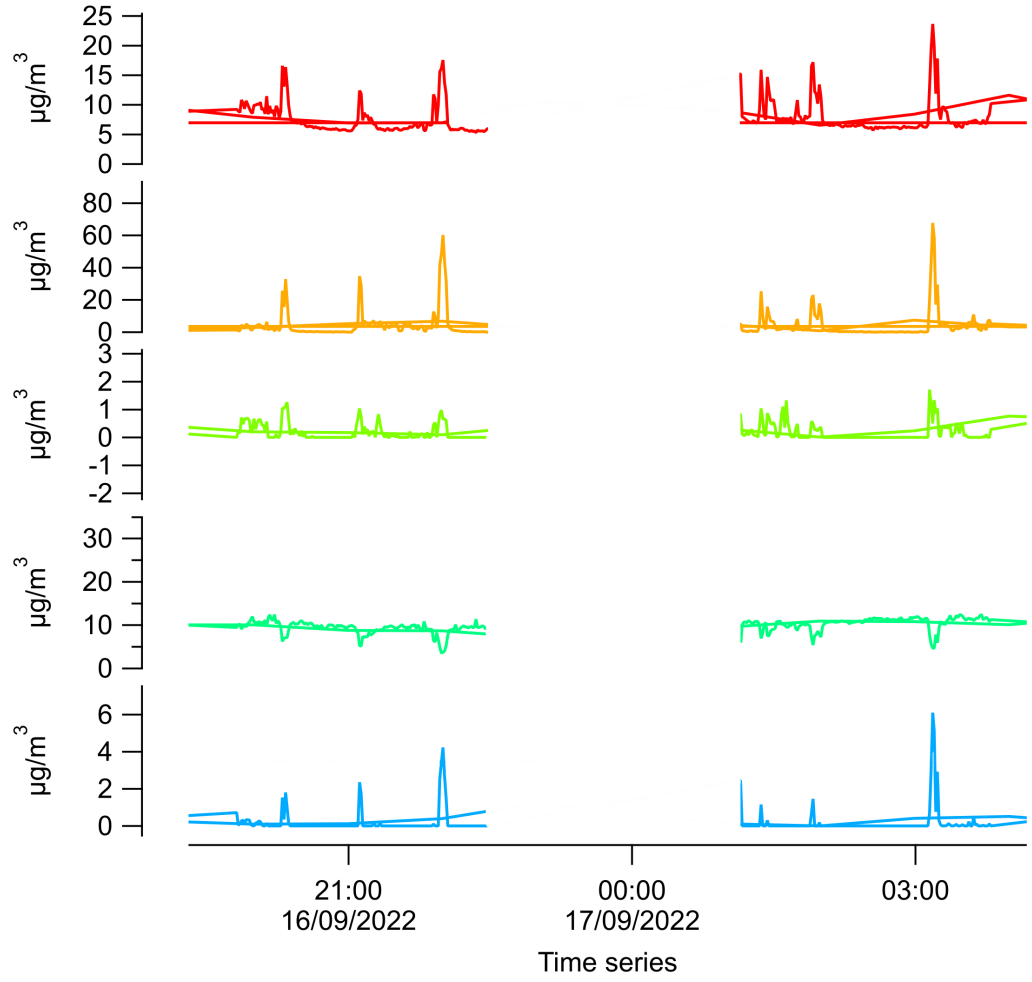

Figure 4-32: *Zoom-in on the time series of the 5-factors solution of the MTR-PMF.*

In this solution, with fewer factors than in the MTR-PMF, a larger fraction of the methanol variability is captured by this factor, whereas in the MTR-PMF most of its variability was captured by other factors. Likewise, acetone and acetic acid appear in Factor 1 (4.8% and 3.4%, respectively) and were absent from the ship emission profiles in the native MTR-PMF. This factor further comprises C_4H_8 (6.4%), C_5H_8 (5.9%), cyclopentane (3.9%), and ethane (2.7%), butane (2.2%), ethylene (2.1%) and propane (2%), the same top speciated contributors of the GC profile in the first unconstrained MTR-PMF. The presence of these compounds confirms that this factor corresponds to ship emissions determined before. The inclusion in the wind-constrained PMF of compounds largely explained by other factors in the 5-factor MTR-PMF solution is expected to rebalance the ship emission contributions in these factors. This adjustment opens the way for a more exclusive identification of ship emissions, which will be examined in the following section through the application of Factor 1 as a constraining factor for the global MTR-PMF.

4.4.d Constrained MTR-PMF

For the constrained MTR-PMF, the first factor of a 5-factor solution was seeded with the profile of Factor 1 in the wind-constrained MTR-PMF, according to the methodology of PMF constraint detailed in Section 2.4.b.iii. A range of a-values were tested for the deviation of the seeded profile, from 0 (fully constrained) to 1 (no constraint). Figure 4-34 shows, for example, the solution based on the a-value = 0 solution where the shipping Factor 1 is fully constrained from the profile of the wind-constrained MTR-PMF. The contribution of the methanol and toluene factor, here in position 5, to the modelled ship peaks is reduced, as these particular compounds are constrained in the seeded shipping factor in position 1.

Firstly, the a-value didn't have any impact on the quality of modelling at 5 factors, as seen in Figures 4-35a and 4-35b. Both a-values on the constrained Factor 1 produce a great correlation coefficient between modelled and observed concentrations, meaning that the choice of an a-value should be explored based on its impact on the distribution of shipping peaks in the solution.

Within the favourable time period used in Chapter 3 to calculate the EFs from the PTR-ToF-MS measurements, the relative contribution of Factor 1, comparing each peak's maximum to the maximum modelled concentration for that peak, was calculated. Increasing the deviation of the seeded profile (e.g. raising the a-value) reduces the contribution of Factor 1 to the modelled ship peaks, as can be seen in Figure 4-36. The median contribution of Factor 1 is 60.5% for an a-value of 0, decreasing to 45.6% for an a-value of 0.9. This is consistent with the fact that, the more the profile deviates, the more likely it is to produce the same solution as Factor 2 in the MTR solutions with important contributions to ship peaks distributed in other factors. Therefore, the solution where a-value = 0 is retained as the most representative shipping factor. In other words, the ship emission profile determined from the observations in the favourable wind sector leads to the most representative profile that can be achieved in the MTR-PMF in the Dunkirk campaign of 2022, enabling an optimal and accurate assessment of its contribution.

According to the average contribution of each factor shown in Figure 4-37, the 'shipping' factor contributes 8.5 ± 15.3% to the observed VOC mass during the entire campaign. The Hauts-de-France emission inventory provides the contribution of the 'other transportation' sector to NMVOC emissions in the Dunkirk Urban Community. This sector comprises the transportation sources other than those related to the combustion, evaporative and abrasive sources linked to motorcycle, car and truck traffic, which are included in the 'road transport' sector of emission inventories. It indicates that the 'other transportation' sector contributed 6.2% to the NMVOC emissions in the Urban Community of Dunkirk in 2021. This value is therefore consistent with the contribution of the 'shipping' factor identified in this study, particularly when considering that its contribution in emission inventories increases year on year.

The MTR-PMF solution where the shipping factor accounts for an optimal proportion of the peaks, allows for a more precise comparison of its profile with the ferry EFs. As represented in Figure 4-38, the profile of the constrained MTR-PMF is more consistent with the VOC EF. This detailed speciation allows a meaningful comparison with previous works. For instance, during the SCIPPER campaign, Timonen et al. (2022) reported significant contributions from C_6 – C_{10} VOCs such as ethylbenzene, m&p-xylenes, hexane, heptane and octane, particularly at low load (10%) while running on MGO with catalytic systems. These compounds are likewise among the top contributors to the constrained MTR-PMF shipping profile in this study, which is consistent with the fact that ferries were operating at low load while manoeuvring. They also observed that lighter VOCs dominated their ship emission profiles, notably ethylene, butane, propene and pentene. This finding is consistent with the profile presented here, where propane, butane and ethylene emerge as the main contributors to the ship emission profile of speciated VOCs. Other VOCs as m&p-xylenes, o-xylene and ethylbenzene are found across various studies in ship emissions (Agrawal et al., 2010; Huang et al., 2018; Zhang et al., 2024) and are here the most abundant aromatics in the profile. Also, acetone (and acrolein C_3H_4O) are major contributors to the ship emission profiles and are reported in significant proportions in the literature, such as in Zhang et al. (2024) for ocean-going vessels. While their relative contributions are higher in their study, their presence in the ship emissions profile highlights their relevance as characteristic compounds in ship emissions. The importance of methanol in ship emissions is confirmed as it is both the main contributor to the shipping profile and the largest EF. Constraining the shipping profile helped redistributing the contributions of these oxygenated VOCs, associated to many sources, in the shipping profile. Overall, this agreement between this study and other independent datasets found in the literature not only supports the robustness of the MTR-PMF shipping profile, but also illustrates how combining temporally resolved PTR-ToF-MS data with chemically detailed TD-GC-FID measurements yields a more complete and reliable representation of ship emissions.

(a) Time series.

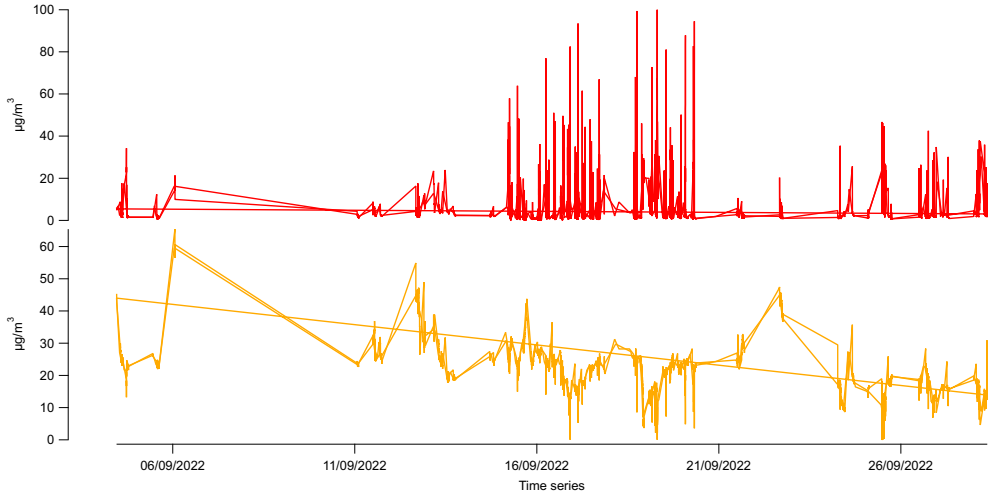

(b) PTR profiles.

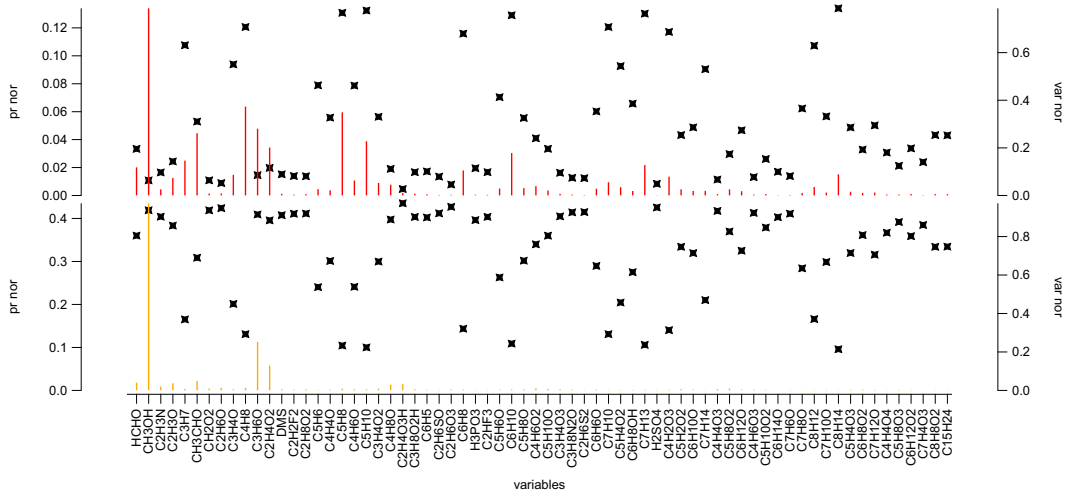

(c) GC profiles.

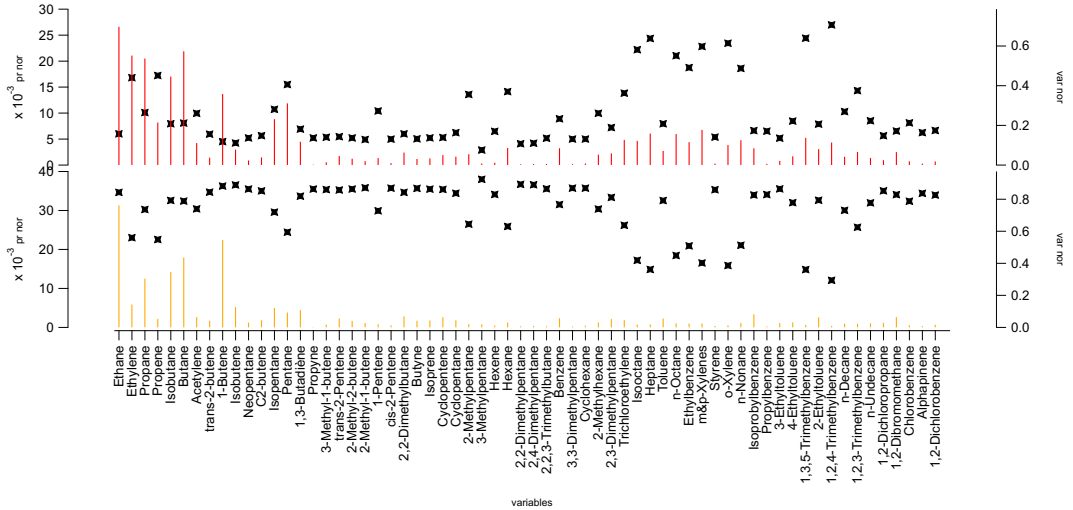

Figure 4-33: *Time series and profiles of the 2-factors solution of the wind-constrained MTR-PMF. The bar plot of the profiles corresponds to the contribution of the variable to the profile (left axis), the dotted plot corresponds to the contribution of the factor to the observed mass of each variable (right axis).*

(a) *Time series.*

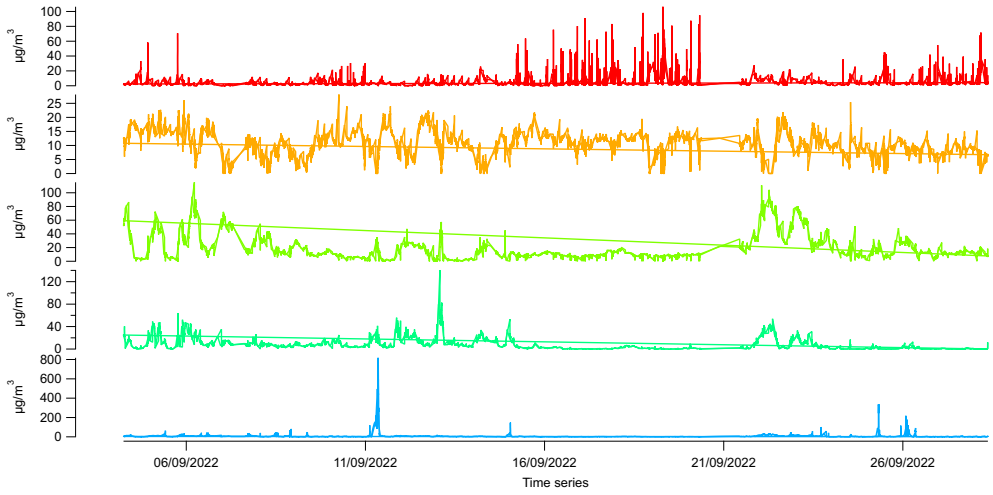

(b) *PTR profiles.*

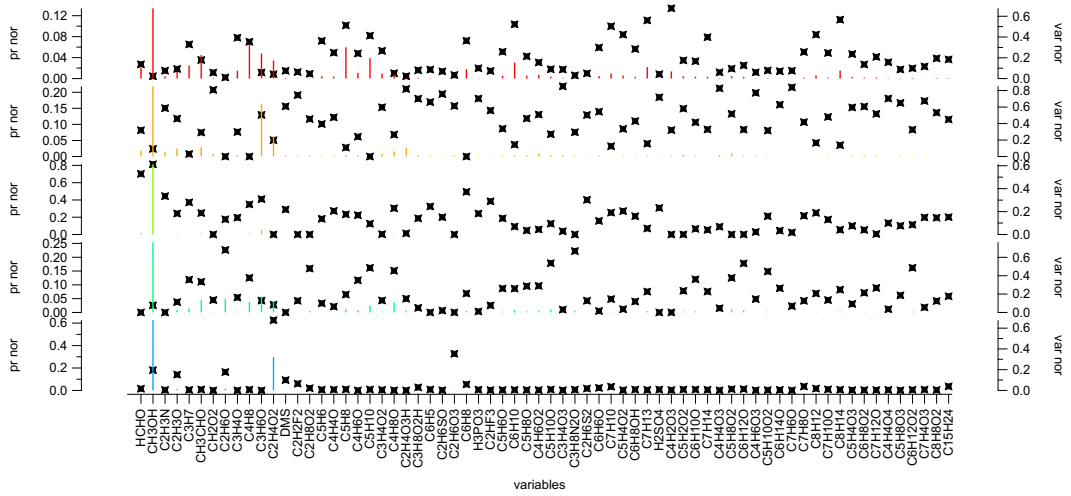

(c) *GC profiles.*

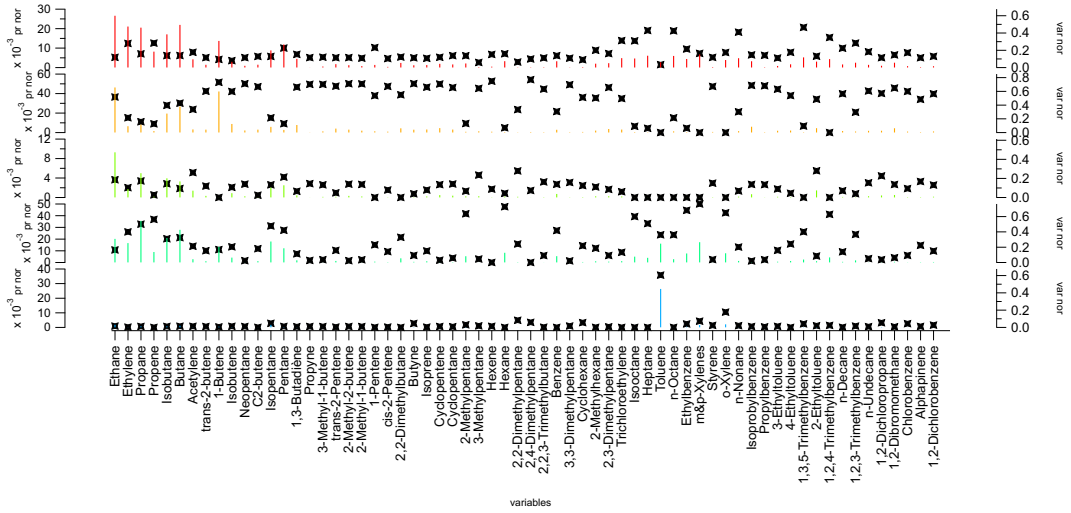

Figure 4-34: *Time series and profiles of the 5-factors solution of the fully constrained MTR-PMF (a-value = 0). The bar plot of the profiles corresponds to the contribution of the variable to the profile (left axis), the dotted plot corresponds to the contribution of the factor to the observed mass of each variable (right axis).*

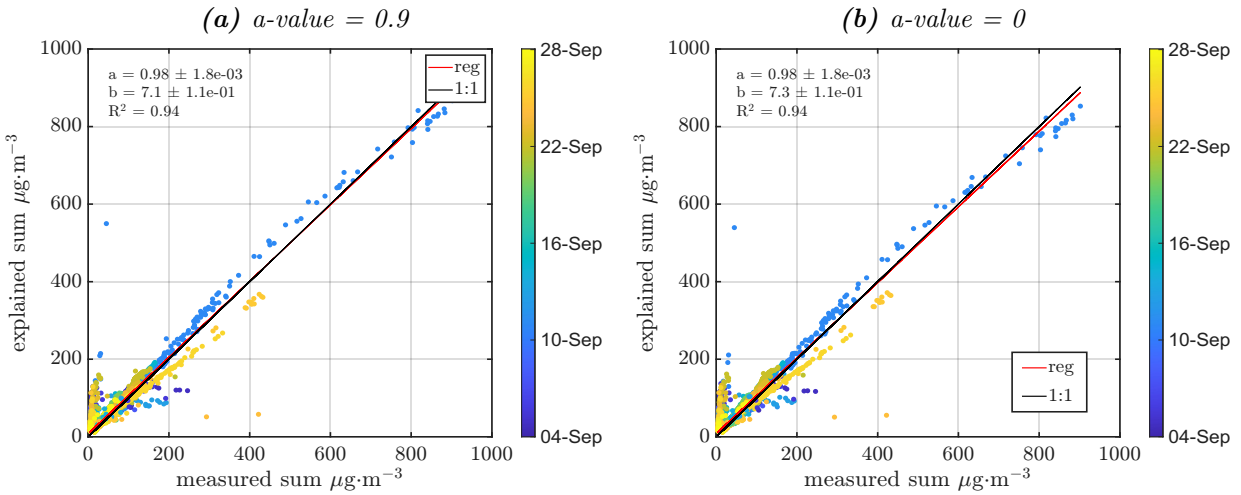

Figure 4-35: *Evolution of the correlation coefficient between observed and modelled concentrations for two a-values of the constrained 'shipping' Factor 1; (a) a-value = 0.9; (b) a-value = 0.*

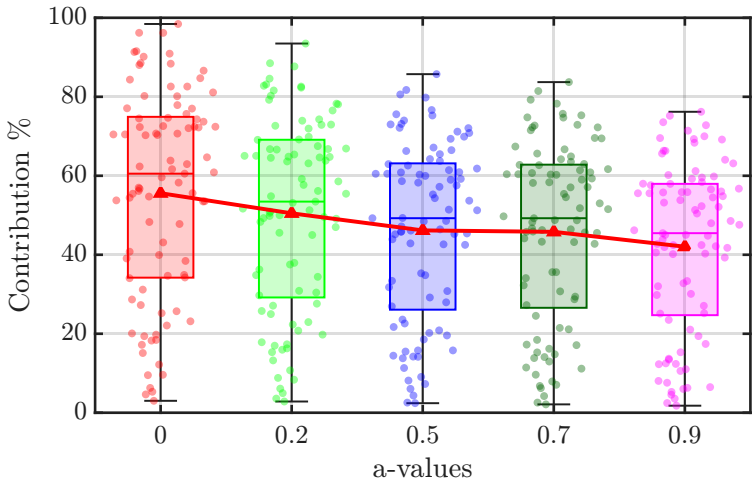

Figure 4-36: *Evolution of the relative contributions of each modelled ship peak of Factor 1 to the total modelled concentrations during ship emissions. The full line in each box in the median, the bottom and top edges of each box are 1st and 3rd quartiles respectively, the bottom and top whiskers are the 10th and 90th percentiles respectively. Triangle/lines indicate the average contribution for each a-value.*

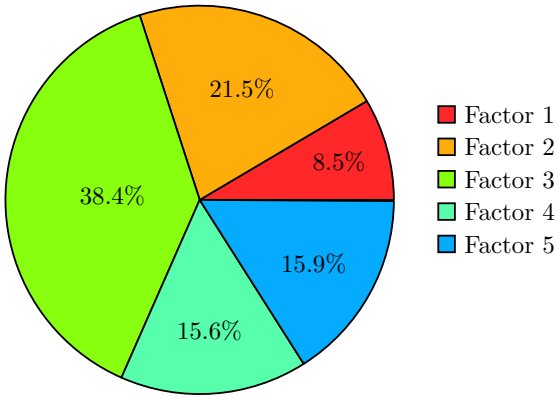

Figure 4-37: *Pie chart of average contribution of the constrained MTR-PMF factors in the 5-factor solution.*

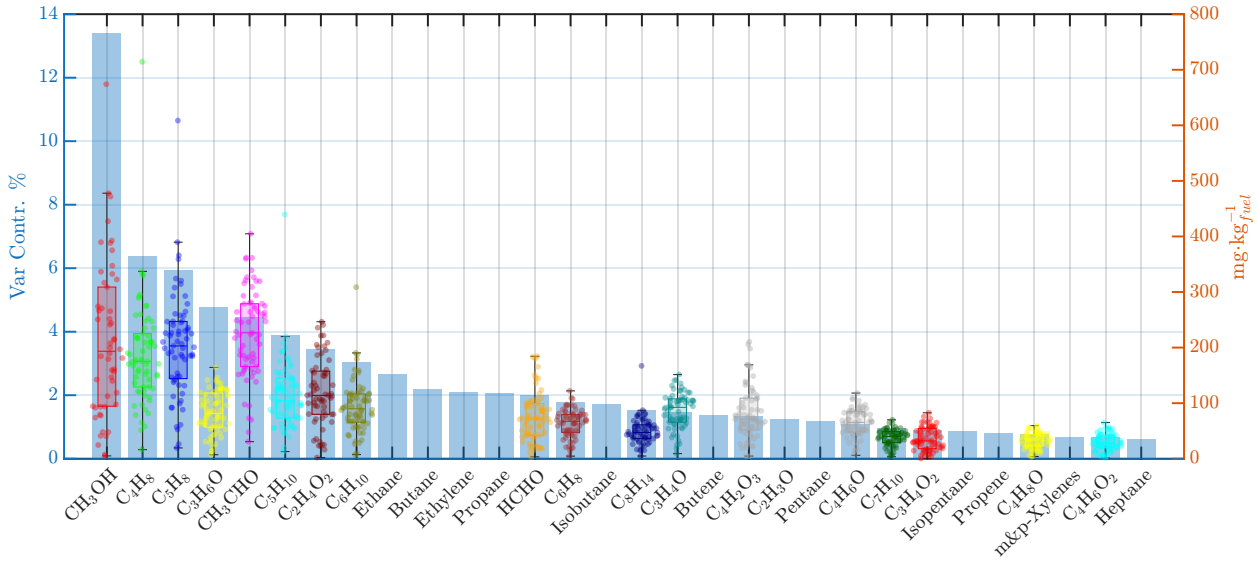

Figure 4-38: *Comparison of the top 30 contributors to the ship emissions profile on the fully constrained MTR-PMF with the Emission Factors determined in Chapter 3. (left axis, blue bar plot) Major contributor to the Factor 1 ship emissions MTR-PMF profile; (box plots, right axis) associated EF calculated in Chapter 3.*

4.5 Implications for the identification of ship emissions from TD-GC-FID observations.

The MTR-PMF shipping profile includes a GC-resolved profile, whose associated time series is represented in Figure 4-39 alongside the time series associated to the PTR ship profile.

As expected from the MTR method in our scenario, this time series is the result of averaging the contribution of the shipping profile observed on the PTR, producing a time series that clearly reflects the evolution of the PTR factor. Furthermore, the GC profile yields a time series exhibiting greater variability and occasionally higher concentrations than the total observed VOC concentration from the GC, as illustrated in Figure 4-40. While this evolution could result from the impact of shipping peaks, it is an artefact of modelling GC concentrations and is not linked to real-world observations of GC.

As the wind-constrained MTR-PMF resulted in the most representative shipping emission profile with both PTR and GC, the same constraint was tested with the GC concentrations to see if it was possible to resolve a ship emission profile from the GC concentrations alone using PMF. The wind-constrained GC-PMF analysis was performed using concentrations filtered for the same wind direction (270 — 20°), resulting in a 231×64 matrix.

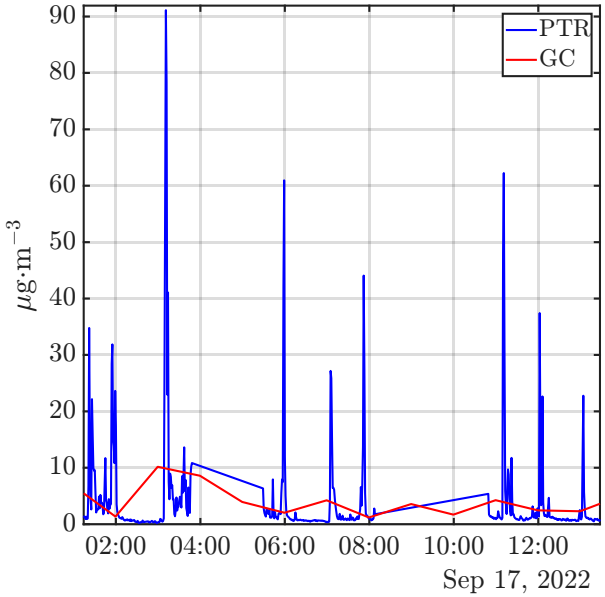

Figure 4-39: *Comparison between the PTR time series of Factor 1 and the GC time series of 'shipping' Factor 1 in the constrained MTR-PMF.*

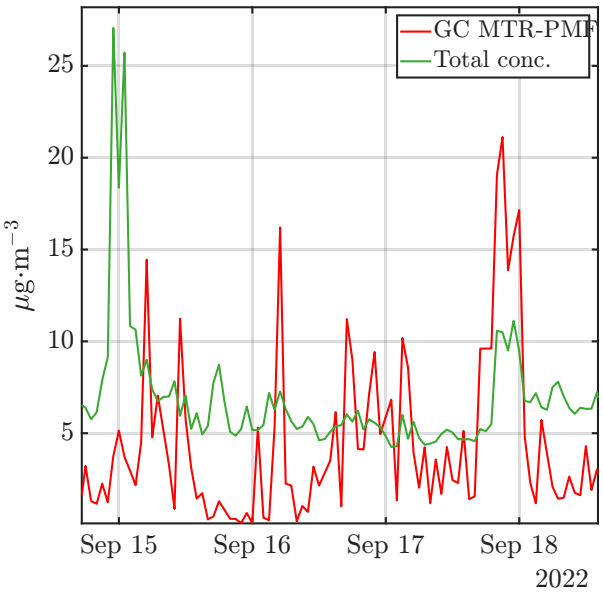

Figure 4-40: *Comparison between the GC time series of 'shipping' Factor 1 in the MTR-PMF and the total concentration of VOCs observed by the TD-GC-FID.*

The 2-factor solution was retained, with $R^2 = 0.56$, since the 3-factor solution had a lower R^2 (0.49) and the 4-factors at 0.46, moreover, two factors are more realistic and consistent with the wind-constrained MTR-PMF.

The solution is presented in Figure 4-41 and shows that the second factor is related to the background, as it accounts for the mass of the same VOCs as the background profiles, such as ethane (95.9%), in a concentration range similar to GC-PMF Factor 2. It provides a Factor 1 that can be linked to combustion processes from its composition, namely 2-methylpentane (6.7%) and hexane (8.6%), as observed for Factor 4 of GC-PMF, and to gasoline evaporation with the presence of isopentane (8.1%) and pentane (10%). However, the overall concentrations (on average 1.5 µg·m^{-3}) and variability remain too low to reflect the influence of ship emissions on VOC levels. These levels are lower than those observed for the GC time series in the constrained MTR-PMF, whose mean concentration was 4.7 µg·m^{-3}, as the way the MTR calculated the GC contribution differ from its use in a native PMF, as mentioned previously and illustrated in Figure 4-40. In terms of profile, the wind-constrained GC factor compares to the GC profile obtained in the MTR-PMF, as shown in Figure 4-42. For example, both profiles show an important relative contribution of the light VOCs, from C_2 to C_5. The profile obtained from the GC-PMF constrained by wind sector shows a stronger contribution of 2-methylpentane and hexane compared to the MTR-PMF. This difference appears to be compensated by a greater contribution of ethane and ethylene in the MTR profile, which balances the mass contributions of the factor. Finally, the two profiles are similar for the remaining VOCs, showing overall a good agreement. The similarity between 2 factors can be tested using the Person-Distance (PD) and Similarity-Identity-Distance (SID) (Belis et al., 2015). They are described as follows:

$$PD = 1 - R^2, \tag{4.1}$$

$$SID = \frac{\sqrt{2}}{m} \sum_{j=1}^{m} \frac{|x_j - y_j|}{x_j + y_j}. \tag{4.2}$$

With R^2 denoting the correlation coefficient between the contribution of each species to each profile, m denoting the number of species and x_j and y_j denoting the relative contribution of each species to the two factors, respectively. More precisely, the SID reports the deviation of the paired contributions of the two factors from the identity line when plotting their correlation. Two factors are considered similar if the SID is less than 0.6 (Belis et al., 2015). The SID calculated using the GC profile contributions to the constrained MTR-PMF and the wind-constrained GC-PMF results in a SID of 0.55, which just meets the similarity criteria. Additionally, we found PD = 0.64 (Figure 4-43), which is consistent with the resemblance criteria between factors of the same category observed by Belis et al. (2015). Therefore, we can conclude that the two profiles are similar and that the PMF analysis using GC data from a narrow wind sector corresponding to ship emissions, reports a chemical fingerprint of VOCs emitted by ferries. Interestingly, the standard GC-PMF described in Section 4.2.b provided a 4-factors solution with a modelling quality that was already satisfactory, with $R^2 = 0.91$. Although the correlation coefficient was improved, it resolved a factor comprising a combination of 2-methylpentane and hexane, as well as isopentane and pentane, which shows similarities with the shipping profile determined in the wind-constrained PMF on the GC data. These VOCs were resolved in two separate factors in previously described 5-factors solution. This 4-factor solution is shown in Figure 4-44. There, the profile of Factor 4 is consistent with the ship emissions profiles identified in the wind-constrained GC-PMF, which is aligned with the GC profile of the shipping factor in constrained MTR-PMF, as shown in Figure 4-45.

However, the PD between these two factors (PD = 0.76) is greater than between the shipping factor of MTR-PMF and the wind-constrained GC-PMF. Moreover, the SID exceeds the satisfactory criterion as it equals 0.79, making the use of TD-GC-FID only in the PMF difficult to identify a shipping factor.

(a) *Time series.*

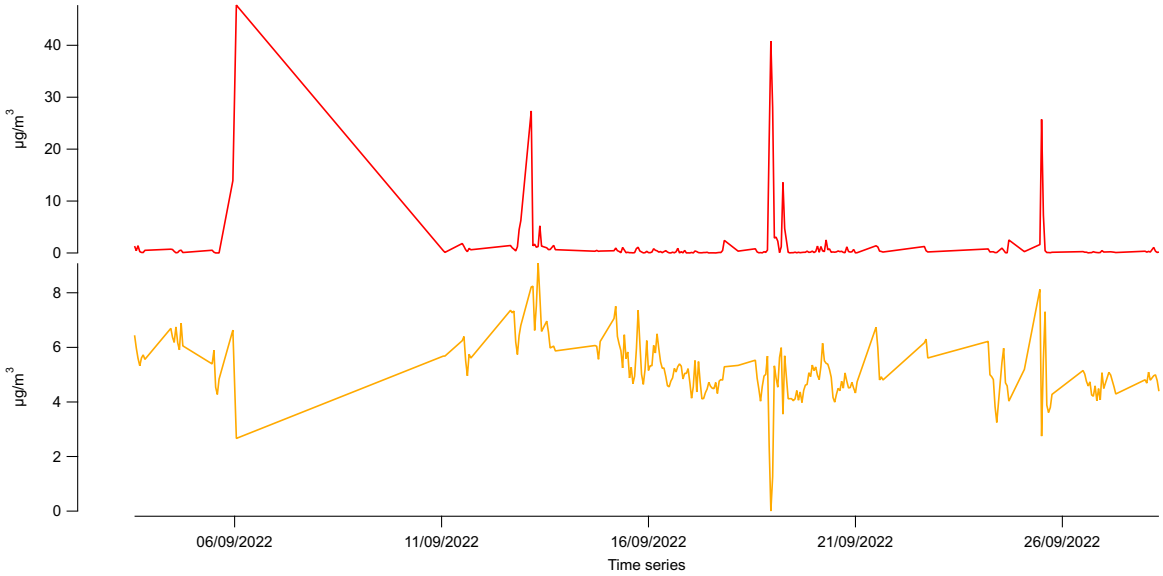

(b) *Chemical profiles.*

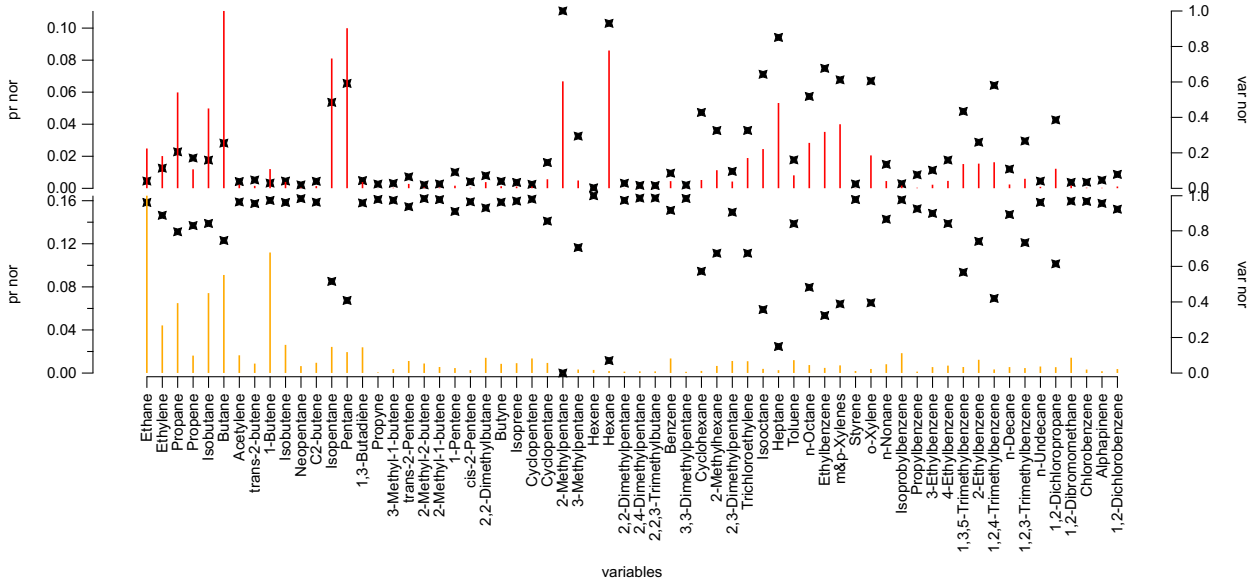

Figure 4-41: *Time series and profiles of the 2-factors solution of the wind-constrained GC-PMF. The bar plot of the profiles corresponds to the contribution of the variable to the profile (left axis), the dotted plot corresponds to the contribution of the factor to the observed mass of each variable (right axis).*

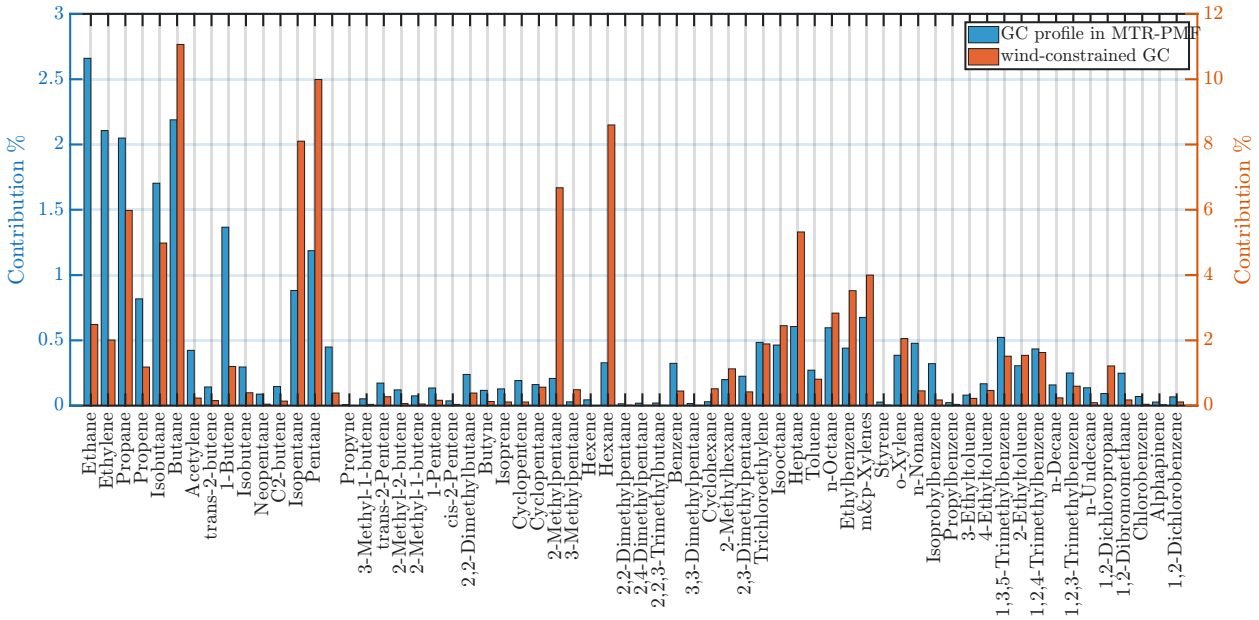

Figure 4-42: *Comparison of the GC 'shipping' profile obtained in the wind-constrained MTR-PMF (blue) versus the GC 'shipping' profile obtained in the wind-constrained GC-PMF (orange).*

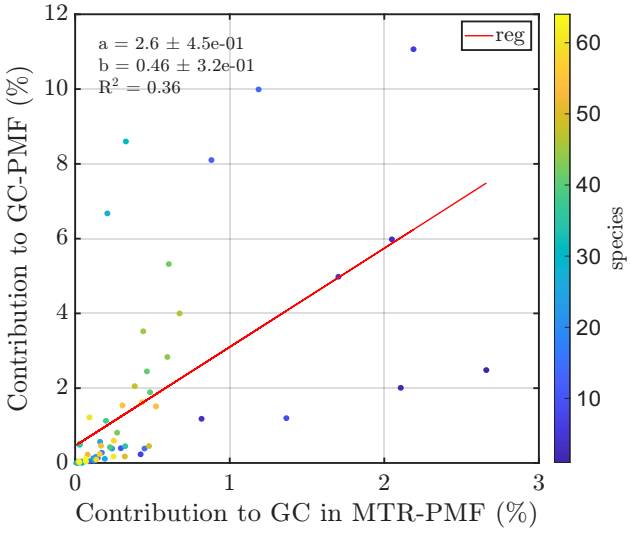

Figure 4-43: *Correlation between the relative contributions (%) of each species to the GC profile of the constrained MTR-PMF (x-axis) and the GC profile of wind-constrained GC-PMF (y-axis), for the calculation of the Pearson Distance (PD). The colorbar refers to the compound number and give an indication on the mass.*

(a) Time series.

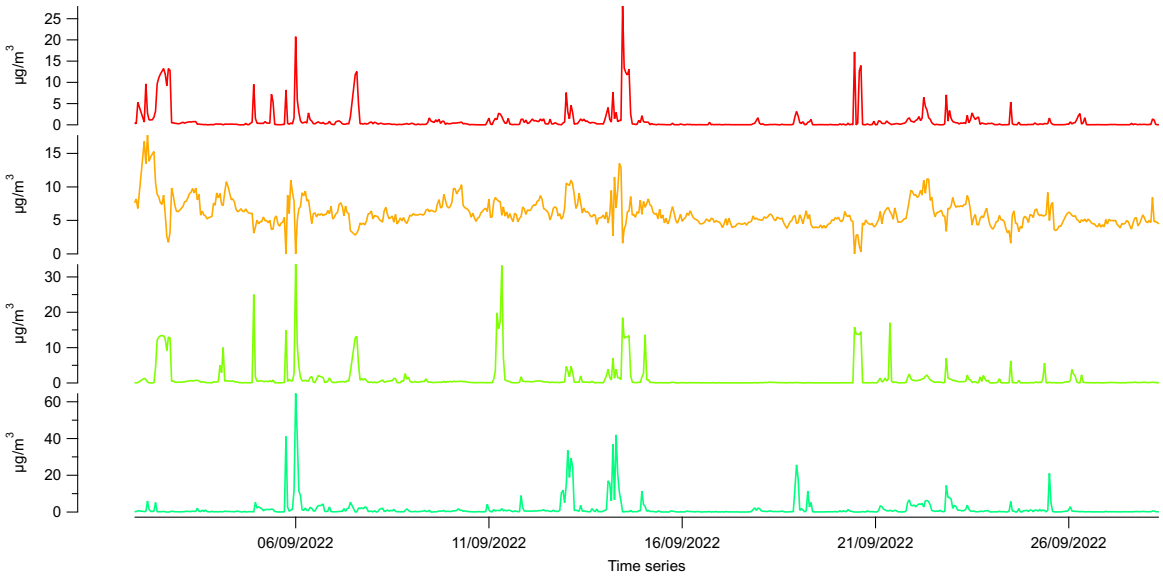

(b) Chemical profiles.

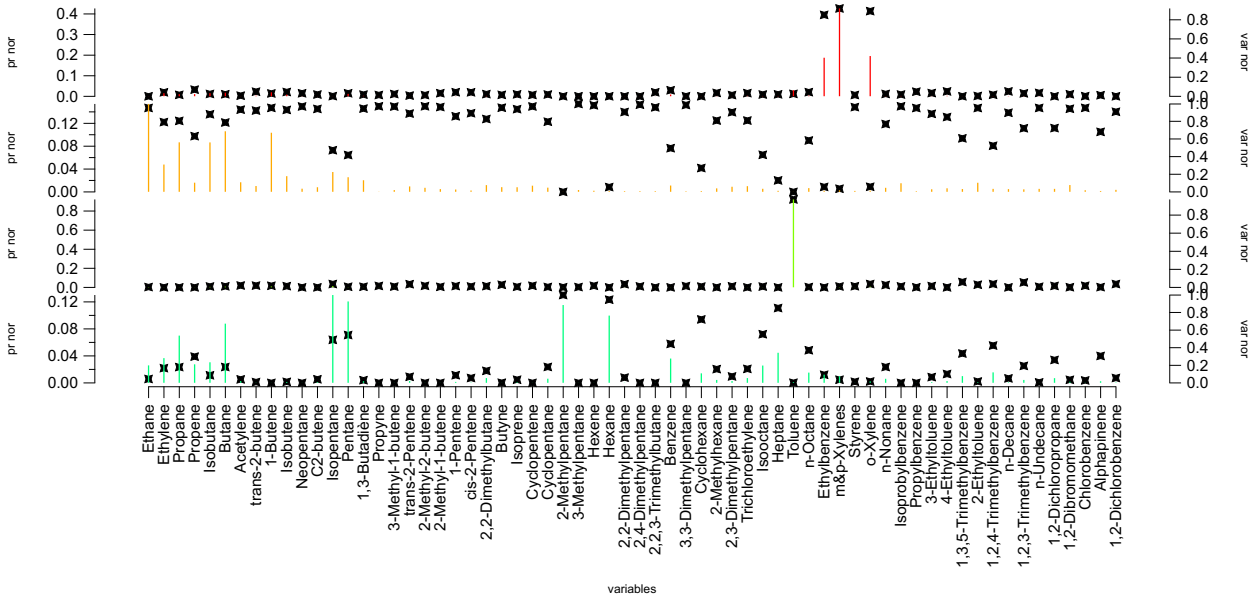

Figure 4-44: *Time series and profiles of the 4-factor solution of the GC-PMF. The bar plot of the profiles corresponds to the contribution of the variable to the profile (left axis), the dotted plot corresponds to the contribution of the factor to the observed mass of each variable (right axis).*

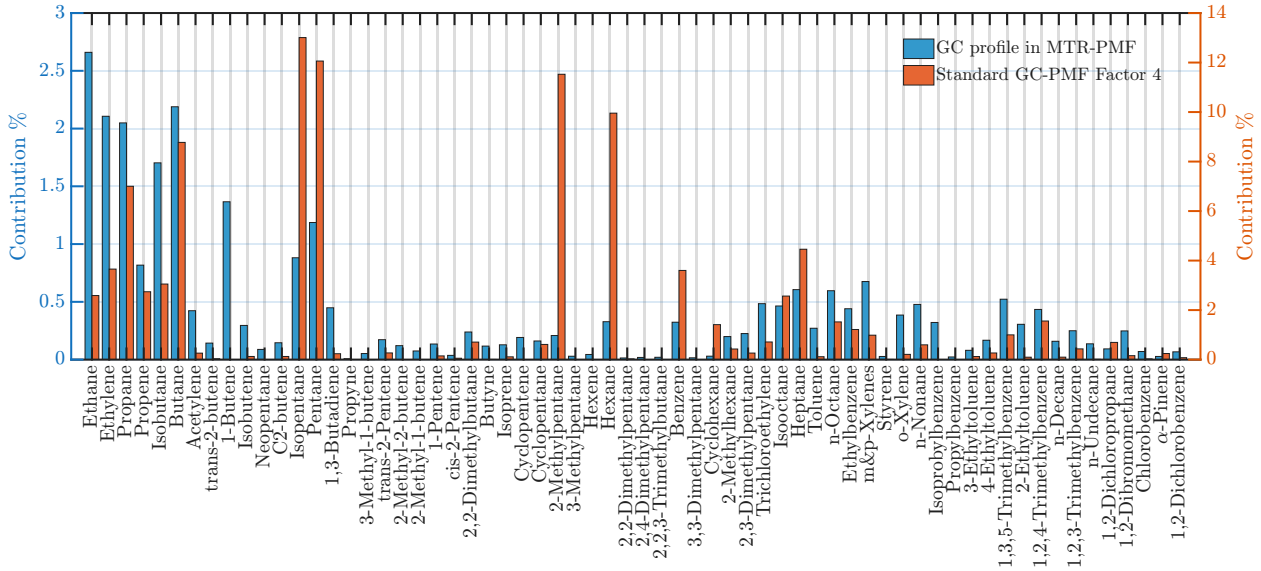

Figure 4-45: *Comparison of the GC profile obtained in the 'shipping' factor of constrained MTR-PMF (blue) versus the GC profile obtained in the standard GC-PMF (orange)*

4.6 Indications on air quality impacts

4.6.a Ozone formation

The Ozone Formation Potential (OFP) can be calculated from the combination of VOC concentrations with their associated Incremental Reactivity (IR), providing an indication of the excess of ozone produces for each mass unit of VOC (Venecek et al., 2018):

$$IR_i(gO_3 \cdot gVOCs^{-1}) = \frac{\Delta O_3}{\Delta VOC_i}, \tag{4.3}$$

with ΔO_3 denoting the excess in ozone and ΔVOC_i denoting the excess of the ith VOC. Particularly for urban areas, such as the one presented in this study, the Maximum Incremental Reactivity (MIR) is used to account for the high-NO_x conditions where VOC gain in reactivity (Venecek et al., 2018). The OFP therefore results in:

$$OFP_i = MIR_i \times [VOC_i] \tag{4.4}$$

as performed in numerous studies (Hanyang et al., 2020; Zulkifli et al., 2022; Li et al., 2022; Gu et al., 2023; Liu et al., 2023; Dufresne et al., 2025). The MIR coefficient values were historically calculated by Carter (1994) from the chemical mechanism model SAPRC90. This resulted in a dataset of MIR values, reported by Carter (2010). Venecek et al. (2018) updated this, using an new version of the model, SAPRC07, to account for more recent and more representative atmospheric conditions of an urban atmosphere.

The median MIRs of the latter were used in this study. Our objective is to determine the contribution of the ship emission Factor 1 to the total OFP of the modelled factors in the constrained MTR-PMF solutions. Therefore, the VOCs used in the calculation were those that were identified as contributing significantly to Factor 1, namely the light VOCs and OVOCs, from formaldehyde to methacylic acid. In addition, aromatics (BTEX), which contribute little to ship emissions, were added in the comparison to account for the contribution of the industrial factors to the total OFP, legitimating the method of calculation their contributions to OFPs. The MIR coefficients of these VOCs are summarised in Table 4-1.

For a mixture of VOCs, its OFP is the sum of each VOC concentration weighted by their respective MIR. When considering the outputs of PMF modelling, the OFP of a PMF factor is calculated with:

$$OFP_{i,k} = \sum_{j=1}^{m} MIR_j \times G_{i,k} \times F_{j,k}, \tag{4.5}$$

with $OFP_{i,k}$ denoting the OFP of the kth factor at its ith observation, m denoting the total number of species the OFP is calculated with, $G_{i,k}$ denoting the contribution (concentration) of the kth factor at the ith observation, $F_{j,k}$ denoting the contribution of the jth species to the kth factor, and MIR_j denoting the MIR of the jth species.

Table 4-1: *MIR coefficients of the VOCs retained for the OFPs determination.*

VOC	**median MIR in Venecek et al. (2018)**
Formaldehyde (HCHO)	7,16
Methanol (CH_3OH)	0,668
Acetaldehyde (CH_3CHO)	6,07
Acrolein (C_3H_4O)	6,98
Acetone (C_3H_6O)	0,343
Acetic acid ($C_4H_2O_3$)	0,728
Crotonaldehyde (C_4H_6O)	8,18
Acrylic acid ($C_3H_4O_2$)	10,9
MEK (C_4H_8O)	5,72
Methacrylic acid ($C_4H_6O_2$)	13,9
Ethane	0,321
Ethylene	8,64
Propane	0,563
Propene	10,8
Isobutane	1,3
Butane	1,33
Acetylene	0,944
Butene	9,3
Isopentane	1,65
Pentane	1,56
Benzene	0,787
Heptane	1,37
Toluene	4,02
Ethylbenzene	3,11
m&p-Xylenes	6,99
o-Xylene	7,17

It enables the OFP of the shipping factor to be compared with those of the other factors in order to evaluate its contribution. Figure 4-46 illustrates the evolution of the relative contribution of each factor to the total OFP of modelled concentration. Using the VOCs presented in Table 4-1, Factor 1 contributes 11 ± 16% to the total OFP, for all modelled factors. The high standard deviation reflects the variability of the OFP during the increases of ship peaks. During ship peaks of Factor 1, the OFP can be entirely attributed to shipping, as observed in Figure 4-46.

By contrast, 'industrial' Factor 3 is the main contributor to the modelled OFPs, averaging 35 ± 18%, closely followed by Factor 2, the unresolved background, with an average OFP of 31 ± 18%. The composition of these factors explains their OFPs, and the contribution of individual VOCs to the factor's OFP will inform on the most ozone forming species for each factor. The relative contribution of species j to the OFP of factor k can be estimated as the ratio of its average contribution to factor k, $F_{j,k}$, weighted by its MIR, to the average OFP of factor k calculated in Equation 4.8:

$$\frac{OFP_{j,k}}{OFP_k}(\%) = \frac{F_{j,k} \times MIR_j}{\overline{OFP_k}} \times 100. \tag{4.6}$$

This value denotes the importance of each species' contribution to the OFP of the kth factor, relative to its composition. Figure 4-47 shows the contribution of the main components of Factor 1 to its OFP. Although methanol is the most abundant VOC in the ship emission factor, it only accounts for 2.3% of its OFP. Acetaldehyde is the main contributor to the OFP at 7.0%, followed by ethylene (4.7%), formaldehyde (3.7%) and 1-butene (3.3%), which confirms their role as important O_3 precursors. The 'background' factor 2 contributes more to the total OFP (30.8%) and is mainly comprised of methanol (22%) and acetone (16%), but 1-butene is the main contributor to the OFP of Factor 2 (3%), although it only contributes 4% to the total modelled mass of Factor 2.

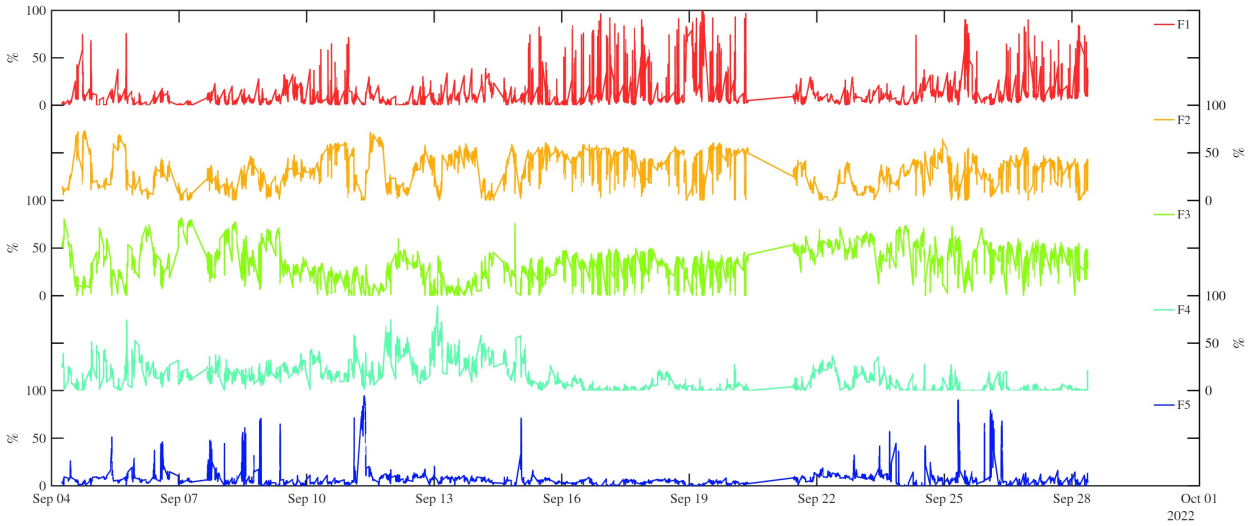

Figure 4-46: *Temporal evolution of the relative contribution of each factor to the total OFP.*

Limitations remain in these OFP calculations, as the MIR coefficients are only valid for high-NO_x regimes. This is a valid hypothesis for the shipping factor, as NO_x is the most important EF according to the results of Chapter 3. However, the other factors may not be affected by high-NO_x, such as the background factor, which may not correspond to high-NO_x conditions. This nuances its position as the most important contributor to the OFP calculated for the Dunkirk 2022 campaign. Additionally, the presence of fragments in the PTR limits the identification of chemical species, which probably causes to miss important contributions to the OFP of these primary ions, which could potentially contribute significantly.

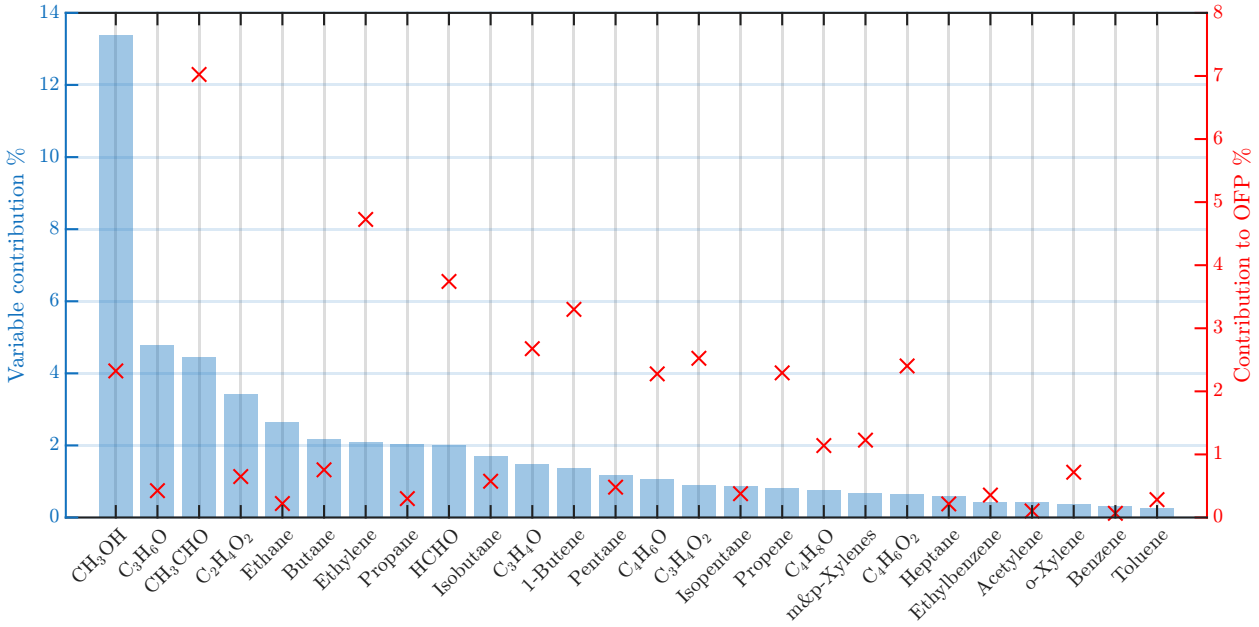

Figure 4-47: *Blue, left axis: VOC contribution to Factor 1; Red crosses, right axis: VOC contribution to the OFP of 'shipping' Factor 1.*

4.6.b SOA formation

Similarly to the OFP, the propensity of VOC to form SOA can be expressed using the Secondary Organic Aerosol Potential (SOAP), illustrating the increase in SOA when a mass of a VOC is added in the atmosphere (Derwent et al., 1998, 2010; Lasne et al., 2023). It is expressed relatively to the SOA formation potential of toluene:

$$SOAP_i = \frac{\Delta[SOA]_{VOC_i}}{\Delta[SOA]_{toluene}} \times 100, \tag{4.7}$$

with $SOAP_i$ denoting the unitless SOAP of the ith VOC, $\Delta[SOA]_{VOC_i}$ the increase of SOA formation linked to the ith VOC and $\Delta[SOA]_{toluene}$ the increase of SOA formation linked to toluene, whose SOAP is taken at 100. Only a few species exceed the SOAP of toluene, namely styrene, benzaldehyde, ethylbenzene and propylbenzene (Derwent et al., 2010). Every speciated VOC, whose SOAP is given in this study, is used for the SOAP calculation, and the SOAPs of the major OVOCs are added, namely methanol, acetic acid, formic acid, acetone, acetaldehyde and formaldehyde. The SOAP of VOCs used in the calculation are presented in Table 4-2.

Table 4-2: *SOAP coefficients used in this study, taken from Derwent et al. (2010).*

Compound	SOAP ($\%_{toluene}$)	Compound	SOAP ($\%_{toluene}$)
Ethane	0.1	Benzene	92.9
Ethylene	1.3	Cyclohexane	0
Propane	0	2-Methylhexane	0
Propene	1.6	2,3-Dimethylpentane	0
Isobutane	0	Heptane	0.1
Butane	0.3	Toluene	100
Acetylene	0.1	n-Octane	0.8
trans-2-butene	4	Ethylbenzene	111.6
1-Butene	1.2	m&p-Xylenes	90
Isobutene	0.6	Styrene	212.3
Neopentane	0.2	o-Xylene	95.5
cis-2-butene	3.6	n-Nonane	1.9
Isopentane	0.2	Isopropylbenzene	95.5
Pentane	0.3	Propylbenzene	109.7
1,3-Butadiène	1.8	1,3,5-Trimethylbenzene	13.5
3-Methyl-1-butene	0.6	1,2,4-Trimethylbenzene	20.6
trans-2-Pentene	4	n-Decane	7
2-Methyl-2-butene	1.9	1,2,3-Trimethylbenzene	43.9
2-Methyl-1-butene	0.9	n-Undecane	16.2
1-Pentene	0	α-pinene	17.4
cis-2-Pentene	3.1	Methanol	0.3
Isoprene	1.9	Acetic Acid	0.1
2-Methylpentane	0	Formic acid	0.1
3-Methylpentane	0.2	Acetone	0.3
Hexane	0.1	Acetaldehyde	0.6
2,2-Dimethylpentane	0	Formaldehyde	0.7s

Just like for the OFP, the total SOAP of a PMF factor is given by the sum of the SOAP of each VOC comprising it:

$$SOAP_{i,k} = \sum_{j=1}^{m} SOAP_j \times G_{i,k} \times F_{j,k}, \tag{4.8}$$

with $SOAP_{i,k}$ denoting the SOA formation produced by the emissions of the kth factor at its ith observation, m denoting the total number of species the SOAP is calculated with, $G_{i,k}$ denoting the contribution (concentration) of the kth factor at the ith observation, $F_{j,k}$ denoting the contribution of the jth species to the kth factor, and $SOAP_j$ denoting the SOAP of the jth species. Similarly to Equation 4.6, the relative contribution of each species to each PMF factor's total SOAP can be obtained by normalising the SOAP-weighted contribution $F_{i,k}$ with the average SOAP of the factor.

$$\frac{SOAP_{j,k}}{SOAP_k}(\%) = \frac{F_{j,k} \times SOAP_j}{\overline{SOAP_k}}. \tag{4.9}$$

Overall, 'shipping' Factor 1 contributes 6 ± 10% to the total SOAP of all PMF factors that were resolved in the constrained MTR-PMF solution. As with the OFP, 'industrial' Factor 3 and 'background' factor 2 are the main contributors to the total SOAP, explaining 52 ± 20% and 24 ± 14% respectively.

Shipping is also the lowest contributor to the total SOAP on average, but may be occasionally responsible for the entirety of the modelled SOAP, as observed in the relative SOAP contribution in Figure 4-48. BTEX are the main contributors to the SOAP of the 'shipping' factor 1 (m-xylene 1.5%, ethylbenzene 1.2%, o-xylene 0.9%, benzene 0.7%, toluene 0.6%), as can be seen in Figure 4-49. However, their limited mass fraction in the ship emissions leads to a smaller propensity for ship emissions to form aerosols compared to other resolved sources.

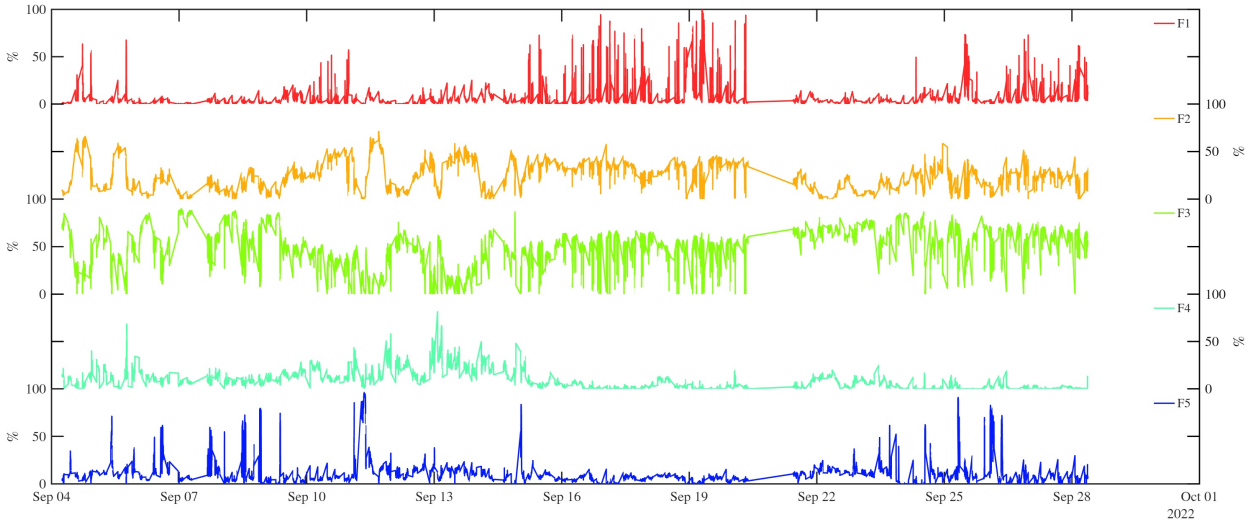

Figure 4-48: *Temporal evolution of the relative contribution of each factor to the total SOAP.*

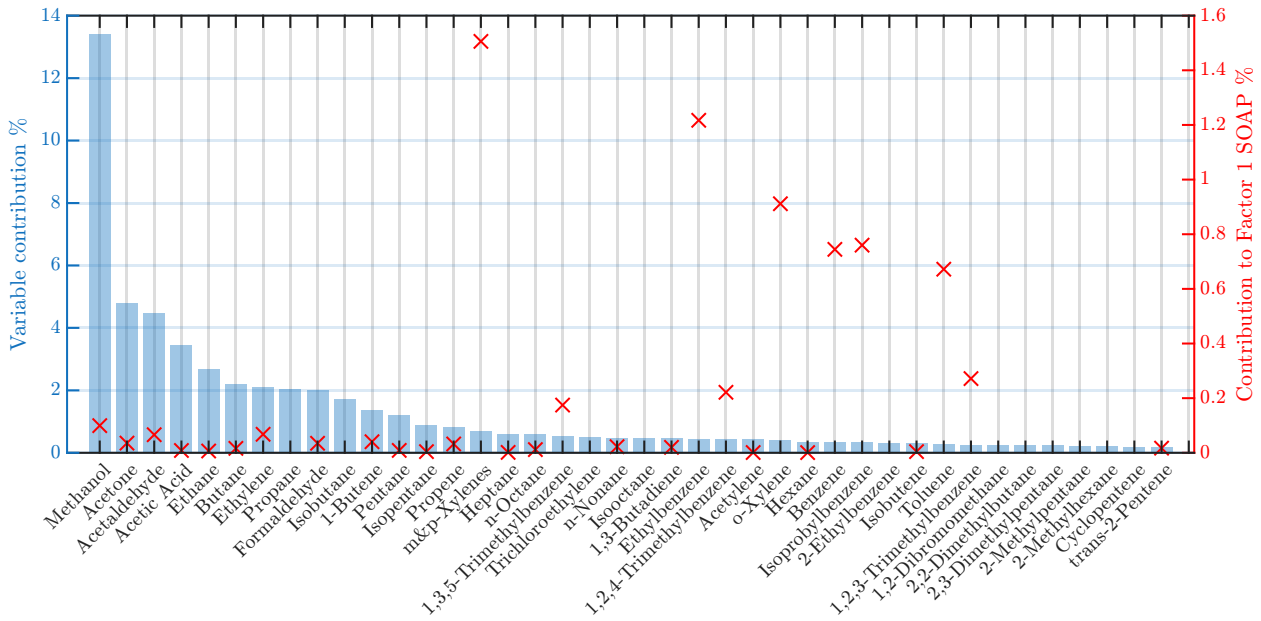

Figure 4-49: *Blue, left axis: VOC contribution to the 'shipping' Factor 1; Red crosses, right axis: VOC contribution to the SOAP of Factor 1. For SOAPs = 0, no symbol is used fo clarity. Only the top 40 contributors to the ship emission profile are represented.*

4.7 Conclusion

This chapter explores the use of PMF to isolate shipping emissions as a source of VOCs and assess their impact. It highlights the difficulty of resolving the shipping factor using TD-GC-FID data due to its low time resolution, which drastically limits the influence of transient ship plumes on VOC levels, resulting in low variability during favourable wind periods. In addition, linking a GC-PMF factor to a ship tracer remains ambiguous, especially for shipping where transient concentration increases reflect ship emissions, as established in the previous chapter for SO_2. While the standard GC-PMF can capture combustion- and fuel-related emission sources in Dunkirk, the dominance of industrial sources associated with hydrocarbon industry, fuel evaporation and storage makes it difficult to unambiguously identify a shipping profile with GC data alone. Time-resolved PTR-ToF-MS measurements, with a resolution of a minute, allowed a clear identification of a shipping profile, as the temporal variability of the 'shipping' factor displayed similar transient increases as those used to derive the ferry EFs. A correlation between the PTR-PMF shipping factor and SO_2, a tracer for ship plumes, was found. This rather weak correlation, due to the transient nature of the ship plumes, comforted the identification of the factor as shipping-related. Next, a combined approach with GC and PTR data was used in a MTR-PMF. This approach provided a more complete VOC fingerprint combining PTR and GC species for the resolved factors. A shipping profile could be isolated for both instruments when the MTR-PMF is fully constrained using a shipping profile obtained by a wind-constrained MTR-PMF. The resulting shipping profile confirmed the significance of oxygenated VOCs (methanol, acetone, acetaldehyde, acetic acid) and other fragments, suggesting the importance of heavier cycloalkenes in shipping emissions, in close agreement with the EFs obtained in chapter 3 with the PTR. In addition, GC speciation revealed the significant contribution of light hydrocarbons to shipping emissions, with ethane, butane, ethylene and propane being the 9th to 12th major contributors to the profile. Overall, the average contribution of VOCs from ship emissions to the total VOC mass modelled is 8.5%, which is in close agreement with regional emission inventories. However, this contribution can reach 100% inside a ship plume, meaning that shipping is transiently the main source of VOCs. As the constrained MTR-PMF gives a most robust shipping profile, insights on its impact were determined from their perspective on their contribution to ozone and SOA formation. It was found to contribute 11% to the total OFP of the PMF-modelled factors, with acetaldehyde, ethylene and formaldehyde being the biggest contributor from the composition of the shipping factor. Also, although propene and BTEX are small contributors to the profile, they contribute significantly to its SOAP, resulting in a 6% contribution to the total SOAP. Overall, these potentials increase drastically when calculated within an influence of a ship plume. This work highlights that while the GC-PMF alone struggles to resolve a robust shipping profile, the MTR-PMF approach allows to include the GC data in a source profile, even for a very transient source such as shipping. This suggests that with carefully designed field campaigns, combining chemically and time-resolved VOC measurements, MTR-PMF could provide complementary evidence for shipping emissions, reinforcing the assessment of this source and expanding the robustness of future observational studies, in a context where ship emissions are expected to evolve to comply with regulations.

This chapter emphasises the importance of the step-by-step approach undertaken. Systematically exploring each dataset independently using the PMF prior to combining them in the MTR-PMF allowed their respective co-variabilities and compositions to be assessed. This progressive methodology ensured that the limitations of each dataset in resolving a shipping factor were clearly identified, enabling more reliable and methodical interpretation of the combined PMF results. This approach strengthens the robustness of the conclusions drawn from the MTR-PMF concerning ship emissions, as these are based on a comprehensive understanding of the individual data sources influencing the Dunkirk harbour site.

CHAPTER 5

Cross-validation of the Volatile Organic Compounds emitted by ships in the harbour of Le Havre

Elaborating the PMF in the Dunkirk harbour revealed a chemical fingerprint representative of VOC emissions from ships. In order to verify the consistency of this profile, it was necessary to investigate whether a comparable PMF factor could be resolved in another industrial harbour and to compare the two profiles. Like Dunkirk, Le Havre is an important industrial harbour where the impact of maritime traffic on air quality can be expected. Therefore, this site was selected as being representative of both ship and industrial VOC emissions.

5.1 Context of Le Havre

The city of Le Havre has the highest number of inhabitants in the Normandy region, with 166,462 inhabitants in 2022 and a surface area of 47.0 km^2. The port of Le Havre is the largest port in France in terms of surface area (16,000 hectares), tonnage (83.6 Mt) and number of cargo containers (3.07 million Twenty-foot Equivalent Units, TEU) (HAROPA, 2022). It also accounts for 2/3 of the exterior exchanges of goods of France. It is part of the HAvre-ROen-PAris port (HAROPA) group since 2020, which, as its name suggests, includes the ports of Rouen and Paris. Its strategic position on the Seine river makes it the main hub for the transportation of goods to the Paris region[1]. As in Dunkirk, this harbour is home to significant industrial activity, primarily associated with the petrochemical and chemical manufacturing sectors, including the production of solvents, lubricants, fertilizers, rubber, and plastics. A large TotalEnergies refinery is located in the industrial zone to the east of the harbour. Unlike Dunkirk, there is no intensive metallurgical infrastructure in the industrial zone.

[1] https://lehavre.fr/ma-ville/decouvrir-le-havre

Studies of VOCs in the harbour of Le Havre are rare. However, in 2020, the Regional Network for Air Quality Monitoring of Normandy (AASQA, Atmo Normandie) put into place a surveillance for the emissions of three VOCs, namely 1,3-butadiene, benzene and acrylonitrile, emitted by known industrial sources in the area (Ney and Le Meur, 2022). Since, they perform four measurement campaigns per year (one per season) to sample these VOCs, at various sites inside and outside the industrial zone. One of these campaigns was performed from 09th to 23rd April 2021. This particular study was retained for comparison, as it displayed the same wind conditions as those encountered in our own study as discussed further below. The highest concentrations of 1,3-butadiene and acrylonitrile were found near Synthomer Speciality Chemicals, a company specialised in the manufacturing of synthetic polymers. The average concentrations obtained in the vicinity of the company were 4.92 µg·m^{-3} and 15 µg·m^{-3} for 1,3-butadiene and acrylonitrile, respectively. With regard to benzene, the area around the TotalEnergies refinery saw significant concentrations, with an average of 5.3 µg·m^{-3} for the April 2021 sampling. The average levels observed for the year 2021 were 4.92 µg·m^{-3} for 1,3-butadiene, 15 µg·m^{-3} for acrylonitrile, and 5.07 µg·m^{-3} for benzene at sites near the mentioned industries. These values exceed the annual exposure limits for the general population for some of the industrial sites tested, highlighting the need for further research into VOCs in the industrial zone of Le Havre (Ney and Delmas, 2024; Gascoin and Legrand, 2025). However, Atmo Normandie took simultaneous measurements of these VOCs in the urban area as part of their 2021 study and found that exposure limits were not exceeded in the urban area. This prompts an investigation into other sources in order to fully assess the surrounding population's exposure to VOCs. As the harbour is closer to the city centre and modelling shows that shipping makes the biggest contribution to ambient NO_2 levels in the city centre (Tokaya et al., 2024), it is unclear whether VOC emissions from ships are more or less important than the levels of VOCs observed in past studies in the industrial zone. The Chemical Transport Modelling (CTM) performed by Tokaya et al. (2024) in Le Havre, among European port cities, revealed that ship emissions had the highest contribution to ambient NO_2 (62%) compared to Rotterdam, Antwerp, Hamburg, Amsterdam and London. The second main contributor to NO_2 in the centre of Le Havre is traffic exhaust (16%). Therefore, the impact of shipping is significant and justifies the study of VOCs from ships in Le Havre, as previously shown in Dunkirk.

5.2 Site description and instrumentation

5.2.a Overview

5.2.a.i Location of the site

The measurement campaign occurred in the harbour of Le Havre between 17th April and 06th June 2023. The period was chosen based on the traffic numbers that were slightly higher in May over the period from 2017-2021, as determined by Atmo Normandie that counted ships navigating in the harbour within the framework of the PIRATE project, which report is presented in Appendix D.1.

The site was located at the east of the cargo terminal "Terminal de l'Atlantique", at the "Écluse François 1er" (Figure 5-1), a lock where ships can enter or leave the harbour. However, the main wind direction over the year 2017-2021 in the month of May was south-west, which might make the detection of vessels at the site less frequent. The François 1er lock is located at the entrance of the western tip of the industrial zone of Le Havre, as presented in Figure 5-2, in perspective of the environmentally-classified industries of the industrial park, potential emitters of VOCs. The main activity in this zone is linked to chemical industry, as well as refinery and coking. The site was located 120 m west from a lock bridge and approximately the 300 m east from the second lock bridge, as presented in Figure 5-2. Hence, a road surrounded the site leading from and to the bridges, seeing traffic from both cars and trucks involved in the exchanges in the port. Measurements were taken using an Atmo Normandie's mobile station, as shown in Figure 5-6a. Its instruments sampled ambient air from a 3 m high mast to capture plumes from ships idling in the lock or arriving to and from the nearby docks.

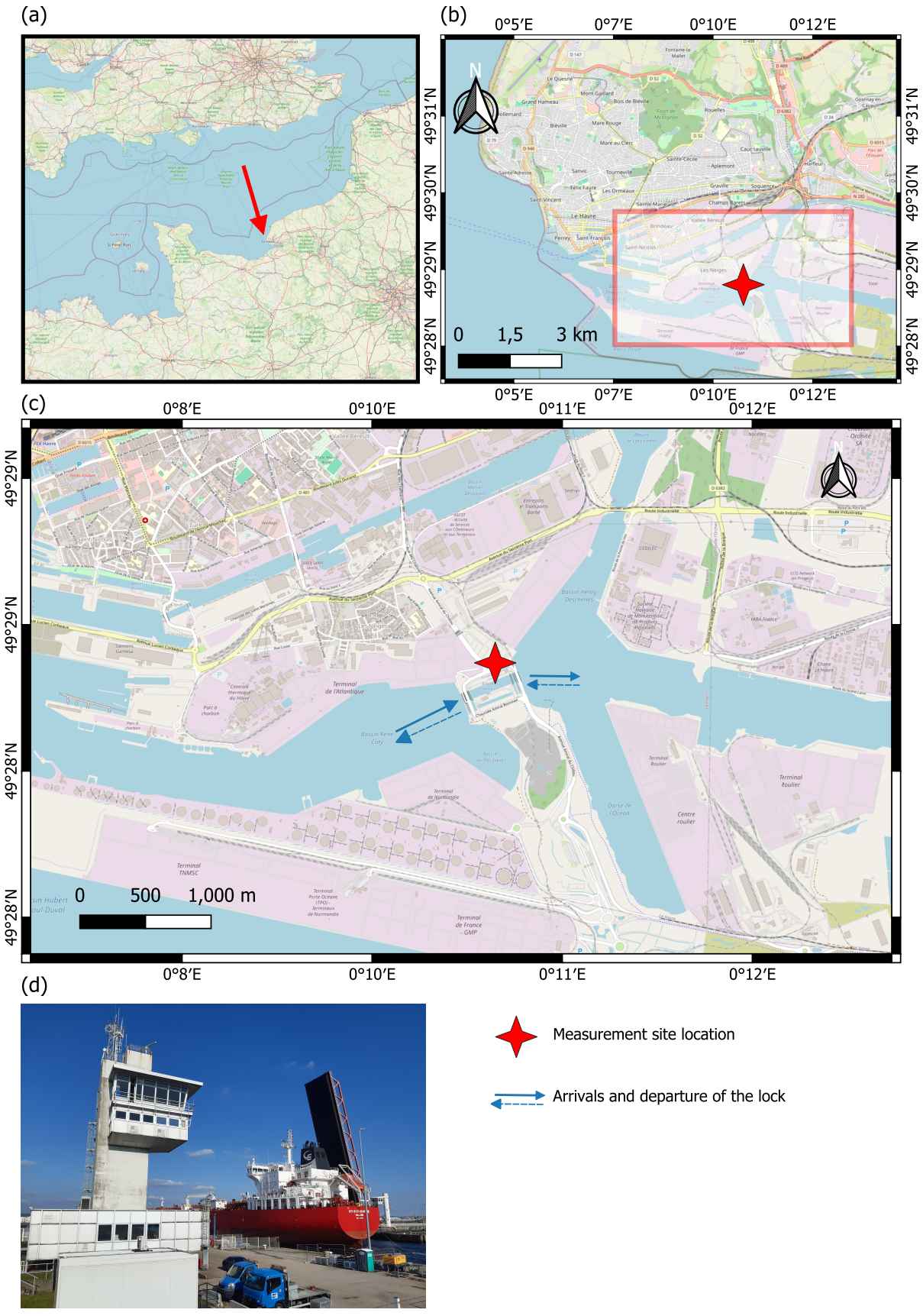

Figure 5-1: *Location of the measurement site at the "Écluse François 1er" in Le Havre. (a) Location of Le Havre in France; (b) Location of the lock in Le Havre; (c) Location of the measurement site next to the terminal and the industrial zone; (d) View on the lock and the bridge used to cross it.*

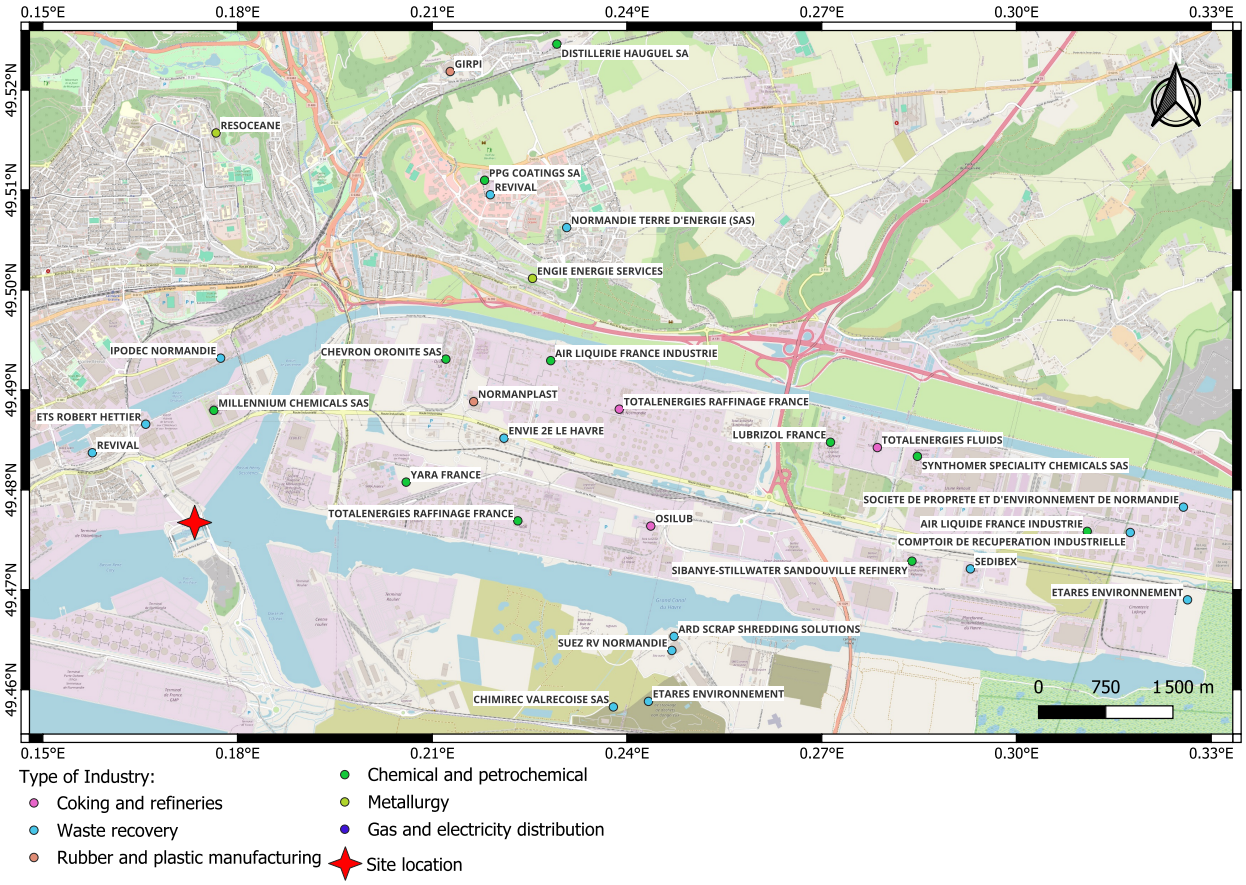

Figure 5-2: *Location of the site in the harbour of Le Havre, in perspective of environmentally classified industries of the industrial park. Spatialized data were taken from the GéoRisques French state data hub. An important number of storage facility of unspecified various materials are present therefore not documented in this map.*

5.2.a.ii Description of criteria pollutants

Various regulated and unregulated pollutants were monitored as summarized in Table 5-1 . Regulated pollutants were measured by the instruments deployed by Atmo Normandie and IMT Nord-Europe measured VOCs using compact GC-FID systems. Meteorological data were also recorded on top of a 10 m-high mast. Throughout the campaign, the temperature remained steady, with temperatures ranging down to 8°C during the night up to 22°C during the day, representative of spring weather.

Table 5-1: *Key pollutants under focus in the campaign of Le Havre.*

Compounds	Instrument	Principle	Time resolution
VOC	Chromatotec C_2-C_6	Gas Chromatography (GC)	60 min
	Chromatotec C_6-C_{12}	Gas Chromatography (GC)	60 min
CO_2, CO, CH_4, H_2O	Picarro G2401	Cavity Ring-Down Spectroscopy (CRDS)	1 s
SO_2	Thermo 43i	UV-fluorescence detector	10 s
NO_x	Teledyne API 200E	Chemiliminescence detector	10 s
PM_{10}, $PM_{2.5}$, PM_1, C_n	PALAS FIDAS 200E	Optical light scattering	10 s
BC	ADDAIR MA350	Optical absorption	1 min
Particle Number	CPC	Optical counting	1 min
Wind direction, speed, RH, P°	Delta Ohm	Ultrasonic signals, capacitive silicon sensor	10 s

Figure 5-3 shows the wind rose for the Le Havre campaign in 2023. It evidences the almost exclusive influence of the NE wind, with winds reaching 8 $m \cdot s^{-1}$. This main wind direction corresponds to the direction of the canyon-like entrance to Le Havre from the eastern highway (A29) which is the city's most important gateway and passes through the town of Harfleur. In this same direction, there are two refrigerated cargo terminals, a logistics company with a container storage area and several industries. Notably, there is an industrial producer of lubricants, Chevron Oronite SAS. Another minimal wind direction ($< 1\%$ of occurrences) is west, suggesting a limited influence of the "Terminal de l'Atlantique" area.

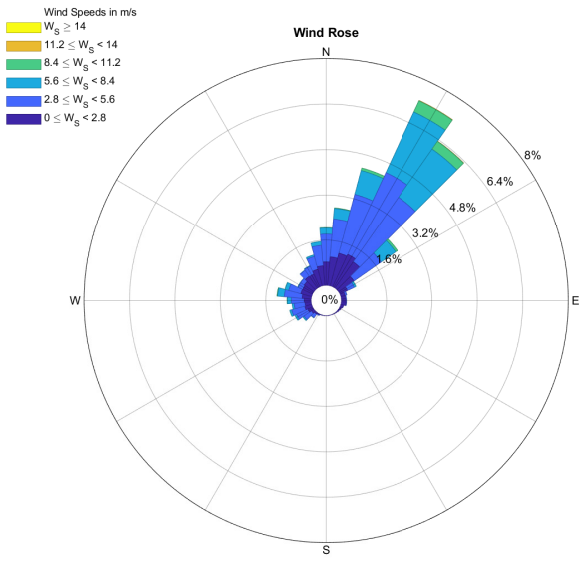

Figure 5-3: *Wind rose of the 2023 campaign of Le Havre.*

Figure 5-4 gathers the concentrations of a selection of criteria pollutants during the campaign, namely SO_2 (violet), CO (blue), NO and NO_2 (red and green) and particle number concentration from the CPC (olive). Each species exhibits transient increases in concentration, as illustrated by the maxima shown in Table 5-2. Figure 5-5a shows the diurnal cycle of the NO/NO_2 ratio, which exhibits its maximum during the day. This highlights the significative increases of NO emissions potentially linked to traffic exhaust close to the measurement site. This is confirmed by the diurnal cycle of NO, shown in Figure 5-5b, showing important increases at 8 am and 5 pm, as shown in Figure 5-5b. This is typical of the impact of traffic exhaust on concentrations (Badol et al., 2008a; Salameh et al., 2014). During the night, the median NO/NO_2 is below 0.1, but frequently exceeds the traffic exhaust value of approximately 0.08 (Kurtenbach et al., 2016; Brimblecombe et al., 2023).

Table 5-2: *Statistics of the concentrations of the criteria pollutants.*

Pollutants	mean	median	min	max	std
PM_1 ($\mu g \cdot m^{-3}$)	9.1	7.1	0.5	40.3	6.5
$PM_{2.5}$ ($\mu g \cdot m^{-3}$)	12.2	10.5	1.0	52.8	6.9
PM_{10} ($\mu g \cdot m^{-3}$)	17.7	16.7	1.3	102.8	8.3
C_n (particles$\cdot cm^{-3}$) – FIDAS	242.8	191.0	11.0	1124.0	175.3
NO (ppb)	3.2	0.6	0	721.5	13.0
NO_2 (ppb)	7.5	5.6	0	101.8	6.5
NO_x (ppb)	10.7	6.4	0	790.3	17.6
SO_2 (ppb)	0.8	0.3	0	253.6	1.8
CO (ppm)	0.1	0.1	0.05	4.8	0.03
CO_2 (ppm)	427.1	424.7	408.3	700.4	10.8
CH_4 (ppm)	2.1	2.1	2.0	3.4	0.1
H_2O (ppm)	1.1	1.1	0.5	1.7	0.2
C_n (particles$\cdot cm^{-3}$) – CPC	11,828.7	8,545.8	0.0	253,191.0	11,719.6

On average, the $PM_{2.5}$ measured by the FIDAS accounts for 67% of the PM_{10} mass, highlighting the impact of fine particles produced by industrial combustion, traffic exhaust or shipping. Furthermore, PM_1 contributes for 49% to the PM_{10}, emphasising the importance of ultrafine particles (UFPs). This is particularly evident when considering the particle number (PN) reported by the CPC, which shows multiple transient peaks reaching $2 \cdot 10^5$ for the most intense signals. The CPC had a smaller cut-off diameter than the FIDAS that reported smaller levels of PN, as observed in Table 5-2, confirming the importance of UFPs to the PM concentrations in Le Havre.

As SO_2 was identified as a tracer for ship emissions in Dunkirk, its correlation with ship passage through the lock was examined in Le Havre. The history of the lock activities was made available and the period corresponding to the ship's passage was extracted. Ship emissions were expected to be intercepted upon arrival at, transit through and departure from the lock. However, as the site mainly encountered wind from the north, there were only very few favourable wind periods for sampling ship plumes, unlike in Dunkirk. Therefore, no correlation between the presence of ships and peaks in SO_2 was found and SO_2 could not be attributed unambiguously to ship emissions.

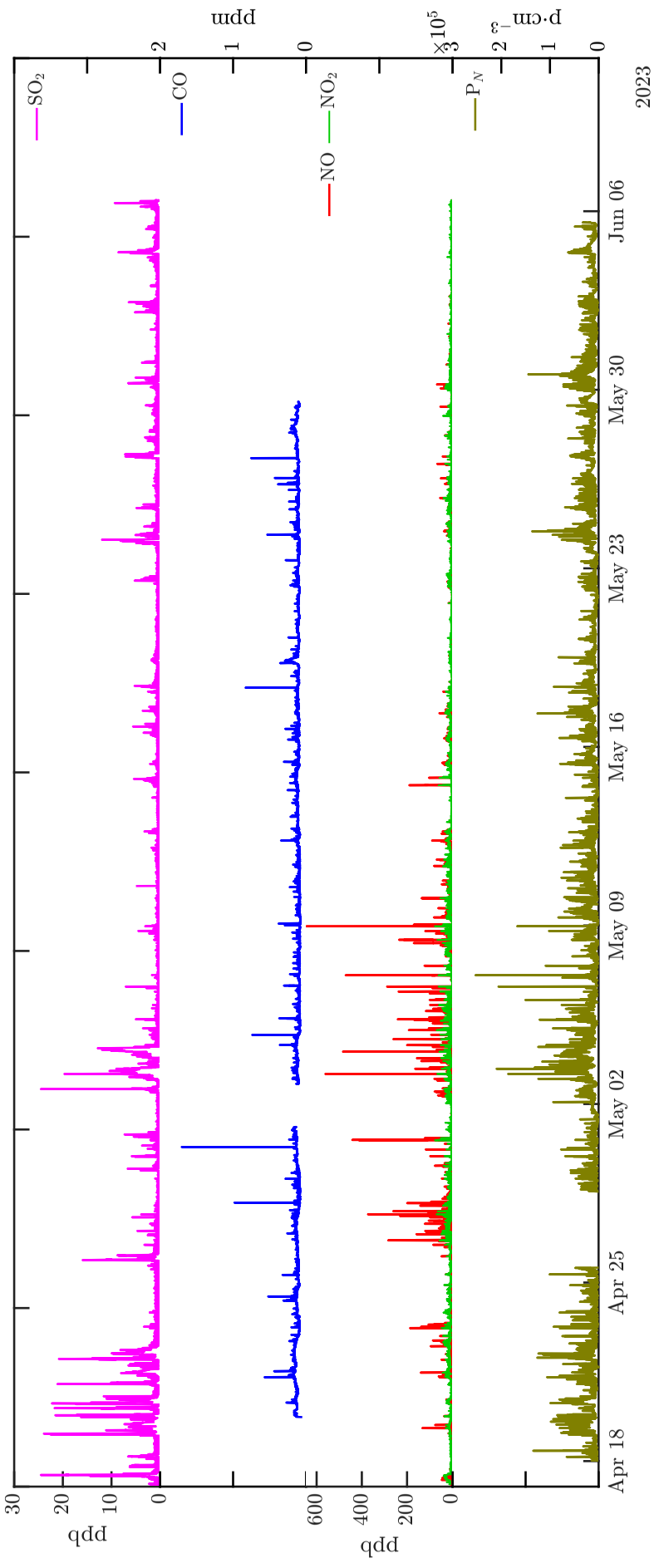

Figure 5-4: *Time series of criteria pollutants; violet: SO_2 (ppb); blue: CO (ppm); red: NO (ppb); green : NO_2 (ppb); olive: PN (particles·cm^{-3}, CPC).*

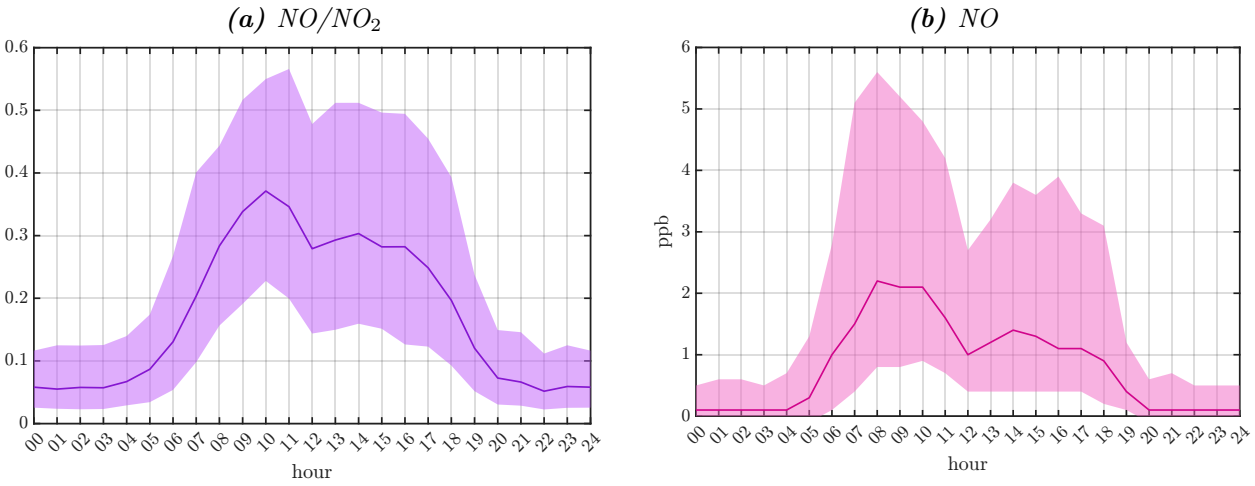

Figure 5-5: *Diurnal cycles related to NO_x, local time. Full lines: hourly medians; shaded area: hourly Inter-Quartile Range (IQR), 25th -the 75th percentiles.*

5.2.b VOC measurements in Le Havre

5.2.b.i Operation of the TD-GC-FID

Two gas chromatography analyzers (TD-GC-FID, AirmoVOC, Chromatotec), one for light VOCs (C_2 – C_6) and one for heavier VOCs (C_6 – C_{20}), were set up in the station as seen in Figure 5-6b and operated according to the same principle as described in Section 2.2.a. The analyzers were installed in a rack alongside a hydrogen generator (Hydroxychrom, Chromatotec) and a calibration unit (AirmoCAL, Chromatotec). Briefly, the AirmoCAL enables automatic dilution during calibration from an external cylinder via two mass flow controllers (MFCs).



(a) *View on the lock where a LNG tanker is passing, with the mobile station in forefront.*

(b) *VOC measurement bay.*

Figure 5-6: *Various views of the measurement site of the 2023 campaign in Le Havre.*

Ambient air was sampled from the 3 m high mast and brought to the AirmoCAL via a heated line to avoid condensational losses. The C_6 – C_{20} was supplied in ambient air by the AirmoCAL through a heated line. The air sample entering the C_2 – C_6 AirmoVOC passed through a Nafion membrane to remove water. Both GCs were supplied with H_2 from a hydrogen generator (Hydroxychrom), which was fed with Ultrapure water and zero air from the AirmoCAL. Chromatograms were integrated using the Vistachrom 1.6 software (Chromatotec). Peak areas that did not exceed the minimum value during integration were considered inferior to the Limit of Detection. The minimum area detectable for integration was set at 50 u.a., which was then retained as the LOD area and further converted into concentration unit. During calibration, an NPL cylinder was connected to the AirmoCAL's calibration inlet, diluting the VOC concentration of the cylinder from 200 ppb to 1 ppb. The content of the NPL cylinder is detailed in Appendix DT1 and allowed the calibration of 28 compounds. The blank corrections of the chromatogram were performed automatically on the C_6 – C_{20}, and manually for the C_2 – C_6 on 05th April, no peak above the LOD has been detected so no correction was performed. Calibrations were performed at the beginning of the campaign, on the 02nd of May, and at the end of the campaign, on 06th June 2023. Four repetitions were taken for each calibration and the last three were used to calculate the average calibration factors (area/ppt). The results are detailed in Figures 5-7a and 5-7b for C_2 – C_6 and C_6 – C_{20}, respectively, for the compounds present in the calibration cylinder. The two calibrations show overall a good agreement, except for propane, which displays significant deviations in the calibration factors. This led to significant uncertainties in the final concentrations for this compound. 2-Methylpentane and n-hexane were analysed on both instruments, but the relative standard deviation was greater for the calibration on the C_2 – C_6 (23% and 8% for 2-methylpentane and hexane, respectively) than for C_6 – C_{20} (14% and 3%, respectively) instrument. Therefore, the C_6 – C_{20} AirmoVOC will be used to determine their final concentrations in the observations. In addition to the VOCs presented in these figures, significant peaks were observed in the chromatograms corresponding to heavy alkanes starting from C_8/C_9, with an important peak between the retention times of m&p-xylenes and ethylbenzene and continuing to C_{16}. The uncertainties of the GC measurements were calculated using the methodology described in Section 2.3.a.i, taking into account the systematic and random errors given in the GAW (2023) guidelines. Further, if the concentration of a compound is below its LOD, the concentration was replaced with half the LOD, and the associated uncertainty was replaced with 5/6 of the LOD (Norris et al., 2014). The uncertainties of the uncalibrated heavy alkanes were calculated by multiplying their concentrations by the median relative standard deviation (RSD) of n-heptane, their chosen reference compound. Additional validation of the VOC concentrations was performed by investigating the correlations of isopentane with pentane, isobutane with butane, and ethane with propane. This validation revealed n-pentane concentrations exceeding 30 $\mu g \cdot m^{-3}$, without any corresponding observation of isopentane. These values resulted from unrealistic integrations, since the actual n-pentane peak was below the detection limit and was therefore not captured correctly. The same was observed for n-butane, with concentrations exceeding 40 $\mu g \cdot m^{-3}$ without isobutane. In total, 38 outliers on 701 observations were removed from these validation, preparing the preliminary investigation of the VOCs in Le Havre.

(a) Calibration factors of 02nd and 06th June for the TD-GC-FID, C_2 – C_6.

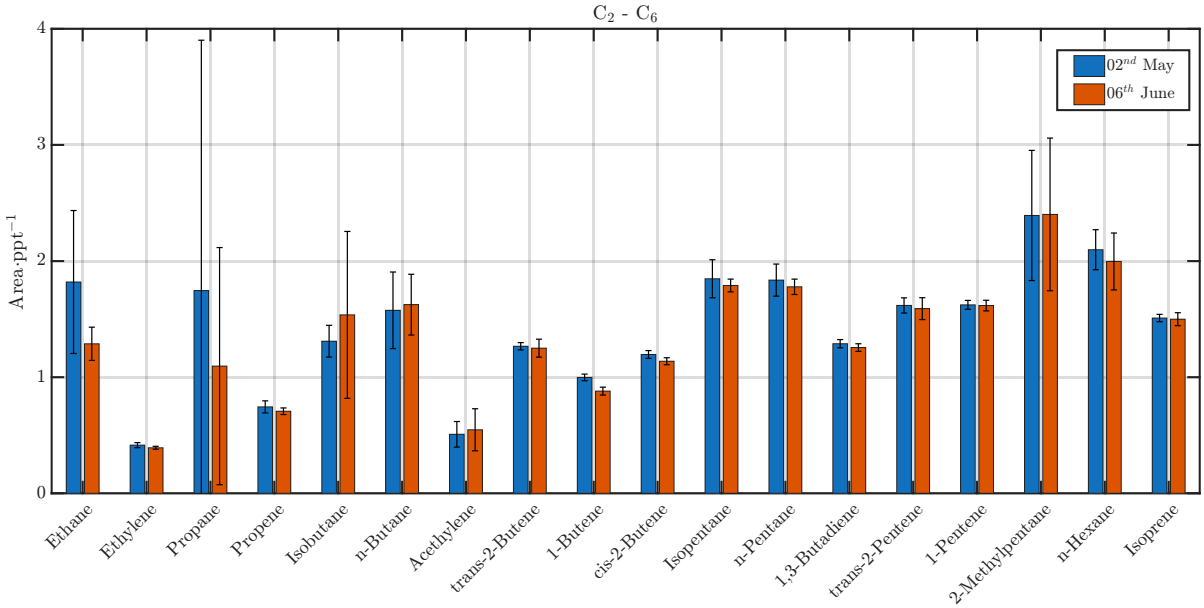

(b) Calibration factors of 02nd and 06th June for the TD-GC-FID, C_6 – C_{20}

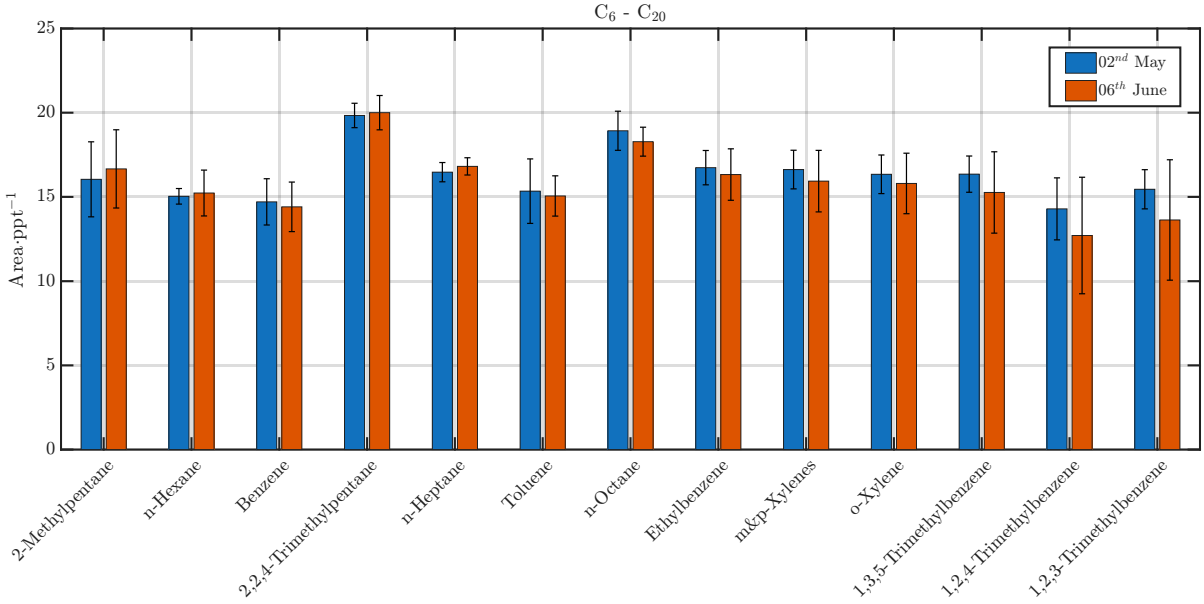

Figure 5-7: *Calibration factors of the two TD-GC-FID during the 2023 campaign of Le Havre.*

5.2.b.ii VOCs in Le Havre compared to Dunkirk

Table 5-3 summarises the statistics of the 36 VOCs measured during the campaign. It is worth noting that acetylene, cis-2-butene, trans-2-butene, 1-butene, trans-2-pentene and 1-pentene were calibrated, but never or almost never detected above the LOD. The low levels of 1-butene (0.06 ± 0.05 µg·m^{-3}) are inconsistent with the concentrations observed in Dunkirk, as it was a compound that was measured in a significant proportion in Dunkirk in September 2022 (0.77 ± 0.33 µg·m^{-3}), with all observations above the LOD. This concentration gap is surprising as 1-butene has an industrial origin and was therefore expected to be present in Le Havre, given that the sampling site was near an industrial area.

The low levels of 1-butene are likely due to its reactivity, meaning it reacted before being sampled. An issue with the Nafion membrane could be suggested as a technical reason, but this was not investigated further.

Table 5-3: *Statistical overview of the VOC concentrations observed in the 2023 campaign of Le Havre. Concentrations are expressed in µg·m^{-3}.*

Compound	mean	median	min	max	std	% >LOD
Ethane	0,66	0,62	0,02	2,19	0,21	99,8
Ethylene	0,09	0,07	0,07	3,56	0,22	1,1
Propane	0,57	0,14	0,03	17,47	1,56	89,9
Propene	0,13	0,06	0,06	33,21	1,33	1,2
Isobutane	0,09	0,04	0,04	1,38	0,16	16,7
n-Butane	0,24	0,04	0,04	6,06	0,54	46,5
Acetylene	0,06	0,05	0,05	7,91	0,30	0,3
1-Butene	0,06	0,06	0,06	1,09	0,05	0,5
Isopentane	0,07	0,04	0,04	0,95	0,10	14,1
n-Pentane	0,11	0,04	0,04	1,15	0,13	48,5
1,3-Butadiene	0,04	0,04	0,04	0,48	0,02	0,2
2-Methylpentane	3,00	2,33	0,04	9,06	1,61	99,8
n-Hexane	0,11	0,09	0,01	0,47	0,07	98,5
Benzene	9,61	8,85	0,01	54,95	11,06	58,4
2,2,4-Trimethylpentane	0,13	0,01	0,01	0,78	0,18	45,3
n-Heptane	0,11	0,10	0,01	1,49	0,12	72,5
Toluene	0,03	0,01	0,01	0,84	0,08	34,2
n-Octane	0,02	0,01	0,01	0,29	0,03	35,9
Ethylbenzene	0,05	0,03	0,01	0,50	0,07	69,8
m&p-Xylenes	0,04	0,03	0,01	0,26	0,03	80,0
o-Xylene	0,05	0,05	0,01	0,32	0,03	98,0
1,3,5-Trimethylbenzene	0,03	0,02	0,01	0,14	0,02	68,3
1,2,4-Trimethylbenzene	0,04	0,04	0,01	0,20	0,03	81,4
1,2,3-Trimethylbenzene	0,66	0,63	0,01	1,53	0,27	99,5
C_8/C_9	5,49	5,37	4,31	7,41	0,64	99,8
C_{10}	2,01	1,98	1,48	2,68	0,25	99,8
C_{11}	0,90	0,89	0,69	1,29	0,10	99,8
C_{12}	0,60	0,59	0,43	1,17	0,08	99,8
C_{13}	0,36	0,35	0,01	0,55	0,05	99,5
C_{14}	0,26	0,25	0,05	0,67	0,04	99,8
C_{15}	0,21	0,21	0,01	0,42	0,05	97,0
C_{16}	0,06	0,02	0,01	0,90	0,09	53,2

Opposingly, benzene appears to be the most abundant VOC, however, a significant dispersion in the benzene peak intensity and retention time was observed during integration, and the cause remains uncertain. The mobile lab was equipped with a CPC operated using butanol, which is known to interfere with benzene on the chromatogram. However, the CPC was equipped with a catalytic oven and tests performed to check the air tightness of our set-up revealed no leaks from inside the lab. Therefore, our best guess is that the catalytic oven did not oxidize all butanol and that the remaining butanol rejected outside the lab, was sampled by the GCs through the sample inlet. Therefore, the concentrations of benzene should be interpreted with great caution. 1,3-Butadiene was the only VOC suspected by Atmo Normandie to be emitted in quantities exceeding exposure limits in the industrial area. It was not detected at significant levels in the harbour of Le Havre during the 2023 campaign, measured on average at 0.04 ± 0.02 µg·m^{-3} by the TD-GC-FID. This confirms the observations of Atmo Normandie that these species are not present at significant levels next to the city.

This may be because the releases of the investigated industries were too infrequent to cause long-term levels above the exposure limits, or because their emissions reacted prior to reaching the site, as was suspected for 1-butene. The comparison of the 20 most abundant VOCs (without considering benzene) between the Dunkirk and Le Havre campaigns, in term of average concentration, is presented in Figure 5-8. It shows that the heavy alkanes (C_8–C_{11}) are the most abundant compounds observed in Le Havre, and are a specificity of this site, as the heavy alkanes are small contributors in Dunkirk, with nonane being the 17th compound among the species measured in common. 2-Methylpentane is the second VOC in Le Havre but measured in lower levels in Dunkirk. Therefore, the Le Havre site was influenced by a more significant source of 2-methylpentane than the Dunkirk site, making this a specificity of the campaign. Finally, the levels of toluene are lower in Le Havre than in Dunkirk, where toluene emissions were associated to methanol. In Le Havre, methanol was not measured and we can thus not identify the same source as in Dunkirk.

The uncertainties associated to the measurements are presented in Table 5-4 alongside their SNR, which was calculated in accordance with Norris et al. (2014). As expected, propane showed the greatest uncertainty due to its high variability during calibration, with an average uncertainty of 0.92 ± 2.79 µg·m^{-3}, 1.3 times its average concentration. Therefore, its SNR is 0, as no observation is greater than its uncertainty. The same observation is made for ethylene, which also displays an SNR of 0.12 despite its stable calibration.

Figure 5-9 shows the total VOC concentrations measured by the TD-GC-FID over the course of the campaign. It confirms that the wind direction was predominantly from the north, with little deviation throughout the campaign. No wind data is available from May 23th to June 1st. Unlike in Dunkirk, there are no intense, punctual peaks in the sum of VOCs and the levels in Le Havre exhibit more evident cyclical behaviour, with 2-methylpentane being the most significant VOC with this pattern. Indeed, a clear diurnal cycle is evident in the VOC sum, as shown in Figure 5-10a. Average concentrations observed during the day are lower than night-time levels, linked to the height of the boundary layer as observed in Figure 5-10b, marking a stronger impact of meteorology on the VOCs in Le Havre compared to Dunkirk.

Individual inspections of the diurnal cycles of the VOCs observed in Le Havre reveal similar dispersion-related diurnal patterns for some VOCs, as demonstrated for 2-methylpentane (Figure 5-11a) and hexane (Figure 5-11b), both of which are prevalent VOCs in the study. They reach a maximum in the early morning at 6 am, and show a minimum in the middle of the afternoon, after which their concentration increases at the beginning of the night . While these two VOCs can be linked to gasoline consumption, the highest concentrations are found under wind directions coming from the industrial zone in the east, as can be seen in the NWR plots for 2-methylpentane and hexane in Figures 5-12a and 5-12b, respectively. Therefore, these two compounds share coherent evolution, as presented in Figure 5-13.

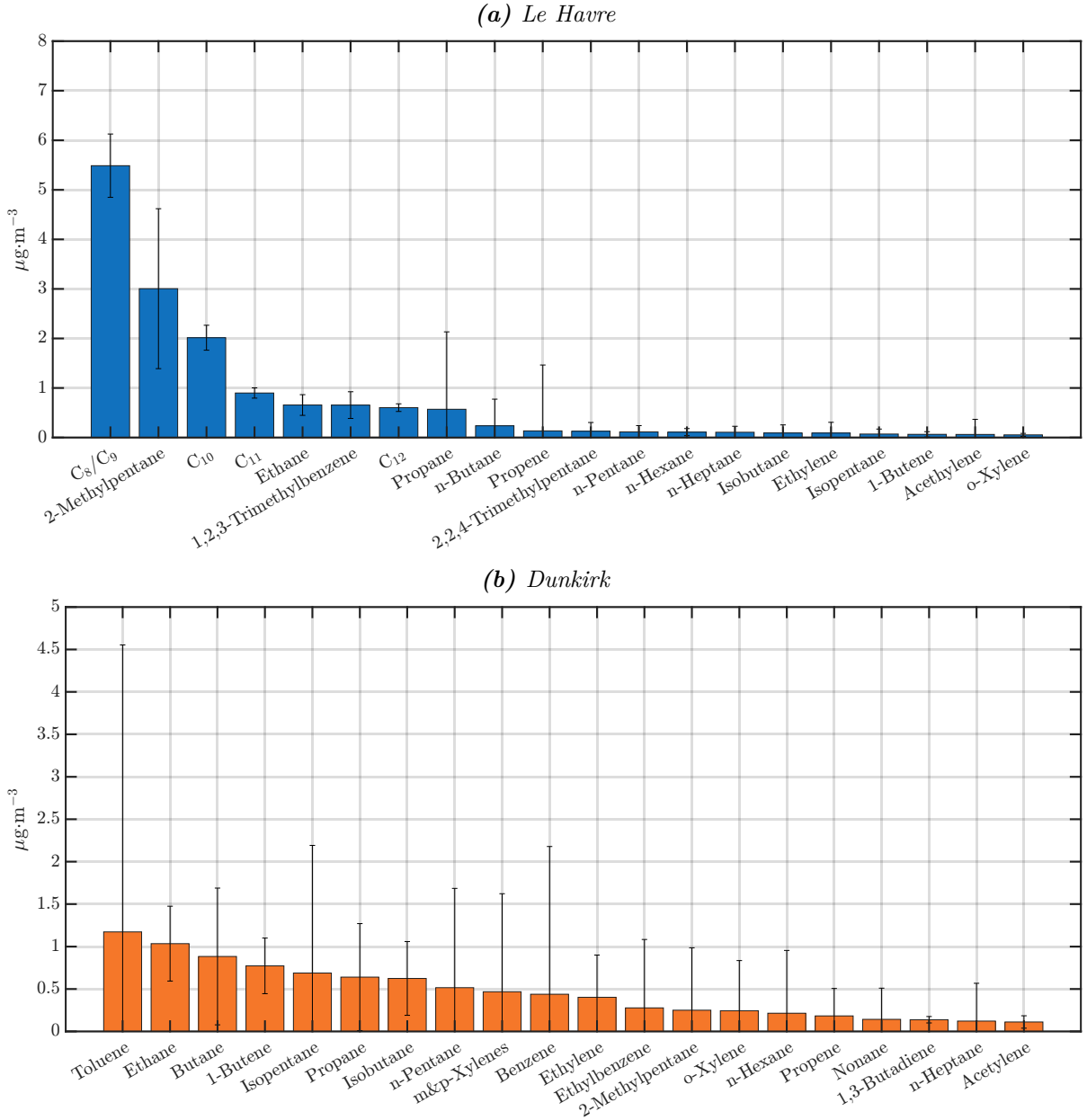

Figure 5-8: *Top 20 most abundant VOCs based on their average in each campaign, respectively (a) Le Havre (without benzene) and (b) Dunkirk, selected for the common species with Le Havre. Error bars: the standard deviation throughout the campaigns.*

Butane and propane, show a sharp peak at 8 am, after which they decrease, as shown in Figures 5-14a and 5-14b. They share a common origin, as seen in Figure 5-15a and 5-15b, in the direction of the industrial zone and follow a similar temporal evolution, as displayed in Figure 5-16. This figure also evidences an interesting co-variability of propane/butane with two other VOC, n-pentane and n-hexane. Overall, the highest concentrations are observed under wind direction coming from the industrial zone, as can be seen in the NWR plot of the sum of VOC concentrations in Figure 5-17. This shows that, although the area was mainly affected by winds bringing air masses from the Le Havre highway entrance, the most intense VOC concentrations occurred when the site was downwind of the industrial zone, which was also observed in Dunkirk.

Table 5-4: *Statistical overview of the uncertainties of the VOC measurements in the 2023 campaign of Le Havre. Uncertainties are expressed in $\mu g \cdot m^{-3}$.*

Compound	mean	median	min	max	std	SNR
Ethane	0,21	0,20	0,03	0,70	0,07	2,1
Ethylene	0,12	0,12	0,10	0,20	0,004	0,1
Propane	0,76	0,20	0,05	23,19	2,07	0
Propene	0,10	0,10	0,08	2,12	0,08	0,1
Isobutane	0,08	0,07	0,07	0,57	0,06	0,2
n-Butane	0,09	0,06	0,06	1,26	0,10	1,0
Acetylene	0,09	0,08	0,08	2,51	0,09	0,004
Isopentane	0,07	0,07	0,06	0,09	0,003	0,4
n-Pentane	0,06	0,07	0,06	0,10	0,005	1,0
1,3-Butadiene	0,07	0,07	0,06	0,07	0,0004	0,01
2-Methylpentane	0,46	0,36	0,06	1,34	0,23	5,4
n-Hexane	0,03	0,03	0,01	0,04	0,003	2,6
Benzene	1,00	0,92	0,01	5,68	1,14	5,0
2,2,4-Trimethylpentane	0,01	0,01	0,01	0,04	0,01	5,9
n-Heptane	0,01	0,02	0,01	0,05	0,003	5,5
Toluene	0,02	0,01	0,01	0,10	0,01	0,4
n-Octane	0,01	0,01	0,01	0,02	0,002	0,9
Ethylbenzene	0,01	0,01	0,01	0,04	0,004	2,4
m&p-Xylenes	0,02	0,02	0,01	0,03	0,01	0,8
o-Xylene	0,03	0,03	0,01	0,04	0,002	1,0
1,3,5-Trimethylbenzene	0,02	0,02	0,01	0,03	0,003	0,5
1,2,4-Trimethylbenzene	0,03	0,03	0,02	0,05	0,01	0,6
1,2,3-Trimethylbenzene	0,13	0,12	0,01	0,30	0,05	3,9
C_8/C_9	0,86	0,84	0,67	1,16	0,10	5,4
C_{10}	0,32	0,31	0,23	0,42	0,04	5,4
C_{11}	0,14	0,14	0,11	0,20	0,02	5,4
C_{12}	0,09	0,09	0,07	0,18	0,01	5,4
C_{13}	0,06	0,06	0,00	0,09	0,01	5,4
C_{14}	0,04	0,04	0,01	0,10	0,01	5,4
C_{15}	0,03	0,03	0,002	0,07	0,01	5,4
C_{16}	0,01	0,004	0,002	0,14	0,01	5,4

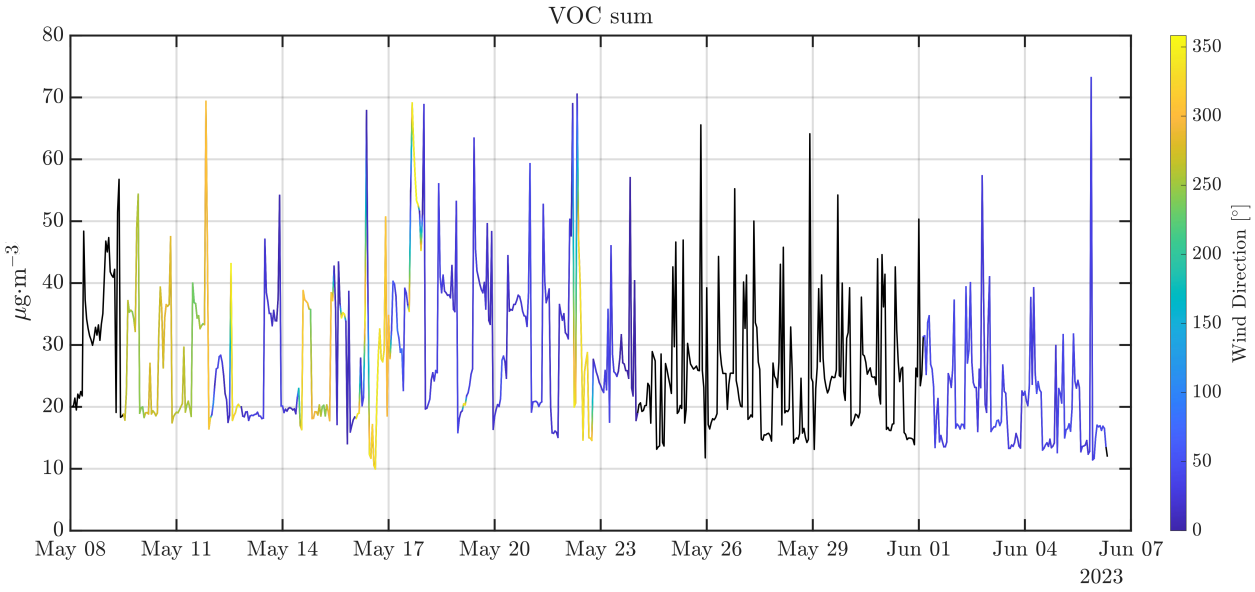

Figure 5-9: *Sum of the VOC concentrations from the TD-GC-FID observed in the 2023 campaign of Le Havre, color coded for wind direction. Black lines represent an absence of wind data.*

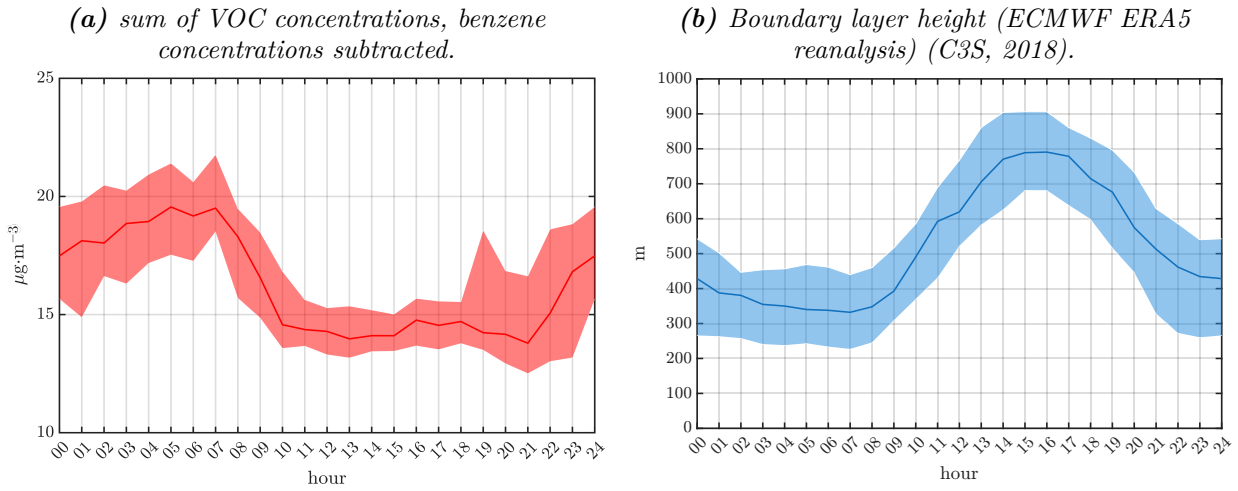

Figure 5-10: *Diurnal cycles of (a) summed concentration of the VOCs deducted from benzene, (b) Boundary Layer Height during the 2023 campaign of Le Havre, local time. Full lines: hourly medians; shaded area: hourly Inter-Quartile Range (IQR), 25th -the 75th percentiles.*

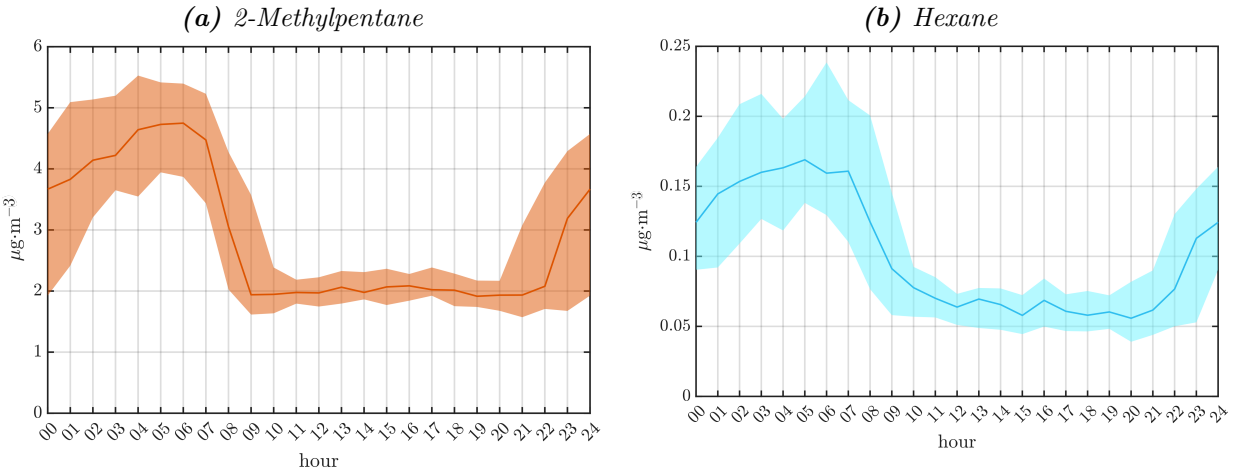

Figure 5-11: *Diurnal cycles of 2-methylpentane (a) and n-hexane (b) during the 2023 campaign of Le Havre, local time. Full lines: hourly medians; shaded area: hourly Inter-Quartile Range (IQR) (25th – 75th percentile)*

Although benzene measurements must be treated with caution, benzene does exhibit co-variability with certain species. This is evidenced by its similar temporal evolution with n-heptane, as represented in Figure 5-18, with higher concentrations observed during the daytime. This is an important consideration for benzene, as this common temporal evolution suggests a common source, and motivates its conservation in the database and use in the PMF approach despite the validation issues mentioned above.

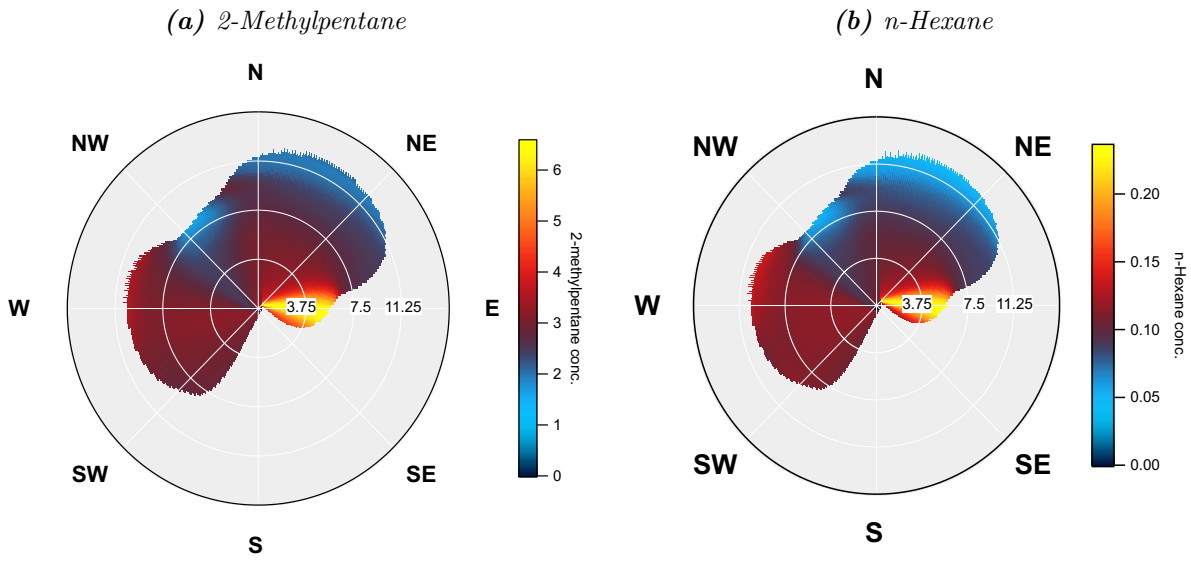

Figure 5-12: *Near Wind Regression (NWR) plots of 2-methylpentane (a) and n-hexane (b).*

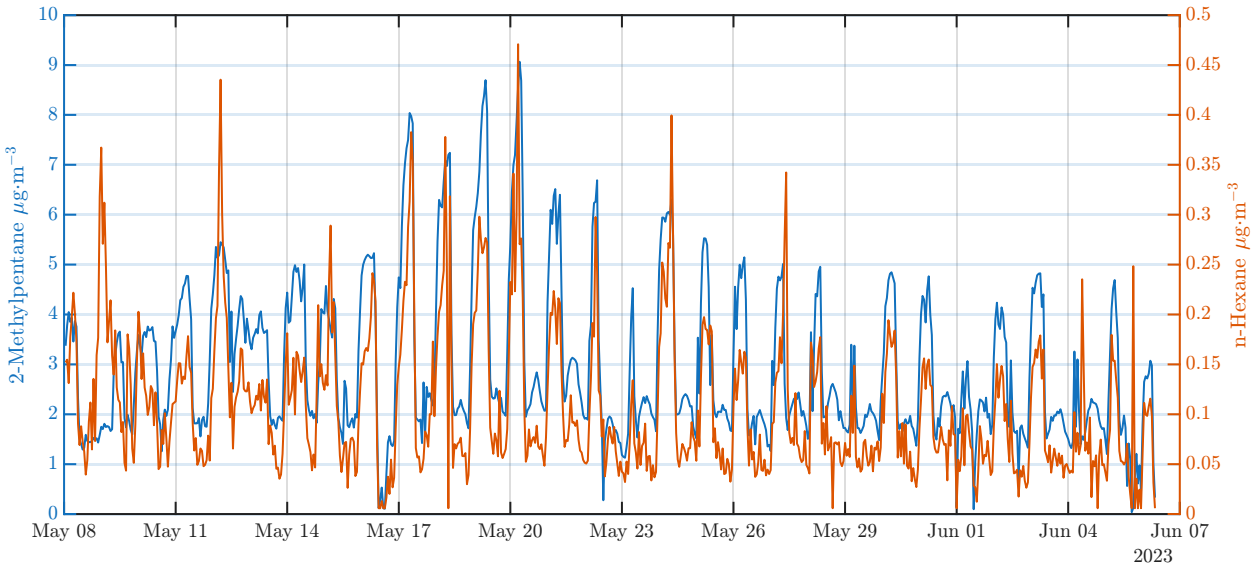

Figure 5-13: *Co-variability of 2-methylpentane (blue, left axis) with n-hexane (orange, right axis).*

The temporal evolution provided by the GC deployed in Le Havre could provide insights into the shipping profile on its own, other than in Dunkirk, as ships are transiting through the lock during minimum 20 minutes. On average, the duration of presence of a ship in the lock is 33 ± 9 min. Under dynamic conditions allowing to sample the shipping plumes, this could be sufficient to observe a significant contribution of the shipping fingerprint in the GC data. However, the predominantly NE wind directions were not favourable to the sampling of the shipping plumes. In Dunkirk, meteorological conditions were more favourable, with a low background period for probing ship plumes. In Le Havre, however, no such period is observed. The observed variability is mainly driven by meteorological factors and the shipping tracer used in Dunkirk, SO_2 , doesn't evolve in response to the presence of ships in the lock. In Le Havre as in Dunkirk, the highest concentrations of many VOCs are found coming from the industrial zone.

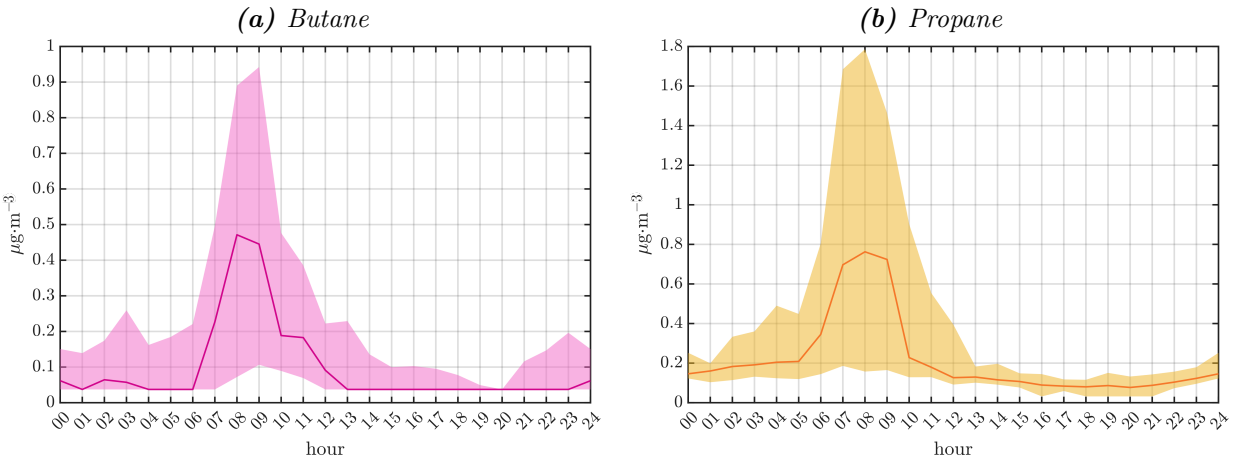

Figure 5-14: *Diurnal cycles of butane (a) and propane (b) during the 2023 campaign of Le Havre, local time. Full lines: hourly medians; shaded area: hourly Inter-Quartile Range (IQR) (25th -75th percentile)*

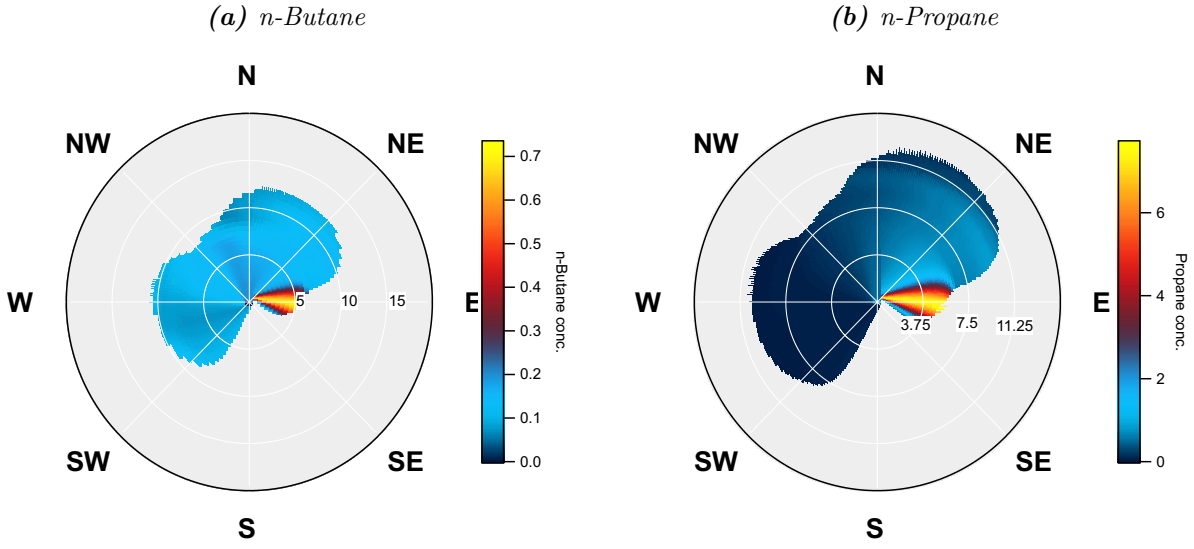

Figure 5-15: *Near Wind Regression (NWR) plots of n-butane (a) and n-propane (b).*

Therefore, as the NWR plot of the GC-PMF profile linked to shipping emissions in Dunkirk was observed to originate from the refinery zone using the 1 hour time resolution, a more in-depth analysis of the data using PMF could potentially reveal ship emissions in Le Havre using the co-variability of species discussed previously.

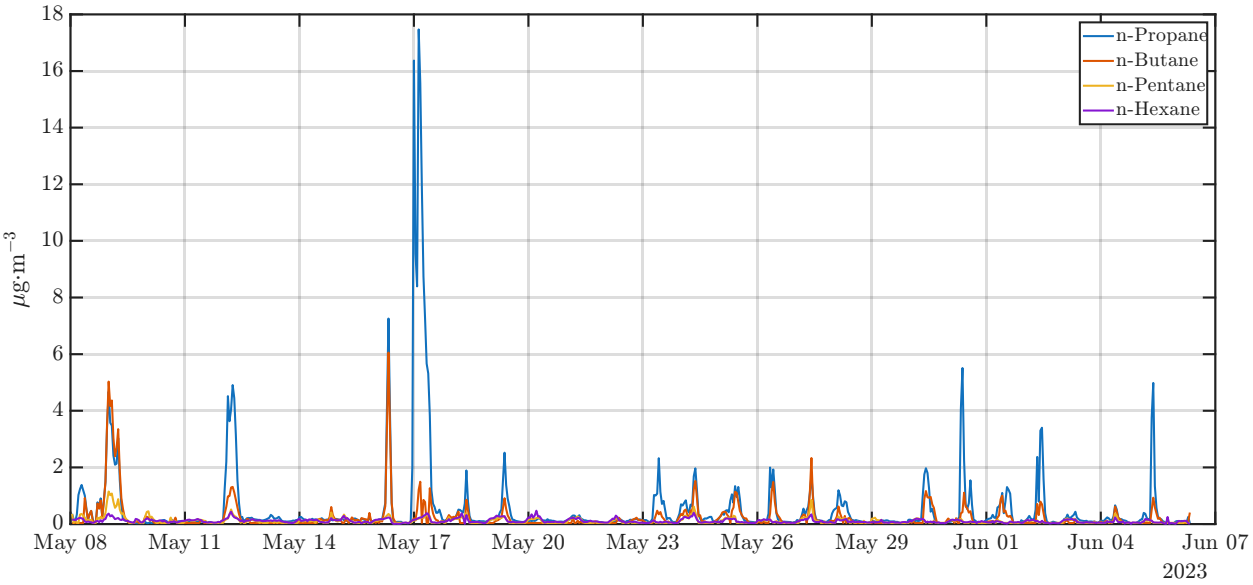

Figure 5-16: *Time series of n-propane, butane, pentane and hexane.*

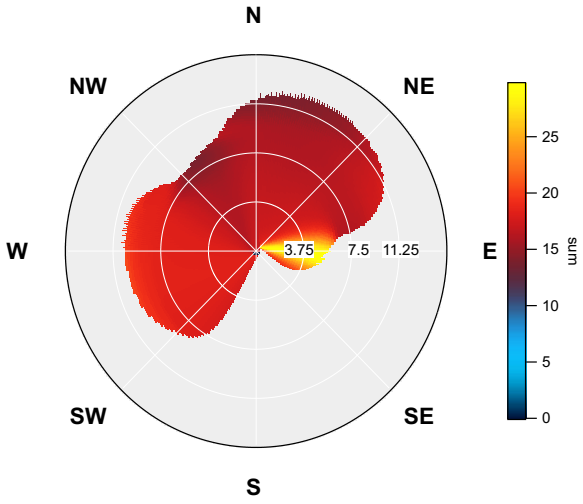

Figure 5-17: *Near Wind Regression (NWR) plots of the sum of VOCs.*

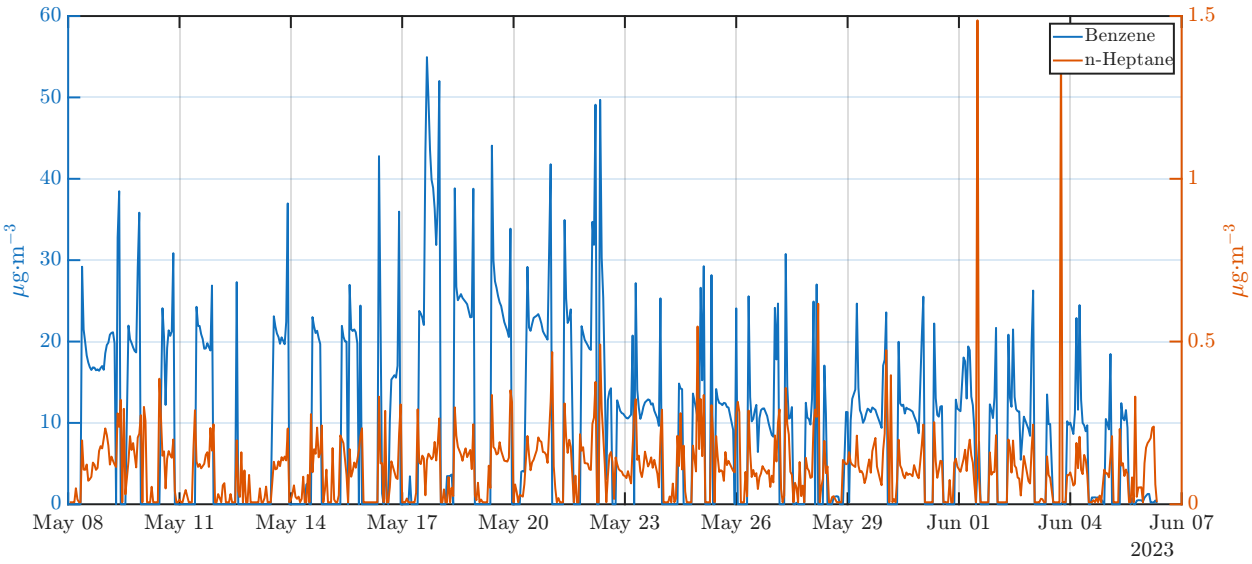

Figure 5-18: *Time series of benzene (blue, left axis); and n-heptane (orange, right axis).*

5.3 Indications on a shipping profile in Le Havre

Upon validation and first investigations of the VOC concentrations, a PMF source apportionment was performed in order to try the resolution of a shipping factor that could be compared with the profile obtained in Dunkirk. This section describes the preliminary PMF analysis performed with the data of the 2023 campaign in the harbour of Le Havre, which provides the first insights and perspective on the robustness of the shipping factor.

5.3.a Stabilizing a PMF solution

The validated input for VOCs results in a 666×36 matrix, which, from the quality criteria given by Norris et al. (2014) applied to Table 5-4, gives 20 compounds qualified as strong quality, 4 as weak and 11 as bad, including the high uncertainty of propane and the pollution of benzene. As a first try, this input matrix was used but no stable solution was found, as the Q/Q_{exp} varied greatly between the different solutions obtained and the correlation coefficient between modelled and observed concentrations didn't exceed 0.2. To understand the reason of this poor modelling, the EPA PMF 5.0 was used with adjusted inputs. It was found that the instability of the PMF solutions was mainly due to the combination of low concentrations and high uncertainty, in particular for propane. This unusually high uncertainty in the propane measurement originates from the calibration at the start of the campaign as previously shown. However, an issue with the calibration on the C_2 – C_6 AirmoVOC would impact several VOCs, which is not the case here. Therefore, we concluded that this error was due to a one-off error in the experiment rather than a systematic analytical issue. Therefore, the uncertainty of propane was lowered to 15% of its initial value to bring it closer to standard calibration conditions. This led to propane being considered of 'strong' quality in the PMF input. Furthermore, benzene was assumed to be subject to signal interference and was initially classified as 'bad' in the first PMF inputs. However, as shown in Figure 5-18, benzene co-evolves with n-heptane. Although there is still some uncertainty regarding the observed concentrations for benzene due to technical issues, its co-variability with n-heptane supports its classification as 'strong' quality.

5.3.b Overview of the factors

Based on these hypotheses, the most stable solution was a 7-factor solution with an $R^2 = 0.75$ between the observed and modelled concentrations. Figure 5-19 shows the time series and the profiles of each factor of this solution. In brief, the profiles display a clear benzene factor, represented by Factor 6 (dark blue), which is linked to the high levels (30 µg·m^{-3}) displayed by this compound, resulting in a factor explaining the majority of the modelled benzene (87.4%), with minor contributions of 2-methylpentane and C_8/C_9. This factor represents the highest concentrations in this PMF solution. The co-variability of benzene with heptane can be found in Factor 2 (orange), which represents the smallest factor in terms of mass fraction. Besides benzene and heptane, further contributions of 2-methylpentane and the C_8/C_9 alkane are found in this factor, whose levels seem particularly influenced by atmospheric dynamics. Factor 2 explains most of the 2-methylpentane (91.6%). Overall, these two compounds are present in relatively high quantities in many factors, such as Factors 1 and 3, which are potential regional background factors.

Factor 4 explains the presence of n-pentane, 2-methylpentane, n-hexane, ethylbenzene and 1,3,5-trimethylbenzene to the greatest extent, and these compounds are potentially linked to traffic exhaust emissions. Surprisingly, BTEX compounds are poorly represented in the PMF, and their resolution could be improved.

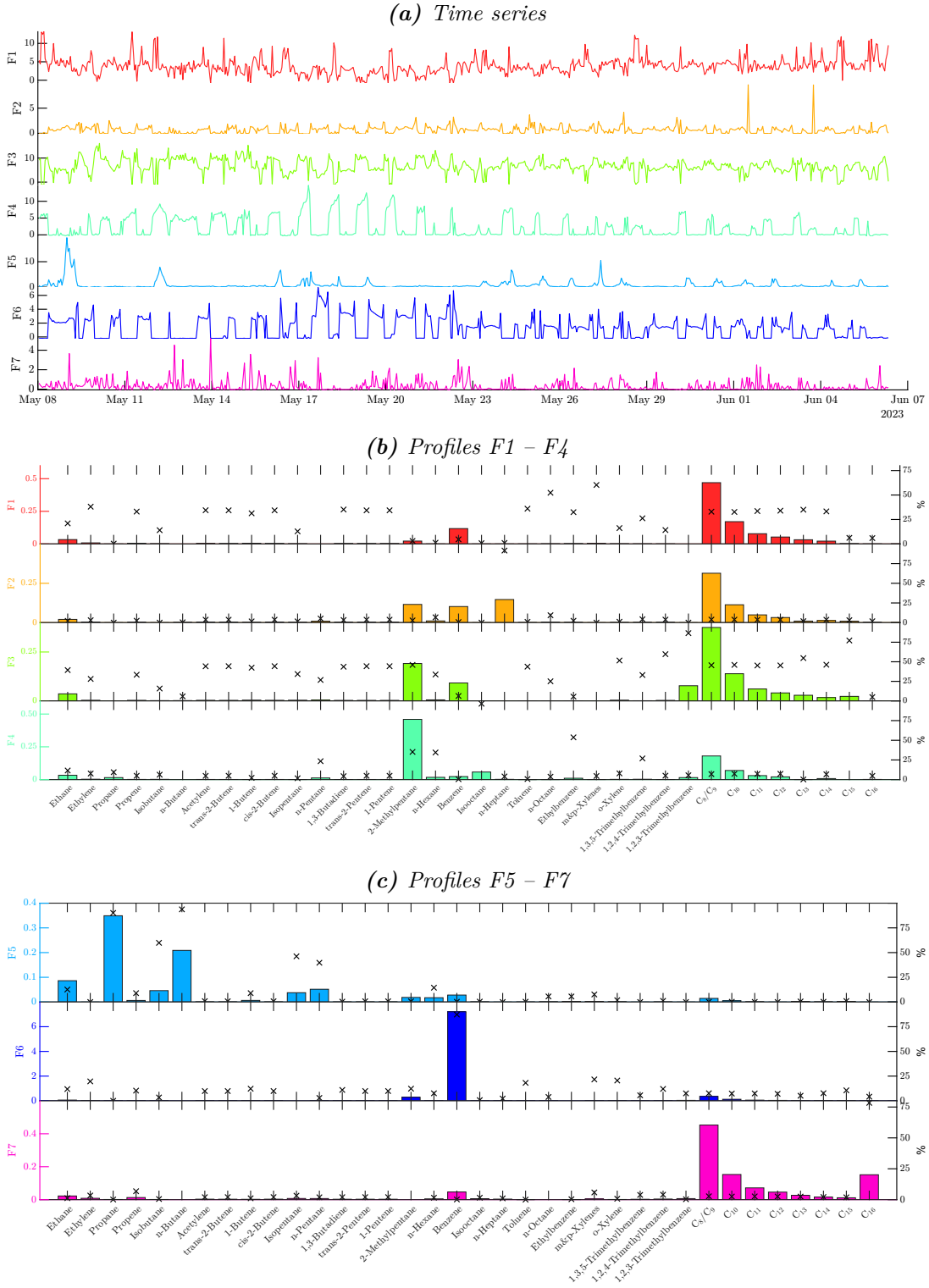

Figure 5-19: *Time series and profiles of the 7-factor solution. (a) Time series ($\mu g \cdot m^{-3}$) of each factor and chemical profiles of (b) Factors 1, 2, 3, 4 and (c) Factors 5, 6, 7 . Left axis (blue): contributions to the profile ($\mu g \cdot m^{-3}$); right axis (red): contributions to the variable (%). Absence of black cross means that the factor contribution is 0.*

This section will focus on Factor 5 (shown in light blue in the time series in Figure 5-19a) to highlight the perspective of this work. Interestingly, its exhibits transient peaks, some of which overlap with those of SO_2, as illustrated in Figure 5-20. Since SO_2 was identified as a ship emission tracer in Dunkirk, this correlation motivates a comparison with the shipping profile obtained in Dunkirk. Figure 5-21 compares the GC profile in the fully constrained MTR-PMF of Dunkirk, considered the most representative of ship emissions there, with Factor 5 in Le Havre. The two factors are primarily composed of light VOCs, such as propane, n-butane, and ethane. The two factors also contain isopentane, pentane, 2-methylpentane, n-hexane and benzene in similar proportions. These two profiles are compared using the Person-Distance (PD) and the Similarity-Identity-Distance (SID) (Belis et al., 2015), as performed in the comparison of the profiles obtained in Dunkirk. Based on the common species presented in Figure 5-21, the PD is 0.6, above similarity criteria (< 0.4), and the SID is 0.97, just meeting the satisfaction criterion ($0 - 1$). However, the lack of similarity can be explained by the absence of common species. Ethylene and propene are not present in Factor 5 in Le Havre because their levels were too low to be detected, therefore, they were not resolved in any PMF factor. The same observation is made for acetylene and the butenes. The BTEX are also not present in significant proportion because they were not properly resolved in this PMF. Therefore, the quality of the data should be investigated further in order to improve the modelling of the compounds expected in a 'shipping' factor. This factor accounts for 5.7% of the modelled VOC concentrations, consistent with the contribution of shipping in Dunkirk and with the proportion of VOC from 'other transportation' in the regional emission inventories of Hauts-de-France (6.2%). The equivalent figure for Normandy wasn't found, but the 2023 contribution of the 'other transportation' sector to benzene emission in Normandy was 1.7%, while the contribution of the potential 'shipping' factor to ambient benzene concentrations is 0.26% based on these PMF results. The absence of details on the contribution of the aeronautical and railway sectors on the benzene inventory prevents the ranking of shipping compared to other sources in terms of VOC.

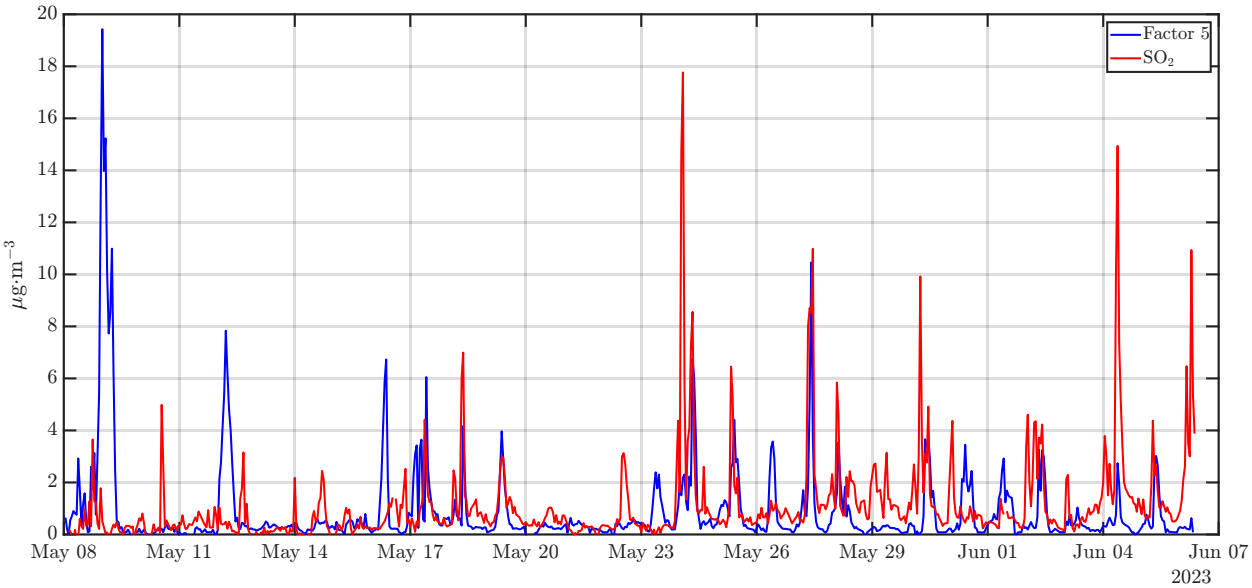

Figure 5-20: *Time series ($\mu g \cdot m^{-3}$). (blue): Factor 5 in the 7-factor solutions of Le Havre; (red): SO_2.*

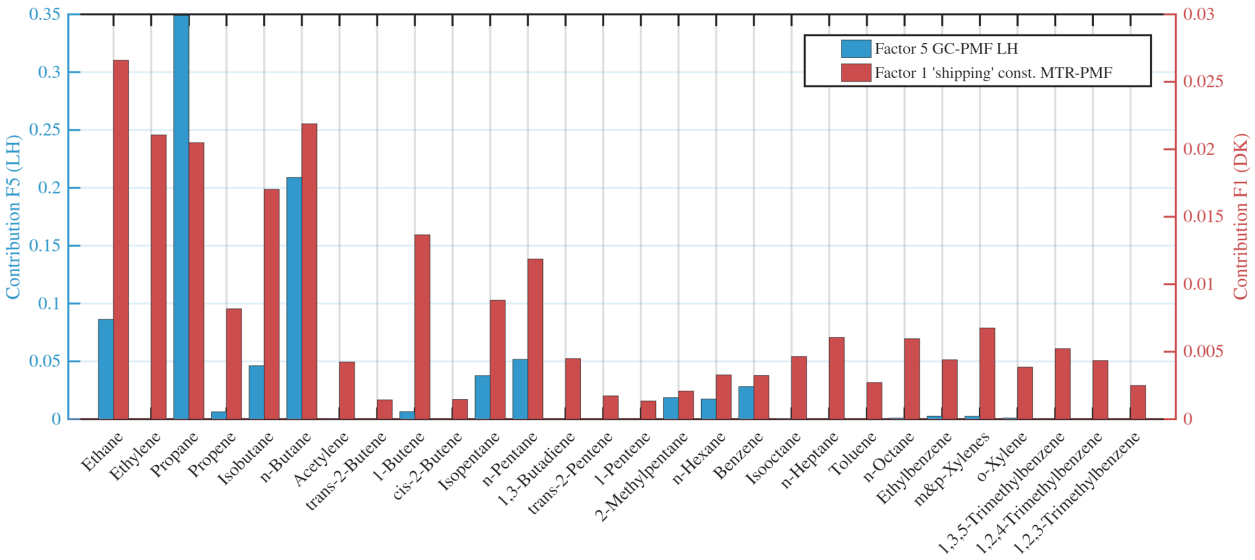

Figure 5-21: *Comparison of the GC profiles. (blue, left axis): GC profile of Factor 5 in the 7-factor solutions of Le Havre; (red, right axis): GC profile in the 'shipping' factor of the fully constrained MTR-PMF in Dunkirk (2022).*

5.4 Conclusion

This final chapter explores the robustness of a campaign in another industrial harbour in order to assess the representativeness of the shipping fingerprint determined in Dunkirk. This campaign took place between April and June 2023 in the harbour Le Havre, a representative industrial harbour that compares to Dunkirk and other European port. The site was located near a ship lock, used by ships to enter or leave the cargo terminal. This behaviour is expected to produce ship emission peaks upon arrival and departure of this lock the same way ships emitted in Dunkirk upon arrival and departure in the terminal. However, different types of ships were expected on this new location. Indeed, while in Dunkirk, the intercepted ship plumes were from ferries, the ships in the vicinity were mainly large cargo ships in Le Havre. Even if the main wind direction was north-east throughout the campaign, bringing in air from the direction of the highway, higher concentrations were met when the site was downwind from the industrial zone, although this occurred less frequently. In this context, the PMF using TD-GC-FID data was performed, requiring a reevaluation of the validation of the inputs in order to achieve the best possible modelling. This allowed a comparison with the GC profile determined by the constrained MTR-PMF performed in Dunkirk from the species observed in common. The final solution was a 7-factor solution, and although the correlation coefficient (R^2 = 0.75) between the observed and modelled concentrations could be improved, the profiles provide an interesting assessment of the sources, notably for factor 5 resembling ship emissions. This factor's profile shows signs of resemblance to the GC profile of shipping in Dunkirk, based solely on the species common to both datasets. The overall concentrations in Le Havre were lower than in Dunkirk, and mainly influenced by atmospheric dynamics, resulting in an absence of certain species observed in Dunkirk but not in Le Havre in the shipping factor. Attributing this factor to a potential shipping profile is subject to limitations, mainly because no exclusive tracer for shipping could be confirmed in this setting. Indeed, the SO_2 peaks evolving with Factor 5 are much longer than the ferries' peaks in Dunkirk, calling into question the exclusivity of SO_2 to ship emissions in such an industrial harbour, where other combustion sources could lead to SO_2 emissions.

Overall, this study provides valuable insights into the methodology of measuring shipping emissions using only GC, which is a more simplified experimental setup than that used in the Dunkirk campaign. Despite similar phases of ship operation being observed in Le Havre as in Dunkirk, namely arrival, departure and berthing, SO_2 doesn't show elevations upon the arrival and departure of ships, as was observed in Dunkirk. Therefore, the relevance of SO_2 as a ship emission tracer in the port of Le Havre is called into question, as industrial emissions may predominate over those from ships in the wind directions observed in the campaign. As in Dunkirk, the GC measurements did not report any increase in concentrations during ship manoeuvres. The impact of berthing periods on the GC concentrations could not be assessed, as southerly winds were almost non-existent during the 2023 campaign, limiting the sampling of ship plumes. Another possible explanation is that the site was located too close to the lock to effectively capture the ferry plumes from ships in the lock. However, the first investigation into the validity of the VOC shipping profile obtained by PMF in Dunkirk seems encouraging as applied to the Le Havre results, but prompts further investigation and validation using GC dataset from other harbour settings.

General Conclusion

The emissions of Volatile Organic Compounds (VOCs) from ships in harbour cities under evolving practices are not well described thus far, nor are their impacts on local air quality. In a context of more stringent regulations on shipping emissions inducing the use of new fuels and new practices, in particular in Emission Control Areas (ECAs), VOCs are still receiving less attention than historically regulated pollutants such as nitrogen oxides (NO_x), sulphur oxides (SO_2) and Particulate Matter (PM). However, VOCs are particularly important for air quality due to their ubiquity in both urban and rural areas and their reactivity, which leads to the formation of harmful secondary pollutants such as ozone and Secondary Organic Aerosols (SOAs). In light of the lack of information on VOC emissions and the anticipated increase in shipping traffic due to the expansion of harbours, the aim of this thesis was to enhance our understanding of VOC emissions from ships in the port of Dunkirk, which is representative of those navigating in the industrial ports of the ECA in the Hauts-de-France region. In addition, its important industrial activity allows the assessment of the contribution of ship emissions to ambient VOCs in such environment.

The approach of this work relied on the analysis of an intensive field campaign in the harbour of Dunkirk in 2022, where VOCs were measured with two TD-GC-FID and a PTR-ToF-MS, making it an exclusive dataset to assess the VOCs with both chemical- and time-resolved measurements. Other criteria pollutants and meteorology were recorded in partnership with the the Regional Network for Air Quality Monitoring of Hauts-de-France (AASQA, Atmo Hauts-de-France), and the Laboratoire de Chimie de l'Environnement (LCE, Marseille), resulting in a first descriptive analysis of the campaign. This highlighted the importance of the wind sector to be able to isolate the ship emissions in an atmosphere that showed highly changing pollution levels in function of the wind directions.

In a specific northern wind sector, intense but short transient peaks of pollutants were observed, such as CO_2, NO_x and SO_2, that corresponded to the arrival or departure of ships in the harbour. The latter was kept as a tracer for ship emissions because it displayed the most systematic and unique peaks during the arrival and departures of the ships. The first result of this thesis was that the SO_2 can still be used as a tracer for ship emissions in a regulated area of a harbour, despite its lower levels, to objectively of identify ship emissions in an industrial harbour, on condition that the background concentrations are sufficiently low.

The increase of SO_2 upon departure and arrival of three sister ferries operating between Dunkirk and Dover were used to isolate these ships' emission peaks in the dataset. Emission factors (EFs) were calculated from these peaks for each instrument used during the campaign, including a PTR-ToF-MS for VOCs. The calculations showed that NO_x and CO were the most emitted gaseous compounds, with average EFs of 33.8 ± 22.4 g·kg$^{-1}_{\text{fuel}}$ and 6.9 ± 4.2 g·kg$^{-1}_{\text{fuel}}$ respectively. The average EF of SO_2 is 1.4 ± 2.3 g·kg$^{-1}_{\text{fuel}}$, which allowed the Fuel Sulphur Content (FSC) of these ships to be calculated and shows that they comply with the 0.1% limit in the ECA. The EFs of the particulate phase showed that Organic Aerosols (OA) dominate the PM_1 composition (6.12 ± 6.00 g·kg$^{-1}_{\text{fuel}}$), and that the Ultra-Fine Particle (UFP) represent 61% of the PM mass emitted by ships. Regarding VOCs, the sum of their EFs is 2.3 g·kg$^{-1}_{\text{fuel}}$, which was rather consistent with the VOC emission EFs of ships used in regional inventories: 1.8 g·kg$^{-1}_{\text{fuel}}$. However, our sum is an underestimation, as the PTR measurements used to determine the EFs are known to underestimate alkanes, expected to contribute significantly, and as identification of the parent ion of the fragments was not always possible. The EFs of specific VOCs indicate the importance of oxygenated VOCs (OVOCs) in ship emissions, such as acetaldehyde (225.7 ± 80.5 mg·kg$^{-1}_{\text{fuel}}$), methanol (212.0 ± 138.7 mg·kg$^{-1}_{\text{fuel}}$) and acetic acid (119.3 ± 61.4 mg·kg$^{-1}_{\text{fuel}}$), providing information on these specific VOCs in ship emissions. This work on EFs resulted in a submitted article and provides a first chemical fingerprint of emitted VOCs under new regulation in a harbour of France.

Source apportionment was performed on the VOC data in Dunkirk using Positive Matrix Factorisation (PMF) after validation of the inputs and their uncertainties. Applying PMF to the PTR data allowed the identification of a factor associated with ferry emissions, which was supported by its correlation with SO_2 as a tracer and by a similar temporal evolution, with clear peaks observed at the ferries' departure and arrival. In contrast, PMF applied to the GC data provided limited evidence for shipping emissions. This was mainly due to the low temporal resolution of the GC measurements (30 min sampling and analysis), which reduces correlation with potential tracers and leads to lower variability in total GC concentrations during favourable wind conditions to capture ferry plumes.

To overcome these limitations, Multi-Time resolution PMF (MTR-PMF) was explored to combine the high temporal resolution of PTR while benefitting from the chemical resolution of GC using their respective original timesteps. A profile consistent with the temporal evolution of the PMF-PTR 'shipping' factor was obtained.

However, the most effective way to resolve a distinct shipping factor without redistributing ship-related peaks across other factors was to fully constrain the MTR-PMF with a MTR-PMF analysis profile derived from a specific wind sector where ferry plumes were sampled. This approach had previously been applied to calculate the EFs.

This shipping factor was characterized by the presence of OVOCs such as methanol, acetone, acetaldehyde and acetic acid predominate, confirming their significance in ship emissions, as documented in the literature. Light hydrocarbons, including ethane, butane, ethylene and propane, which were measured by GC as speciated VOCs, were found to be the main contributors to the GC shipping profile. This is consistent with observations made during the SCIPPER campaign on a ferry operating at low load (10%, manoeuvring). The major compounds identified in the EF approach correspond to those dominating the shipping factor obtained by PMF, which highlights the robustness and complementarity of the approaches.

On average, the shipping factor obtained represents 8.5 ± 15% of the total VOC concentrations resolved by the PMF. However, a strong variability of this contribution was observed, with significant increases up to 100% during periods when the site was directly affected by shipping. According to the Atmo Hauts-de-France inventories, the 'other transportation' sector accounted for 6.2% of total VOC emissions in 2021, a figure which has steadily increased in recent years. Therefore, the contribution of the sector could reach in 2022 a similar value as found in the PMF used with the campaign data. Furthermore, we estimated that the shipping factor accounted for approximately 10% of the O_3 formation potential (OFP) for the total VOCs modelled, using the MIR approach. Additionally, the shipping factor represents around 5% of the total SOA formation potential, with increased contributions during plume episodes (up to 100%). These results provide a (rough) first indication of the potential impacts on shipping on air quality in the area of Dunkirk, evidencing that industrial sources far outweigh shipping for their impacts on air quality on average.

Overall, the key to resolving the shipping factor amongst the other sources, mainly composed of industrial activities and traffic exhaust, was the use of PMF with high-resolution VOC measurements. This work provides an exclusive shipping chemical fingerprint of VOCs resulting from the combination of speciated VOCs from GC and the high-time resolution of PTR. This profile is confronted in another field campaign conducted in 2023 in Le Havre, another important industrial harbour of France.

The second campaign conducted in Le Havre between April and June 2023, near the cargo terminal's ship lock, provided an opportunity to test the robustness of the Dunkirk ship emission factor. During this campaign, VOCs were measured exclusively by TD-GC-FID, enabling a comparison with the species in common with the constrained MTR-PMF GC profile from Dunkirk. A PMF factor potentially associated with shipping emissions was identified based on similarities with the Dunkirk GC profile in terms of composition, as well as on its agreement with the SO_2 tracer. However, significant limitations were encountered, primarily the low VOC levels and substantial uncertainties, particularly for benzene and propane.

The difficulty of achieving a stable PMF solution degraded the identification of the expected profile. Nevertheless, this initial exploration of GC-PMF in Le Havre highlights the potential to capture a shipping-related factor, while emphasising the need for further studies to overcome the limitations met with the Le Havre dataset concerning the low-time resolution observations.

Taken together, these achievements demonstrate that the objectives set out at the beginning of this thesis have been successfully realised. Ship emissions were evidenced in the dataset of Dunkirk using two complementary approaches, by correlation with a tracer and source apportionment of high-time-resolution VOC measurements. These methods were confronted and confirmed the identification of the ship peaks. Using the EFs and the PMF, a consistent VOC fingerprint of shipping was identified, emphasising the significance of OVOCs (PTR) and light VOCs (GC) for the ferries navigating in ECA. The PMF factor enables the contribution of VOCs to be calculated, providing a consistent figure that aligns with regional inventories. Then, confronting the VOC fingerprint with data from another campaign and performing the PMF with data from the port of Le Havre yielded insights similar to those from shipping in Dunkirk, delivering a new VOC fingerprint for marine diesel combustion.

This work, which is based on field studies, has provided results that have been compared with on-board or stack measurements of ship emissions. This approach typically provides direct quantification of emissions, notably through the calculation of EFs, which are determined under controlled operating conditions. This enables accurate classification of emissions in relation to operating conditions, fuel, engine load, speed and manoeuvres. However, such measurements generally represent idealised conditions and may not capture the complexity of real-world emissions, such as the influence of reactivity, meteorology, and dynamics. Furthermore, they do not allow consideration of their contribution to ambient levels, particularly of VOCs. By contrast, land-based VOC measurements reflect the effects of all these processes, providing a realistic representation of emissions in an industrial harbour environment. Therefore, combining both land- and stack-based approaches provides a comprehensive understanding of ship emissions: stack measurements provide a fingerprint of primary emissions, while ambient measurements validate representativeness under real conditions and help identify secondary formation processes, notably when integrating aerosol measurements, such as the HR-ToF-AMS deployed in Dunkirk by the LCE. Future studies could benefit from joint campaigns in which stack and field measurements are taken simultaneously on the same vessels or in the same harbour areas. This would enable a more robust evaluation of chemical profiles and help to model the impact on air quality.

The main limitation of this study is that it focuses on ferries in Dunkirk. Although their chemical fingerprint was established from a repeatable dataset, as these ferries are similar, they only represent this particular type of passenger vessel that could be encountered in other harbours in ECAs. For example, in Le Havre, fewer passenger vessels frequent the harbour, whereas more tankers were observed. However, similar ferries are found in Calais, Marseille and Toulon and this work could therefore inform on VOC emissions in other regions or countries. The next limitation is linked to the instrumental methodology: the attribution of peaks to ship passage was efficiently resolved due to high-resolution time measurements using the PTR-MS, confirmed by high-time resolved SO_2 measurements. As was observed in Le Havre, GC measurements alone would not have provided sufficient data to identify ship emissions, but the GC profile in the MTR-PMF provides reference information for other campaigns with low-time resolved measurements. Additionally, detailed information on ship passage or presence in the harbour is essential for comparing ship passages with concentration variability.

The achievement of a chemical fingerprint in VOC determined in Dunkirk and a preliminary profile in Le Havre adds a valuable element in the discussions on the update of emission inventories of shipping. These discussions could occur with the CITEPA, in charge of updating the EFs used for the regional inventories by the AASQA. The addition of the speciated compounds found in this study would enhance the representativity of the inventories. Moreover, especially within the framework of the PIRATE and SHIPAIR projects with the CEREA partners (École des Ponts/-ParisTech), the impact of VOC emissions from ships will be better estimated thanks to the update suggested in this work.

Bibliography

Agrawal, H., Welch, W.A., Henningsen, S., Miller, J.W., Cocker, D.R., 2010. Emissions from main propulsion engine on container ship at sea. Journal of Geophysical Research: Atmospheres 115, 2009JD013346. doi:10.1029/2009JD013346.

Agrawal, H., Welch, W.A., Miller, J.W., Cocker, D.R., 2008. Emission Measurements from a Crude Oil Tanker at Sea. Environmental Science & Technology 42, 7098–7103. doi:10.1021/es703102y.

Alanen, J., Isotalo, M., Kuittinen, N., Simonen, P., Martikainen, S., Kuuluvainen, H., Honkanen, M., Lehtoranta, K., Nyyssönen, S., Vesala, H., Timonen, H., Aurela, M., Keskinen, J., Rönkkö, T., 2020. Physical Characteristics of Particle Emissions from a Medium Speed Ship Engine Fueled with Natural Gas and Low-Sulfur Liquid Fuels. Environmental Science & Technology 54, 5376–5384. doi:10.1021/acs.est.9b06460.

Alföldy, B., Lööv, J.B., Lagler, F., Mellqvist, J., Berg, N., Beecken, J., Weststrate, H., Duyzer, J., Bencs, L., Horemans, B., Cavalli, F., Putaud, J.P., Janssens-Maenhout, G., Csordás, A.P., Van Grieken, R., Borowiak, A., Hjorth, J., 2013. Measurements of air pollution emission factors for marine transportation in SECA. Atmospheric Measurement Techniques 6, 1777–1791. doi:10.5194/amt-6-1777-2013. publisher: Copernicus GmbH.

Alver, F., Saraç, B.A., Alver Şahin, , 2018. Estimating of shipping emissions in the Samsun Port from 2010 to 2015. Atmospheric Pollution Research 9, 822–828. doi:10.1016/j.apr.2018.02.003.

Ashok, A., Barrett, S.R., 2016. Adjoint-based computation of U.S. nationwide ozone exposure isopleths. Atmospheric Environment 133, 68–80. doi:10.1016/j.atmosenv.2016.03.025.

Atkinson, R., 2000. Atmospheric chemistry of VOCs and NOx. Atmospheric Environment 34, 2063–2101. doi:10.1016/S1352-2310(99)00460-4.

Badol, C., Locoge, N., Galloo, J.C., 2008a. Using a source-receptor approach to characterise VOC behaviour in a French urban area influenced by industrial emissions Part II : Source contribution assessment using the Chmical Mass Balance Model. Science of The Total Environment 389, 429–440. doi:10.1016/j.scitotenv.2007.09.002.

Badol, C., Locoge, N., Léonardis, T., Galloo, J.C., 2008b. Using a source–receptor approach to characterise VOC behaviour in a French urban area influenced by industrial emissions Part I: Study area description, data set acquisition and qualitative data analysis of the data set. Science of The Total Environment 389, 441–452. doi:10.1016/j.scitotenv.2007.09.003.

Balzani Lööv, J.M., Alfoldy, B., Gast, L.F.L., Hjorth, J., Lagler, F., Mellqvist, J., Beecken, J., Berg, N., Duyzer, J., Westrate, H., Swart, D.P.J., Berkhout, A.J.C., Jalkanen, J.P., Prata, A.J., van der Hoff, G.R., Borowiak, A., 2014. Field test of available methods to measure remotely SO_x and NO_x emissions from ships. Atmospheric Measurement Techniques 7, 2597–2613. doi:10.5194/amt-7-2597-2014. publisher: Copernicus GmbH.

Bates, K.H., Jacob, D.J., Wang, S., Hornbrook, R.S., Apel, E.C., Kim, M.J., Millet, D.B., Wells, K.C., Chen, X., Brewer, J.F., Ray, E.A., Commane, R., Diskin, G.S., Wofsy, S.C., 2021. The Global Budget of Atmospheric Methanol: New Constraints on Secondary, Oceanic, and Terrestrial Sources. Journal of Geophysical Research: Atmospheres 126, e2020JD033439. doi:10.1029/2020JD033439.

Baudic, A., Gros, V., Sauvage, S., Locoge, N., Sanchez, O., Sarda-Estève, R., Kalogridis, C., Petit, J.E., Bonnaire, N., Baisnée, D., Favez, O., Albinet, A., Sciare, J., Bonsang, B., 2016. Seasonal variability and source apportionment of volatile organic compounds (VOCs) in the Paris megacity (France). Atmospheric Chemistry and Physics 16, 11961–11989. doi:10.5194/acp-16-11961-2016.

Bauer, A., 2025. Le trafic maritime en France : très légère baisse du fret en 2024. URL: https://www.statistiques.developpement-durable.gouv.fr/le-trafic-maritime-en-france-tres-legere-baisse-du-fret-en-2024.

Beecken, J., Mellqvist, J., Salo, K., Ekholm, J., Jalkanen, J.P., Johansson, L., Litvinenko, V., Volodin, K., Frank-Kamenetsky, D.A., 2015. Emission factors of SO_2 , NO $_x$ and particles from ships in Neva Bay from ground-based and helicopter-borne measurements and AIS-based modeling. Atmospheric Chemistry and Physics 15, 5229–5241. doi:10.5194/acp-15-5229-2015.

Belis, C.A., Pernigotti, D., Karagulian, F., Pirovano, G., Larsen, B.R., Gerboles, M., Hopke, P.K.,

2015. A new methodology to assess the performance and uncertainty of source apportionment models in intercomparison exercises. Atmospheric Environment 119, 35–44. doi:10.1016/j.atmosenv.2015.08.002.

Bell, M., Davis, D., 2001. Reassessment of the Lethal London Fog of 1952: Novel Indicators of Acute and Chronic Consequences of Acute Exposure to Air Pollution. Environmental health perspectives 109 Suppl 3, 389–94. doi:10.1289/ehp.01109s3389.

Bond, T.C., Doherty, S.J., Fahey, D.W., Forster, P.M., Berntsen, T., DeAngelo, B.J., Flanner, M.G., Ghan, S., Kärcher, B., Koch, D., Kinne, S., Kondo, Y., Quinn, P.K., Sarofim, M.C., Schultz, M.G., Schulz, M., Venkataraman, C., Zhang, H., Zhang, S., Bellouin, N., Guttikunda, S.K., Hopke, P.K., Jacobson, M.Z., Kaiser, J.W., Klimont, Z., Lohmann, U., Schwarz, J.P., Shindell, D., Storelvmo, T., Warren, S.G., Zender, C.S., 2013. Bounding the role of black carbon in the climate system: A scientific assessment. Journal of Geophysical Research: Atmospheres 118, 5380–5552. doi:10.1002/jgrd.50171. publisher: American Geophysical Union (AGU).

Borbon, A., Locoge, N., Veillerot, M., Galloo, J.C., Guillermo, R., 2002. Characterisation of NMHCs in a French urban atmosphere: overview of the main sources. The Science of the Total Environment 292, 177–191. doi:10.1016/s0048-9697(01)01106-8.

Borges, A.V., Champenois, W., Gypens, N., Delille, B., Harlay, J., 2016. Massive marine methane emissions from near-shore shallow coastal areas. Scientific Reports 6, 27908. doi:10.1038/srep27908.

Borrás, E., Tortajada-Genaro, L.A., 2012. Secondary organic aerosol formation from the photo-oxidation of benzene. Atmospheric Environment 47, 154–163. doi:10.1016/j.atmosenv.2011.11.020.

Brimblecombe, P., Chu, M., Liu, C.H., Fu, Y., Wei, P., Ning, Z., 2023. Roadside NO2/NOx and primary NO2 from individual vehicles. Atmospheric Environment 295, 119562. doi:10.1016/j.atmosenv.2022.119562.

Brown, S.G., Eberly, S., Paatero, P., Norris, G.A., 2015. Methods for estimating uncertainty in PMF solutions: Examples with ambient air and water quality data and guidance on reporting PMF results. Science of The Total Environment 518-519, 626–635. doi:10.1016/j.scitotenv.2015.01.022.

C3S, 2018. ERA5 hourly data on single levels from 1940 to present. doi:10.24381/CDS.ADBB2D47.

Calderón-Garcidueñas, L., Ayala, A., 2022. Air Pollution, Ultrafine Particles, and Your Brain: Are Combustion Nanoparticle Emissions and Engineered Nanoparticles Causing Preventable Fatal

Neurodegenerative Diseases and Common Neuropsychiatric Outcomes? Environmental Science & Technology 56, 6847–6856. doi:10.1021/acs.est.1c04706.

Calvert, J., Pitts, J.N., 1966. Photochemestry.

Cames, M., Graichen, J., Siemons, A., Cook, V., 2015. Emission reduction targets for international aviation and shipping. Technical Report.

Canagaratna, M.R., Jayne, J.T., Jimenez, J.L., Allan, J.D., Alfarra, M.R., Zhang, Q., Onasch, T.B., Drewnick, F., Coe, H., Middlebrook, A., Delia, A., Williams, L.R., Trimborn, A.M., Northway, M.J., DeCarlo, P.F., Kolb, C.E., Davidovits, P., Worsnop, D.R., 2007. Chemical and microphysical characterization of ambient aerosols with the aerodyne aerosol mass spectrometer. Mass Spectrometry Reviews 26, 185–222. doi:10.1002/mas.20115.

Canonaco, F., Crippa, M., Slowik, J.G., Baltensperger, U., Prévôt, A.S.H., 2013. SoFi, an IGOR-based interface for the efficient use of the generalized multilinear engine (ME-2) for the source apportionment: ME-2 application to aerosol mass spectrometer data. Atmospheric Measurement Techniques 6, 3649–3661. doi:10.5194/amt-6-3649-2013. publisher: Copernicus GmbH.

Canonaco, F., Slowik, J.G., Baltensperger, U., Prévôt, A.S.H., 2015. Seasonal differences in oxygenated organic aerosol composition: implications for emissions sources and factor analysis. Atmospheric Chemistry and Physics 15, 6993–7002. doi:10.5194/acp-15-6993-2015. publisher: Copernicus GmbH.

Canonaco, F., Tobler, A., Chen, G., Sosedova, Y., Slowik, J.G., Bozzetti, C., Daellenbach, K.R., El Haddad, I., Crippa, M., Huang, R.J., Furger, M., Baltensperger, U., Prévôt, A.S.H., 2021. A new method for long-term source apportionment with time-dependent factor profiles and uncertainty assessment using SoFi Pro: application to 1 year of organic aerosol data. Atmospheric Measurement Techniques 14, 923–943. doi:10.5194/amt-14-923-2021. publisher: Copernicus GmbH.

Capaldo, K., Corbett, J.J., Kasibhatla, P., Fischbeck, P., Pandis, S.N., 1999. Effects of ship emissions on sulphur cycling and radiative climate forcing over the ocean. Nature 400, 743–746. doi:10.1038/23438. publisher: Nature Publishing Group.

Carter, W.P., 1994. Development of Ozone Reactivity Scales for Volatile Organic Compounds. Air & Waste 44. doi:10.1080/1073161X.1994.10467290. publisher: Taylor & Francis pages = 881–899,.

Carter, W.P.L., 2010. Updated maximum incremental reactivity scale and hydrocarbon bin reactivities for regulatory applications. California Air Resources Board Contract 07-339. URL:

https://www.researchgate.net/publication/284060890_Updated_maximum_incremental_reactivity_scale_and_hydrocarbon_bin_reactivities_for_regulatory_applications.

Cazier, F., Genevray, P., Dewaele, D., Nouali, H., Verdin, A., Ledoux, F., Hachimi, A., Courcot, L., Billet, S., Bouhsina, S., Shirali, P., Garçon, G., Courcot, D., 2016. Characterisation and seasonal variations of particles in the atmosphere of rural, urban and industrial areas: Organic compounds. Journal of Environmental Sciences 44, 45–56. doi:10.1016/j.jes.2016.01.014.

Celik, S., Drewnick, F., Fachinger, F., Brooks, J., Darbyshire, E., Coe, H., Paris, J.D., Eger, P., Schuladen, J., Tadic, I., Friedrich, N., Dienhart, D., Hottmann, B., Fischer, H., Crowley, J., Harder, H., Borrmann, S., 2020. Influence of vessel characteristics and atmospheric processes on the gas and particle phase of ship emission plumes: in situ measurements in the Mediterranean Sea and around the Arabian Peninsula. Atmospheric Chemistry and Physics 20, 4713–4734. doi:10.5194/acp-20-4713-2020.

Chapman, S., 1930. XXXV. On ozone and atomic oxygen in the upper atmosphere. The London, Edinburgh, and Dublin Philosophical Magazine and Journal of Science 10, 369–383. doi:10.1080/14786443009461588.

Chebaicheb, H., F. de Brito, J., Chen, G., Tison, E., Marchand, C., Prévôt, A.S.H., Favez, O., Riffault, V., 2023. Investigation of four-year chemical composition and organic aerosol sources of submicron particles at the ATOLL site in northern France. Environmental Pollution 330, 121805. doi:10.1016/j.envpol.2023.121805.

Chebaicheb, H., Riffault, V., Chatain, R.M., 2025. User guide for ACSM data processing and PMF application using SoFi Pro .

Chen, G., Sosedova, Y., Canonaco, F., Fröhlich, R., Tobler, A., Vlachou, A., Daellenbach, K.R., Bozzetti, C., Hueglin, C., Graf, P., Baltensperger, U., Slowik, J.G., El Haddad, I., Prévôt, A.S.H., 2021. Time-dependent source apportionment of submicron organic aerosol for a rural site in an alpine valley using a rolling positive matrix factorisation (PMF) window. Atmospheric Chemistry and Physics 21, 15081–15101. doi:10.5194/acp-21-15081-2021.

Chen, J., Hoek, G., 2020. Long-term exposure to PM and all-cause and cause-specific mortality: A systematic review and meta-analysis. Environment International 143, 105974. doi:10.1016/j.envint.2020.105974. publisher: Elsevier BV.

CITEPA, 2022a. Gaz à effet de serre et polluants atmosphériques, bilan des émissions en France de 1990 à 2021. Technical Report 2071sec / 2022.

CITEPA, 2022b. Rapport OMINEA : Organisation et méthodes des inventaires nationaux des

émissions atmosphériques en France - 19ème édition. Technical Report. URL: https://www.citepa.org/wp-content/uploads/publications/ominea/OMINEA-2022v2.pdf.

Clemitshaw, K.C., 2015. Tropospheric Chemistry and Composition | Hydroxyl Radical, in: North, G.R., Pyle, J., Zhang, F. (Eds.), Encyclopedia of Atmospheric Sciences (Second Edition). Academic Press, Oxford, pp. 232–238. doi:10.1016/B978-0-12-382225-3.00429-1.

Coggon, M.M., Stockwell, C.E., Claflin, M.S., Pfannerstill, E.Y., Xu, L., Gilman, J.B., Marcantonio, J., Cao, C., Bates, K., Gkatzelis, G.I., Lamplugh, A., Katz, E.F., Arata, C., Apel, E.C., Hornbrook, R.S., Piel, F., Majluf, F., Blake, D.R., Wisthaler, A., Canagaratna, M., Lerner, B.M., Goldstein, A.H., Mak, J.E., Warneke, C., 2024. Identifying and correcting interferences to PTR-ToF-MS measurements of isoprene and other urban volatile organic compounds. Atmospheric Measurement Techniques 17, 801–825. doi:10.5194/amt-17-801-2024. publisher: Copernicus GmbH.

Collins, W.J., Sitch, S., Boucher, O., 2010. How vegetation impacts affect climate metrics for ozone precursors. Journal of Geophysical Research: Atmospheres 115. doi:10.1029/2010JD014187.

Contini, D., Gambaro, A., Donateo, A., Cescon, P., Cesari, D., Merico, E., Belosi, F., Citron, M., 2015. Inter-annual trend of the primary contribution of ship emissions to PM2.5 concentrations in Venice (Italy): Efficiency of emissions mitigation strategies. Atmospheric Environment 102, 183–190. doi:10.1016/j.atmosenv.2014.11.065.

Cooper, D., 2003. Exhaust emissions from ships at berth. Atmospheric Environment 37, 3817–3830. doi:10.1016/S1352-2310(03)00446-1.

Cooper, D., Gustafsson, T., 2004. Methodology for calculating emissions from ships: 1. Update of emission factors. URL: https://urn.kb.se/resolve?urn=urn:nbn:se:naturvardsverket:diva-7084.

Cooper, O.R., Parrish, D.D., Ziemke, J., Balashov, N.V., Cupeiro, M., Galbally, I.E., Gilge, S., Horowitz, L., Jensen, N.R., Lamarque, J.F., Naik, V., Oltmans, S.J., Schwab, J., Shindell, D.T., Thompson, A.M., Thouret, V., Wang, Y., Zbinden, R.M., 2014. Global distribution and trends of tropospheric ozone: An observation-based review. Elementa: Science of the Anthropocene 2. doi:10.12952/journal.elementa.000029. publisher: University of California Press.

Corbett, J.J., Winebrake, J.J., Green, E.H., Kasibhatla, P., Eyring, V., Lauer, A., 2007. Mortality from Ship Emissions: A Global Assessment. Environmental Science & Technology 41, 8512–8518. doi:10.1021/es071686z.

Crenn, V., Fronval, I., Petitprez, D., Riffault, V., 2017. Fine particles sampled at an urban background site and an industrialized coastal site in Northern France — Part 1: Seasonal

variations and chemical characterization. Science of The Total Environment 578, 203–218. doi:10.1016/j.scitotenv.2015.11.165.

Dalsøren, S.B., Eide, M.S., Endresen, , Mjelde, A., Gravir, G., Isaksen, I.S.A., 2008. Update on emissions and environmental impacts from the international fleet of ships. The contribution from major ship types and ports doi:10.5194/acpd-8-18323-2008.

De Lauretis, R., 2023. EMEP/EEA air pollutant emission inventory guidebook 2023, 1.A.3.d Navigation (Shipping). Technical Report. EMEP/EEA. URL: https://www.eea.europa.eu/en/analysis/publications/emep-eea-guidebook-2023.

DeCarlo, P.F., Kimmel, J.R., Trimborn, A., Northway, M.J., Jayne, J.T., Aiken, A.C., Gonin, M., Fuhrer, K., Horvath, T., Docherty, K.S., Worsnop, D.R., Jimenez, J.L., 2006. Field-Deployable, High-Resolution, Time-of-Flight Aerosol Mass Spectrometer. Analytical Chemistry 78, 8281–8289. doi:10.1021/ac061249n. publisher: American Chemical Society.

Deniz, C., Kilic, A., Cıvkaroglu, G., 2010. Estimation of shipping emissions in Candarli Gulf, Turkey. Environmental Monitoring and Assessment 171, 219–228. doi:10.1007/s10661-009-1273-2.

Derwent, R.G., Jenkin, M.E., Saunders, S.M., Pilling, M.J., 1998. Photochemical ozone creation potentials for organic compounds in northwest Europe calculated with a master chemical mechanism. Atmospheric Environment 32, 2429–2441. doi:10.1016/S1352-2310(98)00053-3.

Derwent, R.G., Jenkin, M.E., Utembe, S.R., Shallcross, D.E., Murrells, T.P., Passant, N.R., 2010. Secondary organic aerosol formation from a large number of reactive man-made organic compounds. Science of The Total Environment 408, 3374–3381. doi:10.1016/j.scitotenv.2010.04.013.

Diesch, J.M., Drewnick, F., Klimach, T., Borrmann, S., 2013. Investigation of gaseous and particulate emissions from various marine vessel types measured on the banks of the Elbe in Northern Germany. Atmospheric Chemistry and Physics 13, 3603–3618. doi:10.5194/acp-13-3603-2013.

Dixon, J.L., Beale, R., Nightingale, P.D., 2013. Production of methanol, acetaldehyde, and acetone in the Atlantic Ocean: PRODUCTION OF OVOCs IN ATLANTIC WATERS. Geophysical Research Letters 40, 4700–4705. doi:10.1002/grl.50922.

Dodge, M.C., 1976. Combined use of modeling techniques and smog chamber data to derive ozone-precursor relationships. volume II. U.S. Environmental Protection Agency, Research Triangle Park, NC. URL: https://heronet.epa.gov/heronet/index.cfm/reference/download/reference_id/38646.

DREAL, 2021. L'Environnement en Hauts-de-France : l'Industrie au regard de l'Environnement .

Dufresne, M., Salameh, T., Leonardis, T., Gille, G., Armengaud, A., Sauvage, S., 2025. Volatile organic compound sources and impacts in an urban Mediterranean area (Marseille, France). Atmospheric Chemistry and Physics 25, 5977–5999. doi:10.5194/acp-25-5977-2025. publisher: Copernicus GmbH.

Dusanter, S., Holzinger, R., Klein, F., Salameh, T., Jamar, M., 2025. Measurement Guidelines for VOC Analysis by PTR-MS. Technical Report.

EPA, 1999. Compendium Method TO-15: Determination Of Volatile Organic Compounds (VOCs) In Air Collected In Specially-Prepared Canisters And Analyzed By Gas Chromatography/ Mass Spectrometry (GC/MS). Technical Report. Center for Environmental Research Information. URL: https://www3.epa.gov/ttnamti1/files/ambient/airtox/to-15r.pdf.

EPA, 2022. Ports Emissions Inventory Guidance: Methodologies for Estimating Port-Related and Goods Movement Mobile Source Emissions. Technical Report. URL: https://nepis.epa.gov/Exe/ZyPDF.cgi?Dockey=P1014J1S.pdf.

EU, 1999. Directive 1999/13/CE du Conseil du 11 mars 1999 relative à la réduction des émissions de composés organiques volatils dues à l'utilisation de solvants organiques dans certaines activités et installations. URL: http://data.europa.eu/eli/dir/1999/13/oj/fra.

EU, 2000. Directive 2000/69/CE du Parlement européen et du Conseil du 16 novembre 2000 concernant les valeurs limites pour le benzène et le monoxyde de carbone dans l'air ambiant. URL: https://www.legifrance.gouv.fr/jorf/id/JORFTEXT000000696655.

EU, 2008. Directive 2008/50/CE du Parlement européen et du Conseil du 21 mai 2008 concernant la qualité de l'air ambiant et un air pur pour l'Europe. URL: https://www.legifrance.gouv.fr/jorf/id/JORFTEXT000018984836/.

Eyring, V., Isaksen, I.S.A., Berntsen, T., Collins, W.J., Corbett, J.J., Endresen, O., Grainger, R.G., Moldanova, J., Schlager, H., Stevenson, D.S., 2010. Transport impacts on atmosphere and climate: Shipping. Atmospheric Environment 44, 4735–4771. doi:10.1016/j.atmosenv.2009.04.059.

Faber, J., Hanayama, S., Zhang, S., Pereda, P., 2020. Fourth IMO GHG Study 2020 Executive-Summary. Technical Report. IMO.

Fan, Q., Zhang, Y., Ma, W., Ma, H., Feng, J., Yu, Q., Yang, X., Ng, S.K.W., Fu, Q., Chen, L.,

2016. Spatial and Seasonal Dynamics of Ship Emissions over the Yangtze River Delta and East China Sea and Their Potential Environmental Influence. Environmental Science & Technology 50, 1322–1329. doi:10.1021/acs.est.5b03965.

Farhat, M., Afif, C., Zhang, S., Dusanter, S., Delbarre, H., Riffault, V., Sauvage, S., Borbon, A., 2024. Investigating the industrial origin of terpenoids in a coastal city in northern France: A source apportionment combining anthropogenic, biogenic, and oxygenated VOC. Science of The Total Environment 928, 172098. doi:10.1016/j.scitotenv.2024.172098.

Feng, J., Zhang, Y., Li, S., Mao, J., Patton, A.P., Zhou, Y., Ma, W., Liu, C., Kan, H., Huang, C., An, J., Li, L., Shen, Y., Fu, Q., Wang, X., Liu, J., Wang, S., Ding, D., Cheng, J., Ge, W., Zhu, H., Walker, K., 2019. The influence of spatiality on shipping emissions, air quality and potential human exposure in the Yangtze River Delta/Shanghai, China. Atmospheric Chemistry and Physics 19, 6167–6183. doi:10.5194/acp-19-6167-2019.

Filella, I., Penuelas, J., 2006. Daily, Weekly, and Seasonal Time Courses of VOC Concentrations in a Semi-Urban Area Near Barcelona. Atmospheric Environment 40, 7752–7769. doi:10.1016/j.atmosenv.2006.08.002.

Fossum, K.N., Lin, C., O'Sullivan, N., Lei, L., Hellebust, S., Ceburnis, D., Afzal, A., Tremper, A., Green, D., Jain, S., Byčenkienė, S., O'Dowd, C., Wenger, J., Ovadnevaite, J., 2024. Two distinct ship emission profiles for organic-sulfate source apportionment of PM in sulfur emission control areas. Atmospheric Chemistry and Physics 24, 10815–10831. doi:10.5194/acp-24-10815-2024. publisher: Copernicus GmbH.

Freney, E., Sellegri, K., Chrit, M., Adachi, K., Brito, J., Waked, A., Borbon, A., Colomb, A., Dupuy, R., Pichon, J.M., Bouvier, L., Delon, C., Jambert, C., Durand, P., Bourianne, T., Gaimoz, C., Triquet, S., Féron, A., Beekmann, M., Dulac, F., Sartelet, K., 2018. Aerosol composition and the contribution of SOA formation over Mediterranean forests. Atmospheric Chemistry and Physics 18, 7041 – 7056. doi:10.5194/acp-18-7041-2018. publisher: European Geosciences Union.

Fridell, E., Salberg, H., Salo, K., 2021. Measurements of Emissions to Air from a Marine Engine Fueled by Methanol. Journal of Marine Science and Application 20, 138–143. doi:10.1007/s11804-020-00150-6. publisher: Springer Science and Business Media LLC.

Fridell, E., Salo, K., 2016. Measurements of abatement of particles and exhaust gases in a marine gas scrubber. Proceedings of the Institution of Mechanical Engineers, Part M: Journal of Engineering for the Maritime Environment 230, 154–162. doi:10.1177/1475090214543716. publisher: SAGE Publications.

Fry, M.M., Schwarzkopf, M.D., Adelman, Z., West, J.J., 2014. Air quality and radiative forcing im-

pacts of anthropogenic volatile organic compound emissions from ten world regions. Atmospheric Chemistry and Physics 14, 523–535. doi:10.5194/acp-14-523-2014. publisher: Copernicus GmbH.

García-Gómez, E., Gkotsis, G., Nika, M.C., Hassellöv, I.M., Salo, K., Hermansson, A.L., Ytreberg, E., Thomaidis, N.S., Gros, M., Petrović, M., 2023. Characterization of scrubber water discharges from ships using comprehensive suspect screening strategies based on GC-APCI-HRMS. Chemosphere 343, 140296. doi:10.1016/j.chemosphere.2023.140296.

Gascoin, C., Legrand, C., 2025. Mesures du 1.3-butadiène, du benzène et de l'acrylonitrile dans l'air ambiant au niveau des zones industrielles du Havre et de Port-Jérôme : Campagnes mutualisées 2024. Technical Report PI_2025_05. Atmo Normandie. URL: https://www.atmonormandie.fr/publications/mesures-du-13-butadiene-du-benzene-et-de-lacrylonitrile-dans-lair-ambiant-au-niveau.

GAW, 2023. Guidelines for Measurements of Non-Methane Hydrocarbons in the Troposphere. Technical Report 281. World Meteorological Organization, Global Atmosphere Watch. URL: https://library.wmo.int/records/item/66281-guidelines-for-measurements-of-non-methane-hydrocarbons-in-the-troposphere.

Gkatzelis, G.I., Coggon, M.M., McDonald, B.C., Peischl, J., Gilman, J.B., Aikin, K.C., Robinson, M.A., Canonaco, F., Prevot, A.S.H., Trainer, M., Warneke, C., 2021. Observations Confirm that Volatile Chemical Products Are a Major Source of Petrochemical Emissions in U.S. Cities. Environmental Science & Technology 55, 4332–4343. doi:10.1021/acs.est.0c05471.

Goldstein, A.H., Galbally, I.E., 2007. Known and Unexplored Organic Constituents in the Earth's Atmosphere. Environmental Science & Technology 41, 1514–1521. doi:10.1021/es072476p.

Denier van der Gon, H., Hulskotte, J., 2010. Methodologies for estimating shipping emissions in the Netherlands : A documentation of currently used emission factors and data on related activity. Technical Report. TNO. URL: https://www.tno.nl/media/2151/methodologies_for_estimating_shipping_emissions_netherlands.pdf.

González, Y., Rodríguez, S., Guerra García, J.C., Trujillo, J.L., García, R., 2011. Ultrafine particles pollution in urban coastal air due to ship emissions. Atmospheric Environment 45, 4907–4914. doi:10.1016/j.atmosenv.2011.06.002.

de Gouw, J., Warneke, C., 2007. Measurements of volatile organic compounds in the earth's atmosphere using proton-transfer-reaction mass spectrometry. Mass Spectrometry Reviews 26, 223–257. doi:10.1002/mas.20119.

GPMD, 2022. Dossier de presse 2022.

Graedel, T.E., 1979. Terpenoids in the atmosphere. Reviews of Geophysics 17, 937. doi:10.1029/RG017i005p00937.

Grandjean, T., Tapadinhas, L., 2019. L'industrie au regard de l'Environnement. URL: https://www.hauts-de-france.developpement-durable.gouv.fr/IMG/pdf/ire_hdf_2019_v21.pdf.

Graver, B., Zhang, K., Rutherford, D., 2019. CO2 emissions from commercial aviation, 2018 .

Grigoriadis, A., Mamarikas, S., Ioannidis, I., Majamäki, E., Jalkanen, J.P., Ntziachristos, L., 2021. Development of exhaust emission factors for vessels: A review and meta-analysis of available data. Atmospheric Environment: X 12, 100142. doi:10.1016/j.aeaoa.2021.100142.

Gu, Y., Liu, B., Meng, H., Song, S., Dai, Q., Shi, L., Feng, Y., Hopke, P.K., 2023. Source apportionment of consumed volatile organic compounds in the atmosphere. Journal of Hazardous Materials 459, 132138. doi:10.1016/j.jhazmat.2023.132138.

Gueneron, M., Erickson, M.H., VanderSchelden, G.S., Jobson, B.T., 2015. PTR-MS fragmentation patterns of gasoline hydrocarbons. International Journal of Mass Spectrometry 379, 97–109. doi:10.1016/j.ijms.2015.01.001.

Guenther, A., Geron, C., Pierce, T., Lamb, B., Harley, P., Fall, R., 2000. Natural emissions of non-methane volatile organic compounds, carbon monoxide, and oxides of nitrogen from North America. Atmospheric Environment 34, 2205–2230. doi:10.1016/S1352-2310(99)00465-3.

Guenther, A., Hewitt, C.N., Erickson, D., Fall, R., Geron, C., Graedel, T., Harley, P., Klinger, L., Lerdau, M., Mckay, W.A., Pierce, T., Scholes, B., Steinbrecher, R., Tallamraju, R., Taylor, J., Zimmerman, P., 1995. A global model of natural volatile organic compound emissions. Journal of Geophysical Research 100, 8873. doi:10.1029/94JD02950.

Guenther, A., Karl, T., Harley, P., Wiedinmyer, C., Palmer, P.I., Geron, C., 2006. Estimates of global terrestrial isoprene emissions using MEGAN (Model of Emissions of Gases and Aerosols from Nature). Atmospheric Chemistry and Physics 6, 3181–3210. doi:10.5194/acp-6-3181-2006. publisher: Copernicus GmbH.

Guenther, A.B., Jiang, X., Heald, C.L., Sakulyanontvittaya, T., Duhl, T., Emmons, L.K., Wang, X., 2012. The Model of Emissions of Gases and Aerosols from Nature version 2.1 (MEGAN2.1): an extended and updated framework for modeling biogenic emissions. Geoscientific Model Development 5, 1471–1492. doi:10.5194/gmd-5-1471-2012. publisher: Copernicus GmbH.

GéoRisques, . Installations industrielles. URL: https://www.georisques.gouv.fr/donnees/bases-de-donnees/installations-industrielles.

Haagen-Smit, A.J., 1952. Chemistry and Physiology of Los Angeles Smog. Industrial & Engineering Chemistry 44, 1342–1346. doi:10.1021/ie50510a045.

Haagen-Smit, A.J., Fox, M.M., 1954. Photochemical Ozone Formation with Hydrocarbons and Automobile Exhaust. Air Repair 4, 105–136. doi:10.1080/00966665.1954.10467649.

Hansel, A., Jordan, A., Holzinger, R., Prazeller, P., Vogel, W., Lindinger, W., 1995. Proton transfer reaction mass spectrometry: on-line trace gas analysis at the ppb level. International Journal of Mass Spectrometry and Ion Processes 149-150, 609–619. doi:10.1016/0168-1176(95)04294-U.

Hanyang, M., Liu, H., Niu, H., Wang, K., Fanyuan, D., Wang, X., Xiao, Q., Hao, J., 2020. VOC evaporative emissions from vehicles in China: Species characteristics of different emission processes. Environmental Science and Ecotechnology 1, 100002. doi:10.1016/j.ese.2019.100002.

HAROPA, 2022. HAROPA PORT - Dossier de presse. URL: https://www.port.fr/sites/default/files/fichiers/dossier_de_presse_haropa_port_2022.pdf.

Harrison, R.M., Allan, J., Carruthers, D., Heal, M.R., Lewis, A.C., Marner, B., Murrells, T., Williams, A., 2021. Non-exhaust vehicle emissions of particulate matter and VOC from road traffic: A review. Atmospheric Environment 262, 118592. doi:10.1016/j.atmosenv.2021.118592.

Healy, R.M., O'Connor, I.P., Hellebust, S., Allanic, A., Sodeau, J.R., Wenger, J.C., 2009. Characterisation of single particles from in-port ship emissions. Atmospheric Environment 43, 6408–6414. doi:10.1016/j.atmosenv.2009.07.039.

Helmig, D., Bottenheim, J., Galbally, I.E., Lewis, A., Milton, M.J.T., Penkett, S., Plass-Duelmer, C., Reimann, S., Tans, P., Thiel, S., 2009. Volatile Organic Compounds in the Global Atmosphere. Eos, Transactions American Geophysical Union 90, 513–514. doi:10.1029/2009EO520001.

Henry, R., Norris, G.A., Vedantham, R., Turner, J.R., 2009. Source Region Identification Using Kernel Smoothing. Environmental Science & Technology 43, 4090–4097. doi:10.1021/es8011723. publisher: American Chemical Society.

Hopke, P.K., 2000. A Guide to Positive Matrix Factorization URL: https://www3.epa.gov/ttnam

ti1/files/ambient/pm25/workshop/laymen.pdf.

Hopke, P.K., 2006. Chemical Mass Balance, in: Encyclopedia of Environmetrics. John Wiley & Sons, Ltd. doi:10.1002/9780470057339.vac017.

Hopkins, F.E., Bell, T.G., Yang, M., Suggett, D.J., Steinke, M., 2016. Air exposure of coral is a significant source of dimethylsulfide (DMS) to the atmosphere. Scientific Reports 6, 36031. doi:10.1038/srep36031.

Huang, C., Hu, Q., Wang, H., Qiao, L., Jing, S., Wang, H., Zhou, M., Zhu, S., Ma, Y., Lou, S., Li, L., Tao, S., Li, Y., Lou, D., 2018. Emission factors of particulate and gaseous compounds from a large cargo vessel operated under real-world conditions. Environmental Pollution 242, 667–674. doi:10.1016/j.envpol.2018.07.036.

IARC, 2008a. 1,3-Butadiene, Ethylene Oxide and Vinyl Halides (Vinyl Fluoride, Vinyl Chloride and Vinyl Bromide). URL: https://publications.iarc.fr/Book-And-Report-Series/Iarc-Monographs-On-The-Identification-Of-Carcinogenic-Hazards-To-Humans/1-3-Butadiene-Ethylene-Oxide-And-Vinyl-Halides-Vinyl-Fluoride-Vinyl-Chloride-And-Vinyl-Bromide--2008.

IARC, 2008b. Formaldehyde, 2-Butoxyethanol and 1-tert-Butoxypropan-2-ol. URL: https://publications.iarc.fr/Book-And-Report-Series/Iarc-Monographs-On-The-Identification-Of-Carcinogenic-Hazards-To-Humans/Formaldehyde-2-Butoxyethanol-And-1--Em-Tert-Em--Butoxypropan-2-ol-2006.

IARC, 2018. Benzene: IARC Monographs on the Evaluation of Carcinogenic Risks to Human. volume 120. URL: https://publications.iarc.fr/Book-And-Report-Series/Iarc-Monographs-On-The-Identification-Of-Carcinogenic-Hazards-To-Humans/Benzene-2018.

IMO, a. International Convention for the Prevention of Pollution from Ships (MARPOL). URL: https://www.imo.org/en/about/Conventions/Pages/International-Convention-for-the-Prevention-of-Pollution-from-Ships-(MARPOL).aspx.

IMO, b. Special Areas under MARPOL. URL: https://www.imo.org/en/ourwork/environment/pages/special-areas-marpol.aspx.

IMO, 2014. Resolution MEPC.251(66). URL: https://wwwcdn.imo.org/localresources/en/KnowledgeCentre/IndexofIMOResolutions/MEPCDocuments/MEPC.251(66).pdf.

IMO, 2015. Resolution MEPC.259(68): Guidelines for Exhaust Gas Cleaning Systems. URL: https://wwwcdn.imo.org/localresources/en/OurWork/Environment/Documents/MEPC.259(68).pdf.

IMO, 2018. Resolution MEPC.304(72): Initial IMo Strategy on Reduction of GHG Emissions From Ships. URL: https://unfccc.int/sites/default/files/resource/250_IMO%20submission_Talanoa%20Dialogue_April%202018.pdf.

IMO, 2023. Prevention of Air Pollution from Ships. URL: https://www.imo.org/en/.

IPCC, 2013. Climate Change 2013: The Physical Science Basis. Technical Report. URL: https://www.ipcc.ch/report/ar5/wg1/.

Ivatt, P.D., Evans, M.J., Lewis, A.C., 2022. Suppression of surface ozone by an aerosol-inhibited photochemical ozone regime. Nature Geoscience 15, 536–540. doi:10.1038/s41561-022-00972-9. number: 7 Publisher: Nature Publishing Group.

Jenkin, M.E., Clemitshaw, K.C., 2000. Ozone and other secondary photochemical pollutants: chemical processes governing their formation in the planetary boundary layer. Atmospheric Environment 34, 2499–2527. doi:10.1016/S1352-2310(99)00478-1.

Jeon, S., Walker, M.J., Sueper, D.T., Day, D.A., Handschy, A.V., Jimenez, J.L., Williams, B.J., 2023. A searchable database and mass spectral comparison tool for the Aerosol Mass Spectrometer (AMS) and the Aerosol Chemical Speciation Monitor (ACSM). Atmospheric Measurement Techniques 16, 6075–6095. doi:10.5194/amt-16-6075-2023.

Jeong, S., Bendl, J., Saraji-Bozorgzad, M., Käfer, U., Etzien, U., Schade, J., Bauer, M., Jakobi, G., Orasche, J., Fisch, K., Cwierz, P.P., Rüger, C.P., Czech, H., Karg, E., Heyen, G., Krausnick, M., Geissler, A., Geipel, C., Streibel, T., Schnelle-Kreis, J., Sklorz, M., Schulz-Bull, D.E., Buchholz, B., Adam, T., Zimmermann, R., 2023. Aerosol emissions from a marine diesel engine running on different fuels and effects of exhaust gas cleaning measures. Environmental Pollution 316, 120526. doi:10.1016/j.envpol.2022.120526.

Jiang, L., Ge, Y., Shah, A.N., He, C., Liu, Z., 2010. Unregulated emissions from a diesel engine equipped with vanadium-based urea-SCR catalyst. Journal of Environmental Sciences 22, 575–581. doi:10.1016/S1001-0742(09)60148-0.

Johnson, D., Marston, G., 2008. The gas-phase ozonolysis of unsaturated volatile organic compounds in the troposphere. Chemical Society Reviews 37, 699. doi:10.1039/b704260b.

Karjalainen, P., Teinilä, K., Kuittinen, N., Aakko-Saksa, P., Bloss, M., Vesala, H., Pettinen, R., Saarikoski, S., Jalkanen, J.P., Timonen, H., 2022. Real-world particle emissions and secondary aerosol formation from a diesel oxidation catalyst and scrubber equipped ship operating with two fuels in a SECA area. Environmental Pollution 292, 118278. doi:10.1016/j.envpol.2021.118278.

Karl, M., Ramacher, M.O.P., Oppo, S., Lanzi, L., Majamäki, E., Jalkanen, J.P., Lanzafame, G.M., Temime-Roussel, B., Le Berre, L., D'Anna, B., 2023. Measurement and Modeling of Ship-Related Ultrafine Particles and Secondary Organic Aerosols in a Mediterranean Port City. Toxics 11, 771. doi:10.3390/toxics11090771.

Kesselmeier, J., Staudt, M., 1999. Biogenic Volatile Organic Compounds (VOC): An Overview on Emission, Physiology and Ecology. Journal of Atmospheric Chemistry 33, 23–88.

King, M.D., Greenstone, R., Bandeen, R., 2010. Earth Observing System (EOS) Science Plan: The State of Science in the EOS Program. URL: https://eospso.nasa.gov/sites/default/files/publications/SciencePlan.pdf.

Kroll, J.H., Seinfeld, J.H., 2008. Chemistry of secondary organic aerosol: Formation and evolution of low-volatility organics in the atmosphere. Atmospheric Environment 42, 3593–3624. doi:10.1016/j.atmosenv.2008.01.003.

Krupa, S.V., Manning, W.J., 1988. Atmospheric ozone: Formation and effects on vegetation. Environmental Pollution 50, 101–137. doi:10.1016/0269-7491(88)90187-x. publisher: Elsevier BV.

Kuittinen, N., Jalkanen, J.P., Alanen, J., Ntziachristos, L., Hannuniemi, H., Johansson, L., Karjalainen, P., Saukko, E., Isotalo, M., Aakko-Saksa, P., Lehtoranta, K., Keskinen, J., Simonen, P., Saarikoski, S., Asmi, E., Laurila, T., Hillamo, R., Mylläri, F., Lihavainen, H., Timonen, H., Rönkkö, T., 2021. Shipping Remains a Globally Significant Source of Anthropogenic PN Emissions Even after 2020 Sulfur Regulation. Environmental Science & Technology 55, 129–138. doi:10.1021/acs.est.0c03627.

Kuo, C.P., Liao, H.T., Chou, C.C.K., Wu, C.F., 2014. Source apportionment of particulate matter and selected volatile organic compounds with multiple time resolution data. Science of The Total Environment 472, 880–887. doi:10.1016/j.scitotenv.2013.11.114.

Kurtenbach, R., Vaupel, K., Kleffmann, J., Klenk, U., Schmidt, E., Wiesen, P., 2016. Emissions of NO, NO2 and PM from inland shipping. Atmospheric Chemistry and Physics 16, 14285–14295. doi:10.5194/acp-16-14285-2016.

Labit, J., Grandjean, T., 2021. L'environnement en Hauts-de-France : L'industrie au regard de l'environnement .

Lack, D.A., Corbett, J.J., 2012. Black carbon from ships: a review of the effects of ship speed, fuel quality and exhaust gas scrubbing. Atmospheric Chemistry and Physics 12, 3985–4000. doi:10.5194/acp-12-3985-2012.

Lack, D.A., Corbett, J.J., Onasch, T., Lerner, B., Massoli, P., Quinn, P.K., Bates, T.S., Covert, D.S., Coffman, D., Sierau, B., Herndon, S., Allan, J., Baynard, T., Lovejoy, E., Ravishankara, A.R., Williams, E., 2009. Particulate emissions from commercial shipping: Chemical, physical, and optical properties. Journal of Geophysical Research: Atmospheres 114. doi:10.1029/2008JD011300.

Lannuque, V., D'Anna, B., Kostenidou, E., Couvidat, F., Martinez-Valiente, A., Eichler, P., Wisthaler, A., Müller, M., Temime-Roussel, B., Valorso, R., Sartelet, K., 2023. Gas–particle partitioning of toluene oxidation products: an experimental and modeling study. Atmospheric Chemistry and Physics 23, 15537–15560. doi:10.5194/acp-23-15537-2023. publisher: Copernicus GmbH.

Lasne, J., Lostier, A., Romanias, M.N., Vassaux, S., Lesueur, D., Gaudion, V., Jamar, M., Derwent, R.G., Dusanter, S., Salameh, T., 2023. VOC emissions by fresh and old asphalt pavements at service temperatures: impacts on urban air quality. Environmental Science: Atmospheres doi:10.1039/D3EA00034F. publisher: RSC.

LCSQA, 2018. Guide méthodologique pour l'élaboration des inventaires territoriaux (polluants de l'air et gaz à effet de serre). Technical Report. URL: https://www.lcsqa.org/fr/rapport/guide-methodologique-pour-lelaboration-des-inventaires-territoriaux-des-emissions.

Le Berre, L., Temime-Roussel, B., Lanzafame, G.M., D'Anna, B., Marchand, N., Sauvage, S., Dufresne, M., Tinel, L., Leonardis, T., Ferreira de Brito, J., Armengaud, A., Gille, G., Lanzi, L., Bourjot, R., Wortham, H., 2025. Measurement report: In-depth characterization of ship emissions during operations in a Mediterranean port. Atmospheric Chemistry and Physics 25, 6575–6605. doi:10.5194/acp-25-6575-2025. publisher: Copernicus GmbH.

Li, J., Deng, S., Li, G., Lu, Z., Song, H., Gao, J., Sun, Z., Xu, K., 2022. VOCs characteristics and their ozone and SOA formation potentials in autumn and winter at Weinan, China. Environmental Research 203, 111821. doi:10.1016/j.envres.2021.111821.

Li, R., Palm, B.B., Ortega, A.M., Hlywiak, J., Hu, W., Peng, Z., Day, D.A., Knote, C., Brune, W.H., De Gouw, J.A., Jimenez, J.L., 2015. Modeling the Radical Chemistry in an Oxidation Flow Reactor: Radical Formation and Recycling, Sensitivities, and the OH Exposure Estimation Equation. The Journal of Physical Chemistry A 119, 4418–4432. doi:10.1021/jp509534k.

Liao, H.T., Kuo, C.P., Hopke, P.K., Wu, C.F., 2013. Evaluation of a Modified Receptor Model for Solving Multiple Time Resolution Equations: A Simulation Study. Aerosol and Air Quality Research 13, 1253–1262. doi:10.4209/aaqr.2012.11.0322. publisher: Taiwan Association for Aerosol Research.

Lin, C., Ceburnis, D., Hellebust, S., Buckley, P., Wenger, J., Canonaco, F., Prévôt, A.S.H., Huang, R.J., O'Dowd, C., Ovadnevaite, J., 2017. Characterization of Primary Organic Aerosol from Domestic Wood, Peat, and Coal Burning in Ireland. Environmental Science & Technology 51, 10624–10632. doi:10.1021/acs.est.7b01926. publisher: American Chemical Society.

Lin, C., Ceburnis, D., Trubetskaya, A., Xu, W., Smith, W., Hellebust, S., Wenger, J., O'Dowd, C., Ovadnevaite, J., 2021. On the use of reference mass spectra for reducing uncertainty in source apportionment of solid-fuel burning in ambient organic aerosol. Atmospheric Measurement Techniques 14, 6905–6916. doi:10.5194/amt-14-6905-2021. publisher: Copernicus GmbH.

Lindinger, W., Hansel, A., Jordan, A., 1998. On-line monitoring of volatile organic compounds at pptv levels by means of proton-transfer-reaction mass spectrometry (PTR-MS) medical applications, food control and environmental research. International Journal of Mass Spectrometry and Ion Processes 173, 191–241. doi:10.1016/S0168-1176(97)00281-4.

Liu, B., Yang, Y., Yang, T., Dai, Q., Zhang, Y., Feng, Y., Hopke, P.K., 2023. Effect of photochemical losses of ambient volatile organic compounds on their source apportionment. Environment International 172, 107766. doi:10.1016/j.envint.2023.107766.

Lonati, G., Cernuschi, S., Sidi, S., 2010. Air quality impact assessment of at-berth ship emissions: Case-study for the project of a new freight port. Science of The Total Environment 409, 192–200. doi:10.1016/j.scitotenv.2010.08.029.

Lostier, A., Sarica, T., Lasne, J., Roose, A., Sartelet, K., Jamar, M., Gaudion, V., Dusanter, S., Lesueur, D., Chen, H., Salameh, T., Romanias, M.N., 2025. Real-World Asphalt Pavement Emissions: Combining Simulation Chamber Measurements and City Scale Modeling to Elucidate the Impacts on Air Quality. ACS ES&T Air 2, 426–435. doi:10.1021/acsestair.4c00323. publisher: American Chemical Society.

Ltd., D., 2021. Source Finder (SoFi): Manual for the software package SoFi (Pro) and SoFi realtime (RT) in IGOR Wavemetrics Inc. Technical Report.

Légifrance, 1999. Directive 98/70/CE du Parlement européen et du Conseil du 13 octobre 1998 concernant la qualité de l'essence et des carburants diesel et modifiant la directive 93/12/CEE du Conseil.

Légifrance, 2010. Décret n° 2010-1250 du 21 octobre 2010 relatif à la qualité de l'air. URL: https://www.legifrance.gouv.fr/jorf/id/JORFTEXT000022941254.

Mahajan, A.S., Tinel, L., Riffault, V., Guilbaud, S., D'Anna, B., Cuevas, C., Saiz-Lopez, A., 2024. MAX-DOAS observations of ship emissions in the North Sea. Marine Pollution Bulletin 206,

116761. doi:10.1016/j.marpolbul.2024.116761.

Marques, B., Kostenidou, E., Valiente, A.M., Vansevenant, B., Sarica, T., Fine, L., Temime-Roussel, B., Tassel, P., Perret, P., Liu, Y., Sartelet, K., Ferronato, C., D'Anna, B., 2022. Detailed Speciation of Non-Methane Volatile Organic Compounds in Exhaust Emissions from Diesel and Gasoline Euro 5 Vehicles Using Online and Offline Measurements. Toxics 10, 184. doi:10.3390/toxics10040184. publisher: MDPI AG.

Miller, S.T.K., Keim, B.D., Talbot, R.W., Mao, H., 2003. Sea breeze: Structure, forecasting, and impacts. Reviews of Geophysics 41. doi:10.1029/2003RG000124.

Millet, D.B., Jacob, D.J., Custer, T.G., de Gouw, J.A., Goldstein, A.H., Karl, T., Singh, H.B., Sive, B.C., Talbot, R.W., Warneke, C., Williams, J., 2008. New constraints on terrestrial and oceanic sources of atmospheric methanol. Atmospheric Chemistry and Physics 8, 6887–6905. doi:10.5194/acp-8-6887-2008.

Montero, L., Duane, M., Manfredi, U., Astorga, C., Martini, G., Carriero, M., Krasenbrink, A., Larsen, B., 2010. Hydrocarbon emission fingerprints from contemporary vehicle/engine technologies with conventional and new fuels. Atmospheric Environment 44, 2167–2175. doi:10.1016/j.atmosenv.2010.03.027.

Mooibroek, D., Sofowote, U.M., Hopke, P.K., 2022. Source apportionment of ambient PM10 collected at three sites in an urban-industrial area with multi-time resolution factor analyses. Science of The Total Environment 850, 157981. doi:10.1016/j.scitotenv.2022.157981.

Ney, M., Delmas, V., 2024. Mesures du 1.3-butadiène, du benzène et de l'acrylonitrile dans l'air ambiant au niveau des zones industrielles du Havre et de Port-Jérôme : Campagnes mutualisées 2023. Technical Report EN_VRP_405_V01. Atmo Normandie. URL: https://www.atmonormandie.fr/publications/mesures-du-13-butadiene-du-benzene-et-de-lacrylonitrile-dans-lair-ambiant-au-niveau.

Ney, M., Le Meur, S., 2022. Mesures du 1.3-butadiène, du benzène et de l'acrylonitrile dans l'air ambiant au niveau des zones industrielles du Havre et de Port-Jérôme : Campagnes mutualisées 2020 – 2021. Technical Report DQR 017-1. Atmo Normandie. URL: https://www.atmonormandie.fr/publications/mesures-du-13-butadiene-du-benzene-et-de-lacrylonitrile-dans-lair-ambiant-au-niveau.

Norris, G., Duvall, R., Brown, S., Bai, S., 2014. Positive Matrix Factorization (PMF) 5.0 Fundamentals and User Guide .

Ogulei, D., Hopke, P.K., Zhou, L., Paatero, P., Park, S.S., Ondov, J.M., 2005. Receptor modeling

for multiple time resolved species: The Baltimore supersite. Atmospheric Environment 39, 3751–3762. doi:10.1016/j.atmosenv.2005.03.012.

Olson, D.A., Hammond, D.M., Seila, R.L., Burke, J.M., Norris, G.A., 2009. Spatial gradients and source apportionment of volatile organic compounds near roadways. Atmospheric Environment 43, 5647–5653. doi:10.1016/j.atmosenv.2009.07.065.

Orellano, P., Reynoso, J., Quaranta, N., Bardach, A., Ciapponi, A., 2020. Short-term exposure to particulate matter (PM10 and PM2.5), nitrogen dioxide (NO2), and ozone (O3) and all-cause and cause-specific mortality: Systematic review and meta-analysis. Environment International 142, 105876. doi:10.1016/j.envint.2020.105876. publisher: Elsevier BV.

ORS, 2007. Les Composés Organiques Volatiles (COV). Technical Report. URL: https://www.ors-idf.org/fileadmin/DataStorageKit/ORS/Etudes/2007/Etude2007_1/rapport_cov_final_1_.pdf.

Paatero, P., 1997. Least squares formulation of robust non-negative factor analysis. Chemometrics and Intelligent Laboratory Systems 37, 23–35. doi:10.1016/S0169-7439(96)00044-5.

Paatero, P., 1999. The Multilinear Engine—A Table-Driven, Least Squares Program for Solving Multilinear Problems, Including the*n*-Way Parallel Factor Analysis Model. Journal of Computational and Graphical Statistics 8, 854–888. doi:10.1080/10618600.1999.10474853. publisher: Informa UK Limited.

Paatero, P., Tapper, U., 1994. Positive matrix factorization: A non-negative factor model with optimal utilization of error estimates of data values. Environmetrics 5, 111–126. doi:10.1002/env.3170050203.

PACA, A., 2017. Impact des émissions du transport maritime sur la qualité de l'air des zones portuaires. Technical Report. URL: https://www.atmosud.org/sites/sud/files/medias/documents/2022-06/2017._etude_bibliographique_air_et_activites_maritimes_et_portuaires.pdf.

Petit, J.E., Favez, O., Albinet, A., Canonaco, F., 2017. A user-friendly tool for comprehensive evaluation of the geographical origins of atmospheric pollution: Wind and trajectory analyses. Environmental Modelling & Software 88, 183–187. doi:10.1016/j.envsoft.2016.11.022.

Petzold, A., Hasselbach, J., Lauer, P., Baumann, R., Franke, K., Gurk, C., Schlager, H., Weingartner, E., 2008. Experimental studies on particle emissions from cruising ship, their characteristic properties, transformation and atmospheric lifetime in the marine boundary layer. Atmospheric Chemistry and Physics 8, 2387–2403. doi:10.5194/acp-8-2387-2008.

Petzold, A., Lauer, P., Fritsche, U., Hasselbach, J., Lichtenstern, M., Schlager, H., Fleischer, F., 2011. Operation of Marine Diesel Engines on Biogenic Fuels: Modification of Emissions and Resulting Climate Effects. Environmental Science & Technology 45, 10394–10400. doi:10.1021/es2021439.

Piccot, S.D., Watson, J.J., Jones, J.W., 1992. A global inventory of volatile organic compound emissions from anthropogenic sources. Journal of Geophysical Research: Atmospheres 97, 9897–9912. doi:10.1029/92JD00682.

Pirjola, L., Pajunoja, A., Walden, J., Jalkanen, J.P., Rönkkö, T., Kousa, A., Koskentalo, T., 2014. Mobile measurements of ship emissions in two harbour areas in Finland. Atmospheric Measurement Techniques 7, 149–161. doi:10.5194/amt-7-149-2014.

Potier, E., Waked, A., Bourin, A., Minvielle, F., Péré, J.C., Perdrix, E., Michoud, V., Riffault, V., Alleman, L.Y., Sauvage, S., 2019. Characterizing the regional contribution to PM10 pollution over northern France using two complementary approaches: Chemistry transport and trajectory-based receptor models. Atmospheric Research 223, 1–14. doi:10.1016/j.atmosres.2019.03.002.

Priestley, M., Bannan, T.J., Le Breton, M., Worrall, S.D., Kang, S., Pullinen, I., Schmitt, S., Tillmann, R., Kleist, E., Zhao, D., Wildt, J., Garmash, O., Mehra, A., Bacak, A., Shallcross, D.E., Kiendler-Scharr, A., Hallquist, M., Ehn, M., Coe, H., Percival, C.J., Hallquist, M., Mentel, T.F., McFiggans, G., 2021. Chemical characterisation of benzene oxidation products under high- and low-NO_x conditions using chemical ionisation mass spectrometry. Atmospheric Chemistry and Physics 21, 3473–3490. doi:10.5194/acp-21-3473-2021. publisher: Copernicus GmbH.

Quinn, P.K., Bates, T.S., Coffman, D., Onasch, T.B., Worsnop, D., Baynard, T., de Gouw, J.A., Goldan, P.D., Kuster, W.C., Williams, E., Roberts, J.M., Lerner, B., Stohl, A., Pettersson, A., Lovejoy, E.R., 2006. Impacts of sources and aging on submicrometer aerosol properties in the marine boundary layer across the Gulf of Maine. Journal of Geophysical Research: Atmospheres 111. doi:10.1029/2006JD007582.

Rimetz-Planchon, J., Perdrix, E., Sobanska, S., Brémard, C., 2008. PM10 air quality variations in an urbanized and industrialized harbor. Atmospheric Environment 42, 7274–7283. doi:10.1016/j.atmosenv.2008.07.005.

Robinson, A.L., Donahue, N.M., Shrivastava, M.K., Weitkamp, E.A., Sage, A.M., Grieshop, A.P., Lane, T.E., Pierce, J.R., Pandis, S.N., 2007. Rethinking Organic Aerosols: Semivolatile Emissions and Photochemical Aging. Science 315, 1259–1262. doi:10.1126/science.1133061.

Roukos, J., Riffault, V., Locoge, N., Plaisance, H., 2009. VOC in an Urban and Industrial Harbor

on the French North Sea Coast during Two Contrasted Meteorological Situations. Environmental pollution (Barking, Essex : 1987) 157, 3001–9. doi:10.1016/j.envpol.2009.05.059.

Russo, M., Leitão, J., Gama, C., Ferreira, J., Monteiro, A., 2018. Shipping emissions over Europe: A state-of-the-art and comparative analysis. Atmospheric Environment 177, 187–194. doi:10.1016/j.atmosenv.2018.01.025.

Saison, J.Y., 2020. Rapport d'Étude: Suivi de la Qualité de l'Air en Proximité Industrielle sur le Site de Mardyck (59). Technical Report. Atmo Hauts-de-France. URL: https://www.atmo-hdf.fr/sites/hdf/files/content/migrated/Rapport_et_synthese_etudes/2020/Rapport_versalis2019.pdf.

Salameh, T., Afif, C., Sauvage, S., Borbon, A., Locoge, N., 2014. Speciation of non-methane hydrocarbons (NMHCs) from anthropogenic sources in Beirut, Lebanon. Environmental Science and Pollution Research 21, 10867–10877. doi:10.1007/s11356-014-2978-5.

Salameh, T., Sauvage, S., Afif, C., Borbon, A., Locoge, N., 2016. Source apportionment vs. emission inventories of non-methane hydrocarbons (NMHC) in an urban area of the Middle East: local and global perspectives. Atmospheric Chemistry and Physics 16, 3595–3607. doi:10.5194/acp-16-3595-2016. publisher: Copernicus GmbH.

Santos, F.M., Gómez-Losada, , Pires, J.C., 2021. Empirical ozone isopleths at urban and suburban sites through evolutionary procedure-based models. Journal of Hazardous Materials 419, 126386. doi:10.1016/j.jhazmat.2021.126386.

Sauvage, S., Plaisance, H., Locoge, N., Wroblewski, A., Coddeville, P., Galloo, J.C., 2009. Long term measurement and source apportionment of non-methane hydrocarbons in three French rural areas. Atmospheric Environment 43, 2430–2441. doi:10.1016/j.atmosenv.2009.02.001.

Saxe, H., Larsen, T., 2004. Air pollution from ships in three Danish ports. Atmospheric Environment 38, 4057–4067. doi:10.1016/j.atmosenv.2004.03.055.

Schauer, J.J., Kleeman, M.J., Cass, G.R., Simoneit, B.R.T., 2002. Measurement of Emissions from Air Pollution Sources. 5. C $_1$ C $_{32}$ Organic Compounds from Gasoline-Powered Motor Vehicles. Environmental Science & Technology 36, 1169–1180. doi:10.1021/es0108077.

Schauer, J.J., Lough, G.C., Shafer, M.M., Christensen, W.F., Arndt, M.F., DeMinter, J.T., Park, J.S., 2006. Characterization of Metals Emitted from Motor Vehicles. Health Effects Institute 133. URL: https://www.healtheffects.org/system/files/Schauer.pdf.

Seigneur, C., 2018. Pollution atmosphérique: concepts, théorie et applications. Échelles, Belin

éducation, Paris.

Seinfeld, J.H., Pandis, S.N., 2016. Atmospheric chemistry and physics: from air pollution to climate change. Third edition ed., Wiley, Hoboken, New Jersey.

Shah, A.N., Ge, Y.s., Jiang, L., 2011. Impact of a Urea-Selective Catalytic Reduction System on Volatile Organic Compound Emissions from a Diesel Engine. Arabian Journal for Science and Engineering 36, 891–901. doi:10.1007/s13369-011-0072-6.

Shen, H., Sun, Z., Chen, Y., Russell, A.G., Hu, Y., Odman, M.T., Qian, Y., Archibald, A.T., Tao, S., 2021. Novel Method for Ozone Isopleth Construction and Diagnosis for the Ozone Control Strategy of Chinese Cities. Environmental Science & Technology 55, 15625–15636. doi:10.1021/acs.est.1c01567. publisher: American Chemical Society.

Shiraiwa, M., Seinfeld, J.H., 2012. Equilibration timescale of atmospheric secondary organic aerosol partitioning. Geophysical Research Letters 39, 2012GL054008. doi:10.1029/2012GL054008.

Simon, L., Favez, O., Petit, J.E., Canonaco, F., Slowik, J.G., Marchand, C., Gros, V., 2025. Source apportionment of organic gaseous and particulate compounds using a combined positive matrix factorization approach in summer (2020) in the Paris region (France). Atmospheric Environment 354, 121269. doi:10.1016/j.atmosenv.2025.121269.

Sindelarova, K., Granier, C., Bouarar, I., Guenther, A., Tilmes, S., Stavrakou, T., Müller, J.F., Kuhn, U., Stefani, P., Knorr, W., 2014. Global data set of biogenic VOC emissions calculated by the MEGAN model over the last 30 years. Atmospheric Chemistry and Physics 14, 9317–9341. doi:10.5194/acp-14-9317-2014.

Slowik, J.G., Vlasenko, A., McGuire, M., Evans, G.J., Abbatt, J.P.D., 2010. Simultaneous factor analysis of organic particle and gas mass spectra: AMS and PTR-MS measurements at an urban site. Atmospheric Chemistry and Physics 10, 1969–1988. doi:10.5194/acp-10-1969-2010.

Sofiev, M., Winebrake, J.J., Johansson, L., Carr, E.W., Prank, M., Soares, J., Vira, J., Kouznetsov, R., Jalkanen, J.P., Corbett, J.J., 2018. Cleaner fuels for ships provide public health benefits with climate tradeoffs. Nature Communications 9, 406. doi:10.1038/s41467-017-02774-9.

Spivakovsky, C.M., Logan, J.A., Montzka, S.A., Balkanski, Y.J., Foreman-Fowler, M., Jones, D.B.A., Horowitz, L.W., Fusco, A.C., Brenninkmeijer, C.A.M., Prather, M.J., Wofsy, S.C., McElroy, M.B., 2000. Three-dimensional climatological distribution of tropospheric OH: Update and evaluation. Journal of Geophysical Research: Atmospheres 105, 8931–8980. doi:10.1029/1999JD901006.

Stanimirova, I., Rich, D.Q., Russell, A.G., Hopke, P.K., 2023. A long-term, dispersion normalized PMF source apportionment of PM2.5 in Atlanta from 2005 to 2019. Atmospheric Environment 312, 120027. doi:10.1016/j.atmosenv.2023.120027.

Sud, A., 2021. Évaluation de l'évolution des émissions des navires dans le port de Marseille en lien avec la crise sanitaire. Technical Report. URL: https://www.atmosud.org/publications/evaluation-de-levolution-des-emissions-des-navires-dans-le-port-de-marseille-en-lien.

Sulzer, P., Hartungen, E., Hanel, G., Feil, S., Winkler, K., Mutschlechner, P., Haidacher, S., Schottkowsky, R., Gunsch, D., Seehauser, H., Striednig, M., Jürschik, S., Breiev, K., Lanza, M., Herbig, J., Märk, L., Märk, T.D., Jordan, A., 2014. A Proton Transfer Reaction-Quadrupole interface Time-Of-Flight Mass Spectrometer (PTR-QiTOF): High speed due to extreme sensitivity. International Journal of Mass Spectrometry 368, 1–5. doi:10.1016/j.ijms.2014.05.004.

Tang, L., Ramacher, M.O.P., Moldanová, J., Matthias, V., Karl, M., Johansson, L., Jalkanen, J.P., Yaramenka, K., Aulinger, A., Gustafsson, M., 2020. The impact of ship emissions on air quality and human health in the Gothenburg area – Part 1: 2012 emissions. Atmospheric Chemistry and Physics 20, 7509–7530. doi:10.5194/acp-20-7509-2020.

Timonen, H., Teinlä, K., Barreira, L., Simonen, P., Dal Maso, M., Keskinen, J., Kalliokoski, J., Moldonova, J., Salberg, H., Merelli, L., D'Anna, B., Temime-Roussel, B., Lanzafame, G.M., Mellqvist, J., 2022. Ship on-board emissions characterisation. Technical Report. The SCIPPER Project. URL: https://www.scipper-project.eu/library/.

Tkacik, D.S., Presto, A.A., Donahue, N.M., Robinson, A.L., 2012. Secondary Organic Aerosol Formation from Intermediate-Volatility Organic Compounds: Cyclic, Linear, and Branched Alkanes. Environmental Science & Technology 46, 8773–8781. doi:10.1021/es301112c.

Tokaya, J.P., Kranenburg, R., Timmermans, R.M.A., Coenen, P.W.H.G., Kelly, B., Hullegie, J.S., Megaritis, T., Valastro, G., 2024. The impact of shipping on the air quality in European port cities with a detailed analysis for Rotterdam. Atmospheric Environment: X 23, 100278. doi:10.1016/j.aeaoa.2024.100278.

Toolbox, T.E., 2003. Fuels - Higher and Lower Calorific Values. URL: https://www.engineeringtoolbox.com/fuels-higher-calorific-values-d_169.html.

UNCTAD, 2021. Beyond 20/20 WDS. URL: https://unctadstat.unctad.org/wds/ReportFolders/reportFolders.aspx.

Unger, N., 2014. On the role of plant volatiles in anthropogenic global climate change. Geophysical Research Letters 41, 8563–8569. doi:10.1002/2014gl061616. publisher: American Geophysical

Union (AGU).

US EPA, O., 2015. Health Effects of Ozone Pollution. URL: https://www.epa.gov/ground-level-ozone-pollution/health-effects-ozone-pollution.

Van Roy, W., Merveille, J.B., Scheldeman, K., Van Nieuwenhove, A., Schallier, R., Van Roozendael, B., Maes, F., 2023. Assessment of the Effect of International Maritime Regulations on Air Quality in the Southern North Sea. Atmosphere 14, 969. doi:10.3390/atmos14060969. number: 6 Publisher: Multidisciplinary Digital Publishing Institute.

Van Roy, W., Schallier, R., Van Roozendael, B., Scheldeman, K., Van Nieuwenhove, A., Maes, F., 2022a. Airborne monitoring of compliance to sulfur emission regulations by ocean-going vessels in the Belgian North Sea area. Atmospheric Pollution Research 13, 101445. doi:10.1016/j.apr.2022.101445.

Van Roy, W., Van Nieuwenhove, A., Scheldeman, K., Van Roozendael, B., Schallier, R., Mellqvist, J., Maes, F., 2022b. Measurement of Sulfur-Dioxide Emissions from Ocean-Going Vessels in Belgium Using Novel Techniques. Atmosphere 13, 1756. doi:10.3390/atmos13111756.

Venecek, M.A., Carter, W.P., Kleeman, M.J., 2018. Updating the SAPRC Maximum Incremental Reactivity (MIR) scale for the United States from 1988 to 2010. Journal of the Air & Waste Management Association 68, 1301–1316. doi:10.1080/10962247.2018.1498410.

Via, M., Chen, G., Canonaco, F., Daellenbach, K.R., Chazeau, B., Chebaicheb, H., Jiang, J., Keernik, H., Lin, C., Marchand, N., Marin, C., O'Dowd, C., Ovadnevaite, J., Petit, J.E., Pikridas, M., Riffault, V., Sciare, J., Slowik, J.G., Simon, L., Vasilescu, J., Zhang, Y., Favez, O., Prévôt, A.S.H., Alastuey, A., Cruz Minguillón, M., 2022. *Rolling* vs. *seasonal* PMF: real-world multi-site and synthetic dataset comparison. Atmospheric Measurement Techniques 15, 5479–5495. doi:10.5194/amt-15-5479-2022.

Via, M., Yus-Díez, J., Canonaco, F., Petit, J.E., Hopke, P., Reche, C., Pandolfi, M., Ivančič, M., Rigler, M., Prevôt, A.S.H., Querol, X., Alastuey, A., Minguillón, M.C., 2023. Towards a better understanding of fine PM sources: Online and offline datasets combination in a single PMF. Environment International 177, 108006. doi:10.1016/j.envint.2023.108006.

Viana, M., Amato, F., Alastuey, A., Querol, X., Moreno, T., García Dos Santos, S., Herce, M.D., Fernández-Patier, R., 2009. Chemical Tracers of Particulate Emissions from Commercial Shipping. Environmental Science & Technology 43, 7472–7477. doi:10.1021/es901558t. publisher: American Chemical Society.

Viana, M., Hammingh, P., Colette, A., Querol, X., Degraeuwe, B., Vlieger, I.d., van Aardenne,

J., 2014. Impact of maritime transport emissions on coastal air quality in Europe. Atmospheric Environment 90, 96–105. doi:10.1016/j.atmosenv.2014.03.046.

Viana, M., Kuhlbusch, T., Querol, X., Alastuey, A., Harrison, R., Hopke, P., Winiwarter, W., Vallius, M., Szidat, S., Prévôt, A., Hueglin, C., Bloemen, H., Wåhlin, P., Vecchi, R., Miranda, A., Kasper-Giebl, A., Maenhaut, W., Hitzenberger, R., 2008. Source apportionment of particulate matter in Europe: A review of methods and results. Journal of Aerosol Science 39, 827–849. doi:10.1016/j.jaerosci.2008.05.007. publisher: Elsevier BV.

Voliotis, A., Wang, Y., Shao, Y., Du, M., Bannan, T.J., Percival, C.J., Pandis, S.N., Alfarra, M.R., McFiggans, G., 2021. Exploring the composition and volatility of secondary organic aerosols in mixed anthropogenic and biogenic precursor systems. Atmospheric Chemistry and Physics 21, 14251–14273. doi:10.5194/acp-21-14251-2021. publisher: Copernicus GmbH.

Waked, A., Bourin, A., Michoud, V., Perdrix, E., Alleman, L.Y., Sauvage, S., Delaunay, T., Vermeesch, S., Petit, J.E., Riffault, V., 2018. Investigation of the geographical origins of PM10 based on long, medium and short-range air mass back-trajectories impacting Northern France during the period 2009–2013. Atmospheric Environment 193, 143–152. doi:10.1016/j.atmosenv.2018.08.015.

Wang, H., Liu, X., Wu, C., Lin, G., 2024. Regional to global distributions, trends, and drivers of biogenic volatile organic compound emission from 2001 to 2020. Atmospheric Chemistry and Physics 24, 3309–3328. doi:10.5194/acp-24-3309-2024. publisher: Copernicus GmbH.

Wang, Q., Wang, S., Cheng, Y.Y., Chen, H., Zhang, Z., Li, J., Gu, D., Wang, Z., Yu, J.Z., 2022. Chemical evolution of secondary organic aerosol tracers during high-$PM_{2.5}$ episodes at a suburban site in Hong Kong over 4 months of continuous measurement. Atmospheric Chemistry and Physics 22, 11239–11253. doi:10.5194/acp-22-11239-2022. publisher: Copernicus GmbH.

Wang, Y., Ren, X., Ji, D., Zhang, J., Sun, J., Wu, F., 2012. Characterization of volatile organic compounds in the urban area of Beijing from 2000 to 2007. Journal of Environmental Sciences 24, 95–101. doi:10.1016/S1001-0742(11)60732-8.

Warneke, C., Geiger, F., Edwards, P.M., Dube, W., Pétron, G., Kofler, J., Zahn, A., Brown, S.S., Graus, M., Gilman, J.B., Lerner, B.M., Peischl, J., Ryerson, T.B., De Gouw, J.A., Roberts, J.M., 2014. Volatile organic compound emissions from the oil and natural gas industry in the Uintah Basin, Utah: oil and gas well pad emissions compared to ambient air composition. Atmospheric Chemistry and Physics 14, 10977–10988. doi:10.5194/acp-14-10977-2014.

Weschler, C.J., Nazaroff, W.W., 2008. Semivolatile organic compounds in indoor environments. Atmospheric Environment 42, 9018–9040. doi:10.1016/j.atmosenv.2008.09.052.

WHO, 2021. WHO global air quality guidelines: particulate matter (PM2.5 and PM10), ozone, nitrogen dioxide, sulfur dioxide and carbon monoxide. URL: https://www.who.int/publications/i/item/9789240034228.

WMO, 2015. Global atmospheric ozone monitoring. URL: https://public.wmo.int/en/bulletin/global-atmospheric-ozone-monitoring.

Xiang, Y., Delbarre, H., Sauvage, S., Léonardis, T., Fourmentin, M., Augustin, P., Locoge, N., 2012. Development of a methodology examining the behaviours of VOCs source apportionment with micro-meteorology analysis in an urban and industrial area. Environmental Pollution 162, 15–28. doi:10.1016/j.envpol.2011.10.012.

Xiao, Q., Li, M., Liu, H., Fu, M., Deng, F., Lv, Z., Man, H., Jin, X., Liu, S., He, K., 2018. Characteristics of marine shipping emissions at berth: profiles for particulate matter and volatile organic compounds. Atmospheric Chemistry and Physics 18, 9527–9545. doi:10.5194/acp-18-9527-2018.

Xu, W., Lambe, A., Silva, P., Hu, W., Onasch, T., Williams, L., Croteau, P., Zhang, X., Renbaum-Wolff, L., Fortner, E., Jimenez, J.L., Jayne, J., Worsnop, D., Canagaratna, M., 2018. Laboratory evaluation of species-dependent relative ionization efficiencies in the Aerodyne Aerosol Mass Spectrometer. Aerosol Science and Technology 52, 626–641. doi:10.1080/02786826.2018.1439570.

Yamamoto, Y., Kambe, Y., Yamada, H., Tonokura, K., 2012. Measurement of Volatile Organic Compounds in Vehicle Exhaust Using Single-Photon Ionization Time-of-Flight Mass Spectrometry. Analytical Sciences 28, 385–390. doi:10.2116/analsci.28.385. publisher: Springer Science and Business Media LLC.

Yuan, B., Koss, A.R., Warneke, C., Coggon, M., Sekimoto, K., De Gouw, J.A., 2017. Proton-Transfer-Reaction Mass Spectrometry: Applications in Atmospheric Sciences. Chemical Reviews 117, 13187–13229. doi:10.1021/acs.chemrev.7b00325.

Yáñez-Serrano, A.M., Filella, I., LLusià, J., Gargallo-Garriga, A., Granda, V., Bourtsoukidis, E., Williams, J., Seco, R., Cappellin, L., Werner, C., de Gouw, J., Peñuelas, J., 2021. GLOVOCS - Master compound assignment guide for proton transfer reaction mass spectrometry users. Atmospheric Environment 244, 117929. doi:10.1016/j.atmosenv.2020.117929.

Zhang, F., Xiao, B., Liu, Z., Zhang, Y., Tian, C., Li, R., Wu, C., Lei, Y., Zhang, S., Wan, X., Chen, Y., Han, Y., Cui, M., Huang, C., Wang, H., Chen, Y., Wang, G., 2024. Real-world emission characteristics of VOCs from typical cargo ships and their potential contributions to secondary organic aerosol and O_3 under low-sulfur fuel policies. Atmospheric Chemistry and Physics 24,

8999–9017. doi:10.5194/acp-24-8999-2024. publisher: Copernicus GmbH.

Zhang, S., Tison, E., Dusanter, S., Beaugard, C., Gengembre, C., Augustin, P., Fourmentin, M., Delbarre, H., Riffault, V., 2021. Near real-time PM1 chemical composition measurements at a French urban background and coastal site under industrial influence over more than a year: Temporal variability and assessment of sulfur-containing emissions. Atmospheric Environment 244, 117960. doi:10.1016/j.atmosenv.2020.117960.

Zhou, L., Hopke, P.K., Paatero, P., Ondov, J.M., Pancras, J.P., Pekney, N.J., Davidson, C.I., 2004. Advanced factor analysis for multiple time resolution aerosol composition data. Atmospheric Environment 38, 4909–4920. doi:10.1016/j.atmosenv.2004.05.040.

Zhou, S., Zhou, J., Zhu, Y., 2019. Chemical composition and size distribution of particulate matters from marine diesel engines with different fuel oils. Fuel 235, 972–983. doi:10.1016/j.fuel.2018.08.080.

Zulkifli, M.F.H., Hawari, N.S.S.L., Latif, M.T., Hamid, H.H.A., Mohtar, A.A.A., Idris, W.M.R.W., Mustaffa, N.I.H., Juneng, L., 2022. Volatile organic compounds and their contribution to ground-level ozone formation in a tropical urban environment. Chemosphere 302, 134852. doi:10.1016/j.chemosphere.2022.134852.

APPENDIX A

Additional Tables of Chapter 2

Table AT1: *Composition of the NPL gas standard used to calibrate the TD-GC-FID (Chromatotec) and TD-GC-2FID (Perkin-Elmer). Reference of the standard is D723268.*

Compound	Amount fraction µmol· mol^{-1}	Compound	Amount fraction µmol· mol^{-1}
Ethane	205 ± 4.2	2-Methylpentane	213.3 ± 4.3
Ethene	201.8 ± 4.1	n-Hexane	213.3 ± 4.3
Propane	203.1 ± 4.1	Isoprene	212.5 ± 4.3
Propene	201.9 ± 4.1	n-Heptane	213.7 ± 4.3
2-Methylpropane	207 ± 6	Benzene	206.2 ± 4.2
n-Butane	205 ± 6	2,2,4-Trimethylpentane	200.6 ± 4.1
Ethyne	211 ± 11	n-Octane	201.2 ± 4.1
trans-2-But-2-ene	205.8 ± 4.2	Toluene	200 ± 6
But-1-ene	204.7 ± 4.1	Ethylbenzene	217 ± 6
cis-But-2-ene	205.2 ± 4.2	m&p-Xylenes	422 ± 11
2-Methylbutane	202.4 ± 4.1	o-Xylene	207 ± 6
n-Pentane	203.3 ± 4.1	1,3,5-Trimethylbenzene	206 ± 6
1,3-Butadiene	207.5 ± 4.2	1,2,4-Trimethylbenzene	207 ± 6
trans-2-Pent-2-ene	204 ± 6	1,2,3-Trimethylbenzene	204 ± 6
1-Pentene	207.7 ± 4.2		

Table AT2: *Composition of the NPL gas standard used to calibrate the PTR-ToF-MS.*

Compound	Amount fraction µmol·mol^{-1}
Acetaldehyde	1.35 ± 0.14
Methanol	1.69 ± 0.17
Ethanol	1.11 ± 0.12
Isoprene	1.13 ± 0.06
Acetone	1.07 ± 0.06
Dimethyl sulfide	1.05 ± 0.13
Acetonitrile	1.29 ± 0.13
Butan-2-one	1.16 ± 0.06
Benzene	0.854 ± 0.043
1,2,4-Trifluorebenzene	0.928 ± 0.047
Toluene	0.967 ± 0.049
Hexamethycyclotrisiloxane	0.98 ± 0.10
m&p-Xylenes	0.963 ± 0.049
Octamethylcyclotetrasiloxane	1.11 ± 0.12
3-Carene	0.92 ± 0.10
Decamethylcyclopentasiloxane	1.11 ± 0.12
1,2,4-Trichlorobenzene	1.04 ± 0.11

Table AT3: *Calibration factors for calibrated VOCs and uncalibrated VOCs and their compound of reference (if any) for the Chromatotec TD-GC-FID.*

VOC	area / ppt	Reference
2-Methylpentane	17,0359	
3-Methylpentane	16,1378	Hexane
Hexene	15,8688	Hexane
n-Hexane	16,1378	
2,2-Dimethylpentane	18,8274	Hexane
2,4-Dimethylpentane	18,8274	Hexane
2,2,3-Trimethylbutane	18,8274	Hexane
Benzene	15,3098	
3,3-Dimethylpentane	18,5621	Heptane
Cyclohexane	16,1378	Hexane
2-Methylhexane	18,5621	Heptane
1,2-Dichloropropane	8,0689	Hexane
i-Octane	20,5966	
n-Heptane	18,5621	
Toluene	17,0976	
1,2-Dibromomethane	5,3793	Hexane
n-Octane	20,7738	
Chlorobenzene	15,3309	Hexane
Ethylbenzene	18,2814	
m&p-Xylenes	20,7723	
Styrene	20,7723	m&p-Xylenes
o-Xylene	20,9676	
n-Nonane	23,8656	Heptane
α-pinene	19,4660	1,3,5-Trimethylbenzene
Propylbenzene	19,4660	1,3,5-Trimethylbenzene
1,3,5-Trimethylbenzene	19,4660	
1,2,4-Trimethylbenzene	23,9575	
n-Decane	26,5173	Heptane
1,2,3-Trimethylbenzene	22,0597	
1,2-Dichlorobenzene	15,3309	Hexane

Table AT4: *Calibration factors for calibrated VOCs and uncalibrated VOCs and their compound of reference (if so) for the Perkin-Elmer TD-GC-2FID.*

VOC	area / ppt	Reference	VOC	area / ppt	Reference
Ethane	5,0130		Hexane	17,4310	
Ethylene	4,5195		2,2-Dimethylpentane	17,4310	Hexane
Propane	7,6630		2,4-Dimethylpentane	17,4310	Hexane
Propene	7,0786		2,2,3-Trimethylbutane	17,4310	Hexane
Isobutane	10,7251		Benzene	15,0130	
Butane	11,0647		3,3-Dimethylpentane	17,3582	Heptane
Acetylene	4,5086		Cyclohexane	17,4310	Hexane
trans-2-butene	10,3227		2-Methylhexane	17,3582	Heptane
1-Butene	11,2164		2,3-Dimethylpentane	17,3582	Heptane
Isobutene	11,2164	1-Butene	Trichloroethylene	5,0835	Heptane
Neopentane	13,4729	Isopentane	Isooctane	20,0890	
cis-2-butene	10,1641		Heptane	17,3582	
Isopentane	13,4729		Toluene	15,2152	
Pentane	13,7785		n-Octane	17,7211	
1,3-Butadiène	9,3433		Ethylbenzene	18,6513	
Propyne	9,9205	Pentane	m&p-Xylenes	18,0206	
3-Methyl-1-butene	13,0752	trans-2-Pentene	Styrene	18,6999	o-Xylene
trans-2-Pentene	13,0752		o-Xylene	18,9366	
2-Methyl-2-butene	13,0752	trans-2-Pentene	n-Nonane	21,3037	o-Xylene
2-Methyl-1-butene	13,0752	trans-2-Pentene	Isoprobylbenzene	21,3037	o-Xylene
1-Pentene	11,2438		Propylbenzene	21,3037	o-Xylene
cis-2-Pentene	11,2438	1-Pentene	3-Ethyltoluene	25,0818	1,3,5-Trimethylbenzene
2,2-Dimethylbutane	16,5342	Pentane	4-Ethyltoluene	25,0818	1,3,5-Trimethylbenzene
Butyne	11,3378	1-Pentene	1,3,5-Trimethylbenzene	25,0818	
Isoprene	9,8590		2-Ethyltoluene	25,0818	1,3,5-Trimethylbenzene
Cyclopentene	17,1653	2-Methylpentane	1,2,4-Trimethylbenzene	26,0716	
Cyclopentane	17,4563	2-Methylpentane	n-Decane	28,9684	1,2,4-Trimethylbenzene
2-Methylpentane	17,4563		1,2,3-Trimethylbenzene	24,6766	
3-Methylpentane	17,4563	2-Methylpentane	n-Undecane	30,1603	1,2,3-Trimethylbenzene
Hexene	17,1405	Hexane			

Table AT5: *Peak list (1st part) used in the PTRMS Viewer 3. Columns 'low' and 'high' indicate the limits for the peak, 'center' indicates the mass at the maximum of the peak. kRate refers to the ionisation rate k of each ion (Equation 2.5).*

Label	Low	Center	High	Multiplier	kRate	Mode	Gauss %	Gauss Height	Gauss Width	Gauss Center	NumOfPeaks	Sigma	PI (0/1)
m21__H3O+	20.96124	21.02205	21.08584	1	3	0	0	0	0	0	1	0	1
m30__1|m30__2	29.94935	29.99626|30.00732	30.05618	1.00|1.00	2.00|2.00	2	0	0	0	0	2	0.00223	0|0
m31__inorg|m31__HCHO.H+|m31__3	30.73500	30.99471|31.01599|31.05176	31.26500	1.00|1.00|1.00	3.00|2.64|2.00	2	0	0	0	0	3	0.00320	0|0|0
m32__O2+	31.9625	31.98925	32.02689	1	3	0	0	0	0	0	1	0	0
m33__inorg|m33__CH3OH.H+	32.88468	32.99885|33.03487	33.11488	1.00|1.00	3.00|2.19	2	0	0	0	0	2	0.00450	0|0
m__O2+__18	34.85408	34.995	35.14871	1	3	0	0	0	0	0	1	0	0
m37__Cluster	36.94068	37.02755	37.15181	1	3	0	0	0	0	0	1	0	0
m39__Cluster18	38.90096	39.03208	39.15	1	3	0	0	0	0	0	1	0	0
m41__inorg|m41__frag.Isop	40.89909	40.97047|41.03858	41.11598	1.00|1.00	3.00|1.97	2	0	0	0	0	2	0.00536	0|0
m42__org|m42__C2H3N.H+	41.90000	42.01083|42.03669	42.20000	1.00|1.00	3.00|4.70	2	0	0	0	0	2	0.00540	0|0
m43__frag.C2H3O+|m43__frag.C3H7+	42.90000	43.01784|43.05423	43.16188	1.00|1.00	3.00|3.00	2	0	0	0	0	2	0.00526	0|0
m45__CO2.H+|m45__CH3CHO.H+	44.86794	44.99882|45.03561	45.14809	1.00|1.00	3.00|3.60	2	0	0	0	0	2	0.00526	0|0
m46__NO2+|m46__org	45.80252	45.99236|46.03150	46.22263	1.00|1.00	3.00|3.00	2	0	0	0	0	2	0.00566	0|0
m47__CH2O2.H+|m47__C2H6O.H+|m47__3	46.81692	47.02480|47.04901|47.01613	47.32309	1.00|1.00|1.00	2.02|4.74|3.00	2	0	0	0	0	3	0.00586	0|0|0
m55__Cluster	54.93823	55.03868	55.15951	1	3	0	0	0	0	0	1	0	0
m57__C3H4O.H+|m57__frag.C4H8.H+	56.84029	57.03349|57.06988	57.27520	1.00|1.00	3.31|1.76	2	0	0	0	0	2	0.00666	0|0
m59__C3H6O.H+	58.95164	59.04914	59.16714	1	4.1	0	0	0	0	0	1	0	0
m61__C2H4O2.H+	60.81692	61.02840	61.24991	1.00	2.11	0	0	0	0	0	1	0	0
m63__inorg1|m63__inorg2|m63__org1|m63__DMS.H+|m63__org3	62.79868	62.93208|62.96718|63.00929|63.02630|63.04438	63.20385	1.00|1.00|1.00|1.00|1.00	3.00|3.00|3.00|2.53|3.00	2	0	0	0	0	5	0.00940	0|0|0|0|0
m65__?C2H2F2.H+|m65__C2H8O2.H+?	64.88194	65.02030|65.05923	65.19985	1.00|1.00	3.00|3.00	2	0	0	0	0	2	0.00883	0|0
m67__?C5H6.H+	66.88137	67.0536	67.25184	1	3	0	0	0	0	0	1	0	0
m69__C3O2|m69__C4H4O.H+|m69__C5H8.H+	68.80354	68.99711|69.03349|69.06989	69.33995	1.00|1.00|1.20	3.00|1.69|1.97	2	0	0	0	0	3	0.00713	0|0|0
m71__inorg|m71__org|m71__C4H6O.H+|m71__C5H10.H+	70.90219	70.94249|71.01427|71.05036|71.08875	71.20544	1.00|1.00|1.00|1.00	3.00|3.00|4.00|1.90	2	0	0	0	0	4	0.00884	0|0|0|0
m73__inorg|m73__C3H4O2.H+|m73__C4H8O.H+	72.79954	72.93623|73.03158|73.06642	73.27872	1.00|1.00|1.00	3.00|3.00|3.48	2	0	0	0	0	3	0.00887	0|0|0
m75.04406	74.89914	75.04406	75.18164	1	3	0	0	0	0	0	1	0	0
m77__C2H4O3H+|m77__org|m77__C3H8O2H+	76.79873	77.02300|77.04644|77.06000	77.24587	1.00|1.00|1.00	3|3.00|3.00	2	0	0	0	0	3	0.01020	0|0|0
m78__inorg|m78__2|m78__C6H6+	77.80080	77.94115|78.02056|78.04640	78.20251	1.00|1.00|1.00	3|3.00|3	2	0	0	0	0	3	0.01152	0|0|0
m79__inorg|m79__C2H6SO.H+|m79__C2H6O3.H+|m79__C6H6.H+	78.79888	78.94488|78.99732|79.03952|79.05400	79.25688	1.00|1.00|1.00|1.00	2.00|3.00|2.00|1.93	2	0	0	0	0	4	0.01341	0|0|0|0
m81__inorg|m81__2|m81__C6H8.H+	80.86957	80.99322|81.03535|81.07189	81.25476	1.00|1.00|1.00	3.00|3.00|2.25	2	0	0	0	0	3	0.01090	0|0|0
m83__inorg|m83__?H3PO3.H+|m83__?C2HF3.H+|m83__C5H6O.H+|m83__C6H10.H+	82.83714	82.94456|82.98980|83.01090|83.04970|83.08610	83.39667	1.00|1.00|1.00|1.00|1.00	3.00|3.00|3.00|3.00|3.00	2	0	0	0	0	5	0.00810	0|0|0|0|0
m85__inorg__1|m85__inorg__2|m85__org|m85__C5H8O.H+|m85__C6H12	84.73034	84.93956|84.96343|85.02748|85.06530|85.10170	85.38399	1.00|1.00|1.00|1.00|1.00	3.00|3.00|3.00|3.00|3.00	2	0	0	0	0	5	0.01081	0|0|0|0|0
m87__C4H6O2.H+|m87__C5H10O.H+|m87__3	86.90032	87.04460|87.08040|87.00962	87.23292	1.00|1.00|1.00	3.00|2.31|3.00	2	0	0	0	0	3	0.01050	0|0|0
m89__inorg|m89__C3H4O3.H+|m89__3|m89__?C3H8N2O.H+|m89__C5H12O	88.87907	88.95158|89.02390|89.05951|89.07150|89.09609	89.22197	1.00|1.00|1.00|1.00|1.00	3.00|3.00|3.00|3.00|2.16	2	0	0	0	0	5	0.00982	0|0|0|0|0
m91__inorg|m91__2|m91__?C2H6N2O	90.77624	90.94747|91.00564|91.04947	91.20270	1.00|1.00|1.00	3.00|3.00|3.00	2	0	0	0	0	3	0.01260	0|0|0
m93__inorg|m93__org|m93__C7H8.H+	92.82000	92.94692|93.03712|93.06989	93.27501	1.00|1.00|1.00	3.00|3.00|2.14	2	0	0	0	0	3	0.01000	0|0|0
m95__inorg|m95__C2H6S2.H+|m95__org2|m95__C6H6O.H+|m95__C7H10.H+	94.85655	94.94479|94.99892|95.01696|95.04734|95.08553	95.24098	1.00|1.00|1.00|1.00|1.00	3.00|3.00|3.00|2.13|3.00	2	0	0	0	0	5	0.01100	0|0|0|0|0
m97__inorg1|m97__inorg2|m97__C5H4O2.H+|m97__C6H8OH+|m97__C7H13+	96.76079	96.95678|96.99225|97.02700|97.06400|97.10110	97.43647	1.00|1.00|1.00|1.00|1.00	3.00|3.00|3.00|3.00|3.00	2	0	0	0	0	5	0.01120	0|0|0|0|0
m99__?H2SO4.H+|m99__?C4H2O3.H+|m99__C5H2O2.H+|m99__C6H10O.H+|m99__C7H14.H+	98.85407	98.95025|99.00431|99.04406|99.08000|99.11359	99.32824	1.00|1.00|1.00|1.00|1.00	3.00|3.00|3.00|3.00|3.00	2	0	0	0	0	5	0.01220	0|0|0|0|0
m101__inorg|m101__?C4H4O3.H+|m101__C5H8O2.H+|m101__C6H12O.H+	100.82934	100.94223|101.02332|101.05958|101.09608	101.26078	1.00|1.00|1.00|1.00	3.00|3.00|3.00|2.21	2	0	0	0	0	4	0.01141	0|0|0|0
m103__inorg|m103__?C4H6O3.H+|m103__C5H10O2.H+|m103__C6H14O.H+	102.78502	102.94639|103.03897|103.07536|103.11174	103.23406	1.00|1.00|1.00|1.00	3.00|3.00|3.00|2.23	2	0	0	0	0	4	0.01150	0|0|0|0
m105__inorg|m105_org1|m105_org2|m105__C8H8.H+	104.80708	104.94647|105.02190|105.05986|105.07040	105.24203	1.00|1.00|1.00|1.00	3.00|3.00|3.00|3.00	2	0	0	0	0	4	0.01339	0|0|0|0
m107__inorg1|m107__inorg2|m107__C7H6O.H+|m107__C8H10.H+	106.81897	106.93710|106.96368|107.05255|107.07861	107.30508	1.00|1.00|1.00|1.00	3.00|3.00|3.63|2.38	2	0	0	0	0	4	0.01240	0|0|0|0
m109__inorg1|m109__inorg2|m109_org1|m109__?C7H8O.H+|m109__?C8H12.H+	108.74000	108.95718|108.97886|109.02689|109.06530|109.10170	109.28443	1.00|1.00|1.00|1.00|1.00	3.00|3.00|3.00|3.00|3.00	2	0	0	0	0	5	0.01110	0|0|0|0|0
m111__inorg1|m111__org1|m111__org2|m111__?C7H10O.H+|m111__?C8H14.H+	110.81341	110.95954|111.00116|111.04608|111.07864|111.11700	111.28211	1.00|1.00|1.00|1.00|1.00	3.00|3.00|3.00|3.00|3.00	2	0	0	0	0	5	0.01280	0|0|0|0|0
m113__inorg|m113__?C5H4O3.H+|m113__?C6H8O2.H+|m113__?C7H12O.H+|m113_org5	112.82807	112.95340|113.02608|113.06034|113.09460|113.13103	113.25213	1.00|1.00|1.00|1.00|1.00	3.00|3.00|3.00|3.00|3.00	2	0	0	0	0	5	0.01399	0|0|0|0|0
m114__1|m114__2|m114__3|m114__?C6H11NO.H|m114__5	113.84095	113.95116|114.02557|114.05933|114.09636|114.14054	114.30567	1.00|1.00|1.00|1.00|1.00	3.00|3.00|3.00|3.00|3.00	2	0	0	0	0	5	0.01650	0|0|0|0|0
m115__1|m115__2|m115__3|m115__4|m115__5	114.83657	114.95642|115.00233|115.03663|115.07379|115.10916	115.27058	1.00|1.00|1.00|1.00|1.00	3.00|3.00|3.00|3.00|3.00	2	0	0	0	0	5	0.01410	0|0|0|0|0
m117__inorg|m117_org1|m117__?C4H4O4.H+|m117__?C5H8O3.H+|m117__?C6H12O2.H+	116.77561	116.90651|116.94818|117.02143|117.05462|117.09160	117.26017	1.00|1.00|1.00|1.00|1.00	3.00|3.00|3.00|3.00|3.00	2	0	0	0	0	5	0.01430	0|0|0|0|0
m119__inorg1|m119__inorg2|m119__3|m119__4	118.80000	118.90162|118.94176|119.03397|119.08649	119.30000	1.00|1.00|1.00|1.00	3.00|3.00|3.00|3.00	2	0	0	0	0	4	0.01497	0|0|0|0
m121__inorg|m121__org1|m121__org2|m121__org3|m121__org4	120.80000	120.90011|120.95517|121.03176|121.06459|121.10108	121.30000	1.00|1.00|1.00|1.00|1.00	3.00|3.00|3.00|3.00|3.00	2	0	0	0	0	5	0.01570	0|0|0|0|0
m123__inorg1|m123__inorg2|m123_org1|m123__org2|m123__org3	122.79558	122.89911|122.95772|123.04511|123.07388|123.11651	123.25317	1.00|1.00|1.00|1.00|1.00	3.00|3.00|3.00|3.00|3.00	2	0	0	0	0	5	0.01555	0|0|0|0|0
m125__inorg|m125__org1|m125__org2|m125__org3|m125__org4	124.88276	124.95193|125.02438|125.06081|125.09511|125.13319	125.25516	1.00|1.00|1.00|1.00|1.00	3.00|3.00|3.00|3.00|3.00	2	0	0	0	0	5	0.01641	0|0|0|0|0
m127__inorg|m127_org1|m127__org2|m127__org3|m127__org4	126.84997	126.96478|127.04201|127.07622|127.11043|127.14788	127.25202	1.00|1.00|1.00|1.00|1.00	3.00|3.00|3.00|3.00|3.00	2	0	0	0	0	5	0.01548	0|0|0|0|0
m129__inorg1|m129__org1|m129__org2|m129__org3|m129__org4	128.83302	128.96726|129.01649|129.05587|129.08869|129.12588	129.27872	1.00|1.00|1.00|1.00|1.00	3.00|3.00|3.00|3.00|3.00	2	0	0	0	0	5	0.01457	0|0|0|0|0
m131__inorg1|m131__inorg2|m131_org1|m131__org2|m131__org3	130.75966	130.90228|130.98344|131.03271|131.06681|131.10470	131.28049	1.00|1.00|1.00|1.00|1.00	3.00|3.00|3.00|3.00|3.00	2	0	0	0	0	5	0.01609	0|0|0|0|0
m133__sum	132.80252	133.05	133.27527	1.00	3.00	0	0	0	0	0	1	0	0
m135__sum	134.75379	135.05	135.33254	1.00	3	0	0	0	0	0	1	0	0
m137__inorg|m137__C7H4O3.H+|m137__C8H8O2.H+|m137__org|m137__C10H16.H	136.88106	136.95390|137.01730|137.05898|137.09429|137.13248	137.34374	1.00|1.00|1.00|1.00|1.00	3.00|3.00|3.00|3.00|2.25	2	0	0	0	0	5	0.01538	0|0|0|0|0
m139__inorg|m139__org1|m139__org2|m139__org3|m139__org4	138.85698	138.98165|139.03906|139.07350|139.10795|139.14814	139.32677	1.00|1.00|1.00|1.00|1.00	3.00|3.00|3.00|3.00|3.00	2	0	0	0	0	5	0.01657	0|0|0|0|0
m141__org1|m141__org2|m141__org3|m141__org4|m141__org5	140.73817	141.01547|141.05424|141.08675|141.12153|141.16203	141.42228	1.00|1.00|1.00|1.00|1.00	3.00|3.00|3.00|3.00|3.00	2	0	0	0	0	5	0.01779	0|0|0|0|0
m143__inorg|m143__org1|m143__org2|m143__org3|m143__org4	142.88300	142.95961|143.03679|143.07107|143.10504|143.14432	143.31435	1.00|1.00|1.00|1.00|1.00	3.00|3.00|3.00|3.00|3.00	2	0	0	0	0	5	0.01715	0|0|0|0|0
m145__org1|m145__org2|m145__org3|m145__org4|m145__org5	144.85360	144.99408|145.04571|145.07713|145.11890|145.15008	145.30515	1.00|1.00|1.00|1.00|1.00	3.00|3.00|3.00|3.00|3.00	2	0	0	0	0	5	0.01868	0|0|0|0|0

Table AT6: *Peak list (2nd part) used in the PTRMS Viewer 3. Low and high columns indicate the limit of the position of the peak, center indicates the maximum position of the peak in mass. kRate refers to the production rate k of each ion (Equation 2.5).*

Label	Low	Center	High	Multiplier	kRate	Mode	Gauss %	Gauss Height	Gauss Width	Gauss Center	NumOfPeaks	Sigma	PI (0/1)
m147_sum	146.85	147	147.3	1	3	0	0	0	0	0	1	0	0
m149.sum	148.85	149	149.3	1	3	0	0	0	0	0	1	0	0
m151.sum	150.85	151	151.3	1	3	0	0	0	0	0	1	0	0
m153.sum	152.85	153	153.3	1	3	0	0	0	0	0	1	0	0
m155.sum	154.85	155	155.3	1	3	0	0	0	0	0	1	0	0
m157_sum	156.85	157	157.3	1	3	0	0	0	0	0	1	0	0
m159_sum	158.85	159	159.3	1	3	0	0	0	0	0	1	0	0
m161_sum	160.79	161	161.3	1	3	0	0.00	0.00	0.00000	0.00000	1	0	0
m163_sum	162.85	163	163.3	1	3	0	0	0	0	0	1	0	0
m165_sum	164.85	165	165.3	1	3	0	0	0	0	0	1	0	0
m167_sum	166.85	167	167.3	1	3	0	0	0	0	0	1	0	0
m169_sum	168.85	169	169.3	1	3	0	0	0	0	0	1	0	0
m171_sum	170.85	171	171.3	1	3	0	0	0	0	0	1	0	0
m173_sum	172.85	173	173.3	1	3	0	0	0	0	0	1	0	0
m175_sum	174.85	175	175.3	1	3	0	0	0	0	0	1	0	0
m177_sum	176.85	177	177.3	1	3	0	0	0	0	0	1	0	0
m178_sum	177.85	178	178.3	1	3	0	0	0	0	0	1	0	0
m179_sum	178.85	179	179.3	1	3	0	0	0	0	0	1	0	0
m181_sum	180.85	181	181.3	1	3	0	0	0	0	0	1	0	0
m183_sum	182.85	183	183.3	1	3	0	0	0	0	0	1	0	0
m185_sum	184.85	185	185.3	1	3	0	0	0	0	0	1	0	0
m187_sum	186.85	187	187.3	1	3	0	0	0	0	0	1	0	0
m189_sum	188.85	189	189.3	1	3	0	0	0	0	0	1	0	0
m191_sum	190.85	191	191.3	1	3	0	0	0	0	0	1	0	0
m193_sum	192.85	193	193.3	1	3	0	0	0	0	0	1	0	0
m195_sum	194.85	195	195.3	1	3	0	0	0	0	0	1	0	0
m197_sum	196.85	197	197.3	1	3	0	0	0	0	0	1	0	0
m199_sum	198.85	199	199.3	1	3	0	0	0	0	0	1	0	0
m201_sum	200.85	201	201.3	1	3	0	0	0	0	0	1	0	0
m204	203.85000	204	204.07283	1	3	0	0.00	0.00	0.00000	0.00000	1	0	0
m205_inorg|m205_C15H24.H+	204.72024	204.94566|205.19507	205.30000	1.00|1.00	3.00|2.90	2	0	0	0	0	2	0.02500	0|0
m207_sum	205.75168	206	206.5	1	3	0	0.00	0.00	0.00000	0.00000	1	0	0
m209_sum	208.65286	209	209.5	1	3	0	0.00	0.00	0.00000	0.00000	1	0	0
m211_sum	210.85	211	211.5	1	3	0	0	0	0	0	1	0	0
m213_sum	212.85	213	213.5	1	3	0	0	0	0	0	1	0	0

221

Table AT7: *Peak list (3rd part) used in the PTRMS Viewer 3. Low and high columns indicate the limit of the position of the peak, center indicates the maximum position of the peak in mass. kRate refers to the production rate k of each ion (Equation 2.5).*

Label	Low	Center	High	Multiplier	kRate	Mode	Gauss %	Gauss Height	Gauss Width	Gauss Center	NumOfPeaks	Sigma	PI (0/1)
m215_sum	214.65783	215	215.5	1	3	0	0.00	0.00	0.00000	0.00000	1	0	0
m217_sum	216.85	217	217.5	1	3	0	0	0	0	0	1	0	0
m219_sum	218.85	219	219.5	1	3	0	0	0	0	0	1	0	0
m221_sum	220.76139	221	221.5	1	3	0	0.00	0.00	0.00000	0.00000	1	0	0
m223_sum	222.85	223	223.5	1	3	0	0	0	0	0	1	0	0
m225_sum	224.78261	225	225.5	1	3	0	0.00	0.00	0.00000	0.00000	1	0	0
m227_sum	226.85	227	227.5	1	3	0	0	0	0	0	1	0	0
m229_sum	228.85	229	229.5	1	3	0	0	0	0	0	1	0	0
m231_sum	230.85	231	231.5	1	3	0	0	0	0	0	1	0	0
m233_sum	232.85	233	233.5	1	3	0	0	0	0	0	1	0	0
m235_sum	234.85	235	235.5	1	3	0	0	0	0	0	1	0	0
m237_sum	236.85	237	237.5	1	3	0	0	0	0	0	1	0	0
m239_sum	238.85	239	239.5	1	3	0	0	0	0	0	1	0	0
m241_sum	240.85	241	241.5	1	3	0	0	0	0	0	1	0	0
m243_sum	242.85	243	243.5	1	3	0	0	0	0	0	1	0	0
m245_sum	244.85	245	245.5	1	3	0	0	0	0	0	1	0	0
m247_sum	246.85	247	247.5	1	3	0	0	0	0	0	1	0	0
m249_sum	248.85	249	249.5	1	3	0	0	0	0	0	1	0	0
m251_sum	250.85	251	251.5	1	3	0	0	0	0	0	1	0	0
m253_sum	252.85	253	253.5	1	3	0	0	0	0	0	1	0	0
m255_sum	254.85	255	255.5	1	3	0	0	0	0	0	1	0	0
m257_sum	256.85	257	257.5	1	3	0	0	0	0	0	1	0	0
m259_sum	258.85	259	259.5	1	3	0	0	0	0	0	1	0	0
m261_sum	260.85	261	261.5	1	3	0	0	0	0	0	1	0	0
m263_sum	262.85	263	263.5	1	3	0	0	0	0	0	1	0	0
m265_sum	264.85	265	265.5	1	3	0	0	0	0	0	1	0	0
m267_sum	266.85	267	267.5	1	3	0	0	0	0	0	1	0	0
m269_sum	268.85	269	269.5	1	3	0	0	0	0	0	1	0	0
m271_sum	270.85	271	271.5	1	3	0	0	0	0	0	1	0	0
m273_sum	272.85	273	273.5	1	3	0	0	0	0	0	1	0	0
m275_sum	274.85	275	275.5	1	3	0	0	0	0	0	1	0	0
m277_sum	276.85	277	277.5	1	3	0	0	0	0	0	1	0	0
m279_sum	278.85	279	279.5	1	3	0	0	0	0	0	1	0	0
m281_sum	280.85	281	281.5	1	3	0	0	0	0	0	1	0	0
m283_sum	282.85	283	283.5	1	3	0	0	0	0	0	1	0	0
m285_sum	284.85	285	285.5	1	3	0	0	0	0	0	1	0	0

Table AT8: *Peak list (4th part) used in the PTRMS Viewer 3. Low and high columns indicate the limit of the position of the peak, center indicates the maximum position of the peak in mass. kRate refers to the production rate k of each ion (Equation 2.5).*

Label	Low	Center	High	Multiplier	kRate	Mode	Gauss %	Gauss Height	Gauss Width	Gauss Center	NumOfPeaks	Sigma	PI (0/1)
m287_sum	286.85	287	287.5	1	3	0	0	0	0	0	1	0	0
m289_sum	288.85	289	289.5	1	3	0	0	0	0	0	1	0	0
m291_sum	290.85	291	291.5	1	3	0	0	0	0	0	1	0	0
m293_sum	292.85	293	293.5	1	3	0	0	0	0	0	1	0	0
m295_sum	294.85	295	295.5	1	3	0	0	0	0	0	1	0	0
m297_sum	296.85	297	297.5	1	3	0	0	0	0	0	1	0	0
m299_sum	298.85	299	299.5	1	3	0	0	0	0	0	1	0	0
m313_sum	312.85	313	313.5	1	3	0	0	0	0	0	1	0	0
m347_sum	346.60733	347	347.10242	1.00	3	0	0.00	0.00	0.00000	0.00000	1	0	0
m355_sum	354.69898	355	355.59661	1.00	3	0	0.00	0.00	0.00000	0.00000	1	0	0
m371_sum	370.79357	371	371.55423	1.00	3	0	0.00	0.00	0.00000	0.00000	1	0	0
m373_sum	372.76222	373	373.44478	1.00	3	0	0.00	0.00	0.00000	0.00000	1	0	0
m429_sum	428.54084	429	429.58507	1.00	3	0	0.00	0.00	0.00000	0.00000	1	0	0
m445_sum	444.86948	445	445.46664	1.00	3	0	0.00	0.00	0.00000	0.00000	1	0	0
m447_sum	446.86890	447	447.46378	1.00	3	0	0.00	0.00	0.00000	0.00000	1	0	0
m209.0290 D3 frag	208.96625	209.02901	209.09177	1.00	2.160	0	0	0	0	0	1	0	0
m208.0320 D3 frag	207.96953	208.03200	208.09447	1.00	2.160	0	0	0	0	0	1	0	0
m207.0320 D3 frag	206.96982	207.03200	207.09418	1.00	2.160	0	0	0	0	0	1	0	0
m225.0610 D3 frag	224.99364	225.06100	225.12837	1.00	2.160	0	0	0	0	0	1	0	0
m224.0630 D3 frag	223.99593	224.06300	224.13008	1.00	2.160	0	0	0	0	0	1	0	0
m223.0640 D3	222.99721	223.06400	223.13078	1.00	2.160	0	0	0	0	0	1	0	0
m297.0830 D4	296.99493	297.08301	297.17108	1.00	2.990	0	0	0	0	0	1	0	0
m283.0480	282.96396	283.04800	283.13205	1.00	2.990	0	0	0	0	0	1	0	0
m282.0510 D4 frag	281.96725	282.05099	282.13474	1.00	2.990	0	0	0	0	0	1	0	0
m281.0510 D4 frag	280.96753	281.05099	281.13446	1.00	2.990	0	0	0	0	0	1	0	0
m299.0790 D4 frag	298.99036	299.07901	299.16766	1.00	2.990	0	0	0	0	0	1	0	0
m298.0820 D4 frag	297.99365	298.08200	298.17035	1.00	2.990	0	0	0	0	0	1	0	0
m357.0670	D5frag	356.96170	357.06699	357.17227	1.00	3.390	0	0	0	0	0	1	0
m356.0700	D5frag	355.96500	356.07001	356.17502	1.00	3.390	0	0	0	0	0	1	0
m355.0700	D5frag	354.96527	355.07001	355.17474	1.00	3.390	0	0	0	0	0	1	0
m372.1010	D5frag	371.99139	372.10101	372.21063	1.00	3.390	0	0	0	0	0	1	0
m373.0980	D5frag	372.98810	373.09799	373.20789	1.00	3.390	0	0	0	0	0	1	0
m372.1050 D5frag	371.99539	372.10501	372.21463	1.00	3.390	0	0	0	0	0	1	0	0
m371.1010 D5	370.99170	371.10101	371.21033	1.00	3.390	0	0	0	0	0	1	0	0
m331	330.70000	331	331.13287	1	2	0	0.00	0.00	0.00000	0.00000	1	0	0

223

APPENDIX B

Supplementary Information of Chapter 3

Declaration of generative AI and AI-assisted technologies in the writing process

During the preparation of this work the author used DeepL Write in order to improve readability with reformulation. After using this tool/service, the author reviewed and edited the content as needed.

Acknowledgments

Authors would like to acknowledge the Port of Dunkirk (GPMD) for providing access to the measurement site and to supplementary information on the harbour traffic history on request. Authors also acknowledge the technical staff of Atmo Hauts-de-France for supervising the technical support of the Dunkirk harbour 2022 campaign. This research was funded by the National Research Agency (ANR), through the SHIPAIR project (ANR-21-CE22-0015), by the French Agency for Ecological Transition (ADEME) through the project PIRATE (AQACIA), the Laboratory of Excellence Chemical and Physical Properties of the Atmosphere (Labex CaPPA) and the Région Hauts-de-France and the CPER ECRIN.

B.1 Transmission coefficient of the flow tube for correcting the HR-ToF-AMS measurements

The concentrations measured by the HR-ToF-AMS were corrected for the flow tube losses using a transmission coefficient, determined for each diameter bin between 15 and 530 nm. The transmission of the flow tube was calculated in a laboratory experiment, where the mass distribution of a nebulised ammonium sulphate solution was compared at the inlet and the outlet of the tube with a SMPS. The resulting diameter-dependant transmission (Figure BF4) was then applied to all mass distributions of the campaign, measured at the inlet of the tube with a SMPS. A mean transmission coefficient was then calculated for each timestep as the weighted mass average of the mass distribution as represented in Figure BF5. No significant variation of the transmission coefficient was observed for the plumes represented in Figure BF5, and the overall values of mean transmission in ship plumes (0.64 ± 0.04) and outside ship plumes (0.66 ± 0.05) throughout the campaign are similar. This result suggests that the weighted mean transmission of the flow tube used in this study is generally little impacted by the smaller particles (80 nm) in the ship plumes, although they contribute at least as much as the bigger particles (> 200 nm). Yet, assessing the flow tube losses by considering the granulometric mass distributions ensures accurate and precise corrections of concentrations measured by the HR-ToF-MS.

B.2 m/z 69 parent ion identification

Gueneron et al. (2015) investigated the fragmentation patterns of parent ions from typical VOCs from gasoline emissions that dissociate on m/z 69 for two E/N ratios (80 Td and 120 Td) in a laboratory study. They determined fragmentation yields of cycloalkanes and cycloalkenes and found that the yield on m/z 125 is approximately half of the yield at m/z 69 at 120 Td for 3,3,5-trimethylcyclohexene, 1,3,5-trimethylcyclohexane and 1,1,3-trimethylcyclohexane. In our study, the ion drift tube was held at 100 Td and we assume that the fragmentation pattern observed will be halfway in between the ones observed by Gueneron et al. (2015). Hence, the contribution of these VOCs to the m/z 69 should be twice the intensity of the signal of m/z 125. In the same way, 1,3-dimethylcyclohexane and 1,4-dimethylcyclohexane both fragment at m/z 111 with an intensity that is approximately twice the yield at m/z 69, meaning that the contribution of these VOC to m/z 69 should be half the intensity of m/z 111. Figure BF12 represents the time series of the mentioned m/z in Counts Per Seconds (CPS) and the mean contribution of twice m/z 125 and half m/z 111 compared to the total m/z 69. It shows that the fragmentation yields of Gueneron et al. (2015) lead to a 17% overestimation of the sum of the m/z 125 and m/z 111 contributors compared to m/z 69. This overestimation can be explained by the fact that our E/N was 100 Td, which leads to less fragmentation. No specific calibration was performed on the potential VOC precursors that were mentioned, so we can only suggest that the sum of m/z 125 and m/z 111 could explain the entirety of the m/z 69 signal that is observed under the E/N condition of our study. The identification of the precursors of the m/z 69 warrants further investigation to determine their fragmentation under our measurement conditions and to further extend the number of potential VOC that fragment on the m/z 69.

B.3 Additional tables

Table BT1: *Composition of the NPL cylinder used for calibration of the PTR-ToF-MS*

VOC	Amount fraction μmol / mol
Acetaldehyde	1.35 ± 0.17
Methanol	1.69 ± 0.17
Isoprene	1.11 ± 0.12
Acetone	1.13 ± 0.06
Dimethyl sulfide	1.07 ± 0.06
Acetonitrile	1.05 ± 0.13
Butan-2-one	1.29 ± 0.13
Benzene	1.16 ± 0.06
1,2,4-Trifluorobenzene	0.845 ± 0.043
Toluene	0.967 ± 0.049
Hexamethylcyclotrisiloxane	0.98 ± 0.10
m-Xylene	0.963 ± 0.049
Octamethylcyclotetrasiloxane	1.11 ± 0.12
3-Carene	0.92 ± 0.10
Decamethylcyclopentasiloxane	1.11 ± 0.12
1,2,4-Trichlorobenzene	1.01 ± 0.11

Table BT2: *Coefficients of correction for humidity for 16 VOCs. [H_2O] is the concentration of water (absolute humidity) expressed in ppm. The obtained coefficient has to be multiplied by the raw concentrations of VOCs to obtain the final humidity-corrected concentrations.*

Compound	Coefficient
Methanol	$-0.43\times$ [H_2O] $+7.67$
Acetonitrile	$-0.08\times$ [H_2O] $+2.15$
Acetaldehyde	$-0.02\times$ [H_2O] $+1.36$
Acetone	$-0.03\times$ [H_2O] $+1.38$
Isoprene	$-0.02\times$ [H_2O] $+1.26$
2-Butanone	$-0.03\times$ [H_2O] $+1.46$
Benzene	$0.03\times$ [H_2O] $+0.55$
Toluene	$0.01\times$ [H_2O] $+0.86$
o-Xylene	$-0.01\times$ [H_2O] $+1.11$
1,2,4-Trifluorobenzene	$0.04\times$ [H_2O] $+0.33$
3-Carene	$-0.01\times$ [H_2O] $+1.20$
1,2,4-Trimethylbenzene	$-0.01\times$ [H_2O] $+1.19$
DMS	$-0.001\times$ [H_2O] $+1.01$
Hexamethylcyclotrisiloxane	$-0.04\times$ [H_2O] $+1.55$
Octamethylcyclotetrasiloxane	$-0.05\times$ [H_2O] $+1.68$
Decamethylcyclopentasiloxane	$-0.23\times$ [H_2O] $+4.42$

Table BT3: *Statistics of the EFs and FSCs calculated in this study.*

Species	unit	Mean	Median	std	Min	Max	N	Species	unit	Mean	Median	std	Min	Max	N
SO_2	g/kg_{fuel}	1,36	1,10	2,34	0,07	27,06	137	H_3PO_3	mg/kg_{fuel}	0,75	0,71	0,47	0,01	2,15	59
CO	g/kg_{fuel}	6,94	6,42	4,24	1,39	49,44	143	C_2HF_3	mg/kg_{fuel}	0,87	0,71	0,75	0,01	4,60	59
CH_4	g/kg_{fuel}	9,60	0,87	29,74	$4{,}58{\cdot}10^{-3}$	174,39	105	C_5H_6O	mg/kg_{fuel}	23,14	23,54	9,95	1,07	45,30	67
NO_2	g/kg_{fuel}	12,28	11,24	9,95	$2{,}29{\cdot}10^{-5}$	56,06	114	C_6H_{10}	mg/kg_{fuel}	94,20	89,85	47,88	7,48	308,75	68
NO	g/kg_{fuel}	22,18	23,99	14,77	$8{,}54{\cdot}10^{-6}$	60,47	115	C_5H_8O	mg/kg_{fuel}	31,21	30,57	13,21	2,40	54,60	67
NO_x	g/kg_{fuel}	33,84	36,84	22,41	$3{,}14{\cdot}10^{-5}$	117,02	116	$C_4H_6O_2$	mg/kg_{fuel}	29,73	28,29	15,05	1,42	65,02	67
PM_{10}	g/kg_{fuel}	1,11	0,46	1,92	$5{,}54{\cdot}10^{-4}$	14,76	117	$C_5H_{10}O$	mg/kg_{fuel}	15,97	16,60	7,39	1,69	28,78	67
$PM_{2.5}$	g/kg_{fuel}	0,35	0,25	0,38	$3{,}61{\cdot}10^{-3}$	2,64	134	$C_3H_4O_3$	mg/kg_{fuel}	3,23	2,76	1,84	0,28	11,15	60
PM_1 (FIDAS)	g/kg_{fuel}	0,24	0,19	0,18	0,02	0,98	133	$C_3H_8N_2O$	mg/kg_{fuel}	1,95	1,61	1,70	0,20	11,59	56
BC	g/kg_{fuel}	0,53	0,42	0,45	0,01	2,96	137	C_7H_8	mg/kg_{fuel}	30,99	26,97	20,71	0,72	111,91	65
PN (FIDAS)	$partICLES/kg_{fuel}$	$1.06{\cdot}10^{13}$	$8.74{\cdot}10^{12}$	$8.22{\cdot}10^{12}$	$1{,}53{\cdot}10^{11}$	$4{,}56{\cdot}10^{13}$	132	$C_2H_6S_2$	mg/kg_{fuel}	0,65	0,46	0,44	0,04	2,13	62
OA	g/kg_{fuel}	6,12	5,26	6,00	0,12	55,38	93	C_6H_6O	mg/kg_{fuel}	19,13	20,65	9,56	0,54	42,29	66
$SO_4^2 2-$	mg/kg_{fuel}	34,56	24,69	35,01	0,49	247,69	86	C_7H_{10}	mg/kg_{fuel}	38,05	40,00	14,49	3,56	69,99	67
NH_4^+	mg/kg_{fuel}	17,38	12,86	25,38	0,12	213,26	79	$C_5H_4O_2$	mg/kg_{fuel}	28,02	26,58	13,79	0,26	66,47	67
NO_3^-	mg/kg_{fuel}	21,30	14,65	44,64	0,14	412,26	87	C_6H_8O	mg/kg_{fuel}	18,75	19,33	7,87	1,36	37,39	67
Chl	mg/kg_{fuel}	2,21	1,61	2,31	0,04	18,13	87	H_2SO_4	mg/kg_{fuel}	0,80	0,55	1,12	0,08	5,14	18
PM_1 (SMPS)	g/kg_{fuel}	5,03	4,50	3,57	0,27	23,66	144	$C_4H_2O_3$	mg/kg_{fuel}	83,06	71,54	48,00	4,76	210,44	67
PN (SMPS)	$particles/kg_{fuel}$	$2{,}01{\cdot}10^{16}$	$1{,}59{\cdot}10^{16}$	$1{,}59{\cdot}10^{16}$	$9{,}99{\cdot}10^{13}$	$9{,}36{\cdot}10^{16}$	144	$C_5H_2O_2$	mg/kg_{fuel}	18,38	16,64	9,63	2,63	39,56	67
HCHO	mg/kg_{fuel}	74,84	71,81	44,14	3,43	184,34	65	$C_6H_{10}O$	mg/kg_{fuel}	13,62	14,08	5,61	1,23	24,76	67
CH_3OH	mg/kg_{fuel}	212,02	193,41	138,73	5,08	674,09	54	C_7H_{14}	mg/kg_{fuel}	10,40	10,25	4,63	1,73	24,16	68
C_2H_3N	mg/kg_{fuel}	4,96	4,81	2,71	0,42	12,96	61	$C_4H_4O_3$	mg/kg_{fuel}	2,53	2,18	1,88	0,01	8,80	63
CH_3CHO	mg/kg_{fuel}	225,66	226,44	80,52	30,67	404,77	67	$C_5H_8O_2$	mg/kg_{fuel}	17,59	16,85	8,19	1,21	36,53	66
CH_2O_2	mg/kg_{fuel}	4,76	2,84	5,49	0,01	27,20	53	$C_6H_{12}O$	mg/kg_{fuel}	13,61	12,66	5,77	0,70	24,34	67
C_2H_6O	mg/kg_{fuel}	9,89	6,83	12,05	0,49	77,32	54	$C_4H_6O_3$	mg/kg_{fuel}	1,63	1,58	1,06	0,00	6,55	62
C_3H_4O	mg/kg_{fuel}	86,84	92,42	32,03	9,15	151,45	67	$C_5H_{10}O_2$	mg/kg_{fuel}	3,20	3,54	1,71	0,32	7,41	65
C_4H_8	mg/kg_{fuel}	187,85	175,18	96,16	16,34	714,36	67	$C_6H_{14}O$	mg/kg_{fuel}	0,53	0,47	0,38	0,02	1,80	63
C_3H_6O	mg/kg_{fuel}	83,84	81,61	38,04	7,18	164,39	67	C_8H_8	mg/kg_{fuel}	9,76	9,84	4,27	0,21	23,53	67
$C_2H_4O_2$	mg/kg_{fuel}	119,29	113,99	61,36	2,08	246,54	63	C_7H_6O	mg/kg_{fuel}	5,09	4,46	3,14	0,24	13,73	67
DMS	mg/kg_{fuel}	3,51	1,97	4,18	0,20	20,90	45	C_8H_{10}	mg/kg_{fuel}	70,58	49,79	73,46	4,47	365,74	64
$C_2H_2F_2$	mg/kg_{fuel}	1,15	0,98	0,88	0,09	4,31	64	C_7H_8O	mg/kg_{fuel}	8,19	8,70	3,36	1,69	16,03	66
$C_2H_8O_2$	mg/kg_{fuel}	1,48	1,02	1,48	0,02	7,45	58	C_8H_{12}	mg/kg_{fuel}	25,70	27,71	9,53	2,73	45,75	67
C_5H_6	mg/kg_{fuel}	17,75	18,99	7,84	0,93	29,14	68	$C_7H_{10}O$	mg/kg_{fuel}	11,52	12,69	4,70	1,78	22,02	67
C_4H_4O	mg/kg_{fuel}	16,30	17,31	7,03	2,66	33,09	66	C_8H_{14}	mg/kg_{fuel}	50,04	47,15	23,76	4,85	167,07	66
C_5H_8	mg/kg_{fuel}	204,35	202,94	94,65	19,43	608,54	67	$C_5H_4O_3$	mg/kg_{fuel}	12,03	11,85	6,42	0,43	28,31	67
C_4H_6O	mg/kg_{fuel}	64,31	65,29	24,94	6,19	118,20	67	$C_6H_8O_2$	mg/kg_{fuel}	7,04	6,26	3,49	0,23	15,29	67
C_5H_{10}	mg/kg_{fuel}	115,37	104,26	62,18	12,81	439,62	67	$C_7H_{12}O$	mg/kg_{fuel}	9,81	9,81	4,12	1,72	19,44	67
$C_3H_4O_2$	mg/kg_{fuel}	35,90	31,95	20,60	0,33	82,70	66	$C_4H_4O_4$	mg/kg_{fuel}	2,16	1,89	1,18	0,15	5,87	66
C_4H_8O	mg/kg_{fuel}	32,21	33,59	13,96	3,96	59,49	66	$C_5H_8O_3$	mg/kg_{fuel}	2,05	2,24	1,01	0,07	4,94	66
$C_2H_4O_3$	mg/kg_{fuel}	4,56	3,14	4,73	0,25	15,72	33	$C_6H_{12}O_2$	mg/kg_{fuel}	3,20	3,12	1,58	0,00	6,73	65
$C_3H_8O_2$	mg/kg_{fuel}	2,73	1,93	2,32	0,19	11,06	54	$C_7H_4O_3$	mg/kg_{fuel}	0,89	0,88	0,38	0,09	1,83	66
C_2H_6SO	mg/kg_{fuel}	0,78	0,55	0,71	0,01	3,92	53	$C_8H_8O_2$	mg/kg_{fuel}	3,78	3,64	1,68	0,39	8,03	67
$C_2H_6O_3$	mg/kg_{fuel}	2,50	1,45	2,67	0,01	11,13	43	$C_{15}H_{24}$	mg/kg_{fuel}	3,13	3,13	1,31	0,35	5,87	65
C_6H_6	mg/kg_{fuel}	41,08	40,83	19,14	3,60	100,43	66	FSC	% S	0,07	0,06	0,12	0,00	1,36	137
C_6H_8	mg/kg_{fuel}	63,91	67,34	24,77	4,68	122,12	67								

Table BT4: *Comparison of VOC and PM_1 EF with previous studies.*

Studies	Benzene (mg/kg_{fuel})	Toluene (mg/kg_{fuel})	m&p-Xylenes (mg/kg_{fuel})	Ethylbenzene (mg/kg_{fuel})	o-Xylene (mg/kg_{fuel})	1,3-Butadiene (mg/kg_{fuel})
This study	41,8 ± 19,14 (C_6H_6)	30,99 ± 20,71 (C_7H_8)		70,58 ± 73,46 (C_8H_{10})		
Agrawal et al 2010	5,26 ± 0,16	7,81 ± 5,32	5,03 ± 3,13	2,18 ± 1,26	12,55 ± 1,15 mg / kg	1,95 ± 1,25
Zhang et al 2024	7,31 ± 4,14	4,88 ±4,09	12,0 ± 11,2	5,25 ± 5,13	7,51 ± 7,34	
Zhang et al 2024	8,12 ± 5,14	14 ± 26,5	11,5 ± 8,15	4,40 ± 1,89	6,86 ± 4,63	9,57 ± 14,4
Huang et al, 2018	0,84	27,73	3,51	2,10	1,51	0,03
Huang et al, 2018	0,36	6,72	0,49	0,24	0,23	0,01
Huang et al, 2018	2,03	57,69	5,65	2,89	2,82	0,01
Timonen et al, 2022	5,315	0,49 (C_7H_8)		36,97 (C_8H_{10})		
	Acetone (mg/kg_{fuel})	Acrolein (mg/kg_{fuel})	OA (g·kg_{fuel}^{-1})	SO_4^{2-} (mg/kg_{fuel})	NO_3^- (mg/kg_{fuel})	NH_4^+ (mg/kg_{fuel})
This study	83,84 ± 38,04 (C_3H_6O)	86,84 ± 32,03 (C_3H_4O)	5,26	24,69	14,65	12,86
Agrawal et al 2010						
Zhang et al 2024	61,5 ± 49,4	16,8 ± 16,7				
Zhang et al 2024	111 ± 104	19,7 ± 17,7				
Huang et al, 2018	5,59	0,17				
Huang et al, 2018	1,32	0,03				
Huang et al, 2018	16,14	0,35				
Timonen et al, 2022			0,11	25,00		
Le Berre et al, 2024	(Manoeuvering)		1,60	171,00		
Le Berre et al,2024	(At berth)		0,61	28,00		
Le Berre et al, 2024	(General)		1,87	175,00	5,40	5.0

B.4 Additional figures

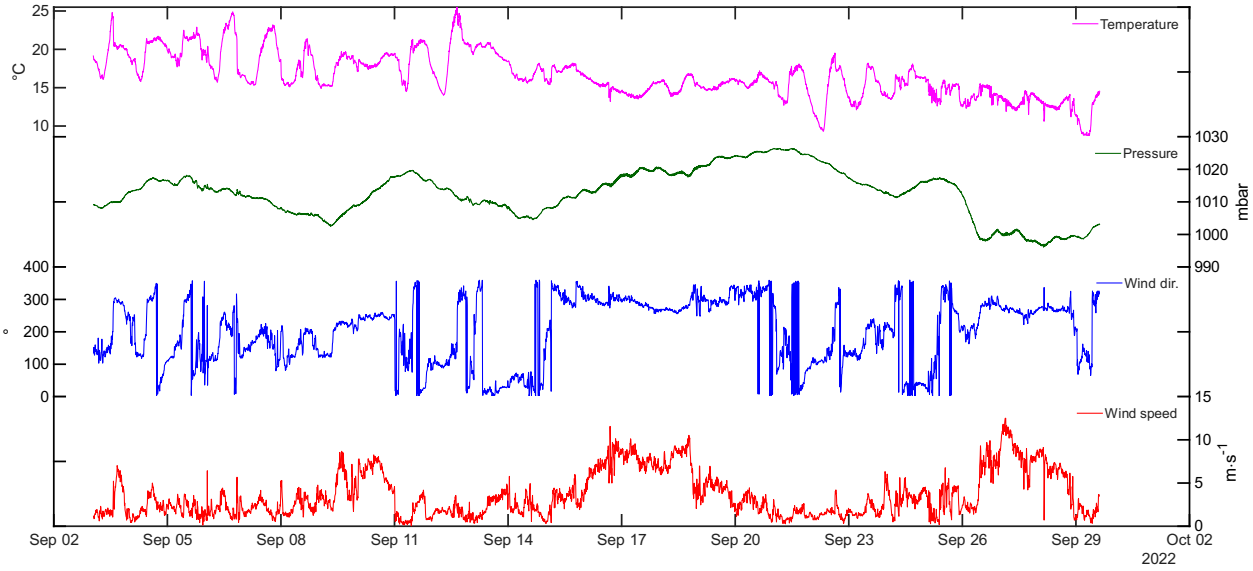

Figure BF1: *Meteorological conditions recorded at the sampling site in Dunkirk. temperature (purple, in °C), pressure (green, in mbar), wind direction (blue, in °), wind speed (red, m·s^{-1})*

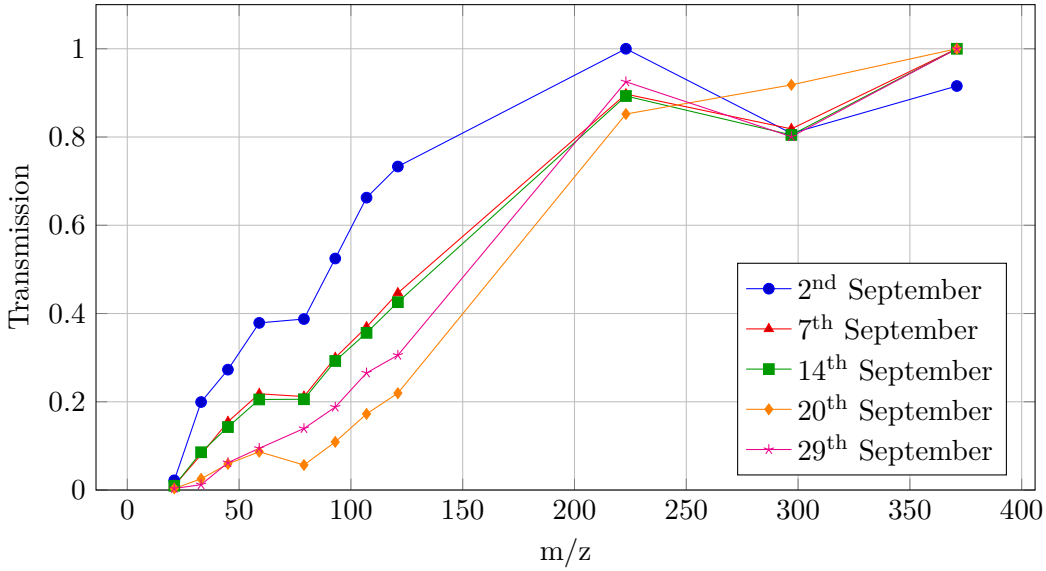

Figure BF2: *Transmission curves for the PTR-ToF-MS determined for each calibration of the campaign.*

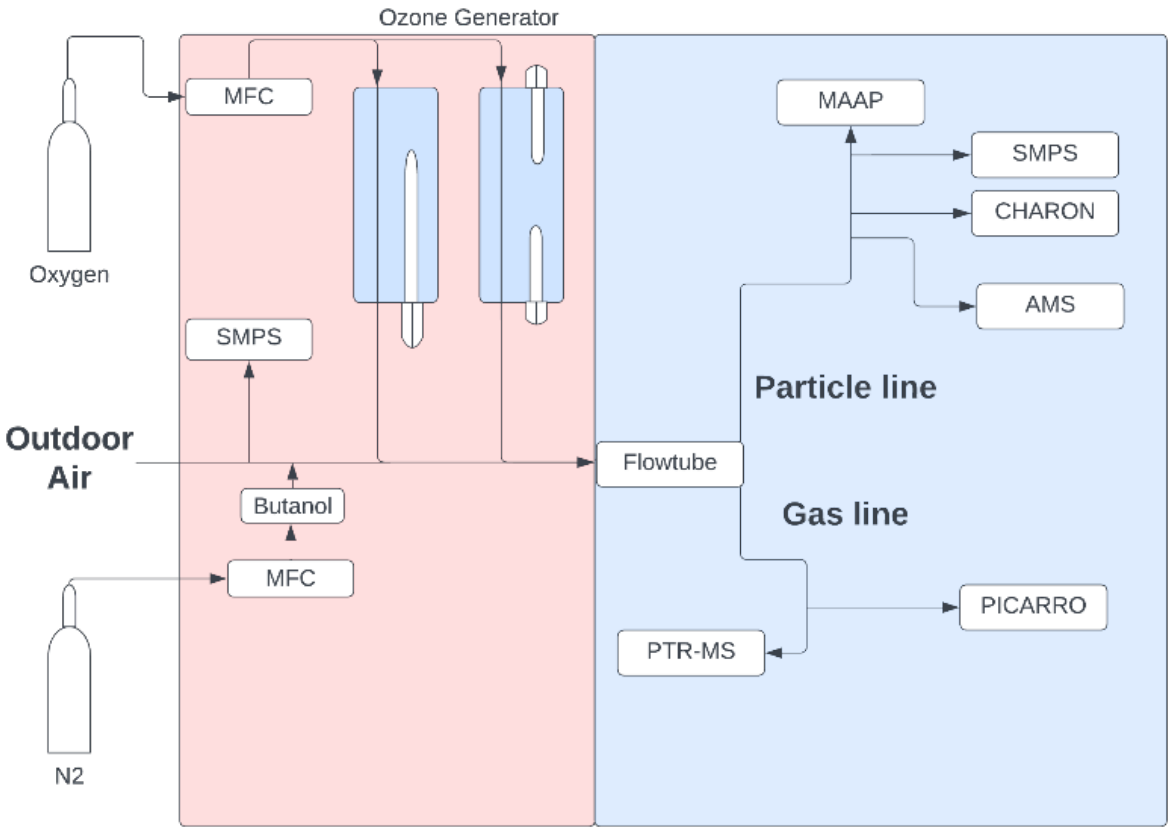

Figure BF3: *Setup of the Aerosol Flow Tube (AFT).*

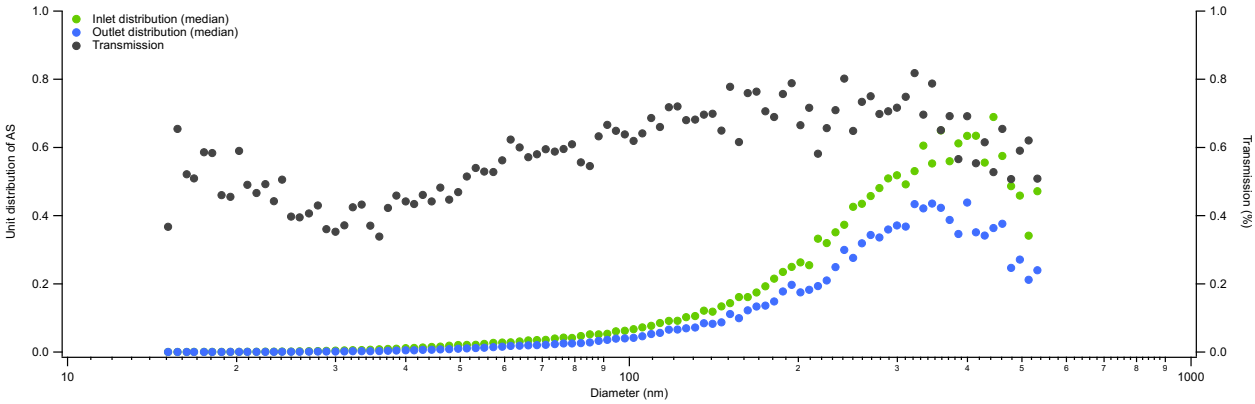

Figure BF4: *Flow tube transmission determined in laboratory experiment. A nebulised ammonium sulphate solution was used and the ratio between inlet (green dots) and outlet (blue dots) masses results in a diameter-dependant transmission efficiency (black dots). Mass distributions were determined using a SMPS, and the final transmission was calculated using the ratio of medians of the inlet and outlet of the distributions at each diameter.*

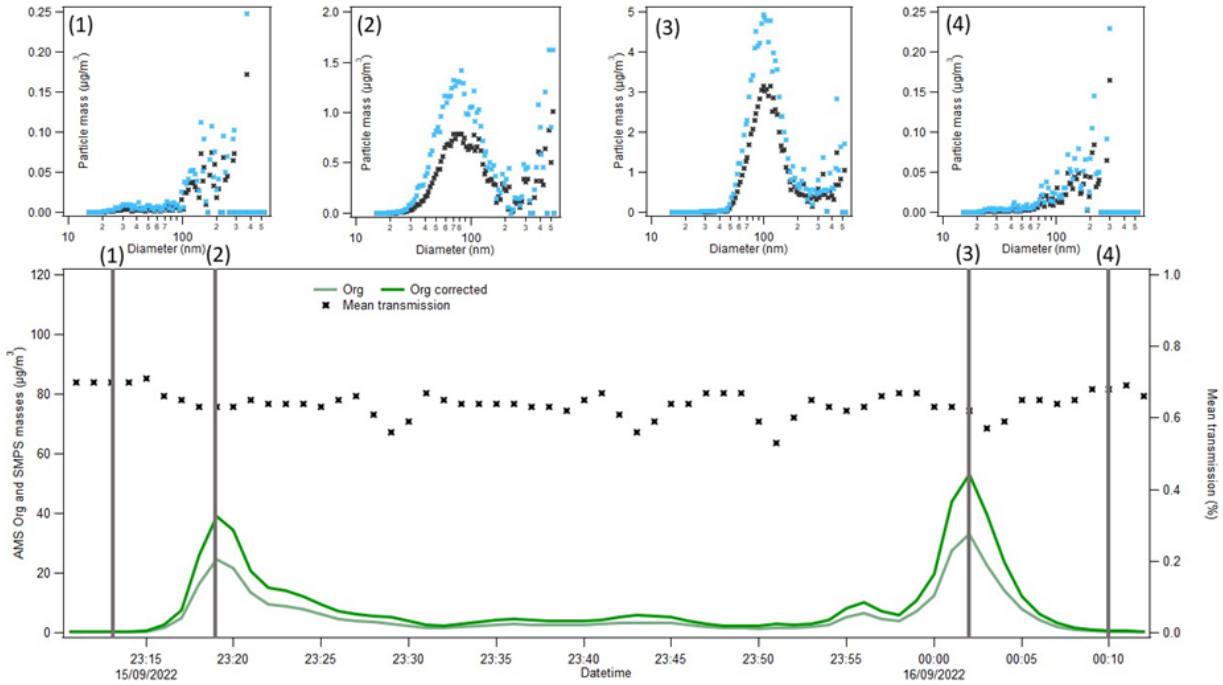

Figure BF5: *Top (1-4): mass distributions of particles at the inlet of the flow tube, corrected (blue dots) and non-corrected (black dots), for each time that is indicated in the time series below. Bottom: concentration time series of corrected OA (dark green), non-corrected OA (light green). Black dots correspond to the mass-weighted mean diameter-dependant transmission efficiency, determined at each time step.*

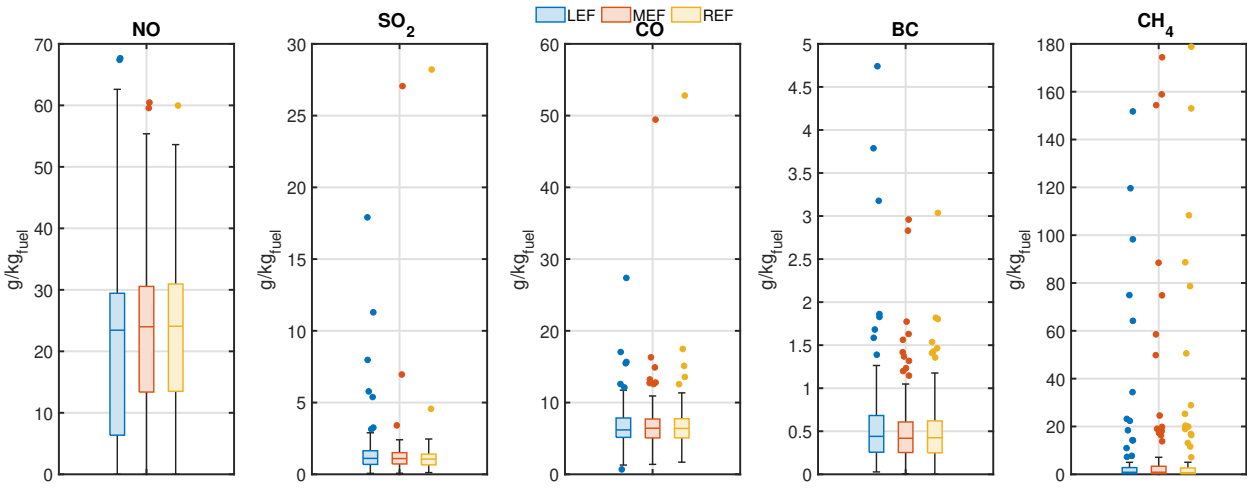

Figure BF6: *Linear fit Based EF (LEF, blue), Median-based EF (MEF, orange) and rolling-median based EF (REF, yellow) distributions for NO, SO2, CO, BC and CH4. The line within the box is the median, the upper and lower edges of the box are respectively 25th and 75th percentile respectively, the bottom and top edges of the whiskers correspond to the median ± 1.5 × Interquartile Range (IQR) of the distributions, outliers are shown as individual points.*

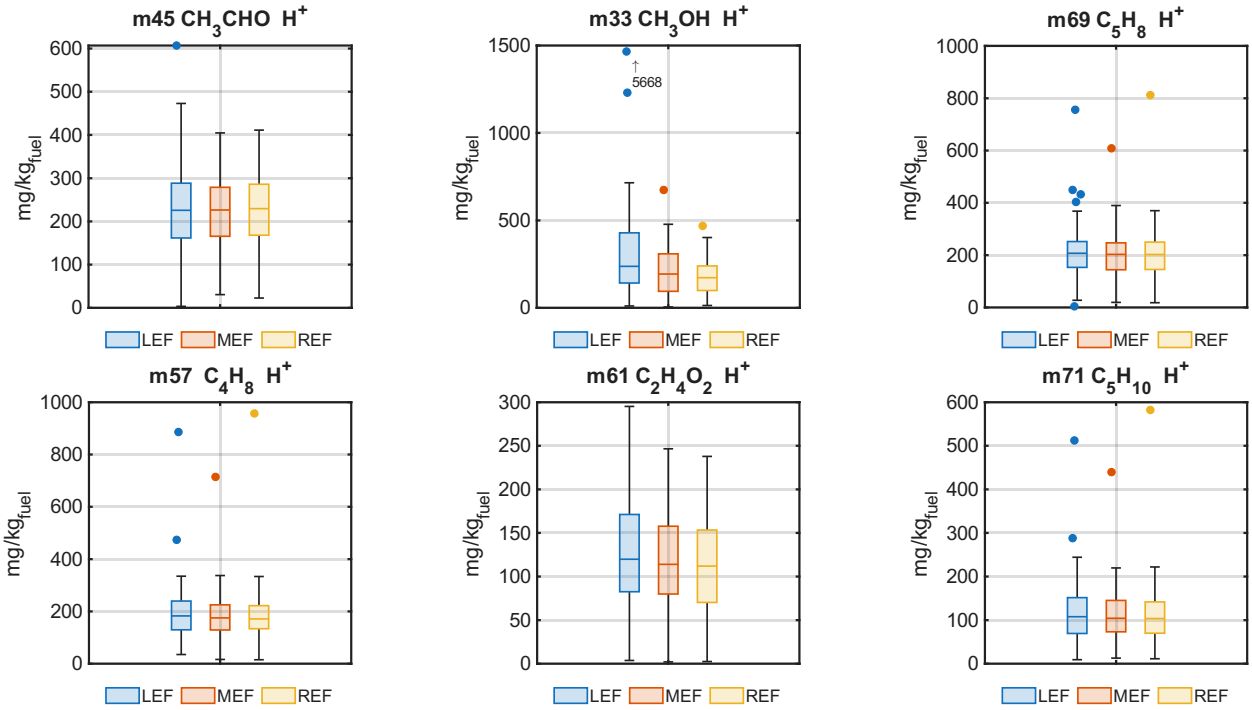

Figure BF7: *Median-based EF distributions (blue) and rolling-median based EF distributions for the 6 major VOCs. The line within the box is the median, the upper and lower edges of the box are respectively 25th and 75th percentile respectively, the bottom and top edges of the whiskers correspond to the median ± 1.5 × Interquartile Range (IQR) of the distributions, outliers are shown as individual points.*

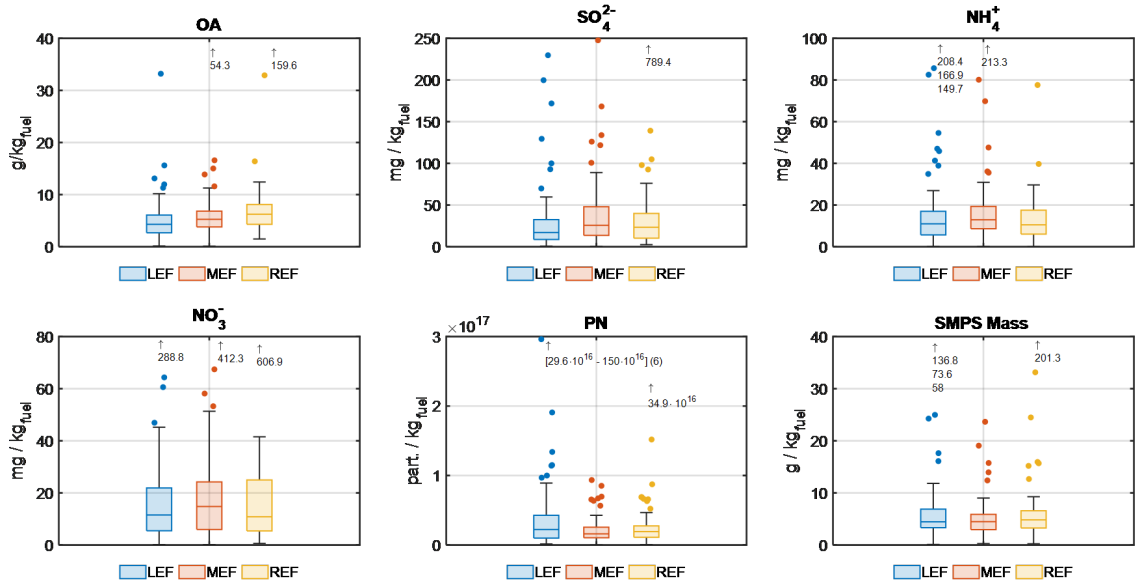

Figure BF8: *Linear fit Based EF (LEF, blue), Median-based EF (MEF, orange) and rolling-median based EF (REF, yellow) distributions for PM_1 composition and PN and mass from the SMPS. The line within the box is the median, the upper and lower edges of the box are respectively 25th and 75th percentile respectively, the bottom and top edges of the whiskers correspond to the median ± 1.5 × Interquartile Range (IQR) of the distributions, outliers are shown as individual points. For readability, some outliers are indicated as values or a range of values that are off-scale.*

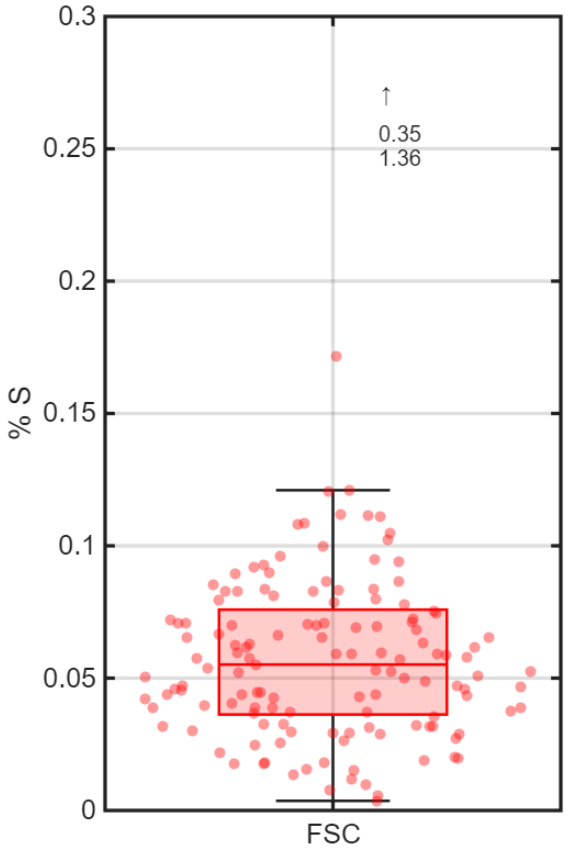

Figure BF9: *Distribution of the FSC derived from each EF of SO_2. The line within the box is the median, the upper and lower edges of the box are respectively 25th and 75th percentile respectively, the bottom and top edges of the whiskers correspond to the median $\pm$ 1.5 $\times$ Interquartile Range (IQR) of the distributions, outliers are shown as individual points. For readability, some outliers are indicated as values or a range of values that are off-scale.*

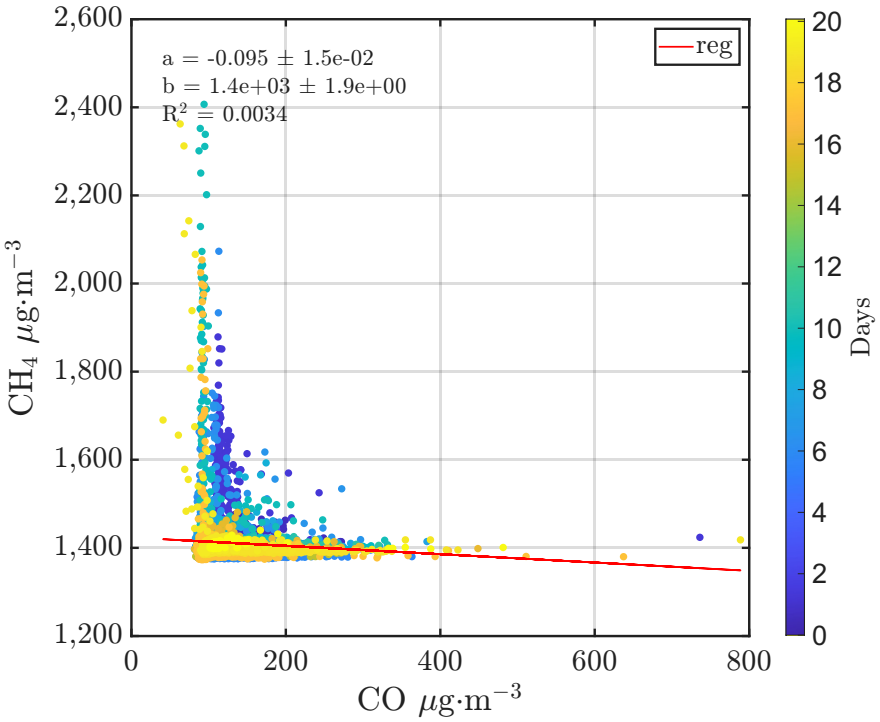

Figure BF10: *Scatter plot of CO vs CH_4. (Red line) linear regression of CO vs CH_4, associated coefficients are in the upper left of the figure. (Color bar) Number of days spent throughout the campaign, 0 is September 9th 2022.*

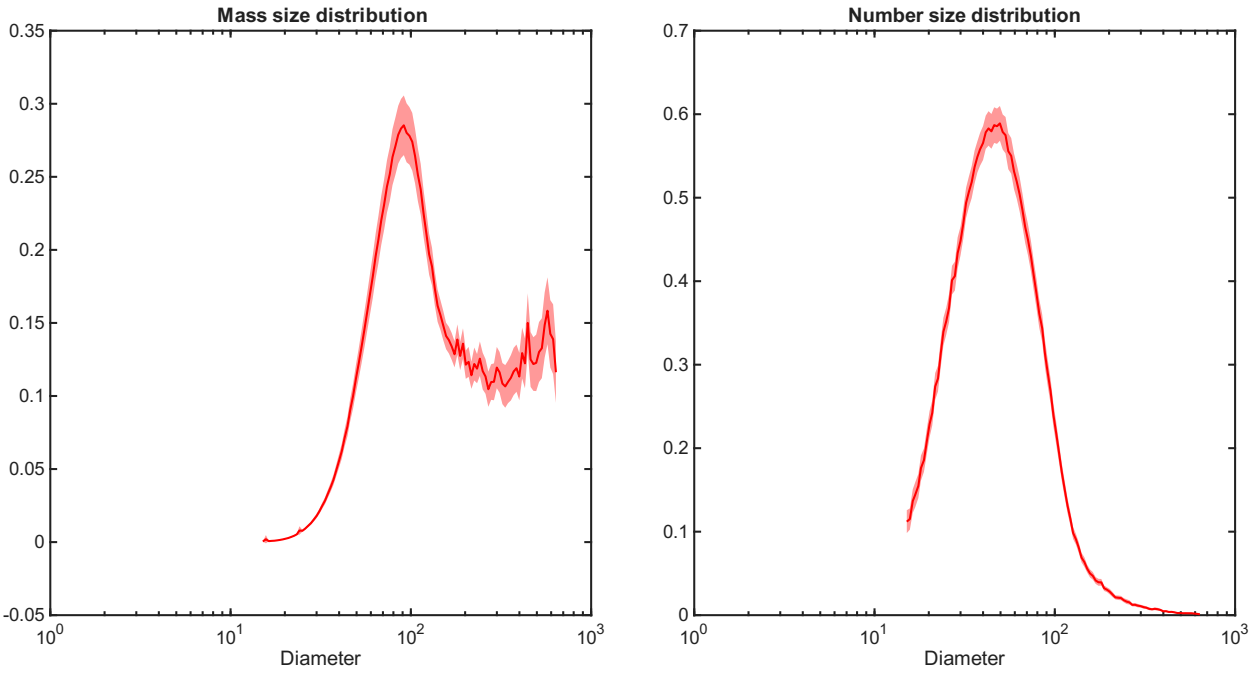

Figure BF11: *Size distributions within the ship plumes determined by the SMPS: (left) normalised mass size distribution , (right) normalised number size distribution*

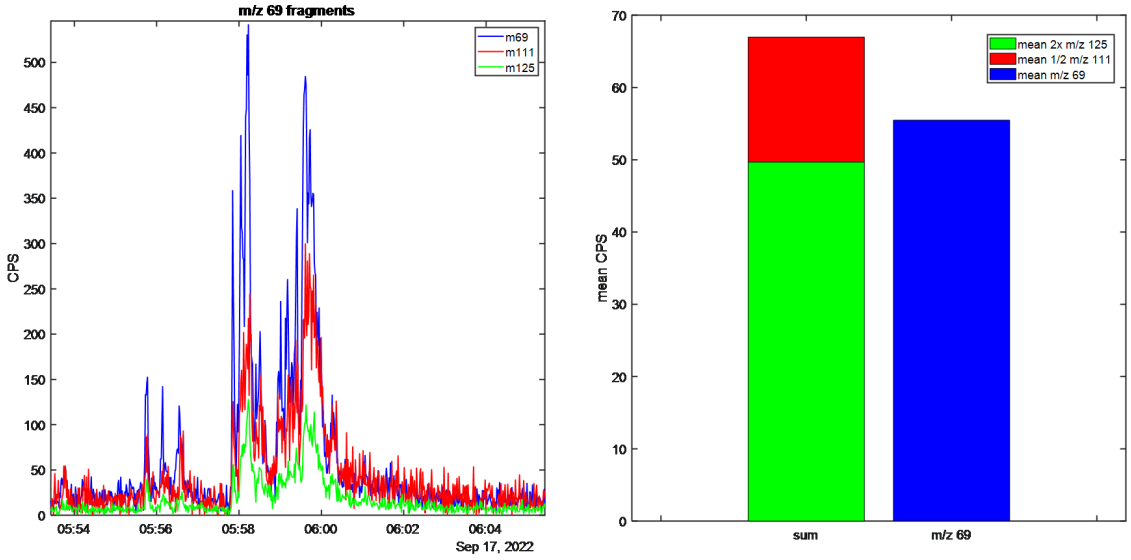

Figure BF12: *Left : time series of raw signals (in Counts Per Second, CPS) of m/z 69 (blue), m/z 111 (red) and m/z 125 (green). Right : bar plots of the mean sum of twice m/z 125 (green) in CPS, half m/z 111 (red) in CPS, and mean m/z 69 in CPS.*

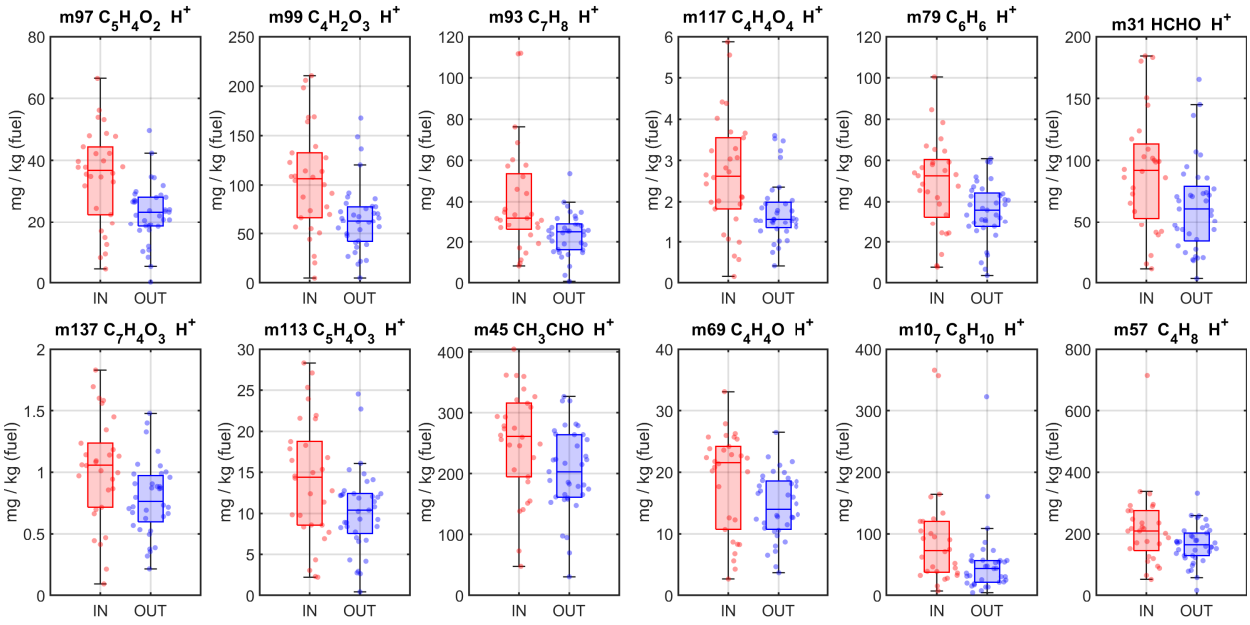

Figure BF13: *Additional comparisons of VOC EF distributions depending on the direction of travel with arrivals EF in red and departures EF in blue.*

APPENDIX C

PMF solution fraction time series of Chapter 4

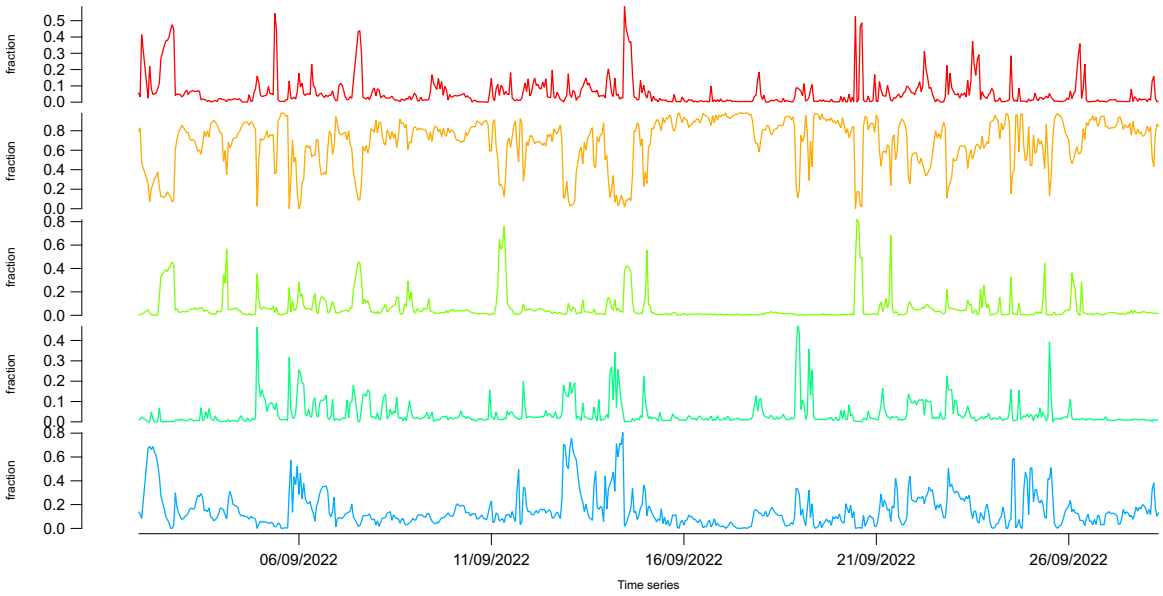

Figure CF1: *Times series of the mass fraction of the 5-factor solution of the PMF ran with TD-GC-FID data.*

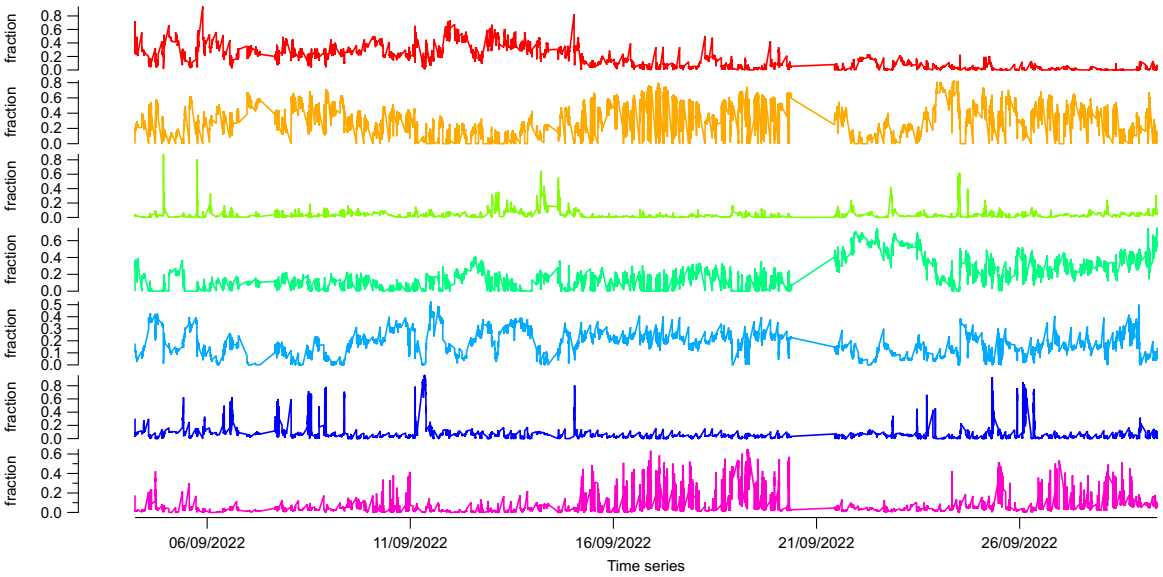

Figure CF2: *Times series of the mass fraction of the 7-factor solution of the PMF ran with PTR-ToF-MS data.*

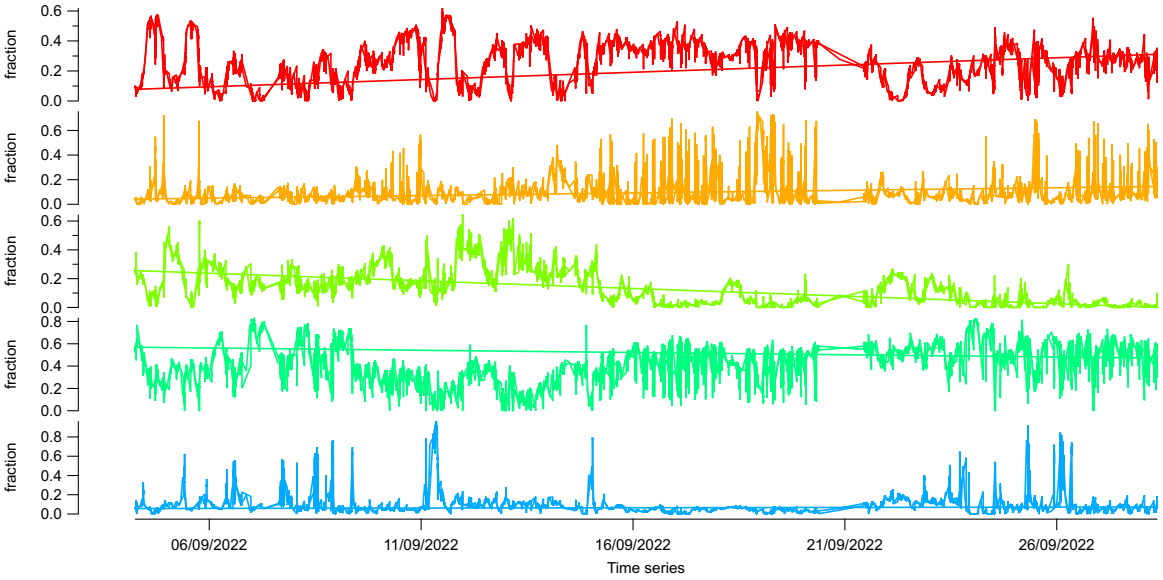

Figure CF3: *Times series of the mass fraction of the 5-factor solution of the MTR-PMF ran with PTR-ToF-MS and TD-GC-FID data.*

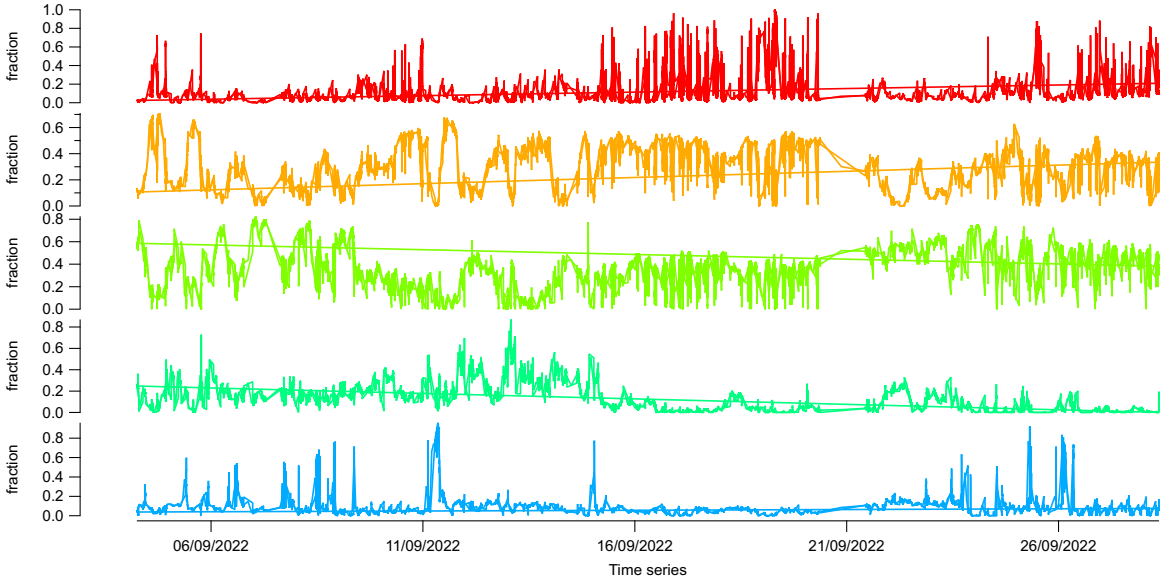

Figure CF4: *Times series of the mass fraction of the 5-factor solution of the constrained MTR-PMF ran with PTR-ToF-MS and TD-GC-FID data.*

APPENDIX D

Appendices of Chapter 5

D.1 Deliverable report of the PIRATE Project by Atmo Normandie

Port Inventories in real time (PIRATE)

Elaboration et validation d'inventaires des émissions portuaires en temps réel



Livrable L3.0a

Février 2023

Choix des sites de mesure pour la campagne intensive du Havre

Dans le cadre du projet PIRATE, une campagne de mesures intensive est prévue en mai 2023 dans l'enceinte de HAROPA Port – Le Havre.

Ce document a pour objectif de présenter les différents éléments (météo, fréquentation, possibilités techniques et électriques, pertinence) qui ont amené à choisir le site de cette campagne de mesure.

Afin de statuer sur le choix du site de mesure, de nombreux échanges ont eu lieu entre HAROPA Port – Le Havre, l'IMT Nord Europe et Atmo Normandie.

1 Bilan des données météorologiques sur la zone

1.1 Localisation des stations

Une étude des conditions de vent (direction, vitesse) a été réalisée à partir des différentes stations météo disponibles sur le territoire.



1.2 Exploitation des données météorologiques

Une exploitation des données météorologiques sous la forme de roses des vents a été réalisée entre 2019 et 2021. Le but est de connaître l'orientation et la vitesse moyennes des vents que nous pourrions rencontrer lors de la campagne de mesure du mois de mai 2023.

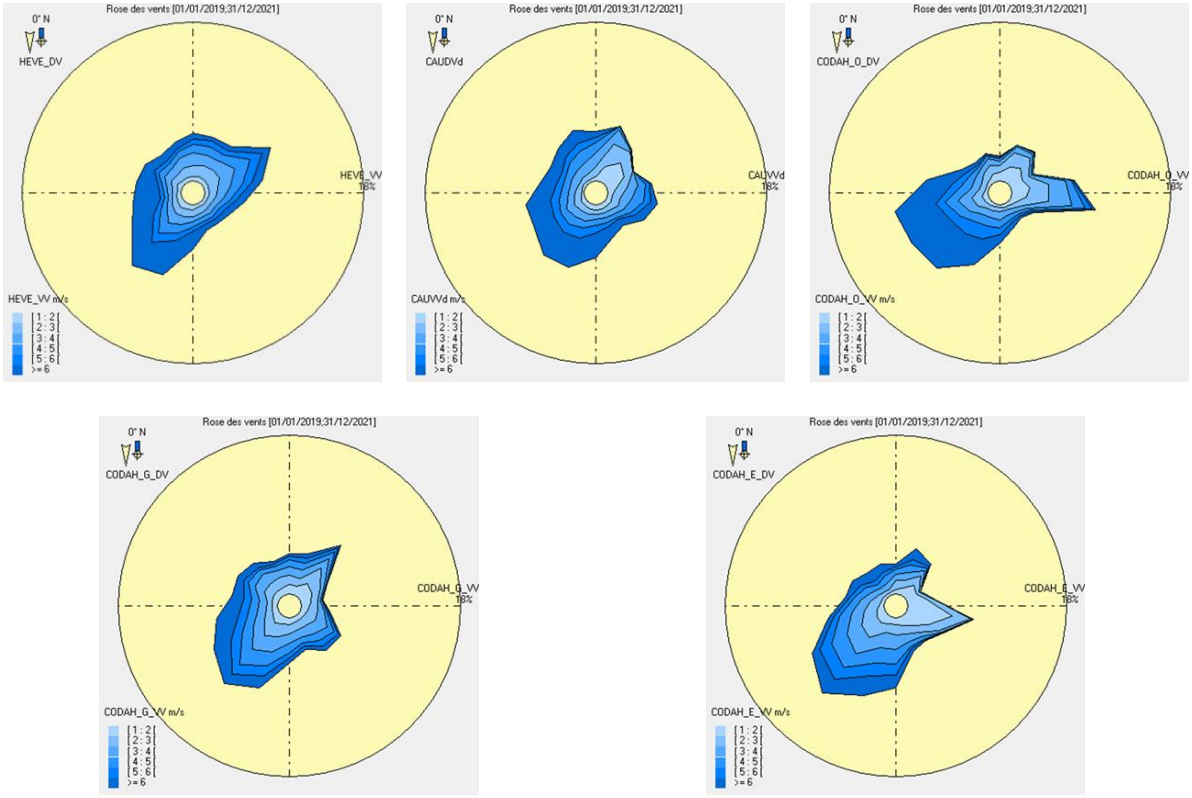

Ces roses des vents font apparaître une prédominance des vents de secteur Sud-Ouest.

D'après cette première analyse, il sera important de sélectionner un site de mesure qui se trouve plutôt au Sud-Ouest des sources d'émissions afin de pouvoir mesurer le plus possible l'influence du transport maritime.

1.3 Analyse du trafic maritime

Pour choisir les éventuels sites pour la campagne de mesure et établir la période plus propice pour effectuer la campagne de mesure, Atmo Normandie a étudié la répartition du trafic selon les différents types de navires qui fréquentent le port du Havre.

L'analyse du trafic du port de 2017 à 2020 a permis de comprendre que pour les containeurs, les tankers et les rouliers aucune saisonnalité n'est observée, le nombre de navires restant relativement constant toute l'année. Par contre, pour les paquebots, le mois de mai concentre le nombre annuel de rotations du port le plus important.

mois	2017	2018	2019	2020	2021
mars	546	592	440	438	417
avril	508	549	492	340	408
mai	550	585	512	300	423
juin	488	518	453	336	398
juillet	521	524	490	384	380

D'après cette analyse, il sera intéressant de pouvoir réaliser la campagne de mesure pendant le mois de mai et en proximité des quais où stationnent les porte-conteneurs et les rouliers.

2.1 Sites proposés par Atmo Normandie et HAROPA Port – Le Havre

Le 13 juillet 2022, nous avions programmé une réunion avec HAROPA Port – Le Havre pour leur proposer plusieurs sites de mesures sous maîtrise d'exploitation du HAROPA Port – Le Havre, afin de faciliter les accès, les autorisations d'installation et le raccordement électrique.

Les sites proposés par Atmo Normandie de commun accord avec HAROPA Port -Le Havre sont les suivants :

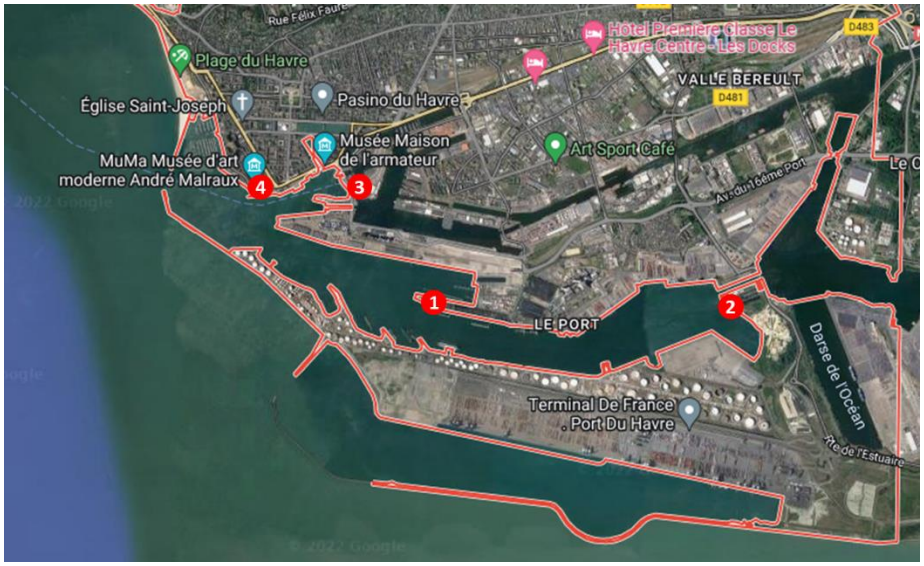

1. **Route du Môle Central**
2. **Avenue Amiral du Chillou**
3. **Bassin de la citadelle : siège d'HAROPA Port – Le Havre**
4. **Port Center – Chaussée John Kennedy**

Après échange entre les équipes d'HAROPA Port – Le Havre, il en ressort que :

- Le site **Route du Môle Central (1)**, bien que répondant aux différents besoins techniques est incertain concernant la sécurité des équipements et leur alimentation électrique. Ce site se trouve en proximité des quais qui accueillent les porte-conteneurs ;

- Le site de l'**avenue Amiral du Chillou (2)**, répond aux contraintes techniques de sécurité des équipements et d'alimentation électrique. Ce site se trouve en proximité des quais qui accueillent les rouliers et les porte-conteneurs ;
- Le site **bassin de la citadelle (3),** répond aux contraintes techniques de sécurité des équipements et d'alimentation électrique. Il n'est cependant pas idéalement situé, car juste à côté des quais d'arrivée des ferries et éloigné par rapport aux autres navires qui débarquent dans le port du Havre.
- Le site **Port Center – Chaussée John Kennedy (4),** n'est pas dans le domaine portuaire, donc il n'a pas été retenu.

2.2 Visite de sites

Le 13 juillet 2002, après la rencontre avec HAROPA Port – Le Havre, Atmo Normandie a visité les lieux dont nous avions discuté lors de la réunion. L'objectif était d'évaluer la faisabilité d'implantation du moyen mobile sur les différents sites repérés ainsi que les facteurs environnementaux des différents sites (position par rapport aux émetteurs, environnement, météo).

Le premier site visité est celui de la **Route du Môle Central (1)** :





Ce site se trouve sous maîtrise d'exploitation d'HAROPA Port – Le Havre. Il ne semble pas très sécurisé et il faut se renseigner pour savoir s'il dispose d'une alimentation électrique. Le site se trouve en proximité de l'arrivée de rouliers.

Le deuxième site visité est celui de l'**avenue Amiral du Chillou (2)** :







Ce site est très intéressant du point de vue de son positionnement, d'autant plus qu'il est à côté d'une station météo appartenant à la communauté urbaine Le Havre Seine Métropole. Il n'est cependant pas sécurisé et la question de l'alimentation électrique s'est posée.

Le 3ème site visité est celui du **Bassin de la citadelle (3)**, à côté du siège social d'HAROPA Port – Le Havre.



Ce site est situé en proximité des quais ferries et se trouve sous les vents lors du passage des navires sortant du port. Il risque donc de ne pas pouvoir être influencé par le trafic des autres navires.

Suite à cette visite, des éléments complémentaires ont été demandés à HAROPA Port – Le Havre :

- Le site de la **route du Môle Central (1),** dispose-t-il d'une alimentation électrique ? Sera-t-il possible de sécuriser le moyen mobile ?
- Le site de l'**avenue Amiral du Chillou (2)**, dispose-t-il d'une alimentation électrique ? Sera-t-il possible de sécuriser le moyen mobile à l'intérieur de l'enceinte grillagée ou à côté du bâtiment ?
- Le site **Bassin de la citadelle (3),** dispose-t-il d'une alimentation électrique ?

3 Choix du site de mesure

3.1 Réponses apportées par HAROPA Port – Le Havre

Suite à la visite de site du 13 juillet 2022, des informations complémentaires avaient été demandées à HAROPA Port – Le Havre.

Les réponses apportées sont les suivantes :

- Pour le site de la **route du Môle Central (1),** il n'existe aucun réseau électrique exploitable ;
- Pour le site de l'**avenue Amiral du Chillou (2),** un raccordement électrique est possible mais le moyen mobile ne pourrait pas être installé dans l'enceinte grillagée et la sécurité n'est pourra pas être assurée ;
- Le site **bassin de la citadelle (3)** dispose d'un réseau électrique utilisable.

3.2 Nouveaux éléments durant le mois de décembre

Durant le mois de décembre, HAROPA Port – Le Havre nous a informé de l'impossibilité de nous fournir un raccordement électrique, notamment en raison de l'augmentation des coûts de l'énergie, et qu'Atmo Normandie devra donc demander un branchement électrique auprès d'ENEDIS. Suite à cette nouvelle, Atmo Normandie a fait part à HAROPA Port – Le Havre la nécessite d'avoir un site sécurisé avec un poste électrique ENEDIS proche, afin de pouvoir demander le raccordement électrique provisoire.

HAROPA Port - Le Havre nous a proposé d'installer le moyen mobile à côté de **l'écluse François 1er (Chaussée du Lazaret) (5),** où les critères de sécurité et de raccordement électrique peuvent être remplis. Ce site se trouve en proximité des quais fréquentés par les rouliers et les ports conteneurs.

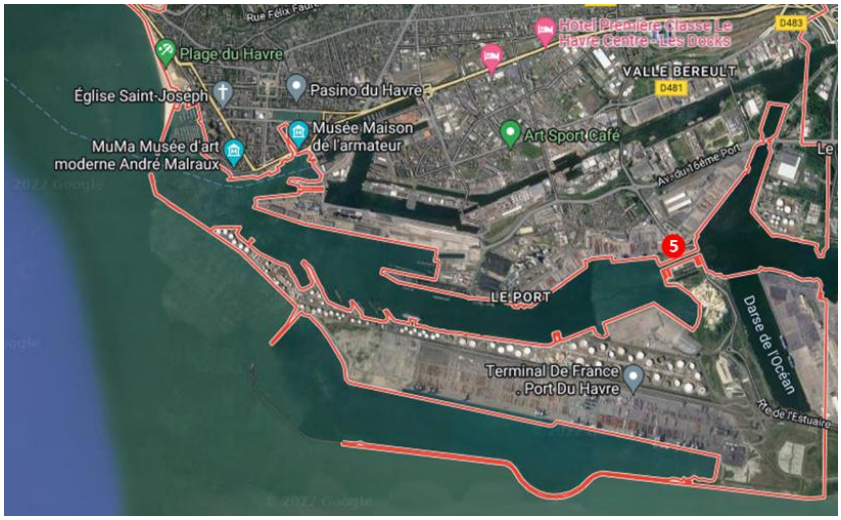

Atmo Normandie a fait une demande d'accordement électrique provisoire : le coffret sera installé le 10 février. HAROPA Port – Le Havre a déjà donné son autorisation d'occuper le lieu pendant la campagne de mesure (courrier du 20 janvier 2023 de la Direction de la transformation de la zone industrialo-portuaire). Par ailleurs, HAROPA Port – Le Havre nous a garanti la sécurisation du moyen mobile au moyen d'un grillage anti-intrusion.

4 Instruments de mesure

Pendant la campagne de mesure seront déployés les instruments de mesure suivants :

- Un FIDAS pour la mesure de PM10, PM2.5 ;
- Un APNA 370 pour la mesure des NOx ;
- Un PICARRO G2401-m pour la mesure du CO_2, CH_4 et CO installé par l'IMT Nord Europe ;
- Un analyseur pour la mesure de SO_2 ;
- Un Envi CPC pour le comptage des particules ;
- Un CHROMATOTEC (installé et géré par l'IMT Nord Europe) pour la mesure de COVs ;
- Un micro-aéthalomètre MA350 pour la mesure du black carbon ;
- Un mât météo télescopique avec une mesure de la vitesse et direction du vent, température et humidité.

Le PAQMAN WATCHER (de l'INU) sera aussi installé par l'IMT Nord Europe pour la campagne de mesure.

Table DT1: *Composition of the NPL gas standard used to calibrate the TD-GC-FID.*

Compound	Amount fraction μmol·mol^{-1}	Compound	Amount fraction μmol·mol^{-1}
Ethane	205,4 ± 4,2	2-Methylpentane	213,3 ± 4,3
Ethylene	201,8 ± 4,1	n-Hexane	213,3 ± 4,3
Propane	203,1 ± 4,1	Isoprene	212,5 ± 4,3
Propene	201,9 ± 4,1	n-Heptane	213,7 ± 4,3
Isobutane	207 ± 6	Benzene	206,2 ± 4,2
Butane	205 ± 6	2,2,4-Trimethylpentae	200,6 ± 4,1
Ethylene	211 ± 11	n-Octane	201,2 ± 4,1
trans-2-Butene	205,8 ± 4,2	Toluene	200 ± 6
cis-2-Butene	204,7 ± 4,1	Ethylbenzene	217 ± 6
2-Methylbutane	202,4 ± 4,1	m&p-Xylenes	422 ± 11
n-Pentane	203,3 ± 4,1	o-Xylene	207 ± 6
1,3-Butadiene	207,5 ± 4,2	1,3,5-Trimethylbenzene	206 ± 6
trans-2-Pentene	204 ± 6	1,2,4-Trimethylbenzene	207 ± 6
1-Pentene	207,7 ± 4,2	1,2,3-Trimethylbenzene	204 ± 6

Scientific Valorisation

Articles

- Volent, E., Gunti, Q., D'Anna, B., De Brito, J. F., Jamar, M., Temime-Roussel, B., Moldanova, J., Timonen, H., Hellén, H., Lanzafame, G., Dal Maso, M., Roze, S., Riffault, V., Tinel, L., Sauvage, S. (2025). Ship Emission Factors for Volatile Organic Compounds and PM_1 from land-based observations in an Emission Control Area of France. Preprint in review.

Posters

- Volent, E., Gunti, Q., D'Anna, B., Jamar, M., Temime-Roussel, B., et al. (2025). Revisiting VOC and PM_1 Emission Factors from ships in Dunkirk. Séminaire interne : Journée de lancement du Cross Disciplinary Project Area, March 2025, Villeneuve d'Ascq, France.

- Volent, E., Tinel, L., & Sauvage, S. (2023). Impact of Volatile Organic Compounds from shipping emissions on air quality in the Channel. 2023 iCACGP-IGAC ECR Online Conference, November 2023, Online, France. doi:10.1021/es071686z

- Tinel, L., Volent, E., Sauvage, S., Riffault, V., Le Berre, L., et al. (2024). Shipping-related emissions of Volatile Organic Compounds (VOCs). SOLAS Open Science Conference, November 2024, Goa, India.

Oral presentations

- Volent, E., Tinel, L., F. de Brito, J., Jamar, M., and Sauvage, S., 2024. Volatile Organic Compounds shipping emissions observed in an industrial harbour of northern France , EGU General Assembly 2024, Vienna, Austria, 14–19 Apr 2024, EGU24-9501, https://doi.org/10.5194/egusphere-egu24-9501, 2024.

- Tinel, L., Volent, E., Gunti, Q., D'Anna, B., Brito, J.F.D., Jamar, M., Temime-Roussel, B., Moldanova, J., Timonen, H., Hellen, H., Lanzafame, G., Maso, M.D., Riffault, V., Sauvage, S., 2025. Determining Volatile Organic Compounds (VOC) and Particulate Matter (PM_1) shipping Emission Factors from land-based, high time resolution observations in an Emission Control Area of northern France. URL:https://meetingorganizer.copernicus.org/EGU25/EGU25-15887.html,doi: 10.5194/egusphere-egu25-15887. conference Name: EGU25

Abstract

Shipping is an important mean of transportation worldwide and a growing source of concern in terms of pollution as its traffic is expected to increase in the coming years. Ship emissions have an impact on a global scale by contributing to global warming and on a regional scale, as emissions mainly occur in coastal areas where populations live. Therefore, regulations have been introduced to address the issue of ship pollutant emissions, such as Annex VI of MARPOL, which establishes Emission Control Areas (ECAs) around the world where ships' fuel sulphur content (FSC) is reduced to a maximum of 0.1%, and where ships' engines are certified in terms of NO_x emissions. In the context of compliance with these regulations, SO_2 and NO_x ship emissions have been reduced, while emissions of emerging pollutants such as Volatile Organic Compounds (VOCs) remain poorly documented. VOCs impact air quality, some are carcinogenic primary pollutants, while others contribute to particulate matter (PM) and ozone (O_3) formation. Therefore, the emissions of VOCs from ships need to be assessed, as their fingerprint is expected to change with evolving practices, like new fuels or technologies. This study presents the results of a campaign conducted in the port of Dunkirk, Hauts-de-France, in September 2022 with the aim to apportion VOC emissions in an industrial harbour context. Additionally, this location within the Northern Sea ECA is a valuable area in which to address ship emissions under new regulations. The experimental setup combines chemical speciation of VOCs using two Gas Chromatography (TD-GC-FID) with time-resolved VOC observations using a Proton Transfer Reaction Time-of-Flight Mass Spectrometer (PTR-ToF-MS). This results in a unique and robust dataset of 68 VOCs, with 12 criteria pollutants and meteorology data that can be used to identify ship emissions. The ship plumes of three ferries were identified in the dataset, revealing that SO_2 still remains a tracer of ship emissions in an ECA. Under favourable wind conditions, it allowed the determination of Emission Factors (EFs) and a VOC fingerprint from the PTR-ToF-MS dataset, since the time resolution was high enough to capture ship plumes. This confirmed the past observations that oxygenated VOCs are the main contributors on average, including methanol (212±139 mg/kg_{fuel}), acetaldehyde (226±81 mg/kg_{fuel}) and acetic acid (119±61 mg/kg_{fuel}). Other fragments, such as C_5H_8 (204±95 mg/kg_{fuel}) and C_4H_8 (188±96 mg/kg_{fuel}), indicate the importance of heavier VOCs, such as cycloalkenes. The classification of these EFs revealed greater emissions of VOC upon arrival for some VOCs. A Positive Matrix Factorisation (PMF) was conducted, primally using the PTR dataset, resulting in a representative shipping factor with the temporal pattern of ship plumes to be resolved. Then, a constrained Multi-Time Resolution PMF (MTR-PMF) has been performed combining both GC and PTR datasets to extend the number of species. The chemical profile for ship emissions confirmed the presence of methanol (13.4%), acetaldehyde (4.4%), acetic acid (3.4%), C_4H_8 (6.4%) and C_5H_8 (5.9%) in ship emissions, in agreement with the EFs. It is completed by ethane (2.7%), butane (2.2%), ethylene (2.1%), and propane (2%). On average, this shipping factor contributed 8.5% of VOC concentrations with a high variability depending on wind conditions. This figure is consistent with the VOC emissions of non-road traffic emissions reported in the Hauts-de-France regional inventories that represented 6.6% of the total VOC emissions in 2021. Finally, the use of GC alone was tested in 2023 in the harbour of Le Havre, Normandy highlighting the limitations of low time resolution for identifying ship emission factors on the PMF. However, a factor similar to the Dunkirk GC profile was suspected, opening the way towards validating a representative chemical fingerprint of ship VOC emissions.

Résumé

Le transport maritime est un mode de transport majeur à l'échelle mondiale, mais également une source croissante de pollution, alors que son trafic continuera d'augmenter dans les prochaines années. Les émissions des navires ont un impact global, en contribuant au réchauffement climatique, et régional, car elles surviennent principalement dans les zones côtières habitées. Des réglementations ont été mises en place, comme l'annexe VI de la convention MARPOL, qui établit des zones de contrôle des émissions (ECA) limitant la teneur en soufre des carburants à 0,1% et encadrant les émissions de NO_x. Dans ce contexte, les émissions de SO_2 et de NO_x ont été réduites, tandis que celles des Composés Organiques Volatils (COV) restent mal documentées. Certains COV sont cancérigènes, d'autres participent à la formation de particules fines (PM) et d'ozone (O_3). Il est donc nécessaire d'évaluer leurs émissions, dont l'empreinte chimique évolue avec l'apparition de nouveaux carburants et technologies. Cette étude présente les résultats d'une campagne menée en septembre 2022 dans le port de Dunkerque (Hauts-de-France) afin de quantifier les émissions de COV dans un contexte portuaire industriel. Situé dans l'ECA de la mer du Nord, ce site est stratégique pour examiner les effets des nouvelles réglementations. Le dispositif expérimental associe la spéciation chimique des COV par deux chromatographes en phase gazeuse (TD-GC-FID) à des mesures à haute résolution temporelle via un PTR-ToF-MS. Cette approche a permis de constituer un jeu de données robuste de 68 COV, au côté de 12 polluants critères, accompagné de données météorologiques. Les panaches de trois ferries ont été identifiés, confirmant que le SO_2 reste un traceur pertinent en zone ECA. Dans des conditions de vent favorables, des facteurs d'émission (EF) et une empreinte chimique ont été déterminés à partir du PTR. Les COV oxygénés sont les principaux contributeurs, notamment le méthanol (212±139 mg/kg_{fuel}), l'acétaldéhyde (226±81 mg/kg_{fuel}) et l'acide acétique (119±61 mg/kg_{fuel}). D'autres composés, tels que les fragments C_5H_8 (204±95 mg/kg_{fuel}) et C_4H_8 (188±96 mg/kg_{fuel}), révèlent l'importance des COV plus lourds tels que les cycloalcènes. Certaines émissions se révèlent aussi plus élevées à l'arrivée des navires. Une Positive Matrix Factorisation (PMF) menée sur les données PTR a permis d'identifier un facteur représentatif des émissions maritimes, en cohérence avec les panaches. Une PMF à multi-résolution temporelle contrainte (MTR-PMF), combinant GC et PTR, a ensuite étendu le spectre des espèces. Le profil chimique obtenu confirme la présence de méthanol (13,4%), d'acétaldéhyde (4,4%), d'acide acétique (3,4%), de C_4H_8 (6,4%) et de C_5H_8 (5,9%), en accord avec les EF, complété par l'éthane (2,7%), le butane (2,2%), l'éthylène (2,1%) et le propane (2%). En moyenne, ce facteur «transport maritime » contribue à 8,5% des concentrations totales de COV, avec une forte variabilité selon le vent. Ce résultat est cohérent avec les inventaires régionaux des Hauts-de-France, où le «transport non routier» représentait 6,6% des émissions de COV en 2021. Enfin, en 2023, l'utilisation seule de GC a été testée dans le port du Havre (Normandie), mettant en évidence les limites de la faible résolution temporelle pour identifier un facteur lié aux émissions maritimes via la PMF. Toutefois, un facteur similaire au profil GC de Dunkerque est suspectée, ouvrant la voie à la validation d'une empreinte chimique représentative des émissions de COV des navires.